Bayesian techniques for inverse uncertainty quantification for multi-physics models of large containment structures

Donatien Rossat

Université Grenoble Alpes

THÈSE

Pour obtenir le grade de

DOCTEUR DE L'UNIVERSITÉ GRENOBLE ALPES

Spécialité : 2MGE : Matériaux, Mécanique, Génie civil, Electrochimie

Arrêté ministériel : 25 mai 2016

Présentée par

Donatien ROSSAT

Thèse dirigée par **Julien BAROTH**, Maitre de Conférences HDR, Université Grenoble Alpes
et co-encadrée par **Frédéric DUFOUR**, Professeur, Grenoble INP
et **Matthieu BRIFFAUT**, Professeur, Ecole Centrale Lille

Thèse préparée au sein du **Laboratoire Sols, Solides, Structures et Risques (3SR)**
dans **l'École Doctorale I-MEP2 - Ingénierie - Matériaux, Mécanique, Environnement, Energétique, Procédés, Production**

Quantification d'incertitudes inverse par inférence Bayésienne pour des modèles multi-physiques de grands ouvrages de confinement

Bayesian techniques for inverse uncertainty quantification for multi-physics models of large containment structures

Thèse soutenue publiquement le **4 octobre 2022**,
devant le jury composé de :

Mme. Clémentine PRIEUR
Professeur, Université Grenoble Alpes, Présidente
M. Franck SCHOEFS
Professeur, Université de Nantes, Rapporteur
M. Frédéric DUPRAT
Professeur, INSA Toulouse, Rapporteur
M. Pierre BEAUREPAIRE
Maître de Conférences, SIGMA Clermont, Examinateur
M. Julien BAROTH
Maître de Conférences HDR, Université Grenoble Alpes, Directeur de thèse
M. Frédéric DUFOUR
Professeur, Grenoble INP, Co-Encadrant
M. Matthieu BRIFFAUT
Professeur, Ecole Centrale Lille, Co-Encadrant
M. Alexandre MONTEIL
Ingénieur, EDF/DIPNN/DT, Co-Encadrant, Invité
Mme. Sylvie MICHEL-PONNELLE
Ingénieur-Chercheur Expert, EDF/R&D, Co-Encadrante, Invitée
M. Benoît MASSON
Ingénieur Expert, EDF/DIPNN/DT, Co-Encadrant, Invité

Résumé

Ce travail s'inscrit dans le contexte du vieillissement de grands ouvrages en béton dotés d'une fonction de confinement, dont les bâtiments réacteurs de centrales nucléaires constituent un exemple archétypal. Il vise notamment à développer une stratégie numérique prévisionnelle du comportement à long terme de tels ouvrages, afin de mieux pouvoir anticiper d'éventuelles réparations dans le cadre de leur maintenance. L'amélioration de la compréhension des phénomènes physiques liés au vieillissement, conjuguée à l'essor des ressources de calcul, ont permis le développement de modèles numériques visant à simuler le comportement Thermo-Hydro-Mécanique et de Fuite (THM-F) à long terme de grands ouvrages de confinement. Néanmoins, les paramètres d'entrées de tels modèles sont entachés d'incertitudes, notamment du fait d'un manque de connaissance à leur sujet, ou d'une variabilité intrinsèque. Par conséquent, cette thèse se base principalement sur le cadre général de la Quantification d'Incertitudes, visant à modéliser explicitement les incertitudes en simulation numérique. Dans ce cadre, les incertitudes des paramètres d'entrées sont typiquement modélisées par des lois de probabilités, pour ensuite être propagées à travers le modèle dans l'optique d'étudier la variabilité de sa réponse, ou d'estimer des quantités d'intérêt spécifiques, tels que des moments ou des quantiles.

Toutefois, les modèles THM-F impliquent typiquement un grand nombre de paramètres incertains, dont la majorité n'est pas mesurable directement. De ce fait, la loi de probabilité modélisant leurs incertitudes est souvent choisie de manière subjective, en se basant sur des avis d'experts. Ainsi, cette thèse se place dans le cadre de l'inférence Bayésienne, afin de mettre à jour un état de connaissance *a priori* sur les paramètres d'entrée à partir de données d'observations bruitées de la réponse de la structure étudiée.

Dans un premier temps, le travail de thèse vise à coupler l'inférence Bayésienne à des techniques numériques adaptées à des modèles THM-F, reposant le plus souvent sur des codes éléments finis coûteux. Dans cette optique, un cadre algorithmique alternatif aux méthodes de type MCMC classiques est étudié, et un couplage avec des techniques de méta-modélisation est proposé afin d'échantillonner la loi *a posteriori* à un coût numérique réduit. Ensuite, une méthodologie générale visant à réaliser des prévisions probabilistes du comportement THM-F d'ouvrages de confinement est présentée. Dans ce contexte, les incertitudes des entrées du modèle THM-F sont quantifiées de manière inverse par inférence Bayésienne, à partir de mesures d'auscultation réalisées à l'échelle de la structure. L'approche proposée est illustrée via une étude de la maquette VeRCoRs (enceinte de confinement à l'échelle 1:3).

Enfin, dans le cadre d'une analyse de fiabilité, cette thèse vise à estimer les risques de dépassement de critères de fuite réglementaires, tout en modélisant l'effet d'éventuelles opérations de maintenance. Dans ce cadre, l'impact du choix de la loi des paramètres d'entrées sur des probabilités de défaillance est évalué, à travers une analyse de robustesse. Enfin, une approche Bayésienne visant à actualiser des probabilités de défaillance à partir de données d'observation est proposée. La méthodologie proposée est appliquée au cas réaliste d'une enceinte de confinement à l'échelle 1:1 opérationnelle.

Mots-clés: Inférence Bayésienne - Génie Civil - Quantification d'incertitudes - Analyse de fiabilité - Simulation numérique - Thermo-hydro-mécanique

Abstract

This work falls within the context of the aging of large concrete containment structures, such as reactor buildings in nuclear power plants. It aims at devising a numerical strategy for forecasting the long-term physical behavior of such structures, in order to better anticipate their maintenance. Recent improvements of the understanding of physical phenomena behind aging and the increase of computational resources have enabled the development of numerical models aiming at simulating the Thermo-Hydro-Mechanical and Leakage (THML) behavior of large aging concrete structures. Nevertheless, the input parameters of such models are tainted with uncertainties, due to a lack of knowledge or to a natural randomness.

Consequently, this thesis is mainly based on the general framework of Uncertainty Quantification (UQ), aiming at explicitly modeling uncertainties in numerical simulation. In this framework, the uncertainties tainting input parameters are typically modeled by probability laws, and are subsequently propagated through the model in order to study the variability of its response, or to estimate specific quantities of interest, such as moments or quantiles. However, THML computational models typically involve a large amount of uncertain parameters, most of them being not measurable directly. For this reason, the input probability law modeling their uncertainties is usually chosen in a subjective way, based on expert judgement. Then, this thesis is placed in the framework of Bayesian inference, in order to update a prior level of knowledge on input parameters from noisy observational data of the response of the structure under study.

Firstly, this work aims at coupling Bayesian inference with numerical techniques adapted with THML computational models, these last most often lying on costly finite element codes. In this perspective, a recent Bayesian computational framework is studied as an alternative to classical MCMC sampling techniques, and a coupling with surrogate modeling techniques is proposed in order to efficiently draw samples from posterior distributions with a reduced computational cost. Next, a general methodology aiming at performing probabilistic forecasts of the long-term THML behavior of containment structures is presented. In this context, the uncertainties of input parameters of the adopted THML model are quantified through Bayesian inference, from *in-situ* monitoring data. The proposed methodology is illustrated through a study of the VeRCoRs mock-up (1:3 scale nuclear containment building).

Lastly, in the framework of a reliability analysis, this thesis aims at estimating risks of exceeding regulatory leakage thresholds, while modeling the effect of eventual maintenance operations. In this framework, the impact of the choice of the inputs' probability law on some quantity of interest (including probabilities of failure) is assessed, through a robustness analysis. Next, a Bayesian approach aiming at updating both probabilities of failure and input parameters from monitoring data is presented. The overall methodology is applied to the realistic case of an operating 1:1 scale nuclear containment building.

Key-words: Bayesian inference - Civil Engineering - Uncertainty Quantification - Reliability analysis - Numerical simulation - Thermo-hydro-mechanical modeling

Remerciements

Ces remerciements, écrits non sans émotion le lendemain de ma soutenance, viennent conclure trois années de thèse formidables, riches de rencontres et d'épanouissement.

Tout d'abord, je tiens à adresser mes plus sincères remerciements à l'ensemble des membres du jury, pour l'intérêt qu'ils ont porté à mes travaux de thèse, et pour m'avoir fait prendre davantage de recul vis-à-vis de ces derniers et de leurs perspectives. À ce titre, je remercie Clémentine Prieur de m'avoir fait l'honneur de présider mon jury de thèse. Je remercie également Franck Schoefs et Frédéric Duprat pour avoir accepté la lourde tâche de rapporter ce manuscrit, ainsi que Pierre Beaurepaire pour avoir examiné mes travaux. Enfin, je réitère mes remerciements à l'adresse de l'ensemble des membres du jury, pour leur enthousiasme et leurs nombreuses questions posées lors de la soutenance.

Le bon déroulement de cette thèse a notamment reposé sur une (nombreuse !) équipe encadrante d'une qualité remarquable, composée de membres du Laboratoire 3SR, de la Direction Technique et de la R&D d'EDF.

Commençons par la composante Grenobloise de l'encadrement. Tout d'abord, je tiens à exprimer ma gratitude à Julien, pour avoir dirigé cette thèse, ainsi que pour ton enthousiasme, ta créativité et ta pédagogie. Tu as su instaurer un climat de confiance dès le début de cette thèse et te rendre très disponible, tout en me laissant une grande marge de manoeuvre pour explorer mes idées, et je t'en suis très reconnaissant. Ensuite, je tiens à remercier Frédéric, pour ta bienveillance, ta rigueur et tes si précieux conseils. Tu m'as beaucoup appris, notamment la rigueur scientifique, à travers nos échanges et tes relectures impressionnantes. Merci également à Matthieu, pour ton soutien et ton investissement dans cette thèse, même après ton changement de poste à Lille !

Poursuivons avec la composante Lyonnaise, sans laquelle cette thèse n'aurait pas pu voir le jour. Un grand merci à Alexandre: cela fait maintenant plus de quatre ans que j'ai eu la chance d'être ton stagiaire au sein du groupe GC de la DT ! Merci également pour m'avoir initié à la passionnante thématique des enceintes, ainsi que pour ta rigueur et ton sens de l'organisation. Tout au long de la thèse, tu as su me rappeler au pragmatisme lorsque cela fut nécessaire, et largement contribué à la valorisation de mes travaux sur le plan industriel. Ensuite, je tiens à témoigner toute ma gratitude à Benoît: merci pour m'avoir donné le goût de la recherche, et pour m'avoir encouragé à poursuivre dans cette voie en me proposant ce projet de thèse. Merci à toi pour ton soutien sans faille, ta bonne humeur et ton sens de l'humour si aiguisé !

Terminons avec la composante Palaisienne: je tiens à remercier chaleureusement Sylvie, pour ton implication dans cette thèse, ta disponibilité et ta gentillesse. Merci également pour ton assistance, et notamment tes réponses à mes (nombreuses !) questions relatives à Code Aster !

Cette thèse m'a également donné la chance de pouvoir travailler au sein de cette formidable grande maison qu'est EDF, que j'ai pu découvrir à travers mon premier stage au sein du groupe GC de la DT il y a maintenant plus de quatre ans. J'ai notamment pu y rencontrer des équipes chaleureuses et travailler sur des sujets passionnants, que ce soit au cours de mon stage ou de ma thèse. Cette ambiance de travail si agréable n'aurait pas été possible sans les membres de la DT et de la R&D d'EDF avec lesquels j'ai eu la chance d'échanger (et sans mon équipe encadrante, bien sûr !).

Dans ce contexte, je tiens tout d'abord à exprimer ma gratitude aux membres du groupe GC de la DT que je n'ai pas encore cités, notamment Julien Niepceron, Damien Thillaye du Boullay, Hugues Philippe, Clément Hervé et Lionel Bouffier. Merci également à Alexis Courtois pour son intérêt pour mes travaux de thèse. Je souhaite également remercier Lionel Germane, pour m'avoir encouragé à poursuivre dans la recherche lors de mon stage à la DT.

Ensuite, je souhaite grandement remercier Charles Toulemonde pour son implication dans cette thèse, et pour m'avoir tant appris, notamment sur le plan de la programmation. La capitalisation de mes travaux de thèse par EDF, notamment sous la forme d'outils numériques, n'aurait pas été possible sans son aide précieuse. Un grand merci à Jean-Luc Adia, notamment pour m'avoir permis de présenter mes travaux dans le cadre du projet CIWAP. Ensuite, j'aimerais remercier Nicolas Bousquet, notamment pour m'avoir invité à présenter mes travaux de thèse dans le cadre du séminaire PSPP du département PRISME. Enfin, merci à Bertrand Iooss et à Merlin Keller, qui m'ont notamment permis de participer à la fort enrichissante formation "Incertitudes Avancées" !

L'agréable ambiance de travail précitée a également reposé sur le Laboratoire 3SR, et je tiens à ce titre à remercier ses doctorants et post-doctorants avec qui j'ai pu échanger. Un grand merci également à Jérôme Branon et à Olivier Senn, qui m'ont grandement aidé à résoudre les problèmes informatiques que j'ai pu rencontrer au cours de cette thèse ! Merci aussi aux membres permanents du laboratoire, notamment ceux de l'équipe RV, avec lesquels j'ai eu d'enrichissantes discussions lors des réunions d'équipe. Ensuite, je tiens à adresser mes plus sincères remerciements à David Bouhjiti: merci à toi pour ton implication tout au long de la thèse et pour tes judicieux conseils. Sur le plan académique, je tiens également à remercier Xavier Dérobert et Géraldine Villain de l'Université Gustave Eiffel (UGE), avec qui j'ai eu l'opportunité de collaborer dans le cadre du projet ENDE. Toujours dans le cadre de ce projet, je souhaite adresser mes remerciements à Jérôme Verdier et à Stéphane Multon du Laboratoire Matériaux et Durabilité des Constructions (LMDC). Je souhaiterais aussi exprimer ma gratitude à Laurent Doyen du Laboratoire Jean Kuntzmann (LJK), pour son intérêt et pour m'avoir invité à présenter mes travaux dans le cadre des séminaires "Modèles Aléatoires pour la Fiabilité et la Maintenance des Systèmes" (FIMA).

Enfin, je tiens à grandement remercier ma famille et mes proches, pour leur soutien tout au long de cette aventure de thèse, et plus généralement, tout au long de mes études. Tout d'abord, merci à mes parents, Vinciane et Philippe : c'est peut-être une tautologie de le dire, mais je ne serais rien sans eux ! Ensuite, merci à mes frères, Édouard, Gabriel et Gaspard (je procède arbitrairement par âge décroissant pour ne froisser personne !). Merci à mon grand-père, Jean: je souhaite également t'adresser un remerciement particulier, pour m'avoir laissé user de ta qualité de professeur agrégé d'Anglais, et pour avoir relu ce manuscrit (je précise que les fautes d'anglais restantes sont uniquement de mon fait) ! Merci à André, pour ton soutien et toutes ces aventures ensemble, de Saint-Alban à Grenoble. Merci à Vincent, pour toutes ces barres de rire, et pour nos discussions interminables. Merci à Pépin, pour m'avoir tant appris (malgré le fait que tu vives dans une pomme). Merci à Matthieu, pour tous ces moments ensemble, entre Strabourg et Karlsruhe !

Je conclus ces remerciements en adressant une pensée particulière à Maëva, ma compagne, et en la remerciant du fond du coeur pour m'avoir soutenu (et supporté !) tout le long de cette thèse.

Grenoble, le 5 octobre 2022.

Contents

Acronyms

BC boundary conditions. 108

BuS Bayesian updating with structural reliability methods. 55

CDF cumulative distribution function. 16

CoV coefficient of variation. 19

ED experimental design. 26

KLD Kullback-Leibler divergence. 44

LARS least angle regression. 27

LHS latin hypercube sampling. 26

LSF limit-state function. 35

MCMC Markov chain Monte Carlo. 12

MCS Monte Carlo simulation. 23

NCB nuclear containment building. 3

PCA principal component analysis. 29

PCE polynomial chaos expansions. 24

PCK polynomial chaos Kriging. 24

PDF probability density function. 17

PII primary influential inputs. 32

PoF probability of failure. 35

QoI quantity of interest. 12

RH relative humidity. 96

RSV representative structural volume. 135

SuS subset simulation. 37

THML thermo-hydro-mechanical-leakage. 7

UQ uncertainty quantification. 4

Notations - UQ

$\mathbf{1}_B$	Indicator function of the set B. 16
$\mathcal{B}(\mathcal{D}_{\boldsymbol{X}})$	Borel σ-algebra on $\mathcal{D}_{\boldsymbol{X}}$. 16
Cov	Covariance. 18
CoV	Coefficient of variation. 19
$\mathcal{D}_f$	Failure domain. 35
D_{KL}	Kullback-Leibler divergence. 44
$\mathcal{D}_{\boldsymbol{X}}$	Input space of the model, subset of $\mathbb{R}^d$. 13
$\mathcal{D}_Y$	Output space of the model, subset of $\mathbb{R}$ ($\mathcal{D}_{\boldsymbol{Y}} \subset \mathbb{R}^n$ in the vector-valued case). 13
$\mathbb{E}$	Expectation. 18
$\mathcal{F}$	σ-algebra on the sample space Ω. 16
$\mathcal{G}$	Limit-state function (or performance function). 35
$\mathcal{L}$	Likelihood function. 42
$\mathcal{M}$	Computational model. 13
Ω	Sample space. 16
P_f	Failure probability. 35
$\pi_{\boldsymbol{X}}$	Probability density function of the random variable $\boldsymbol{X}$. 17
$\boldsymbol{X}^{-1}(B)$	Preimage of the set B under $\boldsymbol{X}$. 16
$\mathbb{P}$	Probability. 16
$\mathbb{P}_{\boldsymbol{X}}$	Probability law of the random variable $\boldsymbol{X}$. 16
$\mathbb{R}$	Real line. 13
Std	Standard deviation. 19
Var	Variance. 18
$\boldsymbol{X} \sim \mathbb{P}_{\boldsymbol{X}}$	$\boldsymbol{X}$ follows the probability law $\mathbb{P}_{\boldsymbol{X}}$. 17
Z	Model evidence (or marginal likelihood). 43

Notations - THML modeling

a_d	Sorption-desorption model parameter [-]. 109
α_{ds}	Desiccation shrinkage coefficient [kg.m^{-3}]. 111
α_l	Local leak model parameter [-]. 118
α_{th}	Concrete thermal dilation coefficient [°C^{-1}]. 111
A	Drying model parameter [m.s^{-2}]. 109
b_d	Sorption-desorption model parameter [-]. 109
β_K	Klinkenberg coefficient [Pa]. 115
B	Drying model parameter [-]. 109
C_c	Leakage rate correction factor accounting for coatings [-]. 179
c_k	Gas relative permeability model parameter [-]. 115
c_c^p	Heat capacity of concrete [J.K^{-1}]. 108
C_w	Volumetric water content [l.m^{-3}]. 109
D_w	Drying diffusion coefficient [m^2.s^{-1}]. 109
E	Young's modulus [Pa]. 139
$\boldsymbol{\varepsilon}$	Total strain tensor [-]. 110
η_{dc}	Desiccation creep viscosity [Pa.s]. 113
η_{id}	Irreversible deviatoric basic creep viscosity [Pa.s]. 112
η_{rd}	Reversible deviatoric basic creep viscosity [Pa.s]. 112
f_d	Sorption-desorption function [-]. 109
γ_c	Coating efficiency parameter [-]. 179
h	Relative humidity [-]. 109
k_{th}	Thermal convective exchange coefficient [W.m^{-1}.K^{-1}]. 108
κ	Basic creep consolidation parameter [-]. 112
$\mathbf{k}_g$	Gas permeability tensor [m^2]. 114

k_0	Intrinsic permeability [m^2]. 115
k_{rd}	Reversible deviatoric basic creep stiffness [Pa]. 112
k_{rg}	Relative gas permeability [-]. 115
λ_c	Thermal conductivity of concrete [$W.m^{-1}.K^{-1}$]. 108
μ_g	Air dynamic viscosity [Pa.s]. 114
$\nabla_{\boldsymbol{s}}$	Nabla operator ∇ with respect to spatial coordinates $\boldsymbol{s}$. 108
ν	Poisson's ratio [-]. 139
ν_{bc}	Basic creep Poisson ratio [-]. 113
$\frac{\partial}{\partial t}$	Partial derivative with respect to time t. 108
p_g	Air pressure [Pa]. 114
ϕ	Concrete porosity [-]. 109
Π	Mechanical macro-variable of the local leak model [-]. 118
$\boldsymbol{q}_{th}$	Thermal flux [$W.m^{-2}$]. 108
$\boldsymbol{q}_d$	Darcy's flux [$m.s^{-1}$]. 114
Q_d	Diffuse leaks leakage rate [$Nm^3.h^{-1}$]. 114
Q_g	Global leakage rate [$Nm^3.h^{-1}$]. 114
Q_l	Local leaks leakage rate [$Nm^3.h^{-1}$]. 114
ρ_c	Density of concrete [$kg.m^{-3}$]. 108
R	Ideal gas constant [$J.K^{-1}.mol^{-1}$]. 109
s_c	Ratio of coated surface [-]. 179
$\boldsymbol{\sigma}$	Cauchy stress tensor [Pa]. 110
$\sigma_{\theta,0}$	Initial tension of tangential prestressing cables [Pa]. 140
$\sigma_{z,0}$	Initial tension of vertical prestressing cables [Pa]. 140
S_w	Water saturation ratio [-]. 114
T	Temperature [K]. 108
T_{bc}^0	Basic creep reference temperature [K]. 112
T_w^0	Drying reference temperature [K]. 109
U_{bc}	Basic creep activation energy [$J.mol^{-1}$]. 112
U_w	Drying activation energy [$J.mol^{-1}$]. 109

General introduction

Industrial and scientific context

Nuclear power plants constitute a substantial part of the French electricity production, mainly ensured by the Électricité de France (EDF) company. Indeed, the French nuclear fleet includes 56 operating reactors, which represent about 78% of the French electricity production (EDF, 2021). This energy mix results from an energy independence policy initiated after the end of the Second World War, and subsequently confirmed during the two oil crises of 1973 and 1979.

All the aforementioned operating reactors are based on the Pressurized Water Reactor (PWR) technology, and can be classified in several families according to their power, namely:

- 32 reactors each developing a power of 900 MWe. These reactors are distributed on 8 sites, and have been constructed between 1971 and 1987.
- 20 reactors each developing a power of 1300 MWe, distributed on 8 sites and built between 1977 and 1993.
- 4 reactors each developing a power of 1450 MWe, distributed on 2 sites and built between 1984 to 1999.

Lastly, the construction of a new reactor based on the European Pressurized Reactor (EPR) technology has been launched on the site of Flamanville, in 2007. This reactor has a characteristic electrical power of 1650 MWe. The geographical distribution of the aforementioned reactors is presented in Fig. i.

Then, the functioning principle of a PWR is depicted in Fig. ii. The reactor core is the locus of nuclear reactions: it is placed in a steel vessel, and comprises several hundreds of nuclear fuel rods. The disintegration reactions of fissile material contained in nuclear fuel induce an important heat release, which is absorbed by the water surrounding fuel rods, evolving in a closed loop, known as *reactor coolant system* or *primary loop* (in yellow in Fig. ii). This water has a temperature varying between 280 and 330 °C, and is pressurized to 155 bars in order to remain liquid. In this way, the heat release in the core is transported to steam generators, which transform this heat into steam in a second closed loop, namely the *secondary loop* (in blue in Fig. ii). This loop converts the thermal energy of the primary loop into mechanical energy, through the injection of steam in a turbine. This last is linked to an alternator, which transforms mechanical energy into electrical energy. Lastly, the steam is re-transformed into water by a condenser, which is linked to a cold source through a *tertiary loop* (or *cooling loop*, in green in Fig. ii). This cold source consists in water usually collected from a river, or the sea, and is possibly completed by a cooling tower.

Figure i: Location of the 56 operating nuclear reactors, and the Flamanville EPR (in construction) in France. The operational phase of Fessenheim's power plant has been stopped in 2020. ©IRSN

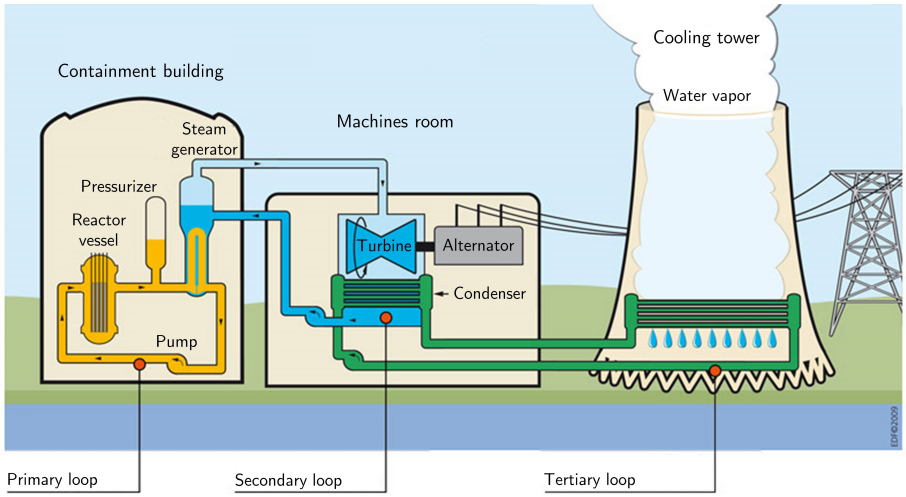

Figure ii: Functioning principle of a pressurized water reactor in a nuclear power plant. ©EDF

The safety of a nuclear reactor mainly hinges on three functions, namely the control of core reactivity, fuel cooling and the containment of radioactive elements. In this context, a reactor comprises three containment barriers:

1. fuel cladding tubes, which constitute the outer layer of fuel rods. They enable to prevent radioactive fission products from contaminating water of the primary loop.

2. the primary loop, notably including the reactor vessel (see Fig. ii).

3. the containment building, which shelters the primary loop (see Fig. ii).

In particular, the containment building ensures two functions, namely the protection of the reactor in the case of external aggressions (*e.g.* impacts), and the protection of the environment from radioactive elements released during an internal accident. Therefore, this building must ensure a sufficient leak tightness in order to fulfill its protective role.

The design principle of nuclear containment buildings (NCB) in French nuclear power plants has progressively evolved since the early 70s (Jacquemain, 2015). Firstly, containment buildings of 900 MWe reactors consist in a single prestressed concrete wall, whose leak tightness is ensured by a steel liner. Then, the containment buildings of 1300 MWe and 1450 MWe reactors have double concrete walls, which comprise an inner prestressed concrete wall without steel liner, and an outer reinforced concrete wall. The protection of the reactor is ensured by the outer wall, whereas leak tightness is ensured by the inner wall. Moreover, an active system keeps the space between the two walls under a constant vacuum, so that potential radioactive elements stemming from accidental situations can be pumped up and filtered instead of being released in the environment.

This thesis is motivated by the problematic of the leak tightness of double-walled NCB. In France, regulatory authorities specify a criterion related to the leakage rate of the inner containment wall: when this last is subjected to an internal pressure of about 5.2 bars, its leakage rate must not exceed 1.5% per day of the mass of air contained inside. In this context, the leakage rate of the containment building is measured before entry to service, and every ten years throughout *decennial pressurization tests*. Meeting the regulatory leak tightness criterion during these tests constitutes a condition for the continuation of the exploitation of the reactor.

Besides, concrete is a complex heterogeneous material, whose properties may evolve in time under the effect of several physical phenomena, related to *aging*. In particular, due to such phenomena, the leakage rate of NCB can evolve over time, which may jeopardize their long-term serviceability. Since such structures cannot be replaced, maintenance operations may be considered in order to fulfill the prescribed leak tightness requirements. Such operations have to be undertaken when the reactor is shut down, and typically involve an important cost. Thus, it is necessary to devise numerical strategies aiming at predicting the leakage rate of NCB, in order to better anticipate potential repair works.

Uncertainty quantification of computational models

Numerical modeling and simulation constitute major tools in modern engineering. Since the end of the twentieth century, the steady increase of computational resources and algorithmic advances in scientific computing have enabled the simulation of more and more complex physical systems. As a result, computational models are nowadays at the core of the design and the management of engineering systems, such as bridges, dams or NCB. In this context, they provide numerical simulators of the behavior of the aforementioned systems, and are usually substituted to real experiments which are generally too costly, too complex, or even impossible to carry out. As an example, in the framework of NCB, numerical simulators have been devised so as to assess the effects of aging on their multi-physic long-term behavior, and evaluate their serviceability. Such computational models may be constituted by simple analytical formulae, or sets of partial differential equations solved with numerical schemes, such as the finite element method.

Nevertheless, despite their increasing fidelity, computational models still constitute idealized representations of the observed reality. Consequently, model inadequacies become unavoidable at some point, notably due to a lack of knowledge about governing physical laws, or due to unresolved scales. Furthermore, the simulation of complex physical phenomena requires a potentially important amount of input parameters. For instance, in the framework of civil engineering structures, such parameters typically include geometrical and material properties, initial and boundary conditions, as well as parameters which may be deprived of physical meaning, or may not be measurable directly. Such parameters are uncertain, typically due to intrinsic randomness of underlying physical phenomena, or due to a limited information. However, uncertainties are often disregarded in practice, since the modeling approaches undertaken in engineering studies remain mostly deterministic.

Uncertainty Quantification (UQ) is the scientific discipline aiming at explicitly modeling uncertainties in numerical simulations (De Rocquigny et al., 2008; Smith, 2014; Sullivan, 2015). It has recently emerged as an active research field, which encompasses a wide range of theoretical and applied features at the interface of statistics, probability theory, applied mathematics and computer science. Furthermore, UQ techniques nowadays disseminate in various branches of engineering and applied sciences (Ghanem et al., 2017; Soize, 2017). This is particularly facilitated by the interdisciplinary and modular nature of the general framework of UQ defined in (De Rocquigny et al., 2008; Iooss, 2009; Sudret, 2007). Such a framework, illustrated in Figure iii, hinges on a chain of few fundamental steps representative of a typical UQ analysis, which are described hereafter:

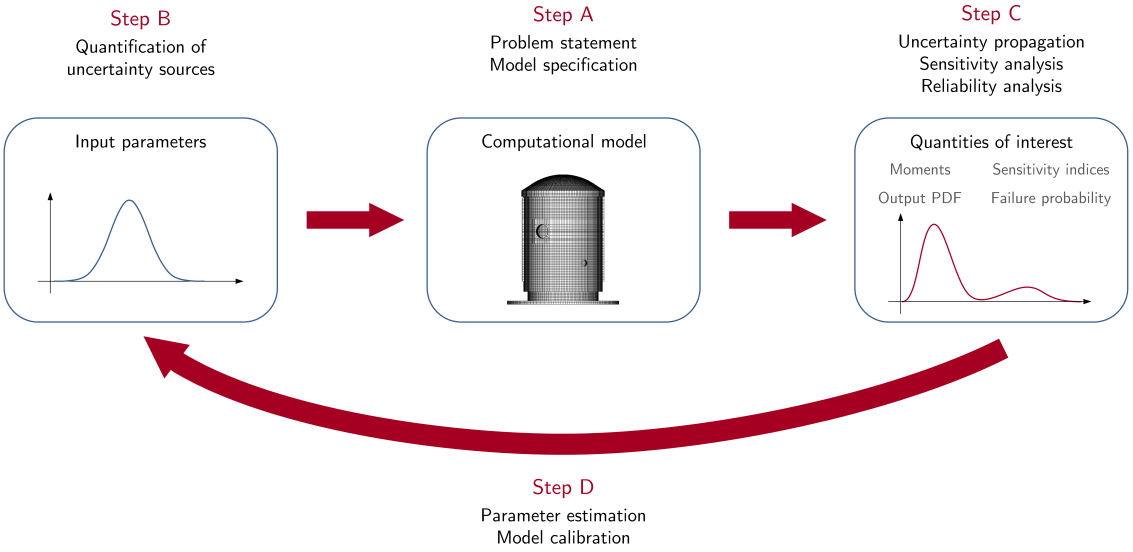

Figure iii: Schematic representation of the Uncertainty Quantification framework, adapted from (De Rocquigny et al., 2008; Sudret, 2007; Wagner, 2021).

- **Step A - Model specification:** the first step consists in specifying a computational model that simulates the physical system under study. Such a model constitutes the core of a typical UQ analysis, and its specification implies the definition of input parameters as well as output variables. In the case of NCB, it may typically involve a multi-physic computational workflow (Bouhjiti, 2018).

- **Step B - Quantification of uncertainty sources:** the second step aims at identifying the sources of uncertainties tainting the input parameters of the model. In this context, uncertainties can be modeled within several different mathematical frameworks, including probability theory or imprecise probabilities.

- **Step C - Characterization of output variables:** the third step consists in characterizing the uncertainties of the output variables of the model. This characterization notably includes methods such as uncertainty propagation (De Rocquigny et al., 2008; Grigoriu, 2012), sensitivity analysis (Iooss and Lemaître, 2015; Saltelli et al., 2004) and structural reliability analysis (Lemaire et al., 2009; Melchers, 1999).

- **Step D - Inverse analysis:** lastly, it is possible to quantify the uncertainties of the input parameters through an inverse analysis, from observations of the response of the simulated physical system (Step D). Such an inverse quantification process encompasses parameter estimation (Kaipio and Somersalo, 2005; Tarantola, 2005), model calibration (Kennedy and O'Hagan, 2001) and data assimilation (Evensen, 2009; Reich and Cotter, 2015). Such tasks may notably be undertaken from a probabilistic viewpoint in the framework of *Bayesian inference*, to which particular attention will be paid in this thesis.

Then, it is worth noting that methods associated to Steps C & D of the UQ framework typically require repeated evaluations of the computational model. Nevertheless, the latter is often time consuming (*e.g.* a complex finite element code), which hinders the application of UQ methods. In order to circumvent this problem, the computational model is usually replaced by inexpensive-to-evaluate mathematical function, called a *surrogate model* (or *metamodel*, or *response surface*) (Fang et al., 2005; Forrester et al., 2008). Likewise, model order reduction (Chinesta et al., 2014; Schilders et al., 2008) approaches aim at finding a compromise between a simpler (and less costly) model and a reasonable accuracy level. Surrogate modeling became an integral part of the UQ framework, and constitute an intermediate step which enables the acceleration of UQ methods.

Contributions and outline of the thesis

Recent modeling approaches dedicated to NCB have been developed in parallel with improvements of the understanding of physical phenomena behind concrete aging, and nowadays serve as a basis for devising computational models able to reasonably well assess the global long-term behavior of large concrete containment structures (see *e.g.* (Boucher, 2016; Jason et al., 2007)). Nevertheless, as mentioned earlier, such approaches mostly remain deterministic, and therefore disregard the immanent uncertainties tainting input parameters. Then, the former work of Bouhjiti (2018) constitutes a pivotal point, since it constitutes a first attempt to quantify uncertainties in the context of the leakage behavior of containment buildings.

Computational models usually adopted to assess the long-term behavior of NCB typically involve a large amount of uncertain input parameters. Concerning parameters that are directly measurable, it is possible to model their uncertainties from experimental data. However, most input parameters are not directly measurable, so that scarce information about them are available. As a result, *expert judgement* (De Rocquigny et al., 2008) is commonly used so as to model the uncertainties of such parameters, as in (Bouhjiti, 2018). In this context, uncertainties are modeled based on the knowledge of one or several analysts, in a more or less subjective fashion. Nevertheless, if large uncertainties are assumed for input parameters, predictions are likely to be tainted with important uncertainties, which impedes decision making related to the maintenance of NCB. Besides, uncertainties of input parameters are most frequently modeled by probability distributions, which are themselves known with various levels of confidence. Consequently, it would be necessary to quantify the impact of the choice of such input distributions on some quantities of interest related to the leakage behavior of the studied NCB, typically a probability of exceeding a regulatory leakage threshold value. The recent UQ branch of *robustness analysis* (Iooss et al., 2021; Lemaître et al., 2015; Sueur et al., 2016) notably aims at addressing such a question.

Besides, recent breakthroughs related to monitoring devices have enabled to acquire a non-negligible amount of data related to the long-term behavior of large concrete structures such as NCB. Hence, monitoring data presents a great interest, since it may be used in order to extract information about uncertain input parameters that cannot be measured directly, and to subsequently perform new predictions of the behavior of the structure. Such an inverse analysis may be achieved through Bayesian inference (Kaipio and Somersalo, 2005; Tarantola, 2005), which enables to update a prior state of knowledge in input parameters from noisy observational data, within a probabilistic framework.

Consequently, based on the UQ framework depicted in Fig. iii, this thesis aims at providing a more comprehensive approach for quantifying uncertainties related to predictions of the long term behavior of containment structures, by pursuing the following objectives:

i. Account for uncertainties in simulations provided by computer models of containment structures, in order to quantify uncertainties of predictions related to their long-term behavior,

ii. Develop a strategy for updating the level of knowledge in uncertain input parameters from noisy and indirect observational data provided by *in-situ* monitoring devices,

iii. Estimate the risks of exceeding regulatory leakage rate thresholds, and evaluate the robustness of such an estimation,

iv. Evaluate the efficiency of potential repair works scenarios, in order to better anticipate maintenance operations of containment structures.

Then, this manuscript is organized as follows: firstly, most of the UQ computational tools considered in this thesis are presented in **Chapter 1**. Several fundamental principles of UQ are firstly introduced, by focusing on probability theory. Afterwards, the basic UQ computational tools that will be used throughout this thesis are briefly presented. In this perspective, *forward* UQ methods (Step C in Fig. iii) including uncertainty propagation,

sensitivity analysis and reliability analysis are introduced, before presenting *inverse* UQ methods (Step D in Fig. iii), by paying particular attention to Bayesian inference.

Subsequently, focusing on Bayesian inference, **Chapter 2** introduces a recent Bayesian computational framework introduced by Straub and Papaioannou (2015), named *Bayesian Updating with Structural reliability methods* (BuS). This framework provides the algorithmic basis for inverse analyses undertaken in further chapters of this thesis. In particular, the involved algorithms require a large amount of model evaluations, and thus may be intractable when dealing with time consuming models. In this context, we propose a novel approach based on adaptive surrogate models, aiming at efficiently accelerating Bayesian computations. The performance of the proposed method is assessed through several academic test cases with varying complexity.

Next, **Chapter 3** establishes the basis for computational models adopted in applications to NCB, through devising a modeling strategy suitable for assessing the long-term Thermo-Hydro-Mechanical and Leakage (THML) behavior of aging concrete containment structures. In particular, this implies the definition of input parameters (*e.g.* Young's modulus, permeability) as well as output variables of interest (*e.g.* strains, leakage rate). To that end, the main physical phenomena related to concrete aging are firstly introduced, in order to provide a better understanding of the physical problem mainly addressed in the next chapters. The THML modeling strategy adopted in this thesis is subsequently presented, by capitalizing on former works dedicated to the physical modeling of NCB (Boucher, 2016; Bouhjiti, 2018).

Then, based on the first three chapters of this thesis, **Chapter 4** constitutes one of our main contributions to the evaluation of the long-term THML behavior of containment structures. In this perspective, we present a general methodology for assessing the long-term behavior of large concrete containment structures subjected to aging, while accounting for uncertainties in predictions in a probabilistic framework. In particular, we propose an approach based on Bayesian inference aiming at updating uncertain input parameters from noisy observational data provided by in-situ monitoring devices. In this perspective, the central case study of this chapter is given by the so-called *VeRCoRs* mock-up, namely a 1:3 scale mock-up of a double-walled NCB built by EDF, for research purposes related to aging.

Our second main contribution to containment structures is presented in **Chapter 5**, which tackles the problem of operating containment structures, and focuses on the assessment of the reliability of their leak tightness. In this context, an operating NCB will constitute the central case-study of this chapter. In particular, operating NCBs involve some specific features compared to the VeRCoRs mock-up studied in the previous chapter, such as maintenance operations aiming at reinforcing leak tightness. Then, we firstly introduce some modeling assumptions in order to assess the effect and the efficiency of repair works. Subsequently, we propose to assess the risks of exceeding regulatory leakage thresholds, based on the framework of reliability analysis. In this context, the effects of the choice of inputs' probability distribution on probabilities of failure are assessed through a robustness analysis. Finally, we propose a Bayesian approach aiming at updating the estimation of such probabilities of failure from *in-situ* monitoring data collected throughout the exploitation of the NCB.

Lastly, **Chapter 6** provides a general conclusion to this thesis. It discusses the limitations of the adopted approaches and exposes perspectives of this work.

Publications and communications

Publications and communications related to this thesis are listed hereafter.

Publications in peer-reviewed international journals

The following publication is related to the contribution presented in Chapter 2 of this thesis:

Rossat, D., Baroth, J., Briffaut, M., and Dufour, F. 2022. Bayesian inversion using adaptive Polynomial Chaos Kriging within Subset Simulation. *Journal of Computational Physics*, 455:110986.

The two publications below constitute my main contributions related to Chapter 4:

Rossat, D., Baroth, J., Briffaut, M., Dufour, F., Masson, B., Monteil, A., and Michel-Ponnelle, S. 2022. Bayesian updating for nuclear containment buildings using both mechanical and hydraulic monitoring data. *Engineering Structures*, 262:114294.

Rossat, D., Baroth, J., Briffaut, M., Dufour, F., Masson, B., Monteil, A., and Michel-Ponnelle, S. 2022. Fast Bayesian inference with correction of model bias and global sensitivity analysis for nuclear containment buildings. *Submitted.*

This publication presents a work realized in parallel to that related to Chapters 4 & 5, and addresses the question of the influence of the choice of the prior distribution, through an application to the VeRCoRs mock-up:

Rossat, D., Baroth, J., Briffaut, M., Dufour, F., Masson, B., Monteil, A., and Michel-Ponnelle, S. 2022. Bayesian updating for predictions of delayed strains of large concrete structures: influence of the prior distribution. *European Journal of Environmental and Civil Engineering.*

The following publication presents a work realized during my first year of PhD, which introduces a simple approach that paved the way to the more general methodology presented in Chapter 4:

Rossat, D., Bouhjiti, D. E.-M., Baroth, J., Briffaut, M., Dufour, F., Monteil, A., Masson, B., and Michel-Ponnelle, S. 2021. A Bayesian strategy for forecasting the leakage rate of concrete containment buildings – Application to nuclear containment buildings. *Nuclear Engineering and Design*, 378:111184.

In parallel to the main topic of my PhD, I had the opportunity to work in collaboration with researchers from the Laboratoire 3SR, the Université Gustave Eiffel (UGE) and the Laboratoire Matériaux et Durabilité des Constructions (LMDC) in the framework of the ENDE[1] project, funded by the French National Research Agency (ANR) and dedicated to non-destructive testing methods for nuclear containment structures.

[1] *Évaluation Non Destructive des Enceintes de confinement des centrales nucléaires*

The two publications below respectively correspond to collaborations with researchers from UGE, and LMDC:

Gupta, R., Rossat, D., Dérobert, X., Baroth, J., Briffaut, M., Villain, G., and Dufour, F. 2022. Blind comparison of saturation ratio profiles on large RC structures by means of NDT and SFE — Application to the VeRCoRs mock-up. *Engineering Structures*, 258:114057.

Verdier, J., Rossat, D., Multon, S., Bouhjiti, D., Sogbossi, H., Baroth, J., Nehme, A., Dufour, F., Cagnon, H., and Briffaut, M. 2022. In-situ measurement and numerical modeling of air leakage in concrete: from the lab specimen up to structural scale. *Submitted*.

Communications in international and national conferences

This communication concerns an alternative Bayesian computational approach considered in the margins of the contents presented in this thesis, namely the Transport Map approach introduced by Prof. Youssef Marzouk and his group at MIT:

Rossat, D., Baroth, J., Briffaut, M., Dufour, F. 2022. Efficient Bayesian inversion with optimal transport maps and Polynomial Chaos surrogates - Application to mechanical inverse problems. *25ème Congrès Français de Mécanique*, Nantes, France.

This communication for the 31st ESREL conference is related to the Chapter 4 of this thesis:

Rossat, D., Baroth, J., Briffaut, M., Dufour, F., Monteil, A., Masson, B., and Michel-Ponnelle, S. 2021. Probabilistic modeling in a Bayesian framework of leak tightness of nuclear containment buildings. *31st European Safety and Reliability Conference (ESREL 2021)*, Angers, France.

Talks in seminars and workshops

During my PhD, I also had the opportunity to give talks in the framework of several seminars and workshops in order to present contents related to Chapters 2 to 5 of this thesis:

Rossat, D., and Baroth, J. 2022. Bayesian inversion using adaptive Polynomial Chaos Kriging within Subset Simulation. *Journée GST Mécanique et Incertain*, Paris, France.

Rossat, D., Baroth, J., Briffaut, M., Dufour, F., Masson, B., Monteil, A., and Michel-Ponnelle, S. 2022. Bayesian updating and reliability analysis for nuclear containment buildings. *60th European Safety, Reliability & Data Association (ESReDA60)*, Grenoble, France.

Rossat, D., and Baroth, J. 2021. Adaptive surrogate models for Bayesian inference - Applications to nuclear containment buildings. *Meeting IMdR - GTR Sécurité et Sûreté des Structures*, Online meeting.

Rossat, D., and Baroth, J. 2020. Actualisation Bayésienne des prévisions du comportement de transfert de grands ouvrages de confinement. *Groupe de travail FIMA: Modèles Aléatoires pour la Fiabilité et la Maintenance des Systèmes*, Grenoble, France.

1

State-of-the-art review on Uncertainty Quantification techniques

Contents

1.1 Introduction

This chapter aims at providing an overall presentation of the framework of Uncertainty Quantification (UQ). Obviously, due to the constantly evolving nature of the field of UQ, such a presentation does not pretend to be exhaustive, but rather aims at giving an overview on the main UQ problems that will be considered throughout this thesis.

The description of the general framework of UQ provided in the introduction of this thesis suggests a classification of UQ methods into two distinct classes (Nagel, 2017; Wagner, 2021), namely *forward UQ* (Step C in Fig. iii), and *inverse UQ* (Step D in Fig. iii). Such a classification is motivated by the input-output relationship embodied by the computational model. Indeed, the model construction supposes that an output is always produced from an input by the model. The reverse situation is not trivial, though. In this context, forward UQ corresponds to methods that quantify the uncertainties in model outputs given the uncertainties in inputs. Conversely, inverse UQ encompasses methods aiming at indirectly quantifying uncertainties on inputs, given observation data related to the model outputs.

This chapter is organized as follows: firstly, Section 1.2 offers an introduction to forward UQ. In this context, computational models are firstly presented as central objects of the UQ framework, and the several sources of uncertainties affecting output quantities of interest (QoI) related to such models are discussed. Then, focusing on a probabilistic description of uncertainties, elements from Probability Theory are presented in order to introduce the framework of uncertainty propagation. The concept of surrogate modeling is subsequently illustrated through the example of polynomial chaos expansions (Ghanem and Spanos, 1991b), which constitute a widely used class of surrogate models. The main concepts of sensitivity and reliability analysis are then presented.

Finally, Section 1.3 introduces inverse UQ methods. The concept of inverse problem is firstly presented, and classical deterministic methods aiming at solving inverse problems are briefly presented. Subsequently, the probabilistic framework of Bayesian inference and its application to inverse problems are introduced. Then, classical Bayesian computational approaches, including Markov chain Monte Carlo (MCMC) methods (Brooks et al., 2011; Robert and Casella, 2004), are reviewed and discussed. Recent alternative computational techniques are also presented and discussed. Eventually, a discussion on the use of surrogate modeling techniques within Bayesian computations is provided.

1.2 Forward uncertainty quantification methods

1.2.1 Computational models

In the context of uncertainty quantification, a computational model is an idealized abstract representation of a physical system. It typically takes the form of a set of equations which may be solved analytically, or numerically through adapted resolution schemes such as the finite element method. For instance, in the framework of civil engineering, an example of computational model typically consists in multi-physics finite element calculations aiming at assessing the long-term physical behavior of a nuclear containment building.

A computational model depends on a set of input parameters, and produces a specific output for a given set of input parameters. Again, in the framework of civil engineering, such input parameters may be related to material properties, initial and boundary conditions of constitutive equations, as well as geometrical characteristics. Furthermore, output variables may typically correspond to temperature, displacements, stresses or strains.

Formally speaking, a computational model may be seen as an input-output map. The mathematical formulation of such an object is given hereafter:

$$\begin{aligned} \mathcal{M} \ : \ \mathcal{D}_{\boldsymbol{X}} \subset \mathbb{R}^d \ &\rightarrow \ \mathcal{D}_Y \subset \mathbb{R} \\ \boldsymbol{x} \ &\mapsto \ y = \mathcal{M}(\boldsymbol{x}) \end{aligned} \tag{1.1}$$

where $\mathcal{M}$ denotes the computational model, which is here assumed to be scalar-valued for the sake of simplicity, $\boldsymbol{x}$ a set of input parameters lying in the *input space* $\mathcal{D}_{\boldsymbol{X}}$, and $y = \mathcal{M}(\boldsymbol{x})$ the corresponding output lying in the *output domain* $\mathcal{D}_Y$.

The model in Eq. (1.1) is supposed to be deterministic, in contrast to *stochastic simulators* (Zhu and Sudret, 2020), which produce different outputs when evaluated repeatedly with the same inputs. Furthermore, a single evaluation of the model $\mathcal{M}$ is generally far from being instantaneous: as previously mentioned, the model $\mathcal{M}$ may typically be constituted by a costly multi-physics computational workflow.

Then, the model in Eq. (1.1) is usually handled in a *black-box* perspective, which means that it is only evaluated in a point-wise manner. Such a structure notably motivates the use of UQ methods that are *non-intrusive*, in the sense that they do not need information on the inner structure and mechanisms of the computational model. An illustration of this non-intrusivity principle may be given in the framework of surrogate modeling, where computational models are emulated from a data set formed by series of inputs and outputs. It is worth mentioning that the term *black-box* does not mean that the understanding of the underlying physical problem has to be disregarded. On the contrary, physical information may typically enable to have a better idea of the effects of some input parameters on model outputs, and guide some modeling choices related to UQ.

Then, the specification of a computational model allows to make forecasts of some physical variables of interest in a deterministic manner. However, inputs always present uncertainties, and inadequacies are immanent in all computational models at some point. Therefore, explicitly accounting for such uncertainties is necessary to provide a more comprehensive description of model forecasts. In this context, a major task in UQ consists in identifying sources of uncertainties, and devising a mathematical framework for modeling them (see Step B in Fig. iii).

1.2.2 Sources of uncertainties

The reliable use of a computational model hinges on the quantification of its predictive power, *i.e.* its ability to predict the response of the studied physical system. Therefore, it is necessary to identify the sources of uncertainties that affect model predictions. In this context, several sources of uncertainties are involved, including:

- *input uncertainties*, which arise from the modeling of input parameters based on available information (*e.g.* scarce and noisy data, expert judgements) (De Rocquigny et al., 2008),
- *variability*, referring to a natural variability of a physical property or phenomenon,
- *measurement noise*, which characterizes imprecision of data (Grabe, 2014). Such a source of uncertainties is typically linked to input uncertainties, as the modeling of inputs may be based on the statistical analysis of measurement data.
- *modeling errors*, related to inadequacies of the model, typically due to missing physics. Such errors also comprise numerical approximation errors (Deuflhard and Hohmann, 2003), as well as surrogate modeling errors, when confronted to expensive computational models.

While these two last sources are extensively studied in the framework of statistical and numerical analysis, UQ mainly focuses on the first two mentioned sources, to a certain extent. Furthermore, from an engineering point of view, two types of uncertainties are usually distinguished, following Der Kiureghian and Ditlevsen (2009):

- *aleatory uncertainties*, referring to a natural randomness of a given physical phenomenon. For instance, in civil engineering, such a type of uncertainties may correspond to the intrinsic variability of material properties, such as Young's modulus or tensile strength (Ghannoum, 2017; Sellier and Millard, 2014). Such uncertainties are considered as *irreducible*, and concern the input parameters $\boldsymbol{x}$ in Eq. (1.1).
- *epistemic uncertainties*, which refer to a lack of knowledge of the analyst. Contrary to aleatory uncertainties, epistemic uncertainties are *reducible* by gathering additional information. This may typically be achieved through collecting and analyzing measurements, or through an inverse analysis from observation data. Epistemic uncertainties are affecting either the input parameters $\boldsymbol{x}$ or the model $\mathcal{M}$ in Eq. (1.1).

Nevertheless, the boundary between these two types of uncertainties is difficult to discern, since most engineering problems involve both epistemic and aleatory uncertainties, and since the nature of uncertainties still constitutes a topic of discussion in the scientific community (Der Kiureghian and Ditlevsen, 2009; Lindley, 2000; Paté-Cornell, 1996). Indeed, Paté-Cornell (1996) suggested that it is possible to clearly distinguish the two aforementioned types, whereas Der Kiureghian and Ditlevsen (2009) proposed that such a distinction has to be made by the analyst. The aim of the latter proposition is to provide a pragmatical way to decide for which source of uncertainties it is possible to allocate some budget to gain information and therefore improve model predictions. For instance, in the case of nuclear buildings, the spatial variability of some material properties (*e.g.* properties related

to moisture transfer in porous media, or mechanical properties) could be faithfully assessed from a large amount of specimens obtained through repeated core sampling. Nevertheless, such operations are not possible due to their cost, and due to the fact that they could jeopardize structural integrity. In this context, non-destructive tests constitute a promising way to achieve such a characterization, though. Alternatively, the existing monitoring devices embedded in the structure enable to indirectly extract information about input parameters of thermo-hydro-mechanical computational models, for instance through a Bayesian inverse analysis.

1.2.3 Uncertainty propagation

Various mathematical concepts have been proposed in the literature so as to model uncertainties in input parameters (see *e.g.* (Paté-Cornell, 1996; Qiu et al., 2008)). In this context, *probability theory* constitutes the most popular and well established framework for modeling uncertainties. Alternative frameworks notably comprise *imprecise probabilities* (Schöbi, 2017; Walley, 2000), which encompass mathematical theories and tools that go beyond classical probabilities, including *evidence theory* (Dempster, 1967; Shafer, 1976), *possibility theory* (Dubois and Prade, 1988), *probability boxes* (or *p-boxes*) (Ferson and Ginzburg, 1996), *fuzzy variables* (Möller and Beer, 2004) and *info-gap theory* (Ajenjo et al., 2022; Ben-Haim, 2006).

Then, it is worth mentioning that if probability theory is widely accepted for describing input uncertainties, the corresponding probability distributions may themselves be uncertain, though. This is notably due to the lack of knowledge about input parameters, as well as contradictory expert judgements, which make input distributions particularly difficult to choose. As a result, uncertainties related to the choice of a probabilistic model may be seen as a *second level* of uncertainties (Stenger, 2020).

Second level UQ approaches recently gained popularity, particularly in engineering applications. Firstly, *robust Bayesian analysis* (Berger, 1990; Ruggeri et al., 2005) constitutes one of the first second level UQ approaches, proposed in the framework of Bayesian inference. This approach aims at quantifying the impact of the choice of the prior distribution on some QoI, through computing lower and upper bounds by modifying the prior within a given set of probability distributions. Similarly, Owhadi et al. (2013) have introduced the optimal UQ (OUQ) framework, which considers uncertainties in the definition of input distributions, and aims at estimating confidence bounds on some QoI. Such bounds are said to be optimal in the sense that they are the sharpest ones, consistently with information and assumptions about input distributions. Such a framework has been recently extended in (Stenger, 2020). Then, in the context of sensitivity analysis, second level UQ became particularly appealing to quantify the impact of uncertainties related to input distributions on sensitivity indices, including the well known Sobol' indices (Hart and Gremaud, 2019). Moreover, recent second level UQ approaches concern the framework of reliability analysis: the so-called *perturbed law indices* (PLI) aim at assessing the impact of modifications of input distributions on estimates of probabilities of failure (Lemaître et al., 2015; Sueur et al., 2016). Such indices have also been extended to other types of QoI, such as quantiles (Iooss and Le Gratiet, 2019; Perrin and Defaux, 2019) or superquantiles (Iooss et al., 2021). In addition, Chabridon (2018) has proposed reliability-oriented Sobol' indices that account for second level input uncertainties.

In this thesis, probability theory will be extensively used to describe and quantify uncertainties. In what follows, basic elements of probability theory are introduced, in order to define the mathematical notions that will be used throughout this thesis. One refers to (Billingsley, 1995; Durrett, 2019; Loève, 1977) for a comprehensive presentation on probability theory.

1.2.3.1 Probability theory

Let $(\Omega, \mathcal{F}, \mathbb{P})$ be a *probability space*, *i.e.* a triplet formed by a sample space Ω of random outcomes, $\mathcal{F}$ a σ-algebra on Ω, and $\mathbb{P}$ a probability measure on $(\Omega, \mathcal{F})$. Moreover, the Borel σ-algebra on the input space $\mathcal{D}_{\boldsymbol{X}}$ is denoted by $\mathcal{B}(\mathcal{D}_{\boldsymbol{X}})$ hereafter.

A *random variable*[1] is a function $\boldsymbol{X} : \Omega \longrightarrow \mathcal{D}_{\boldsymbol{X}}$ that is measurable from $(\Omega, \mathcal{F})$ to $(\mathcal{D}_{\boldsymbol{X}}, \mathcal{B}(\mathcal{D}_{\boldsymbol{X}}))$, that is $\boldsymbol{X}^{-1}(B) \in \mathcal{F}$ for all Borel set $B \in \mathcal{B}(\mathcal{D}_{\boldsymbol{X}})$. Here, $\boldsymbol{X}^{-1}(B) = \{\omega \in \Omega \mid \boldsymbol{X}(\omega) \in B\}$ denotes the *preimage* of $B \in \mathcal{B}(\mathcal{D}_{\boldsymbol{X}})$ under $\boldsymbol{X}$.

Then, it is possible to define a probability measure $\mathbb{P}_{\boldsymbol{X}}$ on $(\mathcal{D}_{\boldsymbol{X}}, \mathcal{B}(\mathcal{D}_{\boldsymbol{X}}))$, by pushing forward the measure $\mathbb{P}$ with $\boldsymbol{X}$:

$$\mathbb{P}_{\boldsymbol{X}}(B) = \mathbb{P}(\boldsymbol{X}^{-1}(B)) \tag{1.2}$$

for all Borel set $B \in \mathcal{B}(\mathcal{D}_{\boldsymbol{X}})$.

The probability measure $\mathbb{P}_{\boldsymbol{X}}$ defined in Eq. (1.2) is the *probability law* (or *probability distribution*) of $\boldsymbol{X}$. For convenience sake, the notation $\mathbb{P}(\boldsymbol{X} \in B) = \mathbb{P}_{\boldsymbol{X}}(B)$ is usually adopted[2]. The measure $\mathbb{P}_{\boldsymbol{X}}$ enables to calculate probabilities of events that "depend" on $\boldsymbol{X}$: for a given $\omega \in \Omega$, one associates a random point (or a *realization*) $\boldsymbol{X}(\omega) \in \mathcal{D}_{\boldsymbol{X}}$, and $\mathbb{P}_{\boldsymbol{X}}(B)$ is the probability that such a random point belongs to $B \in \mathcal{B}(\mathcal{D}_{\boldsymbol{X}})$.

Besides, for any probability measure ν on $(\mathcal{D}_{\boldsymbol{X}}, \mathcal{B}(\mathcal{D}_{\boldsymbol{X}}))$, there exists a canonical way to construct a random vector $\boldsymbol{X}_\nu : \Omega \longrightarrow \mathcal{D}_{\boldsymbol{X}}$ whose probability distribution is ν, *i.e.* $\mathbb{P}_{\boldsymbol{X}_\nu}(B) = \nu(B)$, for all $B \in \mathcal{B}(\mathcal{D}_{\boldsymbol{X}})$. Consequently, it is possible to switch freely between probability measures and random variables. Furthermore, the so-called cumulative distribution function (CDF) of $\boldsymbol{X}$ is defined by:

$$F_{\boldsymbol{X}}(\boldsymbol{x}) = \mathbb{P}(\boldsymbol{X} \leq \boldsymbol{x}) = \int_{\mathcal{D}_{\boldsymbol{X}}} \mathbf{1}_{\prod_{i=1}^{d}]-\infty, x_i]}(\boldsymbol{\xi}) \mathrm{d}\mathbb{P}_{\boldsymbol{X}}(\boldsymbol{\xi}) \tag{1.3}$$

for all $\boldsymbol{x} \in \mathcal{D}_{\boldsymbol{X}}$, where $\mathbf{1}_B$ denotes the indicator function of $B \in \mathcal{B}(\mathcal{D}_{\boldsymbol{X}})$, and where the notation $\boldsymbol{x} \leq \boldsymbol{x}'$ if and only if $x_i \leq x_i'$ for all $i \in \{1, \ldots, d\}$ has been adopted. The CDF $F_{\boldsymbol{X}}$ in Eq. (1.3) fully characterizes the measure $\mathbb{P}_{\boldsymbol{X}}$, in the sense that two random variables $\boldsymbol{X}$ and $\boldsymbol{X}'$ have the same probability distribution if and only if $F_{\boldsymbol{X}} = F_{\boldsymbol{X}'}$.

Two main types of random variables are mostly encountered in practice, namely *discrete* and *continuous* variables. When $\mathcal{D}_{\boldsymbol{X}}$ is countable, the probability distribution of $\boldsymbol{X}$ may be written as follows:

$$\mathbb{P}_{\boldsymbol{X}} = \sum_{\boldsymbol{x} \in \mathcal{D}_{\boldsymbol{X}}} p_{\boldsymbol{x}} \delta_{\boldsymbol{x}} \tag{1.4}$$

[1] the term *random variable* may be sometimes used to refer to the univariate case ($d = 1$), whereas the term of *random vector* being reserved to the multivariate case ($d > 1$). Here, the term *random variable* is deliberately adopted as a generic term if the dimensionality of the input space $\mathcal{D}_{\boldsymbol{X}}$ is not precised.

[2] More specifically, the notations $\mathbb{P}(\boldsymbol{X} = \boldsymbol{x}) = \mathbb{P}_{\boldsymbol{X}}(\{\boldsymbol{x}\})$ and $\mathbb{P}(\boldsymbol{X} \leq \boldsymbol{x}) = \mathbb{P}_{\boldsymbol{X}}\left(\prod_{i=1}^{d}]-\infty, x_i]\right)$ will be adopted, where $\boldsymbol{x} = (x_1, \ldots, x_d) \in \mathcal{D}_{\boldsymbol{X}}$.

where $p_{\boldsymbol{x}} = \mathbb{P}(\boldsymbol{X} = \boldsymbol{x}) = \mathbb{P}(\{\omega \in \Omega \mid \boldsymbol{X}(\omega) = \boldsymbol{x}\})$, and $\delta_{\boldsymbol{x}}$ denotes the Dirac measure at $\boldsymbol{x} \in \mathcal{D}_{\boldsymbol{X}}$ (*i.e.* $\delta_{\boldsymbol{x}}(B) = 1$ if $\boldsymbol{x} \in B$ and 0 else, for all $B \in \mathcal{B}(\mathcal{D}_{\boldsymbol{X}})$). In such a case, the variable $\boldsymbol{X}$ is said to be discrete.

Then, the random variable $\boldsymbol{X}$ is said to be continuous if the measure $\mathbb{P}_{\boldsymbol{X}}$ is absolutely continuous with respect to Lebesgue measure[3]. In this case, Radon-Nikodym theorem states that there exists a Borel function $\pi_{\boldsymbol{X}} : \mathcal{D}_{\boldsymbol{X}} \longrightarrow \mathbb{R}_+$ such that:

$$\mathbb{P}_{\boldsymbol{X}}(B) = \int_B \pi_{\boldsymbol{X}}(\boldsymbol{x})\mathrm{d}\boldsymbol{x} \tag{1.5}$$

for every Borel set $B \in \mathcal{B}(\mathcal{D}_{\boldsymbol{X}})$. The function $\pi_{\boldsymbol{X}}$ is called the probability density function (PDF) of $\boldsymbol{X}$. Moreover, one has $\int_{\mathcal{D}_{\boldsymbol{X}}} \pi_{\boldsymbol{X}}(\boldsymbol{x})\mathrm{d}\boldsymbol{x} = \mathbb{P}(\boldsymbol{X} \in \mathcal{D}_{\boldsymbol{X}}) = 1$. When considering continuous random variables, the denomination of *distribution* is sometimes deliberately confused with the denomination of *density*, although the nature of the two mathematical objects is different. The notation $\boldsymbol{X} \sim \mathbb{P}_{\boldsymbol{X}}$ usually adopted to signify that $\boldsymbol{X}$ follows the distribution $\mathbb{P}_{\boldsymbol{X}}$ will also be extended to $\boldsymbol{X} \sim \pi_{\boldsymbol{X}}$ when $\mathbb{P}_{\boldsymbol{X}}$ admits a density $\pi_{\boldsymbol{X}}$.

Besides, practicioners of calculus-based probability theory usually split probability distributions into discrete and continuous distributions. It is worthwhile to keep in mind that such a classification is a bit restrictive, as underlined by Stenger (2020). Indeed, modern probability theory is based on measure theory and (Lebesgue) integration, allowing to construct more general random variables, since it is possible to define a random variable from an abstract probability measure. Furthermore, when considering random variables taking values in $\mathbb{R}^d$, it is possible to precisely classify probability measures, and therefore random variables. Indeed, a refined form of the Lebesgue measure decomposition theorem (see (Hewitt and Stromberg, 1965)) states that any probability measure ν on $(\mathbb{R}^d, \mathcal{B}(\mathbb{R}^d))$ may be written as follows:

$$\nu = \nu_a + \nu_d + \nu_s \tag{1.6}$$

where ν_a is a measure absolutely continuous with respect to the Lebesgue measure on $\mathbb{R}^d$, ν_d a discrete measure, and ν_s a measure singular with respect to the Lebesgue measure[4]. Therefore, it is worthwhile to keep in mind that there may be probability measures that are neither discrete nor absolutely continuous. Nevertheless, in engineering applications, such cases may be considered as pathological, to a certain extent. Consequently, this thesis will mostly concentrate on continuous random variables.

1.2.3.2 Input distributions

In what follows, the random variable $\boldsymbol{X} : \Omega \longrightarrow \mathcal{D}_{\boldsymbol{X}}$ is assumed to be continuous, with joint density $\pi_{\boldsymbol{X}}$. The components of $\boldsymbol{X}$ are denoted by $(X_1, \ldots, X_d)$, and the input space is written $\mathcal{D}_{\boldsymbol{X}} = \prod_{i=1}^d \mathcal{D}_{X_i}$, where $\mathcal{D}_{X_i} \subset \mathbb{R}$ for all $i \in \{1, \ldots, d\}$. Each component is then given by a scalar-valued random variable $X_i : \Omega \longrightarrow \mathcal{D}_{X_i}$.

The joint CDF of $\boldsymbol{X}$ is given by:

$$F_{\boldsymbol{X}}(\boldsymbol{x}) = \mathbb{P}(X_1 \leq x_1, \ldots, X_d \leq x_d) = \int_{\mathcal{D}_{\boldsymbol{X}}} \mathbf{1}_{\prod_{i=1}^d]-\infty, x_i]}(\boldsymbol{\xi})\pi_{\boldsymbol{X}}(\boldsymbol{\xi})\mathrm{d}\boldsymbol{\xi} \tag{1.7}$$

[3] a measure ν is said to be absolutely continuous w.r.t. a measure μ if $\nu(A) = 0$ for all measurable set A such that $\mu(A) = 0$

[4] a measure ν is said to be singular w.r.t. a measure μ if there exists a measurable set A such that $\mu(A) = 0$ and $\nu(A^c) = 0$, where A^c denotes the complementary set of A.

Furthermore, the distribution of $\boldsymbol{X}$ may be characterized through several quantities, including its first moments, *e.g.* mean $\boldsymbol{\mu_X} \in \mathbb{R}^d$ or covariance matrix $\boldsymbol{\Sigma_X} \in \mathbb{R}^{d\times d}$, provided the latter are well defined and finite. The framework of $\mathbb{L}^p$ spaces (sometimes called Lebesgue spaces) provides the mathematical basis for rigorously defining such quantities. Given a measured space $(E, \mathcal{E}, \nu)$ and $p \geq 1$, one denotes by $\mathscr{L}^p(E, \mathcal{E}, \nu)$ the following function space:

$$\mathscr{L}^p(E, \mathcal{E}, \nu) = \left\{ f : E \longrightarrow \mathbb{R} \text{ measurable } \middle| \int_E |f|^p \mathrm{d}\nu < \infty \right\} \tag{1.8}$$

This space may be equipped with the seminorm defined by $\|f\|_p = \int_E |f|^p \mathrm{d}\nu$. Then, for each $p \geq 1$, the space $\mathbb{L}^p(E, \mathcal{E}, \nu)$ is defined by the quotient of $\mathscr{L}^p(E, \mathcal{E}, \nu)$ by the equivalence relation $\sim$ on $\mathscr{L}^p(E, \mathcal{E}, \nu)$ defined by $(f \sim g) \Leftrightarrow (f = g \quad \nu\text{-almost everywhere})$. In this way, the space $\mathbb{L}^p(E, \mathcal{E}, \nu)$ is a normed space when equipped with $\|\cdot\|_p$, since all functions that are equal to zero ν-almost everywhere are identified to zero. For notation purposes, every equivalence class $[f] \in \mathbb{L}^p(E, \mathcal{E}, \nu)$ will be sloppily identified to one of its representatives f hereafter. The abbreviated notation $\mathbb{L}^p(\nu)$ (or $\mathbb{L}^p(f)$ if ν admits a Lebesgue-density f) will be used if there is no ambiguity concerning the underlying measurable space $(E, \mathcal{E})$. A particular attention will be given to $\mathbb{L}^2$ spaces in the next sections, notably for their Hilbert space structure which plays a key role in the framework of spectral approaches (Ghanem and Spanos, 1991b), which will be considered for surrogate modeling purposes.

Assuming that $X_i \in \mathbb{L}^2(\Omega, \mathcal{F}, \mathbb{P})$ for all $i \in \{1, \ldots, d\}$, the mean $\boldsymbol{\mu_X}$ is well defined, and reads:

$$\boldsymbol{\mu_X} = \mathbb{E}[\boldsymbol{X}] = \int_\Omega \boldsymbol{X}(\omega) \mathrm{d}\mathbb{P}(\omega) \tag{1.9}$$

Then, the well-known *transport theorem* (see (Barbé and Ledoux, 2007)) enables to rewrite the above integral as an integral with respect to the measure $\mathbb{P}_{\boldsymbol{X}}$:

$$\boldsymbol{\mu_X} = \mathbb{E}[\boldsymbol{X}] = \int_{\mathcal{D}_{\boldsymbol{X}}} \boldsymbol{x} \mathrm{d}\mathbb{P}_{\boldsymbol{X}}(\boldsymbol{x}) = \int_{\mathcal{D}_{\boldsymbol{X}}} \boldsymbol{x} \pi_{\boldsymbol{X}}(\boldsymbol{x}) \mathrm{d}\boldsymbol{x} \tag{1.10}$$

Likewise, the covariance matrix $\boldsymbol{\Sigma_X}$ of $\boldsymbol{X}$ is also well defined and writes:

$$\boldsymbol{\Sigma_X} = \mathbb{E}\left[(\boldsymbol{X} - \boldsymbol{\mu_X})(\boldsymbol{X} - \boldsymbol{\mu_X})^\intercal\right] = \int_{\mathcal{D}_{\boldsymbol{X}}} (\boldsymbol{x} - \boldsymbol{\mu_X})(\boldsymbol{x} - \boldsymbol{\mu_X})^\intercal \pi_{\boldsymbol{X}}(\boldsymbol{x}) \mathrm{d}\boldsymbol{x} \tag{1.11}$$

In addition, integration is performed component-wise in Eq. (1.10), which yields $\boldsymbol{\mu_X} = (\mu_{X_1}, \ldots, \mu_{X_d})^\intercal$, μ_{X_i} being the mean of X_i, namely:

$$\mu_{X_i} = \mathbb{E}[X_i] = \int_{\mathcal{D}_{\boldsymbol{X}}} x_i \pi_{\boldsymbol{X}}(\boldsymbol{x}) \mathrm{d}\boldsymbol{x} \tag{1.12}$$

Moreover, the coefficients of the covariance matrix $\boldsymbol{\Sigma_X}$ in Eq. (1.11) are given by:

$$[\boldsymbol{\Sigma_X}]_{ij} = \mathrm{Cov}[X_i, X_j] = \mathbb{E}[(X_i - \mathbb{E}[X_i])(X_j - \mathbb{E}[X_j])] \tag{1.13}$$

for all $i, j \in \{1, \ldots, d\}$.

In particular, diagonal terms of the covariance matrix $\boldsymbol{\Sigma_X}$ in Eq. (1.11) correspond to variances of components of $\boldsymbol{X}$, namely $[\boldsymbol{\Sigma_X}]_{ii} = \mathrm{Var}[X_i] = \mathbb{E}[(X_i - \mathbb{E}[X_i])^2]$. Moreover, the

standard deviation of X_i is denoted by $\sigma_{X_i} = \mathrm{Std}[X_i] = \sqrt{\mathrm{Var}[X_i]}$, whereas the coefficient of variation (CoV) is defined by $\mathrm{CoV}[X_i] = \sigma_{X_i}/\mu_{X_i}$ if $\mu_{X_i} \neq 0$[5].

The linear correlation matrix $\mathbf{R}_{\boldsymbol{X}}$ is also often used in probabilistic modeling. For $i, j \in \{1, \ldots, d\}$, the coefficient $\rho[X_i, X_j] = [\mathbf{R}_{\boldsymbol{X}}]_{ij}$ is given by the so-called *Pearson coefficient* (Pearson, 1895):

$$\rho[X_i, X_j] = \frac{\mathrm{Cov}[X_i, X_j]}{\sigma_{X_i}\sigma_{X_j}} \tag{1.14}$$

provided that $\sigma_{X_i}, \sigma_{X_j} \neq 0$.

Then, two fundamental operations may be considered when handling the joint density $\pi_{\boldsymbol{X}}$ of $\boldsymbol{X}$, namely *marginalization* and *conditioning*. The former consists in analyzing the behavior of marginals X_i of $\boldsymbol{X}$ for $i \in \{1, \ldots, d\}$, and more generally of sub-variables $\boldsymbol{X}_u = (X_i)_{i \in u}$ where $u \subset \{1, \ldots, d\}$. It may be shown that the marginal distribution $\mathbb{P}_{\boldsymbol{X}_u}$ also admits a density $\pi_{\boldsymbol{X}_u}$, which reads:

$$\pi_{\boldsymbol{X}_u}(\boldsymbol{x}_u) = \int_{\mathcal{D}_{\boldsymbol{X}_{\sim u}}} \pi_{\boldsymbol{X}}(\boldsymbol{x}) \mathrm{d}\boldsymbol{x}_{\sim u} \tag{1.15}$$

for all $\boldsymbol{X}_u \in \mathcal{D}_{\boldsymbol{X}_u}$, where the notations $\boldsymbol{x}_u = (x_i)_{i \in u}$ and $\boldsymbol{x}_{\sim u} = (x_i)_{i \notin u}$ have been used (and one similarly denotes $\mathcal{D}_{\boldsymbol{X}_u} = \prod_{i \in \boldsymbol{u}} \mathcal{D}_{X_i}$ and $\mathcal{D}_{\boldsymbol{X}_{\sim u}} = \prod_{i \notin u} \mathcal{D}_{X_i}$). In particular, the density π_{X_i} of the random variable X_i is given by:

$$\pi_{X_i}(x_i) = \int_{\mathcal{D}_{\boldsymbol{X}_{\sim i}}} \pi_{\boldsymbol{X}}(\boldsymbol{x}) \mathrm{d}\boldsymbol{x}_{\sim i} \tag{1.16}$$

Furthermore, *conditioning* aims at describing random variables for which only partial information are available. It is closely related to the notion of *conditional expectation*, which will not be introduced in details here for the sake of concision, and the reader may refer to (Billingsley, 1995, Chapter 6) for a comprehensive presentation. Conditioning also constitutes a core principle of the framework of Bayesian inference, which will be extensively considered throughout this thesis.

Given $u \subset \{1, \ldots, d\}$, $v = \{1, \ldots, d\} \setminus u$ and $\boldsymbol{X}_v \in \mathcal{D}_{\boldsymbol{X}_{\sim u}}$, the *conditional density of* $\boldsymbol{X}_u$ *knowing* $\boldsymbol{X}_v = \boldsymbol{x}_v$ may be defined as follows:

$$\pi_{\boldsymbol{X}_u|\boldsymbol{x}_v}(\boldsymbol{x}_u|\boldsymbol{x}_v) = \frac{\pi_{\boldsymbol{X}}(\boldsymbol{x})}{\pi_{\boldsymbol{X}_v}(\boldsymbol{x}_v)} \tag{1.17}$$

provided that $\pi_{\boldsymbol{X}_v}(\boldsymbol{x}_v) > 0$. Then, the *conditional expectation* of $\boldsymbol{X}_{\boldsymbol{u}}$ knowing $\boldsymbol{X}_v = \boldsymbol{x}_v$ is given by:

$$\mathbb{E}[\boldsymbol{X}_u|\boldsymbol{X}_v = \boldsymbol{x}_v] = \int_{\mathcal{D}_{\boldsymbol{X}_u}} \boldsymbol{x}_u \pi_{\boldsymbol{X}_u|\boldsymbol{x}_v}(\boldsymbol{x}_u|\boldsymbol{x}_v) \mathrm{d}\boldsymbol{x}_u \tag{1.18}$$

It is important to emphasize that the marginals $\mathbb{P}_{X_i}$ may be determined from the joint distribution $\mathbb{P}_{\boldsymbol{X}}$ (see Eq. (1.16)), but the reverse is not true. This observation underlies the notion of *dependence*. The random variables $X_1, \ldots, X_d$ are said to be *mutually independent* if the joint distribution $\mathbb{P}_{\boldsymbol{X}}$ is equal to the tensorial product of distributions of $X_1, \ldots, X_d$, namely:

$$\mathbb{P}_{\boldsymbol{X}} = \mathbb{P}_{X_1} \otimes \cdots \otimes \mathbb{P}_{X_d} \tag{1.19}$$

[5]The notation $\mathrm{CoV}[\cdot]$ used for the CoV shall not be confused with the notation $\mathrm{Cov}[\cdot]$ used for covariance.

In this case, the joint density $\pi_{\boldsymbol{X}}$ of $\boldsymbol{X}$ factorizes as follows:

$$\pi_{\boldsymbol{X}}(\boldsymbol{x}) = \prod_{i=1}^{d} \pi_{X_i}(x_i) \tag{1.20}$$

It is also worth noting that Eq. (1.19) implies that $\mathrm{Cov}[X_i, X_j] = 0$ for all $i, j \in \{1, \ldots, d\}$ such that $i \neq j$. Nevertheless, the zero-covariance property does not systematically imply mutual independence.

In this thesis, the considered input variables will be very often supposed to be mutually independent. Besides, Sklar's theorem (Sklar, 1959) states that for any multivariate distribution, there exists a function $C_{\boldsymbol{X}} : [0,1]^d \longrightarrow [0,1]$ such that:

$$F_{\boldsymbol{X}}(\boldsymbol{x}) = C_{\boldsymbol{X}}(F_{X_1}(x_1), \ldots, F_{X_d}(x_d)) \tag{1.21}$$

where $F_{\boldsymbol{X}}$ denotes the joint CDF, $F_{X_1}, \ldots, F_{X_d}$ the corresponding marginals CDF and $C_{\boldsymbol{X}}$ is a *copula*, namely the joint CDF of a random variable with d marginals uniformly distributed on $[0,1]$. Such a copula is unique when considering continuous random variables (Nelsen, 2006).

As a result, any general multivariate distribution may be fully characterized with its marginals and a copula. Eq. (1.21) suggests a practical and modular way to build multivariate distributions in two main steps, namely by firstly modeling the (univariate) marginals $\mathbb{P}_{X_i}$, and subsequently choosing a copula so as to model the dependence between input variables. In this thesis, the *independent copula* (*i.e.* $C_{\boldsymbol{X}}(u_1, \ldots, u_d) = \prod_{i=1}^{d} u_i$) will be extensively used, whereas *Gaussian copulas* will occasionally be considered. For a comprehensive review on copula theory as well as the various existing classes of copula, the reader may refer to (Nelsen, 2006).

Finally, although the previous presentation emphasized the main ingredients for constructing multivariate distributions in practice, the question of the choice of an appropriate distribution remains not elucidated yet. Two main types of approaches may be considered to infer the distribution of inputs, namely:

- *parametric approaches*, which consist in selecting the distribution among parametric classes of probability distributions, for instance including Gaussian, uniform or log-normal distributions (see Table 1.1). When data sets related to input parameters are available, the parameters of such distributions may be estimated in order to find the distribution that matches best with data. This may be typically achieved through *maximum likelihood estimation* (MLE) (Johansen and Juselius, 1990). Alternatively, parametric distributions may be selected through expert judgement. This is typically the case in the framework of Bayesian inference, when specifying a prior distribution.

- *non-parametric approaches*, which consist in estimating a probability distribution in a non-parametric way, for instance through *kernel density estimation* (KDE) (Parzen, 1962; Silverman, 1986).

Name	**Notation**	**Support**	**CDF** $F_X(x)$	**PDF** $\pi_X(x)$
Exponential	$\mathrm{Exp}(\alpha)$	$\mathbb{R}_+$	$1-\exp(-\alpha x)$	$\alpha\exp(-\alpha x)$
Gaussian	$\mathcal{N}(\mu,\sigma^2)$	$\mathbb{R}$	$\frac{1}{2}\left[1+\mathrm{erf}\left(\frac{x-\mu}{\sigma\sqrt{2}}\right)\right]$	$\frac{1}{\sqrt{2\pi}\sigma}\exp\left(-\frac{(x-\mu)^2}{2\sigma^2}\right)$
Laplace	$\mathrm{Laplace}(\mu,\sigma)$	$\mathbb{R}$	$\begin{cases}\frac{1}{2}\exp\left(\frac{x-\mu}{\sigma}\right) & \text{if} \quad x\leq\mu \\ 1-\frac{1}{2}\exp\left(\frac{\mu-x}{\sigma}\right) & \text{else}\end{cases}$	$\frac{1}{2\sigma}\exp\left(-\frac{\lvert x-\mu\rvert}{\sigma}\right)$
Lognormal	$\mathrm{Log}\mathcal{N}(\mu,\sigma)$	$\mathbb{R}_+^*$	$\frac{1}{2}\left[1+\mathrm{erf}\left(\frac{\log(x)-\mu}{\sigma\sqrt{2}}\right)\right]$	$\frac{1}{\sqrt{2\pi}\sigma x}\exp\left(-\frac{(\log(x)-\mu)^2}{2\sigma^2}\right)$
Uniform	$\mathcal{U}([a,b])$ $(a\leq b)$	$[a,b]$	$\begin{cases}0 & \text{if } x\leq a \\ \frac{x-a}{b-a} & \text{if } x\in[a,b] \\ 1 & \text{else}\end{cases}$	$\begin{cases}\frac{1}{b-a} & \text{if } x\in[a,b] \\ 0 & \text{else}\end{cases}$

Table 1.1: Classical examples of univariate probability distributions. erf *denotes the error function, defined by* $\mathrm{erf}(x)=\frac{2}{\sqrt{\pi}}\int_{-\infty}^{x}\exp(-\xi^2)d\xi$ for all $x\in\mathbb{R}$.

1.2.3.3 Probabilistic transforms

In some cases, it is convenient to transform the distribution $\mathbb{P}_{\boldsymbol{X}}$ into a somewhat simpler one $\mathbb{P}_{\boldsymbol{U}}$, typically a standard normal distribution with independent marginals (*i.e.* $\mathcal{N}(\mathbf{0},\mathbf{I})$, $\mathbf{I}$ denoting the identity matrix of $\mathbb{R}^{d\times d}$), or a uniform distribution on the standard hypercube $[0,1]^d$ (*i.e.* $\mathcal{U}([0,1]^d)$). Such transformations are widely used in the framework of reliability analysis (Der Kiureghian and Liu, 1986; Hohenbichler and Rackwitz, 1981), in order to estimate probabilities of rare events in a somewhat normalized space, with Gaussian random variables. Such a space is usually called *standard Gaussian space*, or *U-space* in the literature.

Let suppose that $\mathbb{P}_{\boldsymbol{U}}$ is the distribution of a random vector $\boldsymbol{U}:\Omega\longrightarrow\mathcal{D}_{\boldsymbol{U}}\subset\mathbb{R}^d$. Mathematically speaking, finding a transformation from the original (or "physical") input space $\mathcal{D}_{\boldsymbol{X}}$ to the standard space $\mathcal{D}_{\boldsymbol{U}}$ which maps $\boldsymbol{X}$ to $\boldsymbol{U}$ is akin to finding a sufficiently regular[6] map $\mathcal{T}:\mathcal{D}_{\boldsymbol{X}}\longrightarrow\mathcal{D}_{\boldsymbol{U}}$ that pushes forward $\mathbb{P}_{\boldsymbol{X}}$ to $\mathbb{P}_{\boldsymbol{U}}$, namely:

$$\mathbb{P}_{\boldsymbol{U}}(B)=\mathbb{P}_{\boldsymbol{X}}(\mathcal{T}^{-1}(B)) \tag{1.22}$$

for every Borel set $B\in\mathcal{B}(\mathcal{D}_{\boldsymbol{U}})$. Eq. (1.22) is often written more compactly $\mathcal{T}_\sharp\mathbb{P}_{\boldsymbol{X}}=\mathbb{P}_{\boldsymbol{U}}$[7]. It is remarked that such a transformation is linked to the notion of *deterministic coupling* encountered in Optimal Transport theory (Santambrogio, 2015; Villani, 2003, 2009), where one finds to push forward a probability measure towards another while minimizing a certain cost function. In the context of probabilistic transforms, the optimality of the sought map (w.r.t. a given cost function) is not needed, though.

In practice, several constructions have been proposed in the literature. One firstly considers the univariate case with a continuous random variable $X:\Omega\to\mathcal{D}_X\subset\mathbb{R}$ with support $\mathcal{D}_X$ and CDF F_X. Then, the random variable $F_X(X)$ follows the uniform distribution $\mathcal{U}([0,1])$ (Santambrogio, 2015). Conversely, if $U\sim\mathcal{U}([0,1])$ is a uniform random variable on $[0,1]$, the random variable $F_X^{-1}(U)$ follows the probability distribution $\mathbb{P}_X$. Note that here $F_X^{(-1)}$

[6] typically a $\mathcal{C}^1$-diffeomorphism. Recall that a $\mathcal{C}^1$ diffeomorphism is a bijective map that is continuously differentiable, and whose inverse is continuously differentiable too.

[7] where $\mathcal{T}_\sharp\mathbb{P}_{\boldsymbol{X}}$ is the *pushforward* measure defined by $\mathcal{T}_\sharp\mathbb{P}_{\boldsymbol{X}}(B)=\mathbb{P}_{\boldsymbol{X}}(\mathcal{T}^{-1}(B))$ for all $B\in\mathcal{B}(\mathcal{D}_{\boldsymbol{U}})$.

denotes the right-continuous inverse of F_X, which is defined for all $q \in [0,1]$ by:

$$F_X^{(-1)}(q) = \inf\{x \in \mathcal{D}_X \mid F_X(x) > q\} \tag{1.23}$$

Consequently, assuming now that $U \sim \mathbb{P}_U$ is a continuous random variable with CDF F_U, the mapping $\mathcal{T} = F_U^{(-1)} \circ F_X$ achieves the desired transformation in Eq. (1.22). Such a mapping is known as the *increasing rearrangement* (Villani, 2009), or also *inverse probability distribution transform*.

Furthermore, in the case of mutually independent multivariate random variables, it is possible to apply the increasing rearrangement in a component-wise fashion. In the case of dependent variables, several transformations may be considered depending on the dependence structure of inputs, namely Nataf transformation (Nataf, 1962), or Rosenblatt transformation[8] (Lebrun and Dutfoy, 2009; Rosenblatt, 1952). Their construction is not detailed here for the sake of brevity (see *e.g.* (Lebrun and Dutfoy, 2009) for further details).

1.2.3.4 Quantities of interest

Let $\mathcal{M} : \mathcal{D}_{\boldsymbol{X}} \to \mathcal{D}_Y$ be the computational model introduced in Section 1.2.1. Assuming that $\mathcal{M}$ is a Borel function, the model output $Y = \mathcal{M}(\boldsymbol{X})$ is a random variable, since $\boldsymbol{X}$ is a random variable. In this context, the main purpose of uncertainty propagation consists in characterizing Y, notably through the determination of QoI of various types, including:

- expectations against the input probability measure $\mathbb{P}_{\boldsymbol{X}}$ (*e.g.* moments),
- the full CDF F_Y of the output Y,
- conservative measures such as α-quantiles (with $\alpha \in]0,1[$):

$$q_\alpha = \inf\{y \in \mathcal{D}_Y \mid F_Y(y) \geq \alpha\} \tag{1.24}$$

- the probability $\mathbb{P}(Y \geq y_*)$ of exceeding a given threshold value $y_* \in \mathcal{D}_{\boldsymbol{Y}}$, whose estimation is at the core of classical reliability analyses.

The first two mentioned quantities are discussed hereafter. Let $\phi : \mathcal{D}_{\boldsymbol{X}} \to \mathbb{R}$ be a scalar function that is integrable with respect to $\pi_{\boldsymbol{X}}$, *i.e.* $\phi \in \mathbb{L}^1(\pi_{\boldsymbol{X}})$. Then, the transport theorem (Barbé and Ledoux, 2007) enables to derive the following expression for the expectation $\mathbb{E}[\phi(\boldsymbol{X})]$:

$$\mathbb{E}[\phi(\boldsymbol{X})] = \int_{\mathcal{D}_{\boldsymbol{X}}} \phi(\boldsymbol{x}) \mathrm{d}\mathbb{P}_{\boldsymbol{X}}(\boldsymbol{x}) = \int_{\mathcal{D}_{\boldsymbol{X}}} \phi(\boldsymbol{x}) \pi_{\boldsymbol{X}}(\boldsymbol{x}) \mathrm{d}\boldsymbol{x} \tag{1.25}$$

Assuming that $\mathcal{M} \in \mathbb{L}^2(\pi_{\boldsymbol{X}})$, the quantities defined in Eq. (1.25) comprise the mean μ_Y and variance σ_Y^2 of the random model output Y, which respectively read:

$$\mu_Y = \mathbb{E}[\mathcal{M}(\boldsymbol{X})] = \int_{\mathcal{D}_{\boldsymbol{X}}} \mathcal{M}(\boldsymbol{x}) \pi_{\boldsymbol{X}}(\boldsymbol{x}) \mathrm{d}\boldsymbol{x} \tag{1.26}$$

$$\sigma_Y^2 = \mathbb{E}\left[(\mathcal{M}(\boldsymbol{X}) - \mu_Y)^2\right] = \int_{\mathcal{D}_{\boldsymbol{X}}} (\mathcal{M}(\boldsymbol{x}) - \mu_Y)^2 \pi_{\boldsymbol{X}}(\boldsymbol{x}) \mathrm{d}\boldsymbol{x} \tag{1.27}$$

[8] also known as *Knothe-Rosenblatt rearrangement* (Carlier et al., 2010; Knothe, 1957).

Likewise, assuming stronger integrability assumptions for the model $\mathcal{M}$, higher order moments such as skewness or kurtosis may also be quantified. Furthermore, the CDF F_Y of the model output Y may also be determined through the transport theorem:

$$F_Y(y) = \mathbb{P}(\mathcal{M}(\boldsymbol{X}) \leq y) = \int_{\mathcal{D}_{\boldsymbol{X}}} \mathbf{1}_{]-\infty,y]}(\mathcal{M}(\boldsymbol{x}))\pi_{\boldsymbol{X}}(\boldsymbol{x})\mathrm{d}\boldsymbol{x} \tag{1.28}$$

1.2.3.5 Monte Carlo simulation

The quantities in Eqs. (1.25) to (1.28) are generally not analytically tractable. Consequently, output QoI are usually estimated by using random sampling techniques. Among the latter, Monte Carlo simulation (MCS) (Metropolis and Ulam, 1949) constitutes the most widely used technique. It consists in drawing independent samples $\mathcal{X} = \{\boldsymbol{x}^{(k)}\}_{1\leq k\leq N} \subset \mathcal{D}_{\boldsymbol{X}}$ from the input distribution of $\boldsymbol{X}$, and subsequently computing the corresponding model outputs $\mathcal{Y} = \{\mathcal{M}(\boldsymbol{x}^{(k)})\}_{1\leq k\leq N}$. Then, QoI such as in Eq. (1.10) may be estimated from the following sample approximation:

$$\hat{\mu}_{Y,N} = \frac{1}{N}\sum_{k=1}^{N} \mathcal{M}(\boldsymbol{x}^{(k)}) \tag{1.29}$$

The *Law of Large Numbers* (LLN) and the *Central Limit Theorem* (CLT) (Billingsley, 1995) constitute the theoretical basis for Monte Carlo simulation. Indeed, assuming that $\mathcal{M} \in \mathbb{L}^1(\pi_{\boldsymbol{X}})$, the LLN states that the estimator $\hat{\mu}_{Y,N}$ converges almost-surely towards the mean μ_Y in Eq. (1.26) when $N \to \infty$. Furthermore, if $\mathcal{M} \in \mathbb{L}^2(\pi_{\boldsymbol{X}})$, the CLT ensures that $\sqrt{N}(\hat{\mu}_{Y,N} - \mu_Y)$ converges in law[9] towards $Z \sim \mathcal{N}(0, \sigma_Y^2)$ when $N \to \infty$, where σ_Y^2 is the output variance defined in Eq. (1.27).

Monte Carlo simulation constitutes a universal method for estimating QoI related to the model output. Moreover, such an approach is robust with respect to the complexity of the integrand in Eq. (1.25), and the dimensionality of the inputs, since it provides dimension-independent convergence rates for sampling errors w.r.t. the number of samples (Robert and Casella, 2004). Nevertheless, such appreciable properties come at the price of slow convergence rates. This notably implies a very large amount of model evaluations to ensure reliable estimators for the studied QoI.

[9]Recall that a sequence $(Z_N)_{N\geq 0}$ of random variables converges in law towards a random variable Z if for all continuous bounded function $\phi : \mathbb{R} \to \mathbb{R}$, one has $\mathbb{E}[\phi(Z_N)] \to \mathbb{E}[\phi(Z)]$ when $N \to \infty$.

1.2.4 Surrogate modeling

When considering costly computational models, classical sampling techniques such as Monte Carlo simulation become intractable, as they may require a very large amount of model evaluations. In this context, surrogate modeling aims at emulating the computational model with a mathematical function that is inexpensive to evaluate. To that end, two main types of surrogate models may be distinguished in the literature (Wagner, 2021):

- *global surrogates*, which provide an approximation of the global behavior of the model, based on some global error measures. Such surrogates include spectral expansions such as polynomial chaos expansions (PCE) (Ghanem and Spanos, 1991a; Wiener, 1938) or Poincaré expansions (Lüthen et al., 2021a), low rank tensor approximations (LRA) (Konakli and Sudret, 2016) and neural networks (Cheng and Titterington, 1994; Goodfellow et al., 2016).

- *local surrogates*, which provide local accuracy in the vicinity of training points. Local surrogates comprises interpolating techniques such as Kriging or Gaussian process (Gp) modeling (Krige, 1951; Matheron, 1963; Sacks et al., 1989; Santner et al., 2003), as well as local regression techniques such as Gaussian process regression (Rasmussen and Williams, 2006) and support vector machines (Steinwart and Christmann, 2008).

Furthermore, Schöbi et al. (2015) introduced a surrogate modeling technique that lies between local and global approaches, namely Polynomial Chaos Kriging (PCK). Such an approach consists in embedding a PCE as a trend of a Kriging, and then enables to combine the global approximation power of PCE with local features provided by the underlying Gaussian process.

Then, it is worth noting that each of the aforementioned techniques presents its own advantages and drawbacks, and their performance may sensibly depend on the considered problem. In this thesis, PCE will be often considered, as they constitute polyvalent and powerful global surrogates, that can be used to perform global sensitivity analyses at a reduced cost (Sudret, 2008). Consequently, a brief review on PCE theory and practice is given herebelow.

1.2.4.1 Polynomial chaos expansions

In what follows, the components of the input random variable $\boldsymbol{X}$ are still assumed to be mutually independent. The reader may refer to (Jakeman et al., 2019) for PCE formulation for dependent input random variables. It is also assumed that $\mathcal{M} \in \mathbb{L}^2(\pi_{\boldsymbol{X}})$, so that the random model response $Y = \mathcal{M}(\boldsymbol{X})$ admits a finite variance.

Firstly, the Hilbert space $\mathbb{L}^2(\pi_{\boldsymbol{X}})$ is equipped with the following inner product:

$$\langle \phi | \psi \rangle_{\pi_{\boldsymbol{X}}} = \mathbb{E}[\phi(\boldsymbol{X})\psi(\boldsymbol{X})] = \int_{\mathcal{D}_{\boldsymbol{X}}} \phi(\boldsymbol{x})\psi(\boldsymbol{x})\pi_{\boldsymbol{X}}(\boldsymbol{x})\mathrm{d}\boldsymbol{x} \tag{1.30}$$

for all $\phi, \psi \in \mathbb{L}^2(\pi_{\boldsymbol{X}})$.

Likewise, for each $i \in \{1, \ldots, d\}$, the space $\mathbb{L}^2(\pi_{X_i})$ is equipped with the inner product defined as follows, for all $\phi, \psi \in \mathbb{L}^2(\pi_{X_i})$:

$$\langle \phi | \psi \rangle_{\pi_{X_i}} = \mathbb{E}[\phi(X_i)\psi(X_i)] = \int_{\mathcal{D}_{X_i}} \phi(x_i)\psi(x_i)\pi_{X_i}(x_i)\mathrm{d}x_i \tag{1.31}$$

Then, under some assumptions related to the input distribution $\mathbb{P}_{X_i}$ (see *e.g.* (Ernst et al., 2012; Xiu and Karniadakis, 2002)), there exists a Hilbert basis[10] $(\psi_k^{(i)})_{k\geq 0}$ formed by univariate polynomials that are orthonormal with respect to $\mathbb{P}_{X_i}$, which reads:

$$\langle \psi_k^{(i)} | \psi_l^{(i)} \rangle_{\pi_{X_i}} = \delta_{kl} \tag{1.32}$$

where δ_{kl} is the Kronecker delta, *i.e.* $\delta_{kl} = 1$ if $k = l$ and 0 else. In this context, classical families of orthogonal polynomials may be linked to parametric probability distributions mentioned in Table 1.1: for instance, Hermite polynomials correspond to Gaussian distributions, and Legendre polynomials correspond to uniform distributions (Xiu and Karniadakis, 2002). When the input distribution is not explicitly given, an orthonormal polynomial family may be constructed numerically through Gram-Schmidt or Stieltjes procedure (Gautschi, 2004). Such an approach has been undertaken in the framework of *arbitrary PCE* (see *e.g.* (Torre et al., 2019)).

Furthermore, under the assumption of mutually independent input variables (see Eq. (1.19)), Soize and Ghanem (2004) proved that the Hilbert space $\mathbb{L}^2(\pi_{\boldsymbol{X}})$ is isomorphic to the tensor product Hilbert space $\bigotimes_{i=1}^d \mathbb{L}^2(\pi_{X_i})$. This allows to build a Hilbert basis $(\psi_{\boldsymbol{\alpha}})_{\boldsymbol{\alpha}\in\mathbb{N}^d}$ of $\mathbb{L}^2(\pi_{\boldsymbol{X}})$ by taking the tensor product of the bases $(\psi_j^{(i)})_{j\geq 0}$:

$$\psi_{\boldsymbol{\alpha}}(\boldsymbol{x}) = \prod_{i=1}^d \psi_{\alpha_i}^{(i)}(x_i) \tag{1.33}$$

for all $\boldsymbol{x} = (x_1, \ldots, x_d) \in \mathcal{D}_{\boldsymbol{X}}$ and $\boldsymbol{\alpha} = (\alpha_1, \ldots, \alpha_d) \in \mathbb{N}^d$. The so-constructed multivariate polynomials are also orthonormal with respect to the joint distribution $\mathbb{P}_{\boldsymbol{X}}$, *i.e.*

$$\langle \psi_{\boldsymbol{\alpha}} | \psi_{\boldsymbol{\beta}} \rangle_{\pi_{\boldsymbol{X}}} = \delta_{\boldsymbol{\alpha}\boldsymbol{\beta}} \tag{1.34}$$

where $\delta_{\boldsymbol{\alpha}\boldsymbol{\beta}} = \prod_{i=1}^d \delta_{\alpha_i\beta_i}$ is the Kronecker delta for multi-indices $\boldsymbol{\alpha}, \boldsymbol{\beta} \in \mathbb{N}^d$. Moreover, the degree of a given polynomial $\psi_{\boldsymbol{\alpha}}$ is encoded by the multi-index $\boldsymbol{\alpha}$, since the degree of the univariate polynomial $\psi_{\alpha_i}^{(i)}$ is equal to α_i for $i \in \{1, \ldots, d\}$, whereas the total degree of $\psi_{\boldsymbol{\alpha}}$ is given by $\|\boldsymbol{\alpha}\|_1 = \sum_{i=1}^d \alpha_i$.

Thus, the random response $Y = \mathcal{M}(\boldsymbol{X})$ may be expanded onto the Hilbert basis $(\psi_{\boldsymbol{\alpha}})_{\boldsymbol{\alpha}\in\mathbb{N}^d}$:

$$\mathcal{M}(\boldsymbol{X}) = \sum_{\boldsymbol{\alpha}\in\mathbb{N}^d} c_{\boldsymbol{\alpha}} \psi_{\boldsymbol{\alpha}}(\boldsymbol{X}) \tag{1.35}$$

where $(c_{\boldsymbol{\alpha}})_{\boldsymbol{\alpha}\in\mathbb{N}^d}$ are the PCE coefficients, which may be written as $c_{\boldsymbol{\alpha}} = \langle \mathcal{M} | \psi_{\boldsymbol{\alpha}} \rangle_{\pi_{\boldsymbol{X}}}$ due to the orthonormality of the PCE basis $(\psi_{\boldsymbol{\alpha}})_{\boldsymbol{\alpha}\in\mathbb{N}^d}$.

Moreover, it is worth noting that the coefficients $(c_{\boldsymbol{\alpha}})_{\boldsymbol{\alpha}}$ in Eq. (1.35) are closely linked to the probabilistic content of the random response $Y = \mathcal{M}(\boldsymbol{X})$. Indeed, due to the orthonormality of the PCE basis, closed-form expressions for the moments of Y can be obtained from the PCE coefficients (Sudret, 2007). Such expressions are given herebelow for the output mean in Eq. (1.26) and variance in Eq. (1.27):

$$\mu_Y = \mathbb{E}[\mathcal{M}(\boldsymbol{X})] = c_{\boldsymbol{0}} \tag{1.36}$$

$$\sigma_Y^2 = \mathrm{Var}[\mathcal{M}(\boldsymbol{X})] = \sum_{\boldsymbol{\alpha}\in\mathbb{N}^d\setminus\{\boldsymbol{0}\}} c_{\boldsymbol{\alpha}}^2 \tag{1.37}$$

[10] considering a Hilbert space $(\mathcal{H}, \langle\cdot|\cdot\rangle)$, a *Hilbert basis* $\{e_n\}_{n\geq 0}$ is an orthonormal basis of $\mathcal{H}$ (*i.e.* $\langle e_i | e_j \rangle = \delta_{ij}$) which is *total*, *i.e.* such that the closure of the linear span of $\{e_n\}_{n\geq 0}$ is equal to $\mathcal{H}$.

1.2.4.2 Truncation schemes

For practical purposes, the representation in Eq. (1.35) has to be truncated on a finite set $\mathcal{A} \subset \mathbb{N}^d$ of multi-indices:

$$\mathcal{M}(\boldsymbol{X}) = \sum_{\boldsymbol{\alpha} \in \mathcal{A}} c_{\boldsymbol{\alpha}} \psi_{\boldsymbol{\alpha}}(\boldsymbol{X}) + \mathcal{R}_{\boldsymbol{\alpha}}(\boldsymbol{X}) \tag{1.38}$$

where $\mathcal{R}_{\boldsymbol{\alpha}}(\boldsymbol{X}) = \sum_{\boldsymbol{\alpha} \in \mathbb{N}^d \setminus \mathcal{A}} c_{\boldsymbol{\alpha}} \psi_{\boldsymbol{\alpha}}(\boldsymbol{X})$ is the error induced by the truncation.

Several types of truncation sets are proposed in the literature. The most popular truncation scheme consists in only keeping polynomials with total degree that not exceeds a prescribed integer $p \in \mathbb{N}$:

$$\mathcal{A}_p = \left\{ \boldsymbol{\alpha} \in \mathbb{N}^d \mid \|\boldsymbol{\alpha}\|_1 \leq p \right\} \tag{1.39}$$

Nevertheless, such a truncation set is subjected to the so-called *curse of dimensionality*, since its number of terms is given by $|\mathcal{A}_p| = (d+p)!/d!p!$, which grows rapidly when the input dimension (and/or the polynomial degree) increases. To alleviate this problem, Blatman and Sudret (2011b) have proposed the following *hyperbolic truncation sets*:

$$\mathcal{A}_{p,q} = \{ \boldsymbol{\alpha} \in \mathbb{N}^d \mid \|\boldsymbol{\alpha}\|_q \leq p \} \tag{1.40}$$

where $p \in \mathbb{N}$, $q \in]0,1]$, and $\|\boldsymbol{\alpha}\|_q = \left(\sum_{i=1}^d |\alpha_i|^q \right)^{1/q}$ is the so-called q-norm of $\boldsymbol{\alpha} \in \mathbb{N}^d$.

Furthermore, an alternative truncation scheme consists in prescribing a maximal *interaction order* for the PCE basis $(\psi_{\boldsymbol{\alpha}})_{\boldsymbol{\alpha} \in \mathbb{N}^d}$, as described in Blatman and Sudret (2008).

1.2.4.3 PCE coefficients computation

Once a truncation set $\mathcal{A} \subset \mathbb{N}^d$ has been specified, the PCE coefficients $(c_{\boldsymbol{\alpha}})_{\boldsymbol{\alpha} \in \mathcal{A}}$ have to be computed. Historically, this was achieved by using *intrusive* techniques in the context of the spectral stochastic finite element method developed in the 90s (Ghanem and Spanos, 1990, 1991b). In this context, Galerkin schemes constitute archetypal examples of intrusive techniques (Frauenfelder et al., 2005). Then, *non-intrusive* techniques emerged as an alternative to Galerkin schemes. Such techniques are said to be non-intrusive in the sense that they only require point-wise evaluations of the computational model. They notably include *quadrature* methods (Novak and Ritter, 1999), *stochastic collocation* (Babuška et al., 2007; Bieri and Schwab, 2009; Xiu and Hesthaven, 2005) and *regression* methods (Berveiller et al., 2006; Blatman and Sudret, 2010; Choi et al., 2004). The latter have been popularized in the recent years, notably through the use of *sparse regression* techniques (Blatman and Sudret, 2011b), which notably enable the construction of accurate *sparse* PCE surrogates from few model evaluations (Lüthen et al., 2021b). Furthermore, sparse PCE have been demonstrated to be more efficient than other classical PCE computational approaches (Lüthen et al., 2021b; Mathelin and Gallivan, 2012). Consequently, sparse regression-based PCE techniques will be preferred in this thesis. A brief description of such techniques is given hereafter.

Firstly, *Ordinary Least Squares* (OLS) constitute the basis of regression-based approaches. Let $\mathcal{X} = \{\boldsymbol{x}^{(k)}\}_{1 \leq k \leq N} \subset \mathcal{D}_{\boldsymbol{X}}$ be an *experimental design* (ED), namely a representative input sample drawn from $\mathbb{P}_{\boldsymbol{X}}$, typically through Monte Carlo sampling, or through *space-filling* techniques such as *Latin Hypercube Sampling* (LHS) (McKay et al., 1979) or *Quasi Monte*

Carlo (QMC) techniques (Niederreiter, 1992). Let $\boldsymbol{y} = (y^{(k)})_{1\leq k\leq N} \in \mathcal{D}_Y^N$ be the vector gathering the corresponding model outputs, *i.e.* $y^{(k)} = \mathcal{M}(\boldsymbol{x}^{(k)})$, for all $k \in \{1,\dots,N\}$. Then, given a reindexing $\{\boldsymbol{\alpha} \in \mathcal{A}\} \leftrightarrow \{\boldsymbol{\alpha}_j \mid j \in \{1,\dots,P\}\}$ where $P = |\mathcal{A}|$ is the number of regressors, the PCE coefficients are gathered in a vector $\boldsymbol{c} = (c_{\boldsymbol{\alpha}_j})_{1\leq j\leq P} \in \mathbb{R}^P$, and the *regression matrix* $\boldsymbol{\Psi} \in \mathbb{R}^{N\times P}$ with entries $\Psi_{kl} = \psi_{\boldsymbol{\alpha}_l}(\boldsymbol{x}^{(k)})$ is subsequently defined. The OLS regression problem is thus defined as follows:

$$\hat{\boldsymbol{c}} = \arg\min_{\boldsymbol{c}\in\mathbb{R}^P} \|\boldsymbol{\Psi}\boldsymbol{c} - \boldsymbol{y}\|_2^2 \tag{1.41}$$

where $\|\cdot\|_2$ denotes the ℓ^2-norm of $\mathbb{R}^N$, *i.e.* $\|\boldsymbol{z}\|_2^2 = \sum_{k=1}^N z_k^2$ for $\boldsymbol{z} \in \mathbb{R}^N$.

The classical OLS problem in Eq. (1.41) admits the following solution:

$$\hat{\boldsymbol{c}} = (\boldsymbol{\Psi}^\intercal\boldsymbol{\Psi})^{-1}\boldsymbol{\Psi}^\intercal\boldsymbol{y} \tag{1.42}$$

which is well-defined if $N \geq P$. Moreover, Fajraoui et al. (2017) have suggested the heuristic number of model evaluations of $N \approx 2P, 3P$ so as to obtain a somewhat robust solution. Nevertheless, such a number may be very large in the case of high-dimensional inputs and/or a high-degree PCE.

Then, sparse regression techniques aim at solving the regression problem in Eq. (1.41) while favoring *sparsity* in the coefficients, in the sense that most PCE coefficients are zero. The use of such techniques is motivated by the fact that the encountered computational models are often *compressible*, in the sense that their random response may be accurately represented by few PCE coefficients (Lüthen et al., 2021b). The so-called *sparsity-of-effects* principle (Montgomery, 2019), stating that most models describing physical phenomena are principally driven by main effects and low-order interactions, also goes in this direction.

Mathematically speaking, sparse regression aims at solving a regularized form of the OLS problem in Eq. (1.41), for instance the ℓ^1-regularized problem:

$$\hat{\boldsymbol{c}} = \arg\min_{\boldsymbol{c}\in\mathbb{R}^P} \|\boldsymbol{\Psi}\boldsymbol{c} - \boldsymbol{y}\|_2^2 + \gamma\|\boldsymbol{c}\|_1 \tag{1.43}$$

where γ is a regularization factor, and $\|\cdot\|_1$ denotes the ℓ^1-norm of $\mathbb{R}^P$, *i.e.* $\|\boldsymbol{z}\|_1 = \sum_{k=1}^P |z_k|$, for $\boldsymbol{z} \in \mathbb{R}^P$.

The problem in Eq. (1.43) may be solved by using various sparse regression techniques, including the *hybrid LARS* procedure introduced by Blatman and Sudret (2011b), based on the *Least Angle Regression* (LARS) algorithm of Efron et al. (2004). For further details about sparse regression-based PCE techniques, the reader may refer to the recent thorough literature and benchmark of Lüthen et al. (2021b).

1.2.4.4 PCE error estimators

Then, the set of PCE coefficients $(\hat{c}_{\boldsymbol{\alpha}})_{\boldsymbol{\alpha}\in\mathcal{A}}$ computed through regression on the data set $\{\mathcal{X}, \boldsymbol{y}\}$ enables to define the following PCE approximation:

$$\hat{\mathcal{M}}(\boldsymbol{X}) = \sum_{\boldsymbol{\alpha}\in\mathcal{A}} \hat{c}_{\boldsymbol{\alpha}}\psi_{\boldsymbol{\alpha}}(\boldsymbol{X}) \tag{1.44}$$

In this context, the so-called *generalization error* is defined by the $\mathbb{L}^2$-norm of the model-surrogate mismatch:

$$E_{\mathrm{G}} = \mathbb{E}\left[\left(\mathcal{M}(\boldsymbol{X}) - \hat{\mathcal{M}}(\boldsymbol{X})\right)^2\right] \tag{1.45}$$

Such an error measure could be estimated through Monte Carlo simulation. However, this would typically require a large amount of additional model calls. Instead, the generalization error in Eq. (1.45) may be estimated from samples of the experimental design $\mathcal{X}$, leading to the so-called *empirical error* estimate:

$$E_{\mathrm{E}} = \frac{1}{N}\sum_{k=1}^{N}\left(y^{(k)} - \hat{\mathcal{M}}(\boldsymbol{x}^{(k)})\right)^2 \tag{1.46}$$

This error measure may be normalized by the output variance:

$$\epsilon_{\mathrm{E}} = \frac{E_{\mathrm{E}}}{\hat{\sigma}_Y^2} \tag{1.47}$$

where $\hat{\sigma}_Y^2$ denotes the empirical variance of the response sample $\mathcal{Y} = \{\mathcal{M}(\boldsymbol{x}^{(k)})\}_{1\leq k\leq N}$:

$$\hat{\sigma}_Y^2 = \frac{1}{N-1}\sum_{k=1}^{N}\left(\mathcal{M}(\boldsymbol{x}^{(k)}) - \hat{\mu}_Y\right)^2 \tag{1.48}$$

with $\hat{\mu}_Y = \frac{1}{N}\sum_{k=1}^{N}\mathcal{M}(\boldsymbol{x}^{(k)})$.

Nevertheless, such an error estimate may sensibly underestimate the generalization error in Eq. (1.45), since it is not sensitive to *overfitting*. The so-called *Leave-One-Out* (LOO) cross-validation error (Blatman and Sudret, 2010) provides a much fair estimate of the generalization error, and is defined by:

$$E_{\mathrm{LOO}} = \frac{1}{N}\sum_{k=1}^{N}\left(y^{(k)} - \hat{\mathcal{M}}^{(\sim k)}(\boldsymbol{x}^{(k)})\right)^2 \tag{1.49}$$

where $\hat{\mathcal{M}}^{(\sim k)}$ is the PCE surrogate constructed on the experimental design $\mathcal{X}\backslash\{\boldsymbol{x}^{(k)}\}$. Instead of constructing N PCE surrogates through regression (see Section 1.2.4.3), the LOO error estimate in Eq. (1.49) may be computed analytically from a single PCE $\hat{\mathcal{M}}$ built on the whole ED $\mathcal{X}$, as derived in (Blatman, 2009, Appendix D):

$$E_{\mathrm{LOO}} = \frac{1}{N}\sum_{i=1}^{N}\left(\frac{y^{(i)} - \hat{\mathcal{M}}(\boldsymbol{x}^{(k)})}{1-a_k}\right)^2 \tag{1.50}$$

where a_k is the k-th diagonal entry of the matrix $\boldsymbol{\Psi}(\boldsymbol{\Psi}^\intercal\boldsymbol{\Psi})^{-1}\boldsymbol{\Psi}^\intercal$, $\boldsymbol{\Psi}$ being the regression matrix defined in Section 1.2.4.3.

Lastly, analogously to Eq. (1.47), a normalized version of the LOO error is given by:

$$\epsilon_{\mathrm{LOO}} = \frac{E_{\mathrm{LOO}}}{\hat{\sigma}_Y^2} \tag{1.51}$$

1.2.4.5 Principal component PCE

The PCE formulation is then extended to vector-valued computational models. Let suppose that the considered computational model is $\mathbb{R}^n$-valued, *i.e.* $\mathcal{M} : \mathcal{D}_{\boldsymbol{X}} \to \mathcal{D}_{\boldsymbol{Y}} \subset \mathbb{R}^n$. One again considers an experimental design $\mathcal{X} = \{\boldsymbol{x}^{(k)}\}_{1 \leq k \leq N} \subset \mathcal{D}_{\boldsymbol{X}}$, and the corresponding model outputs are gathered in $\mathcal{Y} = \{\boldsymbol{y}^{(k)}\}_{1 \leq k \leq N} \subset \mathcal{D}_{\boldsymbol{Y}}$.

Firstly, a straightforward way to build a vector-valued PCE consists in independently constructing n PCE surrogates (*i.e.* one per output dimension) by following the process exposed in the previous sections. Nevertheless, such an approach may be computationally expensive if the output dimension of the model is large. Moreover, some components of the model output may be sensibly correlated, which may induce redundancy between the constructed surrogates.

In order to alleviate this problem, *dimensionality reduction* techniques may be adopted so as to map the output space $\mathcal{D}_{\boldsymbol{Y}}$ to a *reduced* space $\mathcal{D}_{\boldsymbol{z}} \subset \mathbb{R}^r$ with dimension $r < n$. Such techniques include *Principal Component Analysis* (PCA) (Jolliffe, 2002; Pearson, 1901), *Kernel PCA* (KPCA) (Schölkopf et al., 1998) and *autoencoders* (Hinton and Salakhutdinov, 2006). One refers to (Lataniotis, 2019, Chapter 3) for a thorough review on such techniques, and to (Lataniotis et al., 2020) for the presentation of a surrogate modeling framework suitable for high-dimensional problems.

In particular, Blatman and Sudret (2011a) have proposed to combine PCA with PCE to efficiently surrogate vector-valued models. A brief description of this approach, named *Principal Component Polynomial Chaos Expansions* (PC-PCE), is given hereafter. Firstly, the eigendecomposition of the covariance matrix $\boldsymbol{\Sigma}_{\boldsymbol{Y}} \in \mathbb{R}^{n \times n}$ of $\boldsymbol{Y} = \mathcal{M}(\boldsymbol{X})$ is given hereafter:

$$\boldsymbol{\Sigma}_{\boldsymbol{Y}} = \mathbf{W} \boldsymbol{\Lambda} \mathbf{W}^\intercal \tag{1.52}$$

where $\mathbf{W} \in \mathbb{R}^{n \times n}$ is a matrix whose columns are the n eigenvectors $\boldsymbol{w}_1, \ldots, \boldsymbol{w}_n \in \mathbb{R}^n$ of $\boldsymbol{\Sigma}_{\boldsymbol{Y}}$ called *principal components*, and $\boldsymbol{\Lambda} \in \mathbb{R}^{n \times n}$ is the diagonal matrix whose k-th entry is the eigenvalue λ_i of $\boldsymbol{\Sigma}_{\boldsymbol{Y}}$ associated to $\boldsymbol{w}_k$, *i.e.* $\boldsymbol{\Sigma}_{\boldsymbol{Y}} \boldsymbol{w}_k = \lambda_k \boldsymbol{w}_k$. Furthermore, the eigenvalues $(\lambda_k)_{1 \leq k \leq n}$ are sorted in descending order.

Then, one considers the random vector $\boldsymbol{Z} = (Z_1, \ldots, Z_n)$ defined through the following orthogonal transformation:

$$\boldsymbol{Z} = \mathbf{W}^\intercal (\boldsymbol{Y} - \boldsymbol{\mu}_{\boldsymbol{Y}}) \tag{1.53}$$

where $\boldsymbol{\mu}_{\boldsymbol{Y}} = \mathbb{E}[\boldsymbol{Y}]$. Furthermore, due to the orthogonality of $\mathbf{W}^\intercal$, the transformation in Eq. (1.53) is invertible:

$$\boldsymbol{Y} = \boldsymbol{\mu}_{\boldsymbol{Y}} + \mathbf{W} \boldsymbol{Z} = \boldsymbol{\mu}_{\boldsymbol{Y}} + \sum_{k=1}^{n} Z_k \boldsymbol{w}_k \tag{1.54}$$

Eq. (1.54) corresponds to the discrete *Karhunen-Loève* (KL) expansion (Loève, 1977) of the model output $\boldsymbol{Y}$. Then, keeping only the first $r \leq n$ eigenvectors $\boldsymbol{w}_1, \ldots, \boldsymbol{w}_r$ in Eq. (1.54) and gathering them in the matrix $\mathbf{W}^{(r)} \in \mathbb{R}^{n \times r}$ yields the following approximation of $\boldsymbol{Y}$:

$$\boldsymbol{Y} \approx \boldsymbol{\mu}_{\boldsymbol{Y}} + \mathbf{W}^{(r)} \boldsymbol{Z}^{(r)} = \boldsymbol{\mu}_{\boldsymbol{Y}} + \sum_{k=1}^{r} Z_k \boldsymbol{w}_k \tag{1.55}$$

where $\boldsymbol{Z}^{(r)} = (Z_1, \ldots, Z_r)$ are the PCA coefficients associated to the r first principal components.

The number r is usually chosen in order to represent a prescribed fraction of the output *total variance*, defined by the trace of the output covariance matrix $\boldsymbol{\Sigma_Y}$, *i.e.* $\mathrm{tr}(\boldsymbol{\Sigma_Y}) = \sum_{k=1}^{n} \lambda_k$. The so-called *PCA error* (Blatman and Sudret, 2014; Wagner, 2021), resulting from only keeping the r first principal components, is defined by:

$$E_{\mathrm{PCA}} = \sum_{k=r+1}^{n} \lambda_k \tag{1.56}$$

This error measure may be normalized by the total variance as follows:

$$\epsilon_{\mathrm{PCA}} = \frac{E_{\mathrm{PCA}}}{\mathrm{tr}(\boldsymbol{\Sigma_Y})} \tag{1.57}$$

It is worth noting that in practice, the output mean $\boldsymbol{\mu_Y}$ and covariance matrix $\boldsymbol{\Sigma_Y}$ are not known in advance. Consequently, these quantities are usually replaced by appropriate estimators, computed from an input sample (Blatman and Sudret, 2011a).

Next, for each $p \in \{1, \ldots, r\}$, the PCA coefficient Z_p can be seen as a function of the input parameters $\boldsymbol{X}$, and may be therefore surrogated by a PCE:

$$Z_p(\boldsymbol{X}) \approx \hat{Z}_p(\boldsymbol{X}) = \sum_{\boldsymbol{\alpha} \in \mathcal{A}^{(p)}} \hat{c}_{p,\boldsymbol{\alpha}} \psi_{\boldsymbol{\alpha}}(\boldsymbol{X}) \tag{1.58}$$

where $\mathcal{A}^{(p)} \subset \mathbb{N}^d$, and $(\hat{c}_{p,\boldsymbol{\alpha}})_{\boldsymbol{\alpha} \in \mathcal{A}^{(p)}}$ are the corresponding PCE coefficients, and $(\psi_{\boldsymbol{\alpha}})_{\boldsymbol{\alpha} \in \mathcal{A}^{(p)}}$ the PCE basis.

Then, gathering the surrogates $\hat{Z}_1, \ldots, \hat{Z}_r$ in the vector $\hat{\boldsymbol{Z}} = (\hat{Z}_1, \ldots, \hat{Z}_p)^\intercal$, the output $\boldsymbol{Y}$ may be approximated as follows:

$$\boldsymbol{Y} \approx \hat{\mathcal{M}}(\boldsymbol{X}) = \boldsymbol{\mu_Y} + \mathbf{W}^{(r)} \hat{\boldsymbol{Z}}(\boldsymbol{X}) = \boldsymbol{\mu_Y} + \sum_{p=1}^{r} \hat{Z}_p(\boldsymbol{X}) \boldsymbol{w}_p \tag{1.59}$$

Thus, the construction of the PC-PCE surrogate in Eq. (1.59) enables to significantly reduce the computational burden of the initial problem, since the number r of retained principal components is expected to be small compared to the output dimension n of the model $\mathcal{M}$. However, such a construction comes at the price of additional layers of approximation. Indeed, the generalization error in Eq. (1.45) of a PC-PCE surrogate is mainly driven by three sources of error, namely the error stemming from the lossy PCA-based dimensionality reduction (*i.e.* the PCA error), the error induced by the PCE approximation of each component in Eq. (1.58), and the sampling error due to the estimation of the mean $\boldsymbol{\mu_Y}$ and covariance matrix $\boldsymbol{\Sigma_Y}$. As mentioned by Blatman and Sudret (2014), this last error may be deemed to be negligible compared to the two first-mentioned ones, though. Consequently, Blatman and Sudret (2014) have proposed the following estimate for the generalization error in Eq. (1.45):

$$E_{\mathrm{PC-PCE}} = \left(\sqrt{E_{\mathrm{PCA}}} + \sqrt{E_{\mathrm{PCE}}} \right)^2 \tag{1.60}$$

where E_{PCA} is given in Eq. (1.56), and E_{PCE} is defined by:

$$E_{\mathrm{PCE}} = \sum_{p=1}^{r} E_{\mathrm{LOO},p} \tag{1.61}$$

where $E_{\text{LOO},p}$ is the LOO error (see Eq. (1.49)) of the PCE surrogate $\hat{Z}_p$ given in Eq. (1.58). A normalized version of the error defined in Eq. (1.61) is given by:

$$\epsilon_{\text{PCE}} = \frac{E_{\text{PCE}}}{\text{tr}(\boldsymbol{\Sigma}_{\boldsymbol{Y}})} \tag{1.62}$$

Finally, Wagner (2021) has proposed to normalize the PC-PCE error in Eq. (1.60) as follows:

$$\epsilon_{\text{PC-PCE}} = \frac{E_{\text{PC-PCE}}}{\text{tr}(\boldsymbol{\Sigma}_{\boldsymbol{Y}})} = \left(\sqrt{\epsilon_{\text{PCA}}} + \sqrt{\epsilon_{\text{PCE}}}\right)^2 \tag{1.63}$$

1.2.5 Sensitivity analysis

Sensitivity Analysis (SA) aims at studying how the uncertainties in the output of a model can be apportioned to sources of uncertainties in its inputs (Saltelli et al., 2004). Although the field of SA was historically developed independently from UQ techniques, SA nowadays constitutes an integral part of a classical UQ analysis. SA typically enables to determine the most contributing input variables to the output of a model, as well as the less influential input variables, or to identify interactions within the model (Iooss and Lemaître, 2015). It also presents numerous conceptual objectives, including factor prioritization, factor fixing and model verification (Borgonovo, 2017; Saltelli et al., 2004).

A wide variety of SA methods dedicated to the analysis of outputs of black-box computational models is available in the literature[11] (Borgonovo and Plischke, 2016; Iooss, 2009). A brief and non-exhaustive overview of such methods is presented hereafter. For a more comprehensive review, the reader may for instance refer to (Borgonovo and Plischke, 2016; Iooss and Lemaître, 2015). Globally speaking, SA methods may be divided into three main categories, namely:

- *local methods:* these methods constitute the first historical SA methods, and aim at studying the impact of small input perturbations on the model output. Typically, these perturbations are applied around a nominal value, such as the mean of an input variable. Among local methods, it is possible to distinguish *differential* and *adjoint* methods. Differential methods are based on the calculation of partial derivatives of the model at some nominal values. Such derivatives may be calculated analytically (if possible), or numerically, typically through finite-difference (FD) schemes. Automatic differentiation methods may also be considered, if applicable (Griewank and Walther, 2008). Then, adjoint methods may be used when an explicit formulation of the adjoint is available, and they enable to study models with a large number of input variables (Cacuci, 1981). Nevertheless, local methods are not suitable for studying the case of multiple input variables that are simultaneously varied on a wide domain. Furthermore, when considering black-box computational models, the adjoint is rarely available, and derivatives have to be computed with FD schemes which may typically require a large amount of model evaluations.

[11] such methods refer to the denomination of *sensitivity analysis of model output* (SAMO) (Saltelli et al., 1993) often encountered in the literature.

- *screening methods:* such methods are based on a discretization of the input space in several levels, aiming at providing a fast qualitative exploration of the behavior of the model (Iooss and Lemaître, 2015). Screening methods typically enable to identify non-influential input variables for a limited computational cost, and provide a coarse sorting of the most influential inputs, called primary influential inputs (PII), among a potentially large number of variables. The so-called *One factor At Time* (OAT) method constitutes the most widely used screening method, and simply consists in varying each input while fixing the others. However, such a method suffers from several shortcomings, and has been demonstrated to be inefficient at providing a reliable SA (see *e.g.* (Saltelli and Annoni, 2010)). Then, the Morris method (Morris, 1991) constitutes a much complete screening method, based on the repetition of randomized OAT schemes. Furthermore, screening methods comprise *derivative-based global sensitivity measures* (DGSM) (Kucherenko and Iooss, 2015; Sobol' and Gershman, 1995), which may be seen as generalizations to the full input space of local differential SA methods.

- *global methods:* global methods aim at studying the impact of simultaneous variations of inputs over their domain on the model output. In this context, such methods provide *importance measures*, which constitute quantitative sensitivity indices allowing to rank input variables with respect to their relative influence. Sobol' indices (Sobol', 2001, 1993) are the most widely used importance measures when considering independent input variables. Such indices belong to the class of *variance-based* global SA methods (Prieur and Tarantola, 2015), aiming at decomposing the output variance into contributions which can be attributed to input variables or sets of input variables. Furthermore, Shapley effects (Iooss and Prieur, 2019; Owen, 2014; Song et al., 2016) constitute alternative sensitivity indices which provide relevant information compared to Sobol' indices, when considering dependent input variables. Finally, global SA approaches also comprise sensitivity indices based on *dissimilarity measures*, including the Hilbert Schmidt Independence Criterion (HSIC) (Da Veiga, 2015).

In this thesis, one will focus on Sobol' indices, since input variables will be very often supposed to be mutually independent, and since such indices may be efficiently post-processed when the model is approximated by surrogate models, typically PCE or Kriging (Le Gratiet et al., 2017; Sudret, 2008).

1.2.5.1 Sobol' sensitivity indices

Keeping the previously introduced notations, the computational model $\mathcal{M}$ is assumed to be scalar-valued and square-integrable w.r.t. $\pi_{\boldsymbol{X}}$, *i.e.* $\mathcal{M} \in \mathbb{L}^2(\pi_{\boldsymbol{X}})$. Moreover, its input variables $\boldsymbol{X}$ are still assumed to be mutually independent. It is worth noting that generalization of Sobol' indices to the case of dependent input variables have been proposed in the literature (see *e.g.* (Chastaing et al., 2012; Kucherenko et al., 2012)), but will remain out of the scope of this thesis, though.

Sobol' indices rely on the so-called *Hoeffding-Sobol' decomposition*[12] (Hoeffding, 1948; Sobol', 1993), which consists in writing the model output $Y = \mathcal{M}(\boldsymbol{X})$ as the sum of functions

[12] also referred to *functional analysis of variance* (ANOVA), or sometimes also to *high dimensional model representation* (HDMR) (Li et al., 2001).

with an increasing number of input variables:

$$\begin{aligned} Y = \mathcal{M}(\boldsymbol{X}) &= \mathcal{M}_0 + \sum_{1\leq i\leq d} \mathcal{M}_i(X_i) + \sum_{1\leq i\leq j\leq d} \mathcal{M}_{i,j}(X_i, X_j) + \cdots + \mathcal{M}_{1,\ldots,d}(\boldsymbol{X}) \\ &= \sum_{u\subseteq\{1,\ldots,d\}} \mathcal{M}_u(\boldsymbol{X}_u) \end{aligned} \tag{1.64}$$

where $\mathcal{M}_0$ is a constant, $\mathcal{M}_i$ a function of X_i, $\mathcal{M}_{i,j}$ a function of $X_i, X_j, \ldots$, and $\mathcal{M}_{1,\ldots,d}$ is a function of $\boldsymbol{X}$. The functions $(\mathcal{M}_i)_{1\leq i\leq d}$ are called *main effects*, whereas the functions $(\mathcal{M}_{i,j})_{1\leq i,j\leq d}$ and functions with higher input dimension in Eq. (1.64) are called *interactions*. All these functions have been compactly rewritten by using the notations $\mathcal{M}_u$ and $\boldsymbol{X}_u = (X_i)_{i\in u}$ for $u \subseteq \{1,\ldots,d\}$, and setting $\mathcal{M}_\varnothing = \mathcal{M}_0$ for the constant term.

The expansion in Eq. (1.64) exists and is unique if the summands $(\mathcal{M}_u)_{u\subseteq\{1,\ldots,d\}}$ are orthogonal in the sense of $\mathbb{L}^2(\pi_{\boldsymbol{X}})$ (Chastaing et al., 2012; Sobol', 1993), which reads:

$$\langle \mathcal{M}_u | \mathcal{M}_v \rangle_{\pi_{\boldsymbol{X}}} = \mathbb{E}\left[\mathcal{M}_u(\boldsymbol{X}_u)\mathcal{M}_v(\boldsymbol{X}_v)\right] = \int_{\mathcal{D}_{\boldsymbol{X}}} \mathcal{M}_u(\boldsymbol{x}_u)\mathcal{M}_v(\boldsymbol{x}_v)\pi_{\boldsymbol{X}}(\boldsymbol{x})\mathrm{d}\boldsymbol{x} = 0 \tag{1.65}$$

for all $u, v \subseteq \{1,\ldots,d\}$ such that $u \neq v$.

It follows from the orthogonality condition in Eq. (1.65) that $\mathbb{E}\left[\mathcal{M}_u(\boldsymbol{X}_u)\right] = 0$ for all $u \subseteq \{1,\ldots,d\}$ such that $u \neq \varnothing$. Consequently, the output variance admits the following decomposition:

$$\mathrm{Var}[Y] = \sum_{\varnothing\neq u\subseteq\{1,\ldots,d\}} \mathrm{Var}[\mathcal{M}_u(\boldsymbol{X}_u)] \tag{1.66}$$

Moreover, again exploiting the orthogonality property in Eq. (1.65), explicit expressions may be derived for the functions $(\mathcal{M}_u)_{u\subseteq\{1,\ldots,d\}}$ (Chastaing et al., 2012):

$$\mathcal{M}_0 = \mathbb{E}[\mathcal{M}(\boldsymbol{X})] \tag{1.67a}$$

$$\mathcal{M}_i(x_i) = \mathbb{E}[\mathcal{M}(\boldsymbol{X})|x_i] - \mathbb{E}[\mathcal{M}(\boldsymbol{X})] \tag{1.67b}$$

$$\mathcal{M}_u(\boldsymbol{x}_u) = \mathbb{E}[\mathcal{M}(\boldsymbol{X})|\boldsymbol{x}_u] - \sum_{v\subsetneq u} \mathcal{M}_v(\boldsymbol{x}_v) \tag{1.67c}$$

for all $i \in \{1,\ldots,d\}$ and $u \subseteq \{1,\ldots,d\}$ with $|u| \geq 2$.

Furthermore, the term $\mathrm{Var}[\mathcal{M}_u(\boldsymbol{X}_u)]$ in Eq. (1.66) is termed a *partial variance*, and represents the contribution of the set of variables $\boldsymbol{X}_u$ to the total variance $\mathrm{Var}[\mathcal{M}(\boldsymbol{X})]$. The Sobol' index S_u is then defined as the corresponding fraction of the total variance:

$$S_u = \frac{\mathrm{Var}[\mathcal{M}_u(\boldsymbol{X}_u)]}{\mathrm{Var}[\mathcal{M}(\boldsymbol{X})]} \tag{1.68}$$

for all $u \subseteq \{1,\ldots,d\}$ such that $u \neq \varnothing$. In this context, the *first order indices* $(S_i)_{1\leq i\leq d}$ are quantifying the influence of main effects, whereas *second order indices* $(S_{i,j})_{1\leq i,j\leq d}$ are related to the influence of second order (or bivariate) interactions, and so on.

Finally, *total Sobol' indices* are usually used in order to summarize both main effects and interactions involving each input variable (Homma and Saltelli, 1996), and are defined by:

$$T_i = \frac{\mathbb{E}[\mathrm{Var}[\mathcal{M}(\boldsymbol{X})|X_i]]}{\mathrm{Var}[\mathcal{M}(\boldsymbol{X})]} = \sum_{\substack{\varnothing\neq u\subseteq\{1,\ldots,d\} \\ i\in u}} S_u \tag{1.69}$$

for all $i \in \{1,\ldots,d\}$.

1.2.5.2 PCE-based Sobol' indices

The Sobol' indices in Eq. (1.68) may be computed through Monte Carlo simulation, based on several estimators proposed in the literature (see *e.g.* Homma and Saltelli (1996); Janon et al. (2014)). However, such an approach typically requires a large amount of model evaluations, which makes it intractable when considering costly computational models. Alternatively, when considering surrogate models such as PCE or Kriging, Sobol' indices may be computed through an analytical post-processing (Le Gratiet et al., 2017; Sudret, 2008).

Indeed, assuming that the model $\mathcal{M}$ is approximated by a PCE $\hat{\mathcal{M}} = \sum_{\boldsymbol{\alpha}\in\boldsymbol{\mathcal{A}}} \hat{c}_{\boldsymbol{\alpha}}\psi_{\boldsymbol{\alpha}}$ (see Section 1.2.4), a PCE-based Hoeffding-Sobol' decomposition can be derived, and the terms within are given by (Sudret, 2008):

$$\hat{\mathcal{M}}_u(\boldsymbol{X}) = \sum_{\boldsymbol{\alpha}\in\mathcal{A}_u} \hat{c}_{\boldsymbol{\alpha}}\psi_{\boldsymbol{\alpha}}(\boldsymbol{X}) \tag{1.70}$$

where $\mathcal{A}_u = \{\boldsymbol{\alpha} \in \mathcal{A} \mid (\alpha_i \neq 0) \Leftrightarrow (i \in u)\}$, for all $u \subseteq \{1, \ldots, d\}$ such that $u \neq \varnothing$.

Consequently, Sobol' indices in Eq. (1.68) may be approximated as follows:

$$S_u \approx \hat{S}_u = \frac{1}{\mathrm{Var}[Y]} \sum_{\boldsymbol{\alpha}\in\mathcal{A}_u\setminus\{\mathbf{0}\}} \hat{c}^2_{\boldsymbol{\alpha}} \tag{1.71}$$

where $\mathrm{Var}[Y] \approx \sum_{\boldsymbol{\alpha}\in\mathcal{A}} \hat{c}^2_{\boldsymbol{\alpha}}$ (see Eq. (1.37)).

Likewise, total Sobol' indices in Eq. (1.69) may also be approximated from PCE coefficients:

$$T_i \approx \hat{T}_i = \frac{1}{\mathrm{Var}[Y]} \sum_{\boldsymbol{\alpha}\in\mathcal{A}_i^+} \hat{c}^2_{\boldsymbol{\alpha}} \tag{1.72}$$

where $\mathcal{A}_i^+ = \{\boldsymbol{\alpha} \in \mathcal{A} \mid \alpha_i > 0\}$, for all $i \in \{1, \ldots, d\}$.

Finally, the presented analytical approximations may be extended to vector-valued models. Firstly, the formulas in Eqs. (1.71) and (1.72) may obviously be repeatedly applied when PCE surrogate modeling of the model output is performed component-wise. Alternatively, it is also possible to analytically post-process Sobol' indices from PC-PCE surrogates (see Section 1.2.4.5), as described in Appendix A.

1.2.6 Structural reliability analysis

In many engineering disciplines, ensuring the reliability of systems (*e.g.* bridges, nuclear power plants or electronic devices) is of paramount importance. In this context, the considered systems typically must meet high safety requirements, which involves small probabilities of failure. *Structural reliability analysis* aims at estimating the probability of failure (PoF) of a system with respect to a prescribed failure criterion. Structural reliability theory has been developed since the 70s, historically in the field of civil engineering structures. It is also referred to the denomination of *reliability analysis*, or *rare event estimation*.

In the context of a structural reliability analysis, the performance of the studied system is modeled by a so-called *limit-state function*[13] (LSF), whose mathematical formulation is given by:

$$\begin{aligned} \mathcal{G} \ : \ \mathcal{D}_{\boldsymbol{X}} \subset \mathbb{R}^d &\to \mathbb{R} \\ \boldsymbol{x} &\mapsto y = \mathcal{G}(\boldsymbol{x}) \end{aligned} \tag{1.73}$$

where $\mathcal{G}$ denotes the (deterministic) LSF, $\boldsymbol{x}$ a set of input parameters defined in an input space $\mathcal{D}_{\boldsymbol{X}}$, and $y = \mathcal{G}(\boldsymbol{x})$ a scalar output that indicates the performance of the system. Conventionally, the LSF $\mathcal{G}$ is formulated such that:

- $\mathcal{D}_s = \{\boldsymbol{x} \in \mathcal{D}_{\boldsymbol{X}} \mid \mathcal{G}(\boldsymbol{x}) > 0\}$ is the *safe domain*, that indicates a safe system,
- $\mathcal{D}_f = \{\boldsymbol{x} \in \mathcal{D}_{\boldsymbol{X}} \mid \mathcal{G}(\boldsymbol{x}) \leq 0\}$ is the *failure domain*, that indicates a failed system.

In this way, the LSF $\mathcal{G}$ embodies the formalization of the considered failure criterion, by inducing a bipartition of the input space $\mathcal{D}_{\boldsymbol{X}} = \mathcal{D}_s \cup \mathcal{D}_f$. Furthermore, one defines the *limit-state surface* (LSS) as the set $\partial\mathcal{D}_s = \partial\mathcal{D}_f = \{\boldsymbol{x} \in \mathcal{D}_{\boldsymbol{X}} \mid \mathcal{G}(\boldsymbol{x}) = 0\}$. It is worth noting that the so-defined LSF $\mathcal{G}$ is closely linked to the computational model $\mathcal{M}$ considered in the previous sections. The LSF may depend on the input parameters $\boldsymbol{X}$ defined in Section 1.2.3.1 and the model response $\mathcal{M}(\boldsymbol{X})$, but also possibly on additional random variables that are external to the computational model $\mathcal{M}$. For the sake of simplicity, it will be assumed that $\mathcal{G}$ and $\mathcal{M}$ share the same input parameters $\boldsymbol{X}$. In practice, the LSF is typically a deterministic function of the model response, *e.g.* $\mathcal{G}(\boldsymbol{x}) = f(\mathcal{M}(\boldsymbol{x}))$, which includes a thresholded model response $\mathcal{G}(\boldsymbol{x}) = \mathcal{M}(\boldsymbol{x}) - y_*$ (with $y_* \in \mathbb{R}$), which constitutes an archetypal example of LSF encountered in engineering applications.

Given a LSF $\mathcal{G}$, the PoF of the system is defined as follows:

$$P_f = \mathbb{P}(\mathcal{G}(\boldsymbol{X}) \leq 0) \tag{1.74}$$

Then, still assuming that $\boldsymbol{X}$ is a continuous random variable with density $\pi_{\boldsymbol{X}}$, the PoF in Eq. (1.74) may be rewritten as follows:

$$P_f = \int_{\mathcal{D}_{\boldsymbol{X}}} \mathbf{1}_{\mathcal{D}_f}(\boldsymbol{x}) \pi_{\boldsymbol{X}}(\boldsymbol{x}) \mathrm{d}\boldsymbol{x} \tag{1.75}$$

The integral involved in Eq. (1.75) is not analytically tractable in practice, notably due to the fact that the failure domain $\mathcal{D}_f$ implicitly depends on the inputs $\boldsymbol{X}$. In this context, a wide range of methods have been developed in order to solve structural reliability

[13] also known as *performance function* (Lemaire et al., 2009).

problems. A brief and general overview of such techniques is presented hereafter. For a more comprehensive presentation, the reader may refer to the classical textbooks of (Ditlevsen and Madsen, 1996; Lemaire et al., 2009; Melchers, 1999), to name a few. Three main classes of methods may be distinguished in the structural reliability literature:

- *approximation methods:* these methods constitute the first historically developed methods in structural reliability. They typically aim at estimating the integral in Eq. (1.75) through approximating the LSF with its Taylor series expansions. In this context, the *first order reliability method* (FORM) (Hasofer and Lind, 1974; Rackwitz and Flessler, 1978) constitutes the cornerstone of such approaches, and consists in linearizing the LSF near the most probable failure point, namely the so-called *design point*. Then, the *second order reliability method* (Breitung, 1989; Hohenbichler et al., 1987) has been subsequently developed, as an extension of FORM. Approximation techniques have been initially devised to estimate probabilities of failure for a limited number of model calls. Although such techniques may be very efficient in some simple configurations, they typically tend to be inefficient when confronted to high-dimensional problems with possibly complex LSF geometries.

- *simulation methods:* simulation methods provide more robust (and more costly, though) approaches for estimating probabilities of failure. They notably encompass the widely used *Monte Carlo simulation* (MCS) method (Metropolis and Ulam, 1949), *subset simulation* (SuS) (Au and Beck, 2001), *line sampling* (Koutsourelakis et al., 2004), *importance sampling* (IS) (Melchers, 1989) and many IS variants (Dubourg et al., 2011; Uribe et al., 2021).

- *active learning methods:* such methods have been developed more recently, along with the development of powerful surrogate modeling techniques. Active learning methods are based on the coupling of surrogate models with the aforementioned simulation methods, in order to accelerate the latter when considering costly LSFs. The main idea behind active learning methods consists in adaptively enriching an experimental design of a surrogate model, in order to predict the sign of the LSF more accurately. In this context, Kriging surrogates are widely used due to the local features they provide, including local error estimate given by their prediction variance (Kaymaz, 2005). The *efficient global reliability analysis* (EGRA) method of Bichon et al. (2008) constitutes one of the first developed active learning techniques. Then, the so-called *adaptive kriging Monte Carlo simulation* (AK-MCS) (Echard et al., 2011) constitutes the most widely used active learning method. Globally speaking, active learning techniques share a common structure, which may be summarized in fours building bricks (Moustapha et al., 2022), namely: (i) a *learning function* that enables to select enrichment points; (ii) a reliability algorithm that estimates the targeted PoF; (iii) a type of surrogate model; (iv) a *stopping criterion* for the adaptive enrichment. For further details about active learning methods, the reader may refer to the comprehensive survey and benchmark of Moustapha et al. (2022).

In this thesis, the MCS and SuS methods will be considered, and will be possibly coupled with surrogate models in an active learning perspective. A brief presentation of the two aforementioned simulation methods is given hereafter.

1.2.6.1 Monte Carlo simulation

The Monte Carlo simulation (MCS) method presented in Section 1.2.3.5 may be readily applied in the framework of structural reliability, so as to estimate probabilities of rare events. Considering a sample $\{\boldsymbol{x}^{(k)}\}_{1\leq k\leq N} \subset \mathcal{D}_{\boldsymbol{X}}$ formed by independent realizations of the inputs $\boldsymbol{X}$, the PoF in Eq. (1.75) may be estimated by:

$$P_f \approx \hat{P}_{f,N} = \frac{1}{N}\sum_{k=1}^{N} \mathbf{1}_{\mathcal{D}_f}(\boldsymbol{x}^{(k)}) \tag{1.76}$$

The above estimator is unbiased, and has the following theoretical coefficient of variation:

$$\mathrm{CoV}\left[\hat{P}_{f,N}\right] = \sqrt{\frac{1-\hat{P}_{f,N}}{N\hat{P}_{f,N}}} \tag{1.77}$$

Nevertheless, it stems from Eq. (1.77) that MCS sensibly losses efficiency when confronted to small probabilities of failure (*e.g.* $P_f \approx 10^{-6}$). For instance, in order to achieve a target CoV of $\mathrm{CoV}\left[\hat{P}_{f,N}\right] = 10\%$ for the estimate of a PoF of $\hat{P}_{f,N} = 10^{-l}$ ($l \geq 1$), about $N \approx 10^{l+2}$ samples would be necessary. Thus, despite its robust, universal and dimension-independent aspects, the MCS method may typically require a considerably large amount of samples so as to provide reliable estimators of very small probabilities of failure.

1.2.6.2 Subset simulation

Subset Simulation (SuS) is a widely used simulation method originally proposed by Au and Beck (2001). It belongs to the class of Sequential Monte Carlo (SMC) methods (Cérou et al., 2012; Del Moral et al., 2006), and is particularly well suited to estimate small probabilities of failure in high-dimensional problems. Further improvements of the original SuS method may be found in (Bect et al., 2017; Zuev et al., 2012). The main idea behind SuS consists in defining a sequence $(\mathcal{D}_f^{(i)})_{0\leq i\leq m}$ of intermediate failure domains such that $\mathcal{D}_f = \mathcal{D}_f^{(m)} \subset \cdots \subset \mathcal{D}_f^{(1)} \subset \mathcal{D}_f^{(0)} = \mathcal{D}_{\boldsymbol{X}}$, in order to write the PoF in Eq. (1.74) as the product of conditional probabilities:

$$\begin{aligned} P_f = \mathbb{P}(\mathcal{G}(\boldsymbol{X}) \leq 0) &= \mathbb{P}_{\boldsymbol{X}}(\mathcal{D}_f) \\ &= \prod_{j=1}^{m} \mathbb{P}_{\boldsymbol{X}}\left(\mathcal{D}_f^{(j)} | \mathcal{D}_f^{(j-1)}\right) \end{aligned} \tag{1.78}$$

The factors in the product in Eq. (1.78) are called *intermediate probabilities of failure*, and are denoted by $(P_f^{(j)})_{1\leq i\leq m}$. The intermediate failure domains (also called *subsets*) $(\mathcal{D}^{(j)})_{1\leq j\leq m}$ are defined from a sequence $(t_j)_{1\leq j\leq m}$ of intermediate threshold values such that $0 = t_m < \cdots < t_1$:

$$\mathcal{D}_f^{(j)} = \{\boldsymbol{x} \in \mathcal{D}_{\boldsymbol{X}} \mid \mathcal{G}(\boldsymbol{x}) \leq t_j\} \tag{1.79}$$

for all $j \in \{1, \ldots, m\}$.

The aforementioned threshold values are estimated as p_0-quantiles from a set of N samples of LSF outputs $\{\mathcal{G}(\boldsymbol{x}^{(k)})\}_{1\leq k\leq N}$, where $p_0 \in]0,1[$ is the so-called *rarity parameter*, typically set to 0.1 (Au and Beck, 2001). Thus, the rare event estimation problem in Eq. (1.74)

may be reformulated as a sequence of m intermediate problems involving larger probabilities of failure. For the first SuS level $j = 1$, the intermediate PoF reads:

$$P_f^{(1)} = \mathbb{P}_{\boldsymbol{X}}(\mathcal{D}_f^{(1)}) = \mathbb{P}(\mathcal{G}(\boldsymbol{X}) \leq t_1) = \mathbb{E}_{\pi_{\boldsymbol{X}}}\left[\mathbf{1}_{\mathcal{D}_f^{(1)}}(\boldsymbol{X})\right] \tag{1.80}$$

where $\mathbb{E}_\pi$ denotes the expectation with respect to a density $\pi \in \mathbb{L}^1(\mathcal{D}_{\boldsymbol{X}}, \mathcal{B}(\mathcal{D}_{\boldsymbol{X}}), \lambda)$, *i.e.* $\mathbb{E}_\pi[\phi(\boldsymbol{X})] = \int_{\mathcal{D}_{\boldsymbol{X}}} \phi(\boldsymbol{x})\pi(\boldsymbol{x})\mathrm{d}\boldsymbol{x}$.

Furthermore, for $j \in \{2, \ldots, m\}$:

$$P_f^{(j)} = \mathbb{P}_{\boldsymbol{X}}(\mathcal{D}_f^{(j)}|\mathcal{D}_f^{(j-1)}) = \mathbb{E}_{\pi_{\boldsymbol{X}}(\cdot|\mathcal{D}_f^{(j-1)})}\left[\mathbf{1}_{\mathcal{D}_f^{(j)}}(\boldsymbol{X})\right] \tag{1.81}$$

where the conditional density $\pi_{\boldsymbol{X}}(\cdot|\mathcal{D}_f^{(j-1)})$ is defined by:

$$\pi_{\boldsymbol{X}}(\boldsymbol{x}|\mathcal{D}_f^{(j-1)}) = \frac{1}{P_f^{(j-1)}}\pi_{\boldsymbol{X}}(\boldsymbol{x})\mathbf{1}_{\mathcal{D}_f^{(j-1)}}(\boldsymbol{x}) \tag{1.82}$$

Firstly, the probability $P_f^{(1)}$ in Eq. (1.80) may be estimated though Monte Carlo simulation (see Section 1.2.6.1). Then, the remaining probabilities $(P_f^{(j)})_{2\leq j\leq m}$ in Eq. (1.81) are estimated with Markov chain Monte Carlo (MCMC) methods (Robert and Casella, 2004), typically with the *modified Metropolis-Hastings* (mMH) algorithm proposed in (Au and Beck, 2001). Further details concerning MCMC methods will be given in Section 1.3.4. For a comprehensive presentation about MCMC algorithms dedicated to Subset Simulation, the reader may refer to (Papaioannou et al., 2015).

Then, the PoF in Eq. (1.74) may be estimated by:

$$P_f \approx \hat{P}_{f,N} = \prod_{j=1}^{m} \hat{P}_{f,N}^{(j)} \tag{1.83}$$

where $(\hat{P}_{f,N}^{(j)})_{1\leq j\leq m}$ denote the estimator of the intermediate probabilities of failure given in Eqs. (1.80) and (1.81), obtained from N samples per SuS level. Finally, an illustration of the SuS algorithm is given in Fig. 1.1.

The estimator in Eq. (1.83) is biased for a finite number N of samples, due to the correlation between the estimates $(\hat{P}_{f,N}^{(j)})_{1\leq j\leq m}$ induced by MCMC sampling (Au and Beck, 2001). Au and Beck (2001) showed that the bias is of order $\mathcal{O}(1/N)$, and therefore that the estimator in Eq. (1.83) is asymptotically unbiased. Furthermore, this bias may be treated as negligible compared to the coefficient of variation of the estimator in Eq. (1.83), as emphasized by Papaioannou et al. (2015).

Statistics related to the aforementioned estimators are discussed hereafter. Firstly, since the probability $P_f^{(1)}$ is estimated through crude Monte Carlo simulation, the coefficient of variation $\hat{\delta}_1$ of the estimator $\hat{P}_{f,N}^{(1)}$ is given by (see Section 1.2.6.1):

$$\hat{\delta}_1 = \sqrt{\frac{1 - \hat{P}_{f,N}^{(1)}}{N\hat{P}_{f,N}^{(1)}}} \tag{1.84}$$

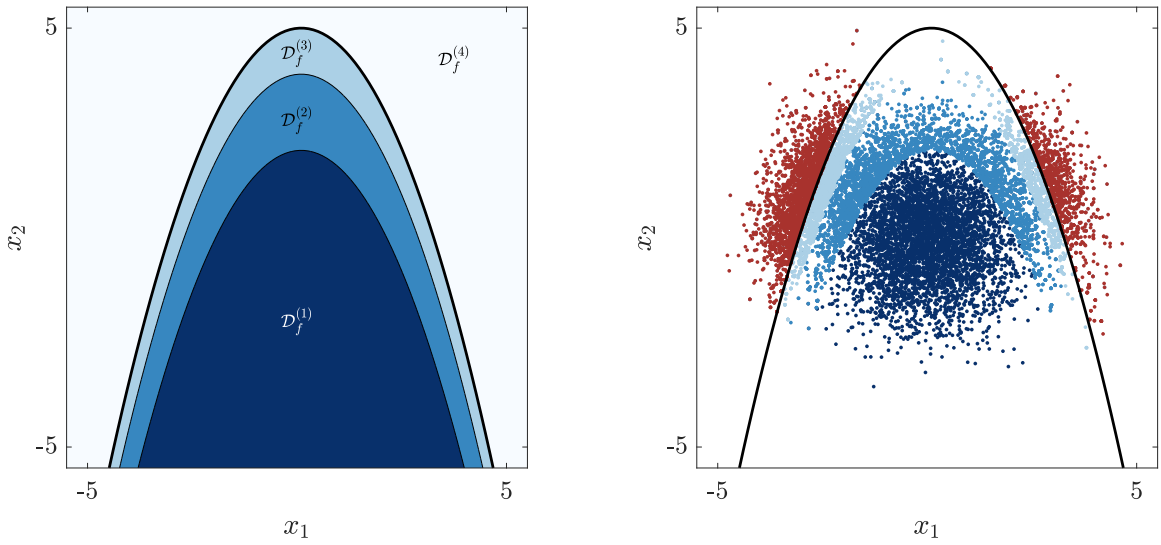

(a) SuS intermediate failure domains **(b)** SuS samples of each intermediate failure domain.

Figure 1.1: Illustration of the SuS method, in the case of a standard normal input distribution $\mathcal{N}(\mathbf{0}, \mathbf{I})$ and a parabolic LSF defined by $\mathcal{G}(x_1, x_2) = 5 - x_2 - a(x_1 - b)^2$, with $a = 0.5$ and $b = 0.1$.

Then, for $j \in \{2, \ldots, m\}$, the coefficient of variation $\hat{\delta}_j$ of $\hat{P}_{f,N}^{(j)}$ is given by (Au and Beck, 2001):

$$\hat{\delta}_j = \sqrt{\frac{1 - \hat{P}_{f,N}^{(j)}}{N \hat{P}_{f,N}^{(j)}} (1 + \gamma_j)} \tag{1.85}$$

where $\gamma_j \geq 0$ is a term which accounts for the intrinsic correlation between samples resulting from MCMC sampling. Its expression is not detailed here for the sake of conciseness, and the reader may refer to (Au and Beck, 2001; Papaioannou et al., 2015) for a derivation of the expression of γ_j. Remark that if the produced samples are independent, then $\gamma_j = 0$ and one retrieves the classical MCS coefficient of variation given in Eq. (1.84). Furthermore, Au and Beck (2001) showed that the coefficient of variation $\hat{\delta}$ of the estimator in Eq. (1.83) may be bounded as follows:

$$\sum_{j=1}^{m} \hat{\delta}_j^2 \leq \hat{\delta}^2 \leq \sum_{1 \leq i,j \leq m} \rho_{ij} \hat{\delta}_i \hat{\delta}_j \tag{1.86}$$

where ρ_{ij} is the correlation between the estimates $\hat{P}_{f,N}^{(i)}$ and $\hat{P}_{f,N}^{(j)}$. In practice, the coefficient of variation $\hat{\delta}$ is commonly estimated by the lower bound in Eq. (1.86), *i.e.* $\hat{\delta} \approx \left(\sum_{j=1}^{m} \hat{\delta}_j^2 \right)^{1/2}$ (Au and Beck, 2001). Such a choice often tends to underestimate the theoretical coefficient of variation of $\hat{P}_{f,N}$, though.

1.3 Inverse uncertainty quantification methods

1.3.1 Inverse problems

As mentioned in Section 1.2, the computational model $\mathcal{M}$ placed at the core of the UQ framework (see Fig. iii) underlies a certain directionality: given an input $\boldsymbol{x} \in \mathcal{D}_{\boldsymbol{X}}$, the model always produces an output $\mathcal{M}(\boldsymbol{x})$. In this context, *forward problems* consist in studying the effects of the inputs on the model output. Conversely, *inverse problems* typically consist in determining the inputs that caused observed data related to the model output. Broadly speaking, an inverse problem is posed when quantities that cannot be observed directly are determined from measurements of the response of a system. Inverse problems are encountered in a wide range of disciplines such as geophysics (Zhdanov, 2015), imaging science (Chalmond, 2003), computerized tomography (Herman, 2009), scattering theory (Colton and Kress, 2013) or engineering mechanics (Stavroulakis, 2001).

Formally speaking, an inverse problem may be written as follows:

$$\text{Find } \boldsymbol{x} \in \mathcal{D}_{\boldsymbol{X}} \text{ such that } \mathcal{M}(\boldsymbol{x}) = \boldsymbol{y} \tag{1.87}$$

where $\mathcal{M} : \mathcal{D}_{\boldsymbol{X}} \to \mathcal{D}_{\boldsymbol{Y}}$ is the *forward model*, which maps an input space $\mathcal{D}_{\boldsymbol{X}} \subset \mathbb{R}^d$ to a *data space* $\mathcal{D}_{\boldsymbol{Y}} \subset \mathbb{R}^n$, $\boldsymbol{x} \in \mathcal{D}_{\boldsymbol{X}}$ the sought input parameters, and $\boldsymbol{y} \in \mathcal{D}_{\boldsymbol{Y}}$ observed data. Here, the adopted terminology slightly differs from that introduced in Section 1.2. The denomination of *forward model* emphasizes the unidirectional nature of the model $\mathcal{M}$, which also embodies the indirect connection between observed data and the input parameters. Furthermore, the meaning of the space $\mathcal{D}_{\boldsymbol{Y}}$ has been enlarged by naming it *data space* rather than *output space*, since inverse problems underly connections between model outputs and observed data, the latter typically stemming from measurements on real-world systems.

Inverse problems fundamentally differ from forward problems, typically through the notion of *well-posedness*. A problem is said to be *well-posed* after Hadamard if the following three properties are satisfied (Hadamard, 1923):

- *existence:* the problem admits a solution, *i.e.* for every $\boldsymbol{y} \in \mathcal{D}_{\boldsymbol{Y}}$ there exists $\boldsymbol{x} \in \mathcal{D}_{\boldsymbol{X}}$ such that $\mathcal{M}(\boldsymbol{x}) = \boldsymbol{y}$,
- *uniqueness:* the problem admits at most one solution, *i.e.* for every $\boldsymbol{y} \in \mathcal{D}_{\boldsymbol{Y}}$ there exists at most one $\boldsymbol{x} \in \mathcal{D}_{\boldsymbol{X}}$ such that $\mathcal{M}(\boldsymbol{x}) = \boldsymbol{y}$,
- *stability:* the solution depends continuously on the data, *i.e.* for every sequence $(\boldsymbol{x}_n)_{n\in\mathbb{N}} \in \mathcal{D}_{\boldsymbol{X}}^{\mathbb{N}}$ such that $\mathcal{M}(\boldsymbol{x}_n) \to \mathcal{M}(\boldsymbol{x})$ when $n \to \infty$, one has $\boldsymbol{x}_n \to \boldsymbol{x}$ when $n \to \infty$[14].

Most physical forward problems are well-posed in this sense. Nevertheless, inverse problems are typically ill-posed, due to the fact that (at least) one of the above properties is not met, which makes such problems particularly challenging. In this context, *regularization* methods have been developed to cope with ill-posed inverse problems (Engl et al., 1996). Such methods typically include the widely used *truncated Singular Value Decomposition* (TSVD) (Hansen, 1987), *Tikhonov regularization* (Tikhonov et al., 1995) and *Landweber*

[14] the limits considered here are understood in the sense of the topologies of $\mathcal{D}_{\boldsymbol{Y}}$ and $\mathcal{D}_{\boldsymbol{X}}$, respectively.

iteration (Landweber, 1951). The reader may refer to (Isakov, 2006; Kirsch, 2011) for a comprehensive overview on classical deterministic approaches related to inverse problems.

In contrast to the aforementioned deterministic approaches, inverse problems may be studied from a more statistical, and Bayesian viewpoint in particular (Kaipio and Somersalo, 2005; Tarantola, 2005). The rationale behind such an approach is to recast the inverse problem in a statistical *quest for information* (Kaipio and Somersalo, 2005), consisting in extracting information from observed data in order to quantify uncertainties in input parameters, based on all the available knowledge related to observation noise, as well as input parameters before observing data. In this context, the variables involved in the problem are modeled by random variables, and degrees of information related to these variables are encoded by probability distributions. The Bayesian paradigm provides a natural mechanism for incorporating observations to a *prior* level of knowledge about parameters encoded by a so-called *prior distribution*, in order to derive a so-called *posterior distribution* through a conditioning operation (Robert, 2007). This posterior distribution summarizes all the available information once observations have been incorporated. Then, when adopting the aforementioned Bayesian approach, the posterior distribution is seen as the solution of the inverse problem. This philosophy contrasts with traditional deterministic approaches for inverse problems: when the latter try to find *the value* of a given parameter, the Bayesian viewpoint aims at determining *the information* about this aforesaid parameter (Kaipio and Somersalo, 2005). This implies different mathematical objects, namely single point estimates for the former, and probability distributions for the latter. Furthermore, formulating an inverse problem in a Bayesian fashion and imposing a prior distribution for the sought parameters may be seen as a regularization procedure (Calvetti and Somersalo, 2018; Idier, 2008). A comprehensive presentation about the mathematical aspects of Bayesian inverse problems may be found in (Stuart, 2010).

The next section aim at providing a general overview on the Bayesian approach for inverse problems. Firstly, the basic concepts of Bayesian inference are presented, in order to subsequently describing the framework of Bayesian inverse problems. Finally, computational approaches for Bayesian inverse problems are presented.

1.3.2 Bayesian inference

1.3.2.1 Likelihood function

The main basics of Bayesian statistical inference are exposed hereafter. For a more comprehensive presentation, the reader may refer to the well-known textbooks (Gelman et al., 2013; Robert, 2007). In this section, $\boldsymbol{X} : \Omega \to \mathcal{D}_{\boldsymbol{X}} \subset \mathbb{R}^d$ denotes the unknown parameters of a statistical model, whereas $\boldsymbol{Y} : \Omega \to \mathcal{D}_{\boldsymbol{Y}} \subset \mathbb{R}^n$ are related observables. Moreover, these two random variables are each assumed to admit a density. Bayesian inference aims at identifying the parameters $\boldsymbol{X}$ from realizations of the observables $\boldsymbol{Y}$, in a statistical fashion. In this context, the connection between parameters and observables is established through the definition of a statistical model explaining the randomness of observations given realizations of parameters. This consists in specifying the conditional density $\pi(\cdot|\boldsymbol{x})$ of observables $\boldsymbol{Y}$ knowing a realization $\boldsymbol{X} = \boldsymbol{x}$, namely:

$$\boldsymbol{Y}|\boldsymbol{x} \sim \pi(\boldsymbol{y}|\boldsymbol{x}) \tag{1.88}$$

The model in Eq. (1.88) typically encapsulates a wide range of assumptions related to the observables: in the framework of Bayesian inverse problems that will be described in Section 1.3.3, such a model may typically summarize uncertainties in measurements, as well as uncertainties and inadequacies of the considered forward model (Kaipio and Somersalo, 2005).

Given observed data $\boldsymbol{y} \in \mathcal{D}_{\boldsymbol{Y}}$, the conditional density $\pi(\boldsymbol{y}|\boldsymbol{x})$ may be seen as a function of $\boldsymbol{x} \in \mathcal{D}_{\boldsymbol{X}}$. In the framework of Bayesian inference, this function is known as the *likelihood function* (Robert, 2007), and is denoted by $\mathcal{L}(\boldsymbol{x}) = \pi(\boldsymbol{y}|\boldsymbol{x})$ hereafter. Note that the dependence on the data $\boldsymbol{y} \in \mathcal{D}_{\boldsymbol{Y}}$ is deliberately omitted in the aforesaid notation, for the sake of conciseness. Moreover, the definition of the likelihood may be readily extended to the case when several observations are available. Indeed, assuming that $\{\boldsymbol{y}^{(k)}\}_{1 \leq k \leq m} \subset \mathcal{D}_{\boldsymbol{Y}}$ are independent realizations of the observables $\boldsymbol{Y}$, the likelihood function reads:

$$\mathcal{L}(\boldsymbol{x}) = \prod_{k=1}^{m} \pi(\boldsymbol{y}^{(k)}|\boldsymbol{x}) \tag{1.89}$$

1.3.2.2 Prior distribution

The Bayesian paradigm involves a subjective interpretation of probabilities: it uses probability distributions so as to model a lack of knowledge related to some variables of interest (Cox, 2006; Robert, 2007). This fundamentally contrasts with the *frequentist* viewpoint, in which probabilities are interpreted as objective frequencies (Samaniego, 2010).

Bayesian inference involves the definition of a *prior distribution* which summarizes the level of knowledge related to the parameters $\boldsymbol{X}$ before making any observation. In the continuous case, this reverts to specify a *prior density*:

$$\boldsymbol{X} \sim \pi(\boldsymbol{x}) \tag{1.90}$$

The choice of the prior distribution constitutes the most crucial point of Bayesian inference, and also the most criticized one (Robert, 2007, Chapter 3). In fact, it is also one of the most difficult step in Bayesian inference. In practice, when a sufficient amount of data concerning parameters is available, several parametric distributions (see Section 1.2.3.2) that fit well the data may exist, which implies to make a choice related to the mathematical definition of the prior distribution itself. Alternatively, the available information concerning parameters may result from a combination of previous experiments, data taken from the literature, and/or an aggregation of expert judgements. In such a case, encoding these various sources of information into a probability distribution constitutes a highly non-trivial task. As a result, the selection of the probabilistic model in Eq. (1.90) constitutes an important modeling choice.

Broadly speaking, prior distributions may be classified according to the degree of information they contain and the function they fulfill (Nagel, 2017). One may distinguish between *informative* priors, which are subjectively defined based on the level of knowledge of one or several analysts, and *non-informative* priors, constructed in a more objective fashion through some formal rules (Kass and Wasserman, 1996). The latter typically trade a subjective choice for a partly automated selection of the prior distribution (Robert, 2007). Such formal rules include the *Jeffreys prior* (Jeffreys, 1946) and the so-called *maximum entropy*

principle (Jaynes, 1957). Furthermore, when considering parametric distribution families, it is also possible to consider *conjugate priors* (Diaconis and Ylvisaker, 1979), which constitute a type of priors that were historically favored so as to facilitate Bayesian calculations.

Thus, it is important to emphasize that uncertainties are immanent to the choice of a prior distribution. This goes in the direction of second level Uncertainty Quantification, evoked in Section 1.2.3. In particular, the framework of *robust Bayesian inference* aims at studying the impact of the choice of the prior on Bayesian inference (Berger, 1990; Ruggeri et al., 2005). Moreover, *hierarchical modeling* (Congdon, 2010; Gelman and Hill, 2006; Nagel and Sudret, 2016b) allows to specify the prior in a multilevel fashion, and then reducing the influence of the choice of the prior on the resulting inference process (Robert, 2007).

1.3.2.3 Posterior distribution

Then, following Eq. (1.17), the conditional density $\pi(\boldsymbol{y}|\boldsymbol{x})$ of $\boldsymbol{Y}$ given $\boldsymbol{X} = \boldsymbol{x}$ may be written as follows:

$$\pi(\boldsymbol{y}|\boldsymbol{x}) = \frac{\pi(\boldsymbol{x}, \boldsymbol{y})}{\pi(\boldsymbol{x})} \tag{1.91}$$

where $\pi(\boldsymbol{x}, \boldsymbol{y})$ is the joint density of $(\boldsymbol{X}, \boldsymbol{Y}) : \Omega \to \mathcal{D}_{\boldsymbol{X}} \times \mathcal{D}_{\boldsymbol{Y}}$, and $\pi(\boldsymbol{x})$ is the prior density of $\boldsymbol{X}$. Likewise, the conditional density $\pi(\boldsymbol{x}|\boldsymbol{y})$ of $\boldsymbol{X}$ knowing $\boldsymbol{Y} = \boldsymbol{y}$ reads:

$$\pi(\boldsymbol{x}|\boldsymbol{y}) = \frac{\pi(\boldsymbol{x}, \boldsymbol{y})}{\pi(\boldsymbol{y})} \tag{1.92}$$

Thus, given $\boldsymbol{y} \in \mathcal{D}_{\boldsymbol{Y}}$, combining Eqs. (1.91) and (1.92) yields the well-known Bayes' theorem for continuous random variables:

$$\pi(\boldsymbol{x}|\boldsymbol{y}) = \frac{\pi(\boldsymbol{x})\mathcal{L}(\boldsymbol{x})}{Z} \tag{1.93}$$

where $\pi(\boldsymbol{x}|\boldsymbol{y})$ is the *posterior density*, $\mathcal{L}(\boldsymbol{x}) = \pi(\boldsymbol{y}|\boldsymbol{x})$ the likelihood function (see Section 1.3.2.1), and $Z = \pi(\boldsymbol{y})$ is a normalizing constant termed *model evidence* or *marginal likelihood*:

$$Z = \int_{\mathcal{D}_{\boldsymbol{X}}} \mathcal{L}(\boldsymbol{x})\pi(\boldsymbol{x})\mathrm{d}\boldsymbol{x} \tag{1.94}$$

The posterior density in Eq. (1.93) summarizes all the available information related to parameters, once observed data have been collected. The corresponding posterior distribution $\mathbb{P}_{\boldsymbol{X}|\boldsymbol{y}}$ is then given by:

$$\mathbb{P}_{\boldsymbol{X}|\boldsymbol{y}}(B) = \int_B \pi(\boldsymbol{x}|\boldsymbol{y})\mathrm{d}\boldsymbol{x} \tag{1.95}$$

for all Borel set $B \in \mathcal{B}(\mathcal{D}_{\boldsymbol{X}})$. Furthermore, expectations with respect to the posterior are given by the transport theorem:

$$\mathbb{E}[\phi(\boldsymbol{X})|\boldsymbol{Y} = \boldsymbol{y}] = \int_{\mathcal{D}_{\boldsymbol{X}}} \phi(\boldsymbol{x})\pi(\boldsymbol{x}|\boldsymbol{y})\mathrm{d}\boldsymbol{x} = \int_{\mathcal{D}_{\boldsymbol{X}}} \phi(\boldsymbol{x})\frac{\mathcal{L}(\boldsymbol{x})}{Z}\pi(\boldsymbol{x})\mathrm{d}\boldsymbol{x} \tag{1.96}$$

for all measurable function $\phi : \mathcal{D}_{\boldsymbol{X}} \to \mathbb{R}$ such that $\phi \in \mathbb{L}^1(\pi(\cdot|\boldsymbol{y}))$. It is worth noting that Eq. (1.96) suggests that integration against the posterior may be recasted as a reweighted integration against the prior, the factor $\mathcal{L}(\boldsymbol{x})/Z$ in Eq. (1.96) being seen as a weight function.

Moreover, in order to quantify prior and posterior uncertainties related to observables $\boldsymbol{Y}$, *predictive* densities defined on the data space $\mathcal{D}_{\boldsymbol{Y}}$ may be constructed from the prior density in Eq. (1.90) and the posterior density in Eq. (1.93) (Robert, 2007). Firstly, the *prior predictive* density is defined by:

$$\pi(\boldsymbol{y}) = \int_{\mathcal{D}_{\boldsymbol{X}}} \pi(\boldsymbol{y}|\boldsymbol{x})\pi(\boldsymbol{x})\mathrm{d}\boldsymbol{x} \tag{1.97}$$

for all $\boldsymbol{y} \in \mathcal{D}_{\boldsymbol{Y}}$. Likewise, and assuming that future data $\boldsymbol{y}' \in \mathcal{D}_{\boldsymbol{Y}}$ and observed data $\boldsymbol{y} \in \mathcal{D}_{\boldsymbol{Y}}$ are conditionally independent, *i.e.* $\pi(\boldsymbol{y}, \boldsymbol{y}'|\boldsymbol{x}) = \pi(\boldsymbol{y}|\boldsymbol{x})\pi(\boldsymbol{y}'|\boldsymbol{x})$, the *posterior predictive* density of $\boldsymbol{Y}$ is defined by:

$$\pi(\boldsymbol{y}'|\boldsymbol{y}) = \int_{\mathcal{D}_{\boldsymbol{X}}} \pi(\boldsymbol{y}'|\boldsymbol{x})\pi(\boldsymbol{x}|\boldsymbol{y})\mathrm{d}\boldsymbol{x} \tag{1.98}$$

This density expresses the probability of observed new data $\boldsymbol{y}' \in \mathcal{D}_{\boldsymbol{Y}}$ given observed data $\boldsymbol{y} \in \mathcal{D}_{\boldsymbol{Y}}$. Such a density constitutes an appealing quantity of interest in the framework of Bayesian calibration (Wagner, 2021), since it incorporates uncertainties related to both parameters and observations in predictions.

1.3.2.4 Information gain

The information gain resulting from the transition from a prior state of knowledge to a posterior one can be quantified from the point of view of *information theory* (Lindley, 2000; MacKay, 2002). In this context, the information gain between the posterior and the prior may be measured by using the *Kullback-Leibler divergence*[15] (KLD) (Kullback and Leibler, 1951). The KLD from the prior $\mathbb{P}_{\boldsymbol{X}}$ to the posterior $\mathbb{P}_{\boldsymbol{X}|\boldsymbol{y}}$ is given by:

$$D_{\mathrm{KL}}(\mathbb{P}_{\boldsymbol{X}|\boldsymbol{y}} \| \mathbb{P}_{\boldsymbol{X}}) = \int_{\mathcal{D}_{\boldsymbol{X}}} \log\left(\frac{\pi(\boldsymbol{x}|\boldsymbol{y})}{\pi(\boldsymbol{x})}\right)\pi(\boldsymbol{x}|\boldsymbol{y})\mathrm{d}\boldsymbol{x} \tag{1.99}$$

This quantity may be seen as a measure of dissimilarity between prior and posterior distributions. Furthermore, it is never negative, and one has $D_{\mathrm{KL}}(\mathbb{P}_{\boldsymbol{X}|\boldsymbol{y}} \| \mathbb{P}_{\boldsymbol{X}}) = 0$ if and only if $\mathbb{P}_{\boldsymbol{X}|\boldsymbol{y}} = \mathbb{P}_{\boldsymbol{X}}$. Therefore, this quantity may indicate the degree of informativeness of observed data: the KLD in Eq. (1.99) is expected to be close to zero if the posterior remains close to the prior.

It is worth noting that the KLD in Eq. (1.99) does not define a distance in the mathematical sense, since it does not define a symmetric function. More precisely, KLD belongs to the class of *divergences* (Ali and Silvey, 1966; Csiszár, 1967). These mathematical objects quantify the dissimilarity between two probability measures by point-wise comparing their mass. One refers to (Peyré and Cuturi, 2019, Chapter 8) for a comprehensive overview on divergences.

1.3.2.5 Model evidence

The model evidence defined in Eq. (1.94) underlies a broader meaning than merely being a normalizing constant (for a fixed set of observed data). A comprehensive interpretation

[15] also known as *relative entropy*.

of this quantity can be made in the context of *Bayesian model selection and averaging* (Claeskens and Hjort, 2001; Wasserman, 2000), which aims at comparing several competing models that explain observed data.

Let $(\mathcal{H}_k)_{1\leq k\leq m}$ be candidate statistical models, each providing a conditional density aiming at modeling observations as in Eq. (1.88), namely:

$$\boldsymbol{Y}|\boldsymbol{x}_{\mathcal{H}_k} \sim \pi(\boldsymbol{y}|\boldsymbol{x}_{\mathcal{H}_k}, \mathcal{H}_k) \tag{1.100}$$

where $\boldsymbol{x}_{\mathcal{H}_k} \in \mathcal{D}_{\mathcal{H}_k} \subset \mathbb{R}^{d_k}$ is a realization of the parameters $\boldsymbol{X}_{\mathcal{H}_k} : \Omega \to \mathcal{D}_{\mathcal{H}_k}$ associated to the model $\mathcal{H}_k$, for each $k \in \{1, \ldots, m\}$. Furthermore, for each $k \in \{1, \ldots, m\}$, the parameters $\boldsymbol{X}_{\mathcal{H}_k}$ of the model $\mathcal{H}_k$ are endowed with a prior density $\pi(\boldsymbol{x}_{\mathcal{H}_k})$.

Bayesian model selection involves the definition of an additional layer of uncertainties related to the choice of a model in $(\mathcal{H}_k)_{1\leq k\leq m}$. One defines a prior discrete probability measure $\mathbb{P}_{\mathcal{H}}$ on the set of models $(\mathcal{H}_k)_{1\leq k\leq m}$, so that $\mathbb{P}_{\mathcal{H}}(\mathcal{H}_k)$ represents the prior plausibility of the hypothesis that $\mathcal{H}_k$ is the best model. Then, given observed data $\boldsymbol{y} \in \mathcal{D}_{\boldsymbol{Y}}$, applying Bayes' theorem in Eq. (1.93) enables to write the posterior distribution $\mathbb{P}_{\mathcal{H}|\boldsymbol{y}}$ as follows:

$$\mathbb{P}_{\mathcal{H}|\boldsymbol{y}}(\mathcal{H}_k|\boldsymbol{y}) = \frac{\mathbb{P}_{\mathcal{H}}(\mathcal{H}_k)\pi(\boldsymbol{y}|\mathcal{H}_k)}{\pi(\boldsymbol{y})} \tag{1.101}$$

where $\pi(\boldsymbol{y}|\mathcal{H}_k)$ is the model evidence associated to the posterior density $\pi(\boldsymbol{x}_{\mathcal{H}_k}|\boldsymbol{y}, \mathcal{H}_k)$ of $\boldsymbol{X}_{\mathcal{H}_k}$, and $\pi(\boldsymbol{y})$ the density of observables $\boldsymbol{Y}$. The former quantity may be written by marginalizing the likelihood $\pi(\boldsymbol{y}|\boldsymbol{x}_{\mathcal{H}_k}, \mathcal{H}_k)$ over the parameters $\boldsymbol{x}_{\mathcal{H}_k}$ of $\mathcal{H}_k$:

$$\pi(\boldsymbol{y}|\mathcal{H}_k) = \int_{\mathcal{D}_{\mathcal{H}_k}} \pi(\boldsymbol{y}|\boldsymbol{x}_{\mathcal{H}_k}, \mathcal{H}_k)\pi(\boldsymbol{x}_{\mathcal{H}_k})\mathrm{d}\boldsymbol{x}_{\mathcal{H}_k} \tag{1.102}$$

The density $\pi(\boldsymbol{y})$ may be written by marginalizing the likelihood $\pi(\boldsymbol{y}|\mathcal{H}_k)$ over the models $(\mathcal{H}_k)_{1\leq k\leq m}$, namely:

$$\pi(\boldsymbol{y}) = \sum_{k=1}^{m} \pi(\boldsymbol{y}|\mathcal{H}_k)\mathbb{P}_{\mathcal{H}}(\mathcal{H}_k) \tag{1.103}$$

Then, assuming a uniform prior for the models $(\mathcal{H}_k)_{1\leq k\leq m}$ (*i.e.* $\mathbb{P}_{\mathcal{H}}(\mathcal{H}_k) = 1/m$, for all $k \in \{1, \ldots, m\}$), the posterior in Eq. (1.101) simply rewrites:

$$\mathbb{P}_{\mathcal{H}|\boldsymbol{y}}(\mathcal{H}_k|\boldsymbol{y}) = \frac{Z_k}{\sum_{l=1}^{m} Z_l} \tag{1.104}$$

where $Z_k = \pi(\boldsymbol{y}|\mathcal{H}_k)$ is the model evidence associated to $\mathcal{H}_k$, for each $k \in \{1, \ldots, m\}$. The probability in Eq. (1.104) expresses how likely is the model $\mathcal{H}_k$ given the observed data $\boldsymbol{y} \in \mathcal{D}_{\boldsymbol{Y}}$. In this context, the notion of *Bayes factors* (Kass, 1993) enables to compare the different models, and hence indicates which model is more likely to have produced the observed data. The Bayes factor B_{kl} between the models $\mathcal{H}_k$ and $\mathcal{H}_l$ is defined by:

$$B_{kl} = \frac{\mathbb{P}_{\mathcal{H}|\boldsymbol{y}}(\mathcal{H}_k|\boldsymbol{y})}{\mathbb{P}_{\mathcal{H}|\boldsymbol{y}}(\mathcal{H}_l|\boldsymbol{y})} = \frac{Z_k}{Z_l} \tag{1.105}$$

where the second equality stems from the assumption of a uniform discrete prior $\mathbb{P}_{\mathcal{H}}$.

The so-called *Jeffreys' scale of evidence* provides an empirical interpretation of Bayes factors (Jeffreys, 1998). Bayesian model selection thus enables to determine which model best explains the data, and moreover enables to select the simplest one in the case when several models perform equally well. Indeed, complex models typically involve complex and large parameter spaces, which tend to present smaller model evidences (Jefferys and Berger, 1991). Thus, Bayesian model selection underlies an automatic *Occam's razor*, or *parsimony principle*. Moreover, the Eq. (1.104) enables to better emphasize the meaning of the model evidence in Eq. (1.94), as well as the relative aspect of Bayesian probabilities in general: indeed, the probabilities defined in Bayesian inference are all conditional to the adopted modeling assumptions (Nagel, 2017), and in particular the model evidence enables to weight several models with respect to their ability to explain the data.

1.3.3 Bayesian inverse problems

The basic principles of Bayesian inference exposed in Section 1.3.2 are now considered in the framework of inverse problems. Let $\mathcal{M} : \mathcal{D}_{\boldsymbol{X}} \subset \mathbb{R}^d \to \mathcal{D}_{\boldsymbol{Y}} \subset \mathbb{R}^n$ be the forward model introduced in Section 1.3.1. In this section, $\boldsymbol{X} : \Omega \to \mathcal{D}_{\boldsymbol{X}}$ denotes the unknown input parameters of $\mathcal{M}$, and $\boldsymbol{Y} : \Omega \to \mathcal{D}_{\boldsymbol{Y}}$ still denotes observables.

Solving an inverse problem seen from a Bayesian viewpoint may be divided in three subtasks (Kaipio and Somersalo, 2005). Firstly, a prior density $\pi(\boldsymbol{x})$ summarizing the available information about $\boldsymbol{X}$ before making any observation has to be elicited. Then, given observed data $\boldsymbol{y} \in \mathcal{D}_{\boldsymbol{Y}}$, a statistical model establishing a connection between the model response and observables is devised. The likelihood function $\mathcal{L}(\boldsymbol{x})$ stemming from the adopted statistical model embodies the aforesaid connection. Finally, applying Bayes' theorem in Eq. (1.93) enables to derive the posterior density $\pi(\boldsymbol{x}|\boldsymbol{y})$. Computational methods aiming at exploring the posterior distribution will be discussed in Sections 1.3.4 and 1.3.5.

Compared to general Bayesian inference presented in Section 1.3.2, the main specificity of Bayesian inverse problems lies in the definition of the likelihood function. Indeed, in the context of inverse problems, the latter encapsulates assumptions related to the discrepancies occurring between observations and the model response. Such discrepancies may typically stem from measurement noise, but also from model inadequacies. Several statistical models often encountered in the framework of Bayesian inverse problems are discussed hereafter.

1.3.3.1 Likelihood functions

In most cases, the discrepancy existing between observables and the model response for a given $\boldsymbol{x} \in \mathcal{D}_{\boldsymbol{X}}$ is modeled by a random noise term, leading to the so-called *additive noise model* denoted by (Kaipio and Somersalo, 2005):

$$\boldsymbol{Y}|\boldsymbol{x} = \mathcal{M}(\boldsymbol{x}) + \boldsymbol{E} \tag{1.106}$$

where $\boldsymbol{E} : \Omega \to \mathcal{D}_{\boldsymbol{Y}}$ is a random variable with zero mean, *i.e.* $\mathbb{E}[\boldsymbol{E}] = \boldsymbol{0}$, and independent from parameters $\boldsymbol{X}$. Assuming that $\boldsymbol{E}$ is a Gaussian random variable with covariance matrix $\boldsymbol{\Sigma} \in \mathbb{R}^{n \times n}$, *i.e.* $\boldsymbol{E} \sim \mathcal{N}(\boldsymbol{0}, \boldsymbol{\Sigma})$, the model in Eq. (1.106) leads to the following conditional distribution for the observables $\boldsymbol{Y}$:

$$\boldsymbol{Y}|\boldsymbol{x} \sim \mathcal{N}(\mathcal{M}(\boldsymbol{x}), \boldsymbol{\Sigma}) \tag{1.107}$$

Hence, given observations $\boldsymbol{y} \in \mathcal{D}_{\boldsymbol{Y}}$, the associated likelihood function reads:

$$\begin{aligned}\mathcal{L}(\boldsymbol{x}) &= \varphi(\boldsymbol{y}; \mathcal{M}(\boldsymbol{x}), \boldsymbol{\Sigma}) \\ &= \det\left(2\pi\boldsymbol{\Sigma}\right)^{-\frac{1}{2}} \exp\left(-\frac{1}{2}(\boldsymbol{y} - \mathcal{M}(\boldsymbol{x}))^{\intercal}\boldsymbol{\Sigma}^{-1}(\boldsymbol{y} - \mathcal{M}(\boldsymbol{x}))\right)\end{aligned} \tag{1.108}$$

where $\varphi(\cdot; \boldsymbol{\mu}, \boldsymbol{\Sigma})$ denotes the density of the distribution $\mathcal{N}(\boldsymbol{\mu}, \boldsymbol{\Sigma})$.

Furthermore, as mentioned in Section 1.3.2, the definition of the likelihood in Eq. (1.108) may be readily extended to the case of several observations $\{\boldsymbol{y}^{(k)}\}_{1 \leq k \leq m} \subset \mathcal{D}_{\boldsymbol{Y}}$: indeed, assuming mutually independent observations and considering a Gaussian additive noise model, the corresponding likelihood writes:

$$\mathcal{L}(\boldsymbol{x}) = \prod_{k=1}^{m} \varphi(\boldsymbol{y}^{(k)}; \mathcal{M}(\boldsymbol{x}), \boldsymbol{\Sigma}) \tag{1.109}$$

Then, it is worth noting that the formulation in Eq. (1.107) assumes that the noise covariance matrix is perfectly known, which is rarely the case in practice. Bayesian inference enables to weaken such an assumption, by devising a parametrized model for the discrepancy involved in the model in Eq. (1.106), and subsequently inferring discrepancy parameters jointly with parameters of the forward model (Nagel and Sudret, 2016b). Considering the Gaussian additive noise model in Eq. (1.107), one defines a parametrized covariance matrix $(\boldsymbol{\Sigma}(\boldsymbol{\eta}))_{\boldsymbol{\eta} \in \mathcal{D}_{\boldsymbol{N}}}$, $\mathcal{D}_{\boldsymbol{N}} \subset \mathbb{R}^p$ denoting the parameter space associated to discrepancy covariance parameters. The latter are modeled by a random variable $\boldsymbol{N} : \Omega \to \mathcal{D}_{\boldsymbol{N}}$, with a prior density $\pi(\boldsymbol{\eta})$. Hence, the conditional distribution of the discrepancy $\boldsymbol{E}$ given a realization $\boldsymbol{N} = \boldsymbol{\eta}$ is simply given by $\mathcal{N}(\boldsymbol{0}, \boldsymbol{\Sigma}(\boldsymbol{\eta}))$, *i.e.* $\boldsymbol{E}|\boldsymbol{\eta} \sim \mathcal{N}(\boldsymbol{0}, \boldsymbol{\Sigma}(\boldsymbol{\eta}))$. In this configuration, the additive model in Eq. (1.106) extends to:

$$\boldsymbol{Y}|\boldsymbol{x}, \boldsymbol{\eta} = \mathcal{M}(\boldsymbol{x}) + \boldsymbol{E}|\boldsymbol{\eta} \tag{1.110}$$

and the corresponding likelihood function reads:

$$\mathcal{L}(\boldsymbol{x}, \boldsymbol{\eta}) = \varphi(\boldsymbol{y}; \mathcal{M}(\boldsymbol{x}), \boldsymbol{\Sigma}(\boldsymbol{\eta})) \tag{1.111}$$

Thus, specifying a joint prior density $\pi(\boldsymbol{x}, \boldsymbol{\eta})$ for $(\boldsymbol{X}, \boldsymbol{N})$, typically by setting $\pi(\boldsymbol{x}, \boldsymbol{\eta}) = \pi(\boldsymbol{x})\pi(\boldsymbol{\eta})$, the posterior density of both model and discrepancy parameters can be derived by applying Bayes' theorem, *i.e.* $\pi(\boldsymbol{x}, \boldsymbol{\eta}|\boldsymbol{y}) \propto \pi(\boldsymbol{x}, \boldsymbol{\eta})\mathcal{L}(\boldsymbol{x}, \boldsymbol{\eta})$.

Finally, it is possible to consider more complex discrepancy models. For instance, it is possible to model systematic modeling biases (Higdon et al., 2004; Kennedy and O'Hagan, 2001), which are disregarded in the models in Eqs. (1.106) and (1.110). In this context, the discrepancy model in Eq. (1.110) may be augmented with a bias term $\boldsymbol{D} : \Omega \to \mathcal{D}_{\boldsymbol{Y}}$ with underlying parameters $\boldsymbol{B} : \Omega \to \mathcal{D}_{\boldsymbol{B}} \subset \mathbb{R}^q$:

$$\boldsymbol{Y}|\boldsymbol{x}, \boldsymbol{\eta}, \boldsymbol{\beta} = \mathcal{M}(\boldsymbol{x}) + \boldsymbol{E}|\boldsymbol{\eta} + \boldsymbol{D}|\boldsymbol{\beta} \tag{1.112}$$

In such a case, Bayesian inference is conducted on the whole set of parameters $(\boldsymbol{X}, \boldsymbol{N}, \boldsymbol{B})$, provided a joint prior density $\pi(\boldsymbol{x}, \boldsymbol{\eta}, \boldsymbol{\beta})$ has been specified.

1.3.3.2 Bayesian linear regression

An illustrative example of a well-known Bayesian inverse problem is presented hereafter. Let us consider the linear forward model defined by $\mathcal{M}(\boldsymbol{x}) = \mathbf{A}\boldsymbol{x}$ for $\boldsymbol{x} \in \mathcal{D}_{\boldsymbol{X}} \subset \mathbb{R}^d$, where $\mathbf{A} \in \mathbb{R}^{n\times d}$. An additive Gaussian noise model is considered for observables $\boldsymbol{Y}$, namely:

$$\boldsymbol{Y}|\boldsymbol{x} = \mathcal{M}(\boldsymbol{x}) + \boldsymbol{E} \tag{1.113}$$

where $\boldsymbol{E} \sim \mathcal{N}(\mathbf{0}, \sigma^2\mathbf{I})$, and $\sigma^2 > 0$ is the noise variance, which is here assumed to be known. Then, given observed data $\boldsymbol{y} \in \mathcal{D}_{\boldsymbol{Y}} \subset \mathbb{R}^n$, the likelihood function associated to the model in Eq. (1.113) simply writes:

$$\mathcal{L}(\boldsymbol{x}) = \varphi(\boldsymbol{y}; \mathbf{A}\boldsymbol{x}, \sigma^2\mathbf{I}) = (2\pi\sigma^2)^{-\frac{n}{2}} \exp\left(-\frac{1}{2\sigma^2}\|\boldsymbol{y} - \mathbf{A}\boldsymbol{x}\|_2^2\right) \tag{1.114}$$

Furthermore, a Gaussian prior with mean $\boldsymbol{\mu}_{\boldsymbol{X}} \in \mathbb{R}^d$ and covariance matrix $\boldsymbol{\Sigma}_{\boldsymbol{X}} \in \mathbb{R}^{d\times d}$ is assumed for the parameters $\boldsymbol{X} : \Omega \to \mathcal{D}_{\boldsymbol{X}}$. Then, it is well known that the posterior distribution is also Gaussian, whose covariance matrix and mean respectively read:

$$\boldsymbol{\Sigma}_{\boldsymbol{X}|\boldsymbol{y}} = (\boldsymbol{\Sigma}_{\boldsymbol{X}}^{-1} + \sigma^{-2}\mathbf{A}^\intercal\mathbf{A})^{-1} \tag{1.115}$$

$$\boldsymbol{\mu}_{\boldsymbol{X}|\boldsymbol{y}} = \boldsymbol{\Sigma}_{\boldsymbol{X}|\boldsymbol{y}}(\boldsymbol{\Sigma}_{\boldsymbol{X}}^{-1}\boldsymbol{\mu}_{\boldsymbol{X}} + \sigma^{-2}\mathbf{A}^\intercal\boldsymbol{y}) \tag{1.116}$$

The posterior mean in Eq. (1.116) gives an insight on the connection between Bayesian inference and classical regularization techniques for inverse problems (Calvetti and Somersalo, 2018). Indeed, when considering a standard normal prior ($\boldsymbol{\mu}_{\boldsymbol{X}} = 0$ and $\boldsymbol{\Sigma}_{\boldsymbol{X}} = \mathbf{I}$), the posterior mean in Eq. (1.116) is equal to the solution of the ℓ^2-penalized Tikhonov-regularized form of the linear inverse problem $\mathbf{A}\boldsymbol{x} = \boldsymbol{y}$ (Wagner, 2021):

$$\arg\min_{\boldsymbol{x}\in\mathcal{D}_{\boldsymbol{X}}} \|\boldsymbol{y} - \mathbf{A}\boldsymbol{x}\|_2^2 + \sigma^2\|\boldsymbol{x}\|_2^2 \tag{1.117}$$

Moreover, it is remarked that when $\sigma^2 \to \infty$, the information provided by observed data tends towards zero and hence the prior knowledge dominates, *i.e.* $\boldsymbol{\mu}_{\boldsymbol{X}|\boldsymbol{y}} = \boldsymbol{\mu}_{\boldsymbol{X}}$ and $\boldsymbol{\Sigma}_{\boldsymbol{X}|\boldsymbol{y}} = \boldsymbol{\Sigma}_{\boldsymbol{X}}$ (Nagel, 2017).

1.3.4 Markov chain Monte Carlo methods

In general, the posterior density in Eq. (1.93) is not known analytically, except in some rare cases involving conjugate distributions (Robert, 2007, Chapter 3), such as the linear inverse problem with a Gaussian prior considered in Section 1.3.3.2. Computationally speaking, exploring the posterior distribution is particularly challenging. Indeed, the model evidence in Eq. (1.94) is typically a multidimensional integral whose calculation may be intractable. Hence, only an unnormalized version of the posterior density in Eq. (1.93), namely the product of the prior density and the likelihood function, is available in practice. Furthermore, in the framework of Bayesian inverse problems, a single evaluation of the likelihood function triggers an evaluation of the forward model (see *e.g.* Eq. (1.108)). In this context, expensive forward models may considerably impede Bayesian computations.

Markov Chain Monte Carlo (MCMC) methods are the most widely used for Bayesian computations. Such methods, originally introduced by Metropolis et al. (1953) in the context

of statistical physics, aim at constructing Markov chains that are suitable for drawing samples from a target distribution. In particular, MCMC methods only require point-wise evaluations of an unnormalized version of the target density. This enables to avoid the calculation of the model evidence in Eq. (1.94), in the context of Bayesian inference.

A general overview on the basic principles of Markov chains as well as classical MCMC algorithms is given hereafter. For a more comprehensive presentation, the reader may refer to (Brooks et al., 2011; Gamerman and Lopes, 2006; Robert and Casella, 2004).

1.3.4.1 Basic principles of MCMC

The definition of a Markov chain rests on the notion of *transition kernel* (Robert and Casella, 2004, Chapter 6). A *transition kernel* is a function $\mathcal{K} : \mathcal{D}_{\boldsymbol{X}} \times \mathcal{B}(\mathcal{D}_{\boldsymbol{X}}) \to [0, 1]$ such that:

1. for all $\boldsymbol{x} \in \mathcal{D}_{\boldsymbol{X}}$, $\mathcal{K}(\boldsymbol{x}, \cdot)$ is a probability measure on $(\mathcal{D}_{\boldsymbol{X}}, \mathcal{B}(\mathcal{D}_{\boldsymbol{X}}))$,
2. for all $B \in \mathcal{B}(\mathcal{D}_{\boldsymbol{X}})$, the function : $\boldsymbol{x} \mapsto \mathcal{K}(\boldsymbol{x}, B)$ is measurable.

Intuitively, these properties state that given a current point $\boldsymbol{x} \in \mathcal{D}_{\boldsymbol{X}}$, the probability measure $\mathcal{K}(\boldsymbol{x}, \cdot)$ enables to randomly choose a new point $\boldsymbol{x}' \in \mathcal{D}_{\boldsymbol{X}}$. This plays a key role in the theory of Markov chains, the latter studying time-dependent random processes, for which the state at time $t + 1$ depends on the state at time t. In what follows, the presentation will focus on *continuous* transition kernels, namely on kernels $\mathcal{K}$ such that $\mathcal{K}(\boldsymbol{x}, \cdot)$ is absolutely continuous w.r.t. Lebesgue measure, for all $\boldsymbol{x} \in \mathcal{D}_{\boldsymbol{X}}$:

$$\mathcal{K}(\boldsymbol{x}, B) = \int_B K(\boldsymbol{x}'|\boldsymbol{x}) \mathrm{d}\boldsymbol{x}' \tag{1.118}$$

where $K(\cdot|\boldsymbol{x})$ denotes the *transition density* associated to $\mathcal{K}(\boldsymbol{x}, \cdot)$.

The notion of Markov chain is introduced hereafter. Let $(\boldsymbol{X}_t)_{t\in\mathbb{N}}$ be a $\mathcal{D}_{\boldsymbol{X}}$-valued stochastic process[16]. Then, $(\boldsymbol{X}_t)_{t\in\mathbb{N}}$ is said to be a *Markov chain* with transition kernel $\mathcal{K}$ if:

$$\begin{aligned} \mathbb{P}\left(\boldsymbol{X}_{t+1} \in B \,\middle|\, \bigcap_{s=0}^{t} \{\boldsymbol{X}_s = \boldsymbol{x}_s\} \right) &= \mathbb{P}(\boldsymbol{X}_{t+1} \in B \,|\, \boldsymbol{X}_t = \boldsymbol{x}_t) \\ &= \mathcal{K}(\boldsymbol{x}_t, B) \end{aligned} \tag{1.119}$$

for all Borel set $B \in \mathcal{B}(\mathcal{D}_{\boldsymbol{X}})$, $\{\boldsymbol{x}_s\}_{0\leq s\leq t} \subset \mathcal{D}_{\boldsymbol{X}}$ and $t \in \mathbb{N}$. In other words, the conditional distribution of $\boldsymbol{X}_{t+1}$ given $\boldsymbol{X}_0, \ldots, \boldsymbol{X}_t$ only depends on $\boldsymbol{X}_t$, and is given by $\mathcal{K}(\boldsymbol{X}_t, \cdot)$. This refers to the so-called *Markov property*: to predict the future $\boldsymbol{X}_{t+1}$ at an instant $t \in \mathbb{N}$, the knowledge of the past $\boldsymbol{X}_0, \ldots, \boldsymbol{X}_t$ does not provide more information than the present $\boldsymbol{X}_t$. Note that here the presentation is restricted to *discrete-time* Markov chains, *i.e.* to the case of variables indexed by an integer $t \in \mathbb{N}$. Furthermore, the transition kernel $\mathcal{K}(\boldsymbol{x}_t, \cdot)$ in Eq. (1.119) defining the conditional distribution of $\boldsymbol{X}_{t+1}$ given $\boldsymbol{X}_t = \boldsymbol{x}_t$ does not depend on t: this refers to a *homogeneous* Markov chain. Conversely, in the case of *inhomogeneous* Markov chains, the transition mechanism between states at instants t and $t + 1$ depends on t. It is also worth noting that a Markov chain is fully characterized by its transition kernel and the distribution of its initial state $\boldsymbol{X}_0$.

[16] *i.e.* $\boldsymbol{X}_t : \Omega \to \mathcal{D}_{\boldsymbol{X}}$ is a random variable, for all $t \in \mathbb{N}$.

Then, a probability distribution with density ρ is said to be an *invariant* (or *stationary*) distribution of the Markov chain $(\boldsymbol{X}_t)_{t\in\mathbb{N}}$ if, for all $\boldsymbol{x}' \in \mathcal{D}_{\boldsymbol{X}}$:

$$\rho(\boldsymbol{x}') = \int_{\mathcal{D}_{\boldsymbol{X}}} K(\boldsymbol{x}'|\boldsymbol{x})\rho(\boldsymbol{x})\mathrm{d}\boldsymbol{x} \tag{1.120}$$

It is worth noting that the invariance property in Eq. (1.120) holds if the following *reversibility* (or *detailed balance*) condition is fulfilled (Robert and Casella, 2004), for all $\boldsymbol{x}, \boldsymbol{x}' \in \mathcal{D}_{\boldsymbol{X}}$:

$$K(\boldsymbol{x}'|\boldsymbol{x})\rho(\boldsymbol{x}) = K(\boldsymbol{x}|\boldsymbol{x}')\rho(\boldsymbol{x}') \tag{1.121}$$

The central idea of MCMC methods is to construct a transition kernel so that the corresponding Markov chain admits the posterior distribution as an invariant distribution (Robert and Casella, 2004; Tierney, 1994). In practice, transition kernels are built in order to satisfy the reversibility condition in Eq. (1.121). Furthermore, under some conditions related to the *irreducibility*, *aperiodicity* and the *ergodicity* of the Markov chain, it is possible to show that the chain converges towards its invariant distribution, in a certain sense. A detailed mathematical description of such properties is not undertaken here, and the reader may refer to (Robert and Casella, 2004) for further details. Then, given an ergodic Markov chain $(\boldsymbol{X}_t)_{t\in\mathbb{N}}$ admitting the posterior in Eq. (1.95) as invariant distribution, the states $\{\boldsymbol{x}_t\}_{1\leq t\leq T}$ of the chain can be used as correlated samples from the posterior, provided the number of steps $T \geq 1$ is sufficiently high. In this context, expectations against the posterior (see Eq. (1.96)) may be estimated by:

$$\mathbb{E}[\phi(\boldsymbol{X})|\boldsymbol{Y} = \boldsymbol{y}] \approx \frac{1}{T}\sum_{t=1}^{T} \phi(\boldsymbol{x}_t) \tag{1.122}$$

for all function $\phi : \mathcal{D}_{\boldsymbol{X}} \to \mathbb{R}$ integrable w.r.t. the posterior, *i.e.* $\phi \in \mathbb{L}^1(\pi(\cdot|\boldsymbol{y}))$.

Eq. (1.122) can be seen as a Law of Large Numbers for ergodic Markov chains (Tierney, 1994, Theorem 3). Moreover, under some additional conditions on the Markov chain (*e.g.* *geometric* or *uniform ergodicity*) (Gelman et al., 1997; Jarner and Hansen, 2000), a central limit theorem holds for the estimate in Eq. (1.122) (see *e.g.* (Tierney, 1994)).

1.3.4.2 Metropolis-Hastings algorithm

The *Metropolis-Hastings* (MH) algorithm (Hastings, 1970; Metropolis et al., 1953) constitutes the cornerstone of MCMC algorithms. Its transition kernel is based on the coupling of a so-called *proposal* distribution with density $q(\boldsymbol{x}'|\boldsymbol{x})$ with an accept-reject correction phase. Firstly, the algorithm is initialized at an arbitrary state $\boldsymbol{x}_0 \in \mathcal{D}_{\boldsymbol{X}}$. Then, at time $t \in \mathbb{N}$, a candidate sample $\boldsymbol{x}_* \sim q(\boldsymbol{x}|\boldsymbol{x}_t)$ is drawn from the proposal distribution, and is subsequently accepted as the next state of the chain, *i.e.* $\boldsymbol{x}_{t+1} = \boldsymbol{x}_*$, with an acceptance probability given by:

$$\alpha(\boldsymbol{x}_t, \boldsymbol{x}_*) = \min\left(1, \frac{\pi(\boldsymbol{x}_*|\boldsymbol{y})q(\boldsymbol{x}_t|\boldsymbol{x}_*)}{\pi(\boldsymbol{x}_t|\boldsymbol{y})q(\boldsymbol{x}_*|\boldsymbol{x}_t)}\right) \tag{1.123}$$

Otherwise, the candidate sample $\boldsymbol{x}_*$ is rejected. The transition density $K(\cdot|\cdot)$ of the MH algorithm may be written as follows:

$$K(\boldsymbol{x}'|\boldsymbol{x}) = \alpha(\boldsymbol{x}, \boldsymbol{x}')q(\boldsymbol{x}'|\boldsymbol{x}) + (1 - \varrho(\boldsymbol{x}))\delta_{\boldsymbol{x}}(\boldsymbol{x}') \tag{1.124}$$

where:

$$\varrho(\boldsymbol{x}) = \int_{\mathcal{D}_{\boldsymbol{X}}} \alpha(\boldsymbol{x}, \boldsymbol{x}') q(\boldsymbol{x}'|\boldsymbol{x}) \mathrm{d}\boldsymbol{x} \tag{1.125}$$

It may be shown that the transition density in Eq. (1.124) satisfies the reversibility condition in Eq. (1.121), and therefore that the constructed Markov chain admits the posterior as invariant distribution (Tierney, 1994). The full MH algorithm is presented in Algorithm 1.1. It is worth noting that the calculation of the acceptance probability in Eq. (1.123) only requires the knowledge of an unnormalized version of the posterior density $\pi(\cdot|\boldsymbol{y})$, due to the presence of the ratio $\pi(\boldsymbol{x}_*|\boldsymbol{y})/\pi(\boldsymbol{x}_t|\boldsymbol{y})$.

Algorithm 1.1 Metropolis-Hastings (MH) algorithm (Hastings, 1970; Metropolis et al., 1953)

Input: posterior density $\pi(\boldsymbol{x}|\boldsymbol{y}) \propto \pi(\boldsymbol{x})\mathcal{L}(\boldsymbol{x})$, proposal density $q(\boldsymbol{x}'|\boldsymbol{x})$

Initialize $\boldsymbol{x}_0 \in \mathcal{D}_{\boldsymbol{X}}$ ▷ Select a seed in the input parameter space
for $t = 0, \ldots, T-1$ **do**
  Draw $\boldsymbol{x}_* \sim q(\boldsymbol{x}|\boldsymbol{x}_t)$ ▷ Draw a candidate sample from the proposal distribution
  Compute $\alpha(\boldsymbol{x}_t, \boldsymbol{x}_*)$ as in Eq. (1.123) ▷ Compute the acceptance probability
  Draw $u \sim \mathcal{U}([0,1])$
  if $u \leq \alpha(\boldsymbol{x}_t, \boldsymbol{x}_*)$ **then** ▷ Accept-reject phase
    Set $\boldsymbol{x}_{t+1} = \boldsymbol{x}_*$ ▷ Accept the candidate sample
  else
    Set $\boldsymbol{x}_{t+1} = \boldsymbol{x}_t$ ▷ Reject the candidate sample
  end if
end for

Output: MCMC samples $\{\boldsymbol{x}_t\}_{1 \leq t \leq T}$

Furthermore, the formulation of the acceptance probability in Eq. (1.123) constitutes a generalization proposed by Hastings (1970) of the original acceptance rule of Metropolis et al. (1953), that was based on less general proposal distributions. Indeed, when considering a *symmetric* proposal density, *i.e.* $q(\boldsymbol{x}'|\boldsymbol{x}) = q(\boldsymbol{x}|\boldsymbol{x}')$, Eq. (1.123) simply rewrites as follows:

$$\alpha(\boldsymbol{x}_t, \boldsymbol{x}_*) = \min\left(1, \frac{\pi(\boldsymbol{x}_*|\boldsymbol{y})}{\pi(\boldsymbol{x}_t|\boldsymbol{y})}\right) \tag{1.126}$$

In this context, a common choice of symmetric proposal is the Gaussian distribution with the following density:

$$q(\boldsymbol{x}'|\boldsymbol{x}) = \det\left(2\pi\boldsymbol{\Sigma}_q\right)^{-\frac{1}{2}} \exp\left(-\frac{1}{2}(\boldsymbol{x}' - \boldsymbol{x})^\intercal \boldsymbol{\Sigma}_q^{-1}(\boldsymbol{x}' - \boldsymbol{x})\right) \tag{1.127}$$

where $\boldsymbol{\Sigma}_q \in \mathbb{R}^{d \times d}$ is the proposal covariance matrix. Such a choice leads to the classical *random walk Metropolis* algorithm. An illustration of this algorithm is given in Fig. 1.2.

Besides, the MH algorithm suffers from several well-known drawbacks. Firstly, due to the Markovian nature of the algorithm, the produced samples are correlated. This typically increases the variance of Monte Carlo estimates in Eq. (1.122), which implies that a longer chain will be required to provide accurate estimates if the inter-correlation between samples is large. This inter-correlation between samples typically stems from the fact that the distance

between two subsequent states $\boldsymbol{x}_t$ and $\boldsymbol{x}_{t+1}$ is small, and/or many candidate points are rejected due to a small acceptance probability in Eq. (1.123). As a result, the proposal distribution has to be properly tuned in order to ensure a sufficiently efficient sampling, as emphasized by Fig. 1.2a, which shows a poor exploration of the posterior due to a badly scaled proposal. This typically consists in adjusting the coefficients of the proposal covariance matrix $\boldsymbol{\Sigma}_q$ in Eq. (1.127) when considering a Gaussian proposal distribution. In practice, such a tuning is often tedious, since the shape of the posterior density is not known in advance.

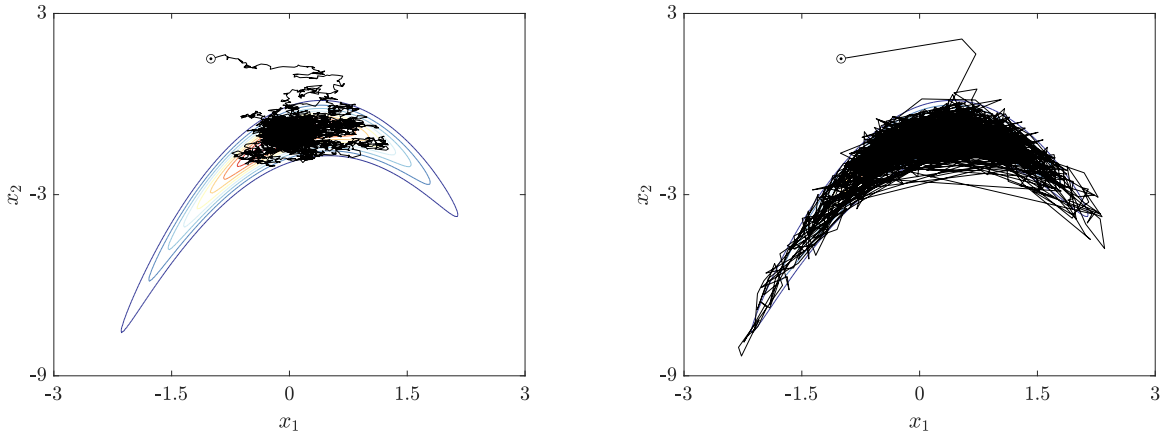

(a) $\sigma_q = 0.05$ **(b)** $\sigma_q = 1$

Figure 1.2: Illustration of the MH algorithm: case of a banana-shaped target distribution, defined as the pushforward of the distribution $\mathcal{N}(\mathbf{0}, \boldsymbol{\Sigma})$ by the map $B : \mathbb{R}^2 \to \mathbb{R}^2$ defined by $B(x_1, x_2) = (x_1, x_2 - (1 + x_2^2))$, with $\boldsymbol{\Sigma} = \begin{pmatrix} 1 & 0.9 \\ 0.9 & 1 \end{pmatrix}$. The proposal distribution is a Gaussian centered at the current state (see Eq. (1.127)), with covariance matrix $\boldsymbol{\Sigma}_q = \sigma_q^2 \mathbf{I}$.

Furthermore, the convergence of MCMC simulations is difficult to diagnose unequivocally in practice. Before the Markov chain converges to its *stationary state* (*viz.* to the posterior distribution), the produced states are possibly not distributed according to the posterior distribution, and may therefore corrupt the set of samples obtained with MCMC. This sequence of states is known as the so-called *burn-in* period (Brooks et al., 2011), and is difficult to determine in practice.

Several heuristics have been proposed in the literature in order to assess the convergence of Markov chains. Firstly, the *acceptance rate*, defined by the ratio of the number of accepted points on the total number of steps, may provide information about the mixing of the chain[17]: in the case of the MH algorithm, a large acceptance rate would indicate a poor exploration of the posterior due to strongly correlated states. Conversely, an acceptance rate close to zero would indicate that proposed samples are located in low-probability regions of the posterior. For instance, in the case of the random walk Metropolis algorithm, these information may serve as guidelines so as to properly scale the proposal covariance matrix. Moreover, the analysis of *trace plots*, that display the time evolution of a chain in each dimension of the parameter space, may serve as a qualitative tool for visualizing the quality of the produced

[17] note that the quality of a chain should not be evaluated only on the basis of acceptance rate values, though.

chains (see Fig. 1.3). Finally, in a more quantitative fashion, the convergence of MCMC simulations may be assessed by using the so-called *Gelman-Rubin diagnostic*, introduced in (Gelman and Rubin, 1992) and later generalized in (Brooks and Gelman, 1998). Based on the results of several independent chains, this indicator typically aims at comparing the second-order moments estimated from individual chains, to the ones estimated from the samples resulting from the combination of all the chains.

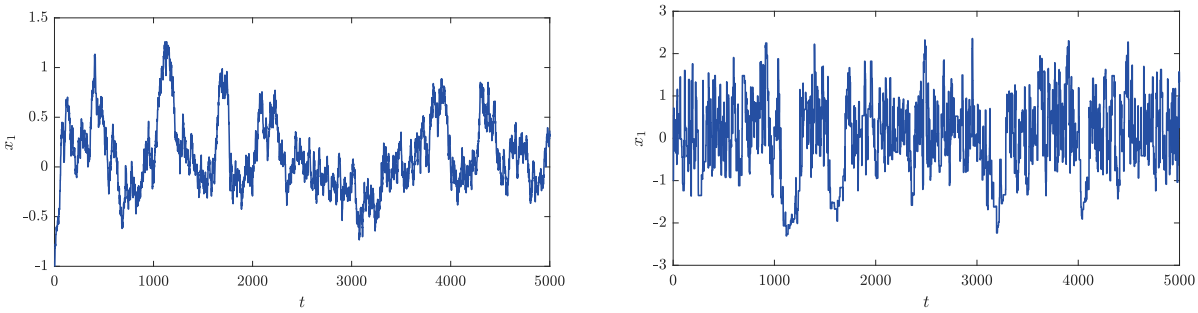

(a) $\sigma_q = 0.05$ **(b)** $\sigma_q = 1$

Figure 1.3: Illustration of the MH algorithm (*bis*): trace plots of the component x_1 of the chains displayed in Fig. 1.2.

1.3.4.3 Overview on MCMC algorithms

As mentioned earlier, the performance of the MH algorithm strongly depends on the choice of the proposal distribution. Broadly speaking, a MCMC algorithm is all the more efficient when the proposal distribution resembles the posterior. Nowadays, a wide variety of MCMC algorithms is available in the literature. Modern MCMC algorithms involve proposal mechanisms that are more sophisticated than those behind the MH algorithm (see Section 1.3.4.2), and typically aim at mimicking the behavior of the target distribution, at least locally. A brief exposition of several popular classes of MCMC algorithms is given herebelow.

- *adaptive Metropolis algorithms:* adaptive variants of the MH algorithm typically consist in tuning the covariance matrix of a Gaussian proposal throughout the sampling procedure (see *e.g.* (Haario et al., 2006, 2001)). For further details about adaptive Metropolis algorithms, the reader may refer to (Andrieu and Thoms, 2008).

- *affine-invariant ensemble samplers:* another popular MCMC algorithm is the *Affine Invariant Ensemble Sampler* (AIES) introduced by Goodman and Weare (2010). This algorithm aims at constructing an ensemble of several Markov chains, which is updated with such a transition mechanism such that the algorithm equally well samples distributions that differ from an affine transformation. In particular, this algorithm is particularly efficient when confronted to strongly correlated and more generally, badly scaled posterior distributions.

- *derivative-based algorithms:* several MCMC algorithms exploit information related to derivatives of the posterior distribution. In this context, some authors have introduced gradient-driven proposals that are constructed by analogy with models taken

from physics. Such algorithms include the *Hamiltonian Monte Carlo* (HMC)[18]. algorithm (Neal, 2011), and the *Metropolis-Adjusted Langevin Algorithm* (MALA) algorithm (Roberts and Tweedie, 1996). Moreover, derivative-based algorithms also include algorithms based on differential geometry, such as the Riemannian manifold algorithms introduced in (Girolami and Calderhead, 2011).

1.3.5 Alternative Bayesian computational techniques

Although MCMC constitutes the widely used class of Bayesian computational techniques, it still suffers from several drawbacks, some of them having been mentioned in Section 1.3.4.2. Firstly, MCMC algorithms produce samples that may be sensibly correlated (see Fig. 1.3), which may alter the accuracy of Monte Carlo estimates of posterior QoI. Furthermore, MCMC lacks of clear convergence criteria in practice, which implies the use of numerous heuristic rules (Brooks and Gelman, 1998; Cowles and Carlin, 1996; Gelman and Rubin, 1992). Classical MCMC may also be not well suited for sampling multi-modal posterior distributions, and may perform poorly when confronted to high-dimensional problems[19] (Papaioannou et al., 2015; Zuev et al., 2012). Lastly, MCMC algorithms require a large amount of likelihood evaluations, which makes them intractable when dealing with computationally expensive models.

In this framework, a widely used alternative to MCMC techniques is given by *Variational Bayesian inference* (VB) (Fox and Roberts, 2011). VB reformulates classical Bayesian inference into a deterministic optimization problem. In this context, the posterior distribution is computed through this optimization problem, by minimizing a dissimilarity measure between the posterior and a distribution sought among a candidate set of parametric distributions. Such a dissimilarity measure is often given by the KLD introduced in Section 1.3.2.4. Nevertheless, the distribution obtained by solving the aforementioned optimization problem is only an approximated form of the posterior, and may sensibly depend on the choice of the parametric class.

More recently, a broad range of alternative Bayesian computational techniques has been proposed in the literature. A selection of alternative techniques is introduced and discussed hereafter:

- *Transport maps:* the *Transport Map* (TM) approach originally introduced by El Moselhy and Marzouk (2012) provides a novel computational framework for Bayesian inference based on ideas from Optimal Transport theory (Villani, 2003, 2009). Such an approach aims at constructing a map that pushes forward the prior measure to the posterior one, by solving an optimization problem. It has also been used so as to improve the efficiency of MCMC algorithms in (Parno and Marzouk, 2018). Moreover, the TM approach has been recently used in the framework of computational mechanics by Rubio (2019), for on-line data assimilation purposes.

- *Spectral approaches:* it is worth mentioning a recent Bayesian computational approach that are neither based on random sampling nor mathematical programming,

[18] originally termed *Hybrid Monte Carlo* by Duane et al. (1987)

[19] note that advanced MCMC algorithms such as derivative-based ones (*e.g.* MALA or HMC) are suitable for high-dimensional problems, however, they may typically require an important additional cost due to evaluations of the gradient of the likelihood function.

namely *spectral likelihood expansions* (SLE). Originally introduced by Nagel and Sudret (2016a), this approach views Bayesian inference from a function approximation viewpoint, and proposes to approximate the likelihood function by a PCE surrogate model. In this framework, Bayesian QoI such as posterior joint and marginal densities, posterior moments or model evidence may be post-processed analytically from PCE coefficients. Nevertheless, as underlined in (Nagel and Sudret, 2016a), likelihood functions constitute highly nonlinear and non-negative functions, which are difficult to approximate with polynomial functions. Consequently, a sensibly large PCE degree is required to provide sufficiently accurate PCE approximations of the likelihood function. In order to alleviate such problems, Wagner et al. (2021) recently proposed an extension of the SLE approach, called *stochastic spectral likelihood embedding* (SSLE), that proposes to approximate the likelihood function with piece-wise PCE surrogates, based on a surrogate modeling approach introduced in (Marelli et al., 2021).

- *Bayesian inference with reliability methods:* lastly, Straub and Papaioannou (2015) recently introduced a novel Bayesian computational framework, known as *Bayesian updating with Structural reliability methods* (BuS). It aims at reformulating classical Bayesian inference into a structural reliability problem. In this framework, exploring the failure domain of the underlying reliability problem is akin to exploring the posterior distribution. Then, the wide portfolio of structural reliability methods may be deployed in the framework of Bayesian computations, including the SuS method (see Section 1.2.6.2), which has been demonstrated to be a powerful and robust method that is suitable for a broad range of structural reliability problems (Au et al., 2007; Schuëller et al., 2004). In particular, SuS has been adapted to the BuS framework in (Betz et al., 2018b), and has been demonstrated to be particularly efficient for sampling posteriors with complex shapes (including multi-modalities) and high dimensionalities (Uribe et al., 2020). Moreover, contrary to MCMC, the BuS framework enables to estimate the model evidence, as a byproduct of the rare event estimation (Straub and Papaioannou, 2015), which makes it suitable for Bayesian model selection (see Section 1.3.2.5).

Consequently, particular attention will be paid to this last framework, in order to provide efficient computational tools for inverse analyses performed throughout this thesis. Such a choice is motivated by the advantages listed above, which make it a promising alternative to classical MCMC sampling techniques (DiazDelaO et al., 2017), and, to a lesser extent, by the fact that structural reliability methods such as SuS are well-known in the field of reliability for civil engineering. As a result, the BuS framework and its computational features (including an adapted version of the SuS method) will be more thoroughly investigated in Chapter 2 of this thesis.

1.3.6 Surrogate modeling within Bayesian computations

Despite the notable advances they have provided, all the aforementioned Bayesian techniques typically require a large amount of evaluations of the likelihood function. Therefore, when dealing with inverse problems with costly forward models, such as multi-physic models for NCB, the aforementioned approaches are not directly tractable, since a likelihood evaluation triggers a run of the forward model (see Section 1.3.3). In such cases, this involves an

additional layer of complexity, since it becomes necessary to maintain a reasonable computational budget while efficiently exploring the posterior distribution related to the problem at hand.

This point motivates the use of surrogate models to accelerate Bayesian computations. A widely used approach consists in replacing the forward model by a surrogate model, including polynomial chaoses (Marzouk and Xiu, 2009; Marzouk and Najm, 2009; Marzouk et al., 2007; Yan and Guo, 2015), Kriging (Damblin et al., 2018; O'Hagan, 2006; Stuart and Teckentrup, 2017; Teckentrup, 2020), or neural networks (Hauser et al., 2011; Yan and Zhou, 2020). In this context, two main classes of approaches can be distinguished in the literature, namely *prior-based* and *adaptive* approaches, and are briefly presented and discussed hereafter.

1.3.6.1 Prior-based surrogates

In the framework of Bayesian inverse problems, most of the surrogate models used to replace forward models are *prior-based*, *i.e.* constructed in an offline fashion before performing Bayesian computations. Broadly speaking, a prior-based surrogate is typically constructed from an experimental design formed by samples drawn from the prior distribution, based on some global error measures that quantify its accuracy on the support of the prior (such as leave-one-out error for PCE, see Section 1.2.4.4). At first glance, such global error measures could provide information on the error on the posterior induced by the surrogate approximation: the fidelity of a surrogate-based posterior is expected to increase when the fidelity of the surrogate forward model increases.

Mathematically speaking, under some conditions related to the prior distribution (see (Ernst et al., 2012)), it is possible to show that a PCE forward model approximation converges in the *prior-weighted* $\mathbb{L}^2$ sense to the full forward model. Then, several authors demonstrated that if the surrogate forward model converges at a certain rate in this prior-weighted $\mathbb{L}^2$ sense, then the surrogate-based posterior converges to the true posterior at the same rate, in the Kullback-Leibler Divergence (KLD) sense (Birolleau et al., 2014; Marzouk and Xiu, 2009; Yan and Zhang, 2017), as well as in the Hellinger distance sense (Stuart, 2010; Yan and Zhang, 2017).

1.3.6.2 From prior-based to adaptive surrogates

Nevertheless, constructing a surrogate forward model which is globally accurate on the support of the prior may be very difficult in practice, typically when confronted to highly nonlinear forward models, with a possibly large input dimension (Li and Marzouk, 2014; Yan and Zhou, 2019). Furthermore, such a global approximation may be unnecessary, since Bayesian inverse problems typically present more structure than prior-based uncertainty propagation problems (Li and Marzouk, 2014). Indeed, when observation data are sufficiently informative, the posterior distribution typically concentrates on a narrow region of the parameter space (see Fig. 1.4 for an illustration). Therefore, to provide a satisfactory approximation of the posterior, the surrogate forward model only needs to be locally accurate near informative zones.

This underlies a well-known failure mechanism of Bayesian inversions accelerated by prior-based surrogate models: as demonstrated by Lu et al. (2015), prior-based PCE may lead to large errors on the approximated posterior, when the posterior mass is shifted suf-

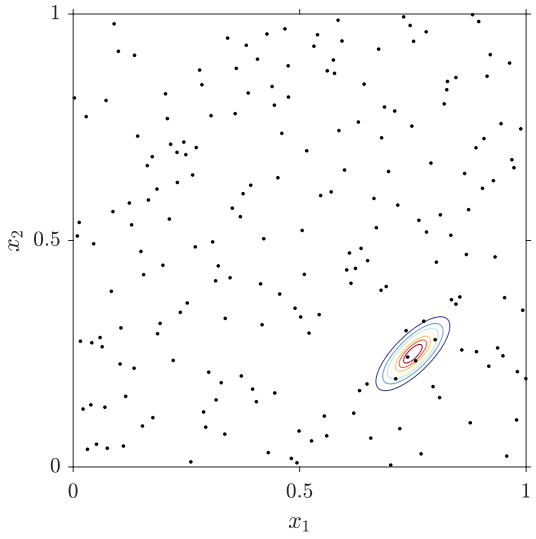

Figure 1.4: Prior-based ED in the case of a concentrated posterior. *Black dots represent samples drawn from the uniform prior* $\mathcal{U}([0,1]^2)$ *through LHS, whereas colored solid lines refer to contours of the posterior density. It is remarked that only few points of the ED fall into the high-probability zone of the posterior.*

ficiently far away from the prior high-probability zones, and/or highly concentrated on a small region of the parameter space in which the PCE forward model is inaccurate. Hence, when data are strongly informative, it may be difficult to ensure that prior-based surrogate forward models are locally accurate near high-probability zones of the posterior, only based on the analysis of global error measures on the support of the prior.

Then, in order to alleviate such problems, several authors proposed *adaptive* surrogate modeling approaches for Bayesian computations. Mostly based on MCMC, such approaches consist in refining approximations of the forward model throughout the sampling procedure. They include adaptive construction schemes for polynomial chaoses (Li and Marzouk, 2014; Yan and Zhou, 2019), deep neural networks (Yan and Zhou, 2020), Gaussian process models (Damblin et al., 2018), local approximations (Conrad et al., 2018, 2016), or reduced-order models (Cui et al., 2014).

Likewise, in the BuS framework, Giovanis et al. (2017) have proposed adaptive artificial neural networks surrogates within SuS, whereas Wang and Shafieezadeh (2020) have proposed a coupling between rejection sampling and adaptive Kriging. In Chapter 2, we will use ideas related to active-learning methods (see Section 1.2.6) in order to devise a novel adaptive surrogate modeling approach within the BuS framework.

Lastly, it is worth mentioning that some authors proposed alternatives to the aforementioned adaptive surrogate modeling approaches, including *two-stage MCMC* schemes (Christen and Fox, 2005; Efendiev et al., 2006; Elsheikh et al., 2014) that use local approximations of the forward model as filters during MCMC accept/reject phases, or approaches introducing a stochastic correction of the error between the forward model and its approximation (Cui et al., 2019; Manzoni et al., 2016).

1.4 Conclusion

This chapter has presented a general state-of-the-art review on the framework of Uncertainty Quantification (UQ). In this context, the general structure of a classical UQ analysis has been discussed, notably by emphasizing the central place occupied by deterministic computational models. The latter are viewed as input-output maps around which classical UQ tasks may be performed in a forward or inverse manner.

In a first section, forward problems in UQ have been introduced. Probability theory has firstly been briefly presented as a general tool for modeling uncertainties, before reviewing basic uncertainty propagation techniques. Surrogate modeling has subsequently been introduced as a crucial task for ensuring the tractability of forward and inverse UQ methods to expensive computational models. Then, classical methods for sensitivity analysis and reliability analysis have been reviewed. In this context, particular attention has been paid to Polynomial Chaos Expansions (PCE), which will be extensively used throughout this thesis. Indeed, PCE constitute powerful surrogates which involve several appealing analytical post-processing features, notably regarding Sobol' indices in the framework of sensitivity analysis. In addition, they may be constructed from a limited amount of model evaluations, by using sparse regression techniques. Moreover, in the framework of reliability analysis, the presentation has been focused on the well-known Subset Simulation (SuS) method, which will be used in several different ways so as to solve Bayesian and reliability problems encountered later in this thesis.

In a second section, inverse UQ methods have been introduced, starting from classical deterministic approaches for inverse problems, for then focusing on the probabilistic framework of Bayesian inference. In this framework, MCMC sampling techniques, which constitute the most widely used class of Bayesian computational methods, have been introduced. Then, more recent alternative Bayesian computational approaches have been presented. Eventually, a discussion related to the use of surrogate modeling to accelerate Bayesian computations in the case of costly computational models has been provided.

Among the aforementioned Bayesian computational approaches, particular attention has been paid to the recent framework of Bayesian updating with Structural reliability methods (BuS), which constitutes a promising alternative to classical MCMC techniques. Such an approach aims at reformulating Bayesian inference into a reliability problem, and therefore enables to use robust and efficient methods such as SuS to draw samples from posterior distributions. This last approach has been recently adapted to the BuS framework, and has been demonstrated to be well suited for Bayesian inverse problems involving possibly multimodal and/or high-dimensional posterior distributions. To a lesser extent, the choice of the BuS framework is also motivated by the connection it provides between Bayesian inference and structural reliability, whose methods are well-known in the field of civil engineering.

The next chapter aims at more thoroughly investigating the BuS framework, in order to provide computational tools which will be used to solve Bayesian inverse problems encountered throughout this thesis. Subsequently, we will propose a novel adaptive surrogate modeling approach aiming at accelerating Bayesian computations performed within the BuS framework.

2

Bayesian updating with structural reliability methods and adaptive surrogate models

Contents

2.1 Introduction

Chapter 1 has provided a general overview of Bayesian computational techniques, including MCMC sampling as well as recent alternative methods. Among the latter, particular attention has been paid to the framework of *Bayesian updating with Structural reliability methods* (BuS) recently introduced by Straub and Papaioannou (2015). Such a framework provides a reformulation of Bayesian inference into a reliability problem, and thereby enables to use powerful reliability methods such as Subset Simulation (SuS) in order to sample posterior distributions. The SuS method has been recently adapted to the BuS framework, and has been demonstrated to be a promising alternative to classical MCMC techniques (Betz et al., 2018b).

However, as any sampling technique, such a method typically requires a large amount of likelihood evaluations. Therefore, it becomes computationally intractable in the case of inverse problems with costly forward models, for instance involving complex finite element codes. In this context, Section 1.3.6 has provided a discussion related to the use of surrogate modeling within Bayesian computations. In particular, *adaptive* surrogate modeling approaches have been described as more robust regarding some drawbacks possibly encountered when considering *prior-based* surrogates.

Besides, adaptive surrogate modeling techniques specific to structural reliability problems have been extensively developed in the literature. In this context, classical simulation methods have been assisted by surrogate models in order to accelerate rare event estimation problems, for instance based on Kriging (Bichon et al., 2008; Echard et al., 2011) or Polynomial Chaos Expansions (PCE) (Marelli and Sudret, 2018). This has led to the emergence of *active-learning* methods (see Section 1.2.6), that constitute powerful approaches for solving structural reliability problems with a limited amount of full model evaluations. Active learning methods do not merely use surrogate models as simple proxies of full models, but as tools that enable to efficiently explore the input parameter space and solving the reliability problem at hand (Moustapha et al., 2022).

Consequently, we propose to fully take advantage of the connection between Bayesian inference and structural reliability established by the BuS framework, by devising an active-learning approach for Bayesian inverse problems. In this context, the proposed approach is based on the implementation of Polynomial Chaos Kriging (PCK) surrogates (see Section 1.2.4) within the SuS algorithm. In particular, the choice of PCK surrogates is motivated by the fact that they provide a global approximation power provided by a PCE trend, as well as local features provided by a the Kriging part, which makes them powerful candidates for rare event estimation, as highlighted in (Schöbi et al., 2017). Thus, the proposed approach aims at firstly building a global prior-based approximation that is adaptively refined, based on a learning criterion that selects enrichment points by exploiting the structure of the posterior distribution.

The content of this chapter is based on the published paper (Rossat et al., 2022a). Firstly, in Section 2.2, the BuS framework is introduced and investigated, and the adaptation of the SuS method to the BuS framework is subsequently presented. Section 2.3 afterwards presents the proposed active learning approach. Then, in Section 2.4, this approach is showcased through applications to several Bayesian inverse problems with varying complexity.

2.2 Bayesian updating with reliability methods

2.2.1 The BuS framework

2.2.1.1 General formulation

The basic principles behind the BuS framework are presented hereafter. Let $(\Omega, \mathcal{F}, \mathbb{P})$ be a probability space, and $\boldsymbol{X} : \Omega \to \mathcal{D}_{\boldsymbol{X}} \subset \mathbb{R}^d$ the input parameters of a forward model $\mathcal{M} : \mathcal{D}_{\boldsymbol{X}} \to \mathcal{D}_{\boldsymbol{Y}}$. The prior distribution of $\boldsymbol{X}$ is denoted by $\mathbb{P}_{\boldsymbol{X}}$ and is assumed to admit a density denoted by π. Furthermore, given observed data $\boldsymbol{y} \in \mathcal{D}_{\boldsymbol{Y}}$, let $\mathcal{L}(\boldsymbol{x}) = \pi(\boldsymbol{y}|\boldsymbol{x})$ be the likelihood function, that expresses a statistical connection between observed data and a realization $\boldsymbol{x} \in \mathcal{D}_{\boldsymbol{X}}$ of the parameters $\boldsymbol{X}$ (see Chapter 1, Section 1.3.2 for further details). The expression of the posterior density derived from Bayes' theorem is then recalled herebelow:

$$\pi(\boldsymbol{x}|\boldsymbol{y}) = \frac{\pi(\boldsymbol{x})\mathcal{L}(\boldsymbol{x})}{Z} \tag{2.1}$$

where Z is the model evidence:

$$Z = \int_{\mathcal{D}_{\boldsymbol{X}}} \mathcal{L}(\boldsymbol{x})\pi(\boldsymbol{x})\mathrm{d}\boldsymbol{x} \tag{2.2}$$

Let $\Upsilon : \Omega \to [0,1]$ be a uniform random variable, *i.e.* $\Upsilon \sim \mathcal{U}([0,1])$, such that $\boldsymbol{X}$ and Υ are mutually independent. The main idea behind BuS is to introduce the following *failure domain* in the augmented space $\mathcal{D}_{\boldsymbol{X}} \times [0,1]$ (Straub and Papaioannou, 2015):

$$\mathcal{D}_f = \{(\boldsymbol{x}, \upsilon) \in \mathcal{D}_{\boldsymbol{X}} \times [0,1] \mid \upsilon \leq C\mathcal{L}(\boldsymbol{x})\} \tag{2.3}$$

where $C > 0$ is a constant chosen such that $C\mathcal{L}(\boldsymbol{x}) \leq 1$, for all $\boldsymbol{x} \in \mathcal{D}_{\boldsymbol{X}}$. One remarks that the failure domain in Eq. (2.3) may be defined from the limit-state function $\mathcal{G} : \mathcal{D}_{\boldsymbol{X}} \times [0,1] \to \mathbb{R}$ given by:

$$\mathcal{G}(\boldsymbol{x}, \upsilon) = \upsilon - C\mathcal{L}(\boldsymbol{x}) \tag{2.4}$$

It is worth noting that the choice of the scaling constant C is non-trivial in practice. An optimal choice would consist in setting C as the inverse of the maximum of the likelihood function, *i.e.* $C^{-1} = \mathcal{L}_{\max} = \max_{\boldsymbol{x} \in \mathcal{D}_{\boldsymbol{X}}} \mathcal{L}(\boldsymbol{x})$ (this last quantity is assumed to be finite in the rest of this chapter). However, such a value is often not known in advance, typically when considering costly forward models for which classical optimization algorithms may be intractable. The choice of the scaling constant will be further discussed in Section 2.2.1.2.

Then, it is possible to show that samples from the prior distribution of $\boldsymbol{X}$ that lie in the failure domain $\mathcal{D}_f$ defined in Eq. (2.3) follow the posterior distribution (Straub and Papaioannou, 2015). Indeed, the posterior density in Eq. (2.1) may be written as follows:

$$\pi(\boldsymbol{x}|\boldsymbol{y}) = \frac{1}{P_f} \int_0^1 \mathbf{1}_{\mathcal{D}_f}(\boldsymbol{x}, \upsilon)\pi(\boldsymbol{x})\mathrm{d}\upsilon \tag{2.5}$$

where $\mathbf{1}_{\mathcal{D}_f}$ is the indicator function of the failure domain defined in Eq. (2.3), and P_f is the probability of failure defined by:

$$P_f = \mathbb{P}(\Upsilon \leq C\mathcal{L}(\boldsymbol{X})) = \mathbb{E}[\mathbf{1}_{\mathcal{D}_f}(\boldsymbol{X}, \Upsilon)] = \int_{\mathcal{D}_{\boldsymbol{X}}} \int_0^1 \mathbf{1}_{\mathcal{D}_f}(\boldsymbol{x}, \upsilon)\pi(\boldsymbol{x})\mathrm{d}\upsilon\mathrm{d}\boldsymbol{x} \tag{2.6}$$

Therefore, the posterior density may be seen as a density conditional on the failure domain $\mathcal{D}_f$, with a normalizing constant equal to the PoF P_f. This establishes the connection between Bayesian inference and structural reliability: sampling from the posterior distribution is equivalent to solving the structural reliability problem with the failure domain $\mathcal{D}_f$ defined in Eq. (2.3). Such a result constitutes the core principle of the BuS framework (see Fig. 2.1 for an illustration). It is intimately linked to classical *rejection sampling*, whose theoretical foundations are provided by the so-called *Fundamental Theorem of Simulation* (Robert and Casella, 2004, Theorem 2.15) and its corollaries (see *e.g.* (Robert and Casella, 2004, Corollary 2.17)). Rejection sampling simply consists in the following two-step procedure (Smith and Gelfand, 1992):

1. Draw a sample $\boldsymbol{x} \in \mathcal{D}_{\boldsymbol{X}}$ from the prior distribution of $\boldsymbol{X}$, and $\upsilon \in [0,1]$ from $\mathcal{U}([0,1])$,
2. If $\upsilon \leq C\mathcal{L}(\boldsymbol{x})$, then set $\boldsymbol{x}' = \boldsymbol{x}$ as the accepted value. Otherwise, return to Step 1.

In this context, we provide an alternative derivation of the validity of the BuS principle. Let $\boldsymbol{X}' : \Omega \to \mathcal{D}_{\boldsymbol{X}}$ be the random variable associated to the accepted values of $\boldsymbol{x}'$ during the rejection sampling procedure described above. Then, for all Borel set $B \in \mathcal{B}(\mathcal{D}_{\boldsymbol{X}})$:

$$\begin{aligned}
\mathbb{P}(\boldsymbol{X}' \in B) &= \mathbb{P}(\boldsymbol{X} \in B | \Upsilon \leq C\mathcal{L}(\boldsymbol{X})) \\
&= \frac{\int_B \int_0^1 \mathbf{1}_{\mathcal{D}_f}(\boldsymbol{x}, \upsilon)\pi(\boldsymbol{x})\mathrm{d}\upsilon\mathrm{d}\boldsymbol{x}}{\int_{\mathcal{D}_{\boldsymbol{X}}} \int_0^1 \mathbf{1}_{\mathcal{D}_f}(\boldsymbol{x}, \upsilon)\pi(\boldsymbol{x})\mathrm{d}\upsilon\mathrm{d}\boldsymbol{x}} \\
&= \frac{\int_B \int_0^{C\mathcal{L}(\boldsymbol{x})} \pi(\boldsymbol{x})\mathrm{d}\upsilon\mathrm{d}\boldsymbol{x}}{\int_{\mathcal{D}_{\boldsymbol{X}}} \int_0^{C\mathcal{L}(\boldsymbol{x})} \pi(\boldsymbol{x})\mathrm{d}\upsilon\mathrm{d}\boldsymbol{x}} \\
&= \int_B \pi(\boldsymbol{x}|\boldsymbol{y})\mathrm{d}\boldsymbol{x}
\end{aligned} \tag{2.7}$$

Thus, $\boldsymbol{X}'$ indeed follows the posterior distribution.

Moreover, it is worth noting that the PoF P_f in Eq. (2.1) is directly linked to the model evidence in Eq. (2.2), since it follows from Eq. (2.1) that:

$$P_f = \int_{\mathcal{D}_{\boldsymbol{X}}} \int_0^{C\mathcal{L}(\boldsymbol{x})} \pi(\boldsymbol{x})\mathrm{d}\upsilon\mathrm{d}\boldsymbol{x} = C \int_{\mathcal{D}_{\boldsymbol{X}}} \mathcal{L}(\boldsymbol{x})\pi(\boldsymbol{x})\mathrm{d}\boldsymbol{x} = CZ \tag{2.8}$$

The above relationship is particularly appealing: if an estimate of the PoF P_f is available, then an estimate for the model evidence is readily available as a byproduct of the rare event estimation procedure (Betz et al., 2018a).

2.2.1.2 BuS scaling constant

The choice of the scaling constant C involved in Eq. (2.3) plays a key role in the BuS framework (Betz et al., 2018a,b; DiazDelaO et al., 2017; Straub and Papaioannou, 2015). As mentioned earlier, the optimal choice is given by $C_{\text{opt}} = \mathcal{L}_{\max}^{-1}$. One the first hand, since the PoF P_f of the equivalent reliability problem decreases linearly with C (see Eq. (2.8)), choosing a too small value for C (*i.e.* $C \leq C_{\text{opt}}$) degrades the efficiency of the BuS approach. In such a case, samples produced by BuS still follow the posterior distribution, though. On

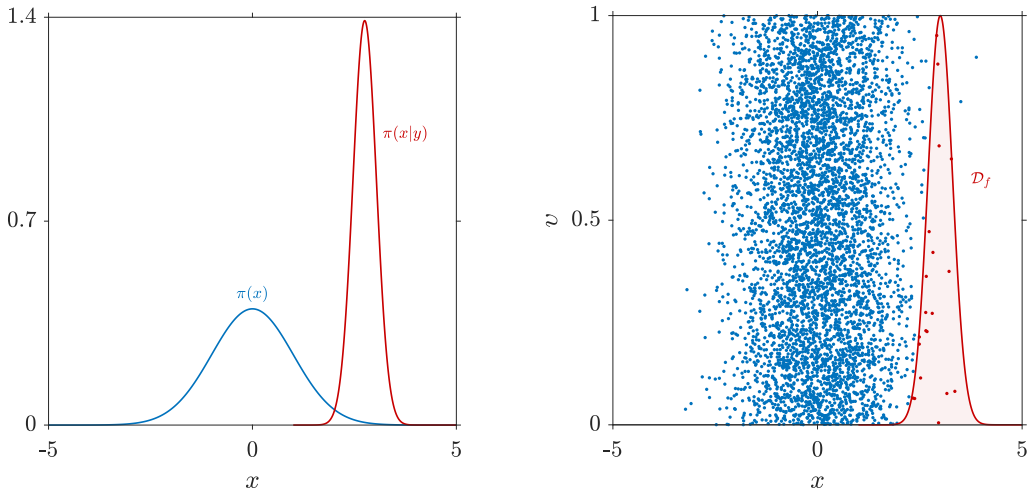

(a) Bayesian inference **(b)** Equivalent reliability problem

Figure 2.1: Illustration of the BuS framework, in the case of rejection sampling with a standard Gaussian prior and likelihood function $\mathcal{L}(x) = \varphi(x; \mu, \sigma)$ with $\mu = 3$ and $\sigma = 0.3$. In such a case, the optimal BuS constant is known and given by $C = \sqrt{2\pi}\sigma$.

the other hand, if a too large value for C (*i.e.* $C \geq C_{\text{opt}}$) is chosen, then samples produced by BuS may not follow the posterior distribution.

The effects of the choice of C are deeper investigated hereafter. Let $\mathcal{D}_C \subset \mathcal{D}_{\boldsymbol{X}}$ be the domain in which the inequality $C\mathcal{L} \leq 1$ is not satisfied, namely:

$$\mathcal{D}_C = \{\boldsymbol{x} \in \mathcal{D}_{\boldsymbol{X}} \mid C\mathcal{L}(\boldsymbol{x}) > 1\} \tag{2.9}$$

Furthermore, let π_C be the density associated to samples produced by the BuS approach, namely:

$$\pi_C(\boldsymbol{x}) = \frac{1}{\mathbb{P}_C} \int_0^1 \mathbf{1}_{\mathcal{D}_f}(\boldsymbol{x}, \upsilon)\pi(\boldsymbol{x})\mathrm{d}\upsilon \tag{2.10}$$

where $\mathbb{P}_C = \mathbb{P}(\Upsilon \leq C\mathcal{L}(\boldsymbol{X}))$ is the probability analogous to Eq. (2.6), in the case of a bad scaling choice, *i.e.* $C \geq C_{\text{opt}}$.

Then, for all $\boldsymbol{x} \in \mathcal{D}_C$, $\mathbf{1}_{\mathcal{D}_f}(\boldsymbol{x}, \upsilon) = 1$ for all $\upsilon \in [0, 1]$ and then the density π_C is proportional to the prior density:

$$\pi_C(\boldsymbol{x}) = \frac{\pi(\boldsymbol{x})}{\mathbb{P}_C} \tag{2.11}$$

Conversely, for all $\boldsymbol{x} \notin \mathcal{D}_C$, the density π_C in Eq. (2.10) is proportional to the posterior density:

$$\pi_C(\boldsymbol{x}) = C\frac{\pi(\boldsymbol{x})\mathcal{L}(\boldsymbol{x})}{\mathbb{P}_C} \propto \pi(\boldsymbol{x}|\boldsymbol{y}) \tag{2.12}$$

Thus, the density π_C in Eq. (2.10) simply rewrites:

$$\pi_C(\boldsymbol{x}) = \frac{\pi(\boldsymbol{x})\mathcal{L}_C(\boldsymbol{x})}{\mathbb{P}_C} \tag{2.13}$$

where $\mathcal{L}_C(\boldsymbol{x}) = \min(1; C\mathcal{L}(\boldsymbol{x}))$, for all $\boldsymbol{x} \in \mathcal{D}_{\boldsymbol{X}}$.

As a result, when a too large value for C is introduced, samples produced with the BuS approach are following a truncated distribution (Betz et al., 2018a; DiazDelaO et al., 2017), whose density is proportional to the prior one on the set $\mathcal{D}_C$, and to the posterior one on the set $\mathcal{D}_{\boldsymbol{X}} \setminus \mathcal{D}_C$. Such a truncated distribution induces a bias in estimates related to posterior QoI (including the model evidence), since the latter may be corrupted by samples lying in the domain $\mathcal{D}_C$.

Then, in order to overcome the selection problem of the scaling constant C, (Betz et al., 2018b, 2014) have proposed an approach consisting in adaptively tuning the BuS scaling constant within a SuS procedure. Further details on this adaptive approach will be given in Section 2.2.2.3.

2.2.1.3 BuS in standard normal space

In the framework of structural reliability problems, probabilities of failure are often estimated in the so-called *standard normal space* (also called *U-space*), *i.e.* by transforming the input distribution of the structural reliability problem into a standard normal Gaussian distribution (see Section 1.2.3.3). This could typically be achieved by using the Nataf (Nataf, 1962) or the Rosenblatt (Rosenblatt, 1952) transformation.

In this context, the structure of BuS problems enables to separately transform the input parameters $\boldsymbol{X}$ and the uniform random variable Υ. Let $\mathcal{T}_0 : \mathcal{D}_{\boldsymbol{X}} \to \mathbb{R}^d$ be a probabilistic transform which pushes forward the prior distribution to the independent standard normal distribution on $\mathbb{R}^d$. Denoting $m = d+1$ to alleviate notations, the joint distribution of $(\boldsymbol{X}, \Upsilon)$ may then be mapped to the standard normal distribution on $\mathbb{R}^m$ through the following transformation:

$$\begin{aligned} \mathcal{T} \; : \; \mathcal{D}_{\boldsymbol{X}} \times [0,1] &\to \mathbb{R}^m \\ (\boldsymbol{x}, \upsilon) &\mapsto (\mathcal{T}_0(\boldsymbol{x}), \Phi^{-1}(\upsilon)) \end{aligned} \tag{2.14}$$

where Φ is the CDF of the standard normal distribution on $\mathbb{R}$.

Therefore, it is possible to define a LSF in the standard normal space that is equivalent to the LSF $\mathcal{G}$ in the so-called *physical space* $\mathcal{D}_{\boldsymbol{X}} \times [0,1]$ defined in Eq. (2.4), by setting:

$$G(\boldsymbol{u}) = \mathcal{G}(\mathcal{T}^{-1}(\boldsymbol{u})) = \Phi(u_m) - C\mathcal{L}(\mathcal{T}_0^{-1}(\boldsymbol{u}_{1:d})) \tag{2.15}$$

for all $\boldsymbol{u} \in \mathbb{R}^m$, where the notation $\boldsymbol{u}_{1:d} = (u_1, \ldots, u_d)$ has been used. The reliability problem in the standard normal space with LSF G is indeed equivalent to that in the original space with LSF $\mathcal{G}$: since the random variable $\boldsymbol{U} = \mathcal{T}(\boldsymbol{X}, \Upsilon)$ follows the Gaussian distribution $\mathcal{N}(\mathbf{0}, \mathbf{I})$, the transport theorem (Barbé and Ledoux, 2007) enables to rewrite the PoF in Eq. (2.6) as follows:

$$P_f = \mathbb{P}(\mathcal{G}(\boldsymbol{X}, \Upsilon) \leq 0) = \mathbb{P}(G(\boldsymbol{U}) \leq 0) = \int_{\mathbb{R}^m} \mathbf{1}_{]-\infty,0]}(G(\boldsymbol{u}))\varphi_m(\boldsymbol{u})\mathrm{d}\boldsymbol{u} \tag{2.16}$$

where φ_m is the density of $\mathcal{N}(\mathbf{0}, \mathbf{I})$[1]. An illustration of the transformation into the standard normal space is given in Fig. 2.2.

[1] note that $\varphi_m(\cdot)$ corresponds to a compressed form of the notation $\varphi_m(\cdot; \mathbf{0}, \mathbf{I})$ introduced in Section 1.2.3.2

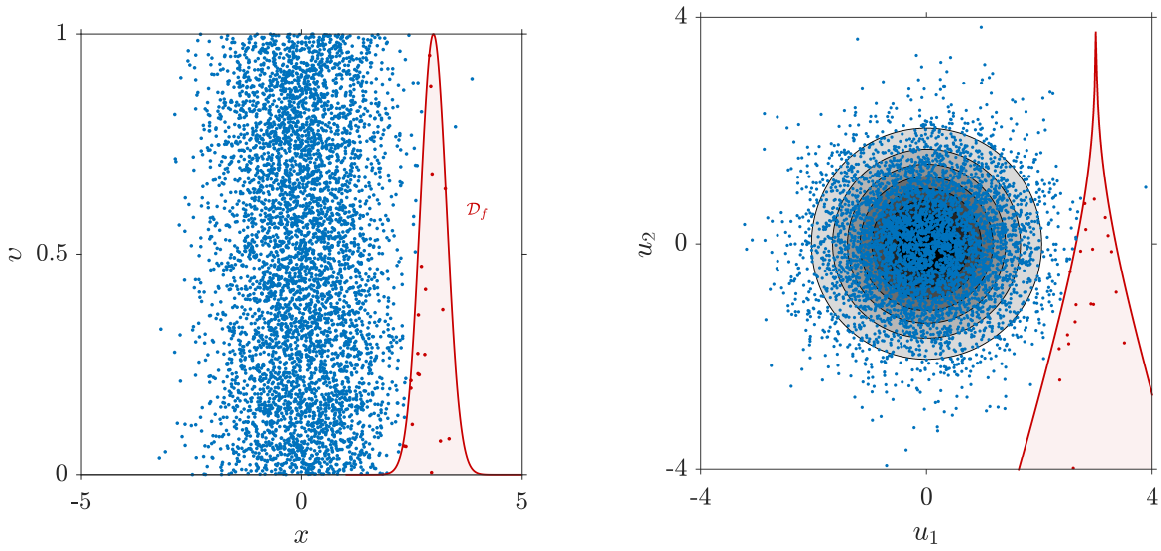

(a) BuS problem in original space **(b)** BuS problem in standard normal space

Figure 2.2: BuS in standard normal space: illustration in the case presented in Fig. 2.1.

From a numerical point of view, such a transformation provides several advantages. Indeed, it acts as a normalization procedure on the parameter space, and enables to work with distributions with unbounded supports (Betz et al., 2016). On the downside, it is worth noting that the transformation in Eq. (2.14) may be a sensibly nonlinear mapping, which introduces an additional layer of complexity.

2.2.2 SuS within the BuS framework

2.2.2.1 General formulation

The formulation of the SuS procedure within the BuS framework is now presented. One firstly recalls that classical SuS aims at constructing a sequence $(\mathcal{D}_f^{(j)})_{0\leq j\leq r}$ of intermediate subsets such that $\mathcal{D}_f = \mathcal{D}_f^{(r)} \subset \cdots \subset \mathcal{D}_f^{(1)} \subset \mathcal{D}_f^{(0)} = \mathcal{D}_{\boldsymbol{X}} \times [0,1]$, in order to write the PoF in Eq. (2.6) as a product of conditional probabilities (Au and Beck, 2001):

$$P_f = \prod_{j=1}^{r} \mathbb{P}_{(\boldsymbol{X},\Upsilon)}(\mathcal{D}_f^{(j)} | \mathcal{D}_f^{(j-1)}) \tag{2.17}$$

where $\mathbb{P}_{(\boldsymbol{X},\Upsilon)} = \mathbb{P}_{\boldsymbol{X}} \otimes \mathbb{P}_{\Upsilon}$ denotes the joint (prior) distribution of $(\boldsymbol{X}, \Upsilon)$.

Furthermore, in classical SuS, the intermediate failure domains $(\mathcal{D}_f^{(j)})_{1\leq j\leq r}$ are usually defined based on a sequence $(t_j)_{1\leq j\leq r}$ of threshold values such that $0 = t_r < \cdots < t_1$:

$$\mathcal{D}_f^{(j)} = \{(\boldsymbol{x}, v) \in \mathcal{D}_{\boldsymbol{X}} \times [0,1] \mid \mathcal{G}(\boldsymbol{x}, v) \leq t_j\} \tag{2.18}$$

where $\mathcal{G}$ is the LSF defined in Eq. (2.4).

Besides, due to the structure of BuS problems, the LSFs in Eqs. (2.4) and (2.15) present a particular format that is not uniquely defined (Betz et al., 2018b). In fact, for a given scaling constant C, any LSF $\mathcal{H}$ such that $\mathcal{H}^{-1}(]-\infty, 0]) = \mathcal{D}_f$ (where $\mathcal{D}_f$ is given by Eq. (2.3)) is

valid to solve the BuS problem at hand. Moreover, in the context of SuS, the formulation of the LSF has a non-negligible impact on the overall performance of the algorithm, since it conditions the shape of the intermediate failure domains (Betz et al., 2018b). Unfortunately, the classical formulation of the subsets in Eq. (2.18) is not well suited to the particular shape of the failure domain of BuS problems. Indeed, in the first intermediate domains of SuS, samples $(\boldsymbol{x}, \upsilon)$ with small values of υ are typically preferred to samples with large values of υ, which correspond to high-probability zones of the posterior. This implies abrupt transitions between subsets which make the SuS sampling procedure more challenging. An illustration of this phenomenon is given in Fig. 2.3a.

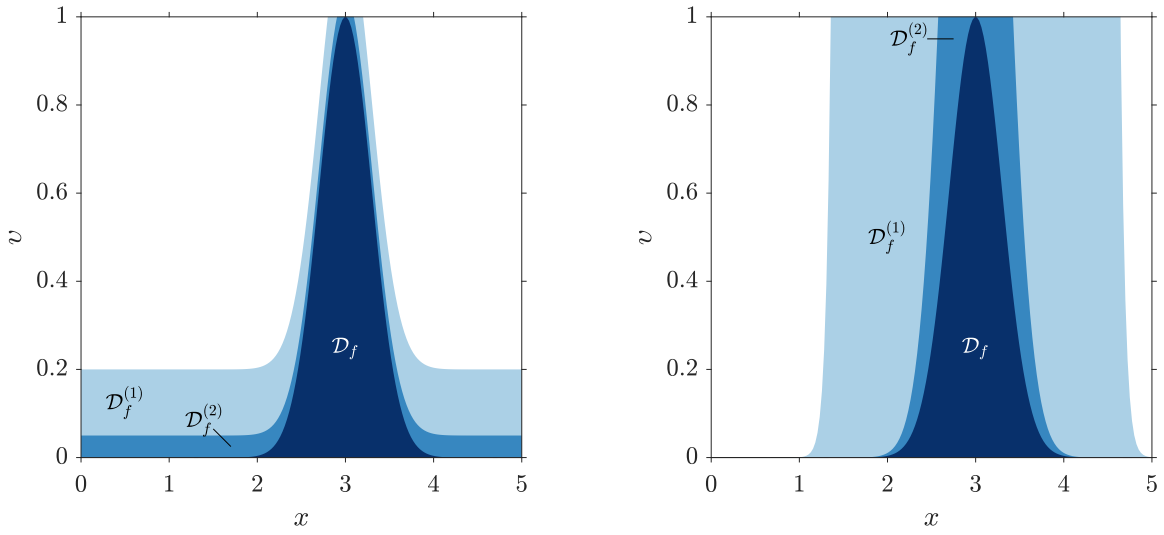

(a) $\mathcal{G}(x, \upsilon) = \upsilon - C\mathcal{L}(x)$ **(b)** $\mathcal{G}_l(x, \upsilon) = \log(\upsilon) + \ell - \log(\mathcal{L}(x))$

Figure 2.3: Impact of the LSF formulation on SuS intermediate failure domains $(\mathcal{D}_f^{(j)})_{1 \leq j \leq r}$, in the case of the problem presented in Fig. 2.1.

Consequently, in order to ensure smoother transitions between subsets and thereby improve the performance of SuS in the BuS framework, the following alternative LSF has been proposed in the literature (Betz et al., 2018b; DiazDelaO et al., 2017):

$$\mathcal{G}_l(\boldsymbol{x}, \upsilon) = \log(\upsilon) + \ell - \log(\mathcal{L}(\boldsymbol{x})) \tag{2.19}$$

where $\ell = -\log C$. Based on this LSF, intermediate failure domains in Eq. (2.18) may be redefined as follows:

$$\mathcal{D}_f^{(j)} = \{(\boldsymbol{x}, \upsilon) \in \mathcal{D}_{\boldsymbol{X}} \times [0, 1] \mid \mathcal{G}_l(\boldsymbol{x}, \upsilon) \leq t_j\} \tag{2.20}$$

Clearly, one has $\mathcal{D}_f^{(r)} = \mathcal{D}_f$, and thus solving the BuS probem associated to the LSF defined in Eq. (2.19) is akin to solving the original problem with the LSF in Eq. (2.4). Moreover, the shape of the subsets corresponding to the LSF $\mathcal{G}_l$ leads to a much more well-behaved sampling procedure. Indeed, contrary to the initial formulation, samples $(\boldsymbol{x}, \upsilon)$ with large values of υ are preferred over samples with small values of υ (see Fig. 2.3b), which provides smoother transitions between subsets (Betz et al., 2018b). Furthermore, such a formulation yields to a better numerical stability, since it is more convenient to work with the log-likelihood rather than with the likelihood directly.

Then, following the classical SuS procedure of Au and Beck (2001) presented in Section 1.2.6.2, the intermediate threshold t_j of the SuS level $j \in \{1, \dots, r\}$ is set as the p_0-quantile of LSF values $\{\mathcal{G}_l(\boldsymbol{x}^{(j-1,k)}, \upsilon^{(j-1,k)})\}_{1\leq k\leq N}$ on samples $\{(\boldsymbol{x}^{(j-1,k)}, \upsilon^{(j-1,k)})\}_{1\leq k\leq N}$ generated in the $(j-1)$-th SuS level. The rarity parameter $p_0 \in]0,1[$ is often set as $p_0 = 0.1$ in the framework of structural reliability (Au and Beck, 2001; Zuev et al., 2012). In the BuS framework, Betz et al. (2018b) have also proposed to use this value, that has led to near-optimal results in several numerical test cases. The full description of the SuS algorithm within BuS is given in Algorithm 2.1. For the sake of conciseness, it is presented in the physical space $\mathcal{D}_{\boldsymbol{X}} \times [0,1]$, but one should keep in mind that MCMC sampling will be performed in the standard normal space (see Section 2.2.2.2).

Algorithm 2.1 SuS within BuS algorithm (Betz et al., 2018b)

Input: BuS scaling constant C, number N of required samples, rarity parameter p_0

Set $j = 1$ and $t_0 = \infty$ ▷ SuS initialization
Draw N samples $\{(\boldsymbol{x}^{(0,k)}, \upsilon^{(0,k)})\}_{1\leq k\leq N}$ from the prior distribution
while $t_j > 0$ **do**
    Set $j \leftarrow j + 1$ ▷ Increase SuS level counter
    Sort the samples $\{(\boldsymbol{x}^{(j-1,k)}, \upsilon^{(j-1,k)})\}_{1\leq k\leq N}$ according to the LSF values $\{\mathcal{G}_l(\boldsymbol{x}^{(j-1,k)}, \upsilon^{(j-1,k)})\}_{1\leq k\leq N}$ in ascending order
    Set t_j as the p_0-quantile of the ordered set $\{\mathcal{G}_l(\boldsymbol{x}^{(j-1,k)}, \upsilon^{(j-1,k)})\}_{1\leq k\leq N}$ ▷ Set the threshold value t_j
    Set $n = \#\{k \in \{1, \dots, N\} \mid \mathcal{G}_l(\boldsymbol{x}^{(j-1,k)}, \upsilon^{(j-1,k)}) \leq \max(t_j, 0)\}$ ▷ Count the samples that lie in the j-th SuS intermediate domain
    if $t_j < 0$ **then**
        Set $t_j = 0$
        Set $P_f^{(j)} = n/N$
    else
        Set $P_f^{(j)} = p_0$
    end if
    Generate the samples $\{(\boldsymbol{x}^{(j,k)}, \upsilon^{(j,k)})\}_{1\leq k\leq N}$ of $\mathcal{D}_f^{(j)}$ with MCMC, by considering n Markov chains with seeds $\{(\boldsymbol{x}^{(j-1,k)}, \upsilon^{(j-1,k)})\}_{1\leq k\leq n}$ and length N/n ▷ Generate the population of the j-th SuS level with MCMC
end while
Set $r = j$ ▷ Final SuS level counter
Set $P_f = \prod_{i=1}^{r} P_f^{(i)}$ ▷ Estimate the PoF
Set $Z = P_f/C$ ▷ Estimate the model evidence

Output: Posterior samples $\{\boldsymbol{x}^{(r,k)}\}_{1\leq k\leq N}$, probability of failure P_f, model evidence Z

2.2.2.2 MCMC sampling within SuS

The SuS algorithm aims at generating samples in the intermediate failure domains $(\mathcal{D}_f^{(j)})_{1\leq j\leq r}$ with MCMC sampling (see Algorithm 2.1, l. 14). In this context, the MH algorithm (see Section 1.3.4.2) may be used so as to achieve this sampling task. Nevertheless, it is well-known that this algorithm performs poorly when the dimension of the problem increases (typically from $d \approx 10$). Indeed, the average acceptance rate of candidates drawn with the MH algorithm rapidly drops when the dimension increases (see *e.g.* (Au and Beck, 2001; Zuev et al., 2012)). Consequently, several alternative MCMC algorithms tailored for SuS and typically suitable for high-dimensional problems have been proposed in the literature (see *e.g.* (Papaioannou et al., 2015) for an in-depth presentation). In this thesis, the so-called *adaptive Conditional Sampling* (aCS) algorithm introduced by Papaioannou et al. (2015) is applied in the SuS procedure, due to its simplicity and to its efficiency compared to classical MCMC algorithms dedicated to SuS (see (Betz et al., 2018b; Papaioannou et al., 2015)). Furthermore, this algorithm is applied within the standard normal space, by transforming the samples and the subsets with the mapping $\mathcal{T} : \mathcal{D}_{\boldsymbol{X}} \times [0,1] \to \mathbb{R}^m$ introduced in Section 2.2.1.3. Further details on the MCMC sampling procedure based on the aCS algorithm within the standard normal space are given in Appendix B.

2.2.2.3 Adaptation of the BuS scaling constant

As highlighted in Section 2.2.1.2, the choice of the BuS scaling constant C plays a crucial role in the sampling of the posterior distribution. In order to circumvent this problem, the approach originally proposed in (Betz et al., 2014) and subsequently improved in (Betz et al., 2018b) consists in adaptively tuning the scaling constant C throughout the SuS procedure. This approach consists in estimating the maximum of the log-likelihood function on the samples generated in each subset. Firstly, at SuS level 0, after l. 2 of Algorithm 2.1, one sets $\ell = \max_{1\leq k\leq N} \log \mathcal{L}(\boldsymbol{x}^{(0,k)})$ (recall that $\ell = -\log C$). Then, at SuS level $j \geq 1$, after l. 14 of Algorithm 2.1, ℓ is set as the maximal log-likelihood value encountered during the simulation, namely:

$$\ell_{\text{new}} = \max\left(\ell_{\text{old}}, \max_{1\leq k\leq N} \log \mathcal{L}(\boldsymbol{x}^{(j,k)})\right) \tag{2.21}$$

ℓ_{old} being the value of ℓ at SuS level $j-1$. Note that such a modification alters the definition of the subset $\mathcal{D}_f^{(j)}$, the latter explicitly depending on the value of C, and thereby ℓ (see Eq. (2.18)). However, Betz et al. (2018b) showed that the updating in Eq. (2.21) does not affect the distribution of the current samples if the threshold value t_j associated to $\mathcal{D}_f^{(j)}$ is modified as follows:

$$t_j^* = t_j - \ell_{\text{old}} + \ell_{\text{new}} \tag{2.22}$$

Moreover, once the above threshold value has been updated, it is possible to decrease the dependence of the samples generated in the current subset, through a resampling step that comes with no additional cost. Indeed, one has $(\boldsymbol{x}, \upsilon) \in \mathcal{D}_f^{(j)}$ if $\upsilon \leq \mathcal{L}(\boldsymbol{x}) \exp(t_j^* - \ell_{\text{new}})$. Consequently, the component υ of each sample $(\boldsymbol{x}, \upsilon)$ that lies in $\mathcal{D}_f^{(j)}$ may be resampled from the uniform distribution $\mathcal{U}([0, \min(1, \mathcal{L}(\boldsymbol{x}) \exp(t_j^* - \ell_{\text{new}})])$. This enables to increase the performance of the SuS procedure, since the rejection of a sample during MCMC sampling implies to duplicate an existing sample.

2.3 Adaptive surrogate modeling

2.3.1 Polynomial Chaos Kriging

Polynomial Chaos Kriging (PCK) is a surrogate modeling technique introduced in (Schöbi et al., 2015), which consists in a universal Kriging whose trend is given by a PCE. Assuming now that the model $\mathcal{M} : \mathcal{D}_{\boldsymbol{X}} \to \mathcal{D}_Y \subset \mathbb{R}$ is scalar-valued, the formulation of PCK may be written by (Schöbi et al., 2015):

$$\mathcal{M}(\boldsymbol{x}) \approx \hat{\mathcal{M}}(\boldsymbol{x}) = \sum_{\boldsymbol{\alpha} \in \mathcal{A}} c_{\boldsymbol{\alpha}} \psi_{\boldsymbol{\alpha}}(\boldsymbol{x}) + \varsigma^2 \mathcal{Z}(\boldsymbol{x}) \tag{2.23}$$

where $\sum_{\boldsymbol{\alpha} \in \mathcal{A}} c_{\boldsymbol{\alpha}} \psi_{\boldsymbol{\alpha}}$ is a PCE truncated on $\mathcal{A} \subset \mathbb{N}^d$ with coefficients $(c_{\boldsymbol{\alpha}})_{\boldsymbol{\alpha} \in \mathcal{A}}$ and basis of multivariate polynomials $(\psi_{\boldsymbol{\alpha}})_{\boldsymbol{\alpha} \in \mathcal{A}}$, and $\mathcal{Z}$ is a centered unit-variance stationary Gaussian process defined by an autocorrelation function $R_{\mathcal{Z}}(\cdot; \boldsymbol{\theta})$ parametrized by a set of hyperparameters $\boldsymbol{\theta}$. ς^2 denotes the variance of the Gaussian process model. Note that for all $\boldsymbol{x} \in \mathcal{D}_{\boldsymbol{X}}$, $\mathcal{Z}(\boldsymbol{x}) : \Omega \to \mathbb{R}$ is a standard Gaussian random variable, *i.e.* $\mathcal{Z}(\boldsymbol{x}) \sim \mathcal{N}(0, 1)$.

The setup of a PCK surrogate consists in two parts, namely:

1. the determination of the optimal set of polynomials contained in the PCE trend (given by the truncation set $\mathcal{A}$),

2. the calibration of the correlation hyperparameters $\boldsymbol{\theta}$, the Gaussian process variance ς^2 and the coefficients $(c_{\boldsymbol{\alpha}})_{\boldsymbol{\alpha} \in \mathcal{A}}$.

In this context, Schöbi et al. (2015) proposed two computational approaches, called *Sequential PCK* (S-PCK) and *Optimal PCK* (O-PCK). The first-mentioned one consists in finding the set $(\psi_{\boldsymbol{\alpha}})_{\boldsymbol{\alpha} \in \mathcal{A}}$ through the LARS-based regression procedure of (Blatman and Sudret, 2011b), and subsequently calibrating the Kriging parameters $\{(c_{\boldsymbol{\alpha}})_{\boldsymbol{\alpha} \in \mathcal{A}}, \boldsymbol{\theta}, \varsigma^2\}$. These parameters are typically estimated through Maximum Likelihood estimation (ML) (Dubourg et al., 2011; Marrel et al., 2008) or Cross Validation (CV) (Bachoc, 2013). Furthermore, the O-PCK approach aims at iteratively constructing a PCK by adding polynomials one-by-one to the trend, and selecting the surrogate which minimizes a global LOO error estimate. One refers to (Schöbi et al., 2015) for a comprehensive presentation of both S-PCK and O-PCK approaches.

Then, once the PCK calibration has been achieved, the prediction of the PCK model in Eq. (2.23) at a point $\boldsymbol{x} \in \mathcal{D}_{\boldsymbol{X}}$ is a Gaussian random variable, whose mean and variance are denoted by $\mu_{\hat{\mathcal{M}}}(\boldsymbol{x})$ and $\sigma^2_{\hat{\mathcal{M}}}(\boldsymbol{x})$, respectively. Their expression are not detailed here, for the sake of brevity (see *e.g.* (Schöbi, 2017, Section 3.4) for a comprehensive presentation). An illustration of a PCK surrogate is given in Fig. 2.4.

The interest of the PCK formulation is twofold: the PCE trend provides a global approximation of the model response on the input domain, whereas the Gaussian process enables to catch local variations of the model response. Furthermore, the prediction variance associated to the Gaussian process provides a local error measure for PCK model predictions, which can be used as an indicator of the sparsity of the ED on which the PCK model is built. Indeed, Kriging is an exact interpolating method, in the sense that predictions are equal to the model response at points of the ED. Thus, the prediction variance is low near

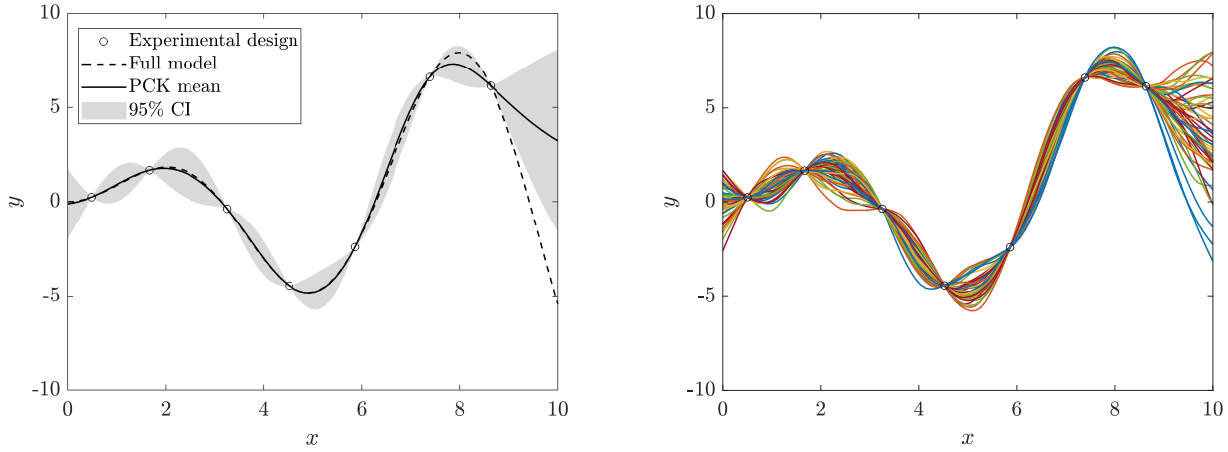

(a) Full model and PCK predictions

(b) Sample paths drawn from the underlying Gaussian process

Figure 2.4: Visualization of a PCK surrogate: case of an analytical model given by $\mathcal{M}(x) = x\sin(x)$, with a uniform input variable $X \sim \mathcal{U}([0, 10])$.

ED points and becomes important in unexplored zones of the parameter space. Such a local indicator may typically be exploited in the framework of adaptive surrogate modeling, in order to enrich EDs (Echard et al., 2011; Schöbi et al., 2017).

2.3.2 Adaptive PCK within SuS algorithm

2.3.2.1 Main algorithm

The proposed approach aims at constructing a PCK surrogate which is adaptively enriched throughout the SuS procedure described by Algorithm 2.1. In this perspective, the log-likelihood $L = \log \mathcal{L}$ is approximated by a PCK surrogate $\hat{L}$:

$$L(\boldsymbol{x}) \approx \hat{L}(\boldsymbol{x}) = \sum_{\boldsymbol{\alpha} \in \mathcal{A}} c_{\boldsymbol{\alpha}} \psi_{\boldsymbol{\alpha}}(\boldsymbol{x}) + \varsigma^2 \mathcal{Z}(\boldsymbol{x}) \tag{2.24}$$

The choice of surrogating the log-likelihood instead of the forward model is mainly motivated by the fact that the definition of Kriging-based adaptation criteria for experimental designs will be facilitated, since the LSF in Eq. (2.19) directly depends on the log-likelihood. Indeed, substituting the log-likelihood L by its PCK surrogate in Eq. (2.24) in the definition of the LSF in Eq. (2.19) yields a surrogate LSF given by:

$$\hat{\mathcal{G}}_l(\boldsymbol{x}, \upsilon) = \log(\upsilon) + \ell - \hat{L}(\boldsymbol{x}) \tag{2.25}$$

Then, since $\hat{L}$ is a Gaussian process, it is remarked that for a given value of ℓ and $\upsilon \in [0, 1]$, the surrogate LSF $\hat{\mathcal{G}}_l(\cdot, \upsilon)$ is also a Gaussian process. Furthermore, its mean and variance at $(\boldsymbol{x}, \upsilon) \in \mathcal{D}_{\boldsymbol{X}} \times [0, 1]$ respectively write:

$$\mu_{\hat{\mathcal{G}}_l}(\boldsymbol{x}, \upsilon) = \log(\upsilon) + \ell - \mu_{\hat{L}}(\boldsymbol{x}) \tag{2.26}$$

$$\sigma^2_{\hat{\mathcal{G}}_l}(\boldsymbol{x}, \upsilon) = \sigma^2_{\hat{L}}(\boldsymbol{x}) \tag{2.27}$$

where $\mu_{\hat{L}}(\boldsymbol{x})$ and $\sigma^2_{\hat{L}}(\boldsymbol{x})$ denote the prediction mean and variance of the PCK $\hat{L}$ at $\boldsymbol{x}$, respectively. Such a LSF structure will be fully exploited to select points in the parameter space to enrich experimental designs, based on local information provided by the underlying Gaussian process of the PCK.

Moreover, another advantage of approximating the log-likelihood rather than the forward model is that the log-likelihood is scalar-valued, contrary to the forward model. Hence, in the case of large output dimensionalities, the calibration of surrogates of the forward models may be computationally expensive (Blatman and Sudret, 2014). On the downside, surrogating the log-likelihood may be more a difficult task than for the forward model. Indeed, when considering an additive Gaussian noise, the log-likelihood is typically given by the composition of a quadratic function with the forward model, which may involve an additional layer of complexity.

Furthermore, the multivariate polynomials $\{\psi_{\boldsymbol{\alpha}}\}$ involved in the trend of the PCK in Eq. (2.24) are chosen to be orthonormal with respect to the prior distribution. This is principally motivated by the fact that under some conditions on the prior (see *e.g.* (Ernst et al., 2012)), the family $(\psi_{\boldsymbol{\alpha}})_{\boldsymbol{\alpha}\in\mathbb{N}^d}$ forms a Hilbert basis of $\mathbb{L}^2(\pi)$. Therefore, if L is square-integrable with respect to the prior, *i.e.* $L \in \mathbb{L}^2(\pi)$, the PCE trend in Eq. (2.24) converges in the $\mathbb{L}^2(\pi)$ sense to the true log-likelihood when the number of terms in the truncation set $\mathcal{A}$ increases. In this context, the surrogate posterior density obtained by substituting the log-likelihood by the trend of its PCK is expected to converge towards the true posterior density, as suggested by results of (Birolleau et al., 2014; Marzouk and Xiu, 2009).

Then, the main steps of the proposed algorithm may be summarized as follows:

1. **Surrogate model initialization:**

   (a) *Initial experimental design:* K_0 samples $\{\boldsymbol{\chi}_k\}_{1\leq k\leq K_0} \subset \mathcal{D}_{\boldsymbol{X}}$ are drawn from the prior, typically by adopting *space-filling* sampling techniques such as Latin Hypercube Sampling (LHS) (McKay et al., 1979), or Sobol' low-discrepancy sequences (Sobol', 1967). Then, the initial ED is set as $\mathcal{X} = \{\boldsymbol{\chi}_k\}_{1\leq k\leq K_0}$. The corresponding log-likelihood values are computed and gathered in $\mathcal{Y} = \{L(\boldsymbol{\chi}_k)\}_{1\leq k\leq K_0}$.

   (b) *Calibration of PCK surrogate:* a PCK surrogate $\hat{L}$ is calibrated from the training data $\{\mathcal{X}, \mathcal{Y}\}$.

2. **Generate samples of SuS level 0:** the N samples $\{(\boldsymbol{x}^{(0,k)}, \upsilon^{(0,k)})\}_{1\leq k\leq N}$ of the SuS level 0 are generated through direct Monte Carlo simulation (see Algorithm 2.1, l. 2).

3. **Initialize the BuS scaling constant ℓ:** the scaling constant $\ell = -\log C$ is estimated from the samples $\{(\boldsymbol{x}^{(0,k)}, \upsilon^{(0,k)})\}_{1\leq k\leq N}$ of the SuS level 0 (see Section 2.3.2.3).

4. **SuS procedure:** at SuS level $j \geq 1$:

   (a) *Compute the threshold t_j and the probability $P_f^{(j)}$:* the threshold value t_j of the current subset $\mathcal{D}_f^{(j)}$ is set as the p_0-quantile of $\{\mu_{\hat{\mathcal{G}}_l}(\boldsymbol{x}^{(j-1,k)}, \upsilon^{(j-1,k)})\}_{1\leq k\leq N}$ (*i.e.* surrogate LSF values computed on the samples from the subset $j-1$), where p_0 is the rarity parameter (see Algorithm 2.1, l. 6). Subsequently, the probability $P_f^{(j)}$ is estimated by following l. 7-13 of Algorithm 2.1.

(b) *Learning stopping criterion:* if the considered stopping criterion is met (see Section 2.3.2.4), the PCK surrogate is deemed to be sufficiently accurate on the support of the posterior distribution, and then the step 4.(c) is skipped.

(c) *Learning phase of the PCK surrogate:* firstly, K points $\mathcal{X}^* = \{\boldsymbol{\chi}_k^*\}_{1\leq k\leq K}$ are selected from a set $\mathcal{S}_0^{(j)}$ of candidate points (see Section 2.3.2.2). The corresponding log-likelihood values are subsequently computed and stored in $\mathcal{Y}^* = \{L(\boldsymbol{\chi}_k^*)\}_{1\leq k\leq K}$. Then, the ED is enriched by setting $\mathcal{X} \leftarrow \{\mathcal{X}, \mathcal{X}^*\}$ and $\mathcal{Y} \leftarrow \{\mathcal{Y}, \mathcal{Y}^*\}$. Finally, the PCK surrogate $\hat{L}$ is recalibrated from the new training data $\{\mathcal{X}, \mathcal{Y}\}$.

(d) *MCMC sampling phase:* the samples $\{\boldsymbol{x}^{(j,k)}, \upsilon^{(j,k)}\}_{1\leq k\leq N}$ of the subset $\mathcal{D}_f^{(j)}$ are generated with MCMC (see l. 14 of Algorithm 2.1), by using the aCS algorithm (see Appendix B for further details). During this phase, the LSF $\mathcal{G}_l$ is replaced by its surrogate counterpart $\hat{\mathcal{G}}_l$.

(e) *Updating of the BuS scaling constant:* the scaling constant ℓ is updated from the samples $\{\boldsymbol{x}^{(j,k)}, \upsilon^{(j,k)}\}_{1\leq k\leq N}$ (see Section 2.3.2.3).

(f) *SuS stopping criterion:* if $t_j \leq 0$, then the SuS procedure is stopped, and the PoF P_f and model evidence Z are estimated as described in Algorithm 2.1, l. 16-18.

The three building bricks of the proposed adaptive approach, namely the learning phase, the learning stopping criterion, and the adaptation phase of the BuS scaling constant are detailed hereafter.

2.3.2.2 Candidate selection

The learning phase consists in selecting one (or several) point(s) in order to enrich the ED of the surrogate. Such a selection procedure relies on the concept of *learning function*, widely used in the framework of active learning schemes for structural reliability methods (Moustapha et al., 2022). A learning function aims at quantifying the value of information gained with respect to a quantity of interest when adding a point $\boldsymbol{x} \in \mathcal{D}_{\boldsymbol{X}}$ to the ED of the surrogate model (Schöbi, 2017). A broad range of learning functions has been developed in the literature, including the *Expected Improvement* (EI) function (Ginsbourger et al., 2013; Jones et al., 1998), the *Expected Feasibility Function* (EFF) (Bichon et al., 2008), the so-called *U-function* (Echard et al., 2011) and the *Fraction of Bootstrap Replicates* (FBR) (Marelli and Sudret, 2018). The reader is referred to the recent in-depth survey of Moustapha et al. (2022) for a more comprehensive presentation on learning functions.

The U-function introduced by Echard et al. (2011) is particularly well suited for Kriging-based adaptive approaches. It is based on properties of the underlying Gaussian process of the surrogate model, and on the notion of *misclassification*, which is explained hereafter. Firstly, recall that samples $(\boldsymbol{x}, \upsilon) \in \mathcal{D}_{\boldsymbol{X}} \times [0,1]$ with non-positive LSF values are classified as failure samples, *i.e.* $(\boldsymbol{x}, \upsilon) \in \mathcal{D}_f$, which traduces in the BuS framework by samples which follow the posterior distribution. Therefore, the potentially important uncertainties on predictions at points which are close to the limit-state surface (LSS) given by $\partial\mathcal{D}_f = \{(\boldsymbol{x}, \upsilon) \in \mathcal{D}_{\boldsymbol{X}} \times [0,1] \mid \mathcal{G}_l(\boldsymbol{x}, \upsilon) = 0\}$ can cause them to change sign, which may lead to misclassification (Echard et al., 2011). In such a case, given a point $(\boldsymbol{x}, \upsilon) \in \mathcal{D}_{\boldsymbol{X}} \times [0,1]$,

the surrogate LSF prediction mean may verify $\mu_{\hat{\mathcal{G}}_l}(\boldsymbol{x}, \upsilon) \leq 0$, while the true LSF verifies $\mathcal{G}_l(\boldsymbol{x}, \upsilon) > 0$, or vice versa.

Besides, as mentioned in Section 2.3.2.1, at each point $(\boldsymbol{x}, \upsilon) \in \mathcal{D}_{\boldsymbol{X}} \times [0,1]$, $\hat{\mathcal{G}}_l(\boldsymbol{x}, \upsilon)$ is a Gaussian random variable with mean $\mu_{\hat{\mathcal{G}}_l}(\boldsymbol{x}, \upsilon)$ and variance $\sigma^2_{\hat{\mathcal{G}}_l}(\boldsymbol{x}, \upsilon)$ given by Eqs. (2.26) and (2.27), respectively. Then, the probability of misclassification $P_m(\boldsymbol{x}, \upsilon)$ may be written by (Bect et al., 2012):

$$P_m(\boldsymbol{x}, \upsilon) = \Phi\left(-\frac{|\mu_{\hat{\mathcal{G}}_l}(\boldsymbol{x}, \upsilon)|}{\sigma_{\hat{\mathcal{G}}_l}(\boldsymbol{x}, \upsilon)}\right) \tag{2.28}$$

Such a probability is bounded between 0 and 0.5. The case $P_m(\boldsymbol{x}, \upsilon) \approx 0$ corresponds to points whose prediction variance is low, and/or points which are far away from the LSS. Conversely, the case $P_m(\boldsymbol{x}, \upsilon) \approx 0.5$ corresponds to points which are close to the LSS and/or whose prediction variance is important. In this context, the U-function proposed by Echard et al. (2011) is defined by:

$$U(\boldsymbol{x}, \upsilon) = \frac{|\mu_{\hat{\mathcal{G}}_l}(\boldsymbol{x}, \upsilon)|}{\sigma_{\hat{\mathcal{G}}_l}(\boldsymbol{x}, \upsilon)} \tag{2.29}$$

Then, the learning phase of the proposed approach is described hereafter. At SuS level $j \geq 1$, before performing MCMC sampling (see Algorithm 2.1, l. 14) n Markov chain seeds $\mathcal{S}_0^{(j)} = \{(\boldsymbol{x}^{(j-1,k)}, \upsilon^{(j-1,k)})\}_{1 \leq k \leq n} \subset \mathcal{D}_f^{(j)}$ are available. These samples are seen as candidate points for enriching the ED $\mathcal{X}$ of the PCK surrogate $\hat{L}$. In the case of a single point enrichment, the optimal point $\boldsymbol{\chi}^* \in \mathcal{D}_{\boldsymbol{X}}$ is selected by minimizing the U-function in Eq. (2.29) or maximizing the misclassification probability in Eq. (2.28):

$$(\boldsymbol{\chi}^*, \upsilon^*) = \underset{(\boldsymbol{x},\upsilon) \in \mathcal{S}_0^{(j)}}{\arg\min}\, U(\boldsymbol{x}, \upsilon) = \underset{(\boldsymbol{x},\upsilon) \in \mathcal{S}_0^{(j)}}{\arg\max}\, P_m(\boldsymbol{x}, \upsilon) \tag{2.30}$$

In this case, the projection on the parameter space $\mathcal{D}_{\boldsymbol{X}}$ of the above optimal point is subsequently added to the current experimental design, *i.e.* $\mathcal{X} \leftarrow \{\mathcal{X}, \boldsymbol{\chi}^*\}$. Note that due to the close connection existing between the misclassification probability in Eq. (2.28) and the U-function in Eq. (2.29), both can be used as learning functions (Schöbi, 2017). An illustration of the proposed point enrichment procedure is given in Fig. 2.5.

Furthermore, multiple point enrichment may also be considered in order to take advantage of parallel computing, if available. Such an approach enables to accelerate the overall computational procedure, but is slightly suboptimal compared to perform several subsequent single point enrichment steps, though (Schöbi et al., 2017). In this context, when $K > 1$ enrichment points per SuS level are desired, the proposed approach uses the *weighted K-means* clustering algorithm (Zaki and Meira, 2014) on the set $\mathcal{S}_0^{(j)}$ of candidate points. The weight of each $(\boldsymbol{x}, \upsilon) \in \mathcal{S}_0^{(j)}$ is set as the corresponding misclassification probability $P_m(\boldsymbol{x}, \upsilon)$. Nevertheless, the surrogate log-likelihood $\hat{L}$ is defined on the original parameter space $\mathcal{D}_{\boldsymbol{X}}$, and then does not depend on values of $\upsilon \in [0,1]$. Hence, performing a clustering in the augmented space $\mathcal{D}_{\boldsymbol{X}} \times [0,1]$ may lead to redundant enrichment points, since the centroids of the identified clusters may lie on lines of the form $\{\boldsymbol{x}\} \times [0,1]$. Consequently, weighted K-means clustering is instead performed on the set given by $\{\boldsymbol{x}^{(j-1,k)}\}_{1 \leq k \leq n}$ by using the same misclassification probabilities $\{P_m(\boldsymbol{x}^{(j-1,k)}, \upsilon^{(j-1,k)})\}_{1 \leq k \leq n}$ as weights. This would typically yield a better coverage of the parameter space $\mathcal{D}_{\boldsymbol{X}}$, and then a better emulation of the

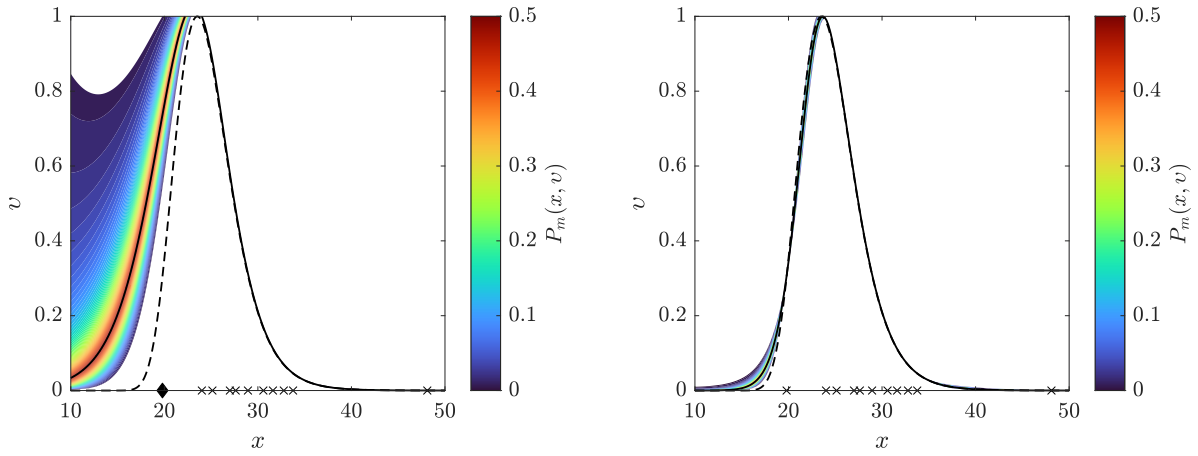

(a) Before point enrichment

(b) After point enrichment

Figure 2.5: Illustration of the point enrichment phase in the case of a single parameter inference: contours of the misclassification probability P_m in Eq. (2.28) and prediction of the LSS (given by a black solid line) obtained from a PCK surrogate of the log-likelihood function. The true LSS is shown by a black dashed line. Points of the experimental design of the surrogate are shown by black crosses (×), whereas the optimal enrichment point in Eq. (2.30) projected in the parameter space is shown by a black diamond (⧫).

log-likelihood function by its PCK surrogate near informative zones. Finally, the enrichment points $\mathcal{X}^* = \{\boldsymbol{\chi}_k^*\}_{1\leq k\leq K}$ are selected as the centroids of the K identified clusters, and are subsequently added to the current ED, *i.e.* $\mathcal{X} \leftarrow \{\mathcal{X}, \mathcal{X}^*\}$.

2.3.2.3 Adaptation of the BuS scaling constant

Following the approach described in Section 2.2.2.3, the BuS scaling constant is adaptively estimated throughout the SuS procedure. Firstly, once the PCK surrogate $\hat{L}$ has been calibrated from the initial ED, the population of SuS first level is generated by drawing N samples $\mathcal{S}^{(0)} = \{\boldsymbol{x}^{(0,k)}, \upsilon^{(0,k)}\}_{1\leq k\leq N}$ from the joint prior distribution of $(\boldsymbol{X}, \Upsilon)$. Then, a critical step is the calculation of an initial value for the scaling constant ℓ. In the approach proposed in (Betz et al., 2018b), this value is set as the largest log-likelihood value on the samples $\mathcal{S}^{(0)}$. When dealing with a PCK surrogate model instead of the true log-likelihood, the estimation of ℓ requires a specific treatment. Indeed, samples drawn through Monte Carlo sampling which are too far away from the ED may lead to inaccurate PCK predictions. This potentially implies to sensibly underestimate the optimal constant $\ell_{\max}$ and then lead to a bias in estimates of posterior QoI, or conversely, to strongly overestimate $\ell_{\max}$ and alter the efficiency of the SuS procedure, as discussed in Section 2.2.1.2.

Consequently, the initial value of ℓ is set as the maximum likelihood on a subset of $\mathcal{S}$, formed by points which are not too far away from points of the ED. At this point, the question is to define a criterion to filter points whose predictions are deemed to be not accurate. A quite natural choice proposed in (Angelikopoulos et al., 2015) and (Giovanis et al., 2017), is based on the convex hull of the points of the current ED.

The convex hull of $\mathcal{X}$, denoted by $\mathbf{co}(\mathcal{X})$, is the smallest convex set which contains the points of $\mathcal{X}$. If the ED points are sufficiently dense, surrogate predictions may be deemed

to be reasonably accurate on this set. Then, the initial constant ℓ is set as the maximum surrogate likelihood on samples of $\mathcal{S}^{(0)}$, namely:

$$\ell = \max_{\boldsymbol{x} \in \mathcal{S}_{\mathcal{X}}^{(0)}} \mu_{\hat{L}}(\boldsymbol{x}) \tag{2.31}$$

where $\mathcal{S}_{\mathcal{X}}^{(0)} = \mathcal{S}^{(0)} \cap \mathbf{co}(\mathcal{X})$. For practical purposes, the convex hull of the ED $\mathcal{X}$ is computed by using the Quickhull algorithm introduced in (Barber et al., 1996).

Likewise, at SuS level $j \geq 1$, once MCMC sampling has been achieved, the following updating is proposed:

$$\ell_{\text{new}} = \max \left(\ell_{\text{old}}, \max_{\boldsymbol{x} \in \mathcal{S}_{\mathcal{X}}^{(j)}} \mu_{\hat{L}}(\boldsymbol{x}) \right) \tag{2.32}$$

where ℓ_{new} and ℓ_{old} denote respectively the scaling constant at the current and previous SuS levels, $\mathcal{S}_{\mathcal{X}}^{(j)} = \mathcal{S}^{(j)} \cap \mathbf{co}(\mathcal{X})$ and $\mathcal{S}^{(j)} = \{(\boldsymbol{x}^{(j,k)}, \upsilon^{(j,k)})\}_{1 \leq k \leq N}$ are the samples generated at SuS level j. Subsequently, the threshold value t_j is modified in order to account for the modification of the value of ℓ, as described in Section 2.2.2.3.

2.3.2.4 Stopping criterion

In the framework of active learning structural reliability methods, several criteria have been proposed in order to stop the enrichment of the surrogate model (Moustapha et al., 2022). Such criteria may be based on the accuracy of PoF estimates (Dubourg et al., 2013; Jian et al., 2017; Marelli and Sudret, 2018), or directly based on learning functions (Bichon et al., 2008; Echard et al., 2011; Lelièvre et al., 2018). The proposed approach uses the stopping criterion proposed by Echard et al. (2011) based on the U-function in Eq. (2.29). At SuS level $j \geq 1$, before the point enrichment phase, this criterion consists in the following lower bound on the set $\mathcal{S}_0^{(j)}$ of candidate points:

$$\min_{(\boldsymbol{x}, \upsilon) \in \mathcal{S}_0^{(j)}} U(\boldsymbol{x}, \upsilon) \geq 2 \tag{2.33}$$

Note that this criterion reverts to impose a maximal misclassification probability in Eq. (2.28) of $\Phi(-2) \approx 0.023$:

$$\max_{(\boldsymbol{x}, \upsilon) \in \mathcal{S}_0^{(j)}} P_m(\boldsymbol{x}, \upsilon) \leq \Phi(-2) \tag{2.34}$$

The choice of such a stopping criterion is motivated by the fact that it focuses on the accuracy of the surrogate model around the limit-state surface, *i.e.* near informative zones. Notwithstanding its widespread use, it should be underlined that this criterion may be too conservative in some cases, typically when confronted to complex LSF and/or high-dimensional problems. One refers to (Moustapha et al., 2022) for a comprehensive review on alternative stopping criteria.

2.3.2.5 Summary of the proposed algorithm

The proposed adaptive algorithm, named PCK-SuS hereafter, is summarized in a pseudo-code presentation in Algorithm 2.2. Lines referring to the adaptive PCK surrogate are shown in blue. The parameters related to the calibration of the PCK surrogate, including parameters related to the PCE trend (*e.g.* degree, truncation set) and to the Gaussian process (*e.g.* the autocorrelation function, optimization parameters) are not mentioned, for the sake of brevity.

Algorithm 2.2 PCK-SuS within BuS algorithm (Rossat et al., 2022a)

Input: Number N of required samples, rarity parameter p_0, initial ED size K_0, number K of enrichment points per learning phase

1: Draw K_0 samples $\{\boldsymbol{\chi}_k\}_{1\leq k\leq K_0}$ from the prior and set $\mathcal{X} = \{\boldsymbol{\chi}_k\}_{1\leq k\leq K_0}$ ▷ Initial ED
2: Compute the log-likelihood values $\mathcal{Y} = \{L(\boldsymbol{\chi}_k)\}_{1\leq k\leq K_0}$
3: Calibrate a PCK surrogate $\hat{L}$ from $\{\mathcal{X}, \mathcal{Y}\}$ ▷ Initial (prior-based) surrogate model
4: Set $j = 1$ and $t_0 = \infty$ ▷ SuS initialization
5: Draw N samples $\mathcal{S}^{(0)} = \{(\boldsymbol{x}^{(0,k)}, \upsilon^{(0,k)})\}_{1\leq k\leq N}$ from the prior
6: Compute the convex hull $\mathbf{co}(\mathcal{X})$ of $\mathcal{X}$ and set $\mathcal{S}_{\mathcal{X}}^{(0)} = \mathcal{S}^{(0)} \cap \mathbf{co}(\mathcal{X})$
7: Set $\ell = \max\{\hat{L}(\boldsymbol{x}, \upsilon) \mid (\boldsymbol{x}, \upsilon) \in \mathcal{S}_{\mathcal{X}}^{(0)}\}$ ▷ Initialize the scaling constant ℓ
8: **while** $t_j > 0$ **do**
9: Set $j \leftarrow j + 1$ ▷ Increase SuS level counter
10: Compute t_j from $\mathcal{S}^{(j-1)} = \{(\boldsymbol{x}^{(j-1,k)}, \upsilon^{(j-1,k)})\}_{1\leq k\leq N}$, as in Algorithm 2.1, l. 5-6
11: Set $\mathcal{S}_0^{(j)} = \{(\boldsymbol{x}, \upsilon) \in \mathcal{S}^{(j-1)} \mid \mu_{\hat{\mathcal{G}}_l}(\boldsymbol{x}, \upsilon) \leq \max(t_j, 0)\}$ and $n = \#\mathcal{S}_0^{(j)}$
12: Estimate the PoF $P_f^{(j)}$ as in Algorithm 2.1, l. 13-18
13: Compute the misclassification probabilities $\mathcal{P}^{(j)} = \{P_m(\boldsymbol{x}, \upsilon) \mid (\boldsymbol{x}, \upsilon) \in \mathcal{S}_0^{(j)}\}$
14: **if** $\max \mathcal{P}^{(j)} > \Phi(-2)$ **then** ▷ Learning stopping criterion
15: Select K points $\mathcal{X}^* = \{\boldsymbol{\chi}_k^*\}_{1\leq k\leq K}$ from $\mathcal{S}_0^{(j)}$ ▷ Point enrichment (Section 2.3.2.2)
16: Compute the log-likelihood values $\mathcal{Y}^* = \{L(\boldsymbol{\chi}_k^*)\}_{1\leq k\leq K}$
17: Set $\mathcal{X} \leftarrow \{\mathcal{X}, \mathcal{X}^*\}$ and $\mathcal{Y} \leftarrow \{\mathcal{Y}, \mathcal{Y}^*\}$ ▷ Enrich the current ED
18: Recompute the convex hull $\mathbf{co}(\mathcal{X})$ of $\mathcal{X}$
19: Recalibrate the PCK surrogate $\hat{L}$ from $\{\mathcal{X}, \mathcal{Y}\}$
20: **end if**
21: Generate the samples $\mathcal{S}^{(j)}$ of $\mathcal{D}_f^{(j)}$ with MCMC, by considering n Markov chains with seeds $\mathcal{S}_0^{(j)}$ and length N/n ▷ Generate the population of the j-th SuS level
22: Set $\mathcal{S}_{\mathcal{X}}^{(j)} = \mathcal{S}^{(j)} \cap \mathbf{co}(\mathcal{X})$, and $\ell^* = \max(\ell, \max_{\mathcal{S}_{\mathcal{X}}^{(j)}} \mu_{\hat{L}})$ ▷ Update ℓ
23: Set $t_j \leftarrow t_j - \ell + \ell^*$, and then $\ell \leftarrow \ell^*$ ▷ Update t_j
24: **end while**
25: Estimate the probability P_f and model evidence Z as in Algorithm 2.1, l. 16-18

Output: Posterior samples $\{\boldsymbol{x}^{(r,k)}\}_{1\leq k\leq N}$, probability of failure P_f, model evidence Z

2.4 Numerical examples

In this section, the proposed algorithm is showcased in the framework of several Bayesian inverse problems with varying complexity. The main algorithmic settings considered in each application are detailed hereafter.

Firstly, PCK surrogates are constructed by using the Optimal PC-Kriging (O-PCK) approach described in (Schöbi et al., 2015), through its implementation in the `UQLab` software (Marelli and Sudret, 2014). The PCE trends $\sum_{\boldsymbol{\alpha}\in\mathcal{A}} c_{\boldsymbol{\alpha}}\psi_{\boldsymbol{\alpha}}$ are constructed by using the adaptive sparse PCE procedure based on the LARS algorithm introduced by Blatman and Sudret (2011b). PCE are built from the classical isotropic truncation sets given by:

$$\mathcal{A}_p = \{\boldsymbol{\alpha} \in \mathbb{N}^d \mid \|\boldsymbol{\alpha}\|_1 \leq p\} \tag{2.35}$$

where the maximum PCE degree p is adaptively chosen in $\{0, \ldots, 10\}$.

Moreover, the Gaussian process of each PCK surrogate is assumed to have an autocorrelation function with the following structure:

$$R_{\mathcal{Z}}(\boldsymbol{x} - \boldsymbol{x}'; \boldsymbol{\theta}) = \prod_{i=1}^{d} R_0\left(\frac{|x_i - x_i'|}{\theta_i}\right) \tag{2.36}$$

where $\boldsymbol{\theta} = (\theta_1, \ldots, \theta_d)$ are the hyperparameters R_0 is the Matérn autocorrelation function with shape parameter $\frac{5}{2}$, given by (Rasmussen and Williams, 2006):

$$R_0(h) = \left(1 + \sqrt{5}h + \frac{5}{3}h^2\right)\exp\left(-\sqrt{5}h\right) \tag{2.37}$$

The hyperparameters $\boldsymbol{\theta}$ are estimated through Cross Validation (CV) (Bachoc, 2013), by using a hybrid genetic strategy: the `Matlab`'s genetic algorithm (GA) is firstly launched, and its final point is used as an initial point for the interior point L-BFGS algorithm of Byrd et al. (1999).

Then, substituting PCK surrogate predictions $\mu_{\hat{L}}$ of the log-likelihood in the definition of the posterior density $\pi^*(\boldsymbol{x}) = \pi(\boldsymbol{x}|\boldsymbol{y})$ yields a surrogate posterior density given by:

$$\hat{\pi}^*(\boldsymbol{x}) = \frac{\pi(\boldsymbol{x})\exp\left(\mu_{\hat{L}}(\boldsymbol{x})\right)}{\hat{Z}} \tag{2.38}$$

where $\hat{Z}$ is the surrogate model evidence given by:

$$\hat{Z} = \int_{\mathcal{D}_{\boldsymbol{X}}} \exp\left(\mu_{\hat{L}}(\boldsymbol{x})\right)\pi(\boldsymbol{x})\mathrm{d}\boldsymbol{x} \tag{2.39}$$

Besides comparing posterior QoI such as mean, standard deviation and model evidence obtained from posterior samples, the accuracy of the proposed approach is assessed through a comparison of reference and surrogate-based posterior univariate marginal densities (typically estimated from samples through kernel density estimation). In this perspective, the error measure introduced in (Wagner et al., 2021) is used:

$$\xi = \frac{1}{d}\sum_{i=1}^{d} D_{\mathrm{JS}}(\hat{\pi}_i^*, \pi_i^*) \tag{2.40}$$

where $D_{\mathrm{JS}}(\hat{\pi}_i^*, \pi_i^*)$ is the Jensen-Shannon Divergence (JSD) (Lin, 1991) between the i-th posterior univariate marginals $\hat{\pi}_i^*$ and π_i^* corresponding to Eqs. (2.38) and (2.1), defined by:

$$D_{\mathrm{JS}}(\hat{\pi}_i^*, \pi_i^*) = \frac{1}{2}\left(D_{\mathrm{KL}}(\pi_i^* \| \bar{\pi}_i^*) + D_{\mathrm{KL}}(\hat{\pi}_i^* \| \bar{\pi}_i^*)\right) \tag{2.41}$$

$D_{\mathrm{KL}}(\cdot\|\cdot)$ being the Kullback-Leibler Divergence (see Section 1.3.2.4), and $\bar{\pi}_i^* = (\pi_i^* + \hat{\pi}_i^*)/2$, for $i \in \{1, \ldots, d\}$. The JSD in Eq. (2.41) constitutes a symmetrized and somewhat regularized form of the KLD. It is also always bounded in $[0, \log(2)]$. Furthermore, the error measure in Eq. (2.40) enables to summarize the accuracy of the approximation of the posterior marginal densities $(\pi_i^*)_{1 \leq i \leq d}$ in a single scalar, which is computationally affordable since it is based on an average of univariate integrals.

In the next sections, reference results are produced with the SuS procedure presented in Section 2.2.2 (see Algorithm 2.1), by using the full likelihood function. The PCK-SuS algorithm is subsequently applied by considering varying initial ED size K_0 and ratios $\kappa = K/K_0$, K being the number of enrichment points at each learning phase. For both SuS and PCK-SuS approaches, a number of $N = 5000$ samples per subset is considered, based on (Betz et al., 2018b; Straub et al., 2016). Furthermore, the rarity parameter p_0 is set as $p_0 = 0.1$, based on recommendations in (Betz et al., 2018b). Moreover, 50 replications of the calculations are produced, in each case, for both SuS and PCK-SuS algorithms. For a single run, the total number of full model calls is denoted by M. For one SuS procedure with N samples per level, this number is simply given by $(r+1)N$, r being the number of SuS levels. In the case of one PCK-SuS procedure with an initial ED size K_0 and K enrichment points per learning phase, this number lies between K_0 and $K_0 + rK$, depending whether and when the learning stopping criterion (see Section 2.3.2.4) has been reached during the procedure.

2.4.1 Two-DOF shear building

2.4.1.1 Problem description

The first numerical example was originally introduced in (Beck and Au, 2002), and then studied in (Betz et al., 2018b; Giovanis et al., 2017; Straub and Papaioannou, 2015; Wang and Shafieezadeh, 2020), and involves a two degrees-of-freedom shear building. The problem consists in estimating the posterior inter-story stiffnesses of the structure, based on measurements of its eigen-frequencies.

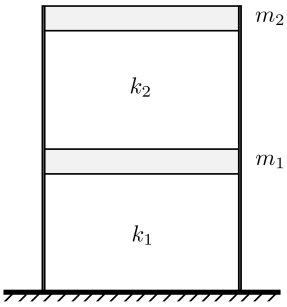

Figure 2.6: Two degrees-of-freedom shear building.

The inter-story stiffnesses are set as $k_i = X_i k_n$ for $i \in \{1, 2\}$, where $k_n = 29.7 \cdot 10^6$ N.m^{-1} and X_1, X_2 are random variables endowed with lognormal priors with modes 1.3 and 0.8, and standard deviations equal to 1. The masses of the two stories are supposed to be deterministic, and are set as $m_1 = 16.531 \cdot 10^3$ kg and $m_2 = 16.131 \cdot 10^3$ kg. Two measured eigen-frequencies $\boldsymbol{y} = (\tilde{f}_1, \tilde{f}_2)$ will be used for Bayesian updating, with $\tilde{f}_1 = 3.13$ Hz and $\tilde{f}_2 = 9.83$ Hz. The corresponding likelihood function writes:

$$\mathcal{L}(\boldsymbol{x}) = \exp\left(-\frac{\mathcal{J}(\boldsymbol{x})}{2\sigma^2}\right) \tag{2.42}$$

where $\sigma = 1/16$ and $\mathcal{J}(\boldsymbol{x})$ is the modal measure-of-fit function given by (Beck and Au, 2002):

$$\mathcal{J}(\boldsymbol{x}) = \sum_{i=1}^{2} \mu_i^2 \left(\frac{f_i(\boldsymbol{x})^2}{\tilde{f}_i^2} - 1\right)^2 \tag{2.43}$$

with $\mu_1 = \mu_2 = 1$, and $(f_i(\boldsymbol{x}))_{i\in\{1,2\}}$ are the eigen-frequencies obtained by solving the equation of motion for un-damped free vibration applied to the structure, given by:

$$\mathbf{M}\ddot{\boldsymbol{u}} + \mathbf{K}\boldsymbol{u} = \mathbf{0} \tag{2.44}$$

where $\mathbf{M} = \begin{pmatrix} m_1 & 0 \\ 0 & m_2 \end{pmatrix}$ is the mass matrix and $\mathbf{K} = \begin{pmatrix} k_1 + k_2 & -k_2 \\ -k_2 & k_2 \end{pmatrix}$ is the stiffness matrix, and $\boldsymbol{u} = (u_1, u_2)^\intercal$ the displacement vector.

The posterior distribution of the parameters $\boldsymbol{X} = (X_1, X_2)$ is bi-modal with significantly distant modes (Beck and Au, 2002; Giovanis et al., 2017), which makes the problem difficult to solve when using classical MCMC sampling approaches.

2.4.1.2 Results

The PCK-SuS algorithm is applied by considering the following parameters:

- an initial ED size of $K_0 \in \{20, 50, 100, 200\}$,
- a ratio $\kappa = K/K_0 \in \{0, 0.1, 0.2, 0.5\}$.

An illustration of an application of the PCK-SuS algorithm (with $K_0 = 50$ and $K = 10$) to the aforementioned Bayesian inverse problem is illustrated in Fig. 2.7. Firstly, an initial ED formed by samples drawn from the prior is defined, and the surrogate log-likelihood is subsequently trained. The first step of SuS procedure enables to define $p_0 K = 500$ seeds to generate the population of the first subset. As shown in Fig. 2.7a, most of these seeds are located in a zone where ED points are sparse. Moreover, the misclassification probability (see Eq. 2.28) of such seeds is sensibly important, which indicates that LSF predictions are classifying posterior samples, and/or that predictions are significantly uncertain in such zones. The multiple point enrichment based on weighted K-means clustering proposed (see Section 2.3.2.2) enables to select points which are quite uniformly spaced in the aforementioned zone (given by white diamonds ($\Diamond$) in Fig. 2.7a). The surrogate model is then recalibrated based on the enriched ED, before performing the MCMC sampling within the first SuS level. Then, as shown in Fig. 2.7c, the seeds of SuS level 2 form two clusters. The point enrichment step proposes K new candidate points which are located in these clusters (Fig. 2.7c). Finally, during the last SuS level (Fig. 2.7e), the surrogate is enriched near high-probability zones of the posterior.

Next, the convergence of the error measure ξ in Eq. (2.40) with respect to the average number of model calls M is shown in Fig. 2.8. The proposed methodology is significantly more efficient when $\kappa > 0$, since ξ values for $\kappa > 0$ are about two orders of magnitude smaller than those for $\kappa = 0$, for a given ED size (see Fig. 2.8b). In the non-adaptive case ($\kappa = 0$), the error ξ is decreasing much more slower as the ED size increases. This is due to the fact that the posterior support is located in low-probability zones of the prior (see Fig. 2.7). Then, without adaptive point enrichment, a very large ED size K_0 is required to draw a sufficient amount of samples in informative zones. In this context, the proposed point enrichment method based on clustering is well suited to the problem, since it allows to enrich the surrogate log-likelihood near the posterior high-probability zones, even in the case of a non-connected posterior support.

Then, posterior samples generated with SuS algorithm and PCK-SuS algorithm are compared in Fig. 2.9. PCK-SuS results for $K_0 = 50$ and $\kappa \in \{0, 0.2, 0.5\}$ are presented. Firstly, the location of posterior modes is well reproduced, for $K_0 = 50$ and $\kappa \geq 0.2$. Broadly speaking, the shape of the joint posterior is well approximated by the proposed approach, with a limited amount of model calls ($M \approx 10^2$). Furthermore, QoI related to left and right clusters of the identified posterior are summarized in Table 2.1 & 2.2. An average number of model calls of about $M \approx 250$ is sufficient to provide an accurate estimation of posterior QoI, which represents a reduction of about 98.8% of the total cost of $2 \cdot 10^4$ model calls required by using the full likelihood function.

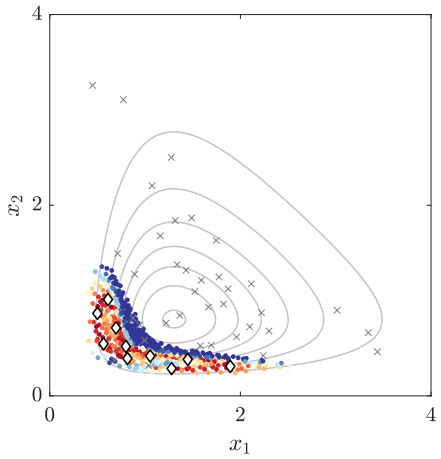

(a) Point enrichment at SuS level 1

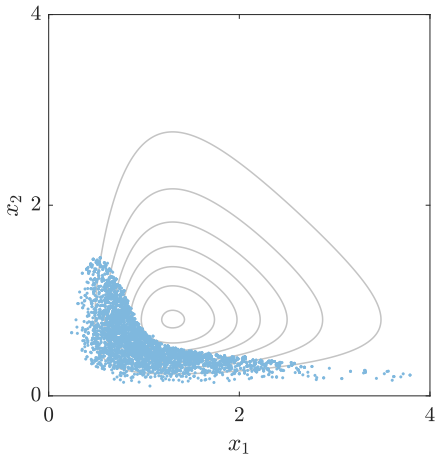

(b) Generated samples of SuS level 1

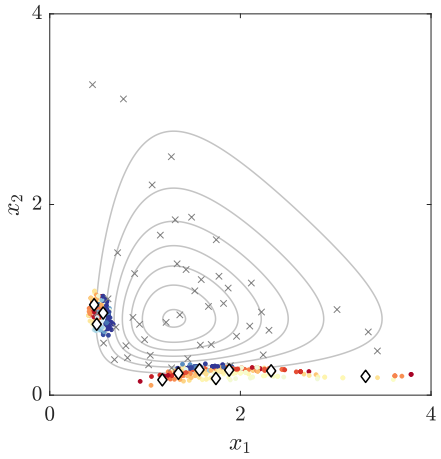

(c) Point enrichment at SuS level 2

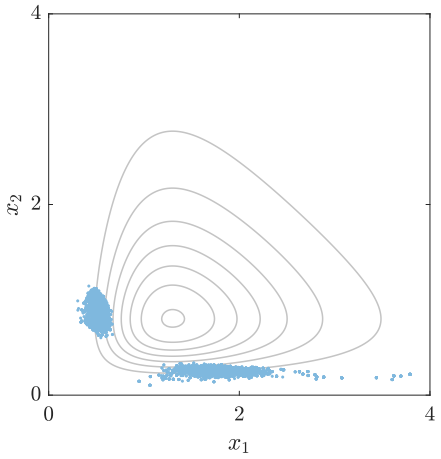

(d) Generated samples of SuS level 2

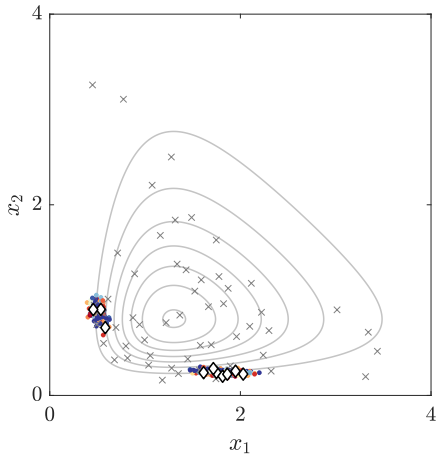

(e) Point enrichment at SuS level 3

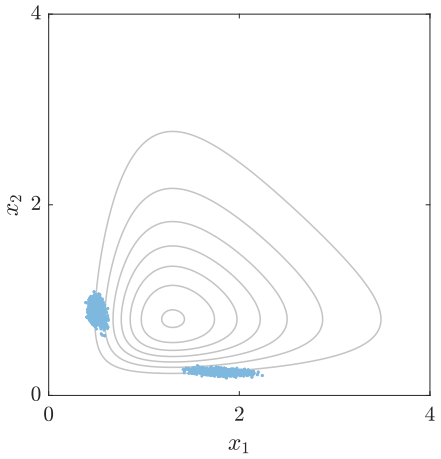

(f) Generated samples of SuS level 3

Figure 2.7: 2 DOF structure: illustration of the PCK-SuS algorithm. The points of the ED are shown by black crosses (×). Enrichment points of the ED are shown by white diamonds (◊). Candidate points (*left column*) are colored by their corresponding misclassification probability (from blue to red). Contours of the joint prior density are shown by grey solid lines.

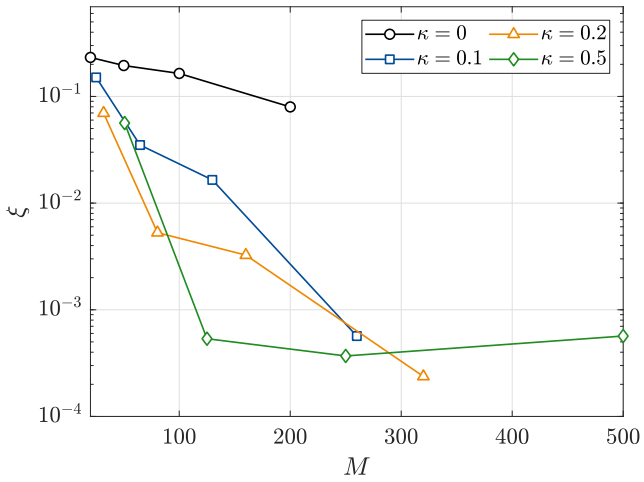

Figure 2.8: 2 DOF structure: convergence of error ξ with respect to the number M of full model calls.

	K_0	κ	M	$\mathbb{E}[X_1\|\boldsymbol{y}]$	$\mathbb{E}[X_2\|\boldsymbol{y}]$	$\mathrm{Std}[X_1\|\boldsymbol{y}]$	$\mathrm{Std}[X_2\|\boldsymbol{y}]$	Z $[\times 10^{-3}]$
PCK-SuS	50	0.2	80	0.502 (0.0)	0.893 (0.7)	0.044 (18.8)	0.086 (23.9)	1.484 (1.3)
	50	0.5	125	0.502 (0.0)	0.898 (0.1)	0.039 (3.5)	0.073 (3.9)	1.474 (1.9)
	100	0.2	160	0.505 (0.6)	0.887 (1.4)	0.045 (21.3)	0.085 (22.0)	1.618 (7.6)
	100	0.5	250	0.502 (0.0)	0.899 (0.0)	0.039 (3.0)	0.072 (2.9)	1.485 (1.2)
	200	0.2	320	0.501 (0.2)	0.900 (0.1)	0.038 (2.1)	0.070 (0.9)	1.509 (0.4)
	200	0.5	500	0.502 (0.0)	0.899 (0.0)	0.038 (0.6)	0.070 (0.3)	1.483 (1.3)
SuS			**20000**	**0.502**	**0.899**	**0.037**	**0.070**	**1.503**

Table 2.1: 2 DOF structure: posterior QoI related to the left cluster. *Relative errors in* % *are given in brackets.*

	K_0	κ	M	$\mathbb{E}[X_1\|\boldsymbol{y}]$	$\mathbb{E}[X_2\|\boldsymbol{y}]$	$\mathrm{Std}[X_1\|\boldsymbol{y}]$	$\mathrm{Std}[X_2\|\boldsymbol{y}]$	Z $[\times 10^{-3}]$
PCK-SuS	50	0.2	80	1.811 (0.2)	0.245 (0.8)	0.178 (25.7)	0.022 (17.9)	1.484 (1.3)
	50	0.5	125	1.812 (0.1)	0.246 (0.2)	0.144 (1.8)	0.020 (5.9)	1.474 (1.9)
	100	0.2	160	1.801 (0.7)	0.246 (0.3)	0.154 (8.5)	0.021 (11.9)	1.618 (7.6)
	100	0.5	250	1.813 (0.1)	0.246 (0.2)	0.144 (1.3)	0.019 (3.6)	1.485 (1.2)
	200	0.2	320	1.814 (0.0)	0.247 (0.0)	0.143 (0.9)	0.019 (0.5)	1.509 (0.4)
	200	0.5	500	1.814 (0.0)	0.247 (0.0)	0.144 (1.3)	0.019 (2.1)	1.483 (1.3)
SuS			**20000**	**1.814**	**0.247**	**0.142**	**0.019**	**1.503**

Table 2.2: 2 DOF structure: posterior QoI related to the right cluster. *Relative errors in* % *are given in brackets.*

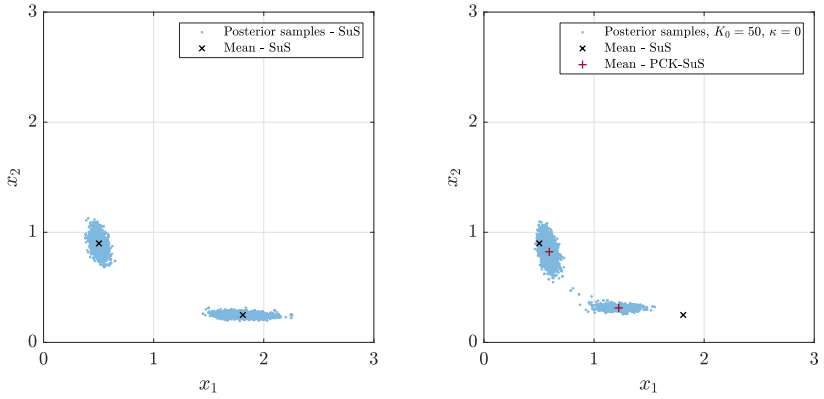

(a) SuS **(b)** PCK-SuS, $K_0 = 50$, $\kappa = 0$

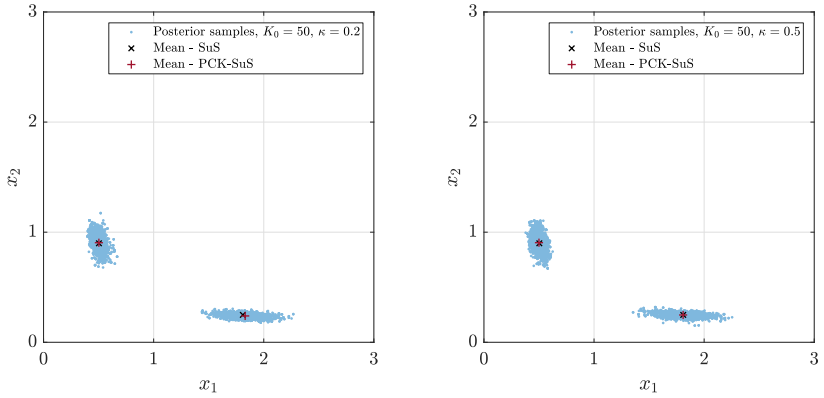

(c) PCK-SuS, $K_0 = 50$, $\kappa = 0.2$ **(d)** PCK-SuS, $K_0 = 50$, $\kappa = 0.5$

Figure 2.9: 2 DOF structure: posterior samples generated with SuS (a) and PCK-SuS (b-d) algorithms. The mean of each cluster is given by black $\times$ markers for SuS samples, and by red $+$ markers for PCK-SuS samples.

2.4.2 Multimodal Gaussian mixture

2.4.2.1 Problem description

The second case study was originally introduced in (Beck and Zuev, 2013), and involves a mixture of Gaussian distributions. A uniform prior over the square $[0, a]^2$ is considered, whereas the likelihood function is defined by:

$$\mathcal{L}(\boldsymbol{x}) = \sum_{j=1}^{q} w_j \varphi_2(\boldsymbol{x}; \boldsymbol{\mu}_j, \sigma^2 \mathbf{I}) \tag{2.45}$$

where the points $\boldsymbol{y} = \{\boldsymbol{\mu}_j\}_{1 \leq j \leq q}$ are drawn from the prior $\mathcal{U}([0, a]^2)$, $\{w_j\}_{1 \leq j \leq q}$ are the weights of the mixture, and $\varphi_2(\cdot; \boldsymbol{\mu}_j, \sigma^2 \mathbf{I})$ is the density of the bivariate Gaussian distribution $\mathcal{N}(\boldsymbol{\mu}_j, \sigma^2 \mathbf{I})$. One sets $a = 10$, $\sigma = 0.1$, $q = 10$ and $w_j = 1/q$ for all $j \in \{1, \ldots, q\}$. The corresponding posterior density $\pi(\boldsymbol{x}|\boldsymbol{y}) \propto \mathbf{1}_{[0,a]^2}(\boldsymbol{x}) \mathcal{L}(\boldsymbol{x})$ is multimodal, with 10 modes.

2.4.2.2 Results

The PCK-SuS algorithm is applied by considering the following parameters:

- an initial ED size of $K_0 \in \{50, 100, 150, 250\}$,
- a ratio $\kappa = K/K_0 \in \{0, 0.1, 0.2\}$.

Posterior samples drawn with SuS and PCK-SuS algorithm are compared in Fig. 2.10. PCK-SuS results are shown for $K_0 \in \{100, 150, 250\}$ and $\kappa = 0.2$. Firstly, as depicted by Fig. 2.10a, posterior samples obtained with the SuS algorithm separate into 10 significantly spaced clusters. This underlines the complexity of the posterior density, which would be difficult to sample with classical MCMC approaches, for which the generated Markov chains may be trapped near few modes (Beck and Zuev, 2013).

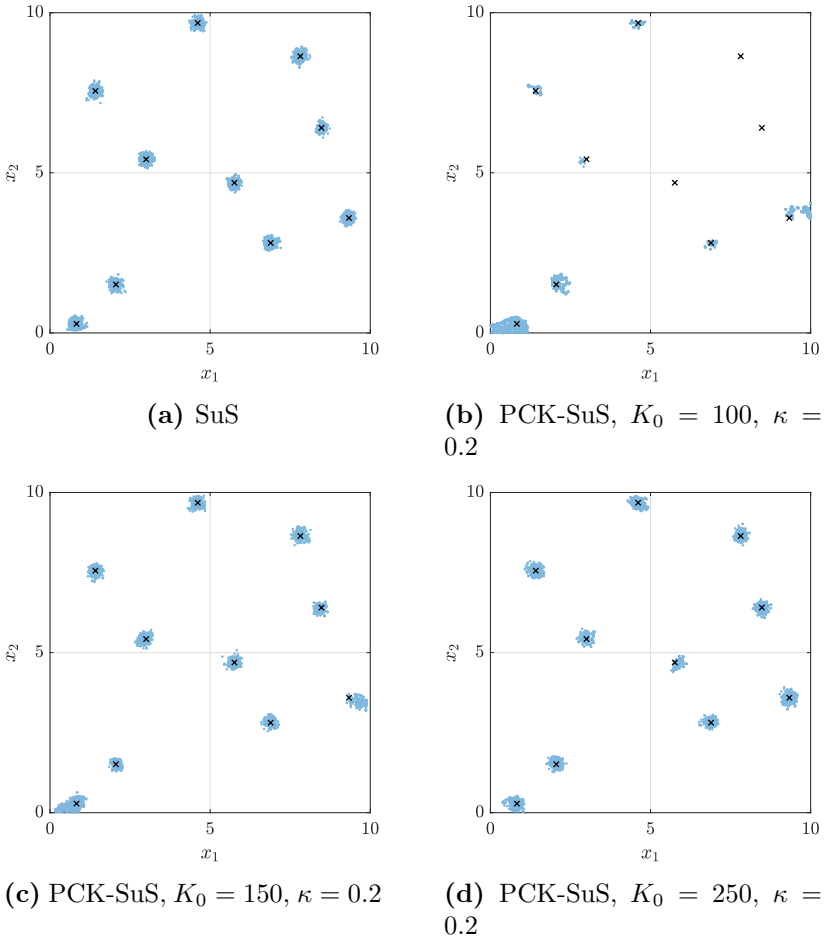

(a) SuS

(b) PCK-SuS, $K_0 = 100$, $\kappa = 0.2$

(c) PCK-SuS, $K_0 = 150$, $\kappa = 0.2$

(d) PCK-SuS, $K_0 = 250$, $\kappa = 0.2$

Figure 2.10: Multimodal Gaussian mixture: posterior samples generated with SuS (a) and PCK-SuS (b-d) algorithms. The modes $\{\boldsymbol{\mu}_j\}_{1 \leq j \leq q}$ of the posterior are shown by black crosses ($\times$).

Next, for $K_0 = 100$ and $\kappa = 0.2$, the proposed approach completely misses 3 modes (see Fig. 2.10b). When $K_0 = 150$ and $\kappa = 0.2$, the proposed approach correctly identifies the 10 modes of the posterior (see Fig. 2.10c), even though the spread of the clusters near $(0, 0)$ and $(10, 3)$ is roughly approximated. Lastly, the 10 modes of the posterior are well reproduced when $K_0 = 250$ and $\kappa = 0.2$ (see Fig. 2.10d).

The convergence of the error ξ in Eq. (2.40) with respect to M is shown in Fig. 2.11. First, when no surrogate model adaptation is performed (*i.e.* $\kappa = 0$), ξ stagnates around a value of 10^{-1}. This may be explained by the highly localized behavior of the likelihood

function, which seems to be difficult to approximate with a fixed ED built from the uniform prior $\mathcal{U}([0,a]^2)$. For a given number of full likelihood calls, significantly lower values of ξ are obtained when $\kappa > 0$. In particular, when $M \geq 200$, the error ξ with $\kappa = 0.2$ is approximately two orders of magnitude smaller than in the case $\kappa = 0$. This underlines the efficiency of the proposed adaptive point enrichment scheme, as mentioned in the example presented in Section 2.4.1. The proposed approach takes advantage of the local features provided by the Gaussian process of the PCK surrogate so as to better catch the likelihood behavior near the modes $\{\boldsymbol{\mu}_j\}_{1\leq j\leq q}$ of the posterior.

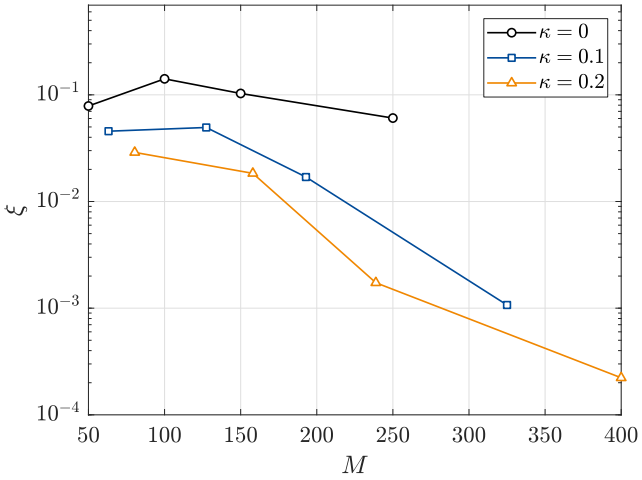

Figure 2.11: Multimodal Gaussian mixture: convergence of error ξ in Eq. (2.40) with respect to M.

	K_0	κ	M	$\mathbb{E}[X_1\|\boldsymbol{y}]$	$\mathbb{E}[X_2\|\boldsymbol{y}]$	$\mathrm{Std}[X_1\|\boldsymbol{y}]$	$\mathrm{Std}[X_2\|\boldsymbol{y}]$	Z
PCK-SuS	100	0.1	127	4.32 (14.6)	4.31 (13.8)	2.73 (7.2)	2.96 (2.2)	0.06 (525.4)
	100	0.2	158	4.58 (9.5)	4.78 (4.4)	2.83 (3.9)	2.97 (3.1)	0.05 (352.0)
	150	0.1	193	4.59 (9.4)	4.79 (4.1)	2.86 (2.9)	2.95 (1.8)	0.02 (138.0)
	150	0.2	239	5.07 (0.1)	4.92 (1.5)	2.95 (0.4)	2.85 (1.5)	0.01 (16.3)
	250	0.1	325	5.05 (0.2)	4.83 (3.4)	2.90 (1.4)	2.84 (1.8)	0.01 (4.4)
	250	0.2	400	5.06 (0.1)	4.95 (0.9)	2.93 (0.5)	2.89 (0.4)	0.01 (2.7)
SuS			**20000**	**5.06**	**4.99**	**2.94**	**2.90**	**0.01**

Table 2.3: Multimodal Gaussian mixture: posterior QoI. *Relative errors in % are given in brackets.*

Lastly, QoI related to the posterior distribution are summarized in Table 2.3. For the sake of brevity, only the components of the posterior mean $\mathbb{E}[\boldsymbol{X}|\boldsymbol{y}]$ and the standard deviation $\mathrm{Std}[\boldsymbol{X}|\boldsymbol{y}]$ are considered as QoI, rather than considering the statistics of each of the 10 clusters of the posterior. The proposed approach provides correct estimates of $\mathbb{E}[X_i|\boldsymbol{y}]$ and $\mathrm{Std}[X_i|\boldsymbol{y}]$ from $K_0 = 100$ and $\kappa = 0.2$. Moreover, fair estimates of the model evidence Z are obtained with $K_0 = 150$ and $\kappa = 0.2$. Finally, it is worth noting that the proposed method provides a quite good approximation of the posterior with a number of full likelihood evaluations of about $M \approx 240$ (see Table 2.3), which corresponds to a reduction of about 98.8% of the total cost of $2 \cdot 10^4$ full likelihood evaluations required by a direct application of the SuS procedure.

2.4.3 Diffusion inverse problem

2.4.3.1 Problem description

The third case study consists in a unidimensional diffusion problem introduced in Straub et al. (2016), as the steady state version of the problem studied in Marzouk and Najm (2009). The problem is described by the following diffusion equation on the unit interval $\mathcal{D} = [0, 1]$:

$$\partial_s \left(a(s) \partial_s u(s) \right) + b(s) = 0 \tag{2.46}$$

where ∂_s refers to the partial derivative w.r.t. the spatial coordinate s, the diffusivity $a(\cdot)$ is represented by a random field, and the source term $b(\cdot)$ is given by:

$$b(s) = \sum_{i=1}^{S} \frac{\varsigma_i}{\sqrt{2\pi}\sigma_i} \exp\left(-\frac{(l_i - s)^2}{2\sigma_i^2} \right) \tag{2.47}$$

This term corresponds to S localized sources with locations $(l_i)_{1 \leq i \leq S}$ and strengths $(\varsigma_i)_{1 \leq i \leq S}$ and widths $(\sigma_i)_{1 \leq i \leq S}$. One considers $S = 3$ sources at locations $l_1 = 0.25$, $l_2 = 0.5$ and $l_3 = 0.75$. The strengths are assumed to be identical, and are set as $\varsigma_i = 10$, as well as the widths, which are fixed to $\sigma_i^2 = 10^{-3}$. Furthermore, Dirichlet boundary conditions $u(0) = u(1) = 0$ are adopted to solve Eq. (2.46). This problem may typically be seen as a prototype for the inverse estimation of an inhomogeneous permeability field in a porous medium (Marzouk and Najm, 2009). It is solved by using linear finite elements, on a uniform grid with spacing $\Delta s = 1/48$.

The problem consists in inferring the diffusivity field $a(\cdot)$ from noisy measurements of the field $u(\cdot)$, provided by a set of $n = 11$ sensors uniformly spaced in $\mathcal{D}$ (excluding the endpoints). The prior of the log-diffusivity field $\log a(\cdot)$ is supposed to be a stationary Gaussian random field, with mean $\mu_{\log a} = 0.1$ and standard deviation $\sigma_{\log a} = 0.2$, and an exponential autocorrelation function given by:

$$R_{\log a}(s, s') = \exp\left(-\frac{|s - s'|}{\vartheta_{\log a}} \right) \tag{2.48}$$

with $\vartheta_{\log a} = 0.3$.

The log-diffusivity random field is represented by a truncated Karhunen-Loève (KL) (Ghanem and Spanos, 1991b; Loève, 1977) expansion:

$$\log a(s) \approx \mu_{\log a} + \sum_{i=1}^{d} \sqrt{\lambda_i} X_i \phi_i(s) \tag{2.49}$$

where $d = 10$ terms are retained, based on (Straub et al., 2016). $(X_i)_{1 \leq i \leq d}$ are d independent standard normal variables, and $(\lambda_i, \phi_i)_{1 \leq i \leq d}$ are the eigenvalues and eigenfunctions associated to the covariance function $\Sigma_{\log a}(s, s') = \sigma_{\log a}^2 R_{\log a}(s, s')$. The latter are satisfying the Fredholm integral equations of the second kind:

$$\int_{\mathcal{D}} \Sigma_{\log a}(s, s') \phi_i(s') \mathrm{d}s' = \lambda_i \phi_i(s) \tag{2.50}$$

for all $i \in \{1, \dots, d\}$, which can be solved analytically in the case of exponential covariance kernels (Ghanem and Spanos, 1991b).

Then, synthetic data $\boldsymbol{y} = \{u_{m,j}\}_{1 \leq j \leq n}$ are generated from a realization of the log-diffusivity random field, by computing the corresponding output field $u_m(\cdot)$ at sensors locations and adding to it a Gaussian noise term with zero mean and standard deviation $\sigma_m = 0.1$. In order to avoid to commit an *inverse crime* (Kaipio and Somersalo, 2005), this synthetic data is generated by using a much finer grid to solve Eq. (2.46). The $d = 10$ Gaussian random variables $(X_i)_{1 \leq i \leq d}$ are subsequently inferred from the generated data. The corresponding likelihood function is given by:

$$\mathcal{L}(\boldsymbol{x}) = \prod_{j=1}^{n} \varphi(u_j(\boldsymbol{x}); u_{m,j}, \sigma_m^2) = (2\pi\sigma_m^2)^{-\frac{n}{2}} \exp\left(-\frac{1}{2\sigma_m^2} \|\boldsymbol{u}(\boldsymbol{x}) - \boldsymbol{u}_m\|^2\right) \tag{2.51}$$

where $u_j(\boldsymbol{x})$ is the field u at the location of the j-th sensor, for a given realization $\boldsymbol{x}$ of the input random variables $\boldsymbol{X} = (X_1, \dots, X_d)$, and $\boldsymbol{u}(\boldsymbol{x}) = (u_j(\boldsymbol{x}))_{1 \leq j \leq n}$ and $\boldsymbol{u}_m = (u_{m,j})_{1 \leq j \leq n}$.

2.4.3.2 Results

The PCK-SuS algorithm is applied by considering the following parameters:

- an initial ED size of $K_0 \in \{50, 100, 250, 500\}$,
- a ratio $\kappa = K/K_0 \in \{0, 0.1, 0.2\}$.

The convergence of the error ξ in Eq. (2.40) with respect to M is shown in Fig. 2.12. For moderate to large ED sizes ($M \geq 250$), the adaptive point enrichment scheme leads to a smaller error than in the non-adaptive case (*i.e.* when $\kappa = 0$). Besides, for $M \leq 250$, the performance of the approach depends less on the adaptation step of the surrogate model, since ξ presents a similar behavior for $\kappa = 0$ and $\kappa > 0$. Such a behavior may be explained by the fact that most of the posterior mass is enclosed in high-probability zones of the prior. In this case, the adaptive point enrichment targets zones in which samples are frequently falling when sampling from the prior. This underlines the fact that the efficiency gain provided by adaptive surrogate modeling approaches is all the more important when the likelihood presents a localized behavior, typically when data are sufficiently informative and/or multi-modalities are encountered.

Then, it is worth noting that the *active dimensionality* of the problem is limited to 6, since the posterior marginals of the four last KL eigenmodes are sensibly close to their prior counterpart. Such a phenomenon has been often encountered in the framework of UQ benchmark problems related to diffusion problems with random diffusivity fields (Fajraoui et al., 2017; Wagner et al., 2021). Consequently, results are analyzed by focusing on the first six variables $(X_i)_{1 \leq i \leq 6}$ hereafter.

Posterior samples drawn with SuS and PCK-SuS algorithms with $(K_0, \kappa) = (250, 0.1)$ are compared in Fig. 2.13. The shape of the posterior distribution is well approximated with the proposed approach, with a quite limited amount of model calls ($M \approx 350$). In particular, the correlation structure of the posterior is well reproduced, notably regarding the couples (X_1, X_3) and (X_2, X_4) which present quite strong linear correlations. Posterior mean and standard deviation values are summarized in Table 2.4 & 2.5. It is also worthwhile

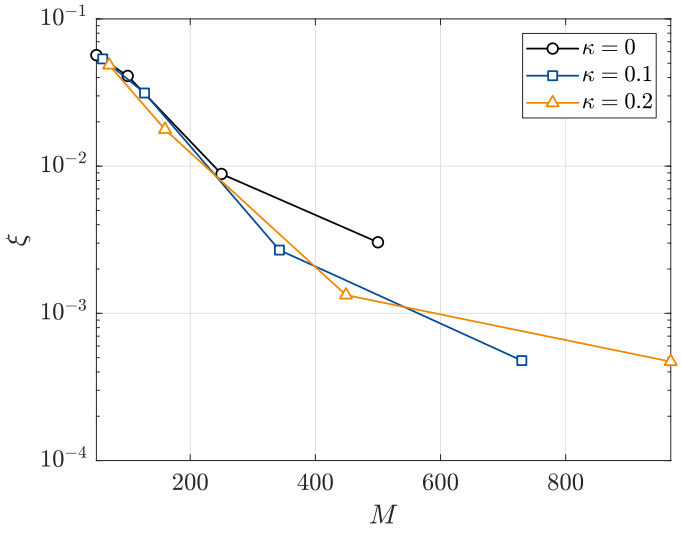

Figure 2.12: Diffusion problem: convergence of error ξ in Eq. (2.40) with respect to M.

noting that the following approach provides a fair estimate of the model evidence with a quite moderate amount of model calls ($\approx 350 - 500$), as underlined by Table 2.6 which summarizes values of the model evidence.

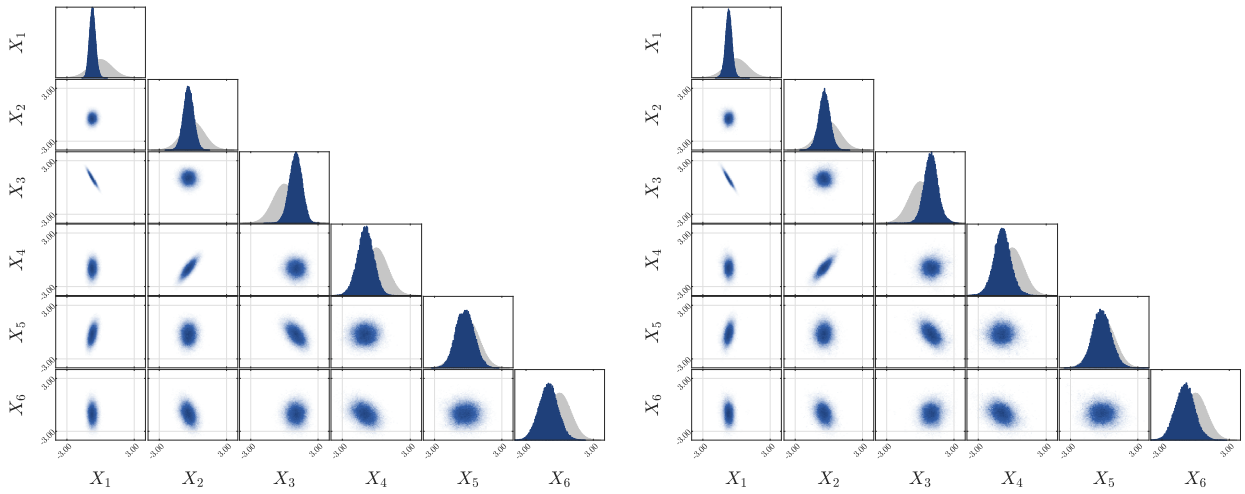

(a) SuS **(b)** PCK-SuS, $K_0 = 250$, $\kappa = 0.1$

Figure 2.13: Diffusion problem: posterior samples generated with SuS (a) and PCK-SuS (b) algorithms. Posterior samples are shown in blue, whereas prior samples are shown in grey.

$\mathbb{E}[X_i\|\boldsymbol{y}]$	K_0	κ	M	X_1	X_2	X_3	X_4	X_5	X_6
PCK-SuS	100	0.1	127	−0.55 (23.4)	−0.13 (68.1)	0.71 (29.6)	−0.57 (41.2)	0.05 (116.0)	−0.54 (46.0)
	100	0.2	160	−0.59 (17.2)	−0.26 (33.0)	0.76 (24.4)	−0.72 (24.7)	−0.01 (95.9)	−0.80 (20.1)
	250	0.1	343	−0.70 (2.9)	−0.41 (3.0)	0.96 (4.3)	−0.89 (7.8)	−0.22 (27.0)	−0.96 (5.1)
	250	0.2	449	−0.70 (2.6)	−0.40 (2.3)	0.97 (3.8)	−0.93 (3.6)	−0.23 (22.1)	−0.96 (5.2)
	500	0.1	730	−0.71 (1.1)	−0.37 (6.5)	0.99 (1.7)	−0.91 (5.2)	−0.28 (5.0)	−1.02 (1.2)
	500	0.2	968	−0.72 (0.1)	−0.38 (4.8)	1.01 (0.3)	−0.92 (4.3)	−0.30 (2.8)	−1.03 (2.6)
SuS			**27600**	**−0.72**	**−0.39**	**1.00**	**−0.96**	**−0.30**	**−1.01**

Table 2.4: Diffusion problem: posterior means of the random variables $(X_i)_{1\leq i\leq 6}$.

$\mathrm{Std}[X_i\|\boldsymbol{y}]$	K_0	κ	M	X_1	X_2	X_3	X_4	X_5	X_6
PCK-SuS	100	0.1	127	0.45 (69.5)	0.71 (59.0)	0.87 (59.1)	0.98 (38.9)	1.13 (43.2)	1.07 (28.0)
	100	0.2	160	0.38 (44.5)	0.62 (40.3)	0.77 (39.6)	0.86 (22.8)	1.00 (26.6)	1.04 (24.1)
	250	0.1	343	0.29 (8.9)	0.49 (10.7)	0.60 (9.1)	0.74 (4.8)	0.82 (3.9)	0.84 (0.7)
	250	0.2	449	0.28 (5.5)	0.48 (7.1)	0.58 (6.3)	0.72 (2.7)	0.81 (3.3)	0.85 (1.3)
	500	0.1	730	0.26 (0.2)	0.45 (1.4)	0.55 (0.2)	0.69 (1.3)	0.79 (0.2)	0.85 (1.8)
	500	0.2	968	0.26 (0.4)	0.45 (0.4)	0.55 (0.3)	0.70 (1.0)	0.77 (2.1)	0.83 (0.4)
SuS			**27600**	**0.26**	**0.44**	**0.55**	**0.70**	**0.79**	**0.84**

Table 2.5: Diffusion problem: posterior standard deviations of the random variables $(X_i)_{1\leq i\leq 6}$.

	K_0	κ	M	Z
PCK-SuS	100	0.1	127	87.09 (254.1)
	100	0.2	160	29.41 (19.6)
	250	0.1	343	22.73 (7.6)
	250	0.2	449	23.36 (5.0)
	500	0.1	730	23.75 (3.4)
	500	0.2	968	24.77 (0.7)
SuS			**27600**	**24.59**

Table 2.6: Diffusion problem: model evidence values.

Next, a comparison between the true log-diffusivity field, and the posterior log-diffusivity fields obtained with SuS and PCK-SuS algorithms is given in Fig. 2.14. Concerning the PCK-SuS algorithm, results are shown for $K_0 \in \{250, 500\}$ and $\kappa = 0.1$. As a validation of reference results, one observes that the posterior log-diffusivity field obtained with SuS matches well with the realization used to generate the synthetic data. Furthermore, the proposed approach provides a fair approximation of the posterior log-diffusivity when $K_0 = 250$ and $\kappa = 0.2$, with a slight overestimation of the variance, though (see Fig. 2.14a). Then, the posterior log-diffusivity field is precisely approximated when $K_0 = 500$ and $\kappa = 0.1$ (see Fig. 2.14b).

Furthermore, contours of the posterior covariance function of the log-diffusivity field obtained from SuS and PCK-SuS samples are shown in Fig. 2.15. Approximately 730 model calls are sufficient to provide an accurate approximation of the covariance function (see Fig. 2.15b). Lastly, it is worth noting that a satisfactory approximation of the posterior is obtained with an average number of model calls of $M = 730$, which represents a reduction of about 97.4% of the total cost of $2.76 \cdot 10^4$ calls required by an inversion using the full likelihood (see Table 2.4 & 2.5).

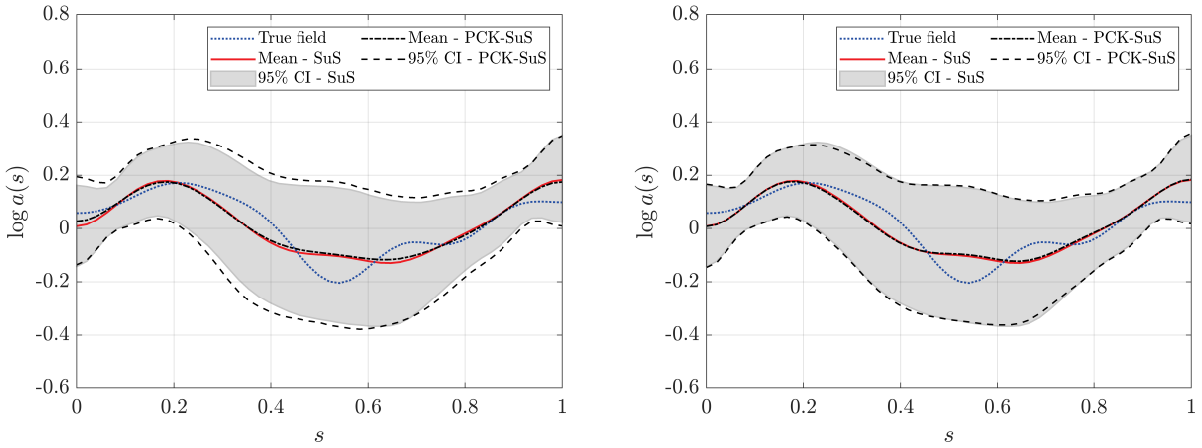

(a) PCK-SuS, $K_0 = 250$, $\kappa = 0.1$ **(b)** PCK-SuS, $K_0 = 500$, $\kappa = 0.1$

Figure 2.14: Diffusion problem: posterior log-diffusivity field $\log a(\cdot)$ estimated from posterior samples generated with SuS and PCK-SuS algorithms.

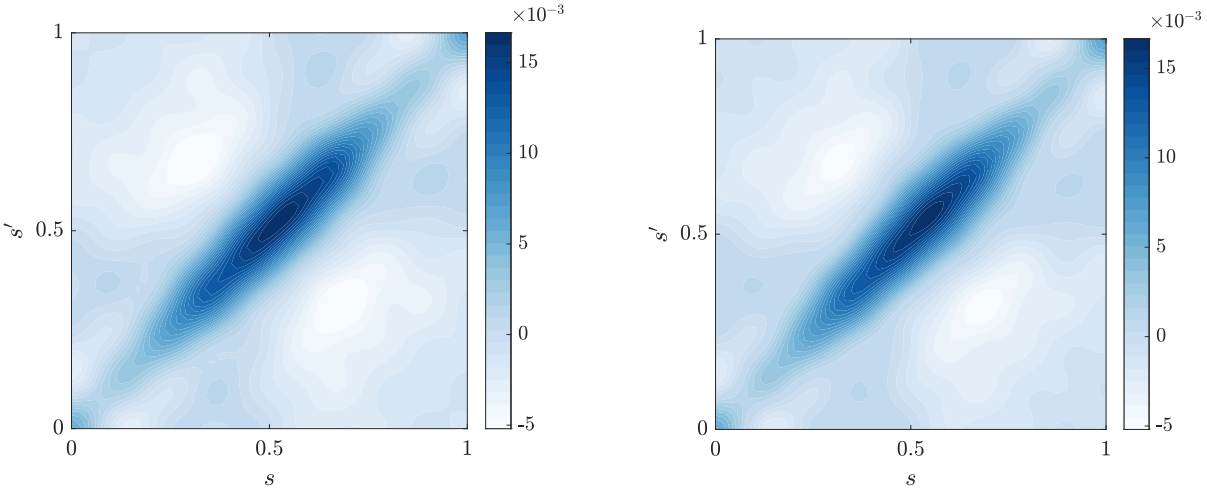

(a) SuS **(b)** PCK-SuS, $K_0 = 500$, $\kappa = 0.1$

Figure 2.15: Diffusion problem: posterior covariance function of the log-diffusivity field estimated from samples generated with SuS and PCK-SuS algorithms.

2.5 Conclusion

The main goal of this chapter was twofold, namely to present the Bayesian computational framework that will be used for solving Bayesian inverse problems in the next chapters of this thesis, and to subsequently introduce a novel adaptive surrogate modeling approach aiming at accelerating Bayesian computations, particularly when dealing with costly computational models.

In this perspective, this chapter has firstly investigated the so-called *Bayesian updating with Structural reliability methods* (BuS) framework originally introduced in (Straub and Papaioannou, 2015), which reinterprets Bayesian inference as a structural reliability problem. This framework allows to deploy a broad range of structural reliability methods to perform Bayesian computations, including the well-known Subset Simulation (SuS) method (Au and Beck, 2001), which has been specifically adapted to the BuS framework in (Betz et al., 2018b). In particular, this last method constitutes an appealing alternative to classical MCMC algorithms, and will be used throughout the next chapters of this thesis in the framework of inverse UQ tasks related to nuclear containment buildings.

Nevertheless, as any sampling technique, the aforementioned SuS method may require a large amount of model evaluations, which makes it computationally intractable when confronted to costly forward models. Then, this chapter presented a novel surrogate-based Bayesian computational approach within the BuS framework, that combines adaptive *Polynomial Chaos Kriging* (PCK) surrogates with the aforementioned SuS method. In this context, a prior-based PCK surrogate model is firstly built in order to catch the global trend of the log-likelihood on the support of the prior. This surrogate model is subsequently enriched throughout the SuS procedure by selecting points in informative regions, based on principles inspired from *active learning* techniques for structural reliability (Moustapha et al., 2022). In particular, the underlying Gaussian process of the PCK surrogate enables to better catching local variations of the log-likelihood, and provides a local error measure which can be used so as to enrich the surrogate model.

The proposed approach has been applied to several academic cases studies with varying complexity, involving a two degrees-of-freedom structure, a multi-modal Gaussian mixture and a diffusion problem with moderate active dimensionality. Numerical investigations have suggested that the proposed approach provides satisfactory approximations of the posterior distributions involved, even in the case of likelihood functions with localized behavior, or multi-modal distributions. Moreover, such approximations have been obtained for a quite limited amount of model calls (*i.e.* $50 - 500$), which makes the proposed approach suitable for computationally demanding models.

Besides, the proposed approach presents several shortcomings that may be addressed in further works. Firstly, it appears from test cases results that the stopping criterion of the point enrichment step has been rarely reached during calculations. This may be due to the fact that the adopted threshold value for the misclassification probability (see Section 2.3.2.4) is too conservative, as underlined in (Cui et al., 2019; Moustapha et al., 2022). Therefore, a more precise stopping criterion may be defined in order to avoid unnecessary model calls throughout Bayesian computations.

Furthermore, although the SuS procedure is well-known for efficiently tackling high-dimensional problems, its coupling with Kriging-based surrogates models typically jeopardizes its application to high-dimensional Bayesian inverse problems with costly forward models. Indeed, the optimization problem involved in the estimation of Kriging parameters may be difficult to solve in high dimensions (Angelikopoulos et al., 2015; Wang and Shafieezadeh, 2020). This is in line with results from the recent survey and benchmark on active learning structural reliability methods of Moustapha et al. (2022), which suggest that PCK surrogate models are well suited for parameter dimensions $d \leq 20$, whereas PCE surrogates perform better in higher dimensions.

Hence, the proposed approach may be adapted to PCE in order to tackle problems with higher dimensions, by using a learning function adapted to PCE (*e.g.* that introduced in (Marelli and Sudret, 2018)). Alternatively, *dimensionality reduction* techniques for Bayesian inverse problems could be used in order to exploit the low-dimensional structure of the posterior distribution, and then construct surrogates on subspaces with smaller dimensionalities, corresponding to few dominant directions of the input parameter space (Zahm et al., 2020). In this context, *active subspaces* (AS) (Constantine et al., 2014, 2016) and *likelihood-informed subspaces* (LIS) (Cui et al., 2014; Cui and Zahm, 2021; Zahm et al., 2022) methods exploit the gradient of the forward model and/or of the likelihood function so as to determine the low-dimensional structure of the posterior. Likewise, Cui et al. (2016) proposed an approach aiming at constructing low-dimensional subspaces of both the parameter space and the state space of the forward model to accelerate large-scale Bayesian inverse problems. Lastly, recent work of Bigoni et al. (2022), not specifically focused on Bayesian inverse problems, proposed a dimension reduction approach for surrogate modeling, that could be used in order to efficiently surrogate high-dimensional forward models or log-likelihood functions.

Then, the first two chapters of this thesis have enabled to establish a basis of UQ computational tools, which will constitute the building bricks of numerical strategies aiming at evaluating the long-term behavior of containment buildings in a probabilistic setting. The following chapters of this thesis are dedicated to the construction of such strategies, and their application to real containment structures. In particular, the next chapter aims at providing an introduction to the physical problem behind the aging of containment buildings, by introducing the main physical phenomena involved by concrete aging, and by subsequently presenting the modeling strategy adopted so as to describe these phenomena.

3

Aging of concrete in large containment structures: physical phenomena and modeling hypotheses

Contents

3.1 Introduction

Concrete is a complex porous and multiphasic material which is in constant thermodynamic disequilibrium with its surrounding environment. As a result, concrete is subjected to several physical processes affecting the evolution of its properties and its response to multi-physic loads over time. Such a transformation is known as *aging*. The aging process of concrete may be divided into two distinct phases, namely:

- an *early age* phase, which mainly corresponds to concrete hydration and hardening, through an ensemble of exothermal chemical reactions existing between the different constituents of concrete (*e.g.* cement, water, sand, aggregates and additives). Its duration is typically about few weeks.

- a *long-term* phase, corresponding to the time evolution of the behavior of hardened concrete under exploitation loads, including ambient thermo-hydric conditions of the operating structure, as well as mechanical loading (*e.g.* prestressing or dead weights). Its duration is about few decades, and the present thesis will be mainly focused on this phase.

During the last decades, experimental research studies have enabled to improve the understanding of physical phenomena related to concrete aging. Along with such experimental advances, a broad range of mathematical models aiming at describing the aforementioned physical phenomena has been developed, including analytical functions, differential equations or partial differential equations. These models serve as a basis to establish numerical strategies aiming at assessing the Thermo-Hydro-Mechanical and Leakage (THML) behavior of concrete, from microscopic to structural scale (Bouhjiti et al., 2018b; Chhun, 2017).

Consequently, the main goal of this chapter is to present a modeling strategy aiming at assessing the long-term THML behavior of aging NCB, that will constitute the core of UQ analyses performed in the next chapters of this thesis. In this context, it is aimed to capitalize on former works related to THML modeling (including (Boucher, 2016; Bouhjiti et al., 2018b)), through the combination, and possibly the modification, of existing behavior laws. In particular, the main buildings bricks of the aforementioned computational model will be selected by following several guidelines promoting the tractability of UQ methods. In this perspective, the devised model should be able to reasonably assess the global THML behavior of aging NCB without requiring a prohibitive computational cost. Furthermore, the so-called *parsimony principle* mentioned in Section 1.3.2.5 will be also used to select models: in the case of several competing models that equally well explain some observed data, the "simpler" model will be preferred. Here, the meaning of the term "simple" has to be interpreted in the sense of mathematical complexity, which includes dimensionality (*i.e.* the number of parameters).

This chapter is organized as follows: firstly, a general overview of the physical phenomena related to concrete aging, as well as the effect of such phenomena on the long-term integrity of containment structures, is given in Section 3.2. Then, the THML modeling strategy adopted in this thesis is described in Section 3.3.

3.2 Physical phenomena of concrete aging in large structures

3.2.1 Thermo-hydration and maturity

During the early age phase, concrete hydration corresponds to chemical reactions between the different phases of cement with water (Bye, 1999; Taylor, 1997). Such reactions corresponds to successive dissolution of anhydric reactants, which form hydrates that are stable in water. Cement essentially contains four compounds, namely dicalcium and tricalcium silicate (C_2S and C_3S), tricalcium aluminate (C_3A) and tetracalcium aluminoferrite (C_4AF) (Neville, 1996). The chemical equations corresponding to hydration of these reactants are given by:

$$C_2S + (\beta + \gamma)H \rightarrow C_\alpha SH_\beta + \gamma CH \tag{3.1a}$$

$$C_3S + (\beta + \delta)H \rightarrow C_\alpha SH_\beta + \delta CH \tag{3.1b}$$

$$C_3A + 3C - S - H_2 + \varepsilon H \rightarrow C_6AS_3H_{\varepsilon+6} \tag{3.1c}$$

$$C_4AF + 3C - S - H_2 + \varepsilon H \rightarrow C_6AFS_3H_{\varepsilon+6} \tag{3.1d}$$

where $C = CaO$, $S = SiO$, $A = Al_2O_3$, $F = Fe_2O_3$ and $H = H_2O$ are notations adopted in cement chemistry (Taylor, 1997), whereas $\alpha, \beta, \gamma, \delta$ and ε denote stoichiometric coefficients.

Concrete hydration is an exothermal reaction, in the sense that it induces a heat release. Therefore, heat production may be seen as an indicator of the hydration progress. In the case of large concrete structures, the temperature may reach approximately 60°C (Benboudjema and Torrenti, 2008). Moreover, hydration is a thermo-activated process (Arrhenius, 1915), which means that hydration kinetics increase with temperature.

The hydration process is summarized in Fig. 3.1. Firstly, during the first minutes of the hydration process, a heat peak is observed, which corresponds to the initial hydration of the surface of cement particles. Then, a so-called *dormant* phase initiates, during which concrete is sensibly deformable. About two hours later, an acceleration of the hydration process is observed, which corresponds to a new heat release. A second heat peak is reached after approximately 10 hours. Then, this second peak is followed by a deceleration phase, which corresponds to a continuous decrease of the heat release. Finally, a so-called *consolidation* phase initiates when hydration is no longer possible at the surface of cement grains. During this period, hydrates become denser through water diffusion oriented towards the interior of cement grains.

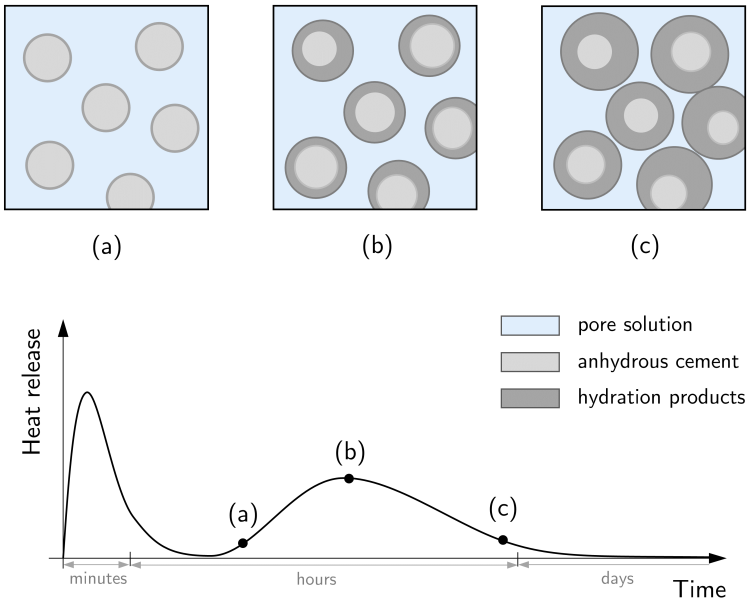

Figure 3.1: Time evolution of heat release during hydration process (bottom) and schematization of the formation of hydrates and their consolidation (top). Adapted from (Scrivener et al., 2015).

Moreover, the end of the second heat peak corresponds to the initiation of concrete setting, which corresponds to the transition to a solid state, induced by the establishment of connected hydrates bridges between cement grains. Such connections between cement grains contribute to the development of the apparent stiffness and strength of concrete. In this context, maturity refers to the percolation process of hydrates which contributes to the development of mechanical properties. As a result, mechanical properties of concrete may be seen as increasing functions of the hydration degree of concrete (De Schutter and Taerwe, 1996), once a sufficient hydration rate has been reached (Acker, 1988).

3.2.2 Desiccation

Water is present in the form of liquid and gaseous phases in the concrete porosity (Benboudjema, 2002). After the concrete setting, the concrete porosity is practically saturated with water, despite the fact that water has been partially consumed during concrete hydration (Baroghel-Bouny, 1994). Therefore, concrete is in a hydric disequilibrium with its surrounding environment, the ambient hygrometry of the latter being sensibly weaker. Desiccation (or drying) refers to the physical process tending to re-establish the thermodynamical equilibrium between liquid and gaseous phases. This process notably induces multiple transport mechanisms, with varying intensity and levels of coupling, depending on the ambient relative humidity (RH) (Chen, 2011; Xi et al., 1994). In this context, under normal temperature and pressure conditions, four main mechanisms may be mentioned (see Fig. 3.2) (Baroghel-Bouny, 1994):

- molecular adsorption or desorption at pore surfaces,
- condensation and evaporation at liquid/gas interfaces,

- molecular diffusion of water vapor (based on Fick's law),
- fluid flow through permeation (based on Darcy's law).

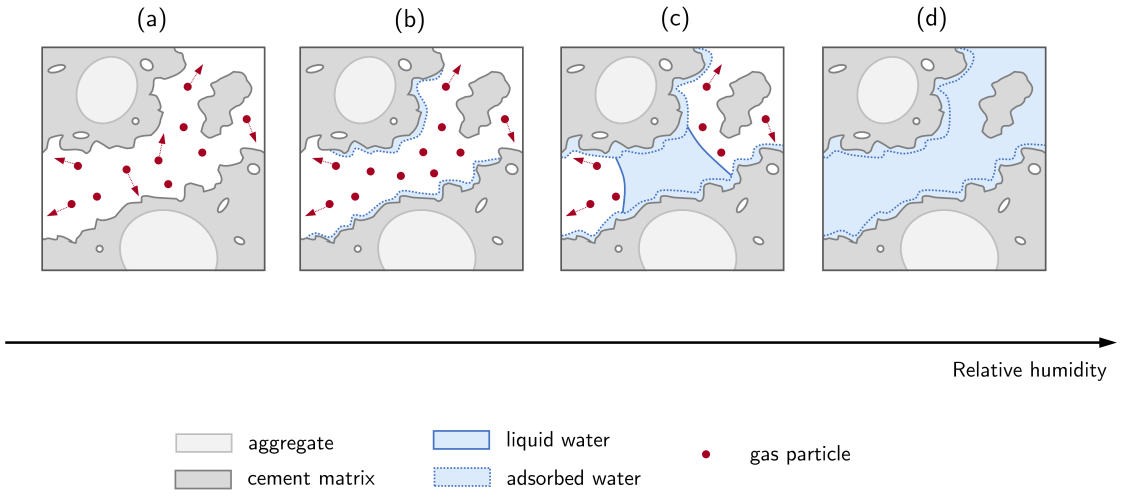

Figure 3.2: Moisture transport mechanisms in concrete according to ambient RH: (a) mono-molecular adsorption and gas diffusion; (b) multi-molecular adsorption (d) water saturation and liquid water diffusion.

Moreover, the variation of the water content of concrete may express a drying of its porosity (*i.e.* desorption), but also humidification (*i.e.* sorption), depending on the gradient of RH existing between concrete's free surface and its surrounding environment (Bouhjiti, 2018). Sorption/desorption experiments aim at analyzing the relationship between the moisture content of concrete and its RH (Zhang et al., 2016). It is worth noting that the obtained sorption/desorption curves may express a non-bijective relationship between the two aforementioned physical quantities: indeed, in the case of drying/humidification cycles, hydric transfers in concrete porosity present an irreversible behavior, and hysteresis phenomena are observed (Granger, 1995).

Nevertheless, in the case of large structures, such phenomena principally concern the hydric behavior of skin concrete, rather than the mean hydric behavior of structure's thickness, as emphasized by Bouhjiti et al. (2018a). Furthermore, desiccation constitutes a thermo-activated process: an increase of temperature induces an acceleration of the diffusion of water molecules in the concrete volume, and affects the concrete diffusivity (Caré, 2008; Granger, 1995), as well as sorption/desorption curves (Poyet, 2009).

3.2.3 Shrinkage

Shrinkage refers to dilation of the volume occurring during or after concrete setting. Such a phenomenon may be induced by concrete hydration, as well as variations of the temperature or moisture content of concrete. In the case of endogenous conditions, three types of shrinkage are identified, namely chemical, auto-desiccation and thermal. In the case of exogenous conditions, including thermo-hydric loads, additional strains are attributable to desiccation shrinkage.

3.2.3.1 Chemical shrinkage

Chemical shrinkage, also known as Le Chatelier's contraction (Le Chatelier, 1904), corresponds to a contraction occuring during the concrete hydration process. Such a contraction stems from the fact that hydration products occupy less absolute volume than the initial concrete mix (Jensen and Hansen, 2001). An illustration of the principle of chemical shrinkage is given in Fig. 3.3.

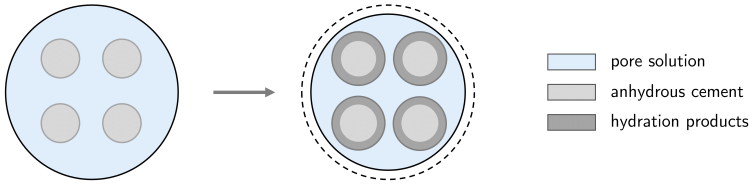

Figure 3.3: Illustration of chemical shrinkage, adapted from Gao et al. (2014).

3.2.3.2 Auto-desiccation shrinkage

After concrete setting, the skeleton of concrete presents a significant stiffness, whereas the hydration process continues to consume water in the capillary porosity of concrete. This yields the formation of internal voids in the concrete matrix (Gao et al., 2014). In the absence of moisture transfer with its external environment, the development of such voids induces the diminution of the internal RH, and the formation of air-water menisci. The aforementioned decrease of RH leads to a decrease of capillary pressures, which are responsible for tensile stresses applied on air-water menisci, according to Laplace-Kelvin's law:

$$p_c = p_g - p_l = \frac{\rho_w RT}{M_g} \log h = \frac{2\gamma}{r_m} \tag{3.2}$$

where p_c denotes the capillary pressure, p_g the air pressure, p_l the water pressure, ρ_w the density of water, $R = 8.314$ J.K^{-1}.mol^{-1} the ideal gas constant, T the temperature, M_g the molar mass of the gaseous phase (*i.e.* air and water vapor), h the RH, γ the superficial tension and r_m is the radius of the air-water menisci.

Tensile stresses applied to air-water menisci are balanced by compression stresses on hydrates, thus producing a global contraction of the solid skeleton. As a result, a global reduction of the concrete volume, called auto-dessication shrinkage, is observed (Persson, 1998). Illustrations of auto-dessication shrinkage and Laplace-Kelvin's law are given in Fig. 3.4.

3.2.3.3 Thermal dilation

Thermal dilation corresponds to volume variations induced by variations of temperature. According to experimental investigations of Piasta (1984) and Hilaire (2014), a linear relation between temperature and thermal dilation strains has been observed for a range of temperatures corresponding to exploitation conditions (*i.e.* $0 - 75°$C). In particular, the exothermal reaction of hydration induces a positive volume variation of concrete, followed by a negative variation during the cooling phase, corresponding to a slow-down of hydration kinetics (Bouhjiti, 2018).

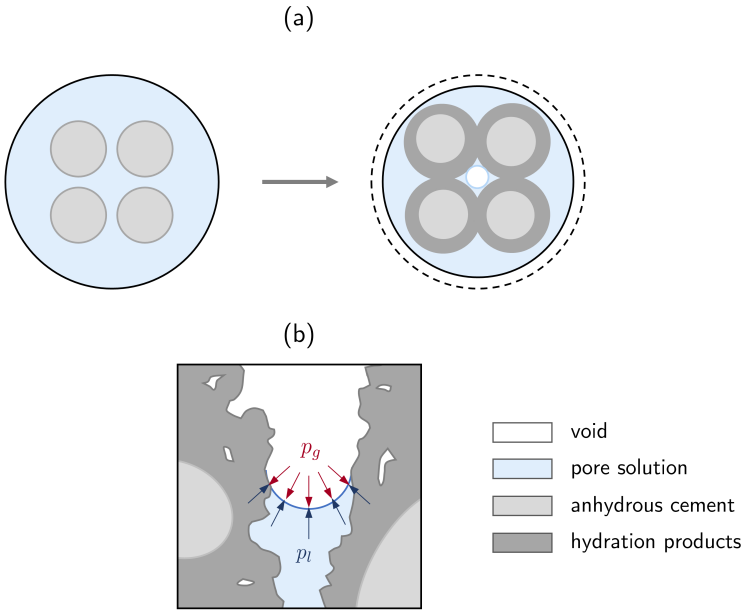

Figure 3.4: (a) illustration of auto-desiccation shrinkage, adapted from (Gao et al., 2014); (b) illustration of Laplace-Kelvin's law in a pore, adapted from (Bouhjiti, 2018).

3.2.3.4 Desiccation shrinkage

As previously mentioned, desiccation shrinkage corresponds to volume variations of concrete induced by desiccation. Desiccation shrinkage may be explained by physical mechanisms which are sensibly analogous to those behind auto-dessication shrinkage (Hilaire, 2014) (see Fig. 3.4). As the humidity of the external environment is lower than the humidity in concrete, the ambient RH in concrete porosity diminishes, which leads to capillary tensile stresses on the surfaces of hydrated grains. As a result, a global volume variation is observed (Bissonnette et al., 1999).

Experimental investigations of Granger (1995) suggested a practically linear relationship between desiccation shrinkage strains and the water content of concrete. Furthermore, Baroghel-Bouny et al. (1999) observed a linear relation between desiccation shrinkage strains and concrete RH, in the case of RH values larger than 50%. It is worth noting that a similar relation has been observed in the case of cement paste, for a wider RH range, though (Baroghel-Bouny et al., 1999; Kinda et al., 2022). Moreover, similarly to the sorption/desorption curve of concrete, several experimental investigations (Granger, 1995; Hilaire, 2014; Sabri and Illston, 1982) highlighted some irreversible and/or hysteresis phenomena for desiccation shrinkage strains, in the case of drying/humidification cycles.

At structural scale, concrete desiccation is a slow and heterogeneous process (Benboudjema, 2002): the RH field of the concrete volume typically presents strong gradients near boundaries participating to hydric transfers. As a result, desiccation shrinkage strains are more important near such boundaries (Bouhjiti, 2018). Conversely, the core of the concrete volume presents a higher RH, which yields restrained shrinkage strains and thus the development of skin tensile stresses. Meanwhile, the core is subjected to compression stresses. Moreover, skin tensile stresses may typically exceed the tensile strength of concrete (Benboudjema et al., 2001), which induces cracking. Then, the presence of cracks might locally

accelerate drying kinetics of concrete, due to higher hydric exchange surfaces. However, as underlined by Granger (1995), the presence of cracks weakly affects the global hydric behavior of the concrete volume at structural scale.

3.2.4 Creep

Creep strains may be divided into two contributions, namely basic creep and desiccation creep strains (Benboudjema, 2002). These two contributions are described hereafter.

3.2.4.1 Basic creep

Basic creep occurs during both early age and long-term phases, and corresponds to the total strain of a concrete volume in non-drying conditions, to which instantaneous and shrinkage strains have been subtracted. Several physical mechanisms are proposed in the literature in order to explain the origins of basic creep. These mechanisms notably highlight the prominent role of water in the development of basic creep (Acker, 1988; Pihlajavaara, 1974). Bažant and Prasannan (1989a,b) have suggested that the evolution of mechanical properties of concrete would be responsible for basic creep, based on the so-called solidification theory. Sellier et al. (2012, 2016) have also proposed that consolidation and micro-cracking in the concrete volume would be responsible for basic creep. Furthermore, Lohtia (1970), Wittmann (1982) and Ulm and Acker (1998) have adopted the so-called water migration theory so as to explain basic creep: external stresses induce the migration of adsorbed water in the capillary porosity, which notably yields a deformation of the solid skeleton. Broadly speaking, basic creep includes two main regimes (Benboudjema, 2002):

- a short-term (reversible) regime, during which applied stresses induce a thermodynamic disequilibrium in the water adsorption zones. Then, according to the aforementioned water migration theory, equilibrium tends to be re-established through the diffusion of adsorbed water through capillary pores (see Fig. 3.5a). As a result, short-term basic creep strains are generated. Such an hypothesis has been corroborated by several experimental studies (Day and Gamble, 1983; Ulm and Acker, 1998).

- a long-term (irreversible) regime, observed after several years, involving a strong effect of aging on the amplitude of basic creep strains. Some authors have proposed that such an aging effect may be linked to the relaxation of micro-stresses in restrained water adsorption zones (Bažant et al., 1997; Ulm and Acker, 1998). This relaxation leads to slipping of C-S-H sheets (Bažant et al., 1997; Lohtia, 1970), which yields long-term basic creep strains (see Fig. 3.5b). Several experimental studies have emphasized the role of the slipping of C-S-H sheets in the development of basic creep strains (Bentur et al., 1979; Ulm and Acker, 1998).

Moreover, a third basic creep regime may be mentioned, namely *tertiary creep* (Torrenti et al., 2008). Such a regime is encountered if the applied loading is sufficiently important, and/or if the latter is applied for a sufficiently long period. In such cases, the micro-cracking network growth, initiated before reaching tertiary creep regime, is accelerated, which leads to the development of damage and macro-cracks. Nevertheless, at the scale of existing large

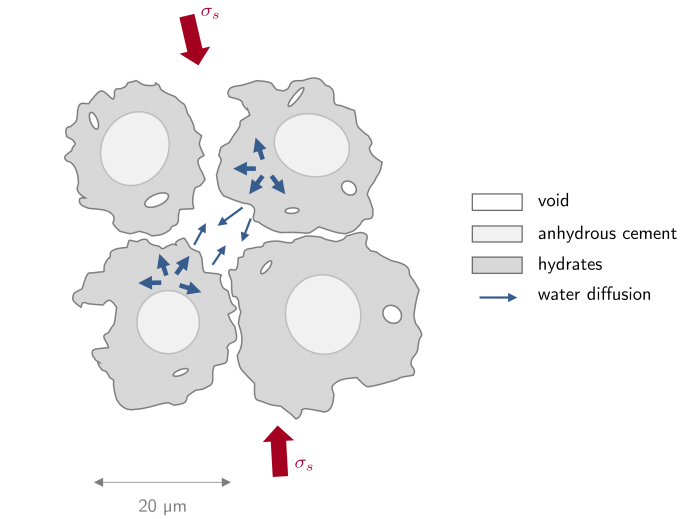

(a) Short-term basic creep

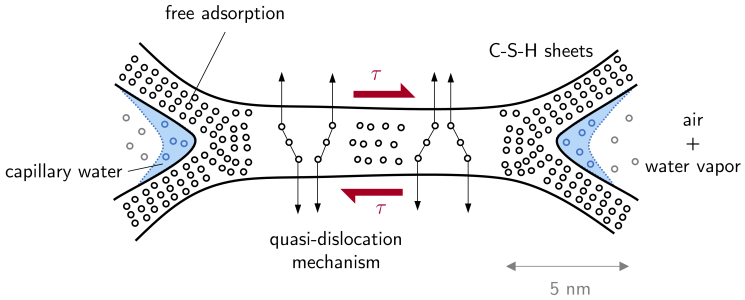

(b) Long-term basic creep

Figure 3.5: Illustration of mechanisms of basic creep, adapted from (Ulm and Acker, 1998)

containment structures such as NCB, the probability to reach such a regime is negligible when considering normal exploitation loads (*i.e.* except accidental situations) (Bouhjiti, 2018).

As previously mentioned, basic creep is sensibly dependent on the moisture content of concrete. Several experimental studies highlighted a quasi-proportionality relation between basic creep strain and RH (Pihlajavaara, 1974; Wittmann, 1970). It is worth noting that such a relationship has been observed for concrete: when considering cement paste, Kinda (2021) observed a nonlinear relationship between basic creep strain and RH, for low RH values. Moreover, the basic creep behavior under compressive stresses seems to be sensibly different than that under tensile stresses (Hilaire, 2014; Rossi et al., 2012). Furthermore, the basic creep behavior of concrete is also driven by the intensity of the applied load, as underlined in (Benboudjema, 2002; Granger, 1995). Then, several studies have highlighted the fact that basic creep sensibly depends on the age of loading: the amplitude of basic creep strains increases with the stiffness of the cement paste (De Schutter, 1999; Niyogi et al., 1973). Moreover, some authors have also pointed out the dependency of basic creep on the concrete formulation (*e.g.* cement type, water/cement ratio) (Li et al., 2001).

3.2.4.2 Desiccation creep

When a concrete volume is subjected to desiccation while being subjected to mechanical load, the observed strain is higher than that obtained in the same configuration with non-drying conditions. Such a phenomenon is known as *Pickett effect* (Pickett, 1942). Desiccation creep corresponds to the total strain, to which the instantaneous elastic strain and the previously mentioned shrinkage and basic creep strains have been subtracted.

The mechanisms that cause desiccation creep are complex and difficult to interpret, so much that there is no consensus in the literature (Benboudjema, 2002; Hilaire, 2014). Bažant and Chern (1985) suggest that desiccation creep is caused by a so-called *"stress-induced-shrinkage"* resulting from two moisture diffusion modes, namely macroscopic diffusion in macro-pores (attributed to drying), and microscopic diffusion in micro-pores. Furthermore, desiccation creep may also be attributed to the relaxation of micro-stresses in restrained water adsorption zones (Bažant et al., 1997), which has been previously mentioned for the case of basic creep. An illustration of the principle of desiccation creep is given in Fig. 3.6.

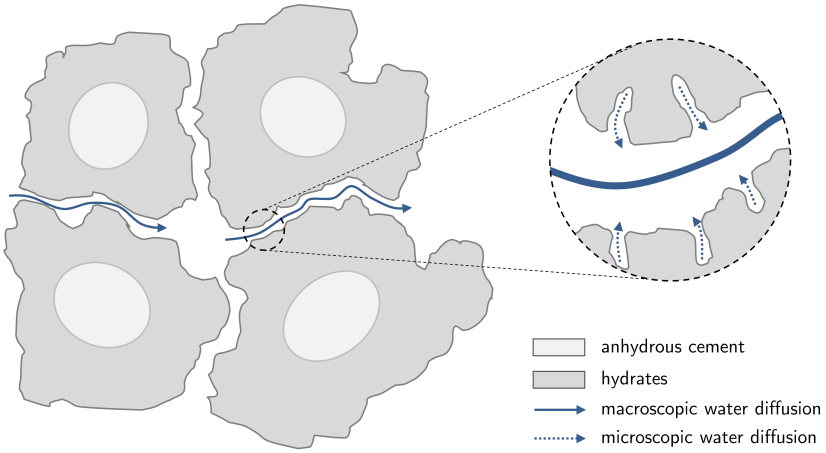

Figure 3.6: Illustration of desiccation creep, adapted from (Benboudjema, 2002)

3.2.5 Cracking

Concrete cracking is mainly driven by the applied mechanical loading (Benboudjema, 2002). In the case of uniaxial tensile stresses, concrete presents a quasi-brittle behavior: the mechanical behavior of concrete is practically linear elastic isotropic, until reaching a stress equal to its tensile strength. This peak stress is directly followed by a softening phase, involving irreversible strains and macroscopic cracking (Kupfer and Gerstle, 1973). In the case of uniaxial compressive stresses, concrete presents a somewhat more ductile behavior: when reaching a stress of about 30% of the compressive strength (Benboudjema, 2002), the elastic linear isotropic phase is followed by a nonlinear phase characterized by the development of micro-cracks in the material, and a progressive loss of stiffness. It is worth noting that concrete presents a sensibly dissymmetric behavior in terms of response to compressive and tensile loads, since its compressive strength is typically 10 times larger than its tensile strength (Benboudjema, 2002)

3.2.5.1 Cracking during early-age phase

Firstly, during the early-age phase, the hydration process of concrete induces a significant heat release yielding an increase of temperature as well as important thermal dilation strain gradients between the core and the surface of the concrete volume (Buffo-Lacarrière et al., 2011; Conceição et al., 2014). As a result, cracking at early-age may be induced by two main mechanisms (Hilaire, 2014):

- auto-stresses due to thermal gradients: the hydration process firstly involves a *free heating phase*, corresponding to an increase of temperature due to the aforementioned heat release. During such a phase, the concrete volume is subjected to a global thermal dilation. Then, during a subsequent *free cooling phase*, a contraction of the concrete volume is observed, whereas the Young's modulus of concrete is higher than during the heating phase. This induces compressive stresses at boundaries and tensile stresses in the core of the concrete volume (Hilaire, 2014). Then, if such tensile stresses reach the tensile strength of concrete, cracking may typically occur near surfaces of the concrete volume (Conceição et al., 2014).

- restrained shrinkage due to massive elements: the stress state induced by the aforementioned differential thermal strains may be altered by the presence of surrounding massive concrete elements: indeed, the cracking risk of a hardening volume increases if the external restraints caused by hardened elements are important (Briffaut et al., 2013; Conceição et al., 2014). Moreover, this effect is increased by endogenous shrinkage (Hilaire, 2014).

3.2.5.2 Cracking during long-term phase

Then, during the long-term phase, the development of cracks is mainly driven by the time evolution of stresses, which itself depends on several factors. Firstly, as previously mentioned, desiccation shrinkage may induce skin cracking, due to the development of tensile stresses at surfaces exposed to hydric fluxes (Benboudjema, 2002; Granger, 1995). Furthermore, in the case of prestressed structures, shrinkage and creep are also responsible for prestressing losses, which may favor tensile stresses and then the development of cracks. Finally, cracking may also be caused by accidental conditions *i.e.* thermo-hydro-mechanical loads that go beyond normal operational conditions (Boucher, 2016; Bouhjiti, 2018; Llau, 2016). In the case of NCB, such conditions may correspond to an overpressure on internal surfaces induced by vapor, accompanied by a increase of the ambient internal temperature.

3.2.6 Air leakage

Leak tightness of large concrete containment structures such as NCB is mainly driven by the permeability of concrete, which is directly dependent on the aforementioned thermo-hydro-mechanical physical processes. Focusing on dry air leak tightness at structural scale, three main flow modes are distinguished in the literature (Bouhjiti, 2018; Mivelaz, 1996), namely:

- flows through concrete porosity,

- flows through cracks,

- flows through structural singularities, which correspond to air leakage near geometrical singularities and construction joints of large concrete containment structures (Asali, 2016; Bouhjiti, 2018). Furthermore, such flows are typically influenced by construction processes on site including the quality of concreting, which may involve the presence of gravel beds, inducing a locally higher porosity. Such flows may also occur at concrete/steel interfaces, where the permeability may be higher due to the thermo-hydro-mechanical behavior at such interfaces (El Dandachy, 2016).

At structural scale, air leakage may present complex flow paths, which stem from a combination of the aforementioned flow modes. Moreover, in addition to flows through sound porosity or macro-cracks, some zones with a somewhat intermediate permeability may be observed, such as construction joints or concrete/steel interfaces, potentially involving a more connected porosity. An illustration of different types of leakage paths in a NCB wall is given in Fig. 3.7.

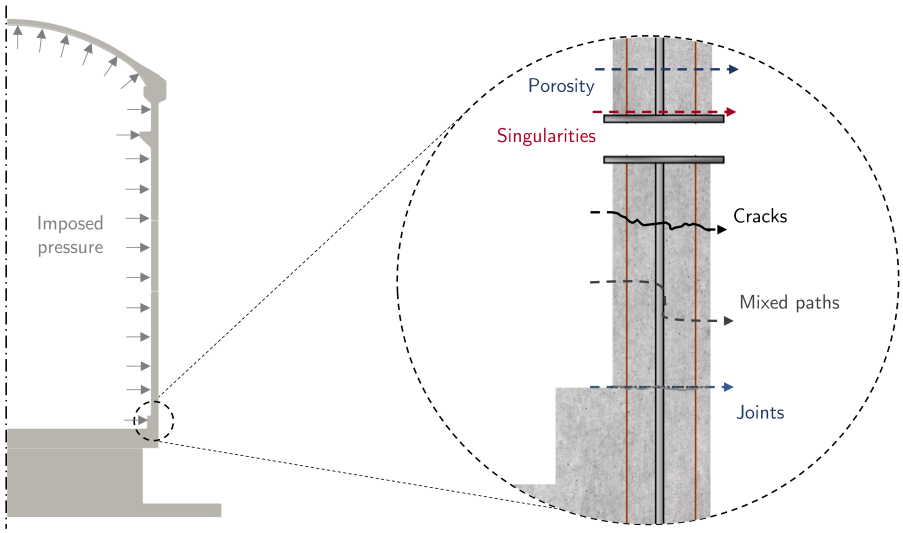

Figure 3.7: Illustration of several leakage paths through the wall of a NCB subjected to a pressurization test.

3.2.6.1 Air flow through concrete porosity

One hereafter focuses on the air permeability of concrete mass and its main influential physical factors. The dependencies established in the literature are described herebelow:

- **structure of the porous medium:** concrete permeability sensibly depends on the connected porosity of concrete, which is mainly formed by its capillary porosity as well as micro-cracks (Rastiello, 2013). Furthermore, the typical size of pores also plays an important role in air transfers through concrete porosity. In a capillary tube, a purely viscous flow implies zero velocity at boundaries of the tube. This is typically the case when the fluid is water. In the case of gases such as air, the flow remains viscous if pore dimensions are larger than the mean free path of air molecules. Otherwise, a slip flow component adds to the viscous flow, due to the non-adherence of gas particles to pore

surfaces (see Fig. 3.8). It is typically the case when concrete pores are sufficiently fine, and contributes to an increase of the air permeability of concrete. This corresponds to the so-called *Klinkenberg* effect (Klinkenberg, 1941), which induces a relationship between air pressure and permeability.

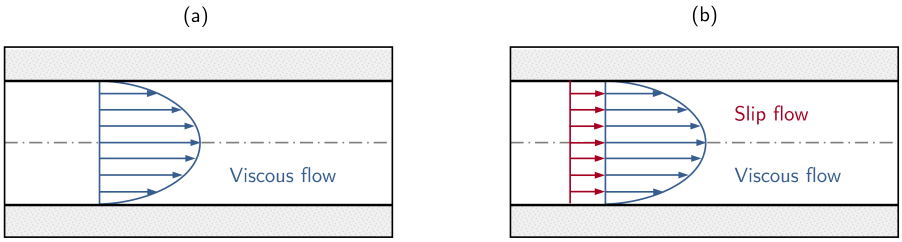

Figure 3.8: Fluid flow through a capillary tube: velocity profiles in the case of a: (a) purely viscous flow; (b) viscous flow with a non-zero slip component.

- **effect of hydric behavior:** the air permeability of concrete is mainly driven by the concrete water saturation (Picandet et al., 2001; Verdier, 2001). Depending on the distribution of water in the concrete porosity, gas transfer may occur for various pore sizes. In the case of a porosity fully saturated with water, the gas permeability of concrete is equal to zero. Conversely, the gas permeability increases when water saturation decreases. As a result, desiccation has a strong influence on the evolution in time of gas permeability, which is notably the case for large concrete structures subjected to drying fluxes (Bouhjiti, 2018). Furthermore, experimental results of Abbas et al. (1999) highlighted that the aforementioned Klinkenberg effect is also influenced by the water saturation state of concrete. Indeed, the same authors observed that the slip flow component becomes more important when water saturation decreases. Such a phenomenon may be explained as follows: according to Laplace-Kelvin's law (see Eq. (3.2)), pores with large dimensions are drying before smaller pores (Chen, 2011), which means that pores with small dimensions become accessible for low levels of water saturation only. An illustration of the effect of the hydric behavior on gas permeability is given in Fig. 3.9.

- **effect of mechanical behavior:** mechanical loads have also a significant influence on the permeability of concrete, notably through the development of diffuse micro-cracking (Choinska, 2006). Such a diffuse micro-cracking may be caused by restrained shrinkage during early-age phase (Hilaire, 2014), or directly by an applied mechanical load (Picandet et al., 2001). Several studies have been conducted in order to analyze the variation of concrete permeability under compression loads (Picandet et al., 2001; Sugiyama et al., 1996) or traction loads (Gérard et al., 1996; Picandet et al., 2009). The reader is referred to the review of (Hoseini et al., 2009) for a more thorough literature survey.

3.2.6.2 Air flow through cracks

As mentioned in Section 3.2.5, cracking in large concrete structures may typically occur during the early-age phase due to restrained shrinkage (thermal or endogenous), or during

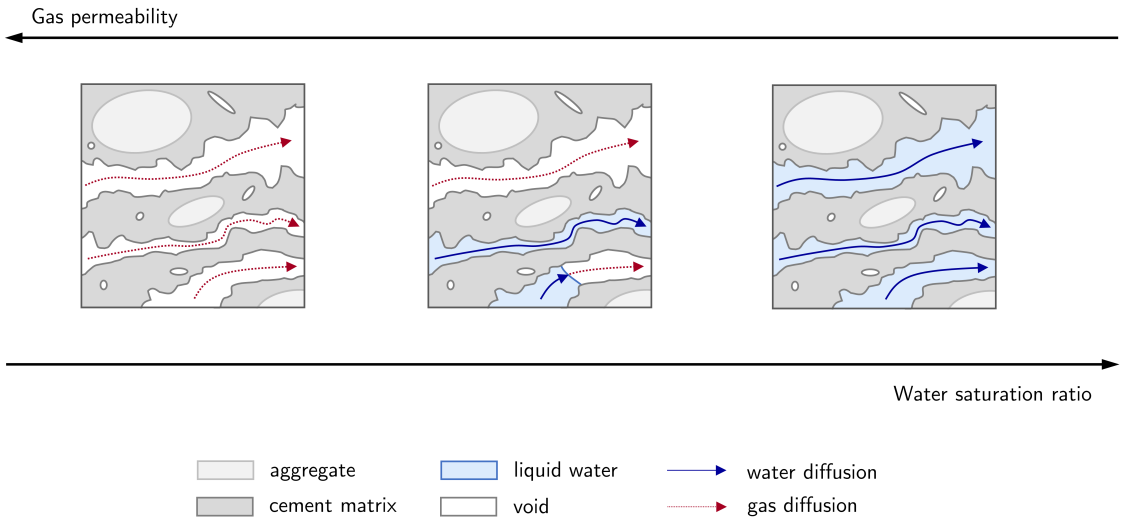

Figure 3.9: Illustration of the influence of the hydric behavior on concrete gas permeability.

the long-term phase, mainly due to thermo-hydro-mechanical operating loads. Here, it is necessary to precise the notion of crack in order to highlight different flow modes: indeed, there exists a more or less progressive transition from a pure Darcy's flow mode through sound concrete porosity to a Poiseuille's flow in a macroscopic crack (Rastiello, 2013). In this context, two steps may be distinguished:

1. a first step characterized by diffuse micro-cracking in the concrete volume, leading to an increase of the connected porosity. Such an effect has already been discussed in Section 3.2.6.1.

2. a second step, characterized by the concentration of micro-cracks, followed by the development of macro-cracks. In such a case, the flow rate through concrete porosity is negligible compared to the flow rate through macro-cracks.

Fluid flows through macro-cracks are very complex to describe, due to the possibly complex geometries involved, including roughness and tortuosity. In particular, a high tortuosity and strong velocity variations may induce the presence of turbulent flows. Furthermore, the boundary between flows through porosity and through macro-cracks is difficult to identify. At structural scale, it is often assumed that the total leak rate is given by the sum of contributions of the concrete porosity and macro-cracks, by assuming that the superposition principle may be applied to Darcy's and Poiseuille's flows (Bouhjiti, 2018). However, such an assumption is *a priori* not valid at the vicinity of a macro-crack: the higher permeability induced by the macro-crack may perturb flow streamlines in the surrounding porosity, whereas the aforementioned second flow regime may occur near the so-called Fracture Process Zone (FPZ) of the crack.

Moreover, at the scale of large structures, it is necessary to distinguish two types of macroscopic cracks, namely through and non-through cracks. Firstly, through cracks constitute the most critical type of macro-cracks (Bouhjiti, 2018; Mivelaz, 1996). Then, non-through cracks may also significantly contribute to the flow rate of the structure, and potentially create preferential leakage paths, for instance through interactions with structural singularities (Bouhjiti, 2018).

3.3 Thermo-Hydro-Mechanical-Leakage modeling

3.3.1 THML modeling strategies

In the literature related to the modeling of the physical behavior of large concrete containment structures, two types of THML modeling strategies may be distinguished, namely *fully-coupled* and *weakly-coupled* strategies (see Fig. 3.10). Fully-coupled approaches consist in simultaneously treating the dependencies between the thermal, hydric, mechanical and leakage behavior (Dal Pont et al., 2007; Gawin et al., 2003) (see Fig. 3.10a), whereas weakly-coupled ones consist in chained calculations related to the aforementioned behaviors (see Fig. 3.10b). It is worth noting that despite their somewhat exhaustive aspect, fully-coupled approaches typically involve a larger amount of uncertain parameters, and require a more important computational cost than weakly-coupled approaches.

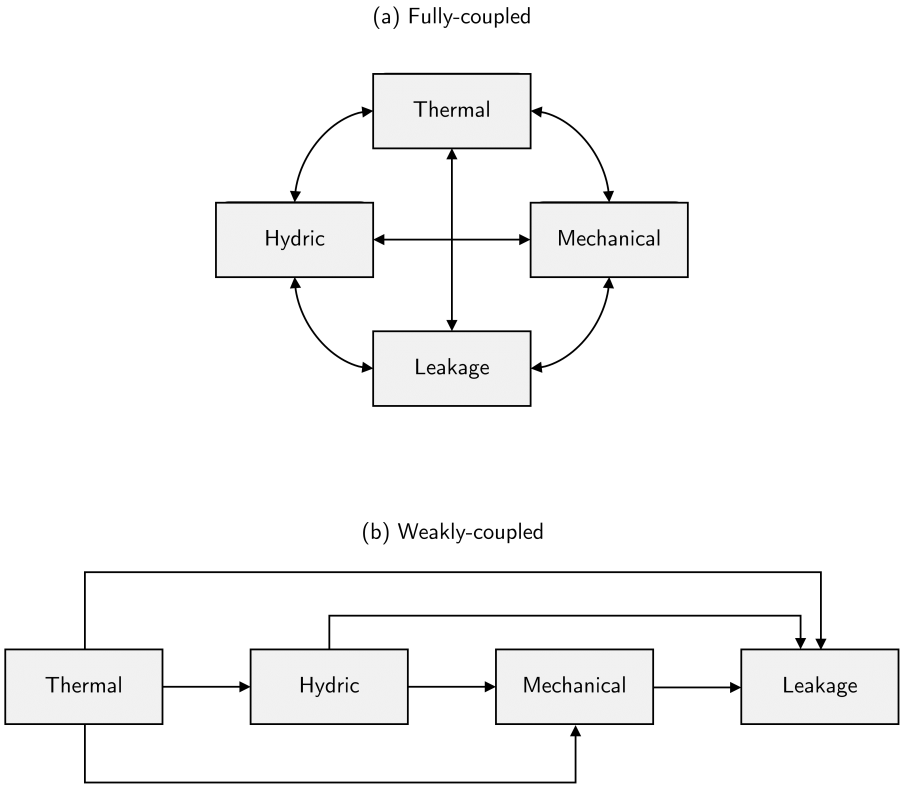

Figure 3.10: THML modeling strategies: (a) fully-coupled; (b) weakly coupled.

In this contribution, a weakly-coupled THML modeling approach will be considered. Such a choice is motivated by the fact that weakly-coupled approaches are suitable for describing the global behavior of aging large concrete structures subjected to normal exploitation loads (Bouhjiti, 2018), and provide affordable computational models based on proven behavior laws. It is worth noting that in the case of accidental conditions, involving notably high temperatures, the assumptions behind weakly-coupled approaches are no longer valid, and fully-coupled approaches are presumed to be more representative of the underlying physical phenomena (Dal Pont et al., 2007). Such situations are out of the scope of this contribution, though.

Besides, it is worth mentioning that whether adopting a weakly-coupled or a full-coupled THML modeling approach does not alters the overall UQ methodology presented in the introduction of this thesis (see Fig. iii), since the computational model is treated in a black-box fashion. A fully-coupled THML model would typically involve an input parameter space with a higher dimensionality, and the time consumed by a single model evaluation would be typically larger. This could make forward and inverse UQ problems more challenging, compared to those associated to a weakly-coupled model.

Then, the constitutive laws relative to the thermal, hydric, mechanical and leakage behavior adopted in this thesis are presented hereafter.

3.3.2 Modeling of the thermal behavior

3.3.2.1 Constitutive equations

Let $\mathcal{D} \subset \mathbb{R}^3$ be the studied domain. In the following, space and time variables are respectively denoted by $\boldsymbol{s} \in \mathcal{D}$ and $t \in \mathbb{R}$. Focusing on the long-term phase, the evolution of the temperature field $T = T(\boldsymbol{s}, t)$ in $\mathcal{D}$ is modeled with the classical heat equation (Fourier, 1822):

$$\rho_c c_c^p \frac{\partial T}{\partial t} = \nabla_{\boldsymbol{s}} \cdot (\lambda_c \nabla_{\boldsymbol{s}} T) \tag{3.3}$$

where ρ_c denotes the density, c_c^p the heat capacity and λ_c the thermal conductivity of hardened concrete. Here, $\frac{\partial}{\partial t}$ denotes partial derivation w.r.t. time.

3.3.2.2 Boundary conditions

The boundary conditions (BC) adopted for the aforementioned heat equation in Eq. (3.3) are next discussed. Dirichlet BC consist in imposing a temperature $\bar{T}$ on boundaries $\partial\mathcal{D}_{\bar{T}} \subset \mathcal{D}$ of the domain, whereas Neumann BC consist in imposing a thermal flux $\bar{q}_{th}$ on $\partial\mathcal{D}_{\bar{q}_{th}} \subset \mathcal{D}$:

$$\begin{cases} T = \bar{T} & \text{on } \partial\mathcal{D}_{\bar{T}} \\ \boldsymbol{q}_{th} \cdot \boldsymbol{n} = \bar{q}_{th} & \text{on } \partial\mathcal{D}_{\bar{q}_{th}} \end{cases} \tag{3.4}$$

where $\boldsymbol{n}$ is the outward unit normal vector field on the boundary $\partial\mathcal{D}$ of $\mathcal{D}$, and where the thermal flux $\boldsymbol{q}_{th}$ is given by Fourier's law (Fourier, 1822):

$$\boldsymbol{q}_{th} = -\lambda_c \nabla_{\boldsymbol{s}} T \tag{3.5}$$

Furthermore, the imposed thermal flux $\bar{q}_{th}$ usually corresponds to convective exchanges (Boucher, 2016):

$$\bar{q}_{th} = k_{th}(T_\infty - T) \tag{3.6}$$

where k_{th} is an equivalent thermal convective exchange coefficient, which is usually assumed to be constant (Briffaut et al., 2012), and T_∞ is the ambient temperature.

3.3.3 Modeling of the hydric behavior

3.3.3.1 Constitutive equations

Next, the considered modeling assumptions related to desiccation induced by the effect of hydric loads during exploitation phase are described hereafter. Based on the simplifying assumptions detailed in (Bouhjiti, 2018), and considering liquid water diffusion only, moisture transfers in concrete are modeled by single diffusion equation similar to the second Fick's law, in which the water content of concrete $C_w = C_w(\boldsymbol{s}, t)$ is the primary variable (Granger, 1995):

$$\frac{\partial C_w}{\partial t} = \nabla_{\boldsymbol{s}} \cdot (D_w(C_w, T) \nabla_{\boldsymbol{s}} C_w) \tag{3.7}$$

where C_w is the water content of concrete, and D_w a phenomenological diffusion coefficient, which is a function of C_w and the temperature field T.

The expression of the diffusion coefficient D_w is precised hereafter. Given the thermo-activated nature of desiccation (see Section 3.2.2), D_w is assumed to follow Arrhenius' law (Bažant and Najjar, 1972; Granger, 1995), namely:

$$D(C_w, T) = D_{w,0}(C_w) \frac{T}{T_w^0} \exp\left[-\frac{U_w}{R}\left(\frac{1}{T} - \frac{1}{T_w^0}\right)\right] \tag{3.8}$$

where $D_{w,0}(C_w)$ is the diffusion coefficient at a reference temperature T_w^0, U_w the activation energy of drying, and R the ideal gas constant.

Furthermore, the model proposed by Mensi et al. (1988) is considered so as to model the coefficient $D_{w,0}(C_w)$:

$$D_{w,0}(C_w) = A \exp(B C_w) \tag{3.9}$$

where A and B are model parameters.

3.3.3.2 Sorption-desorption model

Then, at the scale of large structures, ambient conditions measurements are often given in terms of RH (Boucher, 2016). Therefore, it is more convenient to express BC in terms of RH for the desiccation problem in Eq. (3.7), rather than in terms of water content. Following a remark stated in Section 3.2, drying/humidification cycles are assumed to only affect skin concrete (Bouhjiti et al., 2018a; Granger, 1995). For a given temperature, this last assumption enables to link the concrete (volumetric) water content C_w to its RH h, through a bijective sorption-desorption function f_d:

$$C_w = f_d(h) \tag{3.10}$$

Following Thiery et al. (2007) and Bouhjiti et al. (2018a), the sorption-desorption function of Van Genuchten (1980) will be considered:

$$f_d(h) = \phi \left[1 + (-a_d \log h)^{\frac{1}{1-b_d}}\right]^{-b_d} \tag{3.11}$$

where ϕ is the concrete porosity, and a_d, b_d are model parameters.

It is worth noting that such a model is valid for a given temperature, since it is well-known that sorption-desorption curves sensibly depend on the temperature (Poyet, 2009). As experimental results concerning the temperature-dependency of sorption-desorption curves are rarely available in practice, the model in Eq. (3.11) will be supposed to be fixed. Moreover, adopting a single sorption-desorption curve implies another simplifying assumption, consisting in neglecting hysteresis phenomena due to cyclic hydric loads (Ishida et al., 2007).

3.3.3.3 Boundary conditions

The water diffusion problem in Eq. (3.7) is solved by considering Dirichlet BC in terms of water content, through applying the aforementioned sorption-desorption function to ambient RH, as suggested by Boucher (2016). Such conditions consist in imposing the following water content field on boundaries $\partial\mathcal{D}_{\bar{C}_w} \subset \mathcal{D}$:

$$C_w = \bar{C}_w = f_d(h_\infty) \tag{3.12}$$

where f_d is the aforementioned sorption-desorption model, and h_∞ the ambient RH.

In this way, hydric boundary layer effects are neglected, since the water content corresponding to the ambient RH is imposed directly on the boundary of the structure. Nevertheless, such a simplification may be deemed reasonable if the ambient air of the structure is sufficiently ventilated (Granger, 1995).

3.3.4 Modeling of the mechanical behavior

In the framework of infinitesimal strain theory, the total strain tensor $\boldsymbol{\varepsilon}$ may be written as the sum of five components (focusing on the long-term phase):

$$\boldsymbol{\varepsilon} = \boldsymbol{\varepsilon}^{\mathrm{el}} + \boldsymbol{\varepsilon}^{\mathrm{th}} + \boldsymbol{\varepsilon}^{\mathrm{ds}} + \boldsymbol{\varepsilon}^{\mathrm{bc}} + \boldsymbol{\varepsilon}^{\mathrm{dc}} \tag{3.13}$$

where:

- $\boldsymbol{\varepsilon}^{\mathrm{el}}$ is the elastic strain tensor,
- $\boldsymbol{\varepsilon}^{\mathrm{th}}$ is the thermal strain tensor,
- $\boldsymbol{\varepsilon}^{\mathrm{ds}}$ is the desiccation shrinkage strain tensor,
- $\boldsymbol{\varepsilon}^{\mathrm{bc}}$ is the basic creep strain tensor,
- $\boldsymbol{\varepsilon}^{\mathrm{dc}}$ is the desiccation creep strain tensor.

The modeling assumptions related to each of the contributions to total strains in Eq. (3.13) are described hereafter. In the following, the Cauchy stress tensor will be denoted by $\boldsymbol{\sigma}$, and its decomposition into spherical and deviatoric parts σ_s and $\boldsymbol{\sigma}_d$ will be written as follows:

$$\boldsymbol{\sigma} = \sigma_s \mathbf{I} + \boldsymbol{\sigma}_d \tag{3.14}$$

where $\sigma_s = \mathrm{tr}(\boldsymbol{\sigma})/3$, $\mathrm{tr}(\boldsymbol{\sigma}_d) = 0$, and where $\mathbf{I}$ is the identity tensor.

3.3.4.1 Thermal strains

Firstly, following experimental observations mentioned in 3.2.3.3, the variation of thermal strain $\boldsymbol{\varepsilon}^{\text{th}}$ is supposed to be proportional to temperature variations (Hilaire, 2014), which writes:

$$\dot{\boldsymbol{\varepsilon}}^{\text{th}} = \alpha_{th}\dot{T}\mathbf{I} \tag{3.15}$$

where α_{th} is the thermal dilation coefficient of concrete, and where the notation $\dot{f} = \frac{\partial f}{\partial t}$ has been adopted, for the sake of conciseness.

Moreover, focusing on the mechanical behavior during the long-term phase, the thermal dilation coefficient in Eq. (3.15) is assumed to be constant (Boucher, 2016).

3.3.4.2 Desiccation shrinkage strains

Then, based on the experimental observations mentioned in Section 3.2.3.4, the following linear model in terms of water content is adopted so as to describe dessication shrinkage strains (Benboudjema, 2002; Granger, 1995):

$$\dot{\boldsymbol{\varepsilon}}^{\text{ds}} = \alpha_{ds}\dot{C}_w\mathbf{I} \tag{3.16}$$

where α_{ds} is a desiccation shrinkage coefficient.

3.3.4.3 Basic creep strains

Basic creep strains are described by the Burger rheological model proposed by Foucault et al. (2012), which demonstrated its ability to well reproduce several experimental results (Hilaire, 2014; Reviron, 2009), including the long-term creep experiments of Brooks (2005). The choice of this model is also justified by recent work of Bouhjiti (2018), which enabled to accurately assessing the global delayed mechanical behavior of NCB subjected to normal operating loads.

The model is based on the decomposition of basic creep strain $\boldsymbol{\varepsilon}^{\text{bc}}$ into a reversible part $\boldsymbol{\varepsilon}_r^{\text{bc}}$ and an irreversible part $\boldsymbol{\varepsilon}_i^{\text{bc}}$:

$$\boldsymbol{\varepsilon}^{\text{bc}} = \boldsymbol{\varepsilon}_r^{\text{bc}} + \boldsymbol{\varepsilon}_i^{\text{bc}} = \varepsilon_{rs}^{\text{bc}}\mathbf{I} + \boldsymbol{\varepsilon}_{rd}^{\text{bc}} + \varepsilon_{is}^{\text{bc}}\mathbf{I} + \boldsymbol{\varepsilon}_{id}^{\text{bc}} \tag{3.17}$$

where strain tensors have been decomposed in spherical ($\varepsilon_{rs}^{\text{bc}}$, $\varepsilon_{is}^{\text{bc}}$) and deviatoric ($\boldsymbol{\varepsilon}_{rd}^{\text{bc}}$, $\boldsymbol{\varepsilon}_{id}^{\text{bc}}$) parts. Furthermore, the model consists in the duplication of a Burger rheological model for both spherical and deviatoric parts (see Fig. 3.11a). Such a structure aims at introducing a viscoelastic Poisson effect, through the definition of a creep Poisson ratio (Charpin et al., 2015). Then, for each chain (spherical and deviatoric), reversible basic creep strains ($\varepsilon_{rs}^{\text{bc}}$ and $\boldsymbol{\varepsilon}_{rd}^{\text{bc}}$) are modeled through a Kelvin-Voigt rheological element, whereas irreversible basic creep strains ($\varepsilon_{is}^{\text{bc}}$ and $\boldsymbol{\varepsilon}_{id}^{\text{bc}}$) are modeled by a Maxwell element.

The equations associated to the spherical Burger chain are now presented. Based on water migration theory, the spherical part σ_s of the stress tensor $\boldsymbol{\sigma}$ is associated to the migration of adsorbed water towards capillary porosity, at microscopic and macroscopic scales (Benboudjema, 2002). The following governing equation is adopted for the reversible spherical basic creep strain $\varepsilon_{rs}^{\text{bc}}$, by assuming that basic creep strains are proportional to RH h (Wittmann, 1970):

$$h\sigma_s = k_{rs}\varepsilon_{rs}^{\text{bc}} + \eta_{rs}\dot{\varepsilon}_{rs}^{\text{bc}} \tag{3.18}$$

where k_{rs}, η_{rs} denote the stiffness and the viscosity associated to reversible spherical basic creep, respectively.

Then, the irreversible spherical basic creep strain $\varepsilon_{is}^{\mathrm{bc}}$ is modeled through the following equation:

$$h\sigma_s = \eta_{is}\dot{\varepsilon}_{is}^{\mathrm{bc}} \tag{3.19}$$

where the irreversible spherical basic creep viscosity η_{is} is given by the following expression, originally proposed by Sellier and Buffo-Lacarrière (2009):

$$\eta_{is} = \eta_{is}^0 \exp\left(\frac{\|\boldsymbol{\varepsilon}_i^{\mathrm{bc}}\|_m}{\kappa}\right) \tag{3.20}$$

where κ is a consolidation parameter, and:

$$\|\boldsymbol{\varepsilon}_i^{\mathrm{bc}}(t)\|_m = \max_{\tau\in[0,t]} \sqrt{\boldsymbol{\varepsilon}_i^{\mathrm{bc}}(\tau) : \boldsymbol{\varepsilon}_i^{\mathrm{bc}}(\tau)} \tag{3.21}$$

for all $t \geq 0$, : denoting the double dot product for tensors. It is worth noting that the expression of the viscosity in Eq. (3.20) induces non-linearity in the creep model, since it involves a dependency on the current state of irreversible strains.

Likewise, the constitutive equations associated to the deviatoric chain of the model are described. The deviatoric part $\boldsymbol{\sigma}_d$ of the stress tensor $\boldsymbol{\sigma}$ is associated to the sliding of C-S-H sheets in nano-porosity (Ulm and Acker, 1998). The (reversible) sliding of interfoliar water is modeled by a Kelvin-Voigt element with stiffness k_{rd} and viscosity η_{rd}, whereas the (irreversible) sliding of interlamellar water is modeled by a Maxwell element with viscosity η_{id}. Thus, the reversible deviatoric basic creep strain $\boldsymbol{\varepsilon}_{rd}^{\mathrm{bc}}$ is described with the following equation:

$$h\boldsymbol{\sigma}_d = k_{rd}\boldsymbol{\varepsilon}_{rd}^{\mathrm{bc}} + \eta_{rd}\dot{\boldsymbol{\varepsilon}}_{rd}^{\mathrm{bc}} \tag{3.22}$$

whereas the irreversible deviatoric basic creep strain follows the equation below:

$$h\boldsymbol{\sigma}_d = \eta_{id}\dot{\boldsymbol{\varepsilon}}_{id}^{\mathrm{bc}} \tag{3.23}$$

Furthermore, the viscosity η_{id} is given by an expression purely analogous to Eq. (3.20):

$$\eta_{id} = \eta_{id}^0 \exp\left(\frac{\|\boldsymbol{\varepsilon}_i^{\mathrm{bc}}\|_m}{\kappa}\right) \tag{3.24}$$

Moreover, the adopted model accounts for thermo-activation of basic creep, by adding a temperature-dependency to stiffness and viscosity parameters $k_{rs}, k_{rd}, \eta_{rs}, \eta_{rd}, \eta_{is}$ and η_{id}, based on Arrhenius' law (Arrhenius, 1915). Such a dependency is illustrated for the parameter k_{rs}:

$$k_{rs}(T) = k_{rs}^0 \exp\left[\frac{U_{bc}}{R}\left(\frac{1}{T} - \frac{1}{T_{bc}^0}\right)\right] \tag{3.25}$$

where k_{rs}^0 is the reversible spherical basic creep stiffness at a reference temperature T_{bc}^0, U_{bc} the activation energy of basic creep. Furthermore, a similar expression is adopted for the consolidation parameter κ:

$$\kappa(T) = \kappa_0 \exp\left[-\frac{U_{bc}}{R}\left(\frac{1}{T} - \frac{1}{T_{bc}^0}\right)\right] \tag{3.26}$$

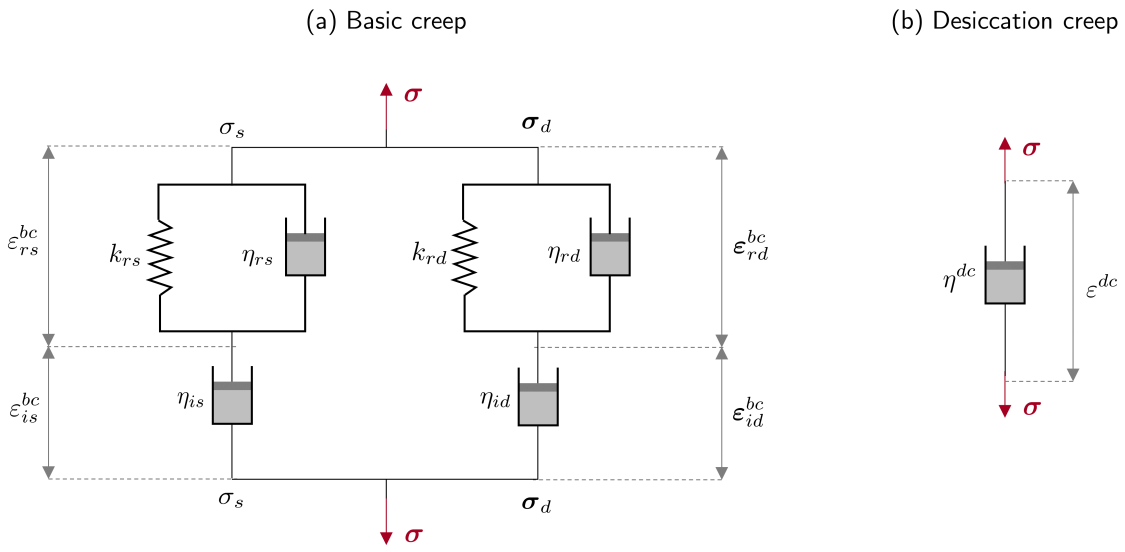

Figure 3.11: Rheological models: (a) basic creep; (b) desiccation creep

where κ_0 is the consolidation parameter at the reference temperature T_{bc}^0.

Finally, the equivalence of spherical and deviatoric chains enables to restrict the number of model parameters, by assuming a constant creep Poisson ratio ν_{bc} (Foucault et al., 2012), given by the following relation:

$$\frac{k_{rs}}{k_{rd}} = \frac{\eta_{rs}}{\eta_{rd}} = \frac{\eta_{is}^0}{\eta_{id}^0} = \frac{1+\nu_{bc}}{1-2\nu_{bc}} \tag{3.27}$$

3.3.4.4 Desiccation creep strains

Then, concerning the modeling of the desiccation creep strain $\boldsymbol{\varepsilon}^{\mathrm{dc}}$, Bažant and Chern (1985) originally proposed the following model:

$$\dot{\boldsymbol{\varepsilon}}^{\mathrm{dc}} = \frac{1}{\eta_{dc}} |\dot{h}| \boldsymbol{\sigma} \tag{3.28}$$

where η_{dc} is a viscosity parameter.

Nevertheless, such a model does not enable to distinguish the creep behavior during desiccation and humidification. Indeed, a disymmetry between these behaviors has been observed by Benboudjema (2002). Then, a modified form of the model in Eq. (3.28), proposed in (Boucher, 2016), will be considered:

$$\dot{\boldsymbol{\varepsilon}}^{\mathrm{dc}} = \frac{1}{\eta_{dc}} \langle \dot{h} \rangle_{-} \boldsymbol{\sigma} \tag{3.29}$$

where:

$$\langle \dot{h}(t) \rangle_{-} = \begin{cases} \dot{h}(t) & \text{if} \quad \dot{h}(t) < 0 \quad \text{and} \quad h(t) < \min_{\tau \in [0,t]} h(\tau) \\ 0 & \text{else} \end{cases} \tag{3.30}$$

Then, such a model neglects the creep desiccation strain due to humidification. Furthermore, desiccation creep occurs only the first encountered desiccation phase, down to a given RH level. An illustration of the corresponding rheological model is given in Fig. 3.11b.

3.3.5 Modeling of the leakage behavior

In the framework of the weakly-coupled THML modeling strategies proposed in the literature (Asali, 2016; Bouhjiti, 2018), the leakage behavior of concrete in large structures is usually separated into two modes, namely (see Fig. 3.7):

- leakage through concrete porosity (sound and/or diffusely damaged),
- leakage through macroscopic cracks.

When cracking is explicitly modeled by means of continuous damage theory (Mazars and Pijaudier-Cabot, 1989), matching laws have been proposed in the literature in order to describe the transition from pure Darcy-type flows through concrete porosity to Poiseuille-type flows through macro-cracks (Bouhjiti et al., 2018b; Choinska et al., 2007a; Pijaudier-Cabot et al., 2009).

Furthermore, at structural scale, the superposition principle is assumed to be applicable to the total leakage rate Q_g (Bouhjiti et al., 2020), namely:

$$Q_g = Q_d + Q_l \tag{3.31}$$

where Q_d refers to the total leakage through concrete porosity (or *diffuse* leaks), and Q_l the leakage rate associated to macroscopic cracks in the structure (or *local* leaks), as well as other type of defects, namely structural singularities (see Fig. 3.7).

3.3.5.1 Air leakage through concrete porosity

Based on simplifying assumptions stated in (Jason et al., 2007), mainly consisting in considering dry air transport only, air leakage through concrete porosity is modeled through the following diffusion equation:

$$(1 - S_w)\phi \frac{\partial p_g}{\partial t} = \nabla_{\boldsymbol{s}} \cdot \left(\frac{\mathbf{k}_g}{2\mu_g} \nabla_{\boldsymbol{s}} p_g^2 \right) \tag{3.32}$$

where S_w denotes the water saturation ratio, ϕ the concrete porosity, $\mathbf{k}_g$ the air permeability tensor, μ_g the dynamic viscosity of air and p_g the air pressure.

Furthermore, considering large containment structures subjected to internal pressure loads, Dirichlet BC in terms of air pressure constitute a somewhat natural choice (Bouhjiti et al., 2020; Jason et al., 2007). Consequently, in order to solve the diffusion equation in Eq. (3.32), a pressure field $\bar{p}_g$ is imposed on boundaries $\partial\mathcal{D}_{\bar{p}_g} \subset \mathcal{D}$:

$$p_g = \bar{p}_g \tag{3.33}$$

Thus, the contribution Q_d attributed to leakage through porosity (see Eq. (3.31)) may be obtained by integrating the Darcy's flux $\boldsymbol{q}_d = -\mu_g^{-1}\mathbf{k}_g \nabla_{\boldsymbol{s}} p_g$ on the surface $\partial\mathcal{D}_{\boldsymbol{q}_d} \subset \partial\mathcal{D}$ of the structure:

$$Q_d = \int_{\partial\mathcal{D}_{\boldsymbol{q}_d}} \boldsymbol{q}_d \cdot \boldsymbol{n} \tag{3.34}$$

where $\boldsymbol{n}$ denotes the outward unit normal vector field on $\partial\mathcal{D}_{\boldsymbol{q}_d}$.

The structure and the dependencies of the permeability tensor $\mathbf{k}_g$ are now described. When considering the sound porosity of concrete, this tensor is usually written as the product of several factors (Jason et al., 2007; Muskat and Meres, 1936), namely:

$$\mathbf{k}_g = \mathbf{k}_0 k_s(p_g, S_w) k_{rg}(S_w) \tag{3.35}$$

where:

- $\mathbf{k}_0$ is the intrinsic permeability tensor, which is characterized by the connected porosity of concrete. It is only relative to the viscous component of the flow through porosity. Such a tensor will be supposed to be isotropic, and one writes $\mathbf{k}_0 = k_0\mathbf{I}$. As a result, the term *intrinsic permeability* will indifferently refer to the tensor $\mathbf{k}_0$ or the scalar k_0 in the following.
- $k_s(p_g, S_w)$ is a factor representative of the slip flow component induced by Klinkenberg's effect (Klinkenberg, 1941). Such a factor is supposed to depend on the gas pressure p_g as well as the water saturation ratio S_w, as underlined by experimental studies (Abbas et al., 1999; Villain et al., 2001) (see Section 3.2.6.1).
- $k_{rg}(S_w)$ is the relative gas permeability of concrete, which is a function of the water saturation ratio S_w (Picandet et al., 2001; Verdier, 2001), as mentioned in Section 3.2.6.1.

Concerning the factor $k_s(p_g, S_w)$, Klinkenberg (1941) originally proposed the following model:

$$k_s(p_g, S_w) = 1 + \frac{\beta_K}{\langle p_g \rangle_s} \tag{3.36}$$

where β_K is the so-called Klinkenberg coefficient, and $\langle p_g \rangle_s$ the average (w.r.t. space) pressure of the flow. However, such a model does not account for the dependency of Klinkenberg effect on the hydric behavior (see Section 3.2.6.1). Then, the model proposed by Abbas et al. (1999) will be considered:

$$k_s(p_g, S_w) = 1 + (1 - S_w)\frac{\beta_K}{\langle p_g \rangle_s} \tag{3.37}$$

Then, several models are available in the literature so as to model the relative gas permeability $k_{rg}(S_w)$ (Monlouis-Bonnaire et al., 2004; Parker et al., 1987; Verdier, 2001), mostly deriving from the model proposed by Van Genuchten (1980). Based on the former work of Bouhjiti (2018), the model proposed by Verdier (2001) will be considered:

$$k_{rg}(S_w) = \sqrt{1 - S_w}\left(1 - S_w^{1/c_k}\right)^{2c_k} \tag{3.38}$$

where c_k is a model parameter.

Finally, it is worth noting that the expression in Eq. (3.35) concerns the gas permeability of the sound porosity of concrete. When considering mechanical simulations using damage modeling, a fourth factor may be added in Eq. (3.35) in order to represent the effect of diffuse damage on gas permeability (Choinska et al., 2007b; Dal Pont and Ehrlacher, 2004; Jason et al., 2007). However, the use of such models implies to explicitly describe damage in the structure, which requires an important computational cost.

Alternatively, diffuse leakage calculations may be performed by using the model in Eq. (3.35) for the porosity of the whole structure. A caveat is that such a simplification implies to carefully interpret the physical meaning of the intrinsic permeability parameter k_0, when identifying the latter from *in-situ* leakage measurements. Indeed, the obtained value would be higher than that obtained with damage calculations, since the identified k_0 would be representative of micro-cracking in the concrete porosity in the case of damage-free calculations.

3.3.5.2 Air leakage through concrete cracks

In the literature, flows through a crack are usually modeled by considering flows between two parallel plates, leading to the so-called *Parallel Plates Model* (PPM) (Snow, 1969). The principle of the PPM model is illutrated in Fig. 3.12. The spacing between the two aforementioned plates is given by the crack opening, denoted by a_c in the following. It is worth noting that such a crack opening is fictitious in mechanical terms: it represents the average hydraulic behavior of the corresponding real crack. Then, the flow rate q_{ppm} of a mono-phasic fluid subjected to a pressure gradient may be quantified through solving Navier-Stokes equations (Temam, 2001). In the case of an incompressible laminar flow (*e.g.* laminar liquid water flows), such a flow rate is given by (Rastiello, 2013):

$$q_{\text{ppm}} = -\rho w \frac{a_c^3}{12\mu} \nabla_s p \tag{3.39}$$

where ρ_l is the density and μ the dynamic viscosity of the fluid, w the crack width, and $\nabla_s p$ the pressure gradient. A similar expression may be obtained in the case of compressible laminar flows (*e.g.* laminar gaseous flows) (Jourdain, 2014):

$$q_{\text{ppm}} = -w \frac{M_g}{RT_g} \frac{a_c^3}{24\mu_g} \nabla_s p_g^2 \tag{3.40}$$

where μ_g is the dynamic viscosity of air. Then, by analogy with Darcy's law, it is possible to define an equivalent crack permeability k_c from Eqs. (3.39) and (3.40) (Rastiello, 2013), by setting $k_c = \frac{a_c^2}{12}$ and $k_c = \frac{M_g}{RT_g}\frac{a_c^2}{24}$, respectively in the incompressible and compressible cases.

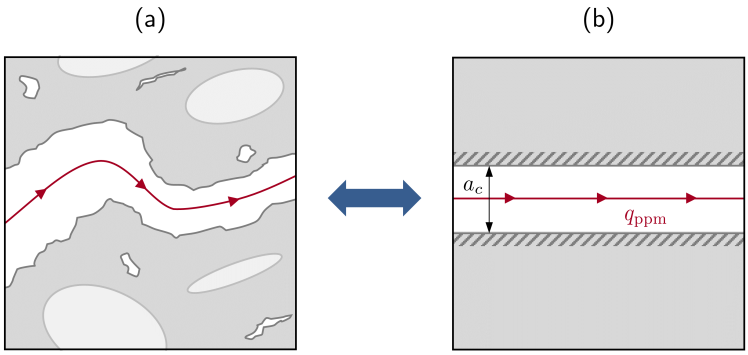

Figure 3.12: Illustration of the PPM model for fluid flows in cracked media: (a) real crack; (b) equivalent parallel plates configuration.

Nevertheless, since the PPM model assumes smooth parallel plates, geometrical features including rugosity and turtuosity (Stroeven, 2000) are not taken into account. Therefore, a correction factor ζ is usually introduced in order to estimate the flow rate q_c of the crack (Mivelaz, 1996):

$$q_c = \zeta q_{\text{ppm}} \tag{3.41}$$

Several models, have been developed in the literature for both the crack flow rate q and the correction factor ζ, including generalizations of Eqs. (3.39) and (3.40) for turbulent flows (Greiner and Ramm, 1995; Mivelaz, 1996; Rizkalla et al., 1984), formulations with a constant correction factor ζ (Picandet et al., 2009) or with an opening-dependent formulation (Rastiello et al., 2015).

Besides, the aforementioned models present several drawbacks: firstly, they present several highly uncertain parameters related to the geometry of the crack (*e.g.* rugosity, turtuosity), which may be very difficult to identify, notably when considering operating large structures such as NCB (Bouhjiti et al., 2020; Rossat et al., 2021). Furthermore, such parameters are only representative of the geometry of a single crack: therefore, modeling the hydraulic behavior of all the cracks of a large structure would require the identification of a sensibly large set of unknown rugosity and tortuosity parameters. Moreover, the use of the aforementioned leakage models supposes a sufficiently precise knowledge about the cracking state of the structure, including cracking paths as well as crack geometries, together with their interactions with rebars and prestressing cables. This notably implies to explicitly modeling cracks through (nonlinear) mechanical calculations. In the framework of structural applications, such calculations may be performed by using continuous damage theory (Mazars and Pijaudier-Cabot, 1989), which introduces the following behavior law in the case of isotropic damage:

$$\boldsymbol{\sigma} = (1 - \mathrm{d})\mathbf{E}_0 : \boldsymbol{\varepsilon} \tag{3.42}$$

where $\boldsymbol{\sigma}$ is the stress tensor, d the damage variable (varying between 0 and 1), $\mathbf{E}_0$ the Hooke's elasticity tensor of sound concrete, and $\boldsymbol{\varepsilon}$ the strain tensor. Based on a continuous-discrete equivalence principle between a zone of localized damage and the discontinuity induced by a macroscopic crack (Bažant and Oh, 1983), several approaches have been proposed in the literature so as to assess crack openings in the framework of damage-based calculations (Dufour et al., 2012; Matallah et al., 2010; Sciumè and Benboudjema, 2017).

The aforementioned approaches involve sensibly nonlinear mechanical calculations, and their application to large structures typically requires an important computational cost. Besides this fact, the explicit modeling of cracking in large structures raises a somewhat more important challenge, related to the initiation of macroscopic cracks in large structure. Indeed, in the case of large structures, cracking may typically occur during the early-age phase, notably due to restrained shrinkages (see Section 3.2.5). Consequently, modeling the hydraulic behavior of macro-cracks based on damage-based mechanical calculations during the long-term phase implies to perform (thermo-hydro-)mechanical calculations during the early age phase, at least in order to assess an initial cracking state (Bouhjiti, 2018). However, the prediction of early age cracking patterns in the case of operating containment structures such as NCB constitutes a very difficult task in general, since scarce information concerning the early age phase of the structure are available.

Then, in addition to the involved computational cost, assessing the hydraulic behavior of cracks implies two main layers of uncertainties, namely the determination of the cracking state of the structure, and the hydraulic behavior of each crack, which is notably driven by highly uncertain parameters related to rugosity, tortuosity, and other geometrical features. This notably involves a sensibly large number of parameters in the presence of multiple cracks.

Consequently, a simple phenomenological model is proposed in this work, in order to assess the long-term evolution of local leaks at structural scale. This model proposes to describe the total contribution of local leaks Q_l in Eq. (3.31) as a function of a macro-variable Π representative of the time evolution of aging effects on the structure's global mechanical behavior:

$$\dot{Q}_l = \alpha_l \dot{\Pi} \tag{3.43}$$

where α_l is a coefficient which characterizes the time evolution of local leaks. In (Rossat et al., 2022b), the macro-variable Π has been taken as the prestressing losses averaged on prestressing cables of the structure, based on purely viscoelastic mechanical calculations (*i.e.* without modeling of damage). Alternatively, such a macro-variable may be chosen as a scalar quantity based on the stress tensor $\boldsymbol{\sigma}$ of the concrete volume.

The choice of such a model is justified hereafter: firstly, due to restrained thermal shrinkage induced during hydration at early age, significant tensile stresses develop in the concrete volume, leading to the appearance of cracks (see Fig. 3.13a). For a given crack, this corresponds to an increase of damage d in a restrained zone, until reaching a maximal value d_0. Then, due to the applied prestressing, early age cracks are (partially) reclosed under the action of compressive stresses (see Fig. 3.13b). Subsequently, these cracks are progressively re-opening due to prestressing losses induced by the effects of aging (see Fig. 3.13c). Such a phenomenon has been observed by Bouhjiti (2018) in the framework of damage-based viscoelastic calculations at the scale of the VeRCoRs mock-up. In this context, the linear model in Eq. (3.43) is inspired from the correlation proposed in (Bouhjiti, 2018), linking the opening of a given crack to the mean residual tensile stresses in the concrete volume.

Moreover, for a given crack, it is assumed that the long-term crack opening does not exceed the maximal opening value obtained at early age. It is also assumed that early age cracks are not propagating, and that new cracks are not initiating during the structure's exploitation phase. Then, according to the second principle of Thermodynamics (stating that $\dot{\mathrm{d}} \geq 0$), these assumptions correspond to postulate that damage remains constant and equal to its maximal value d_0 reached during early age. It is worth noting that the relationship between crack opening and damage is not bijective in general. However, under the previous assumptions, this relationship is indeed bijective during the early age phase (see Fig. 3.13), when cracks are opening for the first time. Furthermore, such assumptions enable to adopt the decoupling of early age and long-term phases suggested by Bouhjiti (2018): in the absence of damage flow (*i.e.* cracks are neither propagating nor initiating during the long-term phase), the time evolution of the hydraulic behavior of cracks may be assessed based on viscoelastic mechanical calculations, which enable to assess the effects of aging on the global mechanical behavior of the structure in the absence of damage rate. This motivates the choice of the macro-variable Π in (Rossat et al., 2022b), which may be calculated in a purely viscoelastic framework.

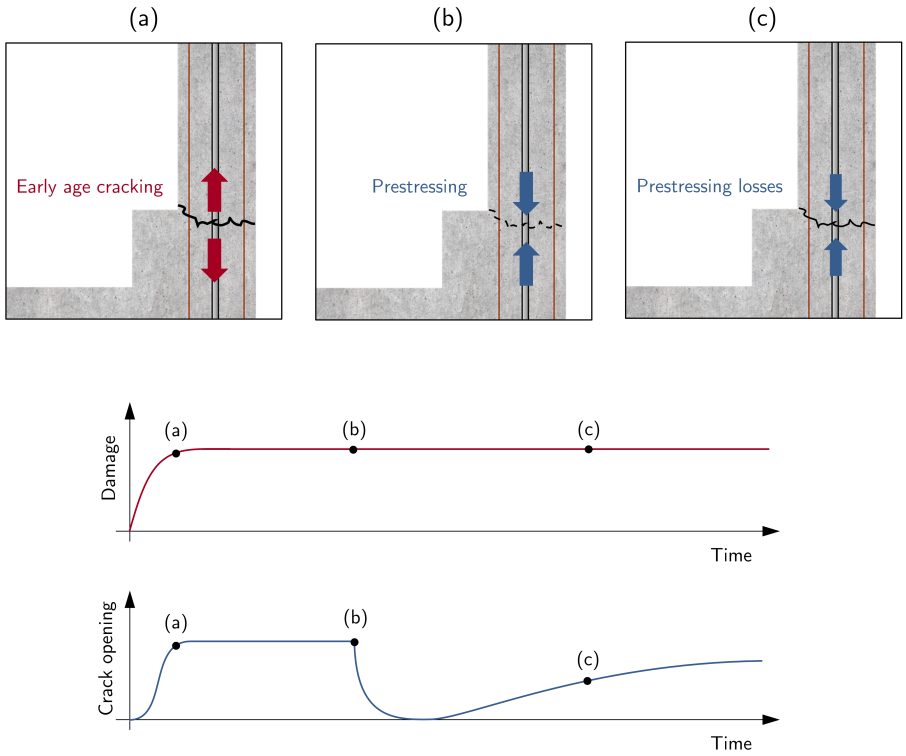

Figure 3.13: Illustration of the proposed phenomenological model for local leaks: (a) early age cracking; (b) crack reclosure due to prestressing; (c) progressive crack re-opening due to prestressing losses induced by aging.

3.4 Conclusion

In this chapter, the main physical phenomena related to concrete aging and their effects on the long-term behavior of large structures have been described and discussed. In the face of the complexity and inter-dependency of such physical phenomena, several assumptions have been adopted in order to adopt a modeling strategy suitable for assessing the long-term Thermo-Hydro-Mechanical and Leakage (THML) behavior of NCB subjected to normal exploitation loads. Such a modeling strategy will serve as a basis in the next chapters of this contribution, so as to devise computational models which will be embedded in the general Uncertainty Quantification (UQ) framework (see Introduction).

In particular, the adopted THML modeling strategy involves a purely viscoelastic description of the delayed mechanical behavior, and disregards explicit damage calculations, which are known to be computationally expensive. Then, the adopted modeling strategy remains valid if the cracking risk during long-term phase is low. Furthermore, some simplifying assumptions have been made regarding the modeling of local leaks, mainly driven by early age cracks in the case of NCB (see Section 3.3.5.2). Indeed, rather than explicitly modeling cracking through damage calculations, so as to subsequently estimate crack openings and then air leakage through each simulated crack, a simple phenomenological model has been proposed in order to assess the evolution in time of the total contribution of local leaks at structural scale.

Such a choice is particularly motivated by the fact that the first-mentioned approach would require a sensibly large number of unknown parameters, as well as an important computational cost. The aforementioned phenomenological model also restrains the description of the leakage behavior of the structure to its *global* leakage rate, and does not provide any information on its *local* leakage behavior, though.

Moreover, such simplifications underlie the following guiding idea: rather than trying to precisely assessing the behavior of a structure since the beginning of its early age phase, the main purpose of the adopted modeling approach consists in combining numerical models with *in-situ* observations of the structure's response during its long-term phase, in order to derive an updated state of knowledge about uncertain model parameters, which stems from a combination of analyst's prior knowledge and noisy observation data. This is notably enabled by the framework of Bayesian inference for inverse problems, which will enable to quantify the uncertainties of uncertain input parameters, and subsequently perform probabilistic predictions of the THML behavior of large structures.

The next chapter presents one of our main contributions related to the probabilistic modeling of the long-term THML behavior of containment structures. In this context, the THML modeling strategy presented in this chapter will be used within a general methodology aiming at updating uncertain input parameters from *in-situ* monitoring data related to the response of the structure under study.

Summary of the THML modeling approach

Phase	Inputs	Constitutive equations	Outputs
Thermal (T)	λ_c, c_c^p ρ_c, k_{th}	$\rho_c c_c^p \frac{\partial T}{\partial t} = \nabla_{\boldsymbol{s}} \cdot (\lambda_c \nabla_{\boldsymbol{s}} T) \quad \text{on } \mathcal{D}$ $T = \bar{T} \quad \text{on } \partial\mathcal{D}_{\bar{T}}$ $\boldsymbol{q}_{\text{th}} \cdot \boldsymbol{n} = k_{th}(T_\infty - T) \quad \text{on } \partial\mathcal{D}_{\bar{q}_{\text{th}}}$	T
Hydric (H)	A, B U_w, T_w^0 a_d, b_d ϕ	$\frac{\partial C_w}{\partial t} = \nabla_{\boldsymbol{s}} \cdot (D(C_w, T) \nabla_{\boldsymbol{s}} C_w) \quad \text{on } \mathcal{D}$ $C_w = f_d(h_\infty) \quad \text{on } \partial\mathcal{D}_{\bar{C}_w}$ $D(C_w, T) = D_0(C_w) \frac{T}{T_w^0} \exp\left[-\frac{U_w}{R}\left(\frac{1}{T} - \frac{1}{T_w^0}\right)\right]$ $D_0(C_w) = A \exp(BC_w)$ $f_d(h) = \phi \left[1 + (-a_d \log h)^{\frac{1}{1-b_d}}\right]^{-b_d}$	C_w, S_w, h
Mechanical (M)	α_{th}, α_{ds} $k_{rd}, \eta_{rd}, \eta_{id}, \kappa$ $\nu_{bc}, U_{bc}, T_{bc}^0$ η_{dc}	$\boldsymbol{\varepsilon} = \boldsymbol{\varepsilon}^{\text{el}} + \boldsymbol{\varepsilon}^{\text{th}} + \boldsymbol{\varepsilon}^{\text{ds}} + \boldsymbol{\varepsilon}^{\text{bc}} + \boldsymbol{\varepsilon}^{\text{dc}}$ $\dot{\boldsymbol{\varepsilon}}^{\text{th}} = \alpha_{th} \dot{T} \mathbf{I}$ $\dot{\boldsymbol{\varepsilon}}^{\text{ds}} = \alpha_{ds} \dot{C}_w \mathbf{I}$ $\boldsymbol{\varepsilon}^{\text{bc}} = \mathcal{F}^{\text{bc}}(\boldsymbol{\sigma}, h; k_{rd}, \eta_{rd}, \eta_{id}, \kappa, \nu_{bc}, U_{bc})$ $\boldsymbol{\varepsilon}^{\text{dc}} = \mathcal{F}^{\text{dc}}(\boldsymbol{\sigma}, h; \eta_{dc})$	$\boldsymbol{\sigma}, \boldsymbol{\varepsilon}, \Pi$
Leakage (L)	μ_g, k_0 β_K, c_k α_l	$(1 - S_w)\phi \frac{\partial p_g}{\partial t} = \nabla_{\boldsymbol{s}} \cdot \left(\frac{\mathbf{k}_g}{2\mu_g} \nabla_{\boldsymbol{s}} p_g^2\right) \quad \text{on } \mathcal{D}$ $p_g = \bar{p}_g \quad \text{on } \partial\mathcal{D}_{\bar{p}_g}$ $\mathbf{k}_g = k_0 k_s(p_g, S_w) k_{rg}(S_w) \mathbf{I}$ $k_s(p_g, S_w) = 1 + (1 - S_w) \frac{\beta_K}{\langle p_g \rangle_{\boldsymbol{s}}}$ $k_{rg}(S_w) = \sqrt{1 - S_w}\left(1 - S_w^{1/c_k}\right)^{2c_k}$ $Q_d = \int_{\partial\mathcal{D}_{\boldsymbol{q}_d}} \boldsymbol{q}_d \cdot \boldsymbol{n}$ $\dot{Q}_l = \alpha_l \dot{\Pi} \quad \text{on } \mathcal{D}$ $Q_g = Q_d + Q_l$	Q_d, Q_l, Q_g

Table 3.1: Summary of the adopted THML modeling approach

4

Bayesian inference for aging containment structures - Case of the VeRCoRs mock-up

Contents

4.1 Introduction

The main goal of this chapter is to devise a general methodology for assessing the long-term THML behavior of large concrete containment structures subjected to aging, while accounting for uncertainties in predictions in a probabilistic setting. In this perspective, the central case study of this chapter is a real structure, namely the VeRCoRs[1] mock-up, consisting in a 1:3 scale mock-up of a double-walled NCB.

Firstly, based on the THML modeling strategy presented in Chapter 3, a computational model aiming at describing the global behavior of the structure is devised. Then, based on Chapter 1, uncertainties in input parameters of the computational model are modeled in a probabilistic setting, in order to subsequently perform forward UQ tasks such as sensitivity analysis and uncertainty propagation. This notably implies the construction of surrogate models so as to alleviate the computational burden involved by UQ tasks. Besides, it is worth noting that the aforementioned forward UQ tasks rely on a probabilistic input that does not integrate observation data related to the response of the structure. Consequently, we propose an approach based on Bayesian inference aiming at updating uncertain input parameters from noisy observational data provided by *in-situ* monitoring devices. In this context, Bayesian computations will be based on the BuS framework presented in Chapter 2. In particular, these computations rely on the SuS algorithm (see Section 2.2.2) which enables to efficiently draw samples from the posterior distribution, that can be used so as to make new predictions of the long-term state of the structure.

The content of this chapter is adapted from the publications (Rossat et al., 2022b,c,d, 2021). Firstly, Section 4.2 provides a presentation of the VeRCoRs mock-up, as well as the monitoring data and the computational model considered in this chapter. Subsequently, surrogate modeling and sensitivity analysis related to physical variables of interest of the structure are presented in Section 4.3. Then, Bayesian inference is considered in Section 4.4, in order to infer uncertain parameters of the THML model from *in-situ* monitoring data related to the response of the structure.

4.2 Structure description and computational model

4.2.1 The VeRCoRs mock-up

The VeRCoRs mock-up consists in a 1:3 scale mock-up of a double-walled NCB of the French nuclear fleet. An aerial view of the VeRCoRs mock-up is given in Fig. 4.1. The ratio of 1:3 has been chosen in order to find an optimum between the structural representativeness and the acceleration of aging of the mock-up. Indeed, according to mathematical considerations on scaling in diffusion equations, the 1:3 scale containment wall is expected to dry nine times faster than full scale one (Granger, 1995). Such an acceleration would also have an effect on desiccation creep and desiccation shrinkage, to a certain extent. It is worth mentioning that basic creep is *a priori* not accelerated by the scale reduction, though. Hence, the aforementioned aging speed-up factor of 9 should be considered as approximate.

[1] VeRCoRs stands for *"Vérification Réaliste du Confinement des Réacteurs"* in French, which translates into *"realistic verification of the containment of reactors"*.

Figure 4.1: Aerial view of VeRCoRs mock up - EDF Lab Les Renardières. ©EDF

The main events occurring during the VeRCoRs mock-up life, including its construction and prestressing phases as well as its pressurization program, are summarized in Table 4.1. Firstly, the construction of the mock-up lasted from July 2014 to April 2015. In this context, the concrete formulation used to construct the mock-up was derived from the concrete mixes of NCBs from the Nogent sur Seine nuclear power plant, notably by using aggregates from the same region (Charpin et al., 2021). Moreover, all structural characteristics that could be constructed at 1:3 scale have been designed accordingly, including wall thicknesses and heights, steel rebars and prestressing cables.

Then, the VeRCoRs pressurization program unfolds in several pressurization tests aiming at applying an absolute air pressure of at most 5.2 bars inside the mock-up. This programs aims at representing the decennial visits of a real operating NCB, during which pressurization tests are performed in order to assess the leak tightness of the inner containment wall. Due to the scale reduction, such tests are performed every year for the VeRCoRs mock-up, instead of every decade for a 1:1 scale NCB. Furthermore, a heating system is used so as to simulate an operating reactor in the inner space of the mock-up. The activation of this heating system enables to start drying, and by extension, the aging process of the mock-up (Charpin et al., 2021).

Then, the rest of this chapter will focus on the inner wall of the VeRCoRs mock-up. This reinforced and prestressed concrete structure has a height of 22.8 m and an external radius of 7.7 m. It is constituted by three main structural volumes, namely a base slab, a cylindrical part and a dome. The base slab and the cylindrical part are linked through a concrete gusset, whereas the junction between the cylindrical part and the dome is ensured by a toric structural element, called *O-ring*.

A visualization of the geometry of the VeRCoRs inner wall is given in Fig. 4.2. The denomination of *standard zone* is usually adopted for designating the zone in the cylindrical part that is sufficiently far away from geometrical singularities, and whose behavior may thereby be assimilated to that of a hollow cylinder. The aforementioned geometrical singularities notably include two ribs in which prestressing cables are anchored, as well as four hatches, namely the equipment hatch, the access hatch, as well as two smaller hatches dedicated to the water supply circuit and the steam circuit (see Fig. 4.2).

Event	**Description - Comments**	**Date**
Start of construction	*Concreting of the raft*	2014-07-24
End of construction	*End of concreting of the dome*	2015-04-28
Start of prestressing	-	2015-05-06
End of prestressing	-	2015-08-12
VPO test	*Pre-operational pressurization test*	2015-11-05
VC1 test	*Control visit pressurization test*	2016-01-27
Start of heating	*Simulation of the operating reactor using a heating system*	2016-03-01
VD1 test	*First decennial test*	2017-03-14
$VD1_{bis}$ test	*Repetition of the first decennial test*	2017-03-21
VD2 test	*Second decennial test*	2018-03-29
VD3 test	*Third decennial test*	2019-03-19
VD4 test	*Fourth decennial test (canceled)*	-
VD5 test	*Fifth decennial test*	2021-03-21

Table 4.1: Summary of main events of VeRCoRs mock-up.

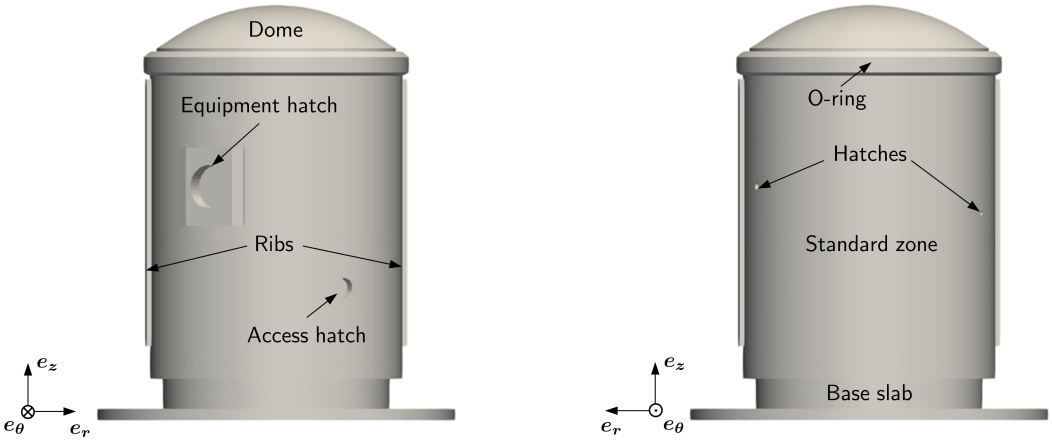

Figure 4.2: Outside view of the VeRCoRs mock-up inner-wall.

The prestressing of the VeRCoRs inner wall is ensured by several types of prestressing cables, namely:

- 57 vertical straight cables, ensuring a part of the prestressing in the vertical direction. These cables are anchored in the base slab and in the O-ring.
- 98 gamma cables, partialy ensuring the vertical prestressing in the standard zone, as well as a part of the prestressing of the dome. These cables are called "gamma" due to their particular shape, reminding the Γ greek letter. Furthermore, such cables are anchored in the base slab and in the O-ring.
- 122 tangential cables, ensuring prestressing in the tangential (or orthoradial) direction. These cables are anchored in the two ribs of the structure, depicted in Fig. 4.2.
- 18 dome cables, ensuring a part of the prestressing of the dome. These cables are anchored in the O-ring.

A visualization of the prestressing cables of the VeRCoRs mock-up is given in Fig. 4.3. During the prestressing phase, after the end of the construction phase, these cables are sequentially tensioned, in order to induce biaxial compressive stresses in the concrete volume. These cables are inserted in ducts and are cement grouted after tension. It is worth noting that the prestressing phase is a complex continuous and iterative process that should lead to compressive stresses of about 12 MPa in the tangential direction and 8.5 MPa in the vertical one, in the standard zone at mid-height (Bouhjiti et al., 2018a; Granger, 1995).

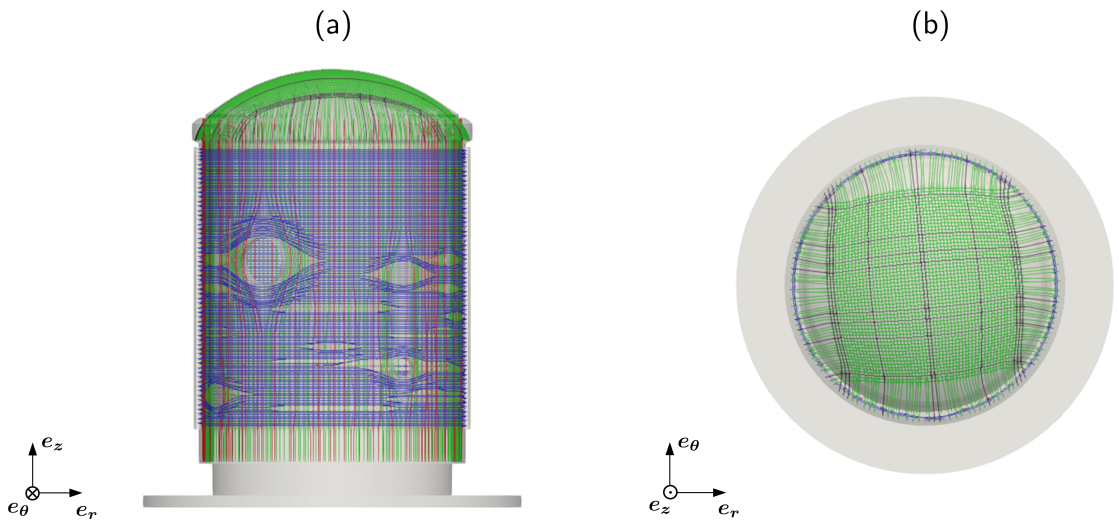

Figure 4.3: Prestressing cables of VeRCoRs mock-up: (a) front view; (b) top view. Vertical cables are shown in red, gamma cables in green, tangential cables in blue and dome cables in black.

4.2.2 Monitoring data

4.2.2.1 Thermo-hydric ambient conditions

The temperature and the relative humidity of the ambient air inside and outside the inner containment wall are continuously measured throughout the lifetime of the structure. Here, the outer space of the inner wall corresponds to the space between the two containment walls of the mock-up. Measurements series of ambient temperature and RH of the inner wall are presented in Fig. 4.4. In what follows, the initial instant $t = 0$ is set as the date of construction start, *i.e.* at 2014-07-24 (see Table 4.1).

Firstly, the ambient temperature and RH vary according to seasonal conditions on site throughout the construction of the mock-up, which explains that measurements related to the internal ambient air are only available from few months after the end of the prestressing phase. Then, the start of the heating system induces an increase of the temperature of internal ambient air, up to about 35°C, whereas the temperature of external air fluctuates around 20°C, between pressurization tests. Likewise, the aforementioned heating system induces also a decrease of the internal ambient RH, to a value of about 30%. This is due to the direct correlation existing between temperature and RH, typically expressed by Magnus' law (see *e.g.* (Boucher, 2016)).

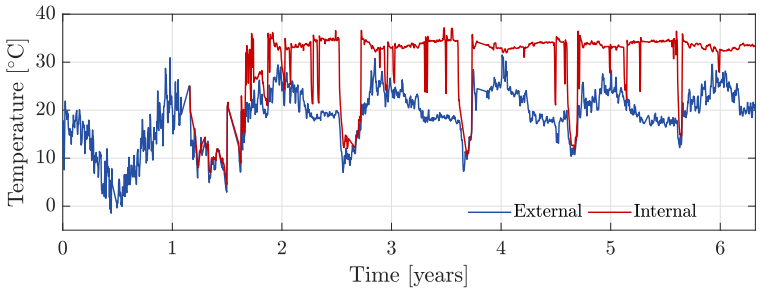

(a) Temperature

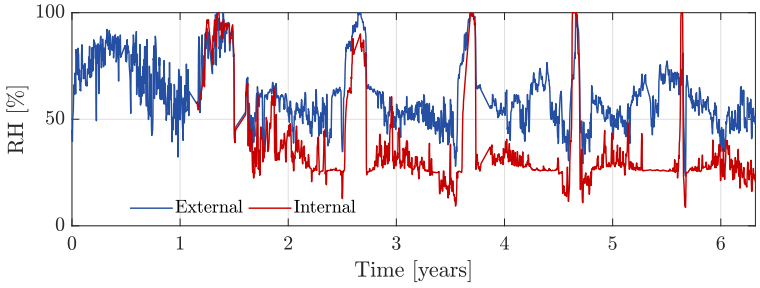

(b) RH

Figure 4.4: Measurements of ambient temperature and RH of the inner and outer air of VeRCoRs inner containment wall, at mid-height.

Then, few weeks before each pressurization test, the shutdown of the operating reactor is simulated by stopping the heating system for a period of about 1 month. This leads to a decrease of the internal ambient temperature, to a value of about 15°C. Such a value is maintained until few weeks after the end of the pressurization test. Likewise, this temperature decrease induces an increase of the ambient RH during the shutdown period of the heating system. Lastly, it is observed that the ambient conditions of the external air of the

inner wall seem to vary along with seasonal conditions, which are more or less delayed by the thickness of the mock-up outer wall.

4.2.2.2 Mechanical monitoring data

The VeRCoRs mock-up constitutes a widely instrumented structure, involving a large amount of sensors aiming at measuring its thermal, hydric and mechanical behavior (Mathieu et al., 2018; Oukhemanou et al., 2016). This notably includes vibrating wire sensors embedded in the thickness of the structure (Courtois, 2019; Hénault et al., 2019), which enable to measure its strains. In particular, the standard zone of the structure at mid-height comprises a zone in which several of these strain sensors are concentrated, on an angular sector of about 25° sufficiently far away from geometrical singularities (such as ribs or hatches). In this way, the strain measurements provided by sensors located in this zone are deemed to be representative of the behavior of the standard zone of the structure. A schematic representation of such a zone is given in Fig. 4.5.

Full strain measurement series in tangential and vertical directions and for intrados and extrados locations (see Fig. 4.5b) are presented in Fig. 4.6 & 4.7. These series are displayed on a time grid with a step of about two weeks, so that strain jumps attributed to internal pressure during integrity tests are not visible. The initial instant $t = 0$ is assumed to be the date of the construction startup (*i.e.* 2014-07-24, see Table 4.1). Moreover, the reference date for strain measurements (*i.e.* the zero strain date) is set as the date of the end of the construction phase (2015-04-28, see Table 4.1) *i.e.* near $t \approx 1$ year.

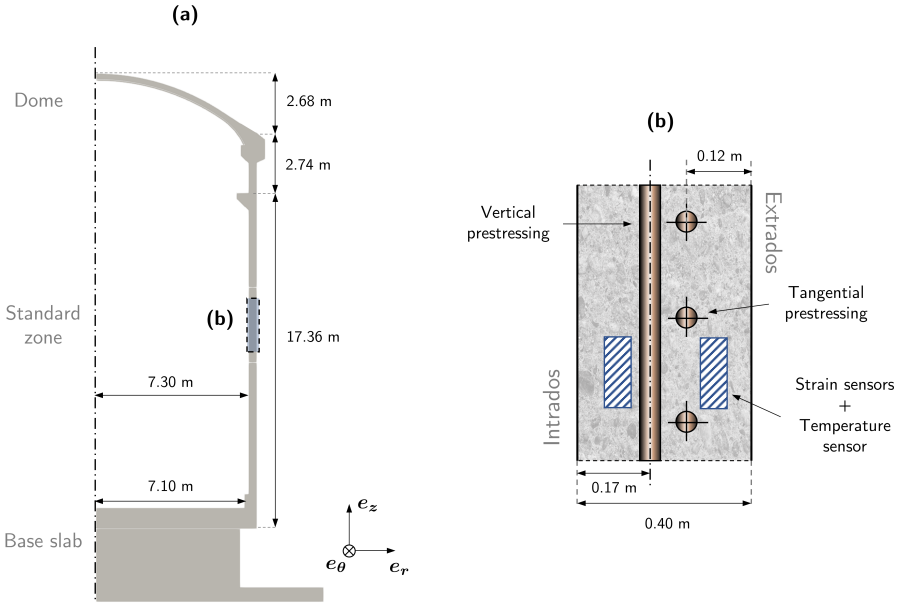

Figure 4.5: VeRCoRs inner wall: (a) 2D view; (b) focus on the standard zone at mid-height.

Firstly, once the prestressing phase is completed, both tangential and vertical strains are slightly decreasing, and fluctuating in correlation with ambient temperature and RH variations (see Fig. 4.4). Then, the increase of the temperature of internal ambient air caused by the start of the heating system involves an acceleration of concrete drying, and thereby of both tangential and vertical strains. Subsequently, few weeks before each pressurization test,

the inner ambient temperature is decreased to a value of about 15°C, in order to simulate the shutdown of the operating reactor. Such a value is maintained until few weeks after the end of the pressurization test.

This implies strain variations near each pressurization test, which are clearly visible in the strain series presented in Fig. 4.6 & Fig. 4.7. Then, between two pressurization tests, strains are continuously decreasing over time. The strain rate tends to be slower as the aging progresses, which could be explained by a stabilization of drying over time.

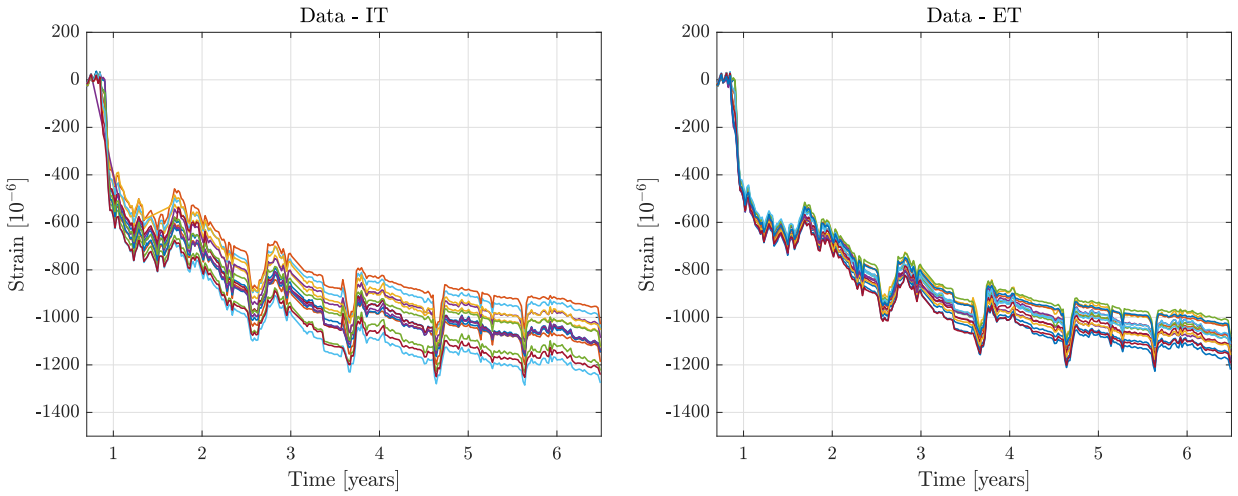

(a) Intrados strains **(b)** Extrados strains

Figure 4.6: Measured tangential strains of VeRCoRs standard zone

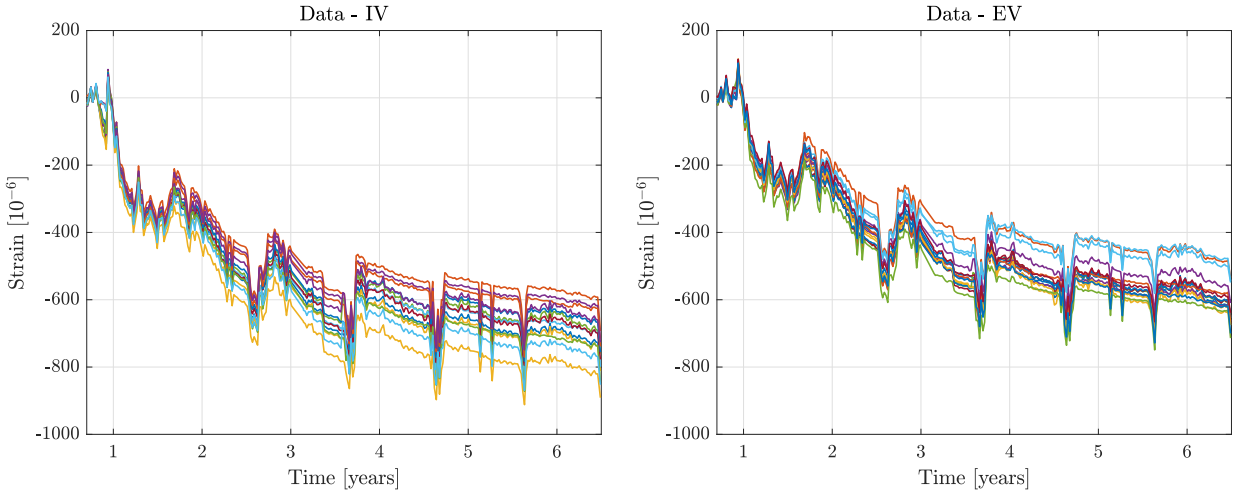

(a) Intrados strains **(b)** Extrados strains

Figure 4.7: Measured vertical strains of VeRCoRs standard zone

Then, in order to provide a synthetic comparison of strain monitoring data, the mean strain measurement series obtained by averaging series provided by sensors of a same data group (*i.e.* intrados/extrados and tangential/vertical strains) are presented in Fig. 4.8. Mean intrados and extrados tangential strain series present sensibly similar values, throughout the structure's service. Furthermore, intrados and extrados vertical strain series present

an offset of about 100 μm.m^{-1}, which is roughly constant since the end of the prestressing phase (near $t = 1.5$ years). Finally, it is worth noting that vertical and tangential strains are evolving in time in a practically parallel way after the end of prestressing phase.

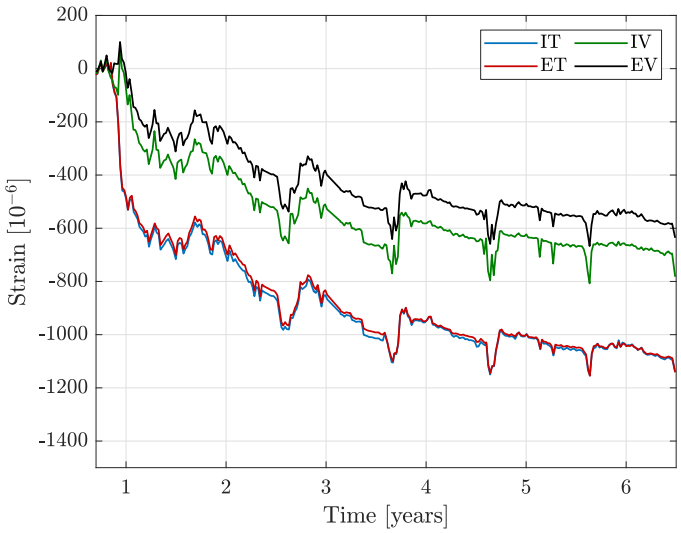

Figure 4.8: Mean strain measurement series. *"I" refers to "intrados", "E" to "extrados", "T" to "tangential", and "V" to "vertical".*

4.2.2.3 Pressurization tests and leakage measurements

During each pressurization test of the VeRCoRs mock-up, the inner pressure of the wall is progressively increased up to a relative value of 4.2 bars, whereas the outer pressure remains equal to the atmospheric pressure (*i.e.* about 1.013 bars). The pressure profiles applied during pressurization tests are given in Fig. 4.9.

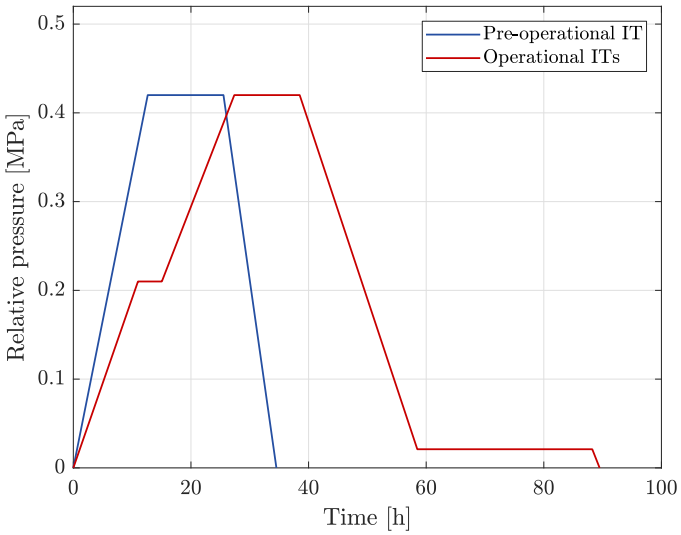

Figure 4.9: Internal pressure imposed during pre-operational and operational pressurization tests of VeRCoRs mock-up.

In-situ leakage measurements may be split into two categories, namely *global* measurements, consisting in estimating the global leakage rate of the structure, and *local* measurements, aiming at establishing a map of local leaks observed on the external surface of the structure.

Firstly, during a pressurization test, the maximal pressure plateau is long enough maintained in order to ensure that the flow is laminar and that the stationary regime is reached. The global leakage rate of the structure is then estimated from pressure and temperature variations of the internal air of the structure. Based on the ideal gas law, the mass of the dry air m_a contained inside the structure may be written as follows:

$$m_a = \frac{p_a V_0}{r_a T_a} \tag{4.1}$$

where $p_a = p - p_v$ is the dry air pressure, p the total pressure in the inner wall, p_v the vapor pressure, V_0 the free volume of the inner containment, T_a the dry air temperature, and $r_a = R/M_a$ the specific ideal gas constant of dry air. R is the ideal gas constant and M_a the molar mass of dry air.

Then, the global leakage rate τ_g (usually given in % per day) of the structure is given by the logarithmic time derivative of the dry air mass m_a. Assuming that variations of the free volume are negligible, this quantity writes:

$$\tau_g = \frac{\dot{m}_a}{m_a} = \frac{\dot{p}_a}{p_a} - \frac{\dot{T}_a}{T_a} \tag{4.2}$$

In practice, the leakage rate in Eq. (4.2) is estimated from measurements of the pressure p_a and the temperature T_a, based on several temperature sensors placed in the free volume of the inner containment (measuring the temperature T_g), moisture probes (measuring the vapor pressure p_v), and manometers measuring the pressure inside and outside the inner containment wall. The leakage rate in Eq. (4.2) may be converted into a (volumetric) flow rate, usually given in $\mathrm{m}^3.\mathrm{h}^{-1}$:

$$Q_g = \tau_g V_0 \tag{4.3}$$

Furthermore, considering only dry air leakage, a specific unit is used to measure the structure leakage rate at each pressurization, namely normal cubic meters per hour ($\mathrm{Nm}^3.\mathrm{h}^{-1}$). A normal cubic meter corresponds to the volume of one cubic meter, for a gas in normal pressure and temperature conditions, such that one disposes of the following conversion formula for the leakage rate in Eq. (4.3), considering a gas at pressure p_a (in bars) and temperature T_a (in K):

$$Q_g^{(\mathrm{Nm}^3.\mathrm{h}^{-1})} = \frac{p_a}{p_n}\frac{T_n}{T_a} Q_g^{(\mathrm{m}^3.\mathrm{h}^{-1})} \tag{4.4}$$

where $p_n = 1.013$ bars and $T_n = 273$ K. Thus, the conversion in Eq. (4.4) provides a normalized leakage rate which does not depend on temperature and pressure conditions of a given test.

Then, during the maximal pressure plateau of a pressurization test, soapy water is sprayed on the external surface of the inner containment wall in order to visually identify local leaks. Such leaks are typically caused by cracks, porosity lines, or local defects created during the construction phase (see Section 3.2.6). A map of local leaks is then established, and the associated local leakage rates are measured with leakage collecting boxes (LCB) equipped with flowmeters. This measurement process is depicted in Fig. 4.10.

Figure 4.10: Measurement of local leaks during a pressurization test with a leakage collecting box, from (Asali, 2016).

Nevertheless, it is worth noting that local leakage measurements present several limitations. Indeed, the size of the LCB may be smaller than some leaking defects, such as long cracks. In such a case, the measured local leakage rate is linearly extrapolated by the operator, which implies an additional layer of uncertainties. Besides, since local leaks are identified through a visual inspection jointly performed with an aspersion of soapy water, which may lead to a non-exhaustive identification. This may be notably explained by the fact that a large surface has to be inspected during a limited period (about 1400 m^2 for VeRCoRs and 9000 m^2 for 1:1 scale NCBs).

As a result, leakage measurements performed on site provide various information involving different scales and levels of uncertainties. Global measurements give an accurate estimation of the global leakage behavior of the structure only, whereas local measurements provide information on the spatial distribution of local leaks, involving sensibly larger measurement uncertainties, though. In Section 4.4, it will be shown how Bayesian inference can be used so as to extract information from both global and local leakage measurements, while accounting for their different level of uncertainties.

Then, global and local leakage measurements performed during the first six pressurization tests of VeRCoRs mock-up are summarized in Table 4.2. Here, the leakage rate associated to local leaks corresponds to the sum of all the individual local leakage rates measured with LCB. Concerning the VD1 test, data taken from the test $VD1_{bis}$ (see Table 4.1) are presented, local leakage measurements of this test being deemed more reliable than those of VD1 test. Following the superposition principle mentioned in Section 3.3.5, the global leakage rate of the structure is assumed to be the sum of two contributions, namely:

- the leakage rate associated to local leaks,
- the leakage rate associated to diffuse leaks, *i.e.* attributed to leakage through concrete porosity.

As a result, the diffuse leakage rate is obtained by subtracting the local leakage rate to the global leakage rate. Hence, only the global and local leakage rates are directly measured.

The time evolution of local and diffuse leakage rates is depicted in Fig. 4.11. The global leakage rate of the structure continuously increases over time, from a value of 4.3 $Nm^3.h^{-1}$ during the pre-operational test to a value of 64.7 $Nm^3.h^{-1}$ at the VD5 test, namely the fifth operational test. In parallel to global leakage, the local leakage rate also increases over time, but seems to stabilize from the third pressurization test, though. Indeed, no evolution of the local leakage rate is observed from the VD3 test to the VD5 test, the leakage rate remaining equal to 38.9 $Nm^3.h^{-1}$. Besides, the global leakage rate continues to increase over time, which may be attributed to an increase of diffuse leaks caused by the evolution of the sound permeability of concrete, which is mainly driven by the water saturation ratio and therefore drying. At this point, it is difficult to conclude for certain regarding the physical phenomena behind such an evolution of global and local leakage rates, notably due to the large uncertainties tainting local leakage measurements. Indeed, as mentioned earlier, global leakage measurements are given with a certain accuracy (*i.e.* with a CoV of about 2%), whereas local leakage measurements present an estimated CoV that may reach 30% (see Table 4.2).

Test	**VPO**	**VC1**	**VD1**	**VD2**	**VD3**	**VD5**
Date	2015-11-05	2016-01-27	2017-03-21	2018-03-29	2019-03-19	2021-03-21
Local leaks [$Nm^3.h^{-1}$]	4.3 (1.5)	7.1 (2.4)	24.8 (5.7)	31.7 (9.7)	38.9 (10.3)	38.9 (11.3)
Global leak [$Nm^3.h^{-1}$]	7.7 (0.2)	9.5 (0.2)	30.3 (0.6)	46.2 (0.9)	57.1 (1.2)	64.7 (1.3)

Table 4.2: Global and local leakage measurements performed during pressurization tests of the VeRCoRs mock-up. Measurements are given with their standard deviation estimated by EDF (in brackets), for information purposes.

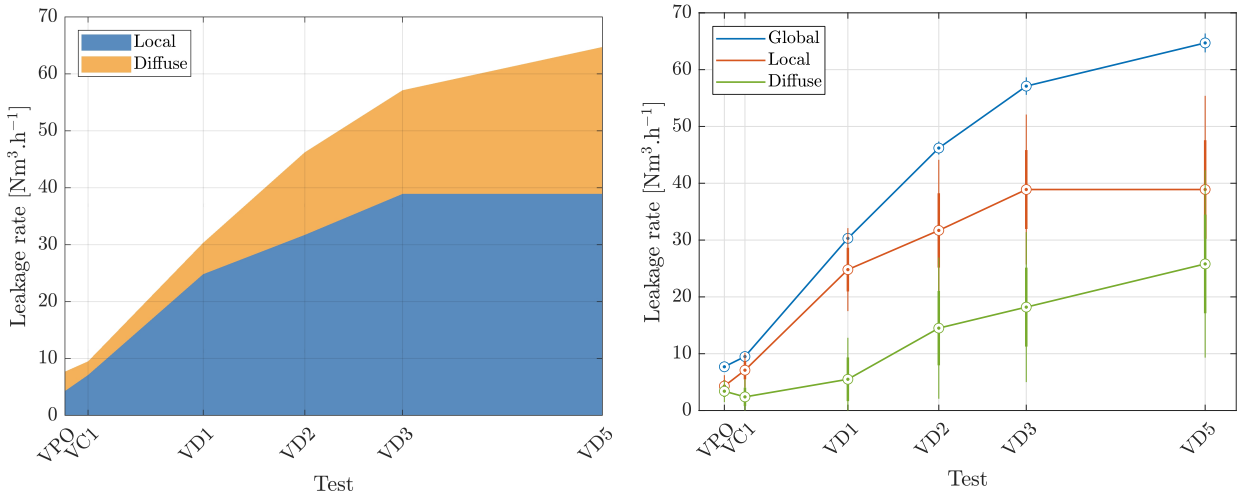

(a) Area chart of local and global leakage rates

(b) Global, local and diffuse leakage rates

Figure 4.11: Time evolution of the measured leakage rates of the VeRCoRs mock-up. *Error bars correspond to 50% CI (thick lines) and 80 % CI (thin lines), assuming centered Gaussian measurement errors.*

4.2.3 Computational model

4.2.3.1 Finite element meshes

Next, the computational model considered in order to assess the global behavior of the VeRCoRs mock-up is presented hereafter. In what follows, a Representative Structural Volume (RSV) of the VeRCoRs standard zone at mid-height will be considered. This choice is motivated by the fact that the standard zone may be deemed as representative of the global behavior of the structure, and that RSVs offer a good compromise between physical representativeness and computational cost (Bouhjiti et al., 2018a; Jason et al., 2007). The geometrical domain corresponding to the chosen RSV consists in a 3D portion of the inner wall, comprising an angular sector of 5° and a height of 0.42 m. Such a volume enables to represent three tangential prestressing cables and two vertical ones. This RSV is depicted in Fig. 4.12a.

Then, weak formulations of the constitutive equations of the THML modeling strategy presented in Chapter 3 are solved by using the finite element method. In this perspective, two finite element meshes are used, namely one for thermo-hydric and diffuse leakage calculations, and one for mechanical calculations. The thermo-hydric mesh is depicted in Fig. 4.12b, whereas the mechanical mesh is presented in Fig. 4.12c & d. Information about these finite element meshes are summarized in Table 4.3.

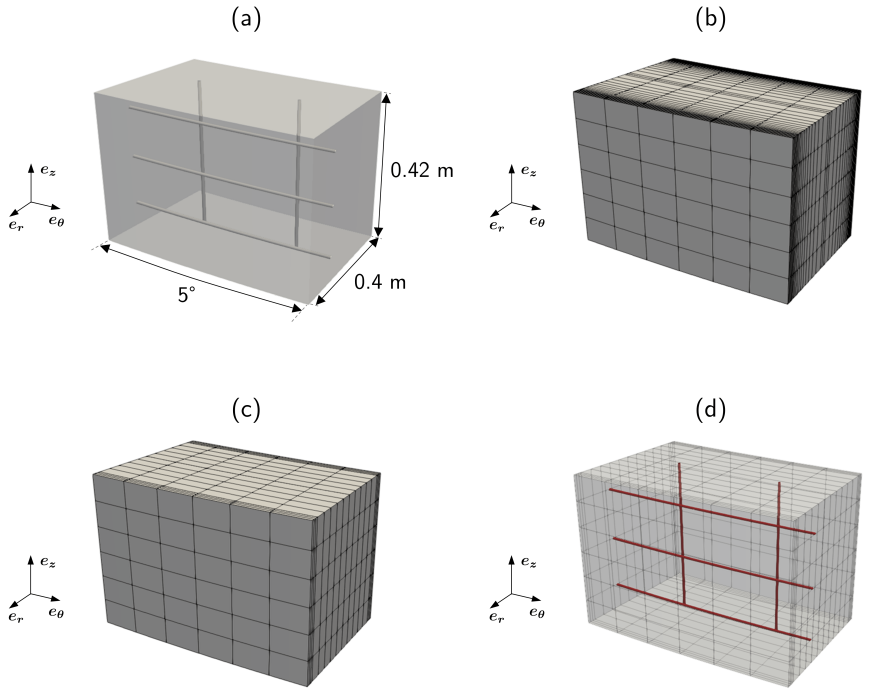

Figure 4.12: Geometry and finite element meshes of the VeRCoRs standard zone RSV: (a) geometry; (b) thermo-hydric mesh; (c) mechanical mesh; (d) prestressing cables mesh.

Phase	Concrete		Prestressing cables	
	Element type	Nodes	Element type	Nodes
TH-L	HEXA8 (linear)	1911	-	-
M	HEXA20 (quadratic)	3097	SEG2 (linear)	49

Table 4.3: Information about finite element meshes of the standard zone RSV.

The mesh adopted for thermo-hydric and leakage calculations (see Sections 3.3.2, 3.3.3 and 3.3.5) is formed by linear finite elements (HEXA8), and is refined near intrados and extrados boundaries of the RSV, in order to evaluate thermo-hydric gradients more precisely. Then, mechanical calculations are carried out on a second mesh, formed by quadratic finite elements for concrete (HEXA20), and linear finite elements (SEG2) for prestressing cables. In the framework of the adopted chained THML modeling strategy, thermo-hydric output fields of interest (*e.g.* temperature, water content) are projected on the aforementioned mechanical mesh. Here, the choice of such a two-step procedure involving two different meshes is justified as follows: in the case of linear finite elements, lumping the thermal mass matrix yields more robust results than that obtained with quadratic elements, when solving discretized thermal problems. Indeed, in some cases, the so-called *maximum principle* (Brezis, 2010) may be violated when using quadratic finite elements. Consequently, thermo-hydric and leakage calculations are performed using linear finite elements and by lumping the mass matrix[2].

4.2.3.2 THML model

As previously mentioned, the constitutive equations of the THML modeling strategy presented in Chapter 3 are solved with the finite element meshes presented in Section 4.2.3.1. Formally speaking, due to the adopted chained modeling strategy, the whole THML computational chain may be seen as an input-output map $\mathcal{M}_{THML} : \mathcal{D}_{\boldsymbol{X}} \subset \mathbb{R}^d \to \mathcal{D}_{\boldsymbol{Y}} \subset \mathbb{R}^n$, which has the following composite structure:

$$\mathcal{M}_{THML} = \mathcal{M}_L \circ \mathcal{M}_M \circ \mathcal{M}_H \circ \mathcal{M}_T \tag{4.5}$$

where $\mathcal{M}_T, \mathcal{M}_H, \mathcal{M}_M, \mathcal{M}_L$ are, in turn, thermal, hydric, mechanical and leakage sub-models. Given a set of input parameters $\boldsymbol{x} \in \mathcal{D}_{\boldsymbol{X}}$, the THML computational model in Eq. (4.5) returns several output of interests through the response of its sub-models, including:

- temperature T,
- water saturation S_w and relative humidity h,
- strains $\boldsymbol{\varepsilon}$ and prestressing losses Π,
- diffuse leaks Q_d, local leaks Q_l and global leakage Q_g.

[2]note that the diffuse leakage constitutive equations presented in Section 3.3.5.1 may be seen as a thermal diffusion problem, as emphasized in (Asali, 2016), which justifies the lumping of the mass matrix in the framework of diffuse leakage calculations.

A schematic representation of the THML model, including the several input-output dependencies involved in the computational chain, is provided in Fig. 4.13.

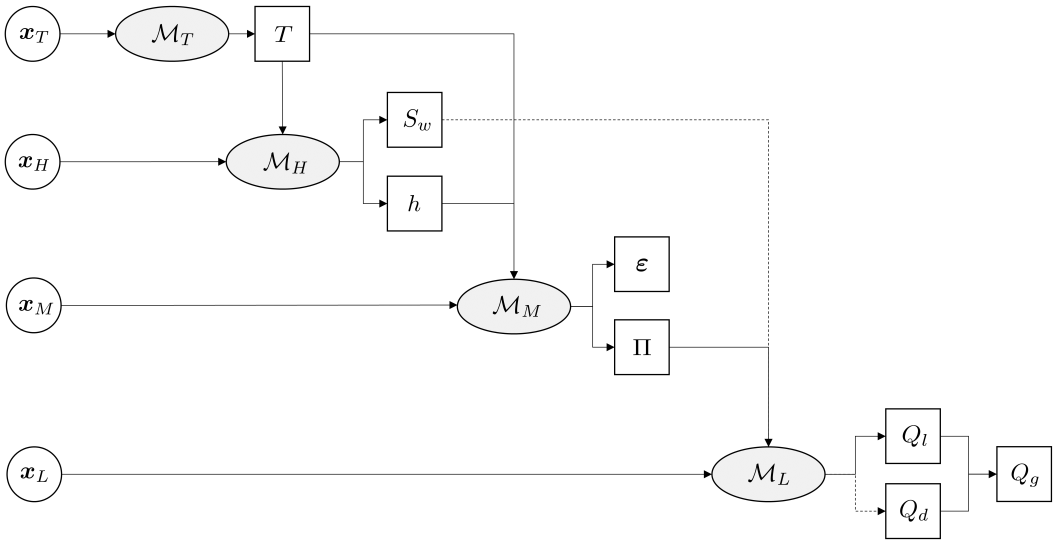

Figure 4.13: Schematic representation of the THML model. Dashed lines are highlighting the fact that water saturation ratio S_w taken as an input of the leakage model $\mathcal{M}_L$ only to compute the diffuse leakage rate Q_d.

The THML computational chain is summarized hereafter. Firstly, writing

$$\boldsymbol{x} = (\boldsymbol{x}_T, \boldsymbol{x}_H, \boldsymbol{x}_M, \boldsymbol{x}_L) \tag{4.6}$$

where the component $\boldsymbol{x}_\star$ denotes the input parameters associated to the sub-model $\mathcal{M}_\star$, the temperature T is obtained as an output of the thermal model $\mathcal{M}_T$ evaluated at $\boldsymbol{x}_T$. Subsequently, hydric variables of interest such as water saturation and RH are computed through the hydric model $\mathcal{M}_H$, by taking as inputs the parameters $\boldsymbol{x}_H$ and the temperature T.

Then, mechanical calculations are performed with the model $\mathcal{M}_M$, by taking as inputs the parameters $\boldsymbol{x}_M$, temperature T (notably for the thermo-activation model for creep, see Section 3.3.4.3) and RH h (for shrinkage and creep models, see Sections 3.3.4.2 to 3.3.4.4).

Lastly, leakage calculations may be split into two decoupled phases, namely the computation of diffuse leaks Q_d and the computation of local leaks Q_l. The first mentioned leakage rate is computed from the input parameters $\boldsymbol{x}_L$, as well as the saturation ratio S_w (notably for the relative gas permeability model, see Section 3.3.5.1). It is thereby remarked that diffuse leaks Q_d only depend on the thermal and hydric phases. Then, local leaks Q_l are computed from mechanical calculations, by taking as inputs the parameters $\boldsymbol{x}_L$ as well a mechanical macro-variable Π (see Section 3.3.5.2), here chosen to be the prestressing losses averaged on cables of the standard zone RSV. Finally, based on the superposition principle mentioned in Section 3.3.5, the global leakage rate Q_g is obtained by summing diffuse and local leakage rates.

4.2.3.3 Boundary conditions and loading

Next, the boundary conditions and loading considered at the scale of the adopted RSV are detailed hereafter. Firstly, Neumann BC in terms of temperature are considered for thermal computations, through the definition of a thermal convective exchange coefficient k_{th} (see Section 3.3.2), for both intrados and extrados surfaces of the RSV, based on the measured temperature histories of ambient air presented in Fig. 4.4a. Furthermore, concerning hydric calculations, Dirichlet BC in terms of water content C_w are adopted on intrados and extrados surfaces of the RSV, as described in Section 3.3.3. Analogously to the temperature histories adopted for thermal calculations, RH histories adopted for the above hydric boundary conditions are defined from the measurements of the RH of ambient air presented in Fig. 4.4b.

Concerning mechanical BC, the vertical component of the displacement field $\boldsymbol{u}$ is set to zero on the lower face of the RSV, and is constrained to be uniform on the RSV upper face. Moreover, the normal displacements on lateral faces of the RSV are blocked (*i.e.* $\boldsymbol{u} \cdot \boldsymbol{n} = 0$ on the corresponding faces, where $\boldsymbol{n}$ is the outward unit normal vector field). Thus, imposing such mechanical BC reverts to treating the standard zone like an infinite hollow cylinder, which constitutes a reasonable assumption when sufficiently far away from geometrical singularities (Bouhjiti et al., 2018a).

Finally, two mechanical loads are considered in this study, namely prestressing and dead weights of concrete volumes located above the RSV. Internal pressure applied during pressurization tests is not modeled in the framework of mechanical calculations, since one only focuses on the aging behavior of the structure, and due to the fact that the mechanical behavior of the standard zone remains essentially elastic during pressurization tests, as underlined by Bouhjiti et al. (2018a). Prestressing is modeled by applying forces at cables end nodes (see Fig. 4.12d). The steel nodes and their coincident concrete nodes are assumed to have a perfect kinematic connection (*i.e.* they have the same displacement). Moreover, prestressing loads are computed as internal nodal forces. Depending on the imposed stress in cables, instantaneous prestressing losses due to anchor recoil and friction are not taken into account at the scale of the considered RSV[3]. Furthermore, dead weights attributed to concrete volumes located above the considered RSV are represented by a vertical stress $\sigma_{z,c}$ imposed on the upper face.

Lastly, diffuse leakage calculations are performed by imposing Dirichlet BC in terms of air pressure p_a on the intrados and extrados surfaces of the RSV (see Section 3.3.5.1). In this context, the pressure profiles presented in Fig. 4.9 are applied on the intrados surface, whereas the pressure on the extrados surface is set to atmospheric pressure.

[3]this is typically the case when the imposed stress corresponds to that imposed at anchors of the structure. A full scale 3D elastic mechanical calculation would indicate that stresses in the standard zone are smaller than those imposed near cables anchors (see *e.g.* (Bouhjiti, 2018)).

4.2.4 Deterministic THML calculations

4.2.4.1 General settings

This section only aims at presenting typical output variables of interest provided by the THML computational model, through deterministic calculations. Hence these output variables are not yet compared with measurements presented in Section 4.2.2. Such observational data and their relationship with model outputs will be thoroughly studied in a Bayesian framework in Section 4.4.

In what follows, the results of a single THML computation are presented, by setting all the 36 input parameters of the THML model to their nominal value. The adopted nominal values of parameters related to concrete are given in Table 4.4, whereas those of parameters related to prestressing cables are given in Table 4.5.

Model	Input parameter	Notation	Unit	Value
$\mathcal{M}_T$	Thermal conductivity	λ_c	$\mathrm{W.m^{-1}.K^{-1}}$	2.8
	Density	ρ_c	$\mathrm{kg.m^{-3}}$	2350
	Heat capacity	c_c^p	$\mathrm{kJ.kg^{-1}.K^{-1}}$	880
	Convective exchange coefficient	k_{th}	$\mathrm{W.m^{-2}.K^{-1}}$	10
$\mathcal{M}_H$	Drying parameter	A	$10^{-15}\ \mathrm{m^2.s^{-1}}$	4.9
	Drying parameter	B	-	0.08
	Initial water content	$C_{w,0}$	$\mathrm{l.m^{-3}}$	160
	Porosity	ϕ	%	16
	Drying reference temperature	T_w^0	°C	15
	Drying activation energy	U_w	$\mathrm{kJ.mol^{-1}}$	59.4
	Sorption model parameter	a_d	-	9.28
	Sorption model parameter	b_d	-	0.39
$\mathcal{M}_M$	Young's modulus	E	GPa	36.7
	Poisson's ratio	ν	-	0.248
	Thermal dilation coefficient	α_{th}	$10^{-6}\ \mathrm{K^{-1}}$	9.2
	Desiccation shrinkage coefficient	α_{ds}	10^{-6}	10
	Basic creep Poisson's ratio	ν_{bc}	-	0.248
	Reversible deviatoric basic creep stiffness	k_{rd}	10^{11} Pa	1.7
	Reversible deviatoric basic creep viscosity	η_{rd}	10^{17} Pa.s	5.0
	Irreversible deviatoric basic creep viscosity	η_{id}	10^{17} Pa.s	5.0
	Basic creep activation energy	U_{bc}	$\mathrm{kJ.mol^{-1}}$	43.1
	Basic creep reference temperature	T_{bc}^0	°C	20
	Basic creep consolidation parameter	κ	10^{-4}	1.0
	Desiccation creep viscosity	η^{dc}	10^9 Pa.s	7.4
	Dead weight of upper concrete lifts	$\sigma_{z,c}$	MPa	0.41
$\mathcal{M}_L$	Relative permeability parameter	c_k	-	0.45
	Klinkenberg coefficient	β_K	MPa	0.18
	Intrinsic permeability	k_0	$10^{-17}\ \mathrm{m^2}$	7.0
	Local leak model parameter	α_l	-	6.0

Table 4.4: Input parameters of the THML model - Concrete.

Model	Input parameter	Notation	Unit	Value
	Young's modulus	E_s	GPa	190
	Poisson's ratio	ν_s	-	0.3
	Density	ρ_s	$kg.m^{-3}$	7850
$\mathcal{M}_M$	Thermal dilation coefficient	$\alpha_{th,s}$	10^{-6} K^{-1}	10
	Section	A_s	mm^2	560
	Initial tension of tangential cables	$\sigma_{\theta,0}$	MPa	1514
	Initial tension of vertical cables	$\sigma_{z,0}$	MPa	1514

Table 4.5: Input parameters of the THML model - Prestressing cables.

Finite element calculations are performed by considering the 2014-07-24 as initial date, and the 2021-04-01 as final date. As a result, the lifetime of the standard zone of VeRCoRs mock-up is simulated up to its fifth pressurization test. A time grid of about 210 instants is used for calculations. This grid is refined near instants of pressurization tests in order to catch variations of temperature and RH. Furthermore, an adaptive refining feature provided by the finite element solver `Code_Aster` is used in order to facilitate the convergence of calculations, when necessary. In the framework of probabilistic calculations presented later in this chapter, the results of each THML model run will be projected on a same time grid.

4.2.4.2 Thermo-hydric calculations

Firstly, the spatio-temporal evolution of the temperature T and water saturation ratio S_w in the thickness of VeRCoRs standard zone are given in Fig. 4.14. In what follows, the zero abscissa in the wall thickness corresponds to the intrados surface. As depicted in Fig. 4.14a, the temperature in the thickness follows the variations of the temperature of the ambient air presented in Fig. 4.4. In particular, the temperature in the whole thickness of the standard zone decreases to a value of about 15°C near pressurization tests.

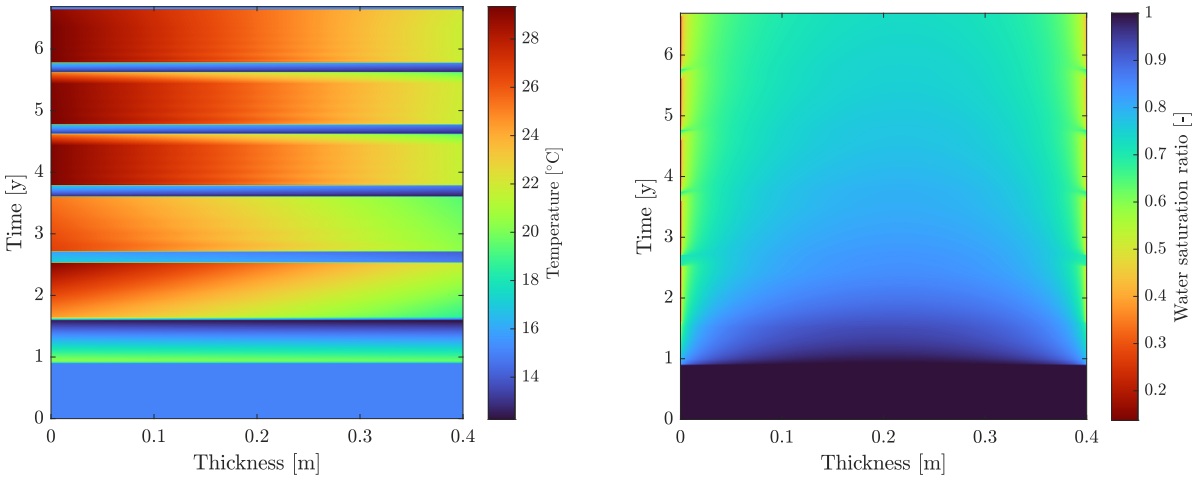

(a) Temperature **(b)** Water saturation ratio

Figure 4.14: Thermo-hydric calculations: spatio-tempral evolution of temperature and water saturation ratio in the thickness of VeRCoRs standard zone.

From the end of the construction of the mock-up to the start of the heating system, practically no drying occurs due to the humidification of both intrados and extrados surface. Then, the start of the heating system induces a progressive decrease of the water saturation ratio in time. During pressurization tests, the decrease of the ambient temperature induces an increase of the ambient RH, which only transfers to few centimeters in the thickness of the wall, near both intrados and extrados surfaces. This may be explained by the fact that moisture transfer (*i.e.* drying and humidification) is a much slower process than heat conduction. Furthermore, few water saturation ratio profiles in the wall thickness are presented in Fig. 4.15. Once the heating system is started, the water saturation ratio field presents strong gradients near both intrados and extrados surfaces. Broadly speaking, drying kinetics tend to slow over time, and the water saturation ratio at the core of the thickness decreases to a value of about 74% at $t = 6$ years.

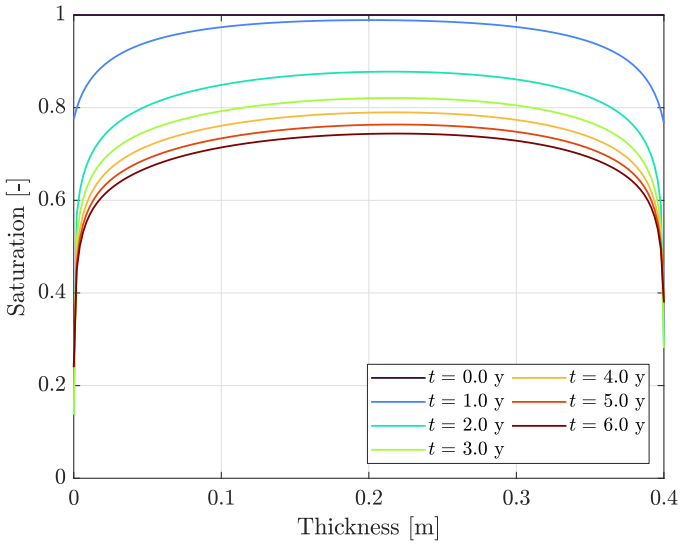

Figure 4.15: Water saturation ratio profiles in the thickness of VeRCoRs standard zone.

4.2.4.3 Mechanical calculations

The time evolution of delayed strains (at intrados/extrados locations and in tangential/vertical directions) and mean prestressing losses computed at the scale of the standard zone RSV are given in Fig. 4.16. Firstly, delayed strains are stagnating around a value of 0 from the end of the construction phase to the start of the prestressing phase. Then, the tensioning of cables induces a significant decrease of strains, near $t \approx 1$ year.

Next, the start of the heating system at $t \approx 1.6$ years induces an acceleration of drying shrinkage and creep strains. Moreover, during pressurization tests, strain variations induced by modification of thermo-hydric ambient conditions are well reproduced by mechanical calculations. It is remarked that the model does not enable to make the distinction between intrados and extrados vertical strains, though. This is due to the idealized cinematic boundary conditions adopted at the scale of the standard zone RSV: indeed, vertical displacements on the upper face of the RSV are constrained to be uniform (see Section 4.2.3.3).

Furthermore, as depicted in Fig. 4.16b, the mean prestressing losses are continuously increasing over time, mainly due to the action of drying, creep and shrinkage strains. It is worth noting that the decrease of the temperature of the inner ambient air during pressurization tests slightly slows the evolution of prestressing losses. This is consistent with strain variations observed during the shutdown period of the heating system, near each pressurization tests.

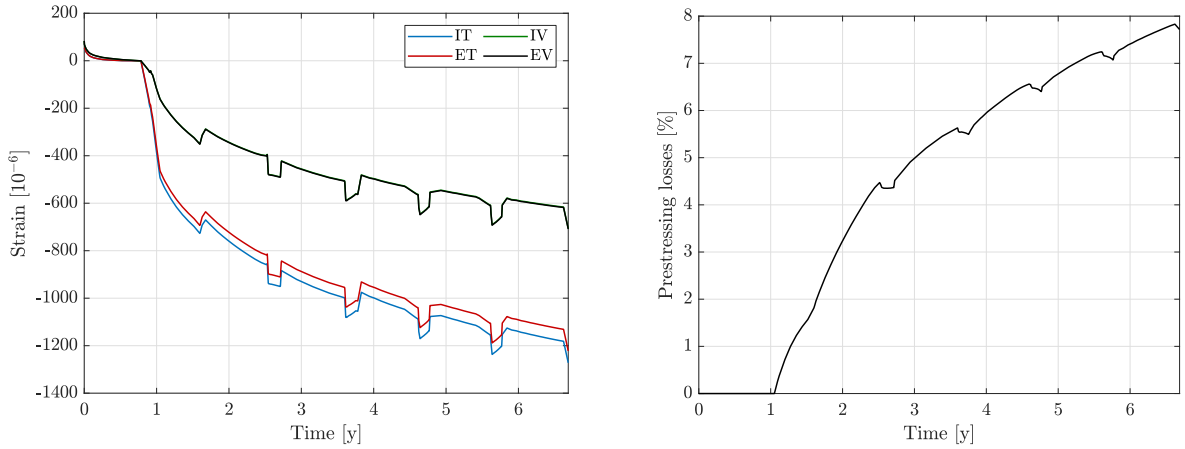

(a) Delayed strains **(b)** Mean prestressing losses

Figure 4.16: Mechanical calculations: temporal evolution of delayed strains and mean prestressing losses of VeRCoRs standard zone. *Concerning delayed strains, "I/E" stand for "intrados/extrados", and "T/V" for "tangential/vertical".*

4.2.4.4 Leakage calculations

Lastly, output quantities related to the leakage model are presented and discussed. The computation of diffuse leaks requires to solve a nonlinear diffusion equation, whose primary unknown variable is given by the air pressure. The time evolution of the diffuse leakage rate of VeRCoRs mock-up during each pressurization test is presented in Fig. 4.17. This diffuse leakage rate is computed by assuming that Darcy's flux is constant over the whole surface of the containment wall. In this way, the structural diffuse leakage rate is simply computed by multiplying the Darcy's flux obtained at the scale of the standard zone RSV by the external surface of VeRCoRs mock-up. This assumption is adopted in first estimate, knowing that the structure is essentially cylindrical. Furthermore, the maximal diffuse leakage rate progressively increases over time, principally due to the decrease of the water saturation ratio in the wall thickness caused by drying. It is also noticed that such a maximal value is reached at an increasingly early instant during each pressurization test, as concrete drying progresses.

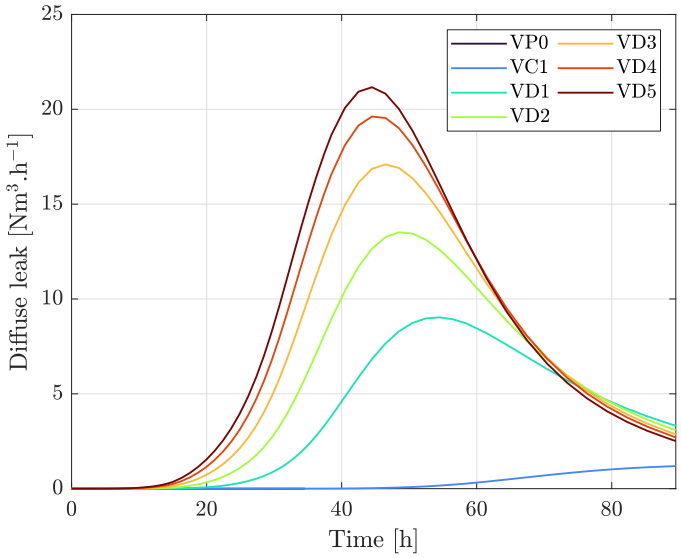

Figure 4.17: Time evolution of diffuse leaks during each pressurization test of VeRCoRs mock-up.

Lastly, the temporal evolution of diffuse and local leakage rates is given in Fig. 4.18. According to the model, the global leakage rate at the pre-operational test is mainly driven by local leaks. Subsequently, the local leakage rate is continuously increasing along with prestressing losses computed with the mechanical model. This is due to the adopted phenomenological local leak model (see Section 3.3.5.2), which does not enable to reproduce the constant local leakage rate observed between VD3 and VD5 tests in Fig. 4.11. Moreover, the proportion of diffuse leaks in the global leakage rate increases over time, as the water saturation in the wall thickness decreases due to drying.

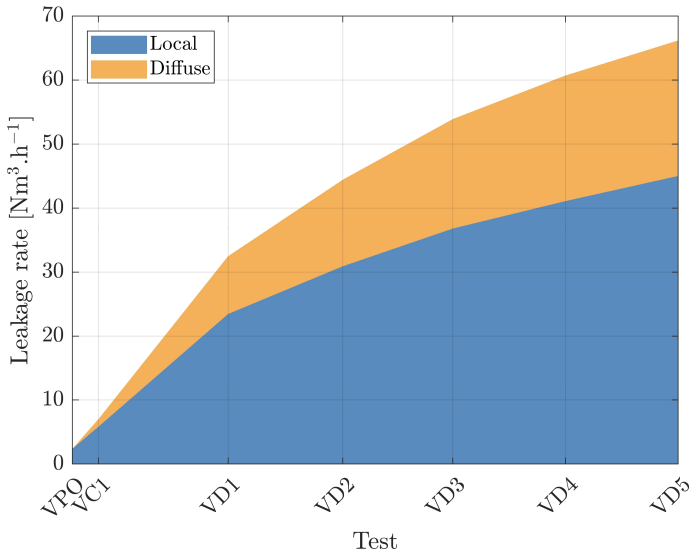

Figure 4.18: Time evolution of the local and diffuse leakage rates of the VeRCoRs mock-up.

4.3 Surrogate modeling and sensitivity analysis

In this section, forward uncertainty quantification techniques are coupled with the computational model presented in Section 4.2, in order to model uncertainties tainting input parameters in a probabilistic framework, and to quantify their effect on the response of the model, including the main output physical variables of interest previously presented (*i.e.* water saturation, strains, leakage rate). Firstly, in Section 4.3.1, the uncertainties of primary influential inputs (PII) are modeled by using probability distributions, following principles presented in Section 1.2.3. Subsequently, in order to ensure the tractability of forward (and inverse) UQ tasks, surrogate modeling is considered in Section 4.3.2. In particular, PCE surrogates are chosen in order to provide global approximations of the model on the support of the devised input probability distribution. Then, based on the analytical post-processing features offered by such surrogates, a global variance-based sensitivity analysis of the main output quantities of the THML model is performed in Section 4.3.3.

4.3.1 Probabilistic input modeling

The computational model presented in Section 4.2 involves about 35 input parameters tainted with more or less important uncertainties. Despite the fact that VeRCoRs mock-up is widely instrumented, and that its material properties are thoroughly studied (Charpin et al., 2021), most of these input parameters remain not well known. Indeed, while a large amount of data is available concerning VeRCoRs material properties that are directly measurable, only scarce information are available for parameters that are not directly measurable. The uncertainties of such parameters are usually quantified through expert judgement.

Furthermore, it is worth noting that the input dimension of the adopted THML model is relatively high, which may impede the computational tractability of UQ techniques. In this context, screening strategies may be considered so as to determine the PII of the model (see Section 1.2.5). Once identified, the latter are modeled as random variables, whereas the remaining input parameters are fixed to their nominal value. In this chapter, the PII of the computational model are selected based on the former work of Bouhjiti (2018), which performed an OAT-based screening in order to determine the most influential parameters of a similar THML computational model, at the scale of a RSV of VeRCoRs mock-up. As a result, a set of 9 input parameters is considered. The marginal distribution of each of these parameters is defined through expert judgement. The set of the retained PII as well as their marginal distributions are summarized in Table 4.6. Moreover, due to the lack of information regarding dependencies, all the aforementioned parameters are assumed to be mutually independent.

Thus, in a Bayesian perspective, the defined joint probability distribution may be seen as a prior distribution for the PII of the THML computational model. It summarizes the level of knowledge in the aforementioned PII before observing and/or analyzing data related to the response of VeRCoRs mock-up. This input distribution will be used in the next sections to construct PCE surrogate models, and performing a global sensitivity analysis of output quantities of the THML model. In Section 4.4, the framework of Bayesian inference will be used so as to combine the defined prior level of knowledge with monitoring data presented in Sections 4.2.2.2 & 4.2.2.3.

Model	n°	Parameter	Unit	Distribution	Mean	Std	CoV
$\mathcal{M}_H$	1	B	-	Lognormal	0.08	0.012	0.15
	2	$C_{w,0}$	l.m^{-3}		160	24	0.15
$\mathcal{M}_M$	3	α_{ds}	10^{-5} kg.m^{-3}	Lognormal	1.0	0.25	0.25
	4	$\sigma_{\theta,0}$	MPa		1514	378.5	0.25
	5	$\sigma_{z,0}$	MPa		1514	378.5	0.25
	6	κ	10^{-4}		1.0	0.25	0.25
$\mathcal{M}_L$	7	k_0	10^{-17} m^2	Lognormal	7.0	3.5	0.5
	8	β_K	MPa		0.18	0.045	0.25
	9	α_l	-		6.0	3.0	0.5

Table 4.6: Marginal distributions of the primary influential inputs of the THML computational model.

4.3.2 Surrogate modeling

4.3.2.1 General settings

Let $(\Omega, \mathcal{F}, \mathbb{P})$ be a probability space. Let $\boldsymbol{X} : \Omega \to \mathcal{D}_{\boldsymbol{X}} \subset \mathbb{R}^d$ the $d = 9$ random input parameters defined in Section 4.3.1. Each output quantity of interest of the THML model (*e.g.* strains) may be seen as a function of $\boldsymbol{X}$, namely an input-output map $\mathcal{M} : \mathcal{D}_{\boldsymbol{X}} \to \mathcal{D}_{\boldsymbol{Y}} \subset \mathbb{R}^n$. Considering only the time evolution of output variables at a given location, the output dimension n here corresponds to the size of the adopted time grid for computing the output variable of interest. Furthermore, each component of the response $\bar{\boldsymbol{Y}} = \mathcal{M}(\boldsymbol{X})$ is assumed to admit a finite variance.

The several output variables of interest of the THML model are computed on different time grids, involving different output dimensionalities. Indeed, leakage rates (diffuse, local and global) are computed at each pressurization test, whereas mechanical fields such as strains are computed on a time grid involving about 210 instants. As a result, two different surrogate modeling approaches are considered hereafter.

Firstly, due to their large output dimensionality, principal component PCE (see Section 1.2.4.5) are used in order to surrogate mechanical variables of interest, namely strains and prestressing losses:

$$\bar{\boldsymbol{Y}} = \mathcal{M}(\boldsymbol{X}) \approx \hat{\mathcal{M}}(\boldsymbol{X}) = \boldsymbol{\mu}_{\bar{\boldsymbol{Y}}} + \sum_{k=1}^{r} \hat{Z}_k(\boldsymbol{X}) \boldsymbol{w}_k \tag{4.7}$$

where $\boldsymbol{\mu}_{\bar{\boldsymbol{Y}}} = \mathbb{E}[\bar{\boldsymbol{Y}}]$ is the output mean, $(\boldsymbol{w}_k)_{1 \leq k \leq r}$ the r first eigenvectors of the output covariance matrix $\boldsymbol{\Sigma}_{\bar{\boldsymbol{Y}}}$, and where $\hat{Z}_k$ is a PCE surrogate given by:

$$\hat{Z}_k(\boldsymbol{X}) = \sum_{\boldsymbol{\alpha} \in \mathcal{A}^{(k)}} \hat{c}_{k,\boldsymbol{\alpha}} \psi_{\boldsymbol{\alpha}}(\boldsymbol{X}) \tag{4.8}$$

Here, $(\psi_{\boldsymbol{\alpha}})_{\boldsymbol{\alpha} \in \mathcal{A}^{(k)}}$ is a family of multivariate polynomials that are chosen to be orthonormal with respect to the input distribution of $\boldsymbol{X}$. This family is indexed with a truncation set $\mathcal{A}^{(k)} \subset \mathbb{N}^d$ which has to be specified. Moreover, $(\hat{c}_{k,\boldsymbol{\alpha}})_{\boldsymbol{\alpha} \in \mathcal{A}^{(k)}}$ denote PCE coefficients, to be computed from point-wise evaluations of the THML model. Furthermore, the number r of principal components in Eq. (4.7) is chosen such that the PCA error (see Section 1.2.4.5) is smaller than 10^{-3}.

Secondly, concerning leakage output quantities (*i.e.* diffuse, local and global leakage rates), component-wise PCE surrogates are considered, due to the low output dimensionality. Indeed, such quantities are computed at only seven instants, namely the dates of the simulated pressurization tests. In this context, multivariate polynomials of the PCE basis are also chosen to be orthonormal with respect to the input distribution defined in Section 4.3.1.

The general settings related to the aforementioned surrogates are summarized hereafter. Firstly, an experimental design $\mathcal{X} = \{\boldsymbol{x}^{(k)}\}_{1 \leq k \leq N} \subset \mathcal{D}_{\boldsymbol{X}}$ of size $N = 1000$ is constructed through Latin Hypercube Sampling (LHS) (McKay et al., 1979). The corresponding THML model outputs are subsequently computed, in order to build a training data set to construct (PC-)PCE surrogate models through regression. The cost of a single model run is about 30 seconds for the thermo-hydric calculations, 8 minutes for mechanical calculations, and 2 minutes for diffuse leakage calculations. As a result, a total cost of about 175 hours is required to compute the 1000 THML model outputs. Using parallel computing on 8 workers, the effective required computational time is about 22 hours.

Then, for each PCE, the following truncation sets are used:

$$\mathcal{A}_p = \left\{ \boldsymbol{\alpha} \in \mathbb{N}^d \mid \|\boldsymbol{\alpha}\|_1 \leq p \right\} \tag{4.9}$$

where p is the maximal PCE degree. PCE coefficients are computed by using the LARS-based procedure of (Blatman and Sudret, 2011b) implemented in UQLab (Marelli and Sudret, 2014). In this context, the maximal PCE degree p is adaptively chosen between 1 and 6. Furthermore, in the case of PC-PCE, the output mean $\boldsymbol{\mu}_{\bar{\boldsymbol{Y}}}$ and covariance matrix $\boldsymbol{\Sigma}_{\bar{\boldsymbol{Y}}}$ are estimated from samples of the experimental design, as proposed in (Blatman and Sudret, 2011a, 2014):

$$\boldsymbol{\mu}_{\bar{\boldsymbol{Y}}} \approx \hat{\boldsymbol{\mu}}_{\bar{\boldsymbol{Y}}} = \frac{1}{N} \sum_{k=1}^{N} \bar{\boldsymbol{y}}^{(k)} \tag{4.10}$$

$$\boldsymbol{\Sigma}_{\bar{\boldsymbol{Y}}} \approx \hat{\boldsymbol{\Sigma}}_{\bar{\boldsymbol{Y}}} = \frac{1}{N-1} \sum_{k=1}^{N} (\bar{\boldsymbol{y}}^{(k)} - \hat{\boldsymbol{\mu}}_{\bar{\boldsymbol{Y}}})(\bar{\boldsymbol{y}}^{(k)} - \hat{\boldsymbol{\mu}}_{\bar{\boldsymbol{Y}}})^{\intercal} \tag{4.11}$$

where $\bar{\boldsymbol{y}}^{(k)} = \mathcal{M}(\boldsymbol{x}^{(k)})$, for all $k \in \{1, \ldots, N\}$.

Lastly, the normalized error measures presented in Section 1.2.4.5 are used so as to assess the accuracy of the constructed (PC-)PCE surrogates. In the case of component-wise PCE surrogates, the LOO error (see Eq. (1.49)) of each PCE is computed. Furthermore, in the case of PC-PCE surrogates, one recalls that the adopted error estimate is given by:

$$\epsilon_{\text{PC}-\text{PCE}} = \left(\sqrt{\epsilon_{\text{PCA}}} + \sqrt{\epsilon_{\text{PCE}}}\right)^2 \tag{4.12}$$

where ϵ_{PCA} is the PCA error defined in Eq. (1.56), and ϵ_{PCE} is the PCE error defined in Eq. (1.61).

4.3.2.2 Mechanical response

The accuracy of the constructed PC-PCE surrogates of mechanical output variables of interest (*i.e.* strains and prestressing losses) is assessed and discussed hereafter. Regarding strains, one will focus on the time evolution of four quantities, namely tangential and vertical strains at sensors locations near intrados and extrados surfaces (see Fig. 4.5b), in order to provide output quantities that are comparable to strain monitoring data (see Fig. 4.8).

Firstly, for illustrative purposes, intrados tangential strains obtained from the $N = 1000$ model runs on the devised experimental design are displayed in strain space and principal component space, in Fig. 4.19. The computed strains are highly correlated in time, especially between integrity tests, as emphasized in Fig. 4.19a. The modifications of thermo-hydric ambient conditions during these tests (see Section 4.2.2.1) tends to break the time auto-correlation of strain series, due to the creation of strain jumps. Moreover, as underlined by Fig. 4.19b, the variability of PCA coefficients $(Z_k)_{1\leq k\leq n}$ rapidly decreases with the number of principal components. This may be explained by the high auto-correlation of delayed strains, which implies that only few principal components are sufficient to accurately represent full strain time series.

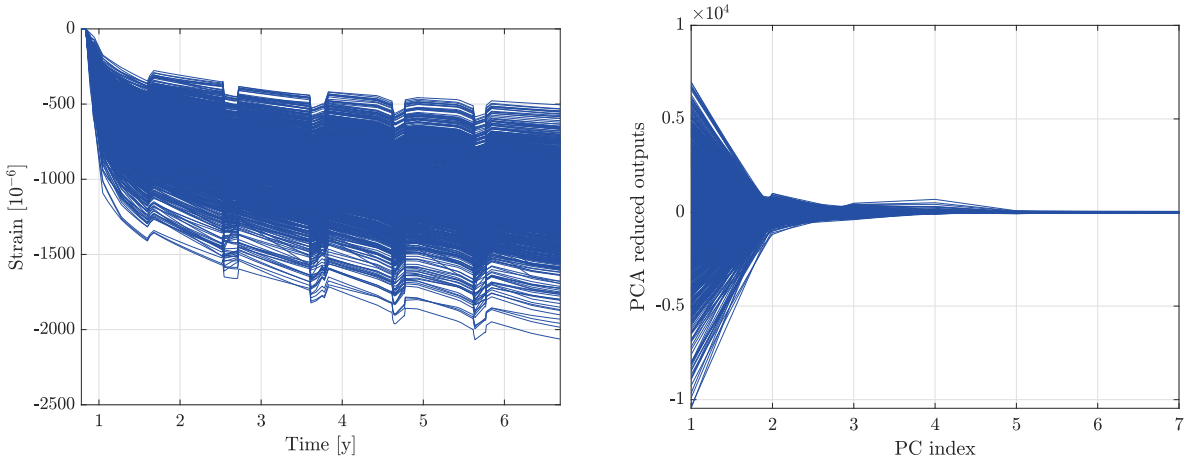

(a) Model outputs in physical space

(b) PCA reduced outputs

Figure 4.19: Intrados tangential strains computed on the constructed experimental design, in physical and principal components spaces

Then, error measures and a cross-plot associated to the PC-PCE surrogate model of intrados tangential strains are given in Fig. 4.20. Results concerning other strain types are sensibly similar, and are thereby not shown, for the sake of brevity. Firstly, the PCA error ϵ_{PCA} decreases exponentially when the number of retained principal components increases. In particular, a PCA error less than 10^{-3}, which corresponds to an fraction of explained total variance of 99.9%, is obtained with only 3 principal components. As previously mentioned, this may be explained by the fact that delayed strains are highly correlated in time. Furthermore, the PCE error ϵ_{PCE} remains practically constant around a value of about $2.4 \cdot 10^{-3}$ when the number of principal components increases. Hence, the PCE surrogates provide a satisfactory approximation of PCA coefficients $(Z_k)_{1\leq k\leq r}$, however, an experimental design with higher size seems to be required to refine this approximation.

Then, the PC-PCE error estimate $\epsilon_{\text{PC}-\text{PCE}}$ decreases when the number of principal components increases, while being constrained by the contribution of PCE error when the number of retained principal components is high. A PC-PCE error of about $4.8 \cdot 10^{-3}$ is obtained with $r = 3$ principal components. Such a value may be considered as satisfactory, compared to the error threshold of $5 \cdot 10^{-2}$ usually considered in engineering applications (Nagel et al., 2020; Wagner et al., 2020). The accuracy of the constructed surrogate model may be qualitatively emphasized in Fig. 4.20, in which a comparison between model and PCE-based predictions of the PCA coefficients $(Z_k)_{1 \leq k \leq r}$ is presented.

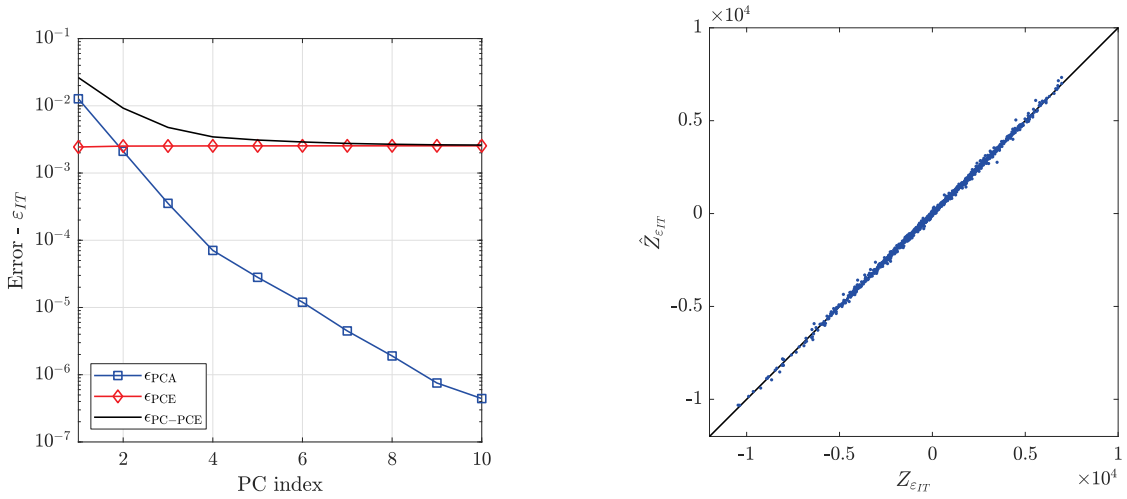

(a) PC-PCE error measures **(b)** PCE cross-plot

Figure 4.20: PC-PCE surrogate model validation - Intrados tangential strains.

Likewise, a similar analysis of the accuracy of the PC-PCE surrogate of prestressing losses is provided in Fig. 4.21. Regarding PC-PCE error measures, the constructed surrogate of prestressing losses presents an analogous behavior to that of the PC-PCE surrogate for strains. This was expected due to fact that prestressing losses are also highly correlated in time (see Section 4.2.4.3), which implies a rapid decrease of the PCA error. As a result, only $r = 2$ principal components are sufficient so as to provide a PCA error smaller than 10^{-3}. The corresponding PC-PCE error is about $4 \cdot 10^{-3}$, which constitutes a satisfactory error value. Again, this is corroborated by the cross-plot of the underlying PCE, shown in Fig. 4.21b.

4.3.2.3 Leakage response

Next, the accuracy of the constructed PCE surrogate of the diffuse leakage response is analyzed and discussed. The associated LOO error estimates computed for each pressurization test, and a cross-plot comparing full model and PCE predictions are given in Fig. 4.22. Firstly, a maximal LOO error of about $2 \cdot 10^{-2}$ is reached at the pre-operational test (VPO test). Then, the LOO error decreases over time, until reaching a value of about $4 \cdot 10^{-4}$ at the fifth pressurization test (VD5 test).

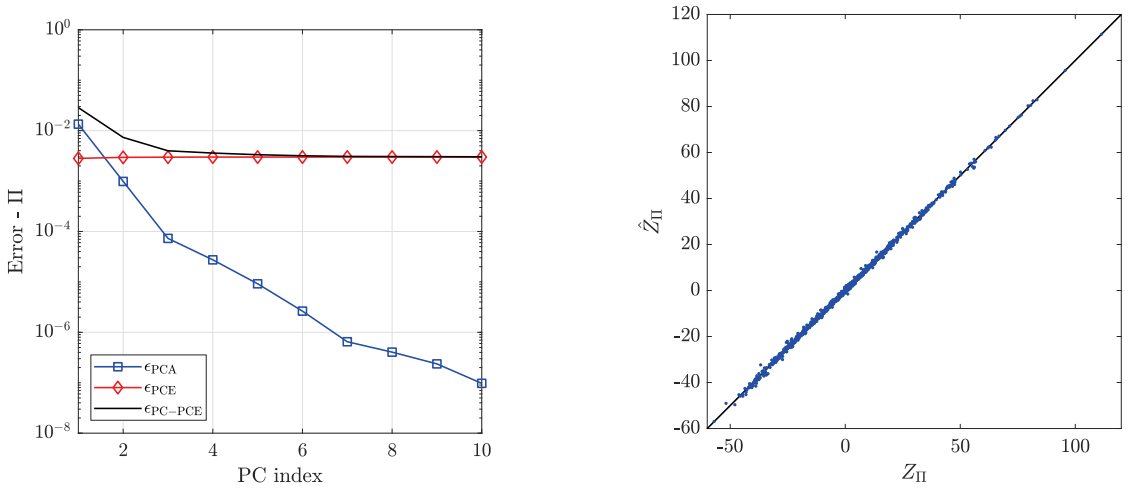

(a) PC-PCE error measures **(b)** PCE cross-plot

Figure 4.21: PC-PCE surrogate model validation - Prestressing losses.

Such a decrease could be explained by the fact that diffuse leakage is essentially affected by the water saturation state of concrete, combined with the fact that the drying process stabilizes over time. This may tend to decrease the level of non-linearity of the function to approximate. Thus, the constructed PCE of the diffuse leakage response may be deemed sufficiently accurate, especially during later pressurization tests. This is emphasized by the cross-plot given in Fig. 4.22b, suggesting a smaller discrepancy between model and surrogate predictions for high leakage rate values.

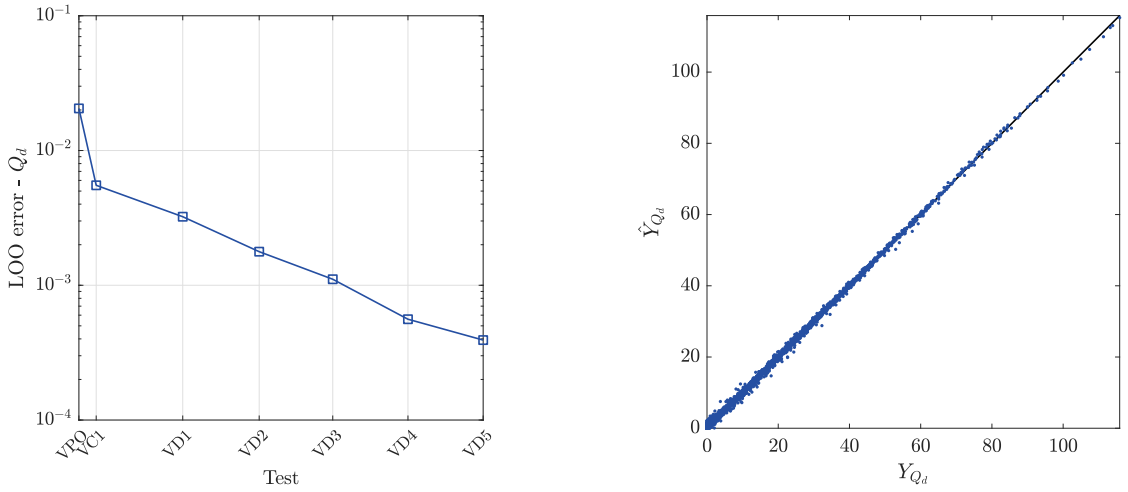

(a) LOO error at each test **(b)** PCE cross-plot

Figure 4.22: PCE surrogate model validation - Diffuse leakage.

4.3.3 Sensitivity analysis

4.3.3.1 General settings

In this section, a global variance-based sensitivity analysis is performed, based on the (PC-)PCE surrogate models constructed in Section 4.3.2. In this context, Sobol' sensitivity indices (see Section 1.2.5) of output quantities of the THML model are aimed to be computed. In the case of (PC-)PCE surrogates, these indices may be post-processed analytically from (PC-)PCE coefficients, as described in Section 1.2.5.2 for PCE surrogates and in Appendix A for PC-PCE surrogates.

Besides, it is worth noting that some output variables of interest are not directly approximated by (PC-)PCE surrogates, which does not enable analytical post-processing of Sobol' indices. Indeed, the local leakage rate Q_l is given by an anaytical function of prestressing losses Π (see Section 3.3.5.2), whereas the global leakage rate Q_g is given by the sum of diffuse and local leakage rates Q_d and Q_l. As a result, the computation of Sobol' indices related to these quantities is subjected to a particular treatment. In this perspective, the aforementioned Sobol' indices are estimated through Monte Carlo simulation, by considering a sample size of 10^6, and by using the UQLab implementation (Marelli and Sudret, 2014) of the Janon-Monod estimators for Sobol' indices (Janon et al., 2014).

In what follows, the analysis of Sobol' sensitivity indices is restricted to total indices, for the sake of brevity (see Section 1.2.5.1). Mechanical output variables of interest are studied in Section 4.3.3.2, whereas leakage rates are studied in Section 4.3.3.3.

4.3.3.2 Mechanical response

Firstly, the time evolution of total Sobol' indices of intrados tangential and vertical strains is given in Fig. 4.23. Results concerning extrados strains are sensibly similar, and are therefore not shown for the sake of brevity. As shown in Fig. 4.23a, the tangential strain response is mainly driven by the initial prestressing of tangential cables $\sigma_{\theta,0}$ during the prestressing phase, starting near $t \approx 1$ year.

Then, from the start of the heating system, the importance of the parameter $\sigma_{\theta,0}$ decreases over time, whereas the importance of the desiccation shrinkage coefficient α_{ds} increases. Note that the importance of the parameter $\sigma_{\theta,0}$ remains significantly high at the end of the simulated lifetime of the structure, though. This is due to the delayed mechanical behavior of the structure, which keeps the applied loading in memory, to a certain extent. The importance of the parameter B driving drying kinetics increases until $t \approx 2$ years, and subsequently slowly decreases as the aging of the structure progresses. This may be attributed to a stabilization of drying over time, which is likely to involve less variability of the strain response with respect to drying parameters.

Furthermore, the importance of the basic creep consolidation parameter κ is negligible until $t \approx 2.5$ years, and then progressively increases over time, while remaining low compared to that of the others input parameters, though. Such an increase is consistent with the fact that the parameter κ concerns very long-term basic creep strains. Moreover, it is also noted that the sum of total Sobol' indices is close to one, which suggests that the variability of the tangential strain response is principally driven by main effects, and that interactions may be deemed negligible.

Finally, the influence of the initial vertical prestressing $\sigma_{z,0}$ is negligible, which corroborates the fact that vertical prestressing creates practically zero tangential strains.

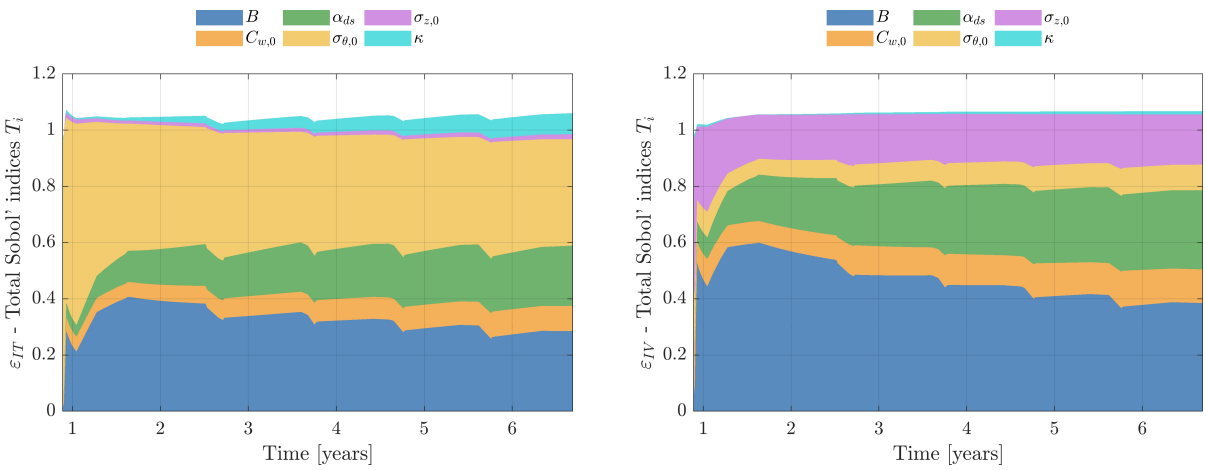

(a) Intrados tangential strains

(b) Intrados vertical strains

Figure 4.23: Time evolution of total Sobol' indices - Intrados strains.

Then, concerning vertical strains, the behavior of total Sobol' indices related to parameters $B, C_{w,0}, \alpha_{ds}$ is comparable to that related to tangential strains, to some extent. The importance of the parameter $\sigma_{z,0}$ is maximal during the prestressing phase, and subsequently decreases over time until $t \approx 2$ years, instant from which the associated total Sobol' indices remains practically constant. It is worth noting that contrary to tangential strains which are dominated by the initial prestressing $\sigma_{\theta,0}$ during the prestressing phase, the vertical strain response is not dominated by the initial vertical prestressing $\sigma_{z,0}$. Furthermore, the drying parameter B is the more important parameter throughout the lifetime of the structure. It is also interesting to note that the initial tangential prestressing $\sigma_{\theta,0}$ has a non-negligible influence on the vertical strain response, which may be explained by geometrical effects at the scale of the standard zone RSV, as well as a Poisson effect linking tangential and vertical strains.

Next, the time evolution of total Sobol' indices of the prestressing losses response are presented in Fig. 4.24. During the first years of the operating phase of the structure, the prestressing losses response is mainly driven by the drying parameter B. Then, the importance of the latter decreases over time, which underlines a plausible stabilization of drying, as mentioned earlier. The importance of the remaining input parameters progressively increases over time. Moreover, it is worth noting that the sum of total Sobol' indices exceeds one from $t \approx 2$ years and increases over time, which suggests the development of interactions having a non-negligible effect on the variability of the prestressing losses response.

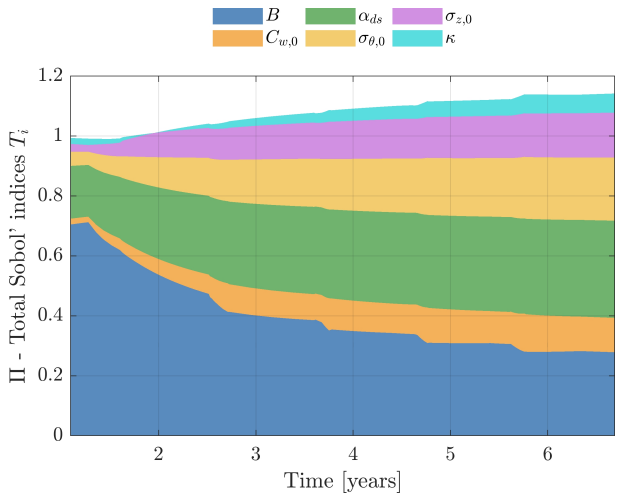

Figure 4.24: Time evolution of total Sobol' indices - Prestressing losses.

4.3.3.3 Leakage response

Next, the time evolution of total Sobol' indices of diffuse and local leakage rates is presented in Fig. 4.25. Firstly, the drying parameter B and the intrinsic permeability k_0 constitute the most important parameters of the diffuse leakage response, as observed in Fig. 4.3.3.3a. Conversely, the influence of the initial water content $C_{w,0}$ and the Klinkenberg coefficient β_K may be deemed to be negligible. The stabilization of drying over time involves a progressive decrease of the importance of B, while the importance of k_0 increases.

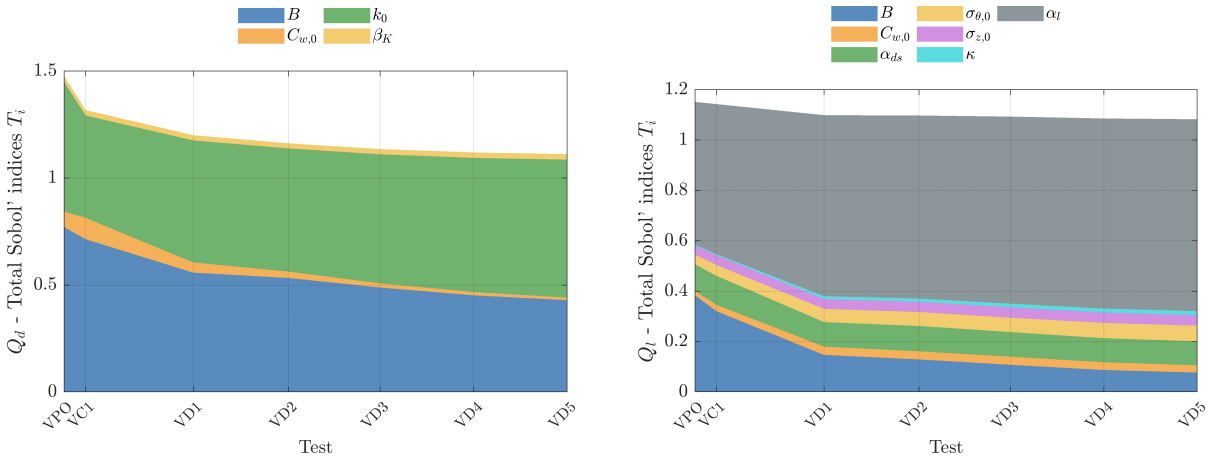

(a) Diffuse leakage **(b)** Local leakage

Figure 4.25: Time evolution of total Sobol' indices - Diffuse and local leakage.

Moreover, the contribution of interactions to the variance of the diffuse leakage response is non-negligible, especially during the first pressurization tests of the VeRCoRs mock-up. Then, as underlined in Fig. 4.25b, the local leakage response is mainly driven by the local leak model parameter α_l. The importance of this parameter slightly increases over time, whereas the importance of the drying parameter B decreases. Furthermore, the remaining input parameters present a relatively low influence.

Lastly, the time evolution of total Sobol' indices of the global leakage response is presented in Fig. 4.26. Three parameters are significantly contributing to the variance of the global leakage rate of the structure, namely the drying parameter B, the relative permeability k_0 and the local leak model parameter α_l. In particular, this emphasizes the crucial influence of the drying parameter B, which significantly contributes to the variance of all the presented output variables of interest of the THML model.

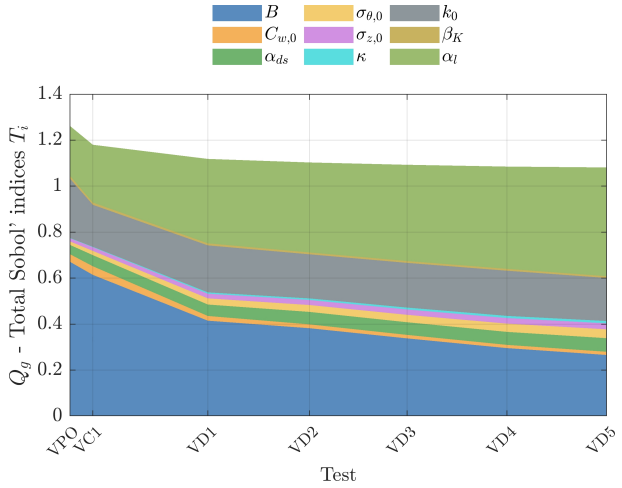

Figure 4.26: Time evolution of total Sobol' indices - Global leakage.

4.4 Bayesian inference for inverse uncertainty quantification

As previously mentioned, the input probability distribution defined in Section 4.3.1 aims at summarizing the level of knowledge about uncertain input parameters of the THML computational model, principally based on expert judgement. As a result, it does not integrate information related to the response of the VeRCoRs mock-up (*e.g.* strains, leakage rate). Nevertheless, *in-situ* monitoring devices provide information on the long-term behavior of the structure, through measurement data related to its mechanical state or leak tightness.

In this section, we propose to use the framework of Bayesian inference in order to provide a more comprehensive quantification of uncertainties in input parameters, by assimilating *in-situ* monitoring data related to the response of the structure so as to update knowledge about parameters in a Bayesian inverse problem setting. In this perspective, this section is organized in two subsequent parts: in Section 4.4.1, we focus on mechanical monitoring presented in Section 4.2.2.2, that are used to extract information about input parameters related to the strain response of the structure. To that end, several statistical models are introduced so as to describe the relationship between model outputs and data, including one model accounting for model biases. Then, in Section 4.4.2, we propose a more global approach enabling to assimilate both mechanical and leakage observational data, in order to update parameters of the whole THML computational chain.

4.4.1 Bayesian inference for the THM behavior

4.4.1.1 Bayesian model setup

Let $\boldsymbol{X} : \Omega \to \mathcal{D}_{\boldsymbol{X}}$ be the random input parameters of the THML model. The prior of these parameters is assumed to be the distribution defined in Section 4.3.1. In order to be consistent with strain measurement series presented in Section 4.2.2.2, we focus on the time evolution of four types of delayed strains, namely:

- intrados and extrados tangential strains, respectively denoted by $\boldsymbol{\varepsilon}_1$ and $\boldsymbol{\varepsilon}_2$,
- intrados and extrados vertical strains, respectively denoted by $\boldsymbol{\varepsilon}_3$ and $\boldsymbol{\varepsilon}_4$.

Then, each of these strains may be seen as a deterministic function $\mathcal{M}_{\boldsymbol{\varepsilon}_k} : \mathcal{D}_{\boldsymbol{X}} \to \mathcal{D}_{\boldsymbol{Y}} \subset \mathbb{R}^n$ of the inputs $\boldsymbol{X}$, where $k \in \{1, \dots, m\}$ (and $m = 4$). Here, n is the number of instants of the time grid adopted for assimilating strain data. In an inverse problem perspective, the m defined functions $(\mathcal{M}_{\boldsymbol{\varepsilon}_k})_{1 \leq k \leq m}$ may be seen as forward models that share the same input parameters. Note that here, only 6 parameters in $\boldsymbol{X}$ (related to the mechanical response of the model, see Section 4.3.1) are involved in the Bayesian inverse problem described herebelow, but the notation $\boldsymbol{X}$ is reused to describe these parameters, for the sake of concision.

Furthermore, the measurement data considered in this section are given by the mean strain measurement series presented in Section 4.2.2.2, on a period starting from the end of the prestressing phase (see Table 4.1) to approximately six years of lifetime. Measurements before the end of prestressing are not considered here, since we focus on the long-term behavior of the structure. Then, projecting these measurements onto the time grid used for mechanical calculations yields a strain data set denoted by $\mathcal{Y}_{\boldsymbol{\varepsilon}} = \{\boldsymbol{y}_{\boldsymbol{\varepsilon}_k}\}_{1 \leq k \leq m} \subset \mathcal{D}_{\boldsymbol{Y}}$.

Next, based on elements taken from the theory of Bayesian inverse problems presented in Section 1.3.3, a statistical model linking model outputs to observed data has to be devised. In this context, we consider an additive Gaussian noise model (see Section 1.3.2.1) so as to model the discrepancy between predicted strains and observed strains. Two variants of this model will be considered, namely one assuming an unbiased forward model (Case (a)), and one accounting for the presence of modeling biases (Case (b)). Formally speaking, the assumption of an additive Gaussian noise model for observables $\boldsymbol{Y}_{\boldsymbol{\varepsilon}_k} : \Omega \to \mathcal{D}_{\boldsymbol{Y}}$ associated to strains $\boldsymbol{\varepsilon}_k$ may be written by:

$$\boldsymbol{Y}_{\boldsymbol{\varepsilon}_k} | \boldsymbol{x} = \mathcal{M}_{\boldsymbol{\varepsilon}_k}(\boldsymbol{x}) + \boldsymbol{E}_k \tag{4.13}$$

where $k \in \{1, \dots, m\}$, and $\boldsymbol{E}_k$ is a centered Gaussian random variable with covariance matrix $\boldsymbol{\Sigma}_{\boldsymbol{E}_k} \in \mathbb{R}^{n \times n}$, *i.e.* $\boldsymbol{E}_k \sim \mathcal{N}(\boldsymbol{0}, \boldsymbol{\Sigma}_{\boldsymbol{E}_k})$. The random variable $\boldsymbol{E}_k$ is also assumed to be independent from the input parameters $\boldsymbol{X}$. Furthermore, for all $k \in \{1, \dots, m\}$, the noise $\boldsymbol{E}_k$ is assumed to be homoscedastic, *i.e.* $\boldsymbol{\Sigma}_{\boldsymbol{E}_k} = \sigma^2 \mathbf{I}$, where σ^2 is the observation noise variance. Note that here, the same variance is considered for each strain type for the sake of simplicity, but more sophisticated parametrized forms of noise covariance matrices are possible.

Case (a): unknown noise variance, unbiased forward model

The noise variance σ^2 involved in the statistical model in Eq. (4.13) may be assumed to be perfectly known, and thereby fixed to a constant value, as in (Berveiller et al., 2012; Perrin, 2008). Besides, such a variance mainly corresponds to two contributions, namely measurement errors that can be properly estimated at the scale of strain sensors, but also model uncertainties that remain most often unknown. Consequently, the noise variance σ^2 is often not perfectly known. Consequently, the noise variance σ^2 is itself modeled by a random variable, which is endowed with a weakly informative prior distribution. In what follows, it is assumed that the prior distribution of σ^2 is given by the uniform distribution $\mathcal{U}([0, \sigma^2_{\max}])$, where $\sigma_{\max} = 100 \cdot 10^{-6}$. The prior density of σ^2 is then given by $\pi(\sigma^2) = \mathbf{1}_{[0,\sigma^2_{\max}]}(\sigma^2)$. The statistical model used in case (a) is then written by, for each $k \in \{1, \ldots, m\}$:

$$\boldsymbol{Y}_{\boldsymbol{\varepsilon}_k} | \boldsymbol{x}, \sigma^2 = \mathcal{M}_{\boldsymbol{\varepsilon}_k}(\boldsymbol{x}) + \boldsymbol{E}_k | \sigma^2 \tag{4.14}$$

where $\boldsymbol{E}_k | \sigma^2 \sim \mathcal{N}(\mathbf{0}, \sigma^2 \mathbf{I})$.

As a result, for each $k \in \{1, \ldots, m\}$, the likelihood function $\mathcal{L}_a^{(k)}$ associated to the statistical model of $\boldsymbol{Y}_{\boldsymbol{\varepsilon}_k}$ in Eq. (4.14) is given by:

$$\begin{aligned} \mathcal{L}_a^{(k)}(\boldsymbol{x}, \sigma^2) &= \varphi_n(\mathcal{M}(\boldsymbol{x}); \boldsymbol{y}_{\boldsymbol{\varepsilon}_k}, \sigma^2 \mathbf{I}) \\ &= (2\pi\sigma^2)^{-\frac{n}{2}} \exp\left(-\frac{1}{2\sigma^2} \| \mathcal{M}_{\boldsymbol{\varepsilon}_k}(\boldsymbol{x}) - \boldsymbol{y}_{\boldsymbol{\varepsilon}_k} \|^2 \right) \end{aligned} \tag{4.15}$$

where $\|\cdot\|$ denotes the Euclidean norm of $\mathbb{R}^n$.

Furthermore, assuming that the noise terms $(\boldsymbol{E}_k)_{1 \leq k \leq m}$ are mutually independent (conditionally on σ^2), the likelihood function $\mathcal{L}_a$ associated to the full data set $\mathcal{Y}_{\boldsymbol{\varepsilon}}$ reads:

$$\mathcal{L}_a(\boldsymbol{x}, \sigma^2) = \prod_{k=1}^{m} \mathcal{L}_a^{(k)}(\boldsymbol{x}, \sigma^2) \tag{4.16}$$

On another note, the joint prior density $\pi_a(\boldsymbol{x}, \sigma^2)$ of input model parameters $\boldsymbol{X}$ and noise variance σ^2 has to be specified. For the sake of simplicity, it is assumed that the aforementioned parameters are mutually independent, which enables to write:

$$\pi_a(\boldsymbol{x}, \sigma^2) = \pi(\boldsymbol{x}) \pi(\sigma^2) \tag{4.17}$$

Thus, applying Bayes' theorem (see Section 1.3.2.3) enables to derived the following expression for the posterior density of case (a):

$$\pi_a(\boldsymbol{x}, \sigma^2 | \mathcal{Y}_{\boldsymbol{\varepsilon}}) \propto \pi_a(\boldsymbol{x}, \sigma^2) \mathcal{L}_a(\boldsymbol{x}, \sigma^2) \tag{4.18}$$

Case (b): unknown noise variance, biased forward model

Next, a similar construction is then presented for case (b), involving the presence of modeling biases. In this context, as an extension of the model of case (a), we propose the following statistical model for observables $(\boldsymbol{Y}_{\varepsilon_k})_{1\leq k\leq m}$:

$$\boldsymbol{Y}_{\varepsilon_k}|\boldsymbol{x},\sigma^2,\beta_k = \mathcal{M}_{\varepsilon_k}(\boldsymbol{x}) + \boldsymbol{E}_k|\sigma^2 + \boldsymbol{\delta}(\beta_k) \tag{4.19}$$

where $\boldsymbol{E}_k|\sigma^2 \sim \mathcal{N}(\boldsymbol{0},\sigma^2\mathbf{I})$, $\boldsymbol{\delta}(\beta_k)\in\mathbb{R}^n$ is a bias term, and β_k is the realization of a random variable $B_k:\Omega\to\mathbb{R}$, for all $k\in\{1,\dots,m\}$. The bias term $\boldsymbol{\delta}(\beta_k)$ is precised hereafter. Let $\boldsymbol{t}=(t_1,\dots,t_n)\in\mathbb{R}^n$ be the time grid shared by predicted and observed strains. One defines the bias term $\boldsymbol{\delta}(\beta_k)$ as follows:

$$\boldsymbol{\delta}(\beta_k) = \beta_k(f(t_1),\dots,f(t_n)) \tag{4.20}$$

where f is the function defined by:

$$f(\tau) = \min\left(\frac{\tau - t_{p,0}}{t_{p,1}-t_{p,0}};1\right) \tag{4.21}$$

for $\tau\geq t_{p,0}$, and $f(\tau)=0$ for $\tau\leq t_{p,0}$, where $t_{p,0}$, $t_{p,1}$ respectively denote the instants of start and end of the prestressing phase.

Such a definition is motivated by the following: the adopted computational model does not make the distinction between intrados and extrados strains, in the vertical direction (see Section 4.2.4.3). This is due to the fact that vertical displacements on the top surface of the standard zone RSV are constrained to be uniform (see Section 4.2.3.3). However, measured intrados and extrados vertical strains present a significant offset (see Fig. 4.8), which seems to be constant from the end of the prestressing phase. Furthermore, such an offset is practically equal to zero before the beginning of the prestressing phase.

Then, for each $k\in\{1,\dots,m\}$, the likelihood function $\mathcal{L}_b^{(k)}$ corresponding to the model in Eq. (4.19) is given by:

$$\begin{aligned}\mathcal{L}_b^{(k)}(\boldsymbol{x},\sigma^2,\beta_k) &= \varphi_n(\mathcal{M}_{\varepsilon_k}(\boldsymbol{x})+\boldsymbol{\delta}(\beta_k);\boldsymbol{y}_{\varepsilon_k},\sigma^2\mathbf{I})\\ &= (2\pi\sigma^2)^{-\frac{n}{2}}\exp\left(-\frac{1}{2\sigma^2}\|\mathcal{M}_{\varepsilon_k}(\boldsymbol{x})+\boldsymbol{\delta}(\beta_k)-\boldsymbol{y}_{\varepsilon_k}\|^2\right)\end{aligned} \tag{4.22}$$

Moreover, in a purely analogous way to case (a), assuming that random noise terms $(\boldsymbol{\mathcal{E}}_k)_{1\leq k\leq m}$ are mutually independent, the likelihood function $\mathcal{L}_b$ corresponding to the full data set $\mathcal{Y}_\varepsilon$ is given by:

$$\mathcal{L}_b(\boldsymbol{x},\sigma^2,\boldsymbol{\beta}) = \prod_{k=1}^{m}\mathcal{L}_b^{(k)}(\boldsymbol{x},\sigma^2,\beta_k) \tag{4.23}$$

where $\boldsymbol{\beta}=(\beta_1,\dots,\beta_m)$.

It is now necessary to define a prior density $\pi(\boldsymbol{\beta})$ for the bias parameters $\boldsymbol{B}=(B_1,\dots,B_m)$. For each $k\in\{1,\dots,m\}$, the prior of B_k is assumed to be a Laplace distribution with zero mean and standard deviation $\sigma_{B_k}=25\cdot10^{-6}$, which leads to the following prior density:

$$\pi(\beta_k) = \frac{1}{\sqrt{2}\sigma_{B_k}}\exp\left(-\sqrt{2}\frac{|\beta_k|}{\sigma_{B_k}}\right) \tag{4.24}$$

Such a choice is motivated by the fact that the density specified above presents a spikier peak around 0, as well as fatter tails than classical Gaussian distributions. This enables to favor small values of biases, while allowing the prior mass to move towards higher values if the latter appear to be plausible. Thus, to a certain extent, such a prior choice favors sparsity in the random vector $\boldsymbol{B}$ (Tibshirani, 1996), as well as robustness with respect to the prior (Nagel et al., 2020).

Then, assuming that the bias parameters $(B_1, \ldots, B_m)$ are supposed to be mutually independent, and that they are independent from model parameters $\boldsymbol{X}$ and noise variance σ^2, the joint prior density $\pi_b(\boldsymbol{x}, \sigma^2, \boldsymbol{\beta})$ is simply given by $\pi_b(\boldsymbol{x}, \sigma^2, \boldsymbol{\beta}) = \pi(\boldsymbol{x})\pi(\sigma^2)\pi(\boldsymbol{\beta})$. Finally, applying Bayes' theorem yields the following posterior density for case (b):

$$\pi_b(\boldsymbol{x}, \sigma^2, \boldsymbol{\beta}|\mathcal{Y}_\varepsilon) \propto \pi_b(\boldsymbol{x}, \sigma^2, \boldsymbol{\beta})\mathcal{L}_b(\boldsymbol{x}, \sigma^2, \boldsymbol{\beta}) \tag{4.25}$$

4.4.1.2 Bayesian computations

Bayesian computations are performed in the BuS framework introduced in Chapter 2. The SuS algorithm (see Section 2.2.2) is used so as to draw samples from the posterior distribution derived in Section 4.4.1.1, in both cases (a) and (b). In this perspective, $N = 10^4$ samples per level are considered, whereas the rarity parameter is set to $p_0 = 0.1$. Furthermore, for both cases (a) and (b), 24 replications are produced by running the SuS algorithm multiple times. Moreover, the PC-PCE surrogates constructed in Section 4.3.2 are used for accelerating the SuS algorithm. Computational costs associated to Bayesian computations are summarized in Table 4.7. The total computational cost of SuS runs in case (b) is about twice that of the total cost in case (a) (namely 12.2 hours vs. 6.2 hours). This may be attributable to the larger dimension of the Bayesian inverse problem of case (b), which implies to solve an equivalent reliability problem with a smaller failure probability to estimate. Besides, SuS runs were parallelized with 8 workers in order to reduce the associated computational time, which led to an effective time of about 45 minutes in case (a) and 90 minutes in case (b).

Case	Cost of a single SuS run		Total computational cost [h]
	Mean [s]	CoV [%]	
(a)	924.7	5.4	6.2
(b)	1825.5	11.7	12.2

Table 4.7: Computational cost of Bayesian computations: cost of a single SuS run and total cost associated to the 24 produced replications.

4.4.1.3 Posterior input parameters

Posterior samples drawn with the SuS algorithm are analyzed hereafter. The prior distribution adopted in cases (a) and (b) is summarized in Table 4.8 for comparison purposes, whereas statistics related to posterior samples in both cases (a) and (b) are given in Tables 4.9 & 4.10. Furthermore, posterior univariate and bivariate marginals of model parameters $\boldsymbol{X} = (B, C_{w,0}, \alpha_{ds}, \sigma_{\theta,0}, \sigma_{z,0}, \kappa)$ estimated from posterior samples in case (a) are given in Fig. 4.27. Posterior samples in case (b) present a similar pairwise correlation structure, and are thereby not shown for the sake of brevity.

The results corresponding to univariate posterior marginals in case (a) are firstly discussed. The mean of the drying parameter B is slightly increased through Bayesian updating, from 0.08 to 0.084, whereas its standard deviation is significantly reduced, from 0.012 to 0.002. Then, the mean of the initial water content $C_{w,0}$ is decreased, from 160 to 142.3 $\mathrm{l.m^{-3}}$, whereas that of parameter α_{ds} is slightly increased from 10.0 to 12.8 10^{-6} $\mathrm{kg.m^{-3}}$. Then, the mean values of both parameters $\sigma_{\theta,0}$ and $\sigma_{z,0}$ are reduced through Bayesian updating. This could be explained by the fact that prior mean values are corresponding to tensions applied at cables anchors of VeRCoRs mock-up. These values are overestimating real tensions in the standard zone, since anchor decline and frictions could not be taken into account at the scale of the studied RSV. Hence, the posterior values of $\sigma_{\theta,0}$ and $\sigma_{z,0}$ are likely corresponding to mean tension values resulting from tension losses due to anchor decline and frictions.

Globally speaking, the obtained posterior standard deviation of model parameters are significantly smaller than their prior counterpart. Such a result suggests that data are sufficiently informative, regarding the uncertainties encoded by the adopted prior distribution. Moreover, in the case (b), similar results are observed, except for the fact that the obtained posterior standard deviations are higher than those obtained in case (a).

n°	Parameter	Units	Distribution	Bounds	Mean	Std	CoV
1	B	10^{-2}	Lognormal	-	8.00	1.20	0.15
2	$C_{w,0}$	$\mathrm{l.m^{-3}}$	Lognormal	-	160.00	24.00	0.15
3	α_{ds}	10^{-6} $\mathrm{kg.m^{-3}}$	Lognormal	-	10.00	2.50	0.25
4	$\sigma_{\theta,0}$	MPa	Lognormal	-	$1.51 \cdot 10^3$	378.50	0.25
5	$\sigma_{z,0}$	MPa	Lognormal	-	$1.51 \cdot 10^3$	378.50	0.25
6	κ	10^{-4}	Lognormal	-	1.00	0.25	0.25
7	σ^2	10^{-12}	Uniform	$[0; 1.00 \cdot 10^4]$	$5.00 \cdot 10^3$	$2.88 \cdot 10^3$	0.58
8	β_1	10^{-6}	Laplace	-	0	25.00	-
⋮	⋮	⋮	⋮	⋮	⋮	⋮	⋮
11	β_4	10^{-6}	Laplace	-	0	25.00	-

Table 4.8: Summary of the prior distribution of parameters $(\boldsymbol{X}, \sigma^2, \boldsymbol{B})$, adopted in cases (a) and (b).

n°	Parameter	Units	Mean	Std	CoV	95 % CI
1	B	10^{-2}	8.36	0.19	0.02	$[7.96, 8.67]$
2	$C_{w,0}$	$\mathrm{l.m^{-3}}$	142.40	12.65	0.09	$[120.51, 170.93]$
3	α_{ds}	10^{-6} $\mathrm{kg.m^{-3}}$	12.80	0.74	0.06	$[11.32, 14.21]$
4	$\sigma_{\theta,0}$	MPa	$1.26 \cdot 10^3$	85.34	0.07	$[1.09 \cdot 10^3, 1.43 \cdot 10^3]$
5	$\sigma_{z,0}$	MPa	$1.10 \cdot 10^3$	148.40	0.13	$[822.98, 1.40 \cdot 10^3]$
6	κ	10^{-4}	0.74	0.10	0.14	$[0.55, 0.96]$
7	σ^2	10^{-12}	$2.98 \cdot 10^3$	255.83	0.09	$[2.50 \cdot 10^3, 3.49 \cdot 10^3]$

Table 4.9: Statistics related to posterior marginals of parameters $(\boldsymbol{X}, \sigma^2)$ - Case (a).

Then, the analysis of bivariate marginals enables to observe the correlation structure of the estimated posterior distribution. Significant linear correlations are observed for parameters $(B, C_{w,0})$, (α_{ds}, κ) and $(\sigma_{\theta,0}, \sigma_{z,0})$. In particular, the strong linear correlation existing for the pair $(\sigma_{\theta,0}, \sigma_{z,0})$ may be attributed to structural effects as well as the Poisson ratio, linking tangential stresses to vertical stresses during the prestressing phase.

n°	Parameter	Units	Mean	Std	CoV	95% CI
1	B	10^{-2}	8.51	0.18	0.02	$[8.17, 8.84]$
2	$C_{w,0}$	l.m^{-3}	142.82	13.89	0.10	$[117.90, 171.76]$
3	α_{ds}	10^{-6} kg.m^{-3}	12.06	0.88	0.07	$[10.28, 13.53]$
4	$\sigma_{\theta,0}$	MPa	$1.26 \cdot 10^3$	120.96	0.10	$[1.07 \cdot 10^3, 1.51 \cdot 10^3]$
5	$\sigma_{z,0}$	MPa	$1.33 \cdot 10^3$	226.45	0.17	$[977.31, 1.83 \cdot 10^3]$
6	κ	10^{-4}	0.83	0.13	0.16	$[0.56, 1.11]$
7	σ^2	10^{-12}	$1.29 \cdot 10^3$	142.25	0.11	$[1.07 \cdot 10^3, 1.60 \cdot 10^3]$
8	β_1	10^{-6}	15.21	14.23	0.94	$[12.9, 40.84]$
9	β_2	10^{-6}	-7.67	13.86	1.81	$[34.0, 19.58]$
10	β_3	10^{-6}	-1.77	23.78	13.46	$[37.3, 75.34]$
11	β_4	10^{-6}	111.44	24.89	0.22	$[73.60, 191.48]$

Table 4.10: Statistics related to posterior marginals of parameters $(\boldsymbol{X}, \sigma^2, \boldsymbol{B})$ - Case (b).

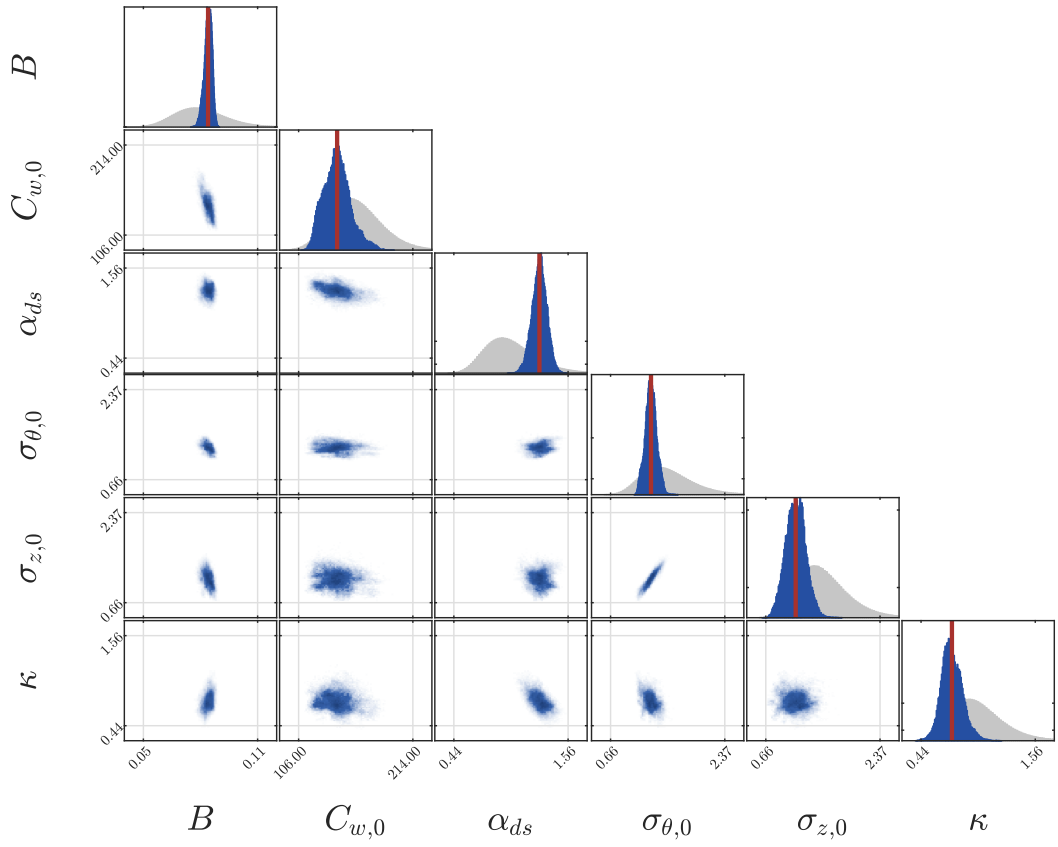

Figure 4.27: Univariate and bivariate marginals from the posterior distribution of model parameters $\boldsymbol{X}$ estimated from samples - Case (a). *Prior samples are shown in grey, whereas posterior samples are shown in blue. The posterior mean value of each parameter is shown by a vertical red line.*

Next, the prior and posterior marginal densities of noise variance σ^2 and bias parameters $\boldsymbol{\beta}$ are depicted in Fig. 4.28. For both cases (a) and (b), the posterior values of the noise variance σ^2 are concentrated in narrow zones, compared to the wide support of its prior distribution. Furthermore, its posterior mean value is higher in case (a) than in case (b). A similar behavior is observed for its standard deviation. Such a phenomenon may be explained by the fact that when the model is assumed to be unbiased, the noise variance is expected to have typically higher values in order to cover the variance of observed data.

Conversely, when modeling biases are taken into account, model predictions are expected to match better with observed data, provided that bias parameters have been well calibrated through Bayesian updating. In such a case, a smaller noise variance would be necessary to cover the observed data. This will be observed later, in Section 4.4.1.4, which presents posterior strain predictions in both cases (a) and (b).

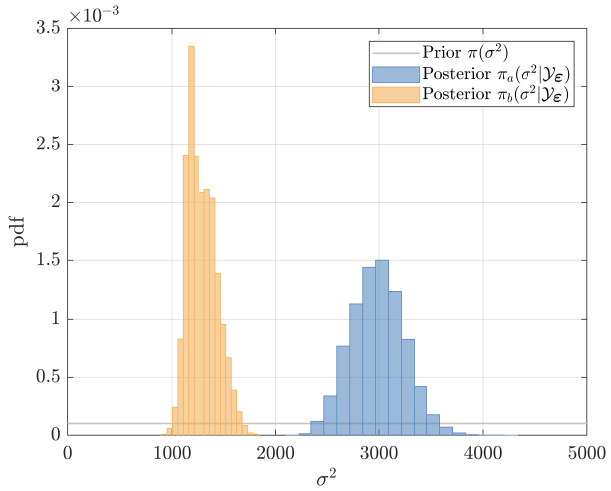

Figure 4.28: Prior density and posterior samples of noise variance σ^2.

Then, in case (b), univariate and bivariate marginals of bias parameters $\boldsymbol{\beta}$ estimated from samples are presented in Fig. 4.29. Firstly, as emphasized in Table 4.10, posterior marginals of bias parameters (B_1, B_2, B_3) seem to be relatively close to their prior counterpart. The parameter B_4, corresponding to the bias of the extrados vertical strain model response, presents a peculiar behavior. Indeed, its posterior mean value is about $100 \cdot 10^{-6}$, which suggests that the computational model presents a bias related to the vertical strain response. It is worth noting that this value of $100 \cdot 10^{-6}$ corresponds to the observed offset between mean measurement series of intrados and extrados vertical strains (see Fig. 4.8). As mentioned earlier, the adopted computational model is not able to make the distinction between intrados and extrados vertical strains, due to the defined mechanical BC at the RSV scale.

Furthermore, observation data emphasize a nearly constant offset between intrados and extrados vertical strains (see Fig. 4.8). Then, Bayesian updating based on the statistical model proposed in case (b) enables to take into account the aforementioned modeling bias, and to correct predictions from the estimated bias parameters. Lastly, it is noted that parameters (B_1, B_2) and (B_3, B_4) present strong linear correlations. Moreover, the bivariate marginals (B_1, B_2) and (B_3, B_4) seem to remain mutually independent, which may be explained by the fact that these pairs are related to different strain directions (tangential for (B_1, B_2), vertical for (B_3, B_4)).

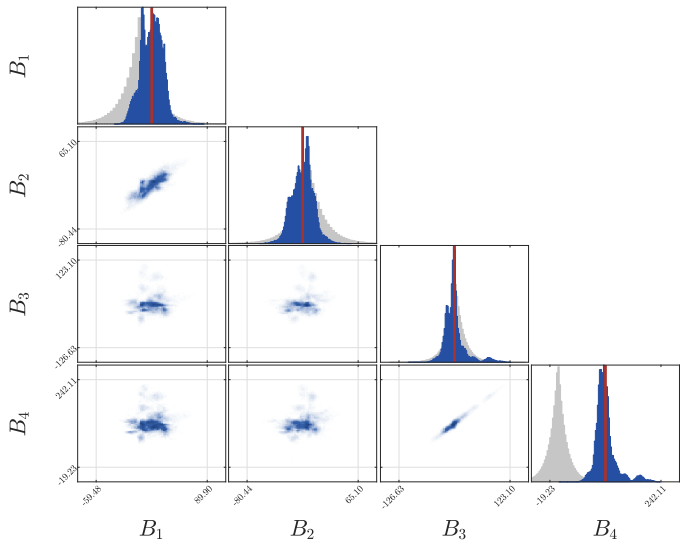

Figure 4.29: Univariate and bivariate marginals from the posterior distribution of bias parameters $\boldsymbol{B}$ estimated from samples - Case (b). *Prior samples are shown in grey, whereas posterior samples are shown in blue. The posterior mean value of each parameter is shown by a vertical red line.*

4.4.1.4 Posterior predictions

Lastly, the strain predictions corresponding to prior distributions, and posterior distributions estimated in the previous section are presented hereafter. In this context, for both cases (a) and (b), the associated prior and posterior predictive distributions (see Section 1.3.2.3) are estimated from prior and posterior samples, respectively. For instance, in case (a), the posterior predictive density (see Eq. (1.98)) of data $\boldsymbol{y} \in \mathcal{D}_{\boldsymbol{Y}}$ given observed ones $\mathcal{Y}_\varepsilon$ may be written by:

$$\pi_a(\boldsymbol{y}|\mathcal{Y}_\varepsilon) = \int_{\mathcal{D}_{\sigma^2}} \int_{\mathcal{D}_{\boldsymbol{X}}} \pi_a(\boldsymbol{y}|\boldsymbol{x},\sigma^2)\pi_a(\boldsymbol{x},\sigma^2|\mathcal{Y}_\varepsilon)\mathrm{d}\boldsymbol{x}\mathrm{d}\sigma^2 \tag{4.26}$$

where $\pi_a(\boldsymbol{y}|\boldsymbol{x},\sigma^2)$ is the likelihood function in Eq. (4.16) associated to data $\boldsymbol{y}$, $\pi_a(\boldsymbol{x},\sigma^2|\mathcal{Y}_\varepsilon)$ the posterior density derived in Eq. (4.18) and $\mathcal{D}_{\sigma^2} = [0, \sigma^2_{\max}]$ is the support of the prior of σ^2. The posterior predictive distribution may be sampled as follows: for instance, in case (a), given a sample $(\boldsymbol{x},\sigma^2) \in \mathcal{D}_{\boldsymbol{X}} \times \mathcal{D}_{\sigma^2}$ drawn from the posterior, a sample $\boldsymbol{y} \in \mathcal{D}_{\boldsymbol{Y}}$ of the corresponding posterior predictive distribution may be generated by drawing $\boldsymbol{y} \sim \mathcal{N}(\mathcal{M}(\boldsymbol{x}), \sigma^2\mathbf{I})$.

Firstly, in case (a), prior and posterior predictions of intrados tangential and vertical strains are shown in Figs. 4.30 & 4.31. Results concerning extrados strains are sensibly similar, and are thereby not presented here for the sake of concision. Prior predictions of tangential strains match quite well with observations in terms of mean value, while presenting sensibly large standard deviations due to the adopted prior distribution. Posterior predictions of tangential strains present significantly narrow credible intervals (CI)[4], whereas the prior mean trend has practically not been modified through Bayesian updating.

[4]it is worth mentioning that the notion of *credible intervals* shall not be confused with the notion of *confidence intervals*. Broadly speaking, the notion of *credible intervals* is mainly used within the context of Bayesian inference, whereas the notion of *confidence intervals* is more used in the framework of frequentist statistics.

Then, the tangential strain observation data used for Bayesian inference (between $t \approx 1.5$ years and $t \approx 6$ years) are well predicted by the model.

Nevertheless, due to the fact that the computational model does not distinguish intrados and extrados vertical strains, the posterior predicted vertical strains in case (a) have been adjusted so that predictions are aligned on the mean of measured intrados and extrados vertical strains (see Fig. 4.31b). This leads to a mismatch between posterior predictions and observation data, for both intrados and extrados vertical strains.

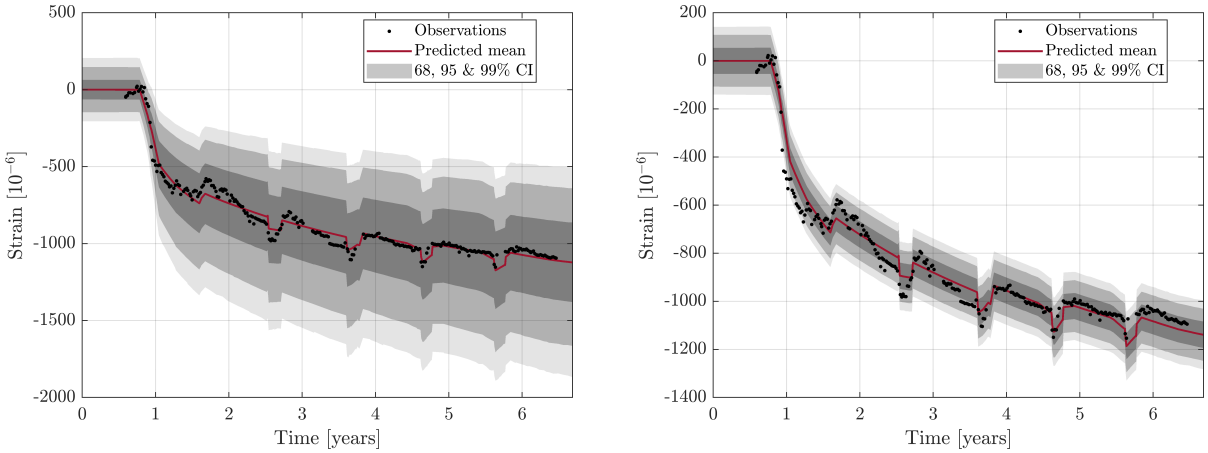

(a) Prior predictions **(b)** Posterior predictions

Figure 4.30: Intrados tangential strains - Prior and posterior predictions - Case (a).

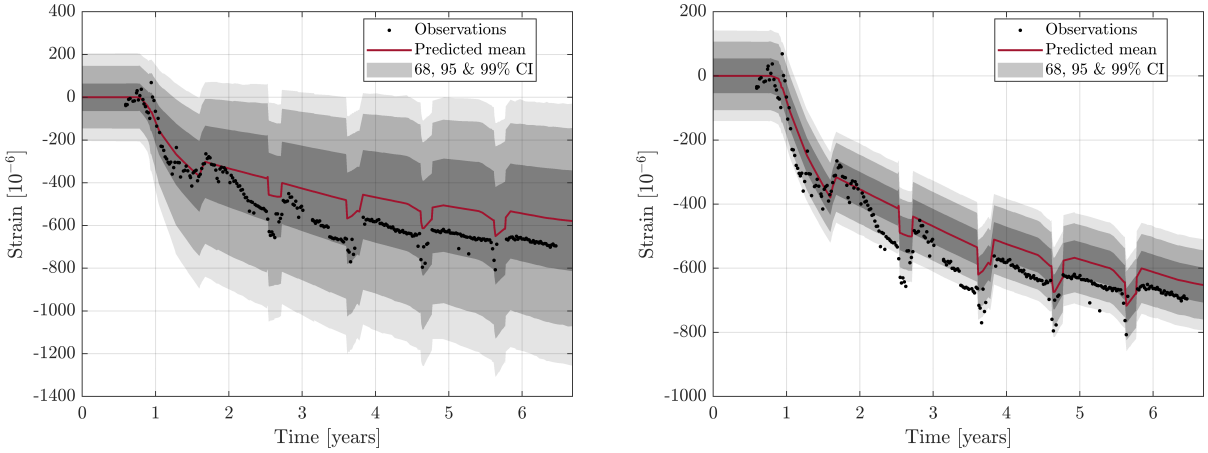

(a) Prior predictions **(b)** Posterior predictions

Figure 4.31: Intrados vertical strains - Prior and posterior predictions - Case (a).

Then, posterior strain predictions obtained in cases (a) and (b) are compared, in order to investigate the effect of accounting for bias terms. The corresponding predictions are depicted in Fig. 4.32. In case (a) (see Fig. 4.32a), posterior predicted tangential strains match well with the corresponding observed data, whereas the mean trend predicted vertical strains is constrained near the average of measured intrados and extrados vertical strains.

In case (b) (see Fig. 4.32b), the identified model bias parameters enable to correct strain predictions, so that a distinction can be made between predicted intrados and extrados vertical strains. In this case, the predictions match well with observed data, for both intrados and extrados vertical strains. Moreover, it is worth noting that the CI of strain predictions in case (b) are narrower than that obtained in case (a). This is consistent with the obtained posterior values for the noise variance σ^2 (see Fig. 4.28): in the case of an unbiased model (case (a)), a larger noise variance is required for covering both intrados and extrados vertical strains (see Fig. 4.32a), contrary to the case (b), where corrected predictions match better with observed data.

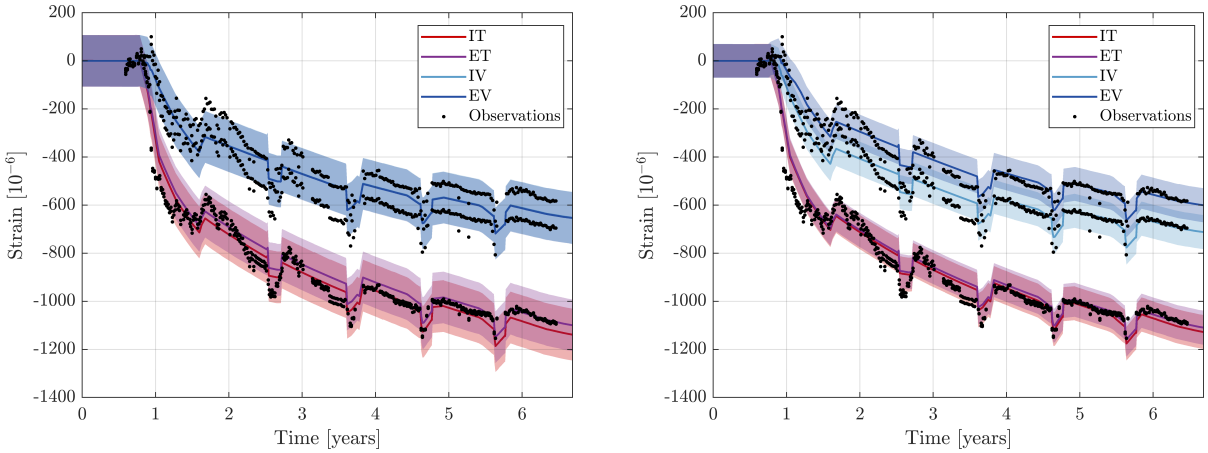

(a) Case (a) (without model bias estimation)

(b) Case (b) (with model bias estimation)

Figure 4.32: Comparison of posterior strain predictions in both cases (a) and (b) - Mean values and 95% CI.

4.4.1.5 Model evidence

Finally, it is worth noting that the SuS algorithm enables to estimate the model evidence as a byproduct of the rare event estimation procedure (see Section 2.2). The model evidences in cases (a) and (b) respectively read:

$$Z_a = \int_{\mathcal{D}_{\sigma^2}} \int_{\mathcal{D}_{\boldsymbol{X}}} \mathcal{L}_a(\boldsymbol{x}, \sigma^2) \pi_a(\boldsymbol{x}, \sigma^2) \mathrm{d}\boldsymbol{x} \mathrm{d}\sigma^2 \tag{4.27}$$

$$Z_b = \int_{\mathcal{D}_{\boldsymbol{B}}} \int_{\mathcal{D}_{\sigma^2}} \int_{\mathcal{D}_{\boldsymbol{X}}} \mathcal{L}_b(\boldsymbol{x}, \sigma^2, \boldsymbol{\beta}) \pi_b(\boldsymbol{x}, \sigma^2, \boldsymbol{\beta}) \mathrm{d}\boldsymbol{x} \mathrm{d}\sigma^2 \mathrm{d}\boldsymbol{\beta} \tag{4.28}$$

where $\mathcal{D}_{\boldsymbol{B}} = \mathbb{R}^4$ is the support of the prior of bias parameters $\boldsymbol{B}$.

The 24 conducted SuS runs yields the estimated values $\log Z_a = -1701.8$ and $\log Z_b = -1565.6$, with coefficient of variations smaller than 0.1%. Thus, based on principles of Bayesian model selection (see Section 1.3.2.5), this suggests that the statistical model proposed in Eq. (4.19) is more likely to have generated the observed data than the model in Eq. (4.14), since $\log Z_b \geq \log Z_a$. Nevertheless, such a conclusion should be nuanced, since the introduction of a bias term which has to be calibrated offers more degrees of freedom, which enable to explain observed data more easily.

4.4.2 Bayesian inference for the THML behavior

4.4.2.1 Bayesian model setup

In Section 4.4.1, the proposed Bayesian inference approach focused on the mechanical behavior of VeRCoRs mock up. In what follows, we propose an approach aiming at inferring the whole set of uncertain parameters of the THML model, from both mechanical and leakage *in-situ* measurement data.

Let $\boldsymbol{X} : \Omega \to \mathcal{D}_{\boldsymbol{X}}$ be the random input parameters of the THML model. Keeping notations introduced in Section 4.4.1, the forward model associated to strains $\boldsymbol{\varepsilon}_k$ is denoted by $\mathcal{M}_{\boldsymbol{\varepsilon}_k} : \mathcal{D}_{\boldsymbol{X}} \to \mathcal{D}_{\boldsymbol{Y}_\varepsilon} \subset \mathbb{R}^{n_1}$, and the strain data set is denoted by $\mathcal{Y}_\varepsilon = \{\boldsymbol{y}_{\boldsymbol{\varepsilon}_k}\}_{1 \leq k' \leq m} \subset \mathcal{D}_{\boldsymbol{Y}_\varepsilon}$. Note that here, the output dimension of the strain forward models $(\mathcal{M}_{\boldsymbol{\varepsilon}_k})_{1 \leq k \leq m}$ is from now on denoted by n_1.

Then, as the aforementioned delayed strains $(\boldsymbol{\varepsilon}_k)_{1 \leq k \leq m}$, both local leakage Q_l and global leakage Q_g predicted by the THML model may be seen as deterministic functions $\mathcal{M}_{Q_l}, \mathcal{M}_{Q_g} : \mathcal{D}_{\boldsymbol{X}} \to \mathcal{D}_{\boldsymbol{Y}_Q} \subset \mathbb{R}^{n_2}$ of the inputs $\boldsymbol{X}$, where n_2 is the number of pressurization tests of the structure. As a result, strains, local and global leakage rates of the structure are predicted by forward models $(\mathcal{M}_{\boldsymbol{\varepsilon}_k})_{1 \leq k \leq m}$, $\mathcal{M}_{Q_l}$ and $\mathcal{M}_{Q_g}$. These models are concatenated by taking their cartesian product in order to define a global forward model:

$$\begin{aligned} \mathcal{M} : \mathcal{D}_{\boldsymbol{X}} &\to \mathcal{D}_{\boldsymbol{Y}} \\ \boldsymbol{x} &\mapsto (\mathcal{M}_{\boldsymbol{\varepsilon}_1}(\boldsymbol{x}), \dots, \mathcal{M}_{\boldsymbol{\varepsilon}_m}(\boldsymbol{x}), \mathcal{M}_{Q_l}(\boldsymbol{x}), \mathcal{M}_{Q_g}(\boldsymbol{x})) \end{aligned} \tag{4.29}$$

where $\mathcal{D}_{\boldsymbol{Y}} = \mathcal{D}_{\boldsymbol{Y}_\varepsilon}^m \times \mathcal{D}_{\boldsymbol{Y}_Q}^2 \subset \mathbb{R}^n$, with $n = mn_1 + 2n_2$.

Furthermore, let $\boldsymbol{y}_{Q_l}, \boldsymbol{y}_{Q_g} \in \mathcal{D}_{\boldsymbol{Y}_Q}$ be the data formed by measurements of local and global leakage rates collected during the first n_2 pressurization tests of the structure. Then, our main goal is to infer the parameters $\boldsymbol{X}$ given the data set $\mathcal{Y} = \mathcal{Y}_\varepsilon \cup \{\boldsymbol{y}_{Q_l}, \boldsymbol{y}_{Q_g}\} = \{\boldsymbol{y}_{\boldsymbol{\varepsilon}_1}, \dots, \boldsymbol{y}_{\boldsymbol{\varepsilon}_m}, \boldsymbol{y}_{Q_l}, \boldsymbol{y}_{Q_g}\} \subset \mathcal{D}_{\boldsymbol{Y}} \subset \mathbb{R}^n$. To that end, a statistical model linking data to model predictions has to be devised. Firstly, let $\boldsymbol{y} \in \mathbb{R}^n$ be the concatenation of all the vectors contained in the data set $\mathcal{Y}$. Likewise, observables $\boldsymbol{Y}_{\boldsymbol{\varepsilon}_1}, \dots, \boldsymbol{Y}_{\boldsymbol{\varepsilon}_m}, \boldsymbol{Y}_{Q_l}, \boldsymbol{Y}_{Q_g}$ related to the strain, local and global leakage responses of the structure are also gathered in a random vector $\boldsymbol{Y}$. Then, we propose the following additive Gaussian noise model:

$$\boldsymbol{Y}|\boldsymbol{x} = \mathcal{M}(\boldsymbol{x}) + \boldsymbol{E} \tag{4.30}$$

where $\boldsymbol{E} \sim \mathcal{N}(\boldsymbol{0}, \boldsymbol{\Sigma})$ is a Gaussian random vector which is independent from $\boldsymbol{X}$.

At this point, the noise covariance matrix $\boldsymbol{\Sigma} \in \mathbb{R}^{n \times n}$ has to be specified. We assume the following block-wise structure:

$$\boldsymbol{\Sigma} = \begin{pmatrix} \boldsymbol{\Sigma}_{\boldsymbol{\varepsilon}_1} & \boldsymbol{0} & \dots & \dots & \boldsymbol{0} \\ \boldsymbol{0} & \ddots & \ddots & & \vdots \\ \vdots & \ddots & \boldsymbol{\Sigma}_{\boldsymbol{\varepsilon}_m} & \ddots & \vdots \\ \vdots & & \ddots & \boldsymbol{\Sigma}_{Q_l} & \boldsymbol{0} \\ \boldsymbol{0} & \dots & \dots & \boldsymbol{0} & \boldsymbol{\Sigma}_{Q_g} \end{pmatrix} \tag{4.31}$$

where $\{\boldsymbol{\Sigma}_{\boldsymbol{\varepsilon}_k}\}_{1 \leq k \leq m}$ are noise covariance matrices associated to strain observations $\{\boldsymbol{y}_{\boldsymbol{\varepsilon}_k}\}_{1 \leq k \leq m}$, and $\boldsymbol{\Sigma}_{Q_l}, \boldsymbol{\Sigma}_{Q_g}$ are noise covariance matrices associated to leakage observations $\boldsymbol{y}_{Q_l}, \boldsymbol{y}_{Q_g}$, respectively.

Furthermore, for each $k \in \{1, \dots, m\}$, one sets $\boldsymbol{\Sigma}_{\boldsymbol{\varepsilon}_k} = \sigma_{\boldsymbol{\varepsilon}}^2 \mathbf{I}$. Here, for the sake of simplicity, the noise variance $\sigma_{\boldsymbol{\varepsilon}_k}^2$ is assumed to be known, and one sets $\sigma_{\boldsymbol{\varepsilon}_k} = 50 \cdot 10^{-6}$, based on results of Section 4.4.1.3. It is worth noting that more general observation models may be adopted, as the model proposed in Eq. (4.19) accounting for an unknown noise variance and modeling biases. Likewise, concerning leakage noise covariance matrices, one sets $\boldsymbol{\Sigma}_{Q_l} = \mathrm{diag}(\sigma_{Q_l,j}^2)_{1 \leq j \leq n_2}$ and $\boldsymbol{\Sigma}_{Q_g} = \mathrm{diag}(\sigma_{Q_g,j}^2)_{1 \leq j \leq n_2}$, where $\sigma_{Q_l,j}$ (respectively $\sigma_{Q_g,j}$) is the standard deviation associated to the measured local (respectively global) leakage during the j-th pressurization test, given in Table 4.2. As for strain measurement data, it is also possible to consider more sophisticated models for the observation noise of leakage data, including a model accounting for an unknown observation noise. Here, the simpler choice of a known observation noise variance is motivated by the fact that only few leakage measurements are available.

Then, the likelihood function associated to the observation model in Eq. (4.30) is given by:

$$\begin{aligned} \mathcal{L}(\boldsymbol{x}) &= \varphi_n(\mathcal{M}(\boldsymbol{x}); \boldsymbol{y}, \boldsymbol{\Sigma}) \\ &= \left(\det\left(2\pi\boldsymbol{\Sigma}\right)\right)^{-\frac{1}{2}} \exp\left[-\frac{1}{2}(\mathcal{M}(\boldsymbol{x}) - \boldsymbol{y})\boldsymbol{\Sigma}^{-1}(\mathcal{M}(\boldsymbol{x}) - \boldsymbol{y})^{\intercal}\right] \end{aligned} \tag{4.32}$$

Thus, denoting by $\pi(\boldsymbol{x})$ the prior density of $\boldsymbol{X}$, the posterior density of $\boldsymbol{X}$ knowing the data set $\mathcal{Y}$ may be derived by applying Bayes' theorem:

$$\pi(\boldsymbol{x}|\mathcal{Y}) \propto \pi(\boldsymbol{x})\mathcal{L}(\boldsymbol{x}) \tag{4.33}$$

4.4.2.2 Bayesian computations

As in Section 4.4.1, the SuS algorithm (see Section 2.2.2) is used to draw samples from the posterior distribution whose density is given by Eq. (4.33). In order to assess the predictive power of the THML model regarding the leakage behavior of the structure, three cases are considered, namely an updating based on data collected until VD1, VD2 and VD3 pressurization tests. Such a choice is also made so as to assess the information gain provided by the increase of the amount of observed data, starting from a same level of knowledge. Furthermore, focusing on the structure operational phase, measurement data collected during pre-operational and control visit tests (*i.e.* VPO and VC1 tests, see Table 4.2) are withdrawn.

For each case, a number of samples per level of $N = 10^4$ is considered, whereas the rarity parameter is again set to $p_0 = 0.1$. Furthermore, 24 independent replications are also produced. Moreover, the (PC-)PCE surrogates of strain and leakage responses constructed in Section 4.3.2 are used to accelerate the SuS algorithm. Computational costs associated to Bayesian computations are summarized in Table 4.7. For each case, the average computational time of a single SuS run is about 2000 seconds, whereas the total computational time associated to the 24 replications is about 14 hours. Parallelizing computations on 8 workers enabled to reduced this total cost to about 1.8 hours.

Case	Cost of a single SuS run		Total computational cost [h]
	Mean [s]	CoV [%]	
VD1	2013.8	7.8	14.0
VD2	2059.1	4.7	13.7
VD3	2119.2	5.2	14.1

Table 4.11: Computational cost of Bayesian computations: cost of a single SuS run and total cost associated to the 24 produced replications.

4.4.2.3 Posterior input parameters

Quantities of interest (QoI) related to samples drawn from the posterior distribution of THML parameters are presented and discussed hereafter. Firstly, a summary of the adopted prior distribution of THML inputs is recalled in Table 4.12, whereas QoI related to posterior marginals in the case of an updating at VD1, VD2 and VD3 tests are presented in Tables 4.13 to 4.15. Furthermore, for the VD1 case, univariate and bivariate marginals from the posterior distribution of THML parameters estimated from samples are shown in Fig. 4.33. Bivariate posterior marginals related to VD2 and VD3 cases present a similar correlation structure, and are thereby not shown for the sake of brevity.

Firstly, the drying parameter B is sensibly impacted by Bayesian updating, through a significant reduction of its standard deviation after updating at VD1 test. Its CoV also decreases from a prior value of 20% to 3%. This may be linked to the fact that this parameter has a significant influence on the variability of both strain and leakage responses (see Section 4.3.3). As a result, extracting information from mechanical and leakage measurement data would provide a significant information gain. Conversely, the first moments (*i.e.* mean and standard deviation) of the Klinkenberg parameter β_K (which may be deemed as weakly influent, see Section 4.3.3) are practically not modified through Bayesian updating. After updating at VD1, the mean of the initial water content $C_{w,0}$ is shifted from 160 to 135 l.m^{-3}, whereas its CoV slightly decreases from 15% to 12%. These values are not significantly evolving after updating at VD2. Nevertheless, the updating at VD3 test involves an increase of the mean of $C_{w,0}$ to a value of 154 l.m^{-3}. Moreover, after updating at VD1 test, the mean value of the desiccation shrinkage parameter α_{ds} is shifted from 10^{-5} to $1.3 \cdot 10^{-5}$ kg.m^{-3}. Its posterior CoV remains around a value of 7% from VD1 to VD3 tests.

Furthermore, it is worth noting that mean values of initial tensions in prestressing cables ($\sigma_{\theta,0}, \sigma_{z,0}$) are reduced once Bayesian updating is performed (see Table 4.13). This has already been observed in the case of an updating based on mechanical monitoring data only (see Section 4.4.1.3).

Then, the mean value of the basic creep consolidation parameter κ is decreased from 10^{-4} to $7 \cdot 10^{-5}$, whereas its CoV slightly decreases from 25% to 18% after updating at VD1. These values are practically not evolving when assimilating data at tests VD2 and VD3. On the contrary, the mean value of the intrinsic permeability is continuously shifted from a value of $5 \cdot 10^{-17}$ m^2 after VD1 to a value of $8 \cdot 10^{-17}$ m^3 after VD3. Such a behavior could be attributed to an underestimation of diffuse leakage during the VD3 test. Lastly, the mean value of the local leak parameter α_l is also slightly increased throughout the Bayesian updating steps, from VD1 to VD3 tests.

n°	Parameter	Units	Distribution	Mean	Std	CoV
1	B	10^{-2}	Lognormal	8.00	1.20	0.15
2	$C_{w,0}$	l.m^{-3}	Lognormal	160.00	24.00	0.15
3	α_{ds}	10^{-6} kg.m^{-3}	Lognormal	10.00	2.50	0.25
4	$\sigma_{\theta,0}$	MPa	Lognormal	$1.51 \cdot 10^3$	378.50	0.25
5	$\sigma_{z,0}$	MPa	Lognormal	$1.51 \cdot 10^3$	378.50	0.25
6	κ	10^{-4}	Lognormal	1.00	0.25	0.25
7	k_0	10^{-17}m^2	Lognormal	7.00	3.50	0.50
8	β_K	MPa	Lognormal	0.18	0.04	0.25
9	α_l	-	Lognormal	6.00	3.00	0.50

Table 4.12: Summary of prior marginals of THML model input parameters.

n°	Parameter	Units	Mean	Std	CoV	95 % CI
1	B	10^{-2}	8.44	0.23	0.03	$[7.99, 8.92]$
2	$C_{w,0}$	l.m^{-3}	135.93	14.85	0.11	$[112.25, 172.98]$
3	α_{ds}	10^{-6} kg.m^{-3}	13.08	0.75	0.06	$[11.83, 14.82]$
4	$\sigma_{\theta,0}$	MPa	$1.23 \cdot 10^3$	108.34	0.09	$[969.48, 1.42 \cdot 10^3]$
5	$\sigma_{z,0}$	MPa	$1.06 \cdot 10^3$	183.73	0.17	$[622.05, 1.39 \cdot 10^3]$
6	κ	10^{-4}	0.74	0.11	0.15	$[0.53, 0.96]$
7	k_0	10^{-17}m^2	5.05	1.55	0.31	$[2.22, 7.85]$
8	β_K	MPa	0.18	0.05	0.26	$[0.11, 0.30]$
9	α_l	-	4.15	0.91	0.22	$[2.35, 5.77]$

Table 4.13: Statistics related to the posterior marginals of THML input parameters, after updating at VD1.

n°	Parameter	Units	Mean	Std	CoV	95 % CI
1	B	10^{-2}	8.30	0.27	0.03	$[7.58, 8.80]$
2	$C_{w,0}$	l.m^{-3}	134.97	16.29	0.12	$[111.64, 188.93]$
3	α_{ds}	10^{-6} kg.m^{-3}	13.48	0.86	0.06	$[11.77, 15.14]$
4	$\sigma_{\theta,0}$	MPa	$1.31 \cdot 10^3$	107.70	0.08	$[1.09 \cdot 10^3, 1.52 \cdot 10^3]$
5	$\sigma_{z,0}$	MPa	$1.19 \cdot 10^3$	177.34	0.15	$[906.24, 1.55 \cdot 10^3]$
6	κ	10^{-4}	0.72	0.13	0.18	$[0.51, 1.06]$
7	k_0	10^{-17}m^2	5.84	1.60	0.27	$[3.42, 10.18]$
8	β_K	MPa	0.19	0.05	0.26	$[0.11, 0.30]$
9	α_l	-	4.67	0.90	0.19	$[2.92, 6.42]$

Table 4.14: Statistics related to the posterior marginals of THML input parameters, after updating at VD2.

Then, based on the bivariate marginals depicted in Fig. 4.33, the correlation structure of posterior THML parameters is analyzed hereafter. A strong linear correlation is observed between parameters $\sigma_{\theta,0}$ and $\sigma_{z,0}$. Such a correlation has already been observed in the case of Bayesian inference from mechanical monitoring data only (see Section 4.4.1). Furthermore, strong linear correlations are also observed for couples $(\sigma_{\theta,0}, \alpha_l)$ and $(\sigma_{z,0}, \alpha_l)$. This could be explained by the nature of the adopted local leak model (see Section 3.3.5.2), which directly links prestressing losses to local leaks.

n°	Parameter	Units	Mean	Std	CoV	95 % CI
1	B	10^{-2}	7.88	0.41	0.05	$[7.28, 8.63]$
2	$C_{w,0}$	$\mathrm{l.m^{-3}}$	153.97	28.04	0.18	$[108.21, 204.97]$
3	α_{ds}	10^{-6} $\mathrm{kg.m^{-3}}$	13.55	1.09	0.08	$[11.34, 15.55]$
4	$\sigma_{\theta,0}$	MPa	$1.38 \cdot 10^3$	117.21	0.08	$[1.15 \cdot 10^3, 1.61 \cdot 10^3]$
5	$\sigma_{z,0}$	MPa	$1.26 \cdot 10^3$	219.41	0.17	$[851.42, 1.73 \cdot 10^3]$
6	κ	10^{-4}	0.65	0.12	0.19	$[0.48, 0.94]$
7	k_0	$10^{-17}\mathrm{m^2}$	8.00	2.78	0.35	$[3.43, 13.16]$
8	β_K	MPa	0.19	0.05	0.25	$[0.11, 0.30]$
9	α_l	-	5.14	1.08	0.21	$[3.22, 7.34]$

Table 4.15: Statistics related to the posterior marginals of THML input parameters, after updating at VD3.

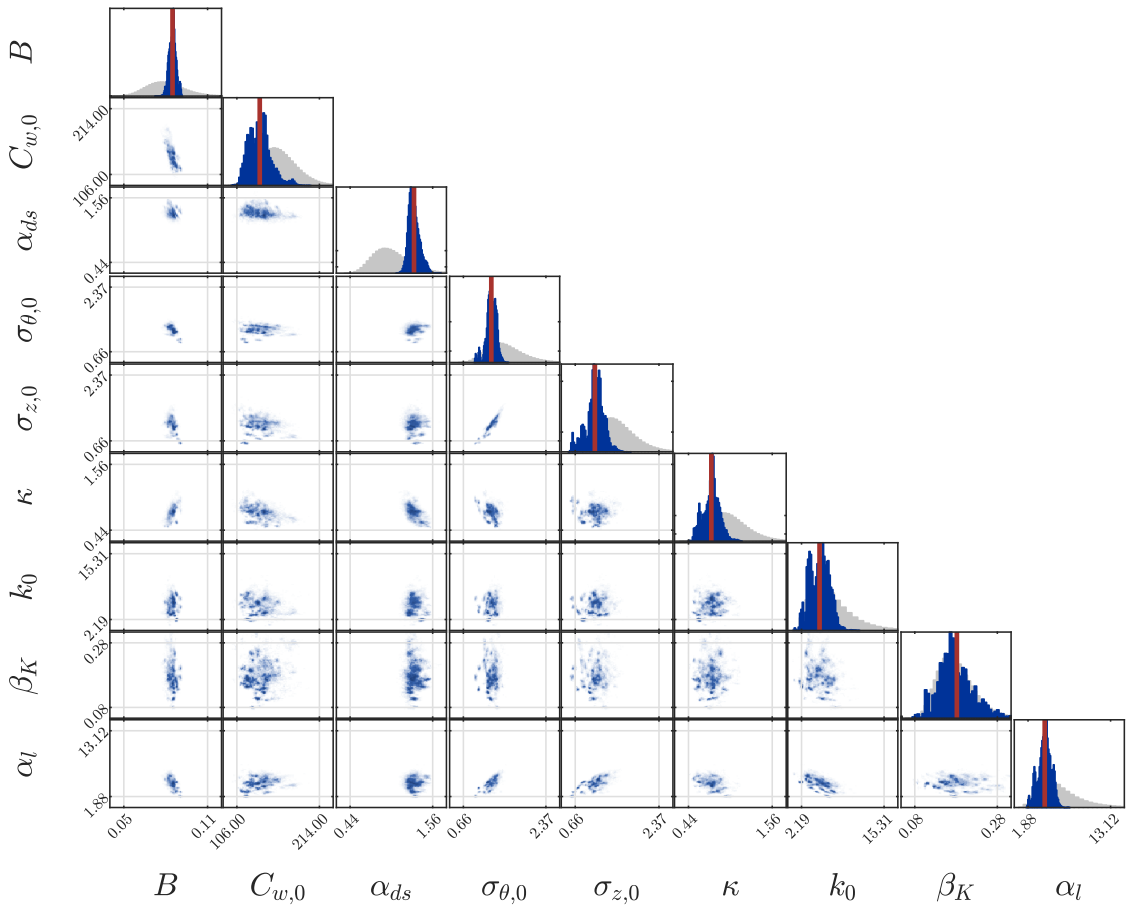

Figure 4.33: Univariate and bivariate marginals from the posterior distribution of THML model input parameters estimated from samples. *Prior samples are shown in grey, whereas posterior samples are shown in blue. The posterior mean value of each parameter is shown by a vertical red line.*

4.4.2.4 Posterior predictions

Next, posterior samples are used in order to perform new predictions of the long-term mechanical and leakage behavior of the structure. Firstly, similarly to Section 4.4.1.4, posterior predictions of delayed strains are performed from samples of the corresponding posterior predictive distributions (see Eq. 4.26). Prior and posterior predictions of tangential and vertical strains are presented in Fig. 4.34. For each direction (*i.e.* tangential or vertical), predicted intrados and extrados strains are averaged, for the sake of readability. As already observed in the case (a) considered in Section 4.4.1.4, prior predictions involve large uncertainties, due to the relatively large uncertainties encoded in the adopted prior input distribution. Furthermore, posterior tangential strains match well with observed tangential strains, whereas posterior vertical strains are aligned on the mean of observed ones.

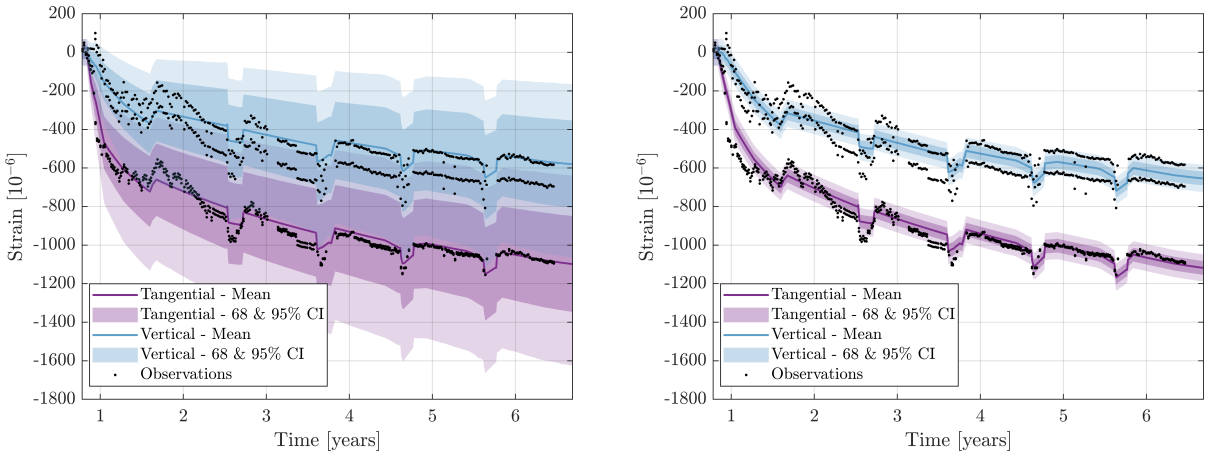

(a) Prior predictions

(b) Posterior predictions

Figure 4.34: Prior and posterior strain predictions after updating at VD3 test.

Next, prior and posterior local leakage predictions are presented in Fig. 4.35. Firstly, as previously observed for prior strain predictions, prior local leakage predictions present sensibly large uncertainties (see Fig. 4.35a). Besides, the prior mean predicted local leakage rate is relatively in good agreement with measurements. Indeed, the predicted mean local leakage rate at VD1 test is about 21.2 $Nm^3.h^{-1}$, whereas the measured leakage rate is about 24.8 $Nm^3.h^{-1}$. Then, after assimilating measurements after VD1 tests, the predicted mean is slightly adjusted, and the width of credible intervals is sensibly reduced. These credible intervals remain relatively large, though. This is notably due to the fact that local leakage measurements involve large uncertainties, as explained in Section 4.2.2.3.

Moreover, it is worth noting that the local leakage rates at VD2 and VD3 tests are also reasonably well predicted in terms of mean value (36.3 $Nm^3.h^{-1}$ predicted vs. 38.9 $Nm^3.h^{-1}$ observed at VD2 test, and 43.9 $Nm^3.h^{-1}$ predicted vs. 38.9 $Nm^3.h^{-1}$ observed at VD3 test). The constant evolution of local leaks between VD3 and VD5 tests suggested by measurements is not reproduced by the model, though. Furthermore, it is also remarked that the assimilation of measurement data after VD2 does not provide significant uncertainty reduction in local leakage predictions, presumably due to the large uncertainties tainting local leakage measurements.

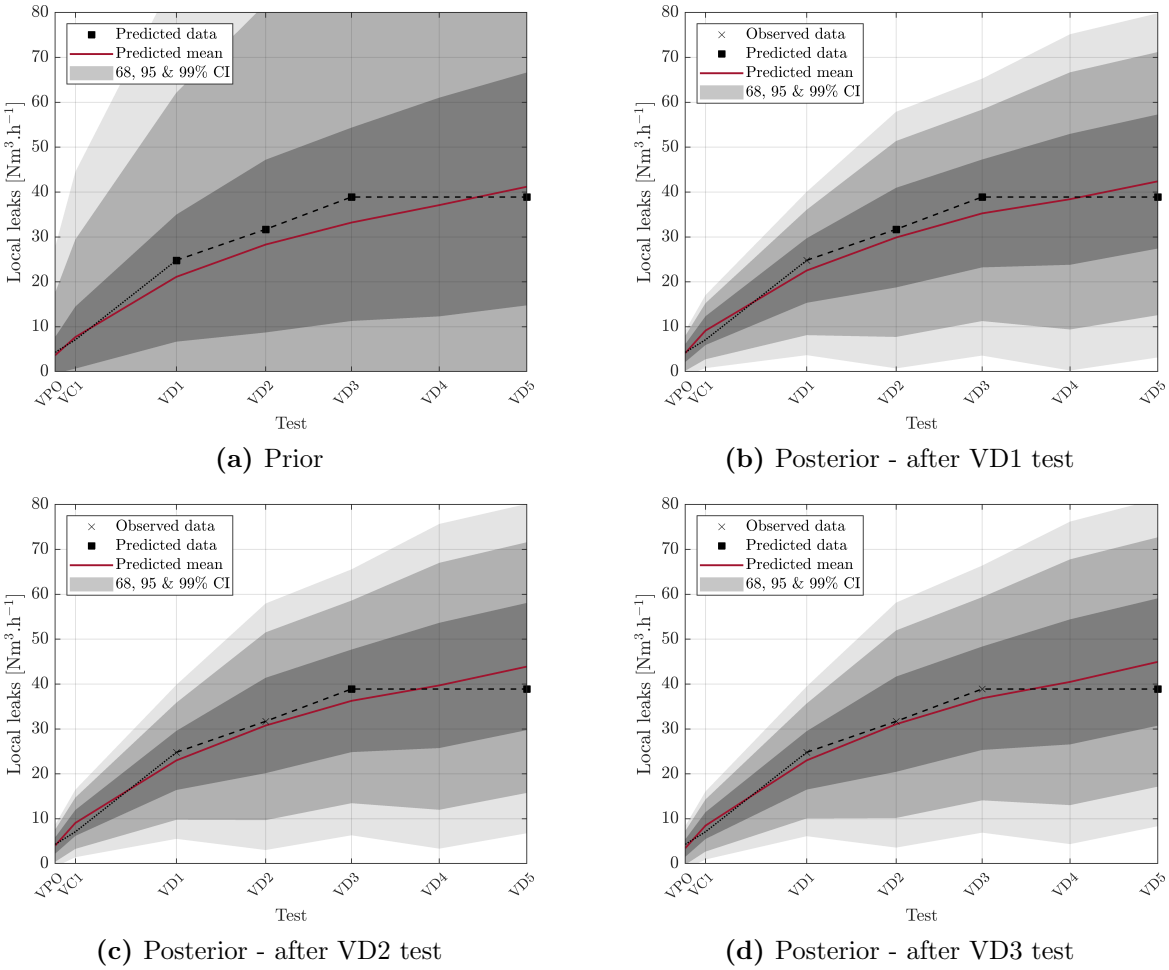

(a) Prior

(b) Posterior - after VD1 test

(c) Posterior - after VD2 test

(d) Posterior - after VD3 test

Figure 4.35: Prior and posterior local leakage predictions.

Lastly, prior and posterior predictions of the global leakage rate of the structure are presented in Fig. 4.36. As for local leakage predictions, prior global leakage predictions obviously involve very large uncertainties. Furthermore, the mean predicted global leakage rate at VD1 test accurately approaches the observed one (32.3 Nm^3.h^{-1} predicted vs. 30.3 Nm^3.h^{-1}). As a result, the mean trend of predictions is practically not affected by Bayesian updating at VD1. However, uncertainties on predictions are strongly reduced, leading to predicted CoVs comparable to that related to observations (*i.e.* about 3%). Then, after Bayesian updating at VD1, the mean predicted global leakage rate at VD2 (41.0 Nm^3.h^{-1}) approaches the observed one (46.2 Nm^3.h^{-1}) with a relative error of about 11.1%. Subsequently, updating at VD2 induces an adjustment of the mean of predictions, so that the mean predicted leakage rate at VD3 (52.0 Nm^3.h^{-1}) approaches the observed one (57.1 Nm^3.h^{-1}) with a relative error smaller than 9%. Finally, after updating at VD3, the mean predicted leakage rate at VD5 is given by 67.6 Nm^3.h^{-1} whereas the measured one is about 64.7 Nm^3.h^{-1}, which corresponds to a relative error of about 4.5%. Thus, Bayesian inference enabled to update and precise predictions of the global leakage behavior of the structure, throughout its operational phase.

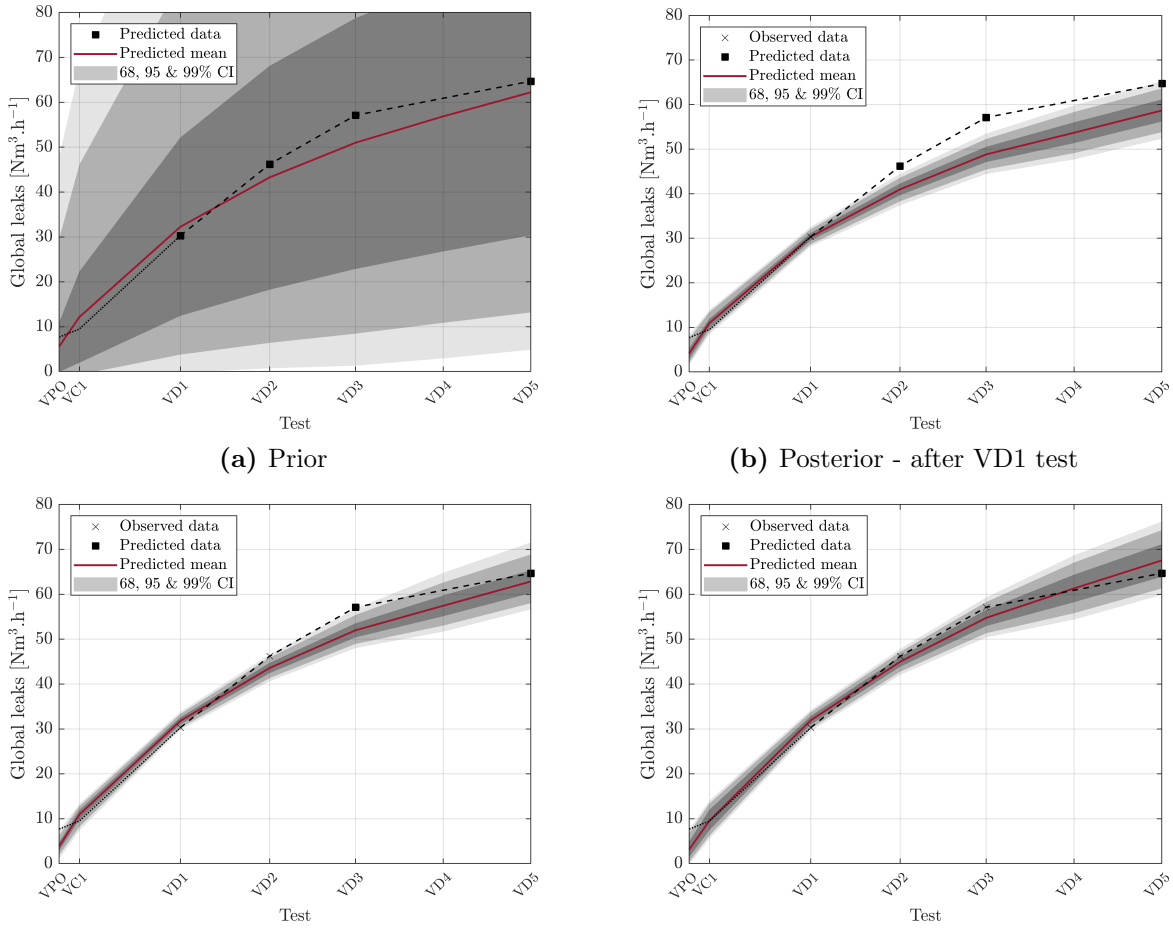

(a) Prior

(b) Posterior - after VD1 test

(c) Posterior - after VD2 test

(d) Posterior - after VD3 test

Figure 4.36: Prior and posterior global leakage predictions.

4.5 Conclusion

In this chapter, we have proposed a global methodology aiming at accounting for uncertainties in simulations of the long-term THML behavior of large concrete containment structures. In this context, the VeRCoRs mock-up has constituted the central case study of this chapter. Firstly, mostly based on expert judgement, the uncertainties tainting input parameters of the THML modeling strategy presented in Chapter 3 have been modeled in a probabilistic setting, through the definition of a prior probability distribution. Then, adapted surrogate modeling techniques have been used to provide inexpensive-to-evaluate approximations of some output variables of interest of the THML model, such as strains or leakage rate. In particular, we considered principal component PCE surrogates so as to take advantage of the structure of strain series and providing an significant reduction of the dimensionality of strain outputs, leading to computationally efficient surrogate model constructions. The aforementioned surrogates have then been used to perform a variance-based sensitivity analysis and propagating prior uncertainties. Next, we have proposed to use Bayesian inference in order to combine the constructed prior with *in-situ* measurement data in order to derive a new state of knowledge about uncertain parameters. In this framework, we have presented a first approach focused on the mechanical behavior of the structure, which notably enabled to manage an unknown observation noise variance and to estimate modeling biases from observed data. Then, we have proposed an approach dealing with both mechanical and leakage measurement data, enabling to update inputs of the whole THML computational chain, and subsequently performing new predictions of both strains and leakage rate of the structure. Results suggest that the proposed approach enables well to update input parameters and precise predictions of the long-term behavior of the structure throughout its exploitation phase, and provided satisfactory estimations of its global leakage rate (with relative errors smaller than 10%).

Besides, the presented work underlies several perspectives: firstly, Bayesian inference results presented in Section 4.4 rely on a single prior distribution, which has been devised through expert judgment, *i.e.* based on a more or less subjective viewpoint. Then, in a second level UQ perspective, it would be interesting to assess the influence of choice of the prior distribution on Bayesian inference results, as proposed in the framework of robust Bayesian inference (Berger, 1990; Ruggeri et al., 2005). In a more practical framework, in the publication (Rossat et al., 2022c), we studied the effect of the choice of the prior through numerical experiments focusing on the mechanical behavior of VeRCoRs mock-up. Furthermore, the considered surrogate modeling techniques (namely PCE and PC-PCE) for approximating time-dependent output variables of the THML model seemed to be well suited to the problem at hand. This is notably due to the fact that aging is a somewhat slow process, which does not involve an increase of non-linearities over time that may cause the failure of (PC-)PCE approaches (Mai, 2016). Lastly, in this chapter, the SuS algorithm used for Bayesian computations (see Section 2.2) has been coupled with prior-based (PC-)PCE surrogates, for the sake of simplicity. Then, it would be possible to use the adaptive PCK approach presented in Chapter 2, in order to sample posterior distributions in a possibly more efficient and robust way. This would require a non-negligible additional cost, though, since prior-based surrogates still have to be constructed so as to performing other UQ tasks (such as prior-based sensitivity analysis and uncertainty propagation).

Finally, the proposed approach focused on the VeRCoRs mock-up, which constitutes a 1:3 scale mock-up of an operating NCB. Such a structure may be seen as a validation support for the proposed probabilistic THML modeling approach, involving well known material properties as well as numerous monitoring devices. Besides, it is worth noting that the presented Bayesian inference approach is mainly based on *in-situ* monitoring data (*e.g.* strain and leakage measurements) that are also available on site in the case of real operating NCBs, in a smaller amount, though. This would suggest the extension of the proposed approach to real operating NCBs.

Nevertheless, the transition from 1:3 scale (VeRCoRs) to 1:1 scale (operating NCBs) induces several problems remaining to be addressed. Indeed, contrary to VeRCoRs mock-up, operating NCBs may be subjected to maintenance operations related to their leak tightness, involving the presence of coatings. Hence, the effect of such coatings on the leakage behavior has to be modeled in order to better plan potential repair works. Furthermore, THML modeling for real operating NCBs subjected to coatings has received a little attention in the literature, and scarce information are available regarding some material properties of such structures, which involves a more vague state of knowledge than in the case of VeRCoRs mock-up. Moreover, contrary to VeRCoRs mock-up which has been built for research purposes, real operating NCBs must satisfy several safety requirements related to their leakage rate, which may condition their long-term exploitation. This notably implies to assess their reliability related to the leak tightness they must ensure, notably through estimating the probability of exceeding some leakage regulatory thresholds. Such problems will be addressed in the next chapter, in which a real operating NCB will be studied.

5

Reliability analysis of the leakage behavior of containment structures - Case of an operating NCB

Contents

5.1 Introduction

In Chapter 4, we have presented a general methodology aiming at performing probabilistic predictions of the long-term THML behavior of containment structures subjected, and updating the uncertainties of input parameters from *in-situ* noisy monitoring data. This methodology has been illustrated and validated at the scale of the VeRCoRs mock-up, which constitutes a 1:3 scale NCB, mainly built for research purposes related to the understanding of the effects of aging on the long-term behavior of NCBs.

Nevertheless, the framework of operating containment structures underlies an additional dimension, namely the evaluation of their reliability regarding the leak tightness function they must ensure. For instance, in the framework of operating NCBs, such safety requirements notably take the form of regulatory leakage thresholds that must not be exceeded. Moreover, operating containment structures imply another specificity compared to the VeRCoRs mock-up, namely the presence of coatings placed on the surface of the structure during maintenance operations. As a result, along with probabilistic predictions of the long-term THML behavior of the structure, it is necessary to quantify the risks of exceeding the aforementioned regulatory thresholds, while assessing the effects of possible repair works. Such a risk quantification could be used so as to better plan the maintenance of the structure, through evaluating several scenarios related to repair works aiming at reinforcing structural leak tightness.

Consequently, the main goal of this chapter is to propose a general methodology for assessing the reliability of the leak tightness of containment structures. In this context, a scale 1:1 operating NCB will constitute the central case-study of this chapter. Firstly, it is worth noting that the modeling of the effects of coatings at the scale of large containment structures is an *a priori* complex task, and has received a very little attention in the literature. Hence, we propose simple modeling assumptions which account for the effect of such repairs, in order to devise a THML computational model suitable for operating NCBs. To that end, the knowledge gained at the scale of VeRCoRs mock-up in terms of THML modeling will be fully exploited to model the behavior of operating NCBs in the absence of coatings.

Besides, the devised THML computational model involves a quite large amount of uncertain input parameters. Hence, in order to facilitate forward and inverse UQ tasks, it is necessary to select the PII on the THML model output variability, and rank them by decreasing influence. To our knowledge, no works dealing with the identification of influential inputs of THML models for scale 1:1 NCBs have been proposed in the literature. At the scale of VeRCoRs mock-up, the former work of Bouhjiti (2018) involved an OAT-based screening for the inputs of a THML model, which enabled to reduce the analysis to about ten uncertain parameters. A crucial question then arises: do the conclusions of Bouhjiti (2018) made at VeRCoRs scale transfer to operating NCBs ? Consequently, we attempt to answer to this question by conducting a global sensitivity analysis based on Sobol' sensitivity indices.

Next, based on the identified PII and their probability distribution, PoF related to the leakage behavior of the structure may be estimated, based on computational tools developed in the framework of structural reliability (see Section 1.2.6). Nevertheless, the input probability distribution retained for the aforementioned PII typically stems from a subjective process aiming at summarizing the available information about them, including expert judgement. As a result, this input distribution itself is known with some level of confidence.

Then, in a second-level UQ perspective (see Section 1.2.3), it would be necessary to quantify the impact of the choice of the input distribution, and to assess the sensitivity of estimated PoF with respect to this choice. In this context, we propose to use a method taken from the new UQ branch of robustness analysis which has recently emerged in the field of sensitivity analysis, namely perturbed-law based sensitivity indices (PLI) (Lemaître, 2014; Lemaître et al., 2015; Sueur et al., 2016).

Finally, it is worth noting that the aforementioned reliability analysis remains based on a probability distribution that does not takes into account monitoring data related to the response of the structure. Following the Bayesian viewpoint adopted throughout this thesis, we propose an approach for updating PoF related to the leakage behavior of the structure, from *in-situ* monitoring data. Then, the proposed approach not merely enables to update the knowledge in uncertain parameters from observed data as in Chapter 4, but also to update the estimation of the risks of exceeding regulatory leakage thresholds.

This chapter is organized as follows: THML modeling assumptions suitable for operating containment structures are described in Section 5.2. Then, the PII of the devised computational model are identified in Section 5.3. Subsequently, a reliability analysis of the leakage behavior of the studied NCB is presented in Section 5.4. In particular, a first prior-based reliability analysis is performed in Section 5.4.1. Next, an introduction to PLI and their application to the leakage behavior of the studied NCB are presented in Section 5.4.2. Lastly, a Bayesian analysis of both input parameters and estimated PoF is undertaken in Section 5.5.

5.2 Computational model setup

In this section, a computational model suitable for assessing the long-term THML behavior of the studied operating NCB is devised. This model is similar to that adopted in Chapter 4 to assess the global behavior of VeRCoRs mock-up, and is mostly based on the THML constitutive equations presented in Chapter 3. Hence, we deliberately adopt a shorter presentation of the studied structure and the computational model, and focus on specificities of operating containment structures.

5.2.1 Finite element meshes

The computational model considered in this chapter is based on a RSV of the standard zone of a operating NCB. As in Chapter 4, two FE meshes are considered for THML calculations, namely one mesh for thermo-hydric and diffuse leakage calculations, and one for mechanical calculations. These meshes are depicted in Fig. 5.1, whereas information about them are summarized in Table 5.1.

5.2.2 Modeling assumptions

During their operational phase, operating NCBs may be subjected to repair works aiming at reinforcing their leak tightness. Such works typically consist in laying composite coatings on internal and/or external surfaces of the structure (see Fig. 5.2). Compared to the typical permeability of concrete, such coatings may be considered to be impervious (Asali, 2016).

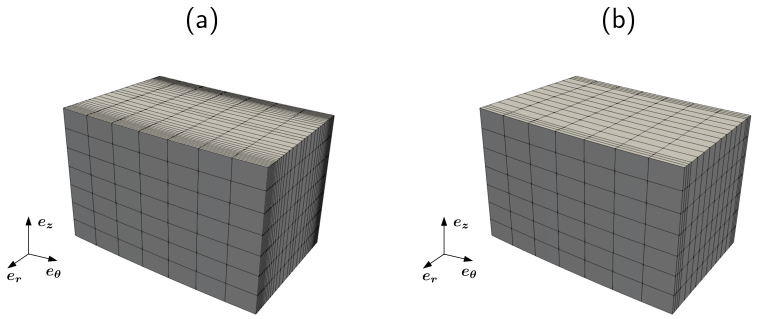

Figure 5.1: FE meshes of the standard zone RSV: (a) mesh for thermo-hydric and diffuse leakage calculations; (b) mesh for mechanical calculations.

Phase	Concrete		Prestressing cables	
	Element type	Nodes	Element type	Nodes
TH-L	HEXA8 (linear)	2240	-	-
M	HEXA20 (quadratic)	4076	SEG2 (linear)	39

Table 5.1: Information about FE meshes of the standard zone RSV.

Figure 5.2: Laying of coatings on the extrados surface of the dome of an operating NCB, during a decennial visit ©EDF.

Physically speaking, the presence of coatings induces several effects on the THML behavior of the structure. Firstly, regarding the hydric behavior, coatings act as a barrier for moisture transfers, as they induce a slowdown of drying kinetics of the concrete wall. This is notably the case when coatings are positioned on the internal surface of the structure, subjected to a higher temperature (and thereby to a lower RH) due to the presence of the operating reactor.

Such modifications of thermo-hydric boundary conditions then have repercussions on the mechanical behavior of the underlying concrete volume, notably through the slowdown of desiccation shrinkage and creep strains. Furthermore, during pressurization tests, the positioning of coatings involve an additional layer of complexity in terms of leakage paths. Indeed, depending on the connectivity of leak paths in the concrete wall (*e.g.* cracks, steel-concrete interfaces, construction joints), the presence of impervious coatings may induce the creation of complex leakage paths, so that some coatings may be by-passed. As a result, although a coating itself is impervious, the combination of the concrete wall and the aforementioned coating may be permeable, to a certain extent. For this reason, the notion of *efficiency* of a given coating will be used to characterize the ability of the combination of this coating with the concrete wall to reduce the leakage rate of a given zone.

From a modeling point of view, explicitly representing coatings as well as their effects on the global THML behavior of the structure would typically require a full scale FE model, involving a possibly prohibitive computational cost. Consequently, some simplifying modeling assumptions are necessary to account for the effects of coatings on the global THML behavior of the structure. To that end, we assume an equivalence principle, linking the leakage response of the structure to the response of the same structure without coatings. In this context, the global leakage rate Q_g of the structure with coatings is supposed to be proportional to the global leakage rate $Q_{g,0}$ of the same structure without coatings:

$$Q_g = C_c Q_{g,0} \tag{5.1}$$

where $C_c \in [0, 1]$ is a correction factor which takes into account the surface and the efficiency of coatings.

The formulation given in Eq. (5.1) enables to assess the behavior of a coated structure through a decoupling of effects of aging and effects of coatings: without any coatings, the global leakage rate of the structure is expected to increase over time, under the effects of aging. In the presence of coatings, only a fraction of the obtained leakage rate is expected to be observed. Thus, this hypothesis allows to reduce the THML modeling to a VeRCoRs-like configuration (*i.e.* without coatings), and to subsequently correct the estimated leakage rate with a factor that integrates the amount of positioned coatings and their efficiency. In this context, the THML modeling strategy presented in Chapter 3 and used at the scale of VeRCoRs mock-up in Chapter 4 is used so as to assess the evolution of the (virtual) leakage rate without coatings $Q_{g,0}$.

Next, the correction factor C_c introduced in Eq. (5.1) is precised hereafter. Firstly, in the simple case of a structure which only presents coatings on one face (*i.e.* internal or external), the aforementioned correction factor is assumed to be written as follows:

$$C_c = 1 - \gamma_c s_c \tag{5.2}$$

where $s_c = S_c/S_t$ is the fraction of coated surface (S_c being the coated surface and S_t the total surface), and $\gamma_c \in [0, 1]$ a so-called *efficiency parameter*. Such a formulation is understood as follows: in the case of a fully efficient device (*i.e.* $\gamma_c = 1$), the leakage reduction is total (*i.e.* $C_c = 0$) if the surface is fully coated.

In practice, operating NCBs may present coatings on both internal and external surfaces. Consequently, we introduce the following extension of Eq. (5.2) for the correction factor C_c:

$$C_c = c(\gamma_{c,i} s_{c,i}, \gamma_{c,e} s_{c,e}) \tag{5.3}$$

where $c : [0,1]^2 \to [0,1]^2$ is a function, $\gamma_{c,i}, \gamma_{c,e}$ are efficiency parameters related to internal and external surfaces, respectively, and $s_{c,i}, s_{c,e}$ the fractions of coated surfaces at internal and external sides. The function c is assumed to be continuous, and for physical reasons, one must have $c(0,0) = 1$ and $c(1,1) = 0$. Furthermore, in the case of fully efficient intrados coatings ($\gamma_{c,i} = 1$), no leakage is expected if all the internal surface is coated, regardless to the surface and the efficiency of extrados coatings (and *vice versa*). Hence, the function c must also satisfy the conditions $c(1,x) = c(x,1) = 0$, for all $x \in [0,1]$. In what follows, the simple polynomial function $c(x,y) = (1-x)(1-y)$ will be considered. This consists in writing the global leakage rate Q_g by:

$$Q_g = (1 - \gamma_{c,i} s_{c,i})(1 - \gamma_{c,e} s_{c,e}) Q_{g,0} \tag{5.4}$$

Finally, assuming the following superposition principle to the (virtual) global leakage $Q_{g,0}$ (see Section 4.2.3.2):

$$Q_{g,0} = Q_{d,0} + Q_{l,0} \tag{5.5}$$

where $Q_{d,0}$ and $Q_{l,0}$ denote the diffuse and local leakage rates without coatings, respectively, formulations analogous to Eq. (5.4) are obtained for the diffuse and local leakage rates with coatings Q_d and Q_l (*i.e.* $Q_\star = (1 - \gamma_{c,i} s_{c,i})(1 - \gamma_{c,e} s_{c,e}) Q_{\star,0}$, with $\star \in \{d, l\}$).

5.2.3 Boundary conditions and loading

The THML boundary conditions and loading applied at the scale of the standard zone RSV are precised hereafter. Firstly, analogously to the VeRCoRs RSV studied in Chapter 4, Neumann boundary conditions in terms of temperature are adopted, through the definition of convective exchange coefficients $k_{th,i}$ and $k_{th,e}$ at intrados and extrados surfaces, respectively. Based on *in-situ* measurements of ambient temperature, simplified temperature histories are considered for the ambient air of the internal and external spaces of the containment wall. Likewise, Dirichlet boundary conditions in terms of water content are imposed at intrados and extrados surfaces, from RH histories composed with a sorption-desorption model. Simplified temperature and RH histories for ambient air based on *in-situ* measurements are summarized in 5.2.

Period	Temperature [°C]		RH [%]	
	Int.	Ext.	Int.	Ext.
Initial state	12.8	12.8	100	100
Reactor startup	12.8	12.8	90	90
Reactor stationary regime	31.0	22.4	43	55

Table 5.2: Simplified temperature and RH histories of the ambient air of the studied NCB.

Then, concerning mechanical boundary conditions, one considers the same kinematic BC than those adopted at the scale of the VeRCoRs RSV presented in Section 4.2.3. Furthermore, prestressing is applied in an identical way. Next, regarding boundary conditions for diffuse leakage calculations, pressure profiles similar to that considered for VeRCoRs mock-up (see Section 4.2.4) are applied on intrados and extrados surfaces of the RSV. Lastly, histories of the (normalized) surface of coatings positioned on intrados and extrados faces are presented in Fig. 5.3. Such histories will be used so as to assess the effects of coatings on the global leakage behavior of the studied structure. From the control visit test (VC1 test), the surface of intrados coatings has been increased over time, until the test of the second decennial visit (VD2 test). Extrados coatings are only positioned from the third decennial visit (VD3), whereas the surface of intrados coatings has not been increased for this visit. Moreover, it is worth noting that coatings surfaces for the fourth decennial visit (VD4) are here assumed to be those planned for the VD3 test.

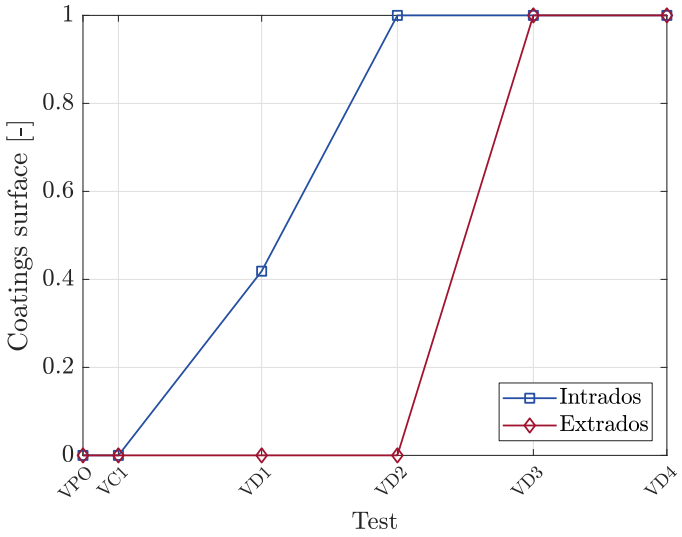

Figure 5.3: Time evolution of the total surface of coatings, on intrados and extrados surfaces. *Coatings surfaces are normalized by the surface planned for VD3 test. Hence, such values shall not be confused with the coated fraction of the surface of the structure.*

5.3 Identification of PII of the THML model

The computational model presented in Section 5.2 involves a large amount (≈ 30) of uncertain parameters, corresponding to those already considered in Chapter 4 (see Section 4.2.4 for a detailed description), as well as coating efficiency parameters introduced in Section 5.2.2. Then, it would be possible to employ screening techniques (see Section 1.2.5) such as the Morris method (Morris, 1991) in order to identify the PII on the variability of output variables of interest of the THML computational model. In this section, we instead choose to compute Sobol' sensitivity indices through the construction of (PC-)PCE surrogates, which enable a more comprehensive sensitivity analysis than classical screening methods, for a comparable amount of model calls. Indeed, based on preliminary numerical experiments, we found that reasonably accurate sparse (PC-)PCE surrogates may be constructed for a cost comparable to that required by classical screening methods, in spite of the quite large the dimension of the problem (≈ 30). This is in line with recent results related to sparse PCE (Blatman and Sudret, 2011b; Lüthen et al., 2021b), which demonstrated their ability to provide accurate approximations with experimental designs of limited size, even in the case of input dimensionalities of $\mathcal{O}(10^2)$.

The probability distribution of the considered THML inputs is defined in Section 5.3.1. The construction of (PC-)PCE surrogates of output variables of interest of the THML model is subsequently described in Section 5.3.2. Lastly, the estimated Sobol' indices are presented and discussed in Section 5.3.3.

5.3.1 Probabilistic input modeling

The probability distribution of each input parameter of the THML computational model are summarized in Table 5.3. The characteristics of such distributions have been mostly defined through expert judgement, due to the scarce available information. Furthermore, due to the lack of information regarding their dependence structure, all these input parameters are assumed to be mutually independent.

5.3.2 Surrogate modeling

5.3.2.1 General settings

The output variables of interest provided by the THML model described in Section 5.2 are the same than that considered at VeRCoRs scale (see *e.g.* Section 4.2.4), except for the leakage behavior, for which the effects of coatings are integrated here. Consequently, surrogate modeling settings considered here are similar to those adopted in Section 4.3.2. The latter are recalled herebelow:

- time-dependent quantities computed on a time grid with size of $\mathcal{O}(10^2)$ (such as water saturation S_w, strains $\boldsymbol{\varepsilon}$ or prestressing losses Π) are approximated by PC-PCE surrogates.

- the (virtual) diffuse leakage $Q_{d,0}$ is approximated by a PCE surrogate, for each pressurization test.

n°	Parameter	Units	Distribution	Bounds	Mean	Std	CoV
1	λ_c	$\mathrm{W.m^{-1}.K^{-1}}$	Lognormal	-	2.33	0.23	0.10
2	c_c^p	10^2 $\mathrm{kJ.kg^{-1}.K^{-1}}$	Lognormal	-	8.80	0.88	0.10
3	$k_{th,i}$	$\mathrm{W.m^{-2}.K^{-1}}$	Lognormal	-	5.00	1.25	0.25
4	$k_{th,e}$	$\mathrm{W.m^{-2}.K^{-1}}$	Lognormal	-	3.00	0.75	0.25
5	A	10^{-13} $\mathrm{m^2.s^{-1}}$	Lognormal	-	1.95	0.49	0.25
6	B	10^{-2}	Lognormal	-	6.80	1.70	0.25
7	U_w	$\mathrm{kJ.mol^{-1}}$	Lognormal	-	39.06	1.17	0.25
8	T_w^0	K	Lognormal	-	20.00	2.00	0.10
9	$C_{w,0}$	$\mathrm{l.m^{-3}}$	Lognormal	-	128.00	32.00	0.25
10	E_c	GPa	Lognormal	-	36.70	9.17	0.25
11	ν	-	Lognormal	-	0.20	0.02	0.10
12	ρ_c	10^3 $\mathrm{kg.m^{-3}}$	Lognormal	-	2.35	0.24	0.10
13	α_{th}	10^{-6} $\mathrm{K^{-1}}$	Lognormal	-	10.00	1.00	0.10
14	α_{ds}	10^{-6} $\mathrm{kg.m^{-3}}$	Lognormal	-	10.00	5.00	0.50
15	ν_c	-	Lognormal	-	0.20	0.02	0.10
16	k_{rd}	10^{10} Pa	Lognormal	-	5.98	2.99	0.50
17	η_{rd}	10^{16} Pa.s	Lognormal	-	8.12	4.06	0.50
18	η_{id}	10^{20} Pa.s	Lognormal	-	1.76	0.88	0.50
19	κ	10^{-4}	Lognormal	-	1.00	0.50	0.50
20	T_{bc}^0	K	Lognormal	-	20.00	2.00	0.10
21	U_{bc}	$\mathrm{kJ.mol^{-1}}$	Lognormal	-	39.06	0.47	0.10
22	η_{dc}	10^9 Pa.s	Lognormal	-	7.39	3.69	0.50
23	$\sigma_{\theta,0}$	MPa	Lognormal	-	$1.48 \cdot 10^3$	371.67	0.25
24	$\sigma_{z,0}$	MPa	Lognormal	-	$1.48 \cdot 10^3$	371.67	0.25
25	$\sigma_{z,c}$	MPa	Lognormal	-	1.37	0.34	0.25
26	β_K	MPa	Lognormal	-	0.20	0.05	0.25
27	k_0	10^{-17} $\mathrm{m^2}$	Lognormal	-	10.00	5.00	0.50
28	c_k	-	Lognormal	-	0.45	0.11	0.25
29	α_l	-	Lognormal	-	10.00	5.00	0.50
30	$\gamma_{c,i}$	-	Truncated Gaussian	$[0;1]$	0.50	0.25	0.50
31	$\gamma_{c,e}$	-	Truncated Gaussian	$[0;1]$	0.50	0.25	0.50

Table 5.3: Summary of the probability distribution of each input THML parameter.

Recall that the local leakage rate without coatings $Q_{l,0}$ is given by an analytical function of prestressing losses Π. Furthermore, the leakage rates with coatings Q_d, Q_l, Q_g are computed from the analytical coating model introduced in Section 5.2.2.

Then, an experimental design of size $K = 1000$ is built through Latin Hypercube Sampling (LHS). The aforementioned output variables of interest are subsequently computed through evaluating the THML computational model. Similarly to the computational times required at the scale of the VeRCoRs RSV (see Section 4.3.2), the cost required by a single model run is about 30 seconds for thermo-hydric calculations, 10 minutes for mechanical calculations, and 2 minutes for leakage calculations. As a result, the total computational cost associated to evaluations of the THML model at samples of the constructed experimental design is about 208 hours, without parallelization.

Furthermore, the LARS-based sparse PCE procedure of Blatman and Sudret (2011b) implemented in `UQLab` (Marelli and Sudret, 2014) is used so as to construct PCE. We use hyperbolic truncation sets $\mathcal{A}_{p,q} = \{\boldsymbol{\alpha} \in \mathbb{N}^d \mid \|\boldsymbol{\alpha}\|_q \leq p\}$ (see Section 1.2.4.2) with $q = 0.8$ in order to limit the number of regressors, since the input dimensionality is quite large ($d = 31$). Moreover, the degree p is adaptively chosen between 1 and 5 throughout the PCE construction procedure. Lastly, concerning PC-PCE surrogates, the number of principal components is chosen such that the PCA truncation-induced error is smaller than 10^{-3}.

5.3.2.2 Error estimation

Next, the validation error of the constructed (PC-)PCE surrogates (see Section 1.2.4.5) is estimated hereafter. Keeping notations introduced in Section 4.4.1 for strains, tangential intrados and extrados strains are denoted $\varepsilon_1, \varepsilon_2$, whereas vertical intrados and extrados strains by $\varepsilon_3, \varepsilon_4$. For each output quantity of interest, (PC-)PCE error estimates as well as the number of retained principal components (in the case of PC-PCEs) to achieve a PCA error smaller than 10^{-3} are summarized in Table 5.4. Regarding the water saturation ratio S_w, only 3 principal components have been retained, and the PC-PCE error of the corresponding surrogate is about $3.7 \cdot 10^{-3}$, which suggests a satisfactory accuracy. Furthermore, regarding strains $(\varepsilon_1, \ldots, \varepsilon_4)$, a number of 5 principal components has been retained, and involve PC-PCE errors of around $1.3 \cdot 10^{-2}$, which still constitutes an acceptable error level. Remark that PC-PCE errors are larger than those obtained in the VeRCoRs case, in Section 4.3.2, where PC-PCE errors of about 10^{-3} have been obtained. This may be attributable to the larger input dimension considered here, which involves a harder approximation problem. Then, prestressing losses Π are approximated with a PC-PCE with 3 principal components, and a PC-PCE error of about $2.7 \cdot 10^{-2}$. Lastly, concerning the diffuse leakage rate $Q_{d,0}$ which is approximated by a PCE (in a component-wise fashion), a PCE error (see Section 1.2.4.5) of about $1.1 \cdot 10^{-2}$ is obtained, which also constitutes a satisfactory error level.

	S_w	ε_1	ε_2	ε_3	ε_4	Π	$Q_{d,0}$
PC number	3	5	5	5	5	3	-
ϵ_{PCA}	$5.3 \cdot 10^{-4}$	$8.8 \cdot 10^{-4}$	$8.9 \cdot 10^{-4}$	$8.0 \cdot 10^{-4}$	$8.0 \cdot 10^{-4}$	$4.5 \cdot 10^{-4}$	-
ϵ_{PCE}	$1.4 \cdot 10^{-3}$	$1.2 \cdot 10^{-2}$	$1.1 \cdot 10^{-2}$	$1.4 \cdot 10^{-2}$	$1.4 \cdot 10^{-2}$	$2.0 \cdot 10^{-2}$	$1.1 \cdot 10^{-2}$
$\epsilon_{\text{PC-PCE}}$	$3.7 \cdot 10^{-3}$	$1.9 \cdot 10^{-2}$	$1.8 \cdot 10^{-2}$	$2.2 \cdot 10^{-2}$	$2.1 \cdot 10^{-2}$	$2.7 \cdot 10^{-2}$	-

Table 5.4: Summary of validation error estimates for (PC-)PCE surrogates of output variables of interest of the THML model.

5.3.3 Variance-based sensitivity analysis

In the following, Sobol' sensitivity indices are computed as in Section 4.3.3, namely either analytically from (PC-)PCE coefficients (see Section 1.2.5.2 and Appendix A), or through Monte Carlo estimation for leakage rates $Q_{l,0}, Q_{g,0}$ and Q_g, with $N = 10^6$ samples.

Besides, when considering models with multivariate outputs, it may be difficult to draw conclusions related to the relative importance of inputs based on Sobol' sensitivity indices. Furthermore, a simple averaging of these indices can be misleading, since a potentially large

weight may be attributed to terms associated to a small output variance. Hence, in order to provide concise indicators, we propose to use generalized Sobol' indices (Gamboa et al., 2013; Lamboni et al., 2011). Such indices consist in averaging all the Sobol' indices weighted by the variance of their corresponding output. Considering a model with n output components $(Y_t)_{1\leq t\leq n}$, the corresponding generalized Sobol' indices are written as follows:

$$GS_u = \frac{\sum_{t=1}^{n} \mathrm{Var}[Y_t] S_{t,u}}{\sum_{t=1}^{n} \mathrm{Var}[Y_t]} \tag{5.6}$$

where $S_{t,u}$ is the Sobol' index corresponding to the output Y_t, for $u \subseteq \{1, \ldots, d\}$.

Likewise, generalized total Sobol' indices are given by:

$$GT_i = \frac{\sum_{t=1}^{n} \mathrm{Var}[Y_t] T_{t,i}}{\sum_{t=1}^{n} \mathrm{Var}[Y_t]} \tag{5.7}$$

where $T_{t,i}$ the total Sobol' index corresponding to Y_t, for $i \in \{1, \ldots, d\}$.

Next, Sobol' sensitivity indices related to output THML variables of interest are presented. For the sake of concision, a particular attention will be paid for total Sobol' indices, which encapsulate the total contribution to the output variance of each single input.

5.3.3.1 Hydric behavior

Firstly, the time evolution of total Sobol' indices related to the water saturation ratio S_w is shown in Fig. 5.4. For the sake of readability, total Sobol' indices $(T_{t,i})_{1\leq t\leq n}$ verifying $\max_{1\leq t\leq n} T_{t,i} \leq 10^{-2}$ are not displayed. Moreover, time is normalized by the last instant of the simulated service period of the structure. Then, it clearly appears that only two parameters are mostly contributing to the output variance (by themselves and by their interactions), namely the drying parameter B and the initial water content $C_{w,0}$. Such a result has been observed at the scale of VeRCoRs mock-up by Bouhjiti (2018).

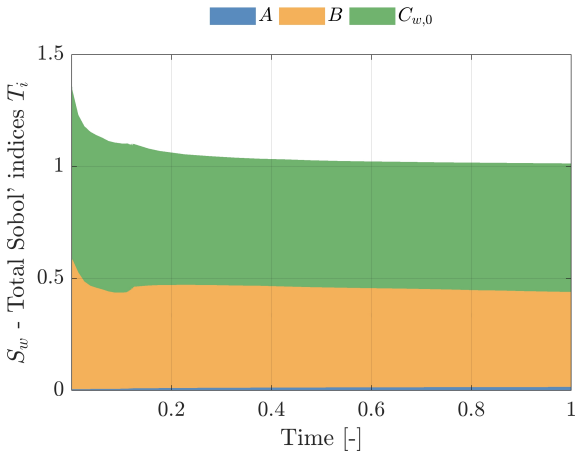

Figure 5.4: Water saturation ratio - Time evolution of total Sobol' indices.

In fact, regarding the drying behavior, the observed similarity between 1:3 and 1:1 scales was more or less expected, given the well-known scaling properties of diffusion equations (Granger, 1995). Indeed, let $f : \mathcal{D} \times \mathbb{R}_+ \to \mathbb{R}$ be a solution of the following diffusion equation on a domain $\mathcal{D} \subset \mathbb{R}^3$:

$$\nabla_{\boldsymbol{s}} \cdot (D(f)\nabla_{\boldsymbol{s}} u) = \frac{\partial f}{\partial t} \tag{5.8}$$

where D is a diffusion coefficient which possibly depends on f.

Moreover, let us consider a scaling constant $k > 0$ and the scaled domain $k\mathcal{D} = \{k\boldsymbol{s} \mid \boldsymbol{s} \in \mathcal{D}\}$. Then, it is possible to show that the function defined by:

$$\begin{aligned} \tilde{f} : k\mathcal{D} \times \mathbb{R}_+ &\to \mathbb{R} \\ (\boldsymbol{s}, t) &\mapsto f\left(\frac{\boldsymbol{s}}{k}, \frac{t}{k^2}\right) \end{aligned} \tag{5.9}$$

is a solution of the diffusion equation (5.8) on the domain $k\mathcal{D}$. It is worth noting that such a rationale has been applied to estimate drying kinetics of VeRCoRs mock-up, which is expected to dry nine times faster than an operating 1:1 scale NCB, as mentioned in Section 4.2.1. Then, the water saturation ratio being computed through solving a diffusion equation (see Section 3.3.3), it can be expected that the associated Sobol' sensitivity indices admit a similar scaling property.

Lastly, it can be seen on Fig. 5.4 that the sum of total Sobol' indices decreases from 1.4 to a value close to 1 at time $t \approx 0.15$, which approximately corresponds to the startup of the operating reactor. When the latter reaches the stationary regime (near $t \approx 0.2$), total Sobol' indices are practically not evolving over time as drying progresses. Moreover, interactions involving B and $C_{w,0}$ become negligible, as the sum of their total indices is practically equal to 1.

5.3.3.2 Mechanical behavior

Next, the time evolution of total Sobol' indices related to intrados strains is shown in Fig. 5.5. Results concerning extrados strains are sensibly similar, and are thereby not shown for the sake of brevity. Total Sobol' indices of tangential strains are firstly discussed (see Fig. 5.5a). During the prestressing phase (occurring before $t \approx 0.1$), the tension of tangential prestressing cables $\sigma_{\theta,0}$ presents the larger total index. The stiffness k_{rs} of reversible deviatoric basic creep also presents a significant importance during the prestressing phase, which vanishes over time once prestressing cables are tensioned. Moreover, a similar behavior is observed for the elastic Young's modulus of concrete E. In summary, the variability of the strain response is mainly driven by mechanical parameters during the prestressing phase. This could be linked to the duration of the prestressing phase, which may be small compared to the drying characteristic time of the containment wall.

Subsequently, after the end of prestressing phase, several parameters are significantly contributing to the output variance through their total effects, including drying parameters B and $C_{w,0}$, desiccation shrinkage coefficient α_{ds}, tangential prestressing $\sigma_{\theta,0}$ and desiccation creep viscosity η_{dc}. Furthermore, once the operating reactor reaches its stationary regime, their relative importance are very slowly evolving over time.

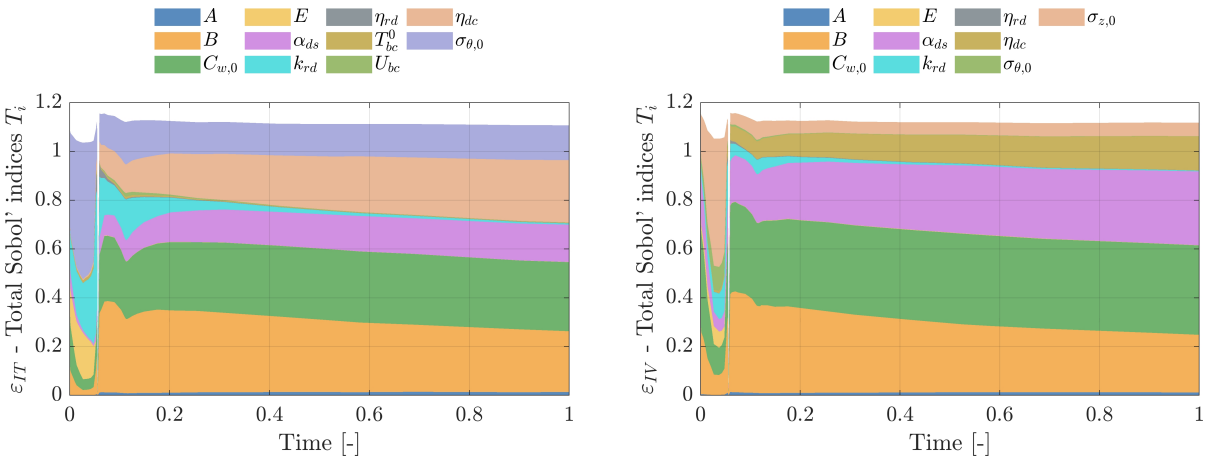

(a) Intrados tangential strains

(b) Intrados vertical strains

Figure 5.5: Intrados strains - Time evolution of total Sobol' indices.

Moreover, it is worth noting that the importance of the desiccation creep viscosity η_{dc} has been found to be negligible in the case of VeRCoRs mock-up (see Section 4.3.3), contrary to the scale 1:1 NCB studied here. This could be explained by the fact that creep is not completely scaled in the case of VeRCoRs. Thus, broadly speaking, in the VeRCoRs case, drying (which is accelerated) is more important than creep, whereas the reverse situation occurs in the case of the studied 1:1 scale NCB.

Next, total Sobol' indices related to vertical strains (see Fig. 5.5b) present a similar behavior to that for tangential strains, with the exception that during the prestressing phase, the tension of vertical cables $\sigma_{z,0}$ is the most important parameter, and the tangential prestressing $\sigma_{\theta,0}$ presents a non-negligible importance. This last effect has already been observed in the VeRCoRs case (see Section 4.3.3), and is plausibly attributable to the geometry of the adopted RSV as well as a Poisson effect linking tangential and vertical directions.

Then, generalized first order and total Sobol' indices related to intrados tangential and vertical strains are depicted in Fig. 5.6. It appears that 8 parameters are significantly contributing to the variability of strains, namely $C_{w,0}, B, \alpha_{ds}, E, \sigma_{\theta,0}, \sigma_{z,0}, k_{rd}$ and η_{dc}. It is worth mentioning that the Young's modulus E is indicated to be significantly important by the computed generalized indices, however, this parameter is only important during the prestressing phase, as highlighted by Fig. 5.5. Furthermore, concerning prestressing losses Π, a similar ranking of input parameters is observed, and therefore Sobol' indices related to Π are not shown for the sake of brevity.

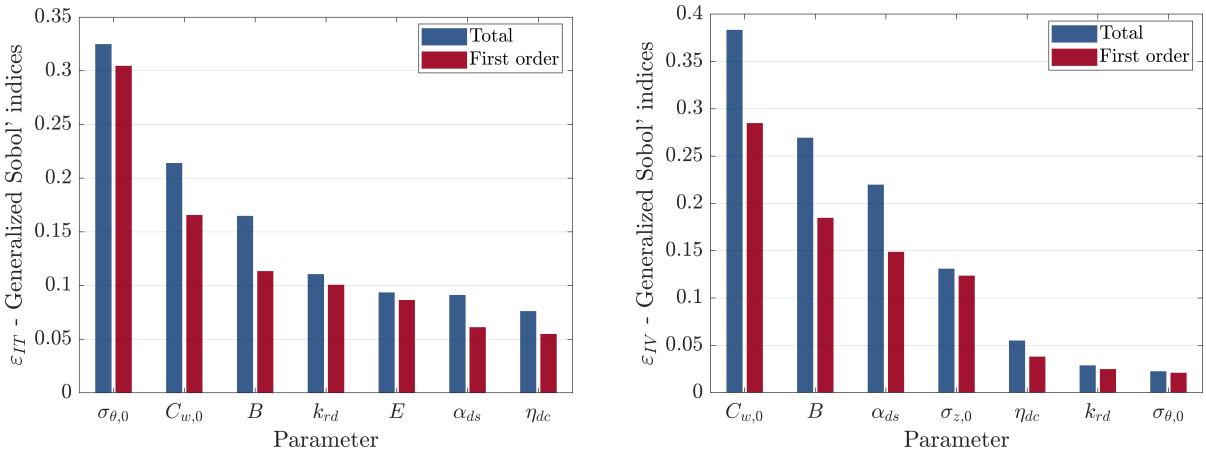

(a) Intrados tangential strains **(b)** Intrados vertical strains

Figure 5.6: Intrados strains - Generalized Sobol' indices.

5.3.3.3 Leakage behavior

Then, Sobol' sensitivity indices related to diffuse, local and global leakage rates are presented and discussed hereafter. Firstly, the time evolution of total Sobol' indices related to diffuse and local leakage rates during simulated pressurization tests is presented in Fig. 5.7. As observed in the VeRCoRs case, 3 parameters are mostly contributing to the output variance of diffuse leakage, namely the drying parameter B, the initial water content $C_{w,0}$, and the intrinsic permeability k_0 (see Fig. 5.7a). The importance of the Klinkenberg coefficient β_K is much smaller.

Furthermore, 5 parameters present a significant importance, namely drying parameters $B, C_{w,0}$, desiccation shrinkage coefficient α_{ds}, desiccation creep viscosity η_{dc} and local leak model parameter α_l. In this context, the parameter α_l is observed to be the most important one, as in the VeRCoRs case (see Section 4.3.3). It is also worth noting that the importance of the aforementioned parameters does practically not evolve over time. Lastly, the important parameters of the diffuse leakage response seem to present significant interactions, especially during the early pressurization tests. Indeed, during these tests, the sum of total Sobol' indices is significantly higher than 1.

Next, the time evolution of total Sobol' indices related to the global leakage rate (without and with coatings) is shown in Fig. 5.8. In the absence of coatings, only 5 parameters mainly explain the output variance through their total effects, over the 31 uncertain inputs of the model. These important parameters are given by the drying parameter B and the initial water content $C_{w,0}$, desiccation shrinkage coefficient α_{ds}, intrinsic permeability k_0 and local leak model parameter α_l.

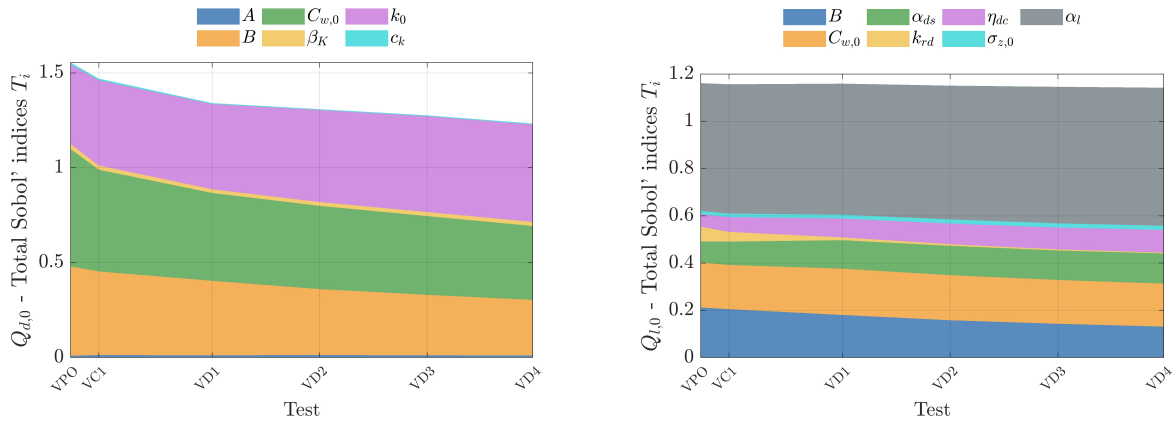

(a) Diffuse leakage rate **(b)** Local leakage rate

Figure 5.7: Diffuse and local leakage rates - Time evolution of total Sobol' indices.

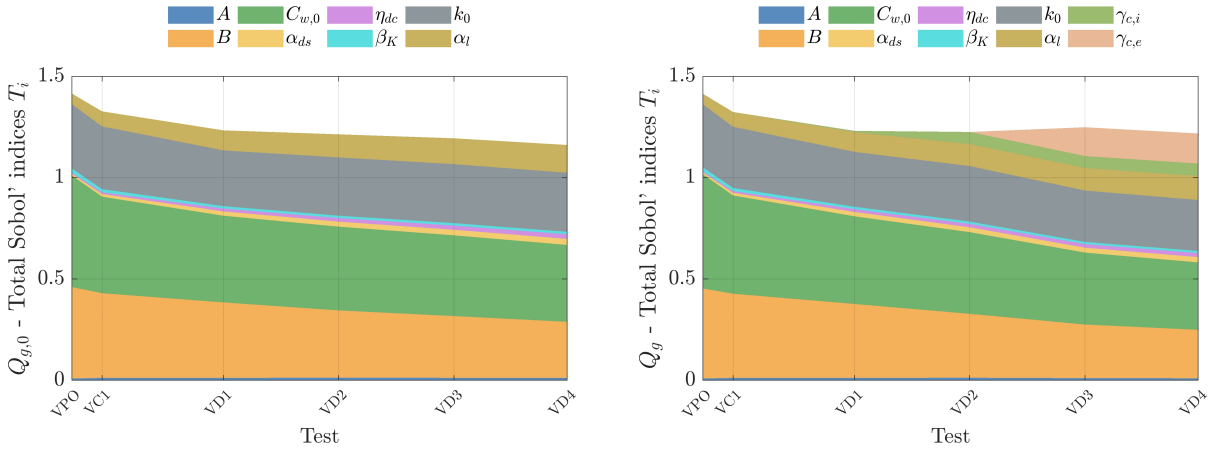

(a) Without coatings **(b)** With coatings

Figure 5.8: Global leakage rate (without and with coatings) - Time evolution of total Sobol' indices.

Then, in the presence of coatings, total Sobol' indices of the aforementioned important parameters present a similar behavior than in the case without coatings. However, from the VD1 pressurization test, the importance of the intrados coatings efficiency parameter $\gamma_{c,i}$ becomes significant. This corresponds to the early positioning of coatings on the intrados surface for the VD1 test (see Fig. 5.3). Likewise, the total Sobol' index of the extrados coatings efficiency parameter $\gamma_{c,e}$ significantly increases from VD3 test, which corresponds to an increase of the surface of extrados coatings, as indicated by Fig. 5.3. The total index of the parameter $\gamma_{c,e}$ is larger than that of parameter $\gamma_{c,i}$, which may be explained by the fact that the surface of extrados coatings is larger than that of intrados ones. Lastly, the most important parameters related to global leakage are summarized in Fig. 5.9, in which generalized first order and total Sobol' indices are presented.

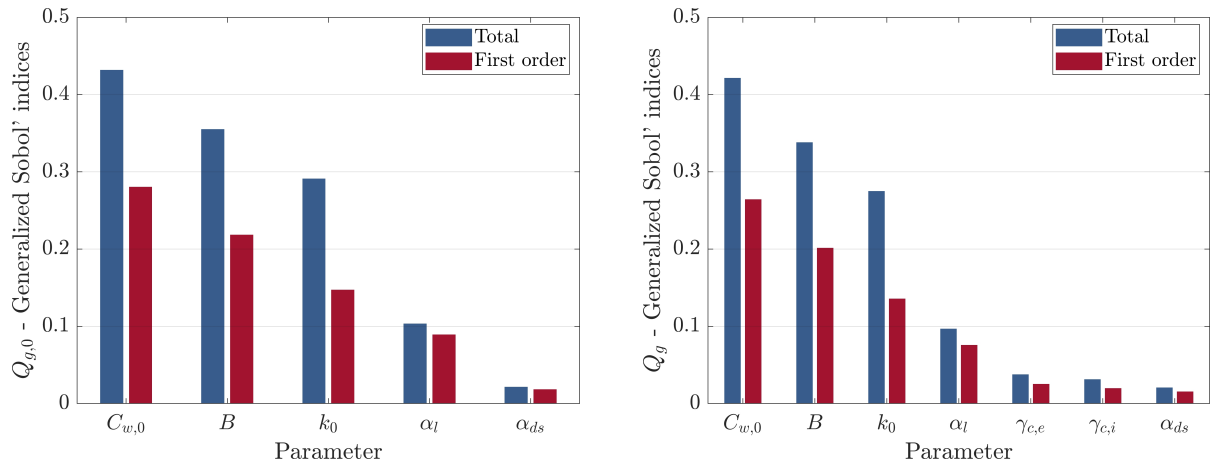

(a) Without coatings **(b)** With coatings

Figure 5.9: Global leakage rate (without and with coatings) - Generalized Sobol' indices.

5.4 Reliability analysis of the leakage behavior

In Section 5.3, a large scale sensitivity analysis based on Sobol' indices has been performed in order to identify the PII on the variability of THML output variables of interest. Amongst the 31 uncertain input parameters of the THML model presented in Section 5.2, about ten have been identified as important, notably regarding the variability of strain and leakage responses. Thus, the input dimensionality of UQ problems (including reliability analysis) can be significantly reduced. Next, based on the identified PII, a reliability analysis related to the leakage behavior of the studied NCB is presented in Section 5.4.1. Subsequently, in Section 5.4.2, we propose to use perturbed-law based sensitivity indices, in order to assess the effect of the choice of the distribution of PII on PoF related to the leakage behavior of the studied NCB.

5.4.1 Prior-based reliability analysis

5.4.1.1 Prior distribution

Firstly, the characteristics of the probability distribution of each of the PII identified in Section 5.3 are summarized in Table 5.4.1. The parameters retained as PII correspond to those identified as important regarding the variability of strain and leakage responses. For the sake of simplicity, these parameters are assumed to be mutually independent. It is worth noting that the Young's modulus E, which presented a significant importance during the prestressing phase (see Section 5.3.3.2), is not modeled by a random variable here, since we focus on the long-term phase of the structure. Then, the remaining THML inputs are fixed to their nominal value, corresponding to the mean value specified in Table 5.3.

From a Bayesian point of view, the defined probability distribution of PII may be seen as a prior, since it does not integrate observational data. In Section 5.5, this prior will be updated from *in-situ* monitoring data of the structure in a Bayesian setting, in order to infer input parameters but also update PoF estimates.

n°	Parameter	Units	Distribution	Bounds	Mean	Std	CoV
1	A	10^{-13} m^2.s^{-1}	Lognormal	-	1.95	0.49	0.25
2	B	10^{-2}	Lognormal	-	6.80	1.70	0.25
3	$C_{w,0}$	l.m^{-3}	Lognormal	-	128.00	32.00	0.25
4	α_{ds}	10^{-6} kg.m^{-3}	Lognormal	-	10.00	2.50	0.25
5	k_{rd}	10^{10} Pa	Lognormal	-	5.98	1.49	0.25
6	κ	10^{-4}	Lognormal	-	1.00	0.25	0.25
7	η_{dc}	10^{9} Pa.s	Lognormal	-	7.39	1.85	0.25
8	$\sigma_{\theta,0}$	MPa	Lognormal	-	$1.48 \cdot 10^3$	371.67	0.25
9	$\sigma_{z,0}$	MPa	Lognormal	-	$1.48 \cdot 10^3$	371.67	0.25
10	β_K	MPa	Lognormal	-	0.20	0.05	0.25
11	k_0	10^{-17} m^2	Lognormal	-	15.00	7.50	0.50
12	α_l	-	Lognormal	-	10.00	5.00	0.50
13	$\gamma_{c,i}$	-	Truncated Gaussian	$[0;1]$	0.50	0.25	0.50
14	$\gamma_{c,e}$	-	Truncated Gaussian	$[0;1]$	0.50	0.25	0.50

Table 5.5: Prior distribution of the PII of the THML model.

5.4.1.2 Surrogate modeling

Then, in order to ensure the tractability of UQ techniques, (PC-)PCE surrogates are constructed with the same settings as in Section 5.3.2, this time based on the prior distribution of PII presented in Section 5.4.1. (PC-)PCE error estimates are briefly summarized in Table 5.6. It is remarked that only slightly smaller error estimates than in Section 5.3.2 are obtained, in spite of the smaller input dimensionality of the approximation problem.

This similarity between error estimates of PII-based (Table 5.6) and full-inputs-based PCEs (Table 5.4) may be explained by the LARS sparse regression algorithm used in the PCE construction procedure of Blatman and Sudret (2011b), which tends to only select regressors that mostly contribute to the output variance. In this way, even in the case of a large input dimensionality, the LARS algorithm enables to exploit the structure of the function to approximate, by focusing on input-output relationships involving PII, to a certain extent.

	ε_1	ε_2	ε_3	ε_4	Π	$Q_{d,0}$
PC number	5	5	5	5	3	-
ϵ_{PCA}	$6.2 \cdot 10^{-4}$	$6.2 \cdot 10^{-4}$	$5.6 \cdot 10^{-4}$	$5.6 \cdot 10^{-4}$	$7.4 \cdot 10^{-4}$	-
ϵ_{PCE}	$9.4 \cdot 10^{-3}$	$9.3 \cdot 10^{-3}$	$1.2 \cdot 10^{-2}$	$1.2 \cdot 10^{-2}$	$1.5 \cdot 10^{-2}$	$6.2 \cdot 10^{-3}$
$\epsilon_{\text{PC}-\text{PCE}}$	$1.4 \cdot 10^{-2}$	$1.4 \cdot 10^{-2}$	$1.8 \cdot 10^{-2}$	$1.8 \cdot 10^{-2}$	$2.3 \cdot 10^{-2}$	-

Table 5.6: Summary of validation error estimates for (PC-)PCE surrogates of output variables of interest of the THML model, based on the prior of PII defined in Section 5.4.1.

5.4.1.3 Probability of failure estimation

Let $(\Omega, \mathcal{F}, \mathbb{P})$ be a probability space. The PII described in Section 5.4.1 are denoted by $\boldsymbol{X} : \Omega \to \mathcal{D}_{\boldsymbol{X}}$, and their joint prior density is denoted by π. Since the components of $\boldsymbol{X}$ are assumed to be mutually independent, this density reads $\pi(\boldsymbol{x}) = \prod_{i=1}^{d} \pi_i(x_i)$ for all $\boldsymbol{x} = (x_1, \ldots, x_d) \in \mathcal{D}_{\boldsymbol{X}}$, where π_i denotes the marginal density of X_i, for $i \in \{1, \ldots, d\}$.

In the following, we focus on the pressurization test of the third decennial visit of the studied NCB (*i.e.* VD3 test). Then, the global leakage rate Q_g during this test may be seen as a scalar-valued deterministic function $\mathcal{M}_{Q_g} : \mathcal{D}_{\boldsymbol{X}} \to \mathbb{R}$. Let $Q_* > 0$ be a leakage threshold value that must be not exceeded. In this setting, the following PoF will constitute our main target quantity of interest:

$$P_f = \mathbb{P}(\mathcal{M}_{Q_g}(\boldsymbol{X}) \geq Q_*) = \int_{\mathcal{D}_{\boldsymbol{X}}} \mathbf{1}_{\{\mathcal{M}_{Q_g} \geq Q_*\}}(\boldsymbol{x}) \pi(\boldsymbol{x}) \mathrm{d}\boldsymbol{x} \tag{5.10}$$

Furthermore, in order to assess the impact of possible repair works, three different coatings scenarios are considered in the following, for illustrative purposes. These scenarios are labeled from (a) to (c), and correspond to an increasing surface of extrados coatings, and a fixed surface of intrados coatings. Then, it is aimed to estimate the PoF given in Eq. (5.10) for each coating scenario. To that end, Monte Carlo simulation (see Section 1.2.6.1) is used, with 10^6 samples. Moreover, for comparison purposes, the SuS algorithm (see Section 1.2.6.2) is also used, with 5000 samples per level. As for SuS computations within the BuS framework (see Chapter 2), MCMC sampling within SuS is performed with the adaptive Conditional Sampling (aCS) algorithm of Papaioannou et al. (2015) presented in Appendix B.

Estimates of the aforementioned PoFs are summarized in Table 5.7. Broadly speaking, the obtained PoF estimates vary from about 0.2 in case (a) to 0.09 in case (c). As expected, the increase of coated surface induces a decrease of the estimated PoF. For all the considered coatings scenarios, values of estimated PoFs are quite large, though. This may be explained by the somewhat large uncertainties encoded in the adopted prior distribution (see Section 5.4.1.1). Furthermore, estimated CoVs are smaller than that obtained with the SuS algorithm, which is explained by the somewhat large PoFs involved and the large amount of MCS samples considered here. Moreover, the SuS algorithm only requires one subset to estimate the target PoF in case (a) and two subsets in case (b), which makes it unnecessary given the efficiency of MCS for this problem, to a certain extent.

Case	Method	Model calls	$\hat{P}_f$	CoV$[\hat{P}_f]$	95% CI
(a)	MCS	10^6	$1.97 \cdot 10^{-1}$	$2.01 \cdot 10^{-3}$	$[1.97;\ 1.98] \times 10^{-1}$
	SuS	$5 \cdot 10^3$	$1.99 \cdot 10^{-1}$	$4.24 \cdot 10^{-2}$	$[1.83;\ 2.16] \times 10^{-1}$
(b)	MCS	10^6	$1.58 \cdot 10^{-1}$	$2.30 \cdot 10^{-3}$	$[1.57;\ 1.59] \times 10^{-1}$
	SuS	$5 \cdot 10^3$	$1.49 \cdot 10^{-1}$	$4.24 \cdot 10^{-2}$	$[1.37;\ 1.61] \times 10^{-1}$
(c)	MCS	10^6	$8.84 \cdot 10^{-2}$	$3.20 \cdot 10^{-3}$	$[8.79;\ 8.90] \times 10^{-2}$
	SuS	10^4	$8.22 \cdot 10^{-2}$	$4.45 \cdot 10^{-2}$	$[7.51;\ 8.94] \times 10^{-2}$

Table 5.7: Prior-based reliability analysis - PoF estimates for two coatings scenarios.

5.4.2 Robustness analysis via perturbed-law based indices

5.4.2.1 Perturbed-law based sensitivity indices

The PoF given in Eq. (5.10) depends on the probability law of the input parameters $\boldsymbol{X}$ presented in Section 5.4.1.1. Besides, as in the framework of other UQ tasks, the choice of such a probability law constitutes a critical hypothesis. Indeed, whatever the way adopted to choose it, the law of inputs $\boldsymbol{X}$ itself is known with some level of confidence, which corresponds to second-level uncertainties. Then, it is necessary to quantify the impact of such second-level uncertainties on the PoF given in Eq. (5.10), in order to provide a more comprehensive reliability analysis of the leakage behavior of the studied NCB.

As mentioned in Section 1.2.3, several approaches have been proposed in the literature so as to handle second-level uncertainties. In particular, the new branch of robustness analysis in UQ has recently emerged in the field of sensitivity analysis (Hart and Gremaud, 2019; Iooss et al., 2021; Perrin and Defaux, 2019). It consists in assessing the impact of the choice of the input distribution, and analyzing variations of some QoI with respect to this choice. In this framework, a particularly interesting approach has been proposed in the framework of reliability-oriented sensitivity analysis, namely perturbed-law based sensitivity indices (PLI) (Lemaître, 2014) (see also (Lemaître et al., 2015; Sueur et al., 2016)). This approach only requires a Monte Carlo sample of model inputs and outputs, and enables to explicitly focus on a QoI specified by the analyst (Iooss et al., 2021). Furthermore, various types of QoI can be handled with this approach: indeed, PLI originally focused on PoFs (Iooss and Le Gratiet, 2019; Lemaître et al., 2015; Sueur et al., 2016), but then have been extended to quantiles (Sueur et al., 2017) and superquantiles (Iooss et al., 2021).

The core idea behind PLI consists in perturbing probability distributions. In this context, Lemaître et al. (2015) proposed to perturb input densities, by replacing each marginal density π_i by a perturbed one $\pi_{i\delta}$, where $\delta \in \mathbb{R}$ is interpreted as a shift of a moment (*e.g.* mean or variance). The simplest case of moment perturbation is given by mean shifting, and consists in finding a density $\pi_{i\delta}$ such that its mean equals $\mathbb{E}[X_i] + \delta$, namely:

$$\int_{\mathcal{D}_{X_i}} x_i \pi_{i\delta}(x_i) \mathrm{d}x_i = \mathbb{E}[X_i] + \delta \tag{5.11}$$

for $i \in \{1, \ldots, d\}$. Furthermore, Lemaître et al. (2015) proposed general perturbation constraints:

$$\int_{\mathcal{D}_{X_i}} g_k(x_i) \pi_*(x_i) \mathrm{d}x_i = \delta_k \tag{5.12}$$

where $g_k : \mathcal{D}_{X_i} \to \mathbb{R}$ is a given function and $\delta_k \in \mathbb{R}$ a prescribed value, for $k \in \{1, \ldots, K\}$. Such constraints notably include variance shifting, by setting $g_1(x_i) = x_i$, $g_2(x_i) = x_i^2$, $\delta_1 = \mathbb{E}[X_i]$ and $\delta_2 = \delta + \mathbb{E}[X_i]^2$ in Eq. (5.12), where $\delta > 0$ is the prescribed variance.

However, even in the simple case of mean shifting, several densities may satisfy the mean shifting constraint in Eq. (5.11). Hence, the definition of constraints in Eq. (5.12) may be ambiguous. In order to address this problem, Lemaître et al. (2015) proposed to define the perturbed density $\pi_{i\delta}$ as the closest one from π_i in the KLD sense, under the perturbation constraints in Eq. (5.12):

$$\pi_{i\delta} = \underset{\pi_* \in \mathcal{P}}{\arg\min}\ D_{\mathrm{KL}}(\pi_* \| \pi_i) \tag{5.13}$$

where $\mathcal{P}$ is the set of probability density functions satisfying the constraints in Eq. (5.12).

In particular, in the simple case of the Gaussian distribution $\mathcal{N}(0,1)$, the density $\pi_{i\delta}$ in Eq. (5.13) is simply given by the density of $\mathcal{N}(\delta,1)$ in the case of a mean shifting of δ (see (Lemaître et al., 2015)). Likewise, in the case of variance shifting, $\pi_{i\delta}$ is given by the density of $\mathcal{N}(0,\delta)$.

Nevertheless, the problem in Eq. (5.13) may not be solved analytically in the general case, and minimizing the KLD in Eq. (5.13) can be difficult numerically (Iooss et al., 2021; Lemaître et al., 2015). Moreover the applied perturbations may be not comparable from an input variable to another, since the variation domains $(\mathcal{D}_{X_i})_{1\leq i\leq d}$ may be not identical. In this context, a simple approach proposed in (Perrin and Defaux, 2019) consists in firstly applying an iso-probabilistic transformation (see Section 1.2.3.3) in order to map each input variable X_i into a standard normal one. Subsequently, the obtained Gaussian variables may be straightforwardly perturbed, following the paragraph above. Besides, it is important to keep in mind that such a simple approach still presents some drawbacks, including the fact that similar perturbations in the standard space may induce sensibly different perturbations in the physical space. In this context, it is worth mentioning that Gauchy et al. (2022) recently presented a more general approach for perturbing probability distributions, based on information geometry. Such an approach is considered to be out of the scope of this chapter, though.

Broadly speaking, a PLI measures the impact of the perturbation of an input density on a given QoI. In the following, we focus on the definition of PLI for PoFs proposed in (Lemaître, 2014) and (Lemaître et al., 2015). Firstly, for $i \in \{1,\dots,d\}$, the i-th marginal density π_i is changed into a perturbed density $\pi_{i\delta}$, by specifying a perturbation level $\delta \in \mathbb{R}$.

Subsequently, replacing the density π_i by its perturbed counterpart $\pi_{i\delta}$ in the expression of the PoF in Eq. (5.10) leads to the following perturbed PoF:

$$P_{i\delta} = \int_{\mathcal{D}_{\boldsymbol{X}}} \mathbf{1}_{\{\mathcal{M}_{Q_g}>Q_*\}}(\boldsymbol{x}) \frac{\pi_{i\delta}(x_i)}{\pi_i(x_i)} \pi(\boldsymbol{x}) \mathrm{d}\boldsymbol{x} \tag{5.14}$$

Then, the PLI related to the i-th input X_i is defined by:

$$S_{i\delta} = \left(\frac{P_{i\delta}}{P_f} - 1\right) \mathbf{1}_{\{P_{i\delta}>P_f\}} + \left(1 - \frac{P_f}{P_{i\delta}}\right) \mathbf{1}_{\{P_{i\delta}<P_f\}} \tag{5.15}$$

where $\mathbf{1}_{\{P_{i\delta}>P_f\}} = 1$ if $P_{i\delta} > P_f$ and 0 else.

The index defined in Eq. (5.15) is equal to zero when $P_f = P_{i\delta}$, *e.g.* when perturbating π_i presents a negligible impact on the PoF, or when the perturbation level δ is small. Furthermore, the sign of $S_{i\delta}$ provides an indication about the way perturbations of inputs affect the PoF: if $S_{i\delta} > 0$, the uncertainties related to the probabilistic modeling of the input X_i tend to increase the failure risk. Such a situation suggests to analyze uncertainties related to X_i more accurately (Lemaître et al., 2015). Conversely, a negative PLI (*i.e.* $S_{i\delta} < 0$) corresponds to a smaller perturbed PoF.

5.4.2.2 Reverse importance sampling for PLI estimation

Let $\mathcal{X} = \{\boldsymbol{x}^{(k)}\}_{1\leq k\leq N} \subset \mathcal{D}_{\boldsymbol{X}}$ be a sample of N independent realizations of the inputs $\boldsymbol{X}$. Firstly, based on classical Monte Carlo simulation (see Section 1.2.6.1), the following estimator is available for the PoF in Eq. (5.10):

$$\hat{P}_{f,N} = \frac{1}{N}\sum_{k=1}^{N} \mathbf{1}_{\{\mathcal{M}_{Q_g}\geq Q_*\}}(\boldsymbol{x}^{(k)}) \tag{5.16}$$

Furthermore, following Lemaître et al. (2015), the perturbed PoFs $(P_{i\delta})_{1\leq i\leq d}$ can be estimated from $\mathcal{X}$ through reverse importance sampling (Hesterberg, 1996):

$$\hat{P}_{i\delta,N} = \frac{1}{N}\sum_{k=1}^{N} \mathbf{1}_{\{\mathcal{M}_{Q_g}\geq Q_*\}}(\boldsymbol{x}^{(k)}) \frac{\pi_{i,\delta}(x_i^{(k)})}{\pi_i(x_i^{(k)})} \tag{5.17}$$

Then, the PLI $S_{i\delta}$ can be estimated by the following plug-in estimator:

$$\hat{S}_{i\delta,N} = \left(\frac{\hat{P}_{i\delta,N}}{\hat{P}_{f,N}} - 1\right)\mathbf{1}_{\{\hat{P}_{i\delta,N}>\hat{P}_{f,N}\}} + \left(1 - \frac{\hat{P}_{f,N}}{\hat{P}_{i\delta,N}}\right)\mathbf{1}_{\{\hat{P}_{i\delta,N}<\hat{P}_{f,N}\}} \tag{5.18}$$

A proof of the asymptotic normality of the estimator in Eq. (5.18) has been provided by Lemaître et al. (2015). Furthermore, the same authors derived an expression for the asymptotic variance of this estimator, which enables to compute confidence intervals for the estimated PLI. This expression is not detailed here for the sake of brevity, and the reader is referred to (Lemaître et al., 2015) for a comprehensive study on theoretical aspects of PLI estimators.

5.4.2.3 Application to the leakage behavior

Next, PLI related to the PoF in Eq. (5.10) are computed from the estimators presented in Section 5.4.2.2. To that end, we use our `Matlab` implementation of PLI, but it is worth noting that such indices are implemented in the `sensitivity` `R` package. Moreover, only the coating scenario (c) (see Section 5.4.1.3) is considered here, for the sake of brevity.

Two types of input density perturbation are considered in the following, namely mean and variance shifting. In this context, the inputs $\boldsymbol{X}$ are beforehand transformed into the standard normal space, as described in Section 5.4.2.1. Since the components of $\boldsymbol{X}$ are assumed to be mutually independent, such an operation simply consists in applying the inverse probability distribution transform (see Section 1.2.3.3) component-wise. Then, concerning mean shifting, the mean of each input is perturbed with $\delta \in [-1.64;\ 1.64]$, following Iooss et al. (2021). This perturbation range corresponds to 5%-quantile and 95%-quantile of a standard normal variable. Regarding variance shifting, the variance of each input is perturbed with $\delta \in [1/20, 2.5]$. Furthermore, a Monte Carlo sample of $N = 10^6$ samples is considered so as to estimate PLI through Eqs. (5.16) to (5.18).

Firstly, the computed mean shifting PLI are presented in Fig. 5.10, and are discussed hereafter. Only the 6 most influential parameters are shown, for the sake of readability. Broadly speaking, parameters with significant PLI values roughly correspond to parameters

with large Sobol' sensitivity indices related to the global leakage response (see Fig. 5.8). However, the meaning of PLI indices is different from Sobol' indices, since PLI quantify the impact of the lack of knowledge about the law of inputs $\boldsymbol{X}$.

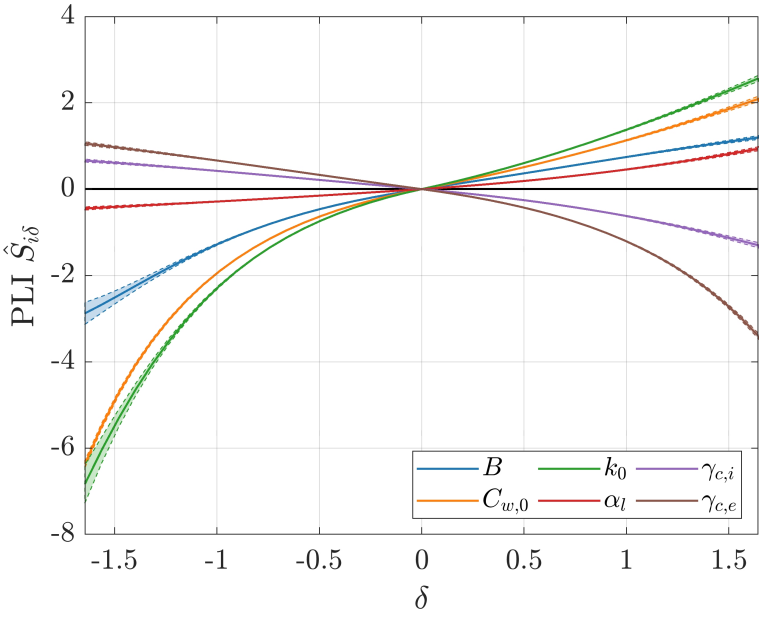

Figure 5.10: PLI related to the leakage PoF in Eq. (5.10) - Mean shifting. *PLI estimates are plotted with their* 95% *CI, shown in dashed lines.*

The PLI associated to the drying parameter B continuously increases when the perturbation level δ increases, and have the same sign as δ. Hence, a decrease of the mean of B induces a smaller PoF, whereas an increase of the mean tends to increase the risk of exceeding the prescribed leakage threshold Q_*. This is consistent with the fact that decreasing the mean of B tends to slow drying, which leads to a higher water saturation and then a lower gas permeability. It is also worth noting that confidence intervals of the PLI of B become larger when δ decreases. This may be explained by the fact that smaller PoFs have to be estimated when δ takes negative values, which tends to increase the CoV of PoF estimates since a fixed Monte Carlo sample size is considered here (see *e.g.* (Sueur et al., 2016) for a more efficient sampling scheme for PLI estimation).

Then, PLI related to the initial water content $C_{w,0}$ and the intrinsic permeability k_0 present a similar behavior to that observed for B, but amplified in terms of absolute values. In particular, a positive perturbation of the mean of k_0 leads to a significant increase of the failure risk, which is consistent with the fact that the global leakage behavior is mainly driven by diffuse leaks, and thus by Darcy's permeability of the containment wall. Next, the PLI of the local leak model parameter α_l also presents a similar behavior than that of PLI of parameters $B, C_{w,0}$ and k_0, with smaller absolute values, though. As mentioned earlier (see Section 5.3.3.3), these smaller values suggest that local leaks are less contributing to the global leakage rate at 1:1 scale.

Lastly, PLI of coatings efficiency parameters $\gamma_{c,i}$ and $\gamma_{c,e}$ present a peculiar behavior compared to the other parameters. Positive perturbations of their mean value lead to decrease the risk of exceeding the leakage threshold. This simply translates the beneficial effect of an efficient coating device regarding the leakage behavior of the structure. Conversely, a

negative δ induces an increase of the failure risk, which is expected in the case of less efficient coating devices. Moreover, in terms of absolute values, the PLI associated to extrados coatings efficiency s$\gamma_{c,e}$ are larger than the PLI of $\gamma_{c,i}$. Such a difference may be explained by the fact that the surface of extrados coatings is higher than that of intrados ones.

Next, variance shifting PLI are presented in Fig. 5.11. The most influential inputs in terms of mean shifting PLI are also the most influential in terms of variance shifting PLI. The variance shifting PLI of the parameter $\gamma_{c,i}$ is not shown here, though, since its values are close to zero. The PLI of the remaining parameters all present the same behavior with respect to the applied variance perturbation. Indeed, for each input, a variance reduction (*i.e.* $\delta < 1$) induces a reduced PoF, whereas a variance increase (*i.e.* $\delta > 1$) tends to increase the failure risk. The PLI of the intrinsic permeability k_0 is the largest index in absolute values, followed by the PLI of the initial water content $C_{w,0}$. Furthermore, PLI of the other parameters are sensibly close to each others.

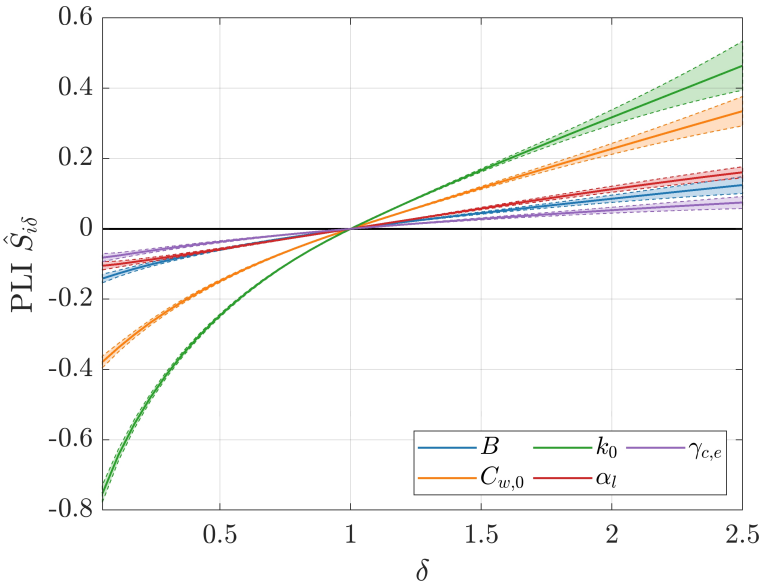

Figure 5.11: PLI related to the leakage PoF in Eq. (5.10) - Variance shifting. *PLI estimates are plotted with their* 95% *CI, shown in dashed lines.*

Thus, the presented PLI enabled a comprehensive study of the effect of each input parameter on the risk of exceeding the considered leakage threshold. In particular, such indices enabled to highlight parameters for which uncertainties in their probabilistic modeling may lead to increase the leakage failure risk. This suggests to analyze more thoroughly the uncertainties tainting the concerned input parameters. In the next section, Bayesian inference will be used to quantify the uncertainties of these parameters in an inverse manner, from observations of the response of the studied NCB.

5.5 Bayesian inverse analysis

In this section, we propose to quantify the uncertainties tainting input parameters in an inverse manner, through Bayesian inference, from observations of the response of the structure. In Chapter 4, we have presented a general methodology aiming at achieving this goal, notably through estimating the posterior distribution resulting from the combination of the prior and observed monitoring data. However, this posterior distribution induces an update of the PoF in Eq. (5.10) related to the leakage behavior of the structure. Hence, a particular attention being paid here for the estimation of the risk of exceeding leakage thresholds, we propose an approach for updating both input parameters and PoFs from observational data. In this context, this approach uses the BuS framework presented in Chapter 2, and shares a common basis with the methodology presented in Chapter 4.

Firstly, the proposed reliability-oriented Bayesian approach is presented, and subsequently applied to the studied structure in Section 5.5.1. Next, as the proposed approach also provides samples from the posterior distribution, the latter may be analyzed and then used so as to perform new predictions of the THML behavior of the structure, in the same fashion as in Chapter 4. Then, characteristics of the estimated posterior distribution are presented in Section 5.5.2, and posterior predictions of the THML response of the studied NCB are performed in Section 5.5.3.

5.5.1 Bayesian updating of probabilities of failure

5.5.1.1 Formulation

Firstly, based on the methodology presented in Chapter 4, a statistical model linking predictions of the THML model described in Section 5.2 to observations of the response of the structure is devised. In the following, three observation data sets will be considered, namely *in-situ* strain measurements provided by vibrating wire sensors embedded in the standard zone of the studied NCB for a period starting from the end of the prestressing phase to the VD2 test, as well as local and global leakage measurements performed during the VD2 test.

Keeping notations introduced in Section 4.4.2, the whole observation data set is denoted by $\mathcal{Y} = \{y_{Q_l}, y_{Q_g}\}$, and the (vector-valued) model mapping input parameters to the strain, local and global leakage responses is denoted by $\mathcal{M} : \mathcal{D}_{\boldsymbol{X}} \rightarrow \mathcal{D}_{\boldsymbol{Y}}$. Then, denoting by $\boldsymbol{Y} = (\boldsymbol{Y}_{\varepsilon}, \boldsymbol{Y}_{Q_l}, \boldsymbol{Y}_{Q_g})$ observables related to strain, local and global leakage responses, the following Gaussian additive model is considered:

$$\boldsymbol{Y}|\boldsymbol{x} = \mathcal{M}(\boldsymbol{x}) + \boldsymbol{E} \tag{5.19}$$

where $\boldsymbol{E} \sim \mathcal{N}(\boldsymbol{0}, \boldsymbol{\Sigma})$ is a centered Gaussian random variable with covariance matrix $\boldsymbol{\Sigma}$. For the sake of simplicity, this matrix is assumed to have the same diagonal structure than in Section 4.4.2, with known entries. Then, the posterior density of inputs $\boldsymbol{X}$ given the observed data set $\mathcal{Y}$ is given by:

$$\pi(\boldsymbol{x}|\mathcal{Y}) \propto \pi(\boldsymbol{x})\mathcal{L}(\boldsymbol{x}) \tag{5.20}$$

where $\mathcal{L}$ denotes the likelihood function associated to $\mathcal{Y}$ (see Section 4.4.2 for further details).

Up to this point, there is no difference with the Bayesian framework presented in Chapter 4. In this chapter, a particular attention is paid to the estimation of PoF related to the leakage behavior of NCB. Then, in comparison to the prior-based PoF defined in Eq. (5.10), observing the data $\mathcal{Y}$ leads to a posterior PoF given by:

$$P_{f|\mathcal{Y}} = \mathbb{P}(\mathcal{M}_{Q_g}(\boldsymbol{X}) \geq Q_*|\mathcal{Y}) = \int_{\mathcal{D}_{\boldsymbol{X}}} \mathbf{1}_{\{\mathcal{M}_{Q_g}>Q_*\}}(\boldsymbol{x})\pi(\boldsymbol{x}|\mathcal{Y})\mathrm{d}\boldsymbol{x} \tag{5.21}$$

It is remarked that this posterior PoF is simply obtained by replacing the prior density π by its posterior counterpart in the expression of the prior PoF in Eq. (5.10). Nevertheless, the posterior density $\pi(\cdot|\mathcal{Y})$ is not known explicitly, which makes the estimation of the posterior PoF in Eq. (5.21) more difficult than the estimation of the prior one. A simple approach could consist in generating posterior samples with the approach presented in Chapter 4, and subsequently estimating the PoF in Eq. (5.21) from the generated posterior samples. Nevertheless, such an approach may be not computationally efficient, since a large number of posterior samples may be required.

Consequently, based on the former work of Straub et al. (2016), we propose an alternative approach based on the BuS framework so as to estimate the posterior PoF in Eq. (5.21). Firstly, based on the equivalence principle between Bayesian inference and structural reliability described in Section 2.2, the posterior distribution can be linked to the following equivalent failure event:

$$\mathcal{D}_o = \{(\boldsymbol{x}, \upsilon) \in \mathcal{D}_{\boldsymbol{X}} \times [0,1] \mid \mathcal{H}(\boldsymbol{x}, \upsilon) \leq 0\} \tag{5.22}$$

where $\mathcal{H}(\boldsymbol{x}, \upsilon) = \upsilon - C\mathcal{L}(\boldsymbol{x})$ for all $(\boldsymbol{x}, \upsilon) \in \mathcal{D}_{\boldsymbol{X}} \times [0,1]$, and $C > 0$ is the BuS scaling constant, *i.e.* a constant chosen such that $C\mathcal{L}(\boldsymbol{x}) \leq 1$ for all $\boldsymbol{x} \in \mathcal{D}_{\boldsymbol{X}}$. Recall that the definition in Eq. (5.22) implies to consider an auxiliary random variable $\Upsilon \sim \mathcal{U}([0,1])$, assumed to be independent from $\boldsymbol{X}$. The joint law of $(\boldsymbol{X}, \Upsilon)$ is thereby written by $\mathbb{P}_{(\boldsymbol{X},\Upsilon)} = \mathbb{P}_{\boldsymbol{X}} \otimes \mathbb{P}_{\Upsilon}$. Furthermore, samples $(\boldsymbol{x}, \upsilon) \in \mathcal{D}_{\boldsymbol{X}} \times [0,1]$ that lie in the domain $\mathcal{D}_o$ are distributed according to the posterior distribution (see Section 2.2).

On another side, the failure domain associated to the leakage reliability problem is given by:

$$\mathcal{D}_f = \{\boldsymbol{x} \in \mathcal{D}_{\boldsymbol{X}} \mid \mathcal{G}(\boldsymbol{x}) \leq 0\} \tag{5.23}$$

where $\mathcal{G}(\boldsymbol{x}) = Q_* - \mathcal{M}_{Q_g}(\boldsymbol{x})$, for all $\boldsymbol{x} \in \mathcal{D}_{\boldsymbol{X}}$.

Then, based on the BuS equivalence principle which encodes the Bayesian inference process from data $\mathcal{Y}$ by the failure domain $\mathcal{D}_o$, the posterior PoF in Eq. (5.21) may be rewritten as follows (Straub et al., 2016):

$$\begin{aligned} P_{f|\mathcal{Y}} &= \mathbb{P}(\mathcal{M}_{Q_g}(\boldsymbol{X}) > Q_*|\Upsilon \leq C\mathcal{L}(\boldsymbol{X})) \\ &= \mathbb{P}_{(\boldsymbol{X},\Upsilon)}(\mathcal{D}_f|\mathcal{D}_o) \\ &= \frac{\mathbb{P}_{(\boldsymbol{X},\Upsilon)}(\mathcal{D}_f \cap \mathcal{D}_o)}{\mathbb{P}_{(\boldsymbol{X},\Upsilon)}(\mathcal{D}_o)} \\ &= \frac{\mathbb{P}(\{\mathcal{G}(\boldsymbol{X}) \leq 0\} \cap \{\mathcal{H}(\boldsymbol{X}, \Upsilon) \leq 0\})}{\mathbb{P}(\mathcal{H}(\boldsymbol{X}, \Upsilon) \leq 0)} \end{aligned} \tag{5.24}$$

Thus, the estimation of the posterior PoF in Eq. (5.21) may be split into two subsequent reliability problems, whose respective PoFs are given by the numerator and the denominator in Eq. (5.24). Furthermore, it is remarked that the probability given by the numerator of Eq. (5.24) may be written as follows:

$$\mathbb{P}(\{\mathcal{G}(\boldsymbol{X}) \leq 0\} \cap \{\mathcal{H}(\boldsymbol{X}, \Upsilon) \leq 0\}) = \mathbb{P}(\mathcal{I}(\boldsymbol{X}, \Upsilon) \leq 0) \tag{5.25}$$

where $\mathcal{I} : \mathcal{D}_{\boldsymbol{X}} \times [0,1] \to \mathbb{R}$ is the LSF defined by:

$$\mathcal{I}(\boldsymbol{x}, \upsilon) = \max(\mathcal{G}(\boldsymbol{x}); \mathcal{H}(\boldsymbol{x}, \upsilon)) \tag{5.26}$$

for all $(\boldsymbol{x}, \upsilon) \in \mathcal{D}_{\boldsymbol{X}} \times [0,1]$. Inserting Eq. (5.25) in Eq. (5.24) finally yields:

$$P_{f|\mathcal{Y}} = \frac{\mathbb{P}(\mathcal{I}(\boldsymbol{X}, \Upsilon) \leq 0)}{\mathbb{P}(\mathcal{H}(\boldsymbol{X}, \Upsilon) \leq 0)} \tag{5.27}$$

Then, we propose the following two-step procedure in order to estimate the posterior PoF given in Eq. (5.27):

1. Firstly, the probability $P_o = \mathbb{P}(\mathcal{H}(\boldsymbol{X}, \Upsilon) \leq 0)$ is estimated by using the SuS within BuS algorithm presented in Section 2.2.2. This is akin to draw samples from the posterior distribution of $\boldsymbol{X}$ knowing $\mathcal{Y}$. Moreover, it is worth noting that this step also enables to estimate the BuS scaling constant C, since it is adaptively tuned throughout the SuS sampling procedure (see Section 2.2.2.3).

2. Secondly, the probability $P_{f,o} = \mathbb{P}(\mathcal{I}(\boldsymbol{X}, \Upsilon) \leq 0)$ is estimated by applying the classical SuS algorithm (see Section 1.2.6.2), by considering the LSF $\mathcal{I}$ defined in Eq. (5.26). It is important to note that evaluating this LSF requires the knowledge of the BuS scaling constant C, since the LSF $\mathcal{H}$ itself depends on C. In this context, we set the value of C as the estimated value obtained at the end of the Step 1, namely at the end of the estimation of P_o with the SuS within BuS algorithm.

Lastly, the posterior PoF $P_{f|\mathcal{Y}}$ can simply be estimated from estimates of the two aforementioned probabilities. Moreover, it is worth noting that Step 1 implies the generation of samples that are distributed according to the posterior. Hence, such samples can be used to estimate posterior QoI related to input parameters (*e.g.* mean or standard deviation), as well as performing new predictions of the THML behavior of the studied structure, as in Chapter 4.

5.5.1.2 Posterior PoF estimates

Next, the two-step SuS procedure presented in Section 5.5.1.1 is applied in order to estimate posterior leakage PoFs for the VD3 pressurization test of the structure, for each considered coating scenario. Such estimates may be seen as updated versions of the prior-based PoFs estimated in Section 5.4.1.3, resulting from the assimilation of *in-situ* observation data. Then, for the two SuS algorithms involved in the proposed estimation procedure, a number of $N = 5000$ samples per level is considered, whereas the rarity parameter is set to $p_0 = 0.1$. Estimated posterior PoFs are summarized in Table 5.8.

For comparison purposes, the prior PoFs estimated with the SuS algorithm in Section 5.4.1.3 are also shown. Note that the probability P_o (*i.e.* the denominator in Eq. (5.27)) is computed once for all the considered coatings scenarios, since only the probability $P_{f,o}$ (*i.e.* the numerator in Eq. (5.27)) depends on the extrados coatings surface.

Firstly, concerning coatings scenarios (b) and (c), the estimated posterior PoFs are sensibly smaller than their prior counterpart. Such a reduction may be attributable to the information provided by Bayesian updating, which led to a reduction of uncertainties for several input parameters (posterior input parameters will be thoroughly examined in Section 5.5.2). Such a reduction of the aforementioned PoFs could also be explained by a sufficiently important coating surface. Indeed, in the coating scenario (a), in which a small extrados coatings surface is involved, the posterior PoF is slightly larger than the prior one (*i.e.* 0.3 vs. 0.2). At least, the estimated prior PoF lies within the 95% confidence interval of the estimated posterior PoF. Such a situation would indicate that the considered coating surface is not sufficient to significantly limit the risk of exceeding the considered leakage threshold.

Case	$\hat{P}_f$ (Prior)	$\hat{P}_o$	$\hat{P}_{f,o}$	$\hat{P}_{f\|\mathcal{Y}}$ (Posterior)
(a)	$1.99 \cdot 10^{-1}$ (0.04)		$7.34 \cdot 10^{-7}$ (0.20)	$3.13 \cdot 10^{-1}$ (0.25)
(b)	$1.49 \cdot 10^{-1}$ (0.04)	$2.34 \cdot 10^{-6}$ (0.16)	$1.21 \cdot 10^{-7}$ (0.22)	$5.17 \cdot 10^{-2}$ (0.27)
(c)	$8.22 \cdot 10^{-2}$ (0.04)		$5.19 \cdot 10^{-10}$ (0.30)	$2.21 \cdot 10^{-4}$ (0.34)

Table 5.8: Reliability analysis of the leakage behavior at VD3 test - Prior and posterior PoF estimates. *CoVs associated to the estimated PoFs are given in brackets.*

Moreover, the posterior PoF is very much smaller for the coating scenario (c) than for scenarios (a) and (b) (namely about $2{\cdot}10^{-4}$ for (c) vs. $5{\cdot}10^{-2}$ for (b)). This simply emphasizes the fact that a larger coated surface leads to a smaller global leakage rate, and therefore to a smaller risk of exceeding the leakage threshold. Thus, according to the estimated PoF, choosing the coating scenario (c) would lead to a sensibly lower failure probability.

5.5.2 Posterior input parameters

As mentioned in Section 5.5.1.1, posterior samples are available as a byproduct of the proposed two-step SuS procedure. Several QoI related to posterior marginals of parameters $\boldsymbol{X}$ estimated from posterior samples are summarized in Table 5.9. Furthermore, univariate and bivariate marginals from the posterior distribution of THML parameters estimated from samples are shown in Fig. 5.12. Recall that the considered observation data corresponds to the available information up to and including VD2 test. Moreover, the extrados coatings efficiency parameter $\gamma_{c,e}$ is not concerned by Bayesian updating, since extrados coatings are only positioned at VD3 test (see Fig. 5.3).

Broadly speaking, only 7 parameters are significantly informed through Bayesian updating, namely the parameters $B, C_{w,0}, \alpha_{ds}, \sigma_{\theta,0}, \sigma_{z,0}, k_0$ and α_l. These parameters roughly correspond to the most influential ones identified through the variance-based sensitivity analysis presented in Section 5.3. The posterior marginals related to the other input parameters remain close to their prior counterpart (see Tables 5.5 & 5.9). Furthermore, as underlined by Fig. 5.12, the estimated posterior distribution presents a similar correlation structure to that already observed in the VeRCoRs case (see Section 4.4), except for coating parameters which are only involved in the case of operating NCBs. Indeed, the same positive posterior linear correlation is observed for the pair $(\sigma_{\theta,0}, \sigma_{z,0})$, which possibly traduces a Poisson effect as well as geometrical effects of the adopted RSV model. Moreover, a non-negligible linear correlation coefficient is observed for pairs $(k_0, \gamma_{c,i})$ and $(\alpha_l, \gamma_{c,i})$, which may be explained by the coating model proposed in Section 5.2.2, involving both diffuse and local leaks parameters with coating efficiency parameters.

n°	Parameter	Units	Mean	Std	CoV	95 % CI
1	A	10^{-13} m^2.s^{-1}	1.93	0.46	0.24	$[1.21, 3.03]$
2	B	10^{-2}	7.76	1.24	0.16	$[5.68, 10.38]$
3	$C_{w,0}$	l.m^{-3}	$1.26 \cdot 10^2$	18.80	0.15	$[95.33, 1.67 \cdot 10^2]$
4	α_{ds}	10^{-6} kg.m^{-3}	8.23	1.45	0.18	$[5.74, 11.32]$
5	k_{rd}	10^{10} Pa	5.69	1.28	0.22	$[3.67, 8.76]$
6	κ	10^{-4}	0.99	0.25	0.25	$[0.60, 1.58]$
7	η_{dc}	10^9 Pa.s	8.17	1.57	0.19	$[5.48, 11.65]$
8	$\sigma_{\theta,0}$	MPa	$1.42 \cdot 10^3$	$1.58 \cdot 10^2$	0.11	$[1.13 \cdot 10^3, 1.74 \cdot 10^3]$
9	$\sigma_{z,0}$	MPa	$1.25 \cdot 10^3$	$2.31 \cdot 10^2$	0.18	$[8.56 \cdot 10^2, 1.73 \cdot 10^3]$
10	β_K	MPa	0.20	$4.75 \cdot 10^{-2}$	0.24	$[0.13, 0.31]$
11	k_0	10^{-17} m^2	15.69	4.11	0.26	$[8.85, 24.60]$
12	α_l	-	15.93	3.07	0.19	$[10.88, 22.79]$
13	$\gamma_{c,i}$	-	0.40	0.20	0.50	$[3.51 \cdot 10^{-2}, 0.78]$

Table 5.9: Statistics related to the posterior marginals of THML input parameters, after updating at VD2 test.

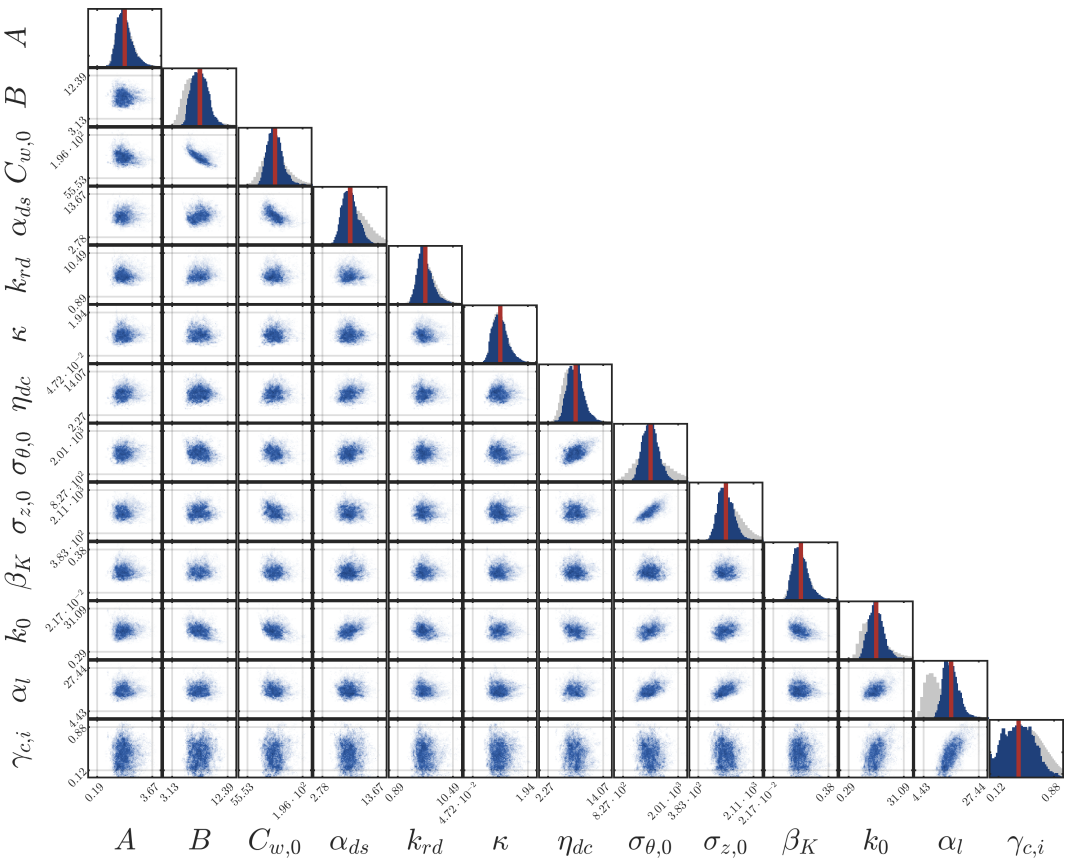

Figure 5.12: Univariate and bivariate marginals from the posterior distribution of THML model input parameters estimated from samples, after updating at VD2 test. *Prior samples are shown in grey, whereas posterior samples are shown in blue. The posterior mean value of each parameter is shown by a vertical red line.*

5.5.3 Posterior predictions

Next, the posterior samples presented in the previous section are used to perform new predictions of the long-term THML behavior of the studied NCB, analogously to posterior predictions presented in Section 4.4.2. Firstly, for illustrative purposes, a comparison of prior and posterior predictions of the (normalized) time evolution of tangential strains[1] of the standard zone is presented in Fig. 5.13. Results related to vertical strains are sensibly similar, and are thereby not shown for the sake of brevity. As intuitively expected, prior predictions are tainted with large uncertainties, due to the vague state of knowledge which has been encoded in the prior input distribution. The prior mean trend is in good agreement with strain measurements, though. Then, posterior predictions present sensibly reduced uncertainties, with a slightly adjusted mean trend. Roughly speaking, the predicted time evolution of long-term strains of VeRCoRs mock-up (see Section 4.4) and the studied NCB are quite similar, up to a proper time scaling. This emphasizes the fact that delayed strains at 1:1 scale are expected to by a time-scaled version of strains at 1:3 scale, under similar THM boundary conditions (Charpin et al., 2021).

[1] obtained by averaging intrados and extrados tangential strains

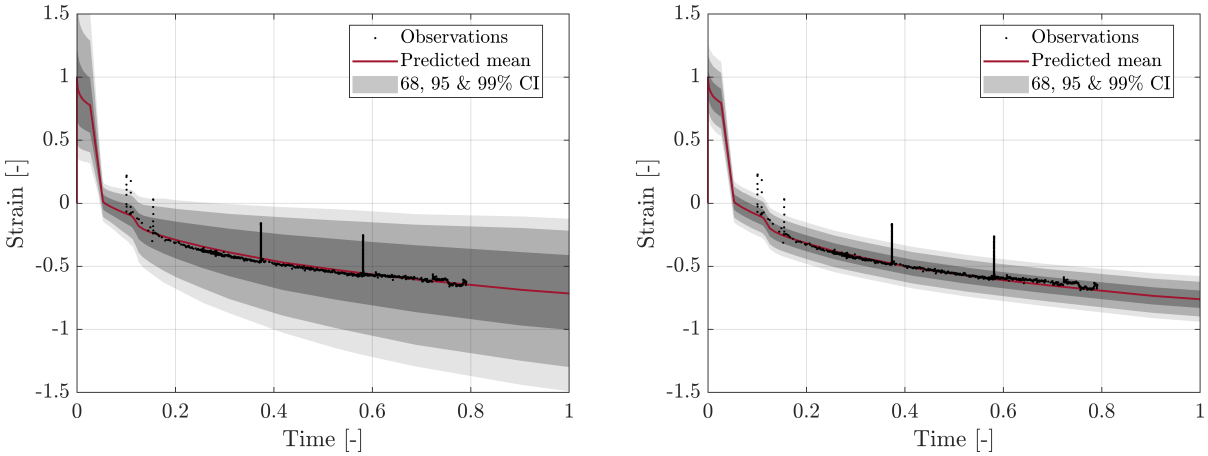

(a) Prior predictions

(b) Posterior predictions

Figure 5.13: Time evolution of tangential strains: prior and posterior predictions.

Then, prior and posterior leakage predictions are presented in Fig. 5.14. Due to the very large uncertainties tainting prior predictions, only global leakage rate values are shown in Fig. 5.14a, for the sake of readability. Then, posterior predictions of the time evolution of global and local leakage rates and their comparison with leakage measurements are depicted in Fig. 5.14b. The time evolution of the predicted virtual global leakage rate (*i.e.* without coatings) is also presented.

First, the uncertainty reduction provided for several THML input parameters (see Section 5.5.2) leads to sensibly reduced credible bounds for both global and local leakage rates, as well as an adjustment of the mean trend of prior predictions. This leads to an accurate (blind) prediction of the global leakage rate at VD3 test: indeed, the mean predicted leakage rate approaches the observed one with a relative error of about 8%. Moreover, the observed local leakage rate is also reasonably predicted, as measurements are contained in the 80% credible intervals of predictions.

Finally, the comparison of the global leakage rate with and without coatings enables to have an idea of the efficiency of the coating scenario considered here. Firstly, the leakage rates with and without coatings are equal, since no coatings are positioned before VD1 test (see Fig. 5.3). From this last test, the surface of intrados coatings is increased, which leads to a decrease of the global leakage rate. Subsequently, due to the progressive increase of coated surface at both intrados and extrados sides, the global leakage rate slightly increases from VD1 to VD2 before significantly decreasing from VD2 to VD3. Then, the evolution kinetics of the global leakage rate is sensibly slowed by the positioning of coatings. The virtual global leakage rate, for its part, continuously increases over time, as in the case of VeRCoRs mock-up (see Chapter 4), which is not subjected to coating repair works. Thus, combined with the reliability-oriented Bayesian approach presented in Section 5.5.1.1, such leakage predictions may be used so as to assess the reduction of the virtual leakage rate caused by a given coating scenario, and to provide a decision aid tool related to the maintenance of the structure.

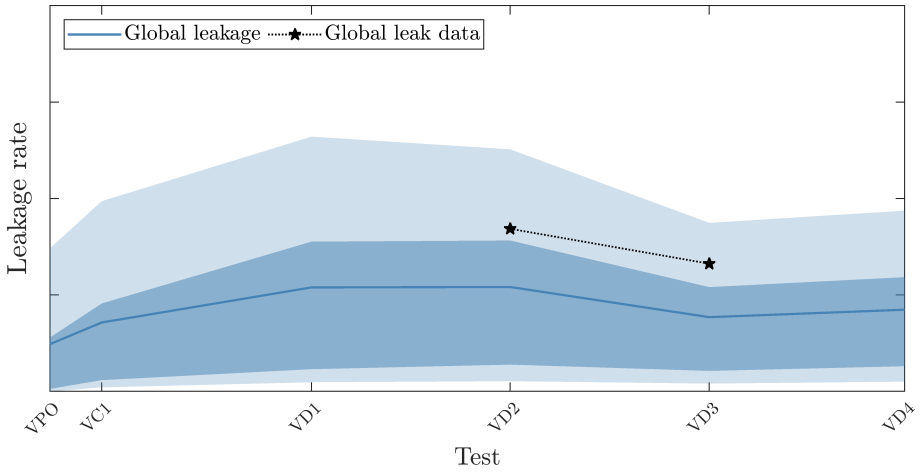

(a) Prior predictions.

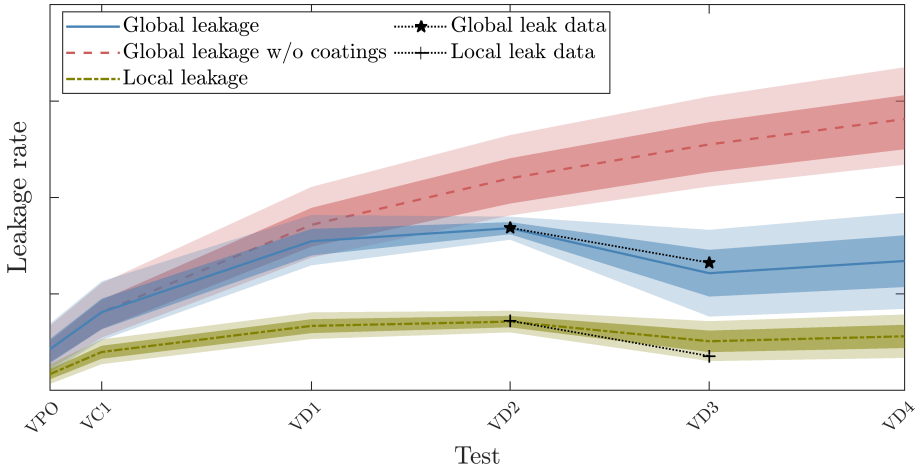

(b) Posterior predictions, after updating at VD2.

Figure 5.14: Prior and posterior leakage predictions - Mean, 50 and 80% CI.

5.6 Conclusions

This chapter has focused on the reliability analysis of the leakage behavior of large concrete containment structures. In this context, a real operating NCB has constituted the central case study of this chapter. Firstly, several modeling assumptions have been proposed in order to take into account the potential presence of coatings aiming at reinforcing leak tightness, and subsequently devising a THML modeling strategy suitable for operating containment structures. Then, a large-scale sensitivity analysis based on Sobol' indices has been performed in order to rank parameters by their relative importance on the variability of output variables of interest. Next, based on the identified PII, a reliability analysis related to the leakage behavior has been presented. In this context, we have proposed to account for uncertainties related to the choice of the input distribution, and to quantify the impact of this choice on leakage PoFs. To that end, we have considered the so-called perturbed-law based sensitivity indices (PLI), which have been developed in the recent field of robustness analysis (Iooss et al., 2021; Lemaître et al., 2015; Sueur et al., 2016).

Furthermore, following the Bayesian viewpoint adopted throughout this thesis, we have proposed an approach aiming at updating PoF along with input parameters in a Bayesian setting, from *in-situ* monitoring data. The proposed methodology has then been applied to the aforementioned operating NCB so as to assess the impact of repair scenarios, and predicting the global leakage rate of the structure.

Then, this chapter raises several perspectives, which are discussed hereafter. Firstly, particular attention has been paid for a particular type of QoI, namely PoFs related to the leak tightness of the structure. However, several alternative QoI could be considered, such as a high-order quantile (*e.g.* 95%) of the predicted leakage rate, or a superquantile (Iooss et al., 2021). It is worth mentioning that in the present work, we focus on methodological aspects rather than regulatory ones: indeed, it is the role of regulatory authorities to define criteria related to the allowable risk level related to the leakage behavior of containment structures.

Furthermore, in the framework of the presented reliability analysis, (PC-)PCE surrogates have been used in order to accelerate structural reliability methods such as MCS or SuS. Such a choice has been motivated by the versatility of (PC-)PCE surrogates, which enables to provide inexpensive-to-evaluate global approximations for a limited construction cost as well as analytical post-processing features for Sobol' sensitivity indices. Then, in order to solve structural reliability problems more efficiently, active-learning surrogate-based techniques (Echard et al., 2011; Moustapha et al., 2022) could be used instead of fixed (PC-)PCE surrogates. Likewise, alternative sampling techniques to Monte Carlo may be considered to estimate PLI more efficiently (see *e.g.* Sueur et al. (2016)).

Finally, it is worth noting that the methodologies presented in Chapters 4 & 5 only enable to assess the global leakage behavior of containment structures. Besides, it would be of great interest to have a *local* description of the leakage behavior, in order to optimize the positioning of coatings. Nevertheless, this underlies a way more difficult problem that the global one. As a first attempt, we have developed a methodology aiming at predicting local leak fields in a Bayesian framework, based on a simple description of the physical phenomena behind local leakage (see Appendix C for further details). Such an approach enables to predict the spatio-temporal evolution of plausible local leak zones, and could be used as a complement to the aforementioned global approaches so as to better plan the maintenance of containment structures.

6

Conclusion and perspectives

Conclusion

The purpose of this thesis was to develop a numerical strategy aiming at accounting for uncertainties in the framework of multi-physics simulations of the long-term behavior of containment structures. To that end, the present work was based on the general framework of Uncertainty Quantification (UQ), which enables a comprehensive management of uncertainties in the simulation of complex engineering systems.

In this framework, based on a Thermo-Hydro-Mechanical and Leakage (THML) modeling strategy, the uncertainties of input parameters are modeled by probability distributions, in order to perform probabilistic forecasts of the time evolution of the leak tightness of containment structures. Then, a particular feature of the proposed approach was to establish a dialog between numerical models and noisy observational data. In this perspective, we have proposed to use Bayesian inference in order to update the uncertainties of input parameters of the THML model from *in-situ* monitoring data related to the response of the real structure. This notably requires to devise adapted computational tools for ensuring their tractability in the framework of THML models, which typically rely on costly finite element schemes. Subsequently, these updated uncertainties can be propagated through the adopted THML model so as to provide new forecasts of the long-term behavior of the structure under study. Moreover, such an inference process can also be used to update the assessment of risks of exceeding some leak tightness regulatory thresholds, or to evaluate the efficiency of several repair works scenarios in the framework of maintenance operations.

Following a broad introduction and state-of-the-art review on UQ techniques (Chapter 1), this thesis has firstly focused on methodological and computational aspects related to Bayesian inference. In Chapter 2, the so-called Bayesian updating with Structural reliability methods (BuS) recently introduced by Straub and Papaioannou (2015) has been investigated as an alternative to classical MCMC sampling techniques. Such a framework reinterprets Bayesian inference into a structural reliability problem, and then enables to use robust and efficient rare event estimation algorithms so as to sample posterior distributions. In particular, a version of the well-known Subset Simulation (SuS) algorithm adapted to the BuS framework in (Betz et al., 2018b) has been adopted in this thesis.

Nevertheless, as any random sampling technique, the SuS algorithm requires an important amount of model evaluations, which makes it intractable when dealing with costly computational models, including THML models for containment structures. Consequently, we have proposed to couple the aforementioned SuS algorithm to an adaptive surrogate modeling scheme, based on the Polynomial Chaos Kriging (PCK) method introduced in (Schöbi et al., 2015). In particular, our method aims at constructing a PCK surrogate whose accuracy is adaptively refined throughout the SuS sampling procedure, based on ideas taken from *active learning* reliability methods (Echard et al., 2011). The performance of this method has been assessed through several academic test cases with varying complexity. Results have emphasized that the proposed adaptive method performs at least as well as in the prior-based case (*i.e.* with fixed surrogates built from the prior distribution), and enables to exploit the structure of the posterior distribution to limit the number of likelihood calls, particularly in the case of concentrated or multi-modal distributions.

Next, the overall strategy presented in this thesis is structured around a given THML computational model, which has to be suitable for assessing the long-term global behavior of

containment structures subjected to aging. In this context, in Chapter 3, we have presented a THML modeling strategy which serves as a basis for computational models considered in the applications to containment structures presented in this thesis. The adopted modeling strategy shares a common structure with that considered in the several former works (including Asali (2016); Boucher (2016); Bouhjiti (2018)), namely a weakly-coupled (or chained) structure. In this context, we have proposed several simplifying assumptions regarding these former works, in order to ensure that UQ techniques may be coupled with the adopted THML model at a reasonable cost. In particular, such assumptions notably aimed at limiting the number of uncertain parameters, and avoiding the use of costly damage calculations through the use of a phenomenological model describing the evolution of local leaks. In this way, a single model call requires several minutes, compared to several hours with damage calculations.

Chapter 4 has presented a methodology constituting the core of the global strategy developed in this thesis, based on the case study of the VeRCoRs mock-up, which consists in a realistic 1:3 scale mock-up of a double-walled nuclear containment building. Based on the first three chapters of this thesis, the proposed methodology enables to perform probabilistic forecasts of the THML behavior of the structure, and provides a connection between the adopted numerical model and *in-situ* monitoring measurements through Bayesian inference. In this context, the Bayesian inference process is used to update the uncertainties tainting input parameters of the THML model, from noisy monitoring data related to the mechanical and leakage behavior of the structure. Furthermore, such an inverse analysis may be preceded and/or followed by a forward UQ analysis, typically including uncertainty propagation or sensitivity analysis. From a computational point of view, the proposed Bayesian methodology relies on the SuS algorithm introduced in Chapter 2, which enables to efficiently sample posterior distributions. Moreover, in order to ensure the tractability of the proposed approach at a reasonable cost, PCE surrogate modeling has been adopted to construct inexpensive-to-evaluate approximations of the different sub-models constituting the THML model. In particular, we used principal component PCE in order to efficiently approximate time-dependent sub-models (including strains), involving large output dimensionalities ($\mathcal{O}(10^{2-3})$).

Then, the proposed approach has been applied in two cases, one focused on the mechanical behavior of the VeRCoRs mock-up, and another one considering its full THML behavior. In the first case, we notably proposed an approach which enabled to deal with unknown observational noise, as well as the presence of modeling biases. In this context, results have emphasized that the proposed Bayesian approach enables to identify and estimate modeling biases related to the adopted mechanical model, through inference from *in-situ* strain measurements. In a second part, we have proposed an extended approach enabling to deal with both mechanical and leakage observational data, in order to infer a full set of THML input parameters and to subsequently perform new predictions of the global leakage rate of the structure. Results have notably highlighted that the proposed approach enabled well to update the knowledge in uncertain parameters, and to precise THML predictions throughout the exploitation phase of the structure.

Besides, the methodology presented in Chapter 4 mainly aimed at providing a probabilistic framework for long-term THML predictions, and has been validated at the scale of the VeRCoRs mock-up. However, the transition from such a structure to 1:1 scale operating

containment buildings underlies some specific points, including the existence of regulatory criteria related to leak tightness, as well as maintenance operations. Consequently, by adopting a reliability analysis viewpoint, we have proposed an approach for assessing probabilities of exceeding leakage rate regulatory thresholds, while accounting for the effect of maintenance operations on the leak tightness of the structure (Chapter 5). The proposed approach has been illustrated through the case study of an operating nuclear containment building. Firstly, we have introduced simple modeling hypotheses for accounting for the effect of coatings on the global leakage rate. Next, as a preliminary task, we have proposed to perform a large-scale variance-based sensitivity analysis based on Sobol' indices in order to identify the most influential inputs on the THML response at 1:1 scale. This has enabled to compare the ranking of THML input parameters with that obtained in the VeRCoRs case.

Next, based on a given input probability distribution and classical reliability methods, the probability of exceeding a leakage regulatory threshold has been estimated for several scenarios of repair works. Nevertheless, it is worth noting that the specified input distribution, which could be seen as a prior distribution in the framework of Bayesian inference, is itself known with some level of confidence. Hence, in order to account for such second-level uncertainties and assess their impact on estimated probabilities of failure, we have proposed to use Perturbed Law-based sensitivity Indices (PLI), taken from the recent UQ field of robustness analysis (Iooss et al., 2021; Lemaître et al., 2015; Sueur et al., 2016). Lastly, following the Bayesian viewpoint adopted in Chapter 4, we have proposed an approach for updating probabilities of failure along with the THML input parameters, from *in-situ* monitoring data. Thus, the proposed approach provides a comprehensive probabilistic framework for assessing risks related to the leak tightness of operating containment buildings, and could be used as an aid decision tool within the framework of their maintenance.

Perspectives

Then, the contributions presented in this thesis raise several improvement perspectives, and pave the way for further research works. These perspectives are listed by theme herebelow:

THML modeling

Firstly, it is necessary to recall the validity domain of the THML modeling strategy adopted in this thesis: indeed, its main purpose was to assess the main effects of aging on the global long-term THML behavior of concrete containment structures, under normal operating conditions in terms of thermal, hydric and mechanical loads. In particular, the leakage calculations performed with this strategy were notably based on purely viscoelastic mechanical calculations, and on a simple phenomenological model describing the evolution of local leaks due to aging.

Hence, such a modeling strategy is at most adapted for modeling the evolution of leak tightness of containment structures during their exploitation phase outside accidental situations, notably involving severe conditions in terms of temperature and pressure. In such situations, weakly-coupled approaches may become no longer valid, and coupled approaches would be required (Dal Pont et al., 2007). Moreover, damage calculations would have to be considered in order to anticipate the possible initiation of cracks.

However, it is worth recalling the modular nature of the UQ framework (see Fig. iii), and that the UQ techniques considered in this thesis are non-intrusive, in the sense that they do not require to modify the internal structure of the adopted computational model. As a result, it is entirely possible to switch from chained to coupled THML modeling strategies within the general UQ methodology. Such a modification of the model would imply different mathematical properties, though. Indeed, coupled THML approaches would typically require a larger amount of input parameters, and involve more complex constitutive equations which could imply different regularity properties for the resulting input-output map of the THML model. Furthermore, such approaches typically require a larger numerical cost, which underlies more challenging UQ computational problems.

Lastly, regarding applications to NCB presented in this thesis, it is worth noting that a single representative structural volume (RSV) of the standard zone has been considered within THML calculations, focusing on the global behavior of the structure. In this context, multiple RSVs could be considered in order to provide a more comprehensive description of the local behavior. Such an extension may present a reasonable numerical cost, provided that parallel computing is available.

Bayesian inference

Next, several perspectives related to Bayesian inference are discussed hereafter:

- **Observation models:** firstly, the Bayesian inverse problems considered in Chapters 4 & 5 all considered Gaussian additive models (see Section 1.3.3). Furthermore, for a given observable, the noise has been assumed to be homoscedastic, *i.e.* the noises corresponding to each component of the observable are assumed to be independent and identically distributed. Then, it is possible to consider more sophisticated observation models, for instance involving a correlated noise, and/or non-Gaussian distributions. Such models could enable a somewhat more realistic modeling of observation noise.

- **Bayesian model selection:** as briefly presented in Section 1.3.2.5, Bayesian inference offers a way to choose the "best" model from a set of competing models aiming at explaining a given data set. This refers to *Bayesian model selection* (Wasserman, 2000). For instance, such a process could be used in the framework of the modeling of local leaks (see Section 3.13), in order to select the model which best explains observations of the structure under study, from a set of phenomenological models proposed by one or several analysts.

- **Hierarchical models:** hierarchical (or multilevel) Bayesian modeling constitutes a powerful extension of the classical framework of Bayesian inference (see *e.g.* (Nagel and Sudret, 2016b)). For instance, it could be used in the case of prior distributions whose parameters are not known exactly, through the definition of *hyperparameters* which parametrize the prior. Nevertheless, it is worth mentioning that this more comprehensive framework typically requires more parameters to identify, and thus involves inverse problems which are more challenging to solve in practice.

- **Robust Bayesian analysis:** a crucial (and somewhat general) arising question is given by the influence of the choice of the prior distribution on results of Bayesian inference. Indeed, the prior distributions considered in this thesis are mostly based on expert judgement, and are therefore known with various levels of confidence. Then, it would be necessary to assess the impact of such second-level uncertainties on the posterior distribution obtained through the inference process, as well as on some posterior QoI. Such a question falls within the field of Robust Bayesian Analysis (see *e.g.* (Berger, 1990; Ruggeri et al., 2005)), which offers a mathematical setting for studying this question. The recent work of (Stenger, 2020, Section 5.6) also provided some insights related to Robust Bayesian Analysis, in the framework of Optimal UQ. From a more practical point of view, we have attempted to address the question of the influence of the choice of the prior in a qualitative manner, in the specific case of the VeRCoRs mock-up (Rossat et al., 2022c). Lastly, it is worth mentioning a new research perspective, which would enable to assess the impact of uncertainties in the prior with PLI measures: indeed, the BuS framework studied in Chapter 2, which reformulates Bayesian inference into a reliability problem, could be combined to the PLI measures introduced in (Lemaître et al., 2015) and used in Section 5.4.2, in order to provide sensitivity indices related to perturbed version of the prior.

- **Alternative computational techniques:** lastly, in this thesis, Bayesian computations have been performed within the BuS framework introduced by Straub and Papaioannou (2015), which notably relies on the use of sampling techniques such as SuS. Alternatively, sampling-free techniques may be considered, such as the Transport Maps approach (Baptista et al., 2020; El Moselhy and Marzouk, 2012), which constitutes a promising alternative Bayesian computational framework.

Surrogate modeling for Bayesian computations

Firstly, as mentioned in Chapter 2, the proposed adaptive approach based on PCK surrogates presents some improvement perspectives: indeed, PCK surrogates may become inefficient when dealing with high-dimensional models. Then, in order to tackle Bayesian inverse problems with larger input dimensionalities (*e.g.* $\mathcal{O}(10^{2-3})$), dimensionality reduction techniques for Bayesian inverse problems could be used in order to exploit the low-dimensional structure of the posterior distribution. To that end, active subspaces (AS) (Constantine et al., 2014, 2016) and likelihood-informed subspaces (LIS) (Cui et al., 2014; Cui and Zahm, 2021; Zahm et al., 2022) methods could be used. Alternatively, recent work of Bigoni et al. (2022) proposed a dimension reduction approach for surrogate modeling that could be used so as to efficiently approximate forward models with high input dimensionalities.

Besides, a classical UQ analysis typically consists in a chaining of several fundamental steps, including subsequent forward and inverse analyses (for instance, prior-based forward UQ problems followed by a Bayesian inverse problem). While adaptive approaches often outperform prior-based ones in the framework of Bayesian inverse problems, these approaches typically focus on the support of the posterior distribution, and may therefore be less accurate for other UQ tasks based on the prior distribution (*e.g.* sensitivity analysis, uncertainty propagation). Hence, constructing a single prior-based surrogate model may be appealing, since the major part of the computational cost of the whole UQ analysis would correspond

to its construction. Constructing a surrogate model that is specific to Bayesian inference then involves an additional computational cost (typically, the order of magnitude of the construction of a prior-based surrogate). For such reasons, and for the simplicity sake, we have considered prior-based PCE surrogate models for all the UQ tasks considered in the applications to containment buildings presented in Chapter 4 & 5. Thus, an improvement perspective would consist in applying the adaptive PCK-based method introduced in Chapter 2 to the Bayesian inverse problems considered in the aforementioned applications.

Eventually, PCE surrogates have been considered in Chapters 4 & 5 for approximating output QoI of the adopted THML model. The choice of such surrogates has been mainly motivated by their global aspect, their approximation power, and the analytical post-processing features (notably for sensitivity analysis) they provide. Such surrogates have seemed to be well suited to the problems presented in the aforementioned chapters, notably due to the fact that aging is a somewhat slow process, which does not involve an increase of non-linearities over time that may cause the failure of PCE surrogates. In the case of dynamical systems, e.g. including structures subjected to earthquakes or impact loads, adapted surrogate modeling techniques should be considered (see *e.g.* (Mai, 2016) for further details).

Reliability analysis

Next, the reliability analysis presented in Chapter 5 underlies some improvements, notably linked to surrogate modeling. Indeed, (prior-based) PCE surrogates have been adopted in order to accelerate the estimation of probabilities of failure. In order to provide potentially more efficient and reliable estimations, active learning techniques (Echard et al., 2011; Moustapha et al., 2022) may be used instead of PCE.

Moreover, concerning the estimation of PLI measures, sampling schemes that are more efficient than Monte Carlo simulation may be considered, such as the approach proposed in (Sueur et al., 2016). Furthermore, the estimation of PLI typically requires a large amount of model evaluations ($\mathcal{O}(10^{5-6})$). In Chapter 5, fixed PCE surrogates have been considered to alleviate this computational burden, but adaptive surrogate modeling techniques could be devised in order to be coupled with the aforementioned improved sampling scheme, while efficiently limiting the number of model calls.

Non-destructive testing methods

Lastly, non-destructive testing (NDT) techniques have been recently developed for applications to large concrete structures, notably in order to provide measurements of some physical variables of interest, such as water saturation, Young's modulus or permeability (Gupta et al., 2022; Verdier et al., 2022). Such techniques present a great interest for further modeling purposes related to the THML behavior of containment structures, since they could be deployed at the scale of operating NCBs, and provide a non-negligible amount of data. For instance, these data could be used so as to represent some material properties by random fields, and/or be used within the framework of Bayesian inference in order to update the knowledge in some input parameters, possibly represented by random fields.

Appendices

Contents

A PC-PCE-based Sobol' sensitivity indices

In this section, a derivation of analytical expressions of Sobol' sensitivity indices based on PC-PCE coefficients is presented. It is worth mentioning that Wagner et al. (2020) derived expressions for total indices, whereas Nagel et al. (2020) derived expressions for first-order indices. In Section A.1, we provide a derivation of closed Sobol' indices, based on conditional expectations. In Section A.2, this derivation is applied to retrieve the expressions of total indices originally derived in (Wagner et al., 2020).

Let $(\Omega, \mathcal{F}, \mathbb{P})$ be a probability space. Let $\boldsymbol{X} : \Omega \to \mathcal{D}_{\boldsymbol{X}} \subset \mathbb{R}^d$ be a continuous random variable with density π and mutually independent components. Let $\mathcal{M} : \mathcal{D}_{\boldsymbol{X}} \to \mathcal{D}_{\boldsymbol{Y}} \subset \mathbb{R}^n$ be a (centered) PC-PCE (see Section 1.2.4.5) written by:

$$\mathcal{M}(\boldsymbol{X}) = \boldsymbol{\mu}_{\boldsymbol{Y}} + \sum_{k=1}^{r} \left(\sum_{\boldsymbol{\alpha} \in \mathcal{A}^{(k)}} c_{k,\boldsymbol{\alpha}} \psi_{\boldsymbol{\alpha}}(\boldsymbol{X}) \right) \boldsymbol{w}_k \tag{A.1}$$

where $(\boldsymbol{w}_k)_{1 \leq k \leq r}$ are principal components and, for each $k \in \{1, \ldots, r\}$, $(c_{k,\boldsymbol{\alpha}})_{\boldsymbol{\alpha} \in \mathcal{A}^{(k)}}$ are PCE coefficients, and $(\psi_{\boldsymbol{\alpha}})_{\boldsymbol{\alpha} \in \mathcal{A}^{(k)}}$ a family formed by multivariate polynomials that are orthonormal with respect to the probability distribution of $\boldsymbol{X}$, which reads:

$$\mathbb{E}[\psi_{\boldsymbol{\alpha}}(\boldsymbol{X}) \psi_{\boldsymbol{\beta}}(\boldsymbol{X})] = \int_{\mathcal{D}_{\boldsymbol{X}}} \psi_{\boldsymbol{\alpha}}(\boldsymbol{x}) \psi_{\boldsymbol{\beta}}(\boldsymbol{x}) \pi(\boldsymbol{x}) \mathrm{d}\boldsymbol{x} = \delta_{\boldsymbol{\alpha}\boldsymbol{\beta}} \tag{A.2}$$

for all $\boldsymbol{\alpha}, \boldsymbol{\beta} \in \mathcal{A}^{(k)}$. Due to the independence of components $(X_1, \ldots, X_d)$ of $\boldsymbol{X}$, the following tensorized form is assumed for polynomials $(\psi_{\boldsymbol{\alpha}})_{\boldsymbol{\alpha}}$:

$$\psi_{\boldsymbol{\alpha}}(\boldsymbol{X}) = \prod_{i=1}^{d} \psi_{\alpha_i}^{(i)}(X_i) \tag{A.3}$$

where the univariate polynomials $(\psi_j^{(i)})_j$ are orthonormal with respect to the marginal distribution of X_i, *i.e.* $\mathbb{E}[\psi_j^{(i)}(X_i) \psi_k^{(i)}(X_i)] = \delta_{jk}$.

Next, given $t \in \{1, \ldots, n\}$, the t-th component of the response $\boldsymbol{Y} = \mathcal{M}(\boldsymbol{X})$ is denoted by $Y_t = \mathcal{M}_t(\boldsymbol{X})$ hereafter, and writes:

$$Y_t = \mathcal{M}_t(\boldsymbol{X}) = \mu_{Y_t} + \sum_{k=1}^{r} \left(\sum_{\boldsymbol{\alpha} \in \mathcal{A}^{(k)}} c_{k,\boldsymbol{\alpha}} \psi_{\boldsymbol{\alpha}}(\boldsymbol{X}) \right) w_{k,t} \tag{A.4}$$

The ANOVA decomposition of $\mathcal{M}_t$ is then recalled herebelow (see Section 1.2.5.1):

$$\begin{aligned} \mathcal{M}_t(\boldsymbol{X}) &= \mathcal{M}_0 + \sum_{1 \leq i \leq d} \mathcal{M}_{t,i}(X_i) + \sum_{1 \leq i \leq j \leq d} \mathcal{M}_{t;i,j}(X_i, X_j) + \cdots + \mathcal{M}_{t;1,\ldots,d}(\boldsymbol{X}) \\ &= \sum_{u \subseteq \{1,\ldots,d\}} \mathcal{M}_{t,u}(\boldsymbol{X}_u) \end{aligned} \tag{A.5}$$

Furthermore, the following expressions may be derived for the terms $(\mathcal{M}_{t,u}(\boldsymbol{X}_u))_{u\subseteq\{1,\dots,d\}}$ (Chastaing et al., 2012):

$$\mathcal{M}_{t,0} = \mathbb{E}[Y_t] \tag{A.6a}$$
$$\mathcal{M}_{t,i}(X_i) = \mathbb{E}[Y_t|X_i] - \mathbb{E}[Y_t] \tag{A.6b}$$
$$\mathcal{M}_{t,u}(\boldsymbol{X}_u) = \mathbb{E}[Y_t|\boldsymbol{X}_u] - \sum_{v\subsetneq u} \mathcal{M}_{t,v}(\boldsymbol{X}_v) \tag{A.6c}$$

for all $i \in \{1,\dots,d\}$ and $u \subseteq \{1,\dots,d\}$ with $|u| \geq 2$.

Then, for $u \subseteq \{1,\dots,d\}$, the Sobol' sensitivity index $S_{t,u}$ is defined by (Chastaing et al., 2012):

$$S_{t,u} = \frac{\mathrm{Var}[\mathcal{M}_{t,u}(\boldsymbol{X}_u)]}{\mathrm{Var}[Y_t]} \tag{A.7}$$

Moreover, the closed Sobol' index $\underline{S}_{t,u}$ with respect to grouped variables $\boldsymbol{X}_u = (X_i)_{i\in u}$ is defined by:

$$\underline{S}_{t,u} = \frac{\mathrm{Var}[\mathbb{E}[Y_t|\boldsymbol{X}_u]]}{\mathrm{Var}[Y_t]} \tag{A.8}$$

This index measures the contribution to the total variance of the variables $(X_i)_{i\in u}$, by themselves or in interaction with each other (Gilquin et al., 2015). By comparing Equations (A.6), (A.7) and (A.8), closed Sobol' indices may be linked to Sobol' indices through the following relation:

$$S_{t,u} = \underline{S}_{t,u} - \sum_{v\subset u} S_{t,v} \tag{A.9}$$

For instance, for $i,j \in \{1,\dots,d\}$ such that $i \neq j$, the second-order Sobol' index S_{ij} of variables (X_i, X_j) is equal to the closed index of these variables minus their single effects:

$$S_{t,ij} = \underline{S}_{t,ij} - S_{t,i} - S_{t,j} \tag{A.10}$$

A.1 Closed Sobol' indices

A derivation of analytical expressions for closed Sobol' indices is presented hereafter. Firstly, given $u \subseteq \{1,\dots,d\}$, an expression for the conditional expectation $\mathbb{E}[Y_t|\boldsymbol{X}_u]$ in terms of PC-PCE coefficients is firstly derived. For the sake of simplicity, the notation $\mathcal{A} = \bigcup_{k=1}^{r} \mathcal{A}^{(k)}$ is adopted hereafter, and one sets $c_{k,\boldsymbol{\alpha}} = 0$ for all $\boldsymbol{\alpha} \in \mathcal{A} \setminus \mathcal{A}^{(k)}$ and $k \in \{1,\dots,r\}$.

Exploiting the orthonormality of the polynomials $(\psi_{\boldsymbol{\alpha}})_{\boldsymbol{\alpha}}$, one has:

$$\begin{aligned}
\mathbb{E}[Y_t|\boldsymbol{X}_u] &= \mu_{Y_t} + \sum_{k=1}^{r} w_{k,t} \sum_{\boldsymbol{\alpha}\in\mathcal{A}} c_{k,\boldsymbol{\alpha}} \mathbb{E}[\psi_{\boldsymbol{\alpha}}(\boldsymbol{X})|\boldsymbol{X}_u] \\
&= \mu_{Y_t} + \sum_{k=1}^{r} w_{k,t} \sum_{\boldsymbol{\alpha}\in\mathcal{A}} c_{k,\boldsymbol{\alpha}} \left(\prod_{i\in u} \psi_{\alpha_i}^{(i)}(X_i)\right) \left(\prod_{j\notin u} \delta_{\alpha_j 0}\right) \\
&= \mu_{Y_t} + \sum_{k=1}^{r} w_{k,t} \sum_{\boldsymbol{\alpha}\in\mathcal{A}_u} c_{k,\boldsymbol{\alpha}} \psi_{\boldsymbol{\alpha}}(\boldsymbol{X})
\end{aligned} \tag{A.11}$$

where $\mathcal{A}_u = \{\boldsymbol{\alpha} \in \mathcal{A} \mid (j \notin u) \Leftrightarrow (\alpha_j = 0)\}$. Hence, again exploiting the orthonormality of polynomials $(\psi_{\boldsymbol{\alpha}})_{\boldsymbol{\alpha}}$ the variance of the conditional expectation $\mathbb{E}[Y_t|\boldsymbol{X}_u]$ may be written by:

$$\mathrm{Var}[\mathbb{E}[Y_t|\boldsymbol{X}_u]] = \sum_{k,l=1}^{r} w_{k,t} w_{l,t} \left(\sum_{\boldsymbol{\alpha} \in \mathcal{A}_u^*} c_{k,\boldsymbol{\alpha}} c_{l,\boldsymbol{\alpha}} \right) \tag{A.12}$$

where $\mathcal{A}_u^* = \mathcal{A}_u \setminus \{\mathbf{0}\}$.

Likewise, the total variance $\mathrm{Var}[Y_t]$ reads:

$$\mathrm{Var}[Y_t] = \sum_{k,l=1}^{r} w_{k,t} w_{l,t} \left(\sum_{\boldsymbol{\alpha} \in \mathcal{A}^*} c_{k,\boldsymbol{\alpha}} c_{l,\boldsymbol{\alpha}} \right) \tag{A.13}$$

where $\mathcal{A}^* = \mathcal{A} \setminus \{\mathbf{0}\}$.

Thus, the following expression is derived for the closed index $\underline{S}_{t,u}$:

$$\underline{S}_{t,u} = \frac{1}{\mathrm{Var}[Y_t]} \sum_{k,l=1}^{r} w_{k,t} w_{l,t} \left(\sum_{\boldsymbol{\alpha} \in \mathcal{A}_u^*} c_{k,\boldsymbol{\alpha}} c_{l,\boldsymbol{\alpha}} \right) \tag{A.14}$$

Sobol' indices $(S_{t,u})_{u \subseteq \{1,\dots,d\}}$ may then be computed recursively from closed indices, based on Equation (A.10) and knowing that $\underline{S}_{t,i} = S_{t,i}$ for all $i \in \{1, \dots, d\}$.

A.2 Total Sobol' indices

Next, a derivation of analogous expressions for total Sobol' indices is presented hereafter. Given $i \in \{1, \dots, d\}$, the total Sobol' index $T_{t,i}$ may be written by:

$$T_{t,i} = 1 - \frac{\mathrm{Var}[\mathbb{E}[Y_t|\boldsymbol{X}_{\sim i}]]}{\mathrm{Var}[Y_t]} \tag{A.15}$$

where $\boldsymbol{X}_{\sim i} = (X_j)_{j \neq i}$.

Based on the derivation presented in Section A.1, the following expression is obtained for the conditional expectation $\mathbb{E}[Y_t|\boldsymbol{X}_{\sim i}]$:

$$\mathbb{E}[Y_t|\boldsymbol{X}_{\sim i}] = \mu_{Y_t} + \sum_{k=1}^{r} w_{k,t} \sum_{\boldsymbol{\alpha} \in \mathcal{A}_{\sim i}} c_{k,\boldsymbol{\alpha}} \psi_{\boldsymbol{\alpha}}(\boldsymbol{X}) \tag{A.16}$$

where $\mathcal{A}_{\sim i} = \{\boldsymbol{\alpha} \in \mathcal{A} \mid \alpha_i = 0\}$.

Then, applying the variance to the above conditional expectation yields:

$$\mathrm{Var}[\mathbb{E}[Y_t|\boldsymbol{X}_{\sim i}]] = \sum_{k,l=1}^{r} w_{k,t} w_{l,t} \left(\sum_{\boldsymbol{\alpha} \in \mathcal{A}_{\sim i}^*} c_{k,\boldsymbol{\alpha}} c_{l,\boldsymbol{\alpha}} \right) \tag{A.17}$$

where $\mathcal{A}_{\sim i}^* = \mathcal{A}_{\sim i} \setminus \{\mathbf{0}\}$.

Thus, inserting (A.16) in (A.15) yields:

$$\begin{aligned} T_{t,i} &= \frac{1}{\mathrm{Var}[Y_t]} \left(\mathrm{Var}[Y_t] - \mathrm{Var}[\mathbb{E}[Y_t | \boldsymbol{X}_{\sim i}]] \right) \\ &= \frac{1}{\mathrm{Var}[Y_t]} \sum_{k,l=1}^{r} w_{k,t} w_{l,t} \left(\sum_{\boldsymbol{\alpha} \in \mathcal{A}^*} c_{k,\boldsymbol{\alpha}} c_{l,\boldsymbol{\alpha}} - \sum_{\boldsymbol{\alpha} \in \mathcal{A}^*_{\sim i}} c_{k,\boldsymbol{\alpha}} c_{l,\boldsymbol{\alpha}} \right) \\ &= \frac{1}{\mathrm{Var}[Y_t]} \sum_{k,l=1}^{r} w_{k,t} w_{l,t} \left(\sum_{\boldsymbol{\alpha} \in \mathcal{A}^*_i} c_{k,\boldsymbol{\alpha}} c_{l,\boldsymbol{\alpha}} \right) \end{aligned} \tag{A.18}$$

where $\mathcal{A}^*_i = \{\boldsymbol{\alpha} \in \mathcal{A}^* \mid \alpha_i > 0\}$.

B Adaptive Conditional Sampling algorithm

B.1 MCMC sampling in the standard normal space

In the context of SuS, the MCMC sampling phase is usually conducted in the standard normal space. Firstly, based on the probabilistic transform $\mathcal{T} : \mathcal{D}_{\boldsymbol{X}} \times [0,1] \to \mathbb{R}^m$ defined in Eq. (2.14), equivalent versions of the LSF in Eq. (2.19) and intermediate domains $(D_f^{(j)})_{1\leq j\leq r}$ may be defined in the standard normal space, namely:

$$G_l(\boldsymbol{u}) = \mathcal{G}_l(\mathcal{T}^{-1}(\boldsymbol{u})) \tag{B.1}$$

for all $\boldsymbol{u} \in \mathbb{R}^m$, and:

$$D_f^{(j)} = \{\boldsymbol{u}' \in \mathbb{R}^m \mid G_l(\boldsymbol{u}') \leq t_j\} \tag{B.2}$$

Then, at SuS level $j \in \{1, \ldots, r\}$, one aims at generating samples conditional to $D_f^{(j)}$ through MCMC sampling from the conditional distribution $\mathbb{P}_{\boldsymbol{U}}(\cdot|D_f^{(j)})$, which has the following density:

$$\varphi(\boldsymbol{u}|D_f^{(j)}) = \frac{\varphi(\boldsymbol{u})\mathbf{1}_{D_f^{(j)}}(\boldsymbol{u})}{\mathbb{P}_{\boldsymbol{U}}(D_f^{(j)})} \tag{B.3}$$

for all $\boldsymbol{u} \in \mathbb{R}^m$. Furthermore, one has n samples $\{(\boldsymbol{x}^{(j-1,k)}, \upsilon^{(j-1,k)})\}_{1\leq k\leq n}$ that lie in the intermediate failure domain $\mathcal{D}_f^{(j)}$ in the physical space. By duality, this corresponds to n samples $\{\boldsymbol{u}^{(j-1,k)}\}_{1\leq k\leq n}$ that lie in the domain $D_f^{(j)}$ in the standard normal space, where $\boldsymbol{u}^{(j-1,k)} = \mathcal{T}(\boldsymbol{x}^{(j-1,k)}, \upsilon^{(j-1,k)})$. These samples are taken as the initial states (or *seeds*) of n Markov chains. Since these samples are already in the domain $D_f^{(j)}$ and thereby following the conditional distribution $\mathbb{P}_{\boldsymbol{U}}(\cdot|D_f^{(j)})$, the generated Markov chains have reached their stationary state since the beginning of MCMC sampling (Au and Beck, 2001; Papaioannou et al., 2015; Zuev et al., 2012). Therefore, the chains do not require *burn-in*. Such a behavior is termed *perfect sampling* (see *e.g.* (Zuev et al., 2012)).

B.2 Transition kernel

The adaptive Conditional Sampling (aCS) proposed by Papaioannou et al. (2015) is briefly presented in what follows. Firslty, the transition mechanism of the aCS algorithm is detailed hereafter. Given a current state $\boldsymbol{u} \in \mathbb{R}^m$ in the standard normal space, a candidate sample $\boldsymbol{u}^* \in \mathbb{R}^m$ is generated from the Gaussian distribution with mean $\mathbf{R}\boldsymbol{u}$ and covariance matrix $\mathbf{I} - \mathbf{R}\mathbf{R}^\intercal$, where $\mathbf{R} \in \mathbb{R}^{m\times m}$ has to be specified by the user. This is akin to sample $\boldsymbol{u}^*$ from $\mathcal{N}(\mathbf{0}, \mathbf{I})$ and imposing that $\boldsymbol{u}^*$ and $\boldsymbol{u}$ are jointly Gaussian with cross-correlation matrix $\mathbf{R}$. Then, the candidate sample $\boldsymbol{u}^*$ is accepted as the new Markov chain state if $\boldsymbol{u}^* \in D_f^{(j)}$, and is rejected otherwise. This proposal mechanism is summarized in Algorithm B.1.

Then, the aCS algorithm underlies the following transition density:

$$K(\boldsymbol{u}'|\boldsymbol{u}) = \varphi_m(\boldsymbol{u}'; \mathbf{R}\boldsymbol{u}, \mathbf{I} - \mathbf{R}\mathbf{R}^\intercal)\mathbf{1}_{D_f^{(j)}}(\boldsymbol{u}') + (1 - \varrho(\boldsymbol{u}))\delta_{\boldsymbol{u}}(\boldsymbol{u}') \tag{B.4}$$

where $\delta_{\boldsymbol{u}}$ is the Dirac mass at $\boldsymbol{u} \in \mathbb{R}^m$, and:

$$\varrho(\boldsymbol{u}) = \int_{D_f^{(j)}} \varphi_m(\boldsymbol{u}'; \mathbf{R}\boldsymbol{u}, \mathbf{I} - \mathbf{R}\mathbf{R}^\intercal)\mathrm{d}\boldsymbol{u}' \tag{B.5}$$

It is noted that compared to the classical MH algorithm for SuS, the aCS algorithm always accepts its candidate samples, without compromising the stationary distribution of the produced chains (Papaioannou et al., 2015). Indeed, comparing the first term of the transition density in Eq. (B.4) to that of the MH algorithm (see Chapter 1, Section 1.3.4.2), the acceptance probability associated to a candidate sample $\boldsymbol{u}'$ is equal to one. Furthermore, it can be shown that the transition density in Eq. (B.4) satisfies the reversibility condition (see Section 1.3.4) with respect to the target density given in Eq. (B.3), which ensures that the stationary distribution of the produced Markov chains is indeed the conditional distribution $\mathbb{P}_{\boldsymbol{U}}(\cdot|D_f^{(j)})$ (see (Papaioannou et al., 2015, Appendix A) for a detailed proof).

Algorithm B.1 Conditional Sampling (CS) proposal mechanism (Papaioannou et al., 2015)

Input: Current state $\boldsymbol{u}$ in U-space at SuS level j, proposal correlation matrix $\mathbf{R}$

1: Draw a sample $\boldsymbol{u}^* \sim \mathcal{N}(\mathbf{R}\boldsymbol{u}, \mathbf{I} - \mathbf{R}\mathbf{R}^\intercal)$ ▷ Draw a candidate sample
2: **if** $\boldsymbol{u}^* \in D_f^{(j)}$ **then** ▷ Accept-reject phase
3: Set $\boldsymbol{u}' = \boldsymbol{u}^*$ ▷ Accept the candidate sample
4: **else**
5: Set $\boldsymbol{u}' = \boldsymbol{u}$ ▷ Reject the candidate sample
6: **end if**

Output: New state $\boldsymbol{u}'$ in U-space at SuS level j

B.3 On-the-fly adaptation of proposal scaling

Then, the correlation matrix $\mathbf{R}$ involved in the proposal mechanism of the aCS algorithm has to be specified. A simple choice proposed by Papaioannou et al. (2015) consists in setting $\mathbf{R} = \mathrm{diag}(\rho_1, \ldots, \rho_m)$, where $\rho_i \in [0, 1]$ is a correlation parameter which drives the spread of the MCMC proposal distribution in the i-th dimension. Besides, the performance of the aCS algorithm sensibly depends on the choice of such correlation parameters: too large values of ρ_i will typically lead to highly correlated samples, whereas too small values will lead to a large amount of rejected samples and thereby an acceptance rate close to zero. Consequently, Papaioannou et al. (2015) proposed to adaptively tuning the parameters $(\rho_i)_{1\leq i\leq m}$ throughout the sampling procedure. In this context, based on ideas taken from adaptive MCMC algorithms (Andrieu and Thoms, 2008), the aforementioned parameters are adjusted in order to achieve a target average acceptance rate. As proposed by Betz et al. (2016), this target acceptance rate is set as $\alpha^* = 0.23 + 0.21/m$, based on theoretical results valid for certain classes of distributions (including Gaussian ones) (Gelman et al., 1997; Roberts and Rosenthal, 1998). The full aCS algorithm is presented in Algorithm B.2. The initial proposal scaling parameter is set to $\lambda_1 = 0.6$, whereas the adaptation period is set to $N_a = 100$, based on recommendations in (Betz et al., 2018b; Papaioannou et al., 2015).

Algorithm B.2 Adaptive Conditional Sampling (aCS) algorithm (Papaioannou et al., 2015)

Input: Seeds $\{\boldsymbol{u}^{(j-1,k)}\}_{1\leq k\leq n}$ at SuS level j, number of required samples N, proposal scaling adaptation period N_a, initial proposal scaling parameter λ_1, target acceptance rate α^*

Set $\sigma_{0,i} = 1$, for $i = 1 : m$ ▷ Initialize proposal standard deviations

Randomize the order of the seeds $\{\boldsymbol{u}^{(j-1,k)}\}_{1\leq k\leq n}$ ▷ Necessary to avoid bias during the adaptation of the proposal scaling

for $l = 1 : N/N_a$ **do**

  Set $\sigma_i = \min(\lambda_l \sigma_{0,i}, 1)$, for $i = 1 : m$ ▷ Update proposal standard deviations

  Set $\rho_i = \sqrt{1 - \sigma_i^2}$, for $i = 1 : m$ ▷ Compute the proposal correlation parameters

  for $k = (l-1)N_a + 1 : lN_a$ **do** ▷ MCMC sampling procedure

    Set $\boldsymbol{u}^{(j,N(k-1)/n+1)} = \boldsymbol{u}^{(j-1,k)}$ ▷ Set MCMC seeds

    Generate $N/n - 1$ states $\{\boldsymbol{u}^{(j,N(k-1)/n+s)}\}_{2\leq s\leq N/n}$ with Algorithm B.1, by starting from $\boldsymbol{u}^{(j,N(k-1)/n+1)}$ and setting $\mathbf{R} = \mathrm{diag}(\rho_1, \ldots, \rho_m)$ ▷ Conditional sampling

  end for

  Set $\bar{\alpha}$ as the average acceptance rate of the last N_a chains

  Set $\lambda_{l+1} = \lambda_l \exp\left((\bar{\alpha} - \alpha^*)/\sqrt{l}\right)$ ▷ Adapt the proposal scaling parameter

end for

Output: Samples $\{\boldsymbol{u}^{(j,k)}\}_{1\leq k\leq N}$ from $\mathbb{P}_{\boldsymbol{U}}(\cdot|D_f^{(j)})$ at SuS level j

C Probabilistic predictions of local leak fields

C.1 Introduction

The approaches presented in Chapters 4 & 5 enable to forecast the global leakage behavior of large containment structures. In this context, these approaches notably aim at predicting the time evolution of the global leakage rate in a probabilistic setting, and allow to update the knowledge in input parameters from observation data through Bayesian inference. In particular, the approach presented in Chapter 5 enables to assess the risk of exceeding a threshold value related to the global leakage rate of the structure, notably through the estimation of probabilities of failure (PoF).

This section aims at presenting a methodology aiming at predicting the spatio-temporal evolution of local leaks. In this perspective, a key issue of such an approach is to identify the plausible zones of the surface of the structure in which local leaks are significant, in order to better plan possible repair works by optimizing the positioning of coatings, when necessary. This notably implies a paradigm shift in terms of variables of interest, since leakage fields have to be modeled instead of a single scalar value, namely the global leakage rate of the structure. In summary, while Chapters 4 & 5 aimed at assessing the time evolution of the global leakage rate and evaluating the risks of exceeding a global leakage rate threshold value, this section aims at describing the spatial distribution of local leaks as well as their time evolution.

Besides, the prediction of local leaks fields is even more challenging than the prediction of the global leakage rate, and even more in the case of operating NCBs involving coatings, which induce an additional layer of complexity. Moreover, to the author's knowledge, such a problem has not been yet tackled in the existing literature. Consequently, in the framework of a first attempt, we propose a simple phenomenological model enabling to describe local leak fields, even in the presence of coatings, based on models proposed for the global approaches presented in Chapters 4 & 5. Then, the constructed local leak model involves numerous uncertain input parameters, which are not measurable directly. Consequently, we propose to infer these parameters through Bayesian inference, from *in-situ* observations of local leak fields which are possibly available in a limited quantity. In this context, the posterior distribution of input parameters is estimated by using the same Bayesian computational approach as global approaches presented in Chapters 4 & 5, namely the SuS within BuS algorithm (see Section 2.2.2). Finally, posterior samples can be used to perform new predictions of the local leak field of the structure.

This appendix is organized as follows: firstly, the proposed approach is presented in Section C.2. Then, it is numerically implemented and applied to several realistic test-cases in Section C.3. These test-cases involve the VeRCoRs mock-up presented in Chapter 4, as well as two 1:1 scale operating NCBs. Lastly, this section is summarized and concluded in Section C.4.

C.2 Formulation

C.2.1 General framework

Let $\mathcal{D} \subset \mathbb{R}^3$ be a geometrical domain, which typically corresponds to the (external) surface of a NCB. A simple model for describing the spatio-temporal evolution of local leaks is presented hereafter. The main idea behind this model is based on the definition of a relationship between local leaks and a physical field of interest (*e.g.* water saturation, strains, prestressing losses, stresses), analogously to the phenomenological model proposed in Section 3.3.5.2.

Let $(\Omega, \mathcal{F}, \mathbb{P})$ be a probability space. Let $\Pi : \mathcal{D} \times \mathbb{R}_+ \times \mathcal{D}_{\boldsymbol{X}} \to \mathbb{R}$ be a scalar-valued field. Given spatial coordinates $\boldsymbol{s} \in \mathcal{D}$ and an instant $t \geq 0$, the function $\Pi_{\boldsymbol{s},t} : \boldsymbol{x} \mapsto \Pi(\boldsymbol{s}, t; \boldsymbol{x})$ is assumed to be deterministic function of random input parameters $\boldsymbol{X} : \Omega \to \mathcal{D}_{\boldsymbol{X}} \subset \mathbb{R}^{d_{\boldsymbol{X}}}$. The field Π can typically correspond to a mechanical field obtained from the THML model presented in Chapter 3.

Firstly, one focuses on the modeling of the local leak field of the studied structure in absence of coatings. Denoting by Q_0 the local leak field, we propose the following model to link Q_0 to the aforementioned field Π:

$$Q_0(\boldsymbol{s}, t; \boldsymbol{x}, \boldsymbol{\theta}) = F(\Pi(\boldsymbol{s}, t; \boldsymbol{x}); \boldsymbol{\theta}) \tag{C.1}$$

for all $(\boldsymbol{s}, t, \boldsymbol{x}) \in \mathcal{D} \times \mathbb{R}_+ \times \mathcal{D}_{\boldsymbol{X}}$, where $F : \mathbb{R} \times \mathcal{D}_{\boldsymbol{\Theta}} :\to \mathbb{R}$ is a function which depends on random parameters $\boldsymbol{\Theta} : \Omega \to \mathcal{D}_{\boldsymbol{\Theta}} \subset \mathbb{R}^{d_{\boldsymbol{\Theta}}}$, and establishes a relationship between the fields Q_0 and Π. For instance, F can be simply given by the following power model:

$$F(\xi; \boldsymbol{\theta}) = \theta_1 \xi^{\theta_2} \tag{C.2}$$

for all $\xi \in \mathbb{R}$ and $\boldsymbol{\theta} = (\theta_1, \theta_2) \in \mathbb{R}_+^2$.

The definition of the relationship between Q_0 and Π given in Eq. (C.1) is motivated by the same phenomenology evoked in Section 3.3.5.2: local leaks are expected to larger in zones where prestressing losses (and possibly tensile stresses) are more important, and/or where the water saturation is lower. For instance, a modeling choice would consist in setting Π as the field of prestressing losses within the formulation in Eq. (C.2).

Nevertheless, it is important to underline that physical phenomena behind local leaks are very complex, and might involve some threshold effects which make that the proposed relationship in Eq. (C.1) may not be valid at each location $\boldsymbol{s} \in \mathcal{D}$ and instant $t \geq 0$. Indeed, when considering physical fields that are somewhat spatially homogeneous and continuously evolving in time, applying the model in Eq. (C.1) in a point-wise fashion in $\mathcal{D} \times \mathbb{R}_+$ would lead to a spatially homogeneous local leak field, which would present important leaks on an important surface of the structure. However, as their name suggests, local leaks typically show a strongly localized behavior in practice, that notably stems from the fact that only few leak zones of the structure are triggered during its life (*e.g.* due to crack initiation). As a result, the model in Eq. (C.1) should be restricted to active local leak zones, while setting $Q_0 = 0$ on the remaining zones which present no, or at least negligible, local leaks.

This motivates the notion of *leak support*. Let $\mathcal{S} \subset \mathcal{D}$ be a subset of the considered geometrical domain. Then, one rewrites the model in Eq. (C.1) as follows, for all $(\boldsymbol{s}, t, \boldsymbol{x}, \boldsymbol{\theta}) \in \mathcal{D} \times \mathbb{R}_+ \times \mathcal{D}_{\boldsymbol{X}} \times \mathcal{D}_{\boldsymbol{\Theta}}$:

$$Q_0(\boldsymbol{s}, t; \boldsymbol{x}, \boldsymbol{\theta}) = \mathbf{1}_{\mathcal{S}}(\boldsymbol{s}) F(\Pi(\boldsymbol{s}, t; \boldsymbol{x}); \boldsymbol{\theta}) \tag{C.3}$$

The subset $\mathcal{S}$ is called the leak support, and typically corresponds to zones where local leaks are active. The choice of such a subset is not trivial, though, and has typically to be based on observations of the local leak field performed during pressurization tests. Then, it is important to underline a strong assumption induced by the formulation proposed in Eq. (C.3): the leak support is assumed to not evolve over time, which corresponds to simplifying hypotheses made in Section 3.3.5.2. Such hypotheses notably consist in assuming that cracks are not propagating over time, and that no new cracks are initiating during the long-term phase of the structure, when subjected to normal operating loads. As a result, given an assumed leak support, the approach proposed here is not able to predict the appearance of new local leak zones, but only aims at assessing the spatio-temporal evolution of local leaks within an assumed support. Remark that in practice, the support $\mathcal{S}$ might be updated *a posteriori*, if new local leak zones are observed. An illustration of a leak support on a discretized map (in cylindrical projection) of VeRCoRs mock-up is given in Fig. C.1.

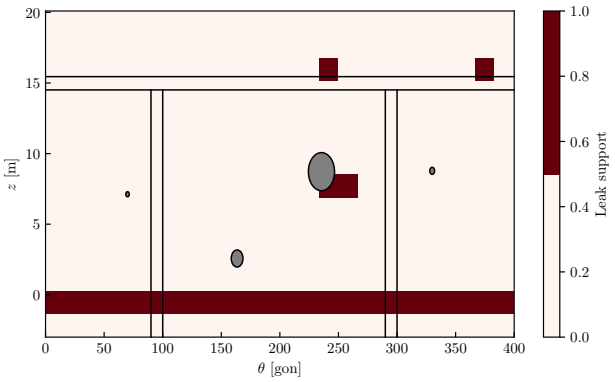

Figure C.1: Example of a leak support on a spatial discretization of VeRCoRs mock-up.

Then, a model aiming at assessing the spatio-temporal of local leaks Q_0 having been presented, we next propose an extension aiming at accounting for the presence of coatings. Such an extension is based on the same principle presented in Section 5.2.2. In this context, the local leak field Q with coatings is assumed to be written by:

$$Q(\boldsymbol{s}, t; \boldsymbol{x}, \boldsymbol{\theta}, \boldsymbol{\gamma}) = C_c(\boldsymbol{s}, t; \boldsymbol{\gamma}) Q_0(\boldsymbol{s}, t; \boldsymbol{x}, \boldsymbol{\theta}) \tag{C.4}$$

where $C_c : \mathcal{D} \times \mathbb{R}_+ \times \mathcal{D}_{\boldsymbol{\Gamma}} \to [0, 1]$ is a function modeling the effects of coatings positioned on the surface of the structure, depending on efficiency parameters $\boldsymbol{\Gamma} : \Omega \to \mathcal{D}_{\boldsymbol{\Gamma}} \subset \mathbb{R}^{d_{\boldsymbol{\Gamma}}}$. The definition of C_c will be precised in the next section.

C.2.2 Spatio-temporal discretization

For computational purposes, one considers a discretization $\mathcal{D} = \bigcup_{k=1}^{m} \mathcal{D}_k$ of the geometrical domain $\mathcal{D}$ into m cells $(\mathcal{D}_k)_{1 \leq k \leq m}$. Likewise, a time grid formed by instants $(t_l)_{1 \leq l \leq n}$ is defined. These instants typically correspond to pressurization tests. Then, from now on, discretized forms of the fields presented in Section C.2.1 (*i.e.* Π, Q_0 and Q) are considered. Discretization of these fields is made such that these last are constant on each cell $\mathcal{D}_k$. Furthermore, the leak support is also discretized so that $\mathcal{S} = \bigcup_{k \in \mathcal{I}} \mathcal{D}_k$, where $\mathcal{I} \subset \{1, \ldots, m\}$.

In this context, the resulting discretized local leak field Q_0 is seen as a $\mathbb{R}^{m\times n}$-valued deterministic function $\boldsymbol{Q}_0$ of parameters $(\boldsymbol{X}, \boldsymbol{\Theta}, \boldsymbol{\Gamma})$, whose output components are given by:

$$Q_0^{(k,l)}(\boldsymbol{x}, \boldsymbol{\theta}) = \delta_k(\mathcal{I}) F(\Pi^{(k,l)}(\boldsymbol{x}); \boldsymbol{\theta}) \tag{C.5}$$

for $(k, l) \in \{1, \ldots, m\} \times \{1, \ldots, n\}$, where $\delta_k(\mathcal{I}) = 1$ if $k \in \mathcal{I}$ and 0 else, and $\Pi^{(k,l)}(\boldsymbol{x})$ corresponds to the field $\Pi(\cdot, t_l; \boldsymbol{x})$ averaged on the cell $\mathcal{D}_k$.

Likewise, the adopted discretization of the local leak field Q with coatings writes as follows:

$$Q^{(k,l)}(\boldsymbol{x}, \boldsymbol{\theta}, \boldsymbol{\gamma}) = C_c^{(k,l)}(\boldsymbol{\gamma}) Q_0^{(k,l)}(\boldsymbol{x}, \boldsymbol{\theta}) \tag{C.6}$$

where $C_c^{(k,l)}(\boldsymbol{\gamma})$ represents the contribution of coatings on the k-th cell and at the l-th instant. Based on the coating model proposed in Section 5.2.2, this contribution is assumed to be defined by:

$$C_c^{(k,l)}(\boldsymbol{\gamma}) = (1 - \gamma_{1,k}\varsigma_1^{(k,l)})(1 - \gamma_{2,k}\varsigma_2^{(k,l)}) \tag{C.7}$$

where $(\gamma_{1,k}, \gamma_{2,k}) \in [0, 1]$ respectively denote efficiency parameters of intrados and extrados coatings of the cell $\mathcal{D}_k$, whereas $\varsigma_1^{(k,l)}, \varsigma_2^{(k,l)}$ respectively denote the fraction of coated surface at intrados and extrados sides of the cell $\mathcal{D}_k$ at time t_l. In this way, if the intrados (respectively extrados) face of the cell $\mathcal{D}_k$ is fully covered by coatings, one has $\varsigma_1^{(k,l)} = 1$ (respectively $\varsigma_2^{(k,l)} = 1$). As a result, the discretized formulation proposed in Eq. (C.7) involves $2m$ unknown coating efficiency parameters. Note that it is possible to reduce this number of unknowns by assuming that coating efficiency parameters are identical on given subsets of the discretized geometrical domain.

Finally, the presented discretization leads to the definition of a local leak field which may be seen as a deterministic map $\boldsymbol{Q} : \mathcal{D}_{\boldsymbol{X}} \times \mathcal{D}_{\boldsymbol{\Theta}} \times \mathcal{D}_{\boldsymbol{\Gamma}} \to \mathbb{R}^{m\times n}$, which depends on the following random input parameters:

- parameters $\boldsymbol{X}$ related to the THM model describing the field Π,
- parameters $\boldsymbol{\Theta}$ related to the assumed relationship between the field Π and the field of (virtual) local leaks Q_0,
- parameters $\boldsymbol{\Gamma}$ related to coatings positioned on the surface of the structure.

C.2.3 Bayesian inference

The local leak model described in the previous sections involves numerous uncertain parameters that cannot be measured directly, for most of them. Besides, local leakage measurements (see Section 4.2.2.3) are available from pressurization tests. Consequently, we propose to infer the aforementioned uncertain parameters from local leakage measurements, in a Bayesian inverse problem perspective.

To that end, a prior distribution for parameters $(\boldsymbol{X}, \boldsymbol{\Theta}, \boldsymbol{\Gamma})$ has firstly to be defined. For the sake of simplicity, these parameters are assumed to be mutually independent. Their prior density is thereby written as follows:

$$\pi(\boldsymbol{x}, \boldsymbol{\theta}, \boldsymbol{\gamma}) = \pi(\boldsymbol{x})\pi(\boldsymbol{\theta})\pi(\boldsymbol{\gamma}) \tag{C.8}$$

On another note, let $\mathcal{Y} = \{y^{(k,l)}\}_{(k,l)\in\{1,\dots,m\}\times\{1,\dots,n\}}$ be a set formed by local leakage measurements projected on the adopted cells $(\mathcal{D}_k)_{1\leq k\leq m}$, for each instant t_l with $l \in \{1,\dots,n\}$. Then, a statistical model has to be devised in order to establish a link between model outputs and observed data. For each instant t_l, denoting by $\boldsymbol{Y}_{\boldsymbol{Q}^{(l)}} : \Omega \to \mathbb{R}^m$ the observed local leak field at instant t_l, the following additive Gaussian model is considered:

$$\boldsymbol{Y}_{\boldsymbol{Q}^{(l)}}|\boldsymbol{x},\boldsymbol{\theta},\boldsymbol{\gamma} = \boldsymbol{Q}^{(l)}(\boldsymbol{x},\boldsymbol{\theta},\boldsymbol{\gamma}) + \boldsymbol{E}^{(l)} \tag{C.9}$$

where $\boldsymbol{Q}^{(l)}(\boldsymbol{x},\boldsymbol{\theta},\boldsymbol{\gamma}) = (Q^{(k,l)}(\boldsymbol{x},\boldsymbol{\theta},\boldsymbol{\gamma}))_{1\leq k\leq m}$ is the predicted local leak field at time t_l, and $\boldsymbol{E}^{(l)} \sim \mathcal{N}(\boldsymbol{0},\boldsymbol{\Sigma}^{(l)})$ is a centered Gaussian random vector with covariance matrix $\boldsymbol{\Sigma}^{(l)}$. For the sake of simplicity, this matrix is assumed to be diagonal, *i.e.* $\boldsymbol{\Sigma}^{(l)} = \mathrm{diag}(\sigma_{1,l}^2,\dots,\sigma_{m,l}^2)$, and its entries are assumed to be known.

Then, for a given instant t_l, the likelihood function $\mathcal{L}^{(l)}$ associated to the model in Eq. (C.9) is given by:

$$\mathcal{L}^{(l)}(\boldsymbol{x},\boldsymbol{\theta},\boldsymbol{\gamma}) = \varphi_m(\boldsymbol{y}^{(l)};\boldsymbol{Q}^{(l)}(\boldsymbol{x},\boldsymbol{\theta},\boldsymbol{\gamma}),\boldsymbol{\Sigma}^{(l)}) \tag{C.10}$$

where $\boldsymbol{y}^{(l)} = (y^{(k,l)})_{1\leq k\leq m} \in \mathbb{R}^m$ denotes observations of the local leak field at time t_l, and $\varphi_m(\cdot;\boldsymbol{\mu},\boldsymbol{\Sigma})$ is the density of $\mathcal{N}(\boldsymbol{\mu},\boldsymbol{\Sigma})$, with $\boldsymbol{\mu} \in \mathbb{R}^m$ and $\boldsymbol{\Sigma} \in \mathbb{R}^{m\times m}$.

Furthermore, assuming that the Gaussian noise terms $(\boldsymbol{E}^{(l)})_{1\leq l\leq n}$ are mutually independent, the likelihood function associated to the whole data set $\mathcal{Y}$ is given by:

$$\mathcal{L}(\boldsymbol{x},\boldsymbol{\theta},\boldsymbol{\gamma}) = \prod_{l=1}^{n} \mathcal{L}^{(l)}(\boldsymbol{x},\boldsymbol{\theta},\boldsymbol{\gamma}) \tag{C.11}$$

Thus, the posterior density of parameters $(\boldsymbol{X},\boldsymbol{\Theta},\boldsymbol{\Gamma})$ given the data set $\mathcal{Y}$ may be derived through applying Bayes' theorem:

$$\pi(\boldsymbol{x},\boldsymbol{\theta},\boldsymbol{\gamma}|\mathcal{Y}) \propto \pi(\boldsymbol{x},\boldsymbol{\theta},\boldsymbol{\gamma})\mathcal{L}(\boldsymbol{x},\boldsymbol{\theta},\boldsymbol{\gamma}) \tag{C.12}$$

For computational purposes, posterior samples can be drawn by using the SuS algorithm presented in Section 2.2.2. Subsequently, new predictions of the local leak field can be performed, based on the generated posterior samples.

C.3 Numerical test-cases

In this section, the approach presented in Section C.2 is applied to several test-cases, including the VeRCoRs mock-up (see Chapter 4) and two operating NCBs. The general settings considered for all these test-cases are precised hereafter. Firstly, the field Π considered here corresponds to prestressing losses computed at the scale of the standard zone. Furthermore, for the sake of simplicity, the underlying THM parameters $\boldsymbol{X}$ are assumed to be deterministic, and are fixed to their nominal value. In the framework of a simple first attempt, this provides a fully analytical local leak model, which significantly reduces the overall computational cost of the approach. As a result, only the parameters $\boldsymbol{\Theta}$, and $\boldsymbol{\Gamma}$ in the presence of coatings, are concerned by Bayesian inference. Moreover, concerning the function F linking (see Eq. (C.1)), the power model in Eq. (C.2).

As local leaks are expected to continuously increase over time as prestressing losses increase, lognormal priors are considered for parameters Θ_1 and Θ_2 (the mean of Θ_2 being

set to 1), so that values of θ_1, θ_2 are positive. Moreover, one set of parameters $(\Theta_{k,1}, \Theta_{k,2})$ is considered for each cell $\mathcal{D}_k$ included in the chosen leak support $\mathcal{S} = \bigcup_{i \in \mathcal{I}} D_{\boldsymbol{s}_i}$, which leads to a number of $d_{\boldsymbol{\Theta}} = 2|\mathcal{I}|$ parameters, $|\mathcal{I}|$ being the number of cells of the support. Note that only parameters related to cells included in the adopted leak support are concerned by Bayesian inference, since the leakage rate outside from the support is set to zero. Furthermore, the components of the resulting inputs $\boldsymbol{\Theta}$ are assumed to be mutually independent. In addition, the $d_{\boldsymbol{\Gamma}} = 2|\mathcal{I}|$ coating parameters $\boldsymbol{\Gamma}$ associated to cells of the leak support are also assumed to be mutually independent, and each parameter is endowed with a uniform prior with support $[0, 1]$.

Next, for each case studied, the entries of observation noise covariance matrices (see Section C.2.3) are assumed to be known, and each standard deviation is computed from estimated standard deviation of measurements of flow meters used during pressurization tests. Note that such a simplifying assumption implies to only consider measurement uncertainties for the observation noise (intrinsic model uncertainties are thereby neglected).

Lastly, Bayesian computations are performed with the SuS algorithm presented in Section 2.2.2, by considering $N = 5000$ samples per level, and a rarity parameter of $p_0 = 0.1$.

C.3.1 VeRCoRs mock-up

The first test case concerns the prediction of local leak fields of the VeRCoRs mock-up, which has been presented in Chapter 4. Here, the problem is simpler than in the case of operating NCBs, since it does not involve coating parameters $\boldsymbol{\Gamma}$.

Firstly, the local leak field observed at VD1 test is used to infer the model parameters $\boldsymbol{\Theta}$, in order to predict the VD2 field. Subsequently, parameters are inferred from observation data of VD1 and VD2 tests in order to predict the VD3 field. Concerning the spatial discretization of the structure, a regular grid with 25×15 cells is adopted. The leak support is defined to be the union of cells whose observed VD1 leakage rate exceeds the threshold value of 100 Nl.h^{-1}, in order to eliminate cells with negligible leaks. The so defined leak support only includes 18 cells, which constitutes a sensibly reduced number of parameters to infer compared to the total number of 375 cells of the adopted grid.

Then, prediction results obtained from posterior samples drawn with the SuS algorithm are presented and discussed hereafter. For the sake of brevity, posterior input parameters are not shown here, in order to rather focus on prediction results. In order to visualize the evolution of local leaks during the considered period (*i.e.* from VD1 to VD3), the observed local leak field at VD1 test is shown in Fig. C.2. Moreover, a comparison of the observed local leak field and the mean of the predicted field at VD2 is given in Fig. C.3. The same comparison for the VD3 test is presented in Fig. C.4.

The visualization of the local leak field observed at VD1 test enables to distinguish two major zones with significant local leaks, namely a zone near the equipment hatch (near 250 gon, at mid-height) and the gusset with the lower standard zone connected to it (near $z = 0$ m). It is worth mentioning that local leaks in this last zone are mainly driven by cracks formed in the concrete volume during the early age phase.

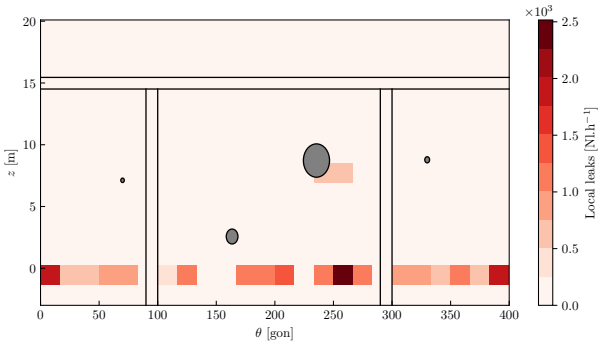

Figure C.2: VeRCoRs - Observed local leak field - VD1 test.

Then, globally speaking, local leak fields at VD2 and VD3 are reasonably well predicted by the proposed approach. This is notably due to the fact that the VD2 field follows the pattern observed at VD1: indeed, the distribution of local leaks seems to not strongly evolve in space, since important leaks observed at VD1 stay in the same zones at VD2. A similar behavior is observed for the VD3 test. This seems to underline the physical phenomena which motivated the definition of the phenomenological local leak model proposed in Section 3.3.5.2 and C.2.1: at the end of prestressing phase, cracks formed during the early age phase are (partially) closed. Subsequently, during the long-term phase, these cracks are continuously reopening under the effect of prestressing losses, which induces the increase of their local leakage rate, from one pressurization test to another.

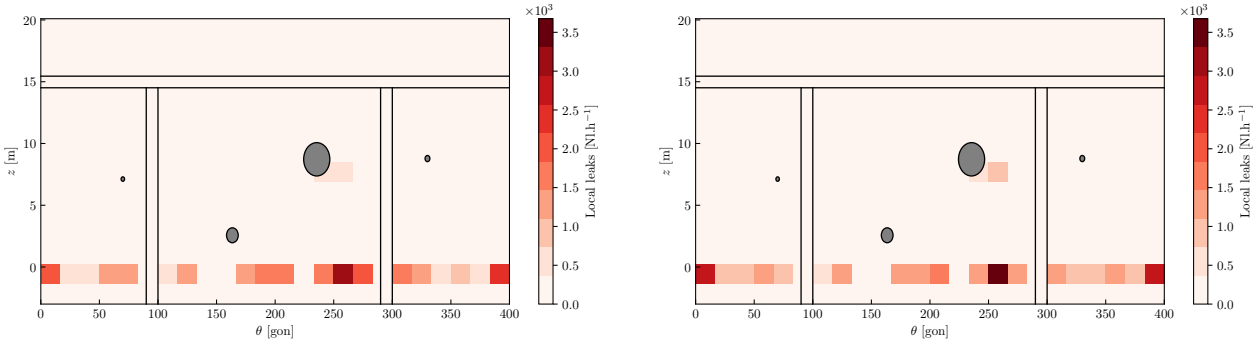

(a) Observed field. **(b)** Predicted field - Mean.

Figure C.3: VeRCoRs - Comparison of observed and predicted local leak fields at VD2 test.

Then, it is worth noting that several QoI related to the predicted local leak field can be estimated from the generated posterior samples. For instance, quantiles of the predicted field can be used so as to visualize extreme values of the field. In particular, high-order quantiles might be interpreted as indicators for zones in which potentially important local leaks may occur. The 5% and 95% quantiles of the VD3 predicted field are shown in Fig. C.5. For most of the cells with significant leaks, observed local leak values are reasonably well bounded the aforementioned predicted quantiles.

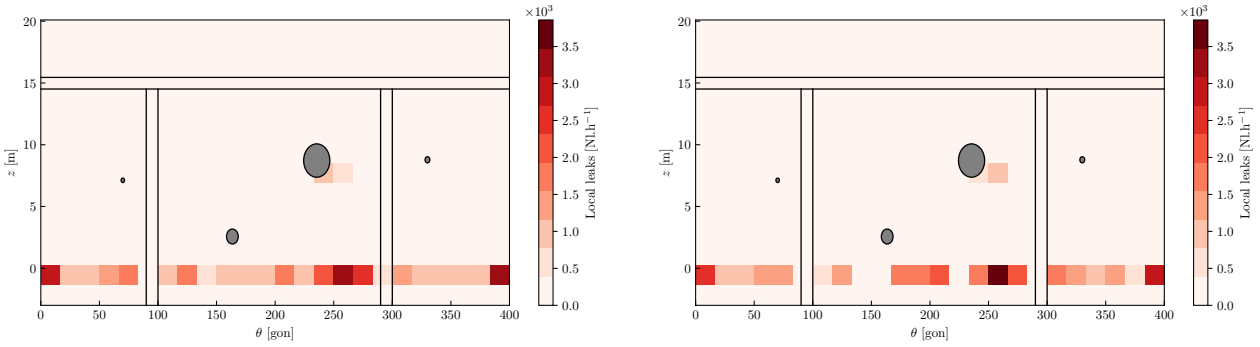

(a) Observed field. **(b)** Predicted field - Mean.

Figure C.4: VeRCoRs - Comparison of observed and predicted local leak fields at VD3 test.

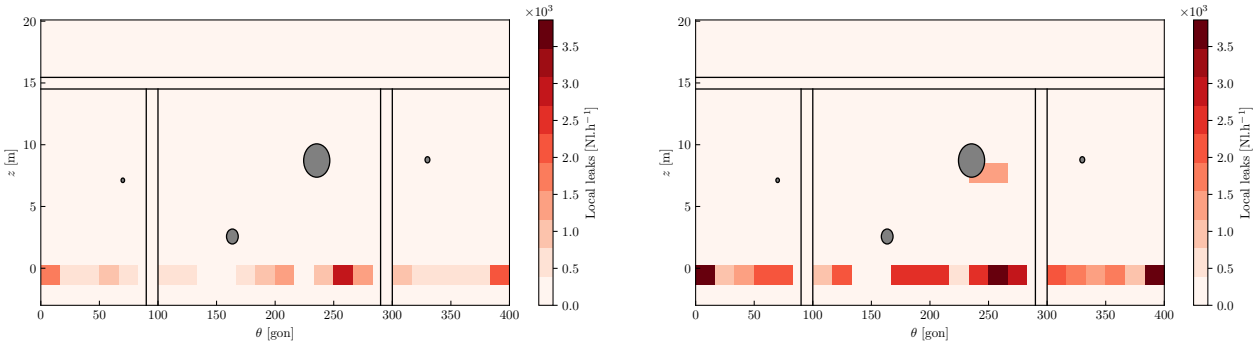

(a) Predicted 5% quantile field. **(b)** Predicted 95% quantile field.

Figure C.5: VeRCoRs - 5% and 95% quantiles of the predicted local leak field at VD3 test

Finally, the predicted field might be used to assess the total local leakage rate of the structure (as in Chapters 4 and 5), simply by summing it on the surface of the latter. In this context, the proposed approach enables to well predict the order of magnitude of the observed total local leakage rate: at VD2 test, the mean of the predicted total leakage rate (29.3 $Nm^3.h^{-1}$) approaches the observed one (31.7 $Nm^3.h^{-1}$) with a relative error of 7.6%. Moreover, at VD3 test, the observed leakage rate is about 38.9 $Nm^3.h^{-1}$, whereas the predicted one is about 34.0 $Nm^3.h^{-1}$, which corresponds to a relative error of 12.6%.

C.3.2 Operating 1:1 scale NCBs

The test case concerning the VeRCoRs mock-up presented in the previous section enabled to assess the predictive power of the model proposed in Section C.2, in the absence of coatings. In this section, two operating NCBs are considered. These two NCBs will be named A and B in the following. In both cases, parameters are inferred from the observed local leak field at VD2, in order to predict the VD3 field. Note that here, the prediction problem is much more difficult than in the VeRCoRs case, and that a small amount of data is available to infer a large amount of uncertain input parameters. Moreover, a coarser grid comprising 8×4 cells is considered here, for the sake of simplicity.

Results concerning the NCB A are firstly presented and discussed. The observed VD2 field used to update input parameters is shown in Fig. C.6. Moreover, a comparison the mean of the predicted field and the observed field at VD3 is given in Fig. C.7. Globally speaking, the VD3 predictions kept in memory some zones which presented a significant leakage rate at VD2, while underestimating the reduction of the leakage rate provided by positioned coatings. Indeed, a zone with an important leakage rate near 300 gon and $z = 0$ during the VD2 test has been coated for the VD3 test, so that its leakage rate at VD3 is practically equal to zero. Such a phenomenon has not been reproduced by the model, which still predicts a significant leakage rate in this zone. Besides, predictions sensibly differ from the observed field at VD3, except maybe near the right half of the dome (from 200 gon to 400 gon), where important leaks are predicted.

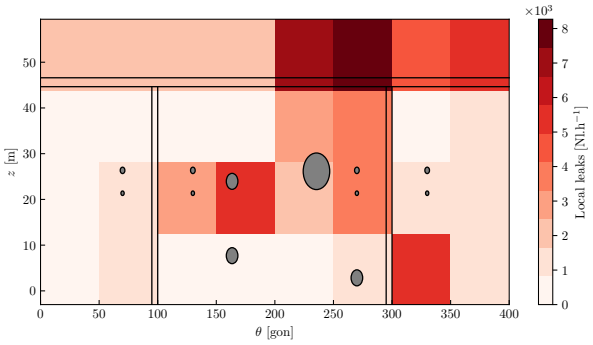

Figure C.6: NCB A - Observed local leak field - VD2 test.

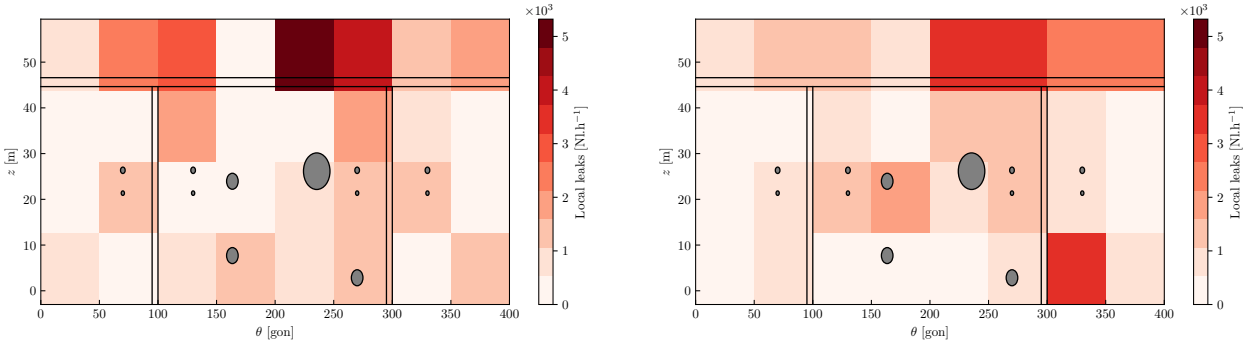

(a) Observed field. **(b)** Predicted field - Mean.

Figure C.7: NCB A - Comparison of observed and predicted local leak fields - VD3 test.

Again, the use of quantiles enables to have an idea of the zones in which important leaks are likely to occur: the 5% and 95% quantiles of the predicted VD3 field are depicted in Fig. C.8. The 95% quantile notably indicates that extreme values of the local leak field are located in several cells of the dome. In a certain extent, such an indicator might be used to guide the positioning of coatings, in order to focus on plausible zones with important leaks.

Finally, it is worth noting that the proposed approach enables to correctly predict the order of magnitude of the total local leakage of the structure, since the observed one is approached with a relative error of about 3% by predictions. However, this probably stems from compensated errors at the local scale, due to the difference observed between the two corresponding fields (see Fig. C.7).

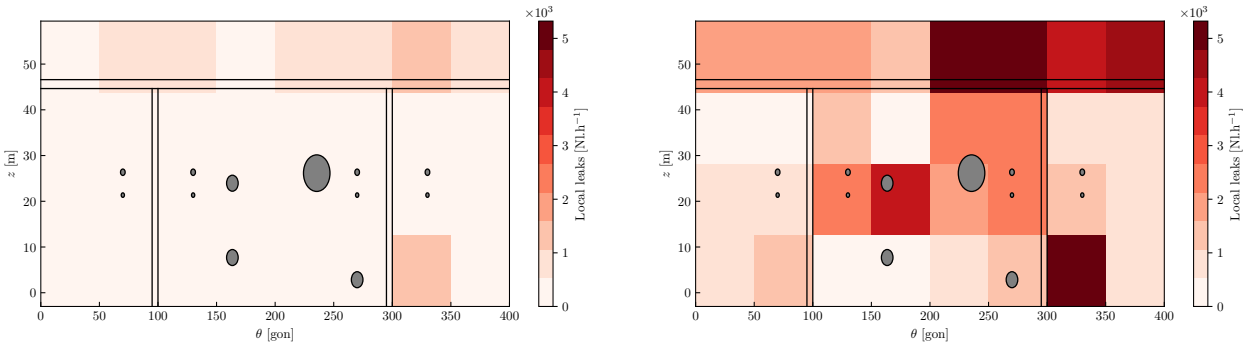

(a) Predicted 5% quantile field.

(b) Predicted 95% quantile field.

Figure C.8: NCB A - 5% and 95% quantiles of the predicted local leak field - VD3 test.

Likewise, results related to NCB B are presented and discussed. The local leak field observed at VD2 is shown in Fig. C.9. Then, the observed local leak field and the mean predicted one at VD3 are compared in Fig. C.10. The considered NCB presents less local leakage zones at VD2, and zones with important leakage rates are concentrated at mid-height, on an angular sector varying from 100 to 350 gon (see Fig. C.9). Then, at VD3, the observed field presents one zone with an important leakage rate, which is located near the equipment hatch (near 200 gon at mid-height). This is well reproduced by predictions. Zones with smaller leakage rates are more roughly predicted by the model, though. Finally, the 5% and 95% quantiles of the VD3 predicted field are depicted in Fig. C.11. The 95% quantile enables to visualize zones with important local leaks, which are mainly located near hatches, at mid-height of the structure.

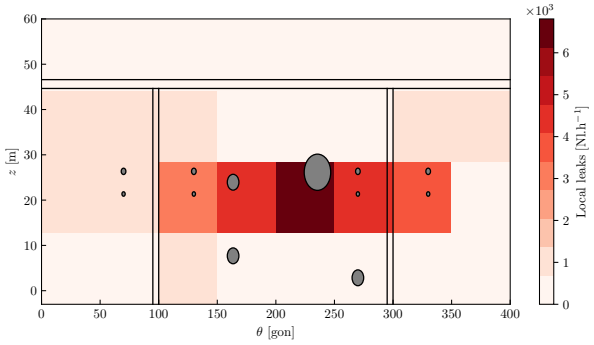

Figure C.9: NCB B - Observed local leak field - VD2 test.

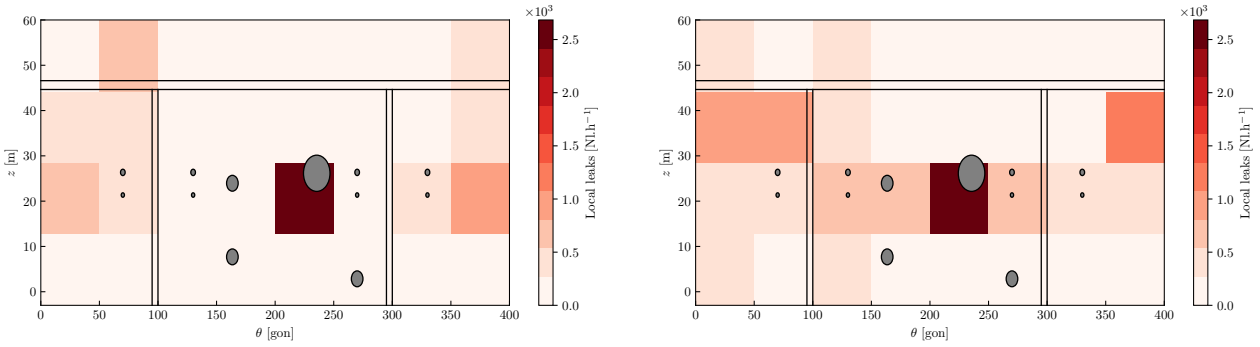

(a) Observed field. **(b)** Predicted field - Mean.

Figure C.10: NCB B - Comparison of observed and predicted local leak fields - VD3 test.

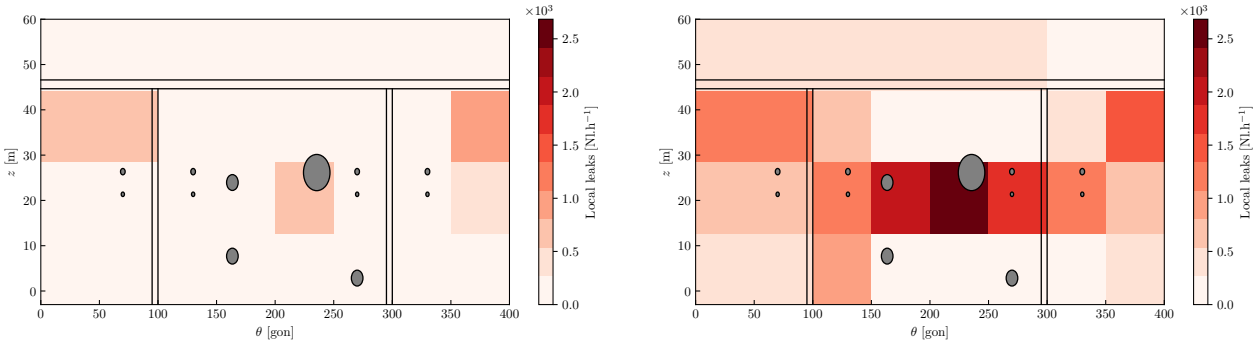

(a) Predicted 5% quantile field. **(b)** Predicted 95% quantile field.

Figure C.11: NCB B - 5% and 95% quantiles of the predicted local leak field - VD3 test.

C.4 Conclusions and perspectives

In this section, a simple methodology aiming at assessing the spatio-temporal evolution of local leaks of NCB has been proposed. This approach is based on a simple phenomenological model linking local leak field to a THM field of interest (*e.g.* water saturation, prestressing or strains), and on a probabilistic description of uncertain input parameters. In this context, the level of knowledge in these input parameters is updated through Bayesian inference, from observations of local leak fields. The proposed approach has been applied to several realistic test-cases, including the VeRCoRs mock-up and two operating 1:1 scale NCBs.

Then, in the VeRCoRs case, results suggest that the proposed local leak model enables to reasonably assess the spatio-temporal evolution of local leaks. In the more complex case of operating NCBs, involving the presence of coatings, results are more mixed, but the proposed model still enables to reasonably well locate zones with large local leakage rates. Broadly speaking, the proposed approach provides a practical visualization of local leak fields with maps of the surface of the studied structure, while proposing probabilistic description of predicted fields, which enables to indicate plausible zones with important leaks. Thus, the proposed approach might be used in complement to global approaches presented in Chapters 4 & 5 in order to potentially optimize the positioning of coatings in the framework of the

maintenance of NCB, through priorizing repair works on the most likely important leakage zones.

Besides, it is worth mentioning that the proposed approach tackles a way more difficult prediction problem than that addressed by global approaches presented in Chapters 4 & 5, since only a small amount of information regarding local leaks is available, and the literature is lacking concerning interactions between leakage and coatings, involving complex transfer phenomena at structural scale. In this context, the proposed simple phenomenological model enables to qualitatively describe the spatio-temporal evolution of local leaks at the scale of the whole structure. The choice of such a simple model is justified as follows: explicitly modeling local leaks through full scale FE calculations would be computationally intractable, since cracking would have to be modeled, for instance with (costly) damage models. Furthermore, such an approach would require a precise knowledge of the location of cracks, as well as their geometrical and hydraulic properties (see Section 3.3.5.2).

The proposed approach constitutes a simple first attempt at predicting local leak fields, and consequently underlies several improvement perspectives. First, the proposed physical model can be obviously refined, regarding the modeling of the evolution of local leaks, as well as the effects of coatings on the hydraulic behavior of the structure. Moreover, it is important to underline that in its actual formulation, the proposed model is only able to predict local leaks in zones in which leaks have already been observed. This is materialized by the notion of leak support, which corresponds to a subset of the studied geometrical domain in which predictions are performed (see Section C.2.1). Hence, the model is not able to detect a potential crack propagation or initiation which would induce the appearance of local leaks in a zone outside of the leak support. Next, in the presented applications, one set of input parameters has been considered for each cell of the adopted spatial discretization of the structure.

Moreover, all the aforementioned parameters are assumed to be mutually independent. Hence, it would be possible to model some inputs by random fields (*e.g.* coating efficiency, local leak evolution parameters), which enable to account for spatial auto-correlation. In this context, such random fields could be inferred through Bayesian inference in a purely analogous way than that presented in the proposed approach, by adopting random field discretization schemes (see *e.g.* (Uribe et al., 2020)). Lastly, regarding alternative modeling approaches for predicting local leak fields, it is worth mentioning the interesting the approach proposed in (Oumouni et al., 2019), based on spatio-temporal Gamma processes, originally used to model degradation phenomena.

D Computational tools and numerical implementations

- Calculations are performed by using a desktop computer, with Intel Xeon W-2145 (8 cores, $3.7 - 4.5$ Ghz Turbo).
- Unless otherwise specified, the algorithms used in this thesis are based on in-house codes developed in `Matlab` and `Python`. Otherwise, some features of the software UQLab (Marelli and Sudret, 2014) for `Matlab`, and OpenTURNS (Baudin et al., 2016) for `Python` are used, notably regarding PCE and PCK surrogate modeling.
- Finite element calculations presented in Chapters 4 & 5 of this thesis are performed with the `Code_Aster` solver developed by EDF R&D. Moreover, finite element meshes are generated by using the `Salome` platform.
- During my PhD, I had the opportunity to collaborate with EDF R&D in order to contribute to an internal software dedicated to digital twins of NCB. In this context, I developed two `Python` software, that are described herebelow:
  - one software enabling to perform a global UQ analysis for the THML behavior of NCB, based on the contents presented in Chapters 4 & 5. In addition to a wide range of scripts enabling to performing finite element THML calculations, this software notably contains features related to Bayesian inference, sensitivity analysis, reliability and robustness analysis. In particular, it comprises in-house codes for several MCMC algorithms (including MH, AM, AIES, see Section 1.3.4), the SuS within BuS algorithm presented in Section 2.2, analytical post-processing features for PC-PCE surrogates, an implementation of MCS and SuS algorithms for reliability analysis, and PLI measures used in Chapter 5.
  - one software corresponding to the method presented in Appendix C aiming at predicting local leak fields of NCB. It notably comprises processing and visualization features for local leak data, and uses probabilistic modeling functionalities of the `OpenTURNS`, the `Salome` platform, as well as a `Python` implementation of the SuS within BuS algorithm (see Section 2.2.2)

E Résumé étendu de la thèse

E.1 Contexte industriel et scientifique

Les centrales nucléaires constituent une part importante de la production d'électricité en France, principalement assurée par l'entreprise Electricité de France (EDF). En effet, le parc nucléaire Français inclut 56 réacteurs opérationnels, représentant environ 78% de la production d'électricité Française (EDF, 2021). Ce mix énergétique résulte notamment d'une politique d'indépendance énergétique initiée après la fin de la Seconde Guerre Mondiale et confirmée par les deux chocs pétroliers de 1973 et 1979.

Les réacteurs opérationnels précités sont tous basés sur la technologie de type Réacteur à Eau Pressurisée (REP), et peuvent être classifiés en plusieurs familles en fonction de leur puissance:

- 32 réacteurs développant chacun une puissance de 900 MWe. Ces réacteurs sont répartis sur 8 sites, et ont été construits entre 1971 et 1987.
- 20 réacteurs chacun dotés une puissance de 1300 MWe, répartis sur 8 sites et construits entre 1977 et 1993.
- 4 réacteurs chacun dotés une puissance de 1450 MWe, répartis sur 2 sites et construits entre 1984 et 1999.

Enfin, la construction d'un nouveau réacteur basé sur la technologie de type Réacteur Pressurisé Européen (EPR) a été initiée sur le site de Flamanville, en 2007. Ce réacteur dispose d'une puissance caractéristique de 1650 MWe. La répartition géographique des réacteurs précités est donnée par la Fig. E.1.

Le principe de fonctionnement d'un réacteur de type REP est schématisé par la Fig. E.2. Premièrement, le coeur du réacteur est le lieu des réactions nucléaires: il est placé dans une cuve en acier, et comprend plusieurs centaines de barres de combustible nucléaire. Les réactions de désintégration des matières fissiles contenus dans le combustible induisent un important dégagement de chaleur, ensuite absorbé par l'eau entourant les barres de combustible. Cette eau évolue dans un circuit fermé, usuellement connu sous le nom de *circuit primaire* (en jaune dans la Fig. E.2). À travers ce circuit, la chaleur dégagée par le coeur du réacteur est transportée vers des générateurs de vapeurs. Ces derniers transforment la chaleur précitée en vapeur au sein d'un second circuit fermé, nommé *circuit secondaire* (en bleu dans la Fig. E.2). Ce circuit convertit l'énergie thermique du circuit primaire en énergie mécanique, à travers l'injection de vapeur dans une turbine reliée à un alternateur, transformant l'énergie mécanique en énergie électrique. Enfin, la vapeur est à nouveau transformée en eau via un condenseur, relié à une source froide par le biais d'un *circuit tertiaire* (ou *circuit de refroidissement*, en vert dans la Fig. E.2). La source froide provient typiquement d'une rivière ou de la mer, et est éventuellement complétée par une tour aéro-réfrigérante.

La sûreté d'un réacteur nucléaire repose principalement sur trois fonctions, à savoir la maîtrise de la réactivité du réacteur, le refroidissement du combustible et le confinement des éléments radioactifs. Dans ce contexte, un réacteur dispose de trois barrières de confinement:

Figure E.1: Localisation des 56 réacteurs du parc nucléaire Français, et de l'EPR de Flamanville (en construction). La centrale nucléaire de Fessenheim a été fermée en 2020. ©IRSN

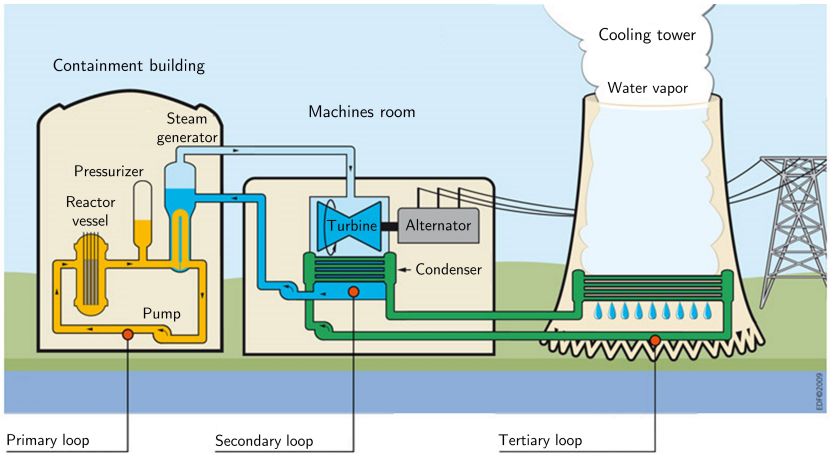

Figure E.2: Schématisation du principe de fonctionnement d'un réacteur de type REP. ©EDF

1. les gaines des barres de combustible, visant à empêcher la migration des produits de fission dans l'eau du circuit primaire,

2. le circuit primaire, comprenant notamment la cuve du réacteur (voir Fig. E.2).

3. l'enceinte de confinement, abritant le circuit primaire (voir Fig. E.2).

En particulier, l'enceinte de confinement assure deux fonctions, à savoir la protection du réacteur en cas d'agressions externes (*e.g.* impacts), et la protection de l'environnement en cas d'accident interne. Par conséquent, cette structure doit disposer d'une étanchéité suffisante afin de remplir son rôle de protection.

Le principe de conception des enceintes de confinement des réacteurs des centrales nucléaires Françaises a progressivement évolué depuis le début des années 1970 (Jacquemain, 2015). Tout d'abord, les enceintes de confinement des réacteurs de 900 MWe consistent en une simple paroi en béton armé et précontraint, dont l'étanchéité est assurée par un liner en acier. Ensuite, les réacteurs de 1300 MWe sont constituées d'une double enceinte en béton, comprenant une enceinte interne en béton armé et précontraint sans liner métallique, ainsi qu'une enceinte externe en béton armé. Dans ce contexte, la protection du réacteur est assurée par l'enceinte externe, tandis que l'étanchéité est assurée par l'enceinte interne. De plus, un système actif maintient un vide dans l'espace entre enceintes, de manière à ce que les éventuels éléments radioactifs provenant de situations accidentelles puissent être collectés et filtrés plutôt que directement relâchés dans l'environnement.

Cette thèse est motivée par la problématique de l'étanchéité des enceintes de confinement à double paroi. En France, les autorités de régulation spécifient un critère relatif au débit de fuite de l'enceinte interne: lorsque cette dernière est soumise à une pression interne de 5.2 bars, son débit de fuite ne doit pas excéder 1.5% par jour de la masse d'air contenue dans l'enceinte. Dans ce contexte, le débit de fuite de l'enceinte est mesuré avant la mise en service du réacteur, puis tous les dix ans, au cours d'essais de pressurisation réalisés à l'occasion de *visites décennales*. Le respect du critère d'étanchéité conditionne la poursuite de l'exploitation du réacteur.

Par ailleurs, le béton constitue un matériau hétérogène complexe, dont les propriétés peuvent évoluer au cours du temps sous l'effet de plusieurs phénomènes physiques liées au *vieillissement*. En particulier, de tels phénomènes peuvent conduire à une augmentation du débit de fuite des enceintes de confinement au cours du temps, ce qui pourrait altérer leur étanchéité à long-terme. Dès lors, les enceintes de confinement ne pouvant pas être remplacées, des opérations de maintenance peuvent être envisagées afin de renforcer leur étanchéité. De telles opérations doivent être réalisées lorsque le réacteur est à l'arrêt, et requièrent un coût potentiellement très important. Ainsi, il est nécessaire de développer des stratégies numériques visant à prévoir l'évolution du débit de fuite d'enceintes de confinement, afin de mieux anticiper d'éventuelles réparations dans le cadre de leur maintenance.

E.2 Quantification d'incertitudes en simulation numérique

La modélisation et la simulation numériques occupent une place centrale dans le cadre de l'ingénierie moderne. Depuis la fin du vingtième siècle, l'essor constant des ressources de calcul et des avancées dans le cadre du calcul scientifique ont permis la simulation de systèmes de plus en plus complexes. De ce fait, les modèles numériques sont aujourd'hui au coeur de la conception et de l'exploitation de systèmes d'ingénierie, tels que les ponts, barrages, ou enceintes de confinement. Dans ce contexte, ils permettent de simuler le comportement de tels systèmes, et sont très souvent substitués à des expériences réelles, généralement trop coûteuses, complexes, voire impossibles à mettre en oeuvre. Par exemple, dans le cadre des enceintes de confinement, des modèles numériques ont été développés dans l'optique d'évaluer l'évolution temporelle de leur comportement multi-physique à long-terme. De tels modèles numériques sont typiquement basés sur des formules analytiques, ou bien des systèmes d'équations aux dérivées partielles, résolues numériquement au moyen de schémas numériques tels que la très usitée méthode des éléments finis.

Toutefois, malgré leur fidélité croissante, les modèles numériques demeurent des représentations idéalisées de la réalité. Ainsi, les écarts entre les prédictions numériques et les observations sont inévitables, notamment du fait d'un manque de connaissance relatif aux lois de comportement physiques, ou du fait d'échelles non résolues. De plus, la simulation de systèmes physiques complexes requiert un nombre potentiellement important de paramètres d'entrée. Par exemple, dans le cadre du génie civil, de tels paramètres peuvent correspondre à des propriétés matériau, géométriques, des conditions aux limites ou des conditions initiales, ainsi qu'à des paramètres non mesurables directement. De tels paramètres sont tous entachés d'incertitudes, typiquement en raison d'un manque de connaissance, ou d'une variabilité intrinsèque. Néanmoins, ces incertitudes sont souvent négligées en pratique, les approches de modélisation classiquement considérées dans les études d'ingénierie demeurant majoritairement déterministes. Ainsi, il est nécessaire de prendre en compte ces incertitudes afin de proposer une approche de modélisation plus rigoureuse et plus complète.

La Quantification d'Incertitudes constitue la discipline scientifique visant à modéliser explicitement les incertitudes en simulation numérique (De Rocquigny et al., 2008; Smith, 2014; Sullivan, 2015). Elle a récemment émergé en tant que domaine de recherche actif, qui englobe un large éventail d'éléments théoriques et appliqués situés à l'interface des Statistiques, de la Théorie des Probabilités, des Mathématiques Appliquées et de l'Informatique. En outre, les techniques de quantification d'incertitudes sont aujourd'hui répandues dans diverses branches de l'ingénierie et des sciences appliquées (Ghanem et al., 2017; Soize, 2017). Ceci est particulièrement facilité par la nature interdisciplinaire et modulaire du cadre général de la quantification d'incertitudes défini dans (De Rocquigny et al., 2008; Iooss, 2009; Sudret, 2007). Ce cadre, illustré par la Fig. E.3, s'articule autour d'une chaîne de quelques étapes fondamentales représentatives d'une analyse typique de quantification d'incertitudes, décrites ci-après:

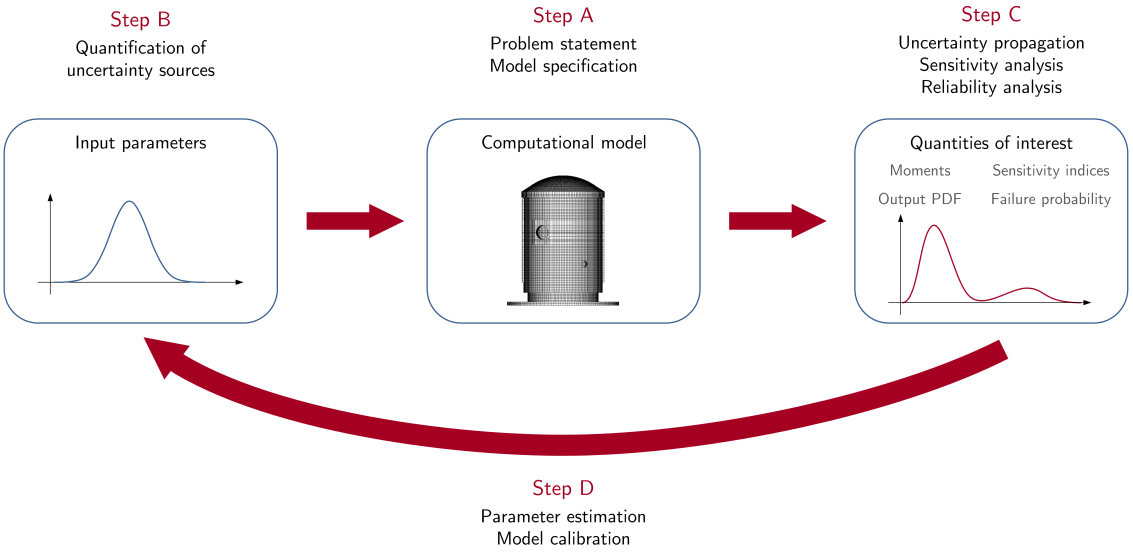

Figure E.3: Représentation schématique du cadre général d'une étude de Quantification d'Incertitudes, adapté de (De Rocquigny et al., 2008; Sudret, 2007; Wagner, 2021).

- **Étape A - Spécification du modèle:** La première étape du cadre de la quantification d'incertitudes consiste à spécifier un modèle de calcul simulant le système physique étudié. Un tel modèle constitue le cœur d'une analyse d'incertitudes, et sa spécification implique la définition des paramètres d'entrée ainsi que des variables de sortie. Dans le cas des enceintes de confinement, il s'agit généralement d'une chaîne de calcul multi-physique basée sur plusieurs codes éléments finis(Boucher, 2016; Bouhjiti, 2018).

- **Étape B - Quantification des sources d'incertitudes:** la deuxième étape vise à identifier les sources d'incertitudes entachant les paramètres d'entrée du modèle. Dans ce contexte, les incertitudes peuvent être modélisées dans plusieurs cadres mathématiques différents, notamment la théorie des probabilités ou les probabilités imprécises.

- **Étape C - Caractérisation des variables de sortie:** la troisième étape consiste à caractériser les incertitudes des variables de sortie du modèle. Cette caractérisation comprend notamment des méthodes issue du cadre de la propagation d'incertitudes (De Rocquigny et al., 2008; Grigoriu, 2012), l'analyse de sensibilité (Iooss and Lemaître, 2015; Saltelli et al., 2004) et de l'analyse de fiabilité (Lemaire et al., 2009; Melchers, 1999).

- **Étape D - Analyse inverse:** enfin, il est possible de quantifier les incertitudes des paramètres d'entrée via une analyse inverse, à partir des observations de la réponse du système physique simulé. Un tel processus de quantification inverse englobe l'estimation de paramètres (Kaipio and Somersalo, 2005; Tarantola, 2005), la calibration de modèles (Kennedy and O'Hagan, 2001) et l'assimilation de données (Evensen, 2009; Reich and Cotter, 2015). De telles tâches peuvent notamment être entreprises d'un point de vue probabiliste dans le cadre de l'inférence Bayésienne, à laquelle une attention particulière sera portée dans cette thèse.

Ensuite, il convient de noter que les méthodes associées aux étapes C & D du cadre de la quantification d'incertitudes nécessitent généralement des évaluations répétées du modèle numérique. Or, ce dernier est souvent coûteux (par exemple un code éléments finis complexe), ce qui entrave l'application des méthodes précitées. Afin de contourner ce problème, le modèle de calcul est généralement remplacé par une fonction mathématique peu coûteuse à évaluer, communément appelée *méta-modèle* (ou *surface de réponse*) (Fang et al., 2005; Forrester et al., 2008). De même, les approches de réduction de modèles (Chinesta et al., 2014; Schilders et al., 2008) visent à trouver un compromis entre un modèle plus simple (et moins coûteux) et un niveau de précision raisonnable. La méta-modélisation (et la réduction de modèle) est devenue une partie intégrante du cadre de la quantification d'incertitudes, et constitue une étape intermédiaire qui permet l'accélération des méthodes de quantification d'incertitudes.

E.3 Contributions et plan de la thèse

Récemment, un large éventail d'approches de modélisation dédiées aux structures de confinement ont pu être développées parallèlement à l'amélioration de la compréhension des phénomènes physiques à l'origine du vieillissement du béton, et servent aujourd'hui de base à la conception de modèles numériques capables d'évaluer raisonnablement le comportement global à long terme de structures de confinement en béton (voir *e.g.* (Asali, 2016; Boucher, 2016; Jason et al., 2007)). Néanmoins, comme mentionné précédemment, ces approches restent le plus souvent déterministes, et ne tiennent donc pas compte des incertitudes omniprésentes entachant les paramètres d'entrée. Les travaux antérieurs de Bouhjiti (2018) constituent alors un point charnière, puisqu'ils constituent une première tentative de quantification d'incertitudes dans le contexte du comportement de fuite des structures de confinement.

Les modèles numériques habituellement adoptés pour évaluer le comportement à long terme de structures de confinement comportent généralement un grand nombre de paramètres d'entrée incertains. En ce qui concerne les paramètres directement mesurables, il est possible de modéliser leurs incertitudes à partir de données expérimentales. Cependant, la plupart des paramètres d'entrée ne sont pas directement mesurables, si bien que peu d'informations sont disponibles à leur sujet. Par conséquent, le *jugement d'expert* (De Rocquigny et al., 2008) est couramment utilisé pour modéliser les incertitudes de ces paramètres, comme par exemple dans (Bouhjiti, 2018). Dans ce contexte, les incertitudes sont modélisées sur la base des connaissances d'un ou plusieurs analystes, de manière plus ou moins subjective. Néanmoins, si de grandes incertitudes sont supposées pour les paramètres d'entrée, les prédictions correspondantes sont susceptibles d'être entachées d'incertitudes importantes, ce qui entrave la prise de décision liée à la maintenance de structures de confinement. En outre, les incertitudes des paramètres d'entrée sont le plus souvent modélisées par des distributions de probabilité, elles-mêmes connues avec différents niveaux de confiance. Par conséquent, il serait nécessaire de quantifier l'impact du choix de telles distributions d'entrée sur des quantités d'intérêt liées au comportement de fuite de la structure étudiée, typiquement une probabilité de dépassement d'un critère réglementaire de fuite. La branche récente de l'*analyse de robustesse* (Iooss et al., 2021; Lemaître et al., 2015; Sueur et al., 2016) vise notamment à répondre à une telle question.

Par ailleurs, les récentes avancées en matière de dispositifs de surveillance ont permis d'acquérir une quantité non négligeable de données relatives au comportement à long terme de grandes structures en béton telles que les enceintes de confinement. Les données de surveillance présentent donc un grand intérêt, car elles peuvent être utilisées pour extraire des informations sur des paramètres d'entrée incertains ne pouvant pas être mesurés directement, et pour ensuite effectuer de nouvelles prédictions du comportement de la structure. Une telle analyse inverse peut être réalisée par le biais de l'inférence Bayésienne, qui permet de mettre à jour un état de connaissance préalable des paramètres d'entrée à partir de données d'observation bruitées, dans un cadre probabiliste.

Par conséquent, sur la base du cadre de la quantification d'incertitudes décrit par la Fig. E.3, cette thèse vise à fournir une approche plus complète pour quantifier les incertitudes liées aux prédictions du comportement à long terme des structures de confinement, en poursuivant les objectifs suivants :

i. Tenir compte des incertitudes dans les simulations de modèles numériques de structure de confinement, afin de quantifier les incertitudes des prédictions de leur comportement à long terme,

ii. Développer une stratégie visant à mettre à jour le niveau de connaissance des paramètres d'entrée incertains à partir de données d'observation bruitées et indirectes fournies par des dispositifs d'auscultation *in-situ*,

iii. Estimer les risques de dépassement des seuils réglementaires de taux de fuite, et évaluer la robustesse d'une telle estimation,

iv. Évaluer l'efficacité d'éventuels scénarios de travaux de réparation, afin de mieux anticiper des opérations de maintenance.

Dès lors, ce manuscrit est organisé comme suit : tout d'abord, un état de l'art général sur le cadre et les méthodes de la Quantification d'Incertitudes est présenté dans le **Chapitre 1**. Les principes fondamentaux de la quantification d'incertitudes sont d'abord introduits, en se concentrant sur la théorie des probabilités. Ensuite, les outils de calcul de base de la quantification d'incertitudes utilisés tout au long de cette thèse sont brièvement présentés. Dans cette perspective, une présentation en deux parties est adoptée, traitant premièrement des méthodes dites *directes* (étape C dans la Fig. E.3) incluant la propagation d'incertitude, l'analyse de sensibilité et l'analyse de fiabilité, avant de présenter des méthodes dites *inverses* (étape D dans la Fig. E.3).

Ensuite, en se concentrant sur l'inférence Bayésienne, le **Chapitre 2** présente un cadre Bayésien récemment introduit par Straub and Papaioannou (2015), nommé *Bayesian Updating with Structural reliability methods* (BuS). Ce cadre constitue la base algorithmique pour les analyses inverses entreprises dans les chapitres suivants de cette thèse. En particulier, les algorithmes impliqués nécessitent un grand nombre d'évaluations du modèle numérique, ce qui rend leur coût prohibitif lorsque des modèles coûteux sont considérés. Dans ce contexte, nous présentons une nouvelle approche basée sur des méta-modèles adaptatifs, visant à accélérer efficacement les méthodes d'échantillonnage Bayésiennes considérées dans cette thèse. Les performances de la méthode proposée sont évaluées à l'aide de plusieurs cas tests académiques de complexité variable.

Ensuite, le **Chapitre 3** établit la base des modèles de calcul adoptés dans les applications aux structures de confinement présentées dans cette thèse, à travers la description d'une stratégie de modélisation adaptée à l'évaluation du comportement Thermo-Hydro-Mécanique et de Fuite (THMF) à long terme des structures de confinement vieillissantes. En particulier, cela implique la définition de paramètres d'entrée (*e.g.* module d'Young, perméabilité) ainsi que de variables de sortie d'intérêt (*e.g.* déformations, taux de fuite). À cette fin, les principaux phénomènes physiques liés au vieillissement du béton sont d'abord introduits, afin de permettre une meilleure compréhension du problème physique principalement abordé dans les chapitres suivants. La stratégie de modélisation THMF adoptée dans cette thèse est ensuite présentée, en capitalisant sur des travaux antérieurs dédiés à la modélisation physique de structures de confinement (Boucher, 2016; Bouhjiti, 2018).

Ensuite, en se basant sur les trois premiers chapitres de cette thèse, le **Chapitre 4** constitue l'une de nos principales contributions à l'évaluation du comportement THMF à long terme de structures de confinement. Dans cette perspective, nous présentons une méthodologie générale visant à évaluer le comportement à long terme des grandes structures de confinement en béton soumises au vieillissement, tout en tenant compte des incertitudes des prédictions dans un cadre probabiliste. En particulier, nous proposons une approche basée sur l'inférence Bayésienne visant à mettre à jour les paramètres d'entrée incertains à partir de données d'observation bruitées fournies par des dispositifs de surveillance *in-situ*. Dans cette perspective, l'étude de cas centrale de ce chapitre est donnée par la maquette VeRCoRs, à savoir une maquette à l'échelle 1:3 d'une enceinte de confinement à double paroi construite par EDF, à des fins de recherche sur le sujet du vieillissement.

Notre deuxième contribution principale au NCB est présentée dans le **Chapitre 5**, qui aborde la thématique des structures de confinement opérationnelles, et se concentre sur l'évaluation de la fiabilité de leur étanchéité. Dans ce contexte, une enceinte de confinement en exploitation (à l'échelle 1:1) constituera l'étude de cas centrale de ce chapitre. En particulier, un tel problème comporte des caractéristiques spécifiques par rapport à la maquette VeRCoRs étudiée dans le chapitre précédent, telles que des opérations de maintenance visant à renforcer l'étanchéité. Dans un premier temps, nous introduisons plusieurs hypothèses de modélisation afin d'évaluer l'effet et l'efficacité de travaux de réparation vis-à-vis de l'étanchéité de la structure. Par la suite, nous proposons d'évaluer les risques de dépassement de seuils réglementaires de fuite, en nous appuyant sur le cadre de l'analyse de fiabilité. Dans ce contexte, les effets du choix de la distribution de probabilité des entrées sur les probabilités de défaillance estimées sont évalués via une analyse de robustesse. Enfin, nous proposons une approche Bayésienne visant à mettre à jour l'estimation des probabilités de défaillance précitées, à partir des données de surveillance *in-situ* collectées tout au long de l'exploitation de la structure.

Enfin, le **Chapitre 6** fournit une conclusion générale à cette thèse. Il discute les limites des approches adoptées et expose les perspectives de ce travail.

E.4 Publications et communications

Les publications et communications liées à cette thèse sont listées ci-dessous.

Articles de revues internationales à comité de lecture

Rossat, D., Baroth, J., Briffaut, M., and Dufour, F. 2022. Bayesian inversion using adaptive Polynomial Chaos Kriging within Subset Simulation. *Journal of Computational Physics*, 455:110986.

Rossat, D., Baroth, J., Briffaut, M., Dufour, F., Masson, B., Monteil, A., and Michel-Ponnelle, S. 2022. Bayesian updating for nuclear containment buildings using both mechanical and hydraulic monitoring data. *Engineering Structures*, 262:114294.

Rossat, D., Baroth, J., Briffaut, M., Dufour, F., Masson, B., Monteil, A., and Michel-Ponnelle, S. 2022. Fast Bayesian inference with correction of model bias and global sensitivity analysis for Nuclear Containment Buildings. *Submitted.*

Rossat, D., Baroth, J., Briffaut, M., Dufour, F., Masson, B., Monteil, A., and Michel-Ponnelle, S. 2022. Bayesian updating for predictions of delayed strains of large concrete structures: influence of the prior distribution. *European Journal of Environmental and Civil Engineering.*

Rossat, D., Bouhjiti, D. E.-M., Baroth, J., Briffaut, M., Dufour, F., Monteil, A., Masson, B., and Michel-Ponnelle, S. 2021. A Bayesian strategy for forecasting the leakage rate of concrete containment buildings – Application to nuclear containment buildings. *Nuclear Engineering and Design*, 378:111184.

Parallèlement aux principaux travaux de cette thèse, j'ai eu l'opportunité de prendre part à des travaux en lien avec le projet Évaluation Non Destructive des Enceintes de confinement des centrales nucléaires (ENDE), financé par l'Agence Nationale de la Recherche (ANR). Ces travaux ont donné lieu à deux publications, résultant de collaborations avec des chercheurs de l'Université Gustave Eiffel (UGE), et du Laboratoire Matériaux et Durabilité des Constructions (LMDC):

Gupta, R., Rossat, D., Dérobert, X., Baroth, J., Briffaut, M., Villain, G., and Dufour, F. 2022. Blind comparison of saturation ratio profiles on large RC structures by means of NDT and SFE — Application to the VeRCoRs mock-up. *Engineering Structures*, 258:114057.

Verdier, J., Rossat, D., Multon, S., Bouhjiti, D., Sogbossi, H., Baroth, J., Nehme, A., Dufour, F., Cagnon, H., and Briffaut, M. 2022. In-situ measurement and numerical modeling of air leakage in concrete: from the lab specimen up to structural scale. *Submitted.*

Communications dans des conférences internationales et nationales

Rossat, D., Baroth, J., Briffaut, M., Dufour, F. 2022. Efficient Bayesian inversion with optimal transport maps and Polynomial Chaos surrogates - Application to mechanical inverse problems. *25ème Congrès Français de Mécanique*, Nantes, France.

Rossat, D., Baroth, J., Briffaut, M., Dufour, F., Monteil, A., Masson, B., and Michel-Ponnelle, S. 2021. Probabilistic modeling in a Bayesian framework of leak tightness of nuclear containment buildings. *31st European Safety and Reliability Conference (ESREL 2021)*, Angers, France.

Exposés dans des séminaires et workshops

Rossat, D., and Baroth, J. 2022. Bayesian inversion using adaptive Polynomial Chaos Kriging within Subset Simulation. *Journée GST Mécanique et Incertain*, Paris, France.

Rossat, D., Baroth, J., Briffaut, M., Dufour, F., Masson, B., Monteil, A., and Michel-Ponnelle, S. 2022. Bayesian updating and reliability analysis for nuclear containment buildings. *60th European Safety, Reliability & Data Association (ESReDA60)*, Grenoble, France.

Rossat, D., and Baroth, J. 2021. Adaptive surrogate models for Bayesian inference - Applications to Nuclear Containment Buildings. *Meeting IMdR - GTR Sécurité et Sûreté des Structures*, Online meeting.

Rossat, D., and Baroth, J. 2020. Actualisation Bayésienne des prévisions du comportement de transfert de grands ouvrages de confinement. *Groupe de travail FIMA: Modèles Aléatoires pour la Fiabilité et la Maintenance des Systèmes*, Grenoble, France.

Bibliography

Abbas, A., Carcasses, M., and Ollivier, J. P. 1999. Gas permeability of concrete in relation to its degree of saturation. *Materials and Structures*, 32(1):3–8. doi: 10.1007/BF02480405. 105, 115

Acker, P. 1988. *Comportement mécanique du béton : apports de l'approche physico-chimique*. PhD thesis, École Nationale des Ponts et Chaussées. 96, 100

Ajenjo, A., Ardillon, E., Chabridon, V., Iooss, B., Cogan, S., and Sadoulet-Reboul, E. 2022. An info-gap framework for robustness assessment of epistemic uncertainty models in hybrid structural reliability analysis. *Structural Safety*, 96:102196. doi: 10.1016/j.strusafe.2022.102196. 15

Ali, S. M. and Silvey, S. D. 1966. A General Class of Coefficients of Divergence of One Distribution from Another. *Journal of the Royal Statistical Society. Series B (Methodological)*, 28(1):131–142. 44

Andrieu, C. and Thoms, J. 2008. A tutorial on adaptive MCMC. *Statistics and Computing*, 18(4):343–373. doi: 10.1007/s11222-008-9110-y. 53, 221

Angelikopoulos, P., Papadimitriou, C., and Koumoutsakos, P. 2015. X-TMCMC: Adaptive kriging for Bayesian inverse modeling. *Computer Methods in Applied Mechanics and Engineering*, 289:409–428. doi: 10.1016/j.cma.2015.01.015. 74, 92

Arrhenius, S. 1915. *Quantitative laws in biological chemistry*. G. Bell, London. 95, 112

Asali, M. 2016. *Modélisation et prévision du comportement thermo-hydro-mécanique d'une paroi en béton : application au cas des enceintes de confinement des bâtiments réacteurs nucléaires*. PhD thesis, Université Lille 1. 104, 114, 133, 136, 177, 209, 241

Au, S., Ching, J., and Beck, J. L. 2007. Application of subset simulation methods to reliability benchmark problems. *Structural Safety*, 29(3):183–193. doi: 10.1016/j.strusafe.2006.07.008. 55

Au, S.-K. and Beck, J. L. 2001. Estimation of small failure probabilities in high dimensions by subset simulation. *Probabilistic Engineering Mechanics*, 16(4):263–277. doi: 10.1016/S0266-8920(01)00019-4. 36, 37, 38, 39, 65, 67, 68, 91, 220

Babuška, I., Nobile, F., and Tempone, R. 2007. A Stochastic Collocation Method for Elliptic Partial Differential Equations with Random Input Data. *SIAM Journal on Numerical Analysis*, 45(3):1005–1034. 26

Bachoc, F. 2013. Cross Validation and Maximum Likelihood estimations of hyper-parameters of Gaussian processes with model misspecification. *Computational Statistics & Data Analysis*, 66:55–69. doi: 10.1016/j.csda.2013.03.016. 69, 77

Baptista, R., Zahm, O., and Marzouk, Y. 2020. An adaptive transport framework for joint and conditional density estimation. url: 10.48550/ARXIV.2009.10303. 212

Barber, C. B., Dobkin, D. P., and Huhdanpaa, H. 1996. The quickhull algorithm for convex hulls. *ACM Transactions on Mathematical Software*, 22(4):469–483. doi: 10.1145/235815.235821. 75

Barbé, P. and Ledoux, M. 2007. *Probabilité*. EDP Sciences, Les Ulis, France. 18, 22, 64

Baroghel-Bouny, V. 1994. *Caractérisation microstructurale et hydrique des pâtes de ciment et des bétons ordinaires et à très hautes performances*. Theses, Ecole Nationale des Ponts et Chaussées. 96

Baroghel-Bouny, V., Mainguy, M., Lassabatere, T., and Coussy, O. 1999. Characterization and identification of equilibrium and transfer moisture properties for ordinary and high-performance cementitious materials. *Cement and Concrete Research*, 29(8):1225–1238. doi: 10.1016/S0008-8846(99)00102-7. 99

Baudin, M., Dutfoy, A., Iooss, B., and Popelin, A.-L. 2016. *OpenTURNS: An Industrial Software for Uncertainty Quantification in Simulation*, pages 1–38. Springer International Publishing, Cham. doi: 10.1007/978-3-319-11259-6_64-1. 235

Bažant, Z. P. and Chern, J. C. 1985. Concrete creep at variable humidity : Constitutive law and mechanisms. *Materials and Structures*, 18:1–20. doi: 10.1007/bf02473360. 102, 113

Bažant, Z. P., Hauggaard, A. B., Baweja, S., and Ulm, F.-J. 1997. Microprestress-Solidification Theory for Concrete Creep. I: Aging and Drying Effects. *Journal of Engineering Mechanics*, 123(11):1188–1194. doi: 10.1061/(ASCE)0733-9399(1997)123:11(1188). 100, 102

Bažant, Z. P. and Najjar, L. J. 1972. Nonlinear water diffusion in nonsaturated concrete. *Matériaux et Construction*, 5(1):3–20. doi: 10.1007/BF02479073. 109

Bažant, Z. P. and Oh, B. H. 1983. Crack band theory for fracture of concrete. *Matériaux et Construction*, 16(3):155–177. doi: 10.1007/BF02486267. 117

Bažant, Z. P. and Prasannan, S. 1989a. Solidification Theory for Concrete Creep. I: Formulation. *Journal of Engineering Mechanics*, 115(8):1691–1703. doi: 10.1061/(ASCE)0733-9399(1989)115:8(1691). 100

Bažant, Z. P. and Prasannan, S. 1989b. Solidification Theory for Concrete Creep. II: Verification and Application. *Journal of Engineering Mechanics*, 115(8):1704–1725. doi: 10.1061/(ASCE)0733-9399(1989)115:8(1704). 100

Beck, J. L. and Au, S.-K. 2002. Bayesian Updating of Structural Models and Reliability using Markov Chain Monte Carlo Simulation. *Journal of Engineering Mechanics*, 128(4):380–391. doi: 10.1061/(asce)0733-9399(2002)128:4(380). 79

Beck, J. L. and Zuev, K. M. 2013. Asymptotically Independent Markov Sampling: A New Markov Chain Monte Carlo Scheme for Bayesian Inference. *International Journal for Uncertainty Quantification*, 3(5):445–474. doi: 10.1615/int.j.uncertaintyquantification.2012004713. 83, 84

Bect, J., Ginsbourger, D., Li, L., Picheny, V., and Vazquez, E. 2012. Sequential design of computer experiments for the estimation of a probability of failure. *Statistics and Computing*, 22(3):773–793. doi: 10.1007/s11222-011-9241-4. 73

Bect, J., Li, L., and Vazquez, E. 2017. Bayesian Subset Simulation. *SIAM/ASA Journal on Uncertainty Quantification*, 5(1):762–786. doi: 10.1137/16m1078276. 37

Ben-Haim, Y. 2006. *Info-Gap Decision Theory: Decisions Under Severe Uncertainty*. Elsevier. 15

Benboudjema, F. 2002. *Modélisation des déformations différées du béton sous sollicitations biaxiales : application aux enceintes de confinement de bâtiments réacteurs des centrales nucléaires*. PhD thesis, Université de Marne-La-Vallée. 96, 99, 100, 101, 102, 103, 111, 113

Benboudjema, F., Meftah, F., and Torrenti, J.-M. 2001. Drying creep: an elasto-plastic damage approach of the structural effect. In *Fourth International Conference on Fracture Mechanics of Concrete and Concrete Structures*, pages 169–176. 99

Benboudjema, F. and Torrenti, J. 2008. Early-age behaviour of concrete nuclear containments. *Nuclear Engineering and Design*, 238(10):2495–2506. doi: 10.1016/j.nucengdes.2008.04.009. 95

Bentur, A., Berger, R., Lawrence, F., Milestone, N., Mindess, S., and Young, J. 1979. Creep and drying shrinkage of calcium silicate pastes III. A hypothesis of irreversible strains. *Cement and Concrete Research*, 9(1):83–95. doi: 10.1016/0008-8846(79)90098-X. 100

Berger, J. O. 1990. Robust Bayesian analysis: sensitivity to the prior. *Journal of Statistical Planning and Inference*, 25(3):303–328. doi: 10.1016/0378-3758(90)90079-A. 15, 43, 172, 212

Berveiller, M., Pape, Y. L., Sudret, B., and Perrin, F. 2012. Updating the long-term creep strains in concrete containment vessels by using Markov chain Monte Carlo simulation and polynomial chaos expansions. *Structure and Infrastructure Engineering*, 8(5):425–440. doi: 10.1080/15732479.2010.539057. 155

Berveiller, M., Sudret, B., and Lemaire, M. 2006. Stochastic finite element: a non intrusive approach by regression. *European Journal of Computational Mechanics*, 15(1-3):81–92. doi: 10.3166/remn.15.81-92. 26

Betz, W., Beck, J. L., Papaioannou, I., and Straub, D. 2018a. Bayesian inference with reliability methods without knowing the maximum of the likelihood function. *Probabilistic Engineering Mechanics*, 53:14–22. doi: 10.1016/j.probengmech.2018.03.004. 62, 64

Betz, W., Papaioannou, I., Beck, J. L., and Straub, D. 2018b. Bayesian inference with Subset Simulation: Strategies and improvements. *Computer Methods in Applied Mechanics and Engineering*, 331:72–93. doi: 10.1016/j.cma.2017.11.021. 55, 60, 62, 64, 65, 66, 67, 68, 74, 78, 79, 91, 208, 221

Betz, W., Papaioannou, I., and Straub, D. 2014. Adaptive variant of the BUS approach to Bayesian updating. In *9th International Conference on Structural Dynamics, EURODYN*. 64, 68

Betz, W., Papaioannou, I., and Straub, D. 2016. Transitional Markov Chain Monte Carlo: Observations and Improvements. *Journal of Engineering Mechanics*, 142(5):04016016. doi: 10.1061/(ASCE)EM.1943-7889.0001066. 65, 221

Bichon, B. J., Eldred, M. S., Swiler, L. P., Mahadevan, S., and McFarland, J. M. 2008. Efficient Global Reliability Analysis for Nonlinear Implicit Performance Functions. *AIAA Journal*, 46(10):2459–2468. doi: 10.2514/1.34321. 36, 60, 72, 75

Bieri, M. and Schwab, C. 2009. Sparse high order FEM for elliptic sPDEs. *Computer Methods in Applied Mechanics and Engineering*, 198(13):1149–1170. doi: 10.1016/j.cma.2008.08.019, HOFEM07. 26

Bigoni, D., Marzouk, Y., Prieur, C., and Zahm, O. 2022. Nonlinear dimension reduction for surrogate modeling using gradient information. *Information and Inference: A Journal of the IMA*. doi: 10.1093/imaiai/iaac006. 92, 212

Billingsley, P. 1995. *Probability and measure*. Wiley, New York, 3rd edition edition. 16, 19, 23

Birolleau, A., Poëtte, G., and Lucor, D. 2014. Adaptive Bayesian Inference for Discontinuous Inverse Problems, Application to Hyperbolic Conservation Laws. *Communications in Computational Physics*, 16(1):1–34. doi: 10.4208/cicp.240113.071113a. 56, 71

Bissonnette, B., Pierre, P., and Pigeon, M. 1999. Influence of key parameters on drying shrinkage of cementitious materials. *Cement and Concrete Research*, 29(10):1655–1662. doi: 10.1016/S0008-8846(99)00156-8. 99

Blatman, G. 2009. *Adaptive sparse polynomial chaos expansions for uncertainty propagation and sensitivity analysis*. PhD thesis, Université Blaise Pascal - Clermont Ferrand II. 28

Blatman, G. and Sudret, B. 2008. Sparse polynomial chaos expansions and adaptive stochastic finite elements using a regression approach. *Comptes Rendus Mécanique*, 336(6):518–523. doi: 10.1016/j.crme.2008.02.013. 26

Blatman, G. and Sudret, B. 2010. An adaptive algorithm to build up sparse polynomial chaos expansions for stochastic finite element analysis. *Probabilistic Engineering Mechanics*, 25(2):183–197. doi: 10.1016/j.probengmech.2009.10.003. 26, 28

Blatman, G. and Sudret, B. 2011a. Adaptive sparse polynomial chaos expansion based on least angle regression. *Journal of Computational Physics*, 230(6):2345–2367. doi: 10.1016/j.jcp.2010.12.021. 29, 30, 146

Blatman, G. and Sudret, B. 2011b. Principal component analysis and Least Angle Regression in spectral stochastic finite element analysis. In *Applications of Statistics and Probability in Civil Engineering*, pages 669–676. CRC Press. doi: 10.1201/b11332-101. 26, 27, 69, 77, 146, 182, 184, 191

Blatman, G. and Sudret, B. 2014. Sparse polynomial chaos expansions of vector-valued response quantities. In *Safety, Reliability, Risk and Life-Cycle Performance of Structures and Infrastructures*, pages 3245–3252. CRC Press. doi: 10.1201/b16387-469. 30, 71, 146

Borgonovo, E. 2017. *Sensitivity Analysis. An Introduction for the Management Scientist*. Springer International Publishing. doi: 10.1007/978-3-319-52259-3. 31

Borgonovo, E. and Plischke, E. 2016. Sensitivity analysis: A review of recent advances. *European Journal of Operational Research*, 248(3):869–887. doi: 10.1016/j.ejor.2015.06.032. 31

Boucher, M. 2016. *Analyse du transfert spatio- temporel des déformations entre le cœur d'un ouvrage épais et son parement : Application aux enceintes de confinement*. PhD thesis, Université Grenoble Alpes. 5, 7, 94, 103, 108, 109, 110, 111, 113, 128, 209, 240, 241, 242

Bouhjiti, D. E.-M. 2018. *Analyse probabiliste de la fissuration et du confinement des grands ouvrages en béton armé et précontraint*. Theses, Université Grenoble Alpes. 4, 5, 6, 7, 97, 98, 99, 101, 103, 104, 105, 106, 107, 109, 111, 114, 115, 117, 118, 138, 144, 176, 185, 209, 240, 241, 242

Bouhjiti, D. E.-M., Boucher, M., Briffaut, M., Dufour, F., Baroth, J., and Masson, B. 2018a. Accounting for realistic Thermo-Hydro-Mechanical boundary conditions whilst modeling the ageing of concrete in nuclear containment buildings: Model validation and sensitivity analysis. *Engineering Structures*, 166:314–338. doi: 10.1016/j.engstruct.2018.03.015. 97, 109, 127, 135, 138

Bouhjiti, D. E.-M., El Dandachy, M. E., Dufour, F., Dal Pont, S., Briffaut, M., Baroth, J., and Masson, B. 2018b. New continuous strain-based description of concrete's damage-permeability coupling. *International Journal for Numerical and Analytical Methods in Geomechanics*, 42(14):1671–1697. doi: 10.1002/nag.2808. 94, 114

Bouhjiti, D.-M., Baroth, J., Dufour, F., Michel-Ponnelle, S., and Masson, B. 2020. Stochastic finite elements analysis of large concrete structures' serviceability under thermo-hydro-mechanical loads – Case of nuclear containment buildings. *Nuclear Engineering and Design*, 370:110800. doi: 10.1016/j.nucengdes.2020.110800. 114, 117

Breitung, K. 1989. Asymptotic approximations for probability integrals. *Probabilistic Engineering Mechanics*, 4(4):187–190. doi: 10.1016/0266-8920(89)90024-6. 36

Brezis, H. 2010. *Functional Analysis, Sobolev Spaces and Partial Differential Equations*. Springer New York. doi: 10.1007/978-0-387-70914-7. 136

Briffaut, M., Benboudjema, F., Laborderie, C., and Torrenti, J.-M. 2013. Creep Consideration Effect on Meso-Scale Modeling of Concrete Hydration Process and Consequences on the Mechanical Behavior. *Journal of Engineering Mechanics*, 139(12):1808–1817. doi: 10.1061/(ASCE)EM.1943-7889.0000607. 103

Briffaut, M., Benboudjema, F., Torrenti, J.-M., and Nahas, G. 2012. Effects of early-age thermal behaviour on damage risks in massive concrete structures. *European Journal of Environmental and Civil Engineering*, 16(5):589–605. doi: 10.1080/19648189.2012.668016. 108

Brooks, J. J. 2005. 30-year creep and shrinkage of concrete. *Magazine of Concrete Research*, 57(9):545–556. doi: 10.1680/macr.2005.57.9.545. 111

Brooks, S., Gelman, A., Jones, G., and Meng, X.-L., Eds. 2011. *Handbook of Markov Chain Monte Carlo*. Chapman and Hall/CRC. doi: 10.1201/b10905. 12, 49, 52

Brooks, S. P. and Gelman, A. 1998. General Methods for Monitoring Convergence of Iterative Simulations. *Journal of Computational and Graphical Statistics*, 7(4):434–455. doi: 10.1080/10618600.1998.10474787. 53, 54

Buffo-Lacarrière, L., Sellier, A., Turatsinze, A., and Escadeillas, G. 2011. Finite element modelling of hardening concrete: application to the prediction of early age cracking for massive reinforced structures. *Materials and Structures*, 44(10):1821–1835. doi: 10.1617/s11527-011-9740-y. 103

Bye, G. 1999. *Portland cement: Composition, production and properties*. Thomas Telford Publishing, 2nd edition edition. doi: 10.1680/pccpap.27664. 95

Byrd, R. H., Hribar, M. E., and Nocedal, J. 1999. An Interior Point Algorithm for Large-Scale Nonlinear Programming. *SIAM Journal on Optimization*, 9(4):877–900. doi: 10.1137/S1052623497325107. 77

Cacuci, D. G. 1981. Sensitivity theory for nonlinear systems. I. Nonlinear functional analysis approach. *Journal of Mathematical Physics*, 22(12):2794–2802. doi: 10.1063/1.525186. 31

Calvetti, D. and Somersalo, E. 2018. Inverse problems: From regularization to Bayesian inference. *WIREs Computational Statistics*, 10(3). doi: 10.1002/wics.1427. 41, 48

Carlier, G., Galichon, A., and Santambrogio, F. 2010. From Knothe's Transport to Brenier's Map and a Continuation Method for Optimal Transport. *SIAM Journal on Mathematical Analysis*, 41(6):2554–2576. doi: 10.1137/080740647. 22

Caré, S. 2008. Effect of temperature on porosity and on chloride diffusion in cement pastes. *Construction and Building Materials*, 22(7):1560–1573. doi: 10.1016/j.conbuildmat.2007.03.018. 97

Chabridon, V. 2018. *Reliability-oriented sensitivity analysis under probabilistic model uncertainty – Application to aerospace systems*. PhD thesis, Université Clermont Auvergne. 15

Chalmond, B. 2003. *Modeling and Inverse Problems in Imaging Analysis*. Springer New York. doi: 10.1007/978-0-387-21662-1. 40

Charpin, L., Le Pape, Y., Coustabeau, E., Masson, B., and Montalvo, J. 2015. EDF Study of 10-Year Concrete Creep under Unidirectional and Biaxial Loading: Evolution of the Poisson Coefficient under Sealed and Unsealed Conditions. url: 10.1061/9780784479346.163. 111

Charpin, L., Niepceron, J., Corbin, M., Masson, B., Mathieu, J.-P., Haelewyn, J., Hamon, F., Åhs, M., Aparicio, S., Asali, M., Capra, B., Azenha, M., Bouhjiti, D. E.-M., Calonius, K., Chu, M., Herrman, N., Huang, X., Jiménez, S., Mazars, J., Mosayan, M., Nahas, G., Stepan, J., Thenint, T., and Torrenti, J.-M. 2021. Ageing and air leakage assessment of a nuclear reactor containment mock-up: VERCORS 2nd benchmark. *Nuclear Engineering and Design*, 377:111136. doi: 10.1016/j.nucengdes.2021.111136. 125, 144, 203

Chastaing, G., Gamboa, F., and Prieur, C. 2012. Generalized Hoeffding-Sobol decomposition for dependent variables - application to sensitivity analysis. *Electronic Journal of Statistics*, 6(none):2420 – 2448. doi: 10.1214/12-EJS749. 32, 33, 217

Chen, W. 2011. *Etude expérimentale de la perméabilité du béton sous conditions thermiques et hydriques variables*. Theses, Ecole Centrale de Lille. 96, 105

Cheng, B. and Titterington, D. M. 1994. Neural Networks: A Review from a Statistical Perspective. *Statistical Science*, 9(1):2 – 30. doi: 10.1214/ss/1177010638. 24

Chhun, P. 2017. *Modélisation du comportement thermo-hydro-chemo-mécanique des enceintes de confinement nucléaire en béton armé-précontraint*. PhD thesis, Université Toulouse 3. 94

Chinesta, F., Keunings, R., and Leygue, A. 2014. *The Proper Generalized Decomposition for Advanced Numerical Simulations*. Springer International Publishing. doi: 10.1007/978-3-319-02865-1. 5, 240

Choi, S.-K., Grandhi, R. V., Canfield, R. A., and Pettit, C. L. 2004. Polynomial Chaos Expansion with Latin Hypercube Sampling for Estimating Response Variability. *AIAA Journal*, 42(6):1191–1198. doi: 10.2514/1.2220. 26

Choinska, M. 2006. *Effets de la température, du chargement mécanique et de leurs interactions sur la perméabilité du béton de structure*. Theses, Ecole Centrale de Nantes (ECN) ; Université de Nantes. 105

Choinska, M., Dufour, F., and Pijaudier-Cabot, G. 2007a. Matching permeability law from diffuse damage to discontinuous crack opening. In *6th International Conference on Fracture Mechanics of Concrete and Concrete Structures*, pages 551–548, Catania, Italy. 114

Choinska, M., Khelidj, A., Chatzigeorgiou, G., and Pijaudier-Cabot, G. 2007b. Effects and interactions of temperature and stress-level related damage on permeability of concrete. *Cement and Concrete Research*, 37(1):79–88. doi: 10.1016/j.cemconres.2006.09.015. 115

Christen, J. A. and Fox, C. 2005. Markov chain Monte Carlo Using an Approximation. *Journal of Computational and Graphical Statistics*, 14(4):795–810. doi: 10.1198/106186005x76983. 57

Claeskens, G. and Hjort, N. L. 2001. *Model Selection and Model Averaging*. Cambridge University Press. doi: 10.1017/cbo9780511790485. 45

Colton, D. and Kress, R. 2013. *Inverse Acoustic and Electromagnetic Scattering Theory*. Springer New York. doi: 10.1007/978-1-4614-4942-3. 40

Conceição, J., Faria, R., Azenha, M., Mamede, F., and Souza, F. 2014. Early-age behaviour of the concrete surrounding a turbine spiral case: Monitoring and thermo-mechanical modelling. *Engineering Structures*, 81:327–340. doi: /10.1016/j.engstruct.2014.10.009. 103

Congdon, P. D. 2010. *Applied Bayesian Hierarchical Methods*. Chapman and Hall/CRC. doi: 10.1201/9781584887218. 43

Conrad, P. R., Davis, A. D., Marzouk, Y. M., Pillai, N. S., and Smith, A. 2018. Parallel Local Approximation MCMC for Expensive Models. *SIAM/ASA Journal on Uncertainty Quantification*, 6(1):339–373. doi: 10.1137/16m1084080. 57

Conrad, P. R., Marzouk, Y. M., Pillai, N. S., and Smith, A. 2016. Accelerating Asymptotically Exact MCMC for Computationally Intensive Models via Local Approximations. *Journal of the American Statistical Association*, 111(516):1591–1607. doi: 10.1080/01621459.2015.1096787. 57

Constantine, P. G., Dow, E., and Wang, Q. 2014. Active Subspace Methods in Theory and Practice: Applications to Kriging Surfaces. *SIAM Journal on Scientific Computing*, 36(4):A1500–A1524. doi: 10.1137/130916138. 92, 212

Constantine, P. G., Kent, C., and Bui-Thanh, T. 2016. Accelerating Markov Chain Monte Carlo with Active Subspaces. *SIAM Journal on Scientific Computing*, 38(5):A2779–A2805. doi: 10.1137/15M1042127. 92, 212

Courtois, A. 2019. *Contribution à la surveillance des structures épaisses en béton : proposition d'une démarche pour intégrer le suivi de la teneur en eau dans le pronostic*. PhD thesis, Université Paris-Saclay. 129

Cowles, M. K. and Carlin, B. P. 1996. Markov Chain Monte Carlo Convergence Diagnostics: A Comparative Review. *Journal of the American Statistical Association*, 91(434):883–904. doi: 10.1080/01621459.1996.10476956. 54

Cox, D. R. 2006. *Principles of Statistical Inference*. Cambridge University Press. doi: 10.1017/cbo9780511813559. 42

Csiszár, I. 1967. Information-Type Measures of Difference of Probability Distributions and Indirect Observations. *Studia Scientiarum Mathematicarum Hungarica*, 2:299–318. 44

Cui, T., Fox, C., and O'Sullivan, M. J. 2019. A posteriori stochastic correction of reduced models in delayed-acceptance MCMC, with application to multiphase subsurface inverse problems. *International Journal for Numerical Methods in Engineering*, 118(10):578–605. doi: 10.1002/nme.6028. 57, 91

Cui, T., Marzouk, Y., and Willcox, K. 2016. Scalable posterior approximations for large-scale Bayesian inverse problems via likelihood-informed parameter and state reduction. *Journal of Computational Physics*, 315:363–387. doi: 10.1016/j.jcp.2016.03.055. 92

Cui, T., Marzouk, Y. M., and Willcox, K. E. 2014. Data-driven model reduction for the Bayesian solution of inverse problems. *International Journal for Numerical Methods in Engineering*, 102(5):966–990. doi: 10.1002/nme.4748. 57, 92, 212

Cui, T. and Zahm, O. 2021. Data-free likelihood-informed dimension reduction of Bayesian inverse problems. *Inverse Problems*, 37(4):045009. doi: 10.1088/1361-6420/abeafb. 92, 212

Cérou, F., Del Moral, P., Furon, T., and Guyader, A. 2012. Sequential Monte Carlo for rare event estimation. *Statistics and Computing*, 22(3):795–808. doi: 10.1007/s11222-011-9231-6. 37

Da Veiga, S. 2015. Global sensitivity analysis with dependence measures. *Journal of Statistical Computation and Simulation*, 85(7):1283–1305. doi: 10.1080/00949655.2014.945932. 32

Dal Pont, S., Durand, S., and Schrefler, B. 2007. A multiphase thermo-hydro-mechanical model for concrete at high temperatures—Finite element implementation and validation under LOCA load. *Nuclear Engineering and Design*, 237(22):2137–2150. doi: 10.1016/j.nucengdes.2007.03.047. 107, 210

Dal Pont, S. and Ehrlacher, A. 2004. Numerical and experimental analysis of chemical dehydration, heat and mass transfers in a concrete hollow cylinder submitted to high temperatures. *International Journal of Heat and Mass Transfer*, 47(1):135–147. doi: 10.1016/S0017-9310(03)00381-8. 115

Damblin, G., Barbillon, P., Keller, M., Pasanisi, A., and Parent, É. 2018. Adaptive Numerical Designs for the Calibration of Computer Codes. *SIAM/ASA Journal on Uncertainty Quantification*, 6(1):151–179. doi: 10.1137/15m1033162. 56, 57

Day, R. and Gamble, B. 1983. The effect of changes in structure on the activation energy for the creep of concrete. *Cement and Concrete Research*, 13(4):529–540. doi: 10.1016/0008-8846(83)90012-1. 100

De Rocquigny, E., Devictor, N., and Tarantola, S., Eds. 2008. *Uncertainty in Industrial Practice*. John Wiley & Sons, Ltd. doi: 10.1002/9780470770733. 4, 5, 6, 14, 239, 240, 241

De Schutter, G. 1999. Degree of hydration based Kelvin model for the basic creep of early age concrete. *Materials and Structures*, 32:260–265. doi: 10.1007/bf02479595. 101

De Schutter, G. and Taerwe, L. 1996. Degree of hydration-based description of mechanical properties of early age concrete. *Materials and Structures*, 29(6):335. doi: 10.1007/BF02486341. 96

Del Moral, P., Doucet, A., and Jasra, A. 2006. Sequential Monte Carlo Samplers. *Journal of the Royal Statistical Society. Series B (Statistical Methodology)*, 68(3):411–436. 37

Dempster, A. P. 1967. Upper and Lower Probabilities Induced by a Multivalued Mapping. *The Annals of Mathematical Statistics*, 38(2):325 – 339. doi: 10.1214/aoms/1177698950. 15

Der Kiureghian, A. and Ditlevsen, O. 2009. Aleatory or epistemic? Does it matter? *Structural Safety*, 31(2):105–112. doi: 10.1016/j.strusafe.2008.06.020, Risk Acceptance and Risk Communication. 14

Der Kiureghian, A. and Liu, P. 1986. Structural Reliability under Incomplete Probability Information. *Journal of Engineering Mechanics*, 112(1):85–104. doi: 10.1061/(ASCE)0733-9399(1986)112:1(85). 21

Deuflhard, P. and Hohmann, A. 2003. *Numerical Analysis in Modern Scientific Computing*. Springer New York. doi: 10.1007/978-0-387-21584-6. 14

Diaconis, P. and Ylvisaker, D. 1979. Conjugate Priors for Exponential Families. *The Annals of Statistics*, 7(2). doi: 10.1214/aos/1176344611. 43

DiazDelaO, F., Garbuno-Inigo, A., Au, S., and Yoshida, I. 2017. Bayesian updating and model class selection with Subset Simulation. *Computer Methods in Applied Mechanics and Engineering*, 317:1102–1121. doi: 10.1016/j.cma.2017.01.006. 55, 62, 64, 66

Ditlevsen, O. and Madsen, H. O. 1996. *Structural Reliability Methods*. John Wiley & Sons Ltd, Chichester. 36

Duane, S., Kennedy, A., Pendleton, B. J., and Roweth, D. 1987. Hybrid Monte Carlo. *Physics Letters B*, 195(2):216–222. doi: 10.1016/0370-2693(87)91197-x. 54

Dubois, D. and Prade, H. 1988. *Possibility Theory: An Approach to Computerized Processing of Uncertainty*. Springer US. 15

Dubourg, V., Sudret, B., and Bourinet, J.-M. 2011. Reliability-based design optimization using kriging surrogates and subset simulation. *Structural and Multidisciplinary Optimization*, 44(5):673–690. doi: 10.1007/s00158-011-0653-8. 36, 69

Dubourg, V., Sudret, B., and Deheeger, F. 2013. Metamodel-based importance sampling for structural reliability analysis. *Probabilistic Engineering Mechanics*, 33:47–57. doi: 10.1016/j.probengmech.2013.02.002. 75

Dufour, F., Legrain, G., Pijaudier-Cabot, G., and Huerta, A. 2012. Estimation of crack opening from a two-dimensional continuum-based finite element computation. *International Journal for Numerical and Analytical Methods in Geomechanics*, 36(16):1813–1830. doi: 10.1002/nag.1097. 117

Durrett, R. 2019. *Probability: Theory and Examples*. Cambridge Series in Statistical and Probabilistic Mathematics. Cambridge University Press, 5 edition. doi: 10.1017/9781108591034. 16

Echard, B., Gayton, N., and Lemaire, M. 2011. AK-MCS: An active learning reliability method combining Kriging and Monte Carlo Simulation. *Structural Safety*, 33(2):145–154. doi: 10.1016/j.strusafe.2011.01.002. 36, 60, 70, 72, 73, 75, 206, 208, 213

EDF 2021. Universal Registration Document (URD). url: https://www.edf.fr/sites/groupe/files/2022-03/edf-2021-universal-registration-document.pdf. 1, 236

Efendiev, Y., Hou, T., and Luo, W. 2006. Preconditioning Markov Chain Monte Carlo Simulations Using Coarse-Scale Models. *SIAM Journal on Scientific Computing*, 28(2):776–803. doi: 10.1137/050628568. 57

Efron, B., Hastie, T., Johnstone, I., and Tibshirani, R. 2004. Least angle regression. *The Annals of Statistics*, 32(2). doi: 10.1214/009053604000000067. 27

El Dandachy, M. E. 2016. *Characterization and modelling of permeability of damaged concrete : application to reinforced concrete structures*. Theses, Université Grenoble Alpes. 104

El Moselhy, T. A. and Marzouk, Y. M. 2012. Bayesian inference with optimal maps. *Journal of Computational Physics*, 231(23):7815–7850. doi: 10.1016/j.jcp.2012.07.022. 54, 212

Elsheikh, A. H., Hoteit, I., and Wheeler, M. F. 2014. Efficient Bayesian inference of subsurface flow models using nested sampling and sparse polynomial chaos surrogates. *Computer Methods in Applied Mechanics and Engineering*, 269:515–537. doi: 10.1016/j.cma.2013.11.001. 57

Engl, H. W., Hanke, M., and Neubauer, A. 1996. *Regularization of Inverse Problems*. Springer Netherlands. 40

Ernst, O. G., Mugler, A., Starkloff, H.-J., and Ullmann, E. 2012. On the convergence of generalized polynomial chaos expansions. *ESAIM: M2AN*, 46(2):317–339. doi: 10.1051/m2an/2011045. 25, 56, 71

Evensen, G. 2009. *Data Assimilation*. Springer Berlin Heidelberg. doi: 10.1007/978-3-642-03711-5. 5, 240

Fajraoui, N., Marelli, S., and Sudret, B. 2017. Sequential Design of Experiment for Sparse Polynomial Chaos Expansions. *SIAM/ASA Journal on Uncertainty Quantification*, 5(1):1061–1085. doi: 10.1137/16M1103488. 27, 87

Fang, K.-T., Li, R., and Sudjianto, A. 2005. *Design and Modeling for Computer Experiments*. Chapman and Hall/CRC. doi: 10.1201/9781420034899. 5, 240

Ferson, S. and Ginzburg, L. R. 1996. Different methods are needed to propagate ignorance and variability. *Reliability Engineering & System Safety*, 54(2):133–144. doi: 10.1016/S0951-8320(96)00071-3, Treatment of Aleatory and Epistemic Uncertainty. 15

Forrester, A. I. J., Sóbester, A., and Keane, A. J. 2008. *Engineering Design via Surrogate Modelling*. Wiley. doi: 10.1002/9780470770801. 5, 240

Foucault, A., Galenne, E., and Michel-Ponnelle, S. 2012. A new creep model for NPP containment behaviour prediction. In *International Conference on Numerical modeling Strategies for sustainable concrete structures*. International Conference on Numerical modeling Strategies for sustainable concrete structures. 111, 113

Fourier, J. 1822. *Théorie analytique de la chaleur*. Chez Firmin Didot, Père et Fils, Paris. doi: 10.1017/cbo9780511693229. 108

Fox, C. W. and Roberts, S. J. 2011. A tutorial on variational Bayesian inference. *Artificial Intelligence Review*, 38(2):85–95. doi: 10.1007/s10462-011-9236-8. 54

Frauenfelder, P., Schwab, C., and Todor, R. A. 2005. Finite elements for elliptic problems with stochastic coefficients. *Computer Methods in Applied Mechanics and Engineering*, 194(2):205–228. doi: 10.1016/j.cma.2004.04.008. 26

Gamboa, F., Janon, A., Klein, T., and Lagnoux, A. 2013. Sensitivity indices for multivariate outputs. *Comptes Rendus Mathematique*, 351(7):307–310. doi: 10.1016/j.crma.2013.04.016. 185

Gamerman, D. and Lopes, H. F. 2006. *Markov Chain Monte Carlo : Stochastic Simulation for Bayesian inference*. Chapman & Hall/CRC, Boca Raton, Florida, USA, 2nd ed. texts in statistical science 68 edition. 49

Gao, P., Zhang, T., Luo, R., Wei, J., and Yu, Q. 2014. Improvement of autogenous shrinkage measurement for cement paste at very early age: Corrugated tube method using non-contact sensors. *Construction and Building Materials*, 55:57–62. doi: 10.1016/j.conbuildmat.2013.12.086. 98, 99

Gauchy, C., Stenger, J., Sueur, R., and Iooss, B. 2022. An Information Geometry Approach to Robustness Analysis for the Uncertainty Quantification of Computer Codes. *Technometrics*, 64(1):80–91. doi: 10.1080/00401706.2021.1905072. 194

Gautschi, W. 2004. *Orthogonal Polynomials: Computation and Approximation*. Oxford University Press. doi: 10.1093/oso/9780198506720.001.0001. 25

Gawin, D., Pesavento, F., and Schrefler, B. A. 2003. Modelling of hygro-thermal behaviour of concrete at high temperature with thermo-chemical and mechanical material degradation. *Computer Methods in Applied Mechanics and Engineering*, 192:1731–1771. doi: 10.1016/s0045-7825(03)00200-7. 107

Gelman, A., Carlin, J. B., Stern, H. S., Dunson, D. B., Vehtari, A., and Rubin, D. B. 2013. *Bayesian Data Analysis*. Chapman and Hall/CRC. doi: 10.1201/b16018. 41

Gelman, A., Gilks, W. R., and Roberts, G. O. 1997. Weak convergence and optimal scaling of random walk Metropolis algorithms. *The Annals of Applied Probability*, 7(1):110 – 120. doi: 10.1214/aoap/1034625254. 50, 221

Gelman, A. and Hill, J. 2006. *Data Analysis Using Regression and Multilevel/Hierarchical Models*. Cambridge University Press. 43

Gelman, A. and Rubin, D. B. 1992. Inference from Iterative Simulation Using Multiple Sequences. *Statistical Science*, 7(4). doi: 10.1214/ss/1177011136. 53, 54

Ghanem, R., Higdon, D., and Owhadi, H., Eds. 2017. *Handbook of Uncertainty Quantification*. Springer International Publishing. doi: 10.1007/978-3-319-12385-1. 4, 239

Ghanem, R. and Spanos, P. 1991a. *Stochastic finite elements - A spectral approach*. Springer Verlag. doi: 10.1007/978-1-4612-3094-6. 24

Ghanem, R. and Spanos, P. D. 1990. Polynomial Chaos in Stochastic Finite Elements. *Journal of Applied Mechanics*, 57(1):197–202. doi: 10.1115/1.2888303. 26

Ghanem, R. G. and Spanos, P. D. 1991b. Spectral Stochastic Finite Element Formulation for Reliability Analysis. *Journal of Engineering Mechanics*, 117(10):2351–2372. doi: 10.1061/(ASCE)0733-9399(1991)117:10(2351). 12, 18, 26, 86, 87

Ghannoum, M. 2017. *Effects of heterogeneity of concrete on the mechanical behavior of structures at different scales*. Theses, Université Grenoble Alpes. 14

Gilquin, L., Prieur, C., and Arnaud, E. 2015. Replication procedure for grouped Sobol' indices estimation in dependent uncertainty spaces. *Information and Inference*, 4(4):354–379. doi: 10.1093/imaiai/iav010. 217

Ginsbourger, D., Rosspopoff, B., Pirot, G., Durrande, N., and Renard, P. 2013. Distance-based kriging relying on proxy simulations for inverse conditioning. *Advances in Water Resources*, 52:275–291. doi: 10.1016/j.advwatres.2012.11.019. 72

Giovanis, D. G., Papaioannou, I., Straub, D., and Papadopoulos, V. 2017. Bayesian updating with subset simulation using artificial neural networks. *Computer Methods in Applied Mechanics and Engineering*, 319:124–145. doi: 10.1016/j.cma.2017.02.025. 57, 74, 79

Girolami, M. and Calderhead, B. 2011. Riemann manifold Langevin and Hamiltonian Monte Carlo methods. *Journal of the Royal Statistical Society: Series B (Statistical Methodology)*, 73(2):123–214. doi: 10.1111/j.1467-9868.2010.00765.x. 54

Goodfellow, I., Bengio, Y., and Courville, A. 2016. *Deep Learning*. MIT Press. http://www.deeplearningbook.org. 24

Goodman, J. and Weare, J. 2010. Ensemble samplers with affine invariance. *Commun. Appl. Math. Comput. Sci.*, 5(1):65–80. doi: 10.2140/camcos.2010.5.65. 53

Grabe, M. 2014. *Measurement Uncertainties in Science and Technology*. Springer International Publishing. doi: 10.1007/978-3-319-04888-8. 14

Granger, L. 1995. *Comportement différé du béton dans les enceintes de centrales nucléaires : Analyse et modélisation*. PhD thesis, École nationale des ponts et chaussées. 97, 99, 100, 101, 103, 109, 110, 111, 124, 127, 186

Greiner, U. and Ramm, W. 1995. Air leakage characteristics in cracked concrete. *Nuclear Engineering and Design*, 156(1):167–172. doi: 10.1016/0029-5493(94)00942-R. 117

Griewank, A. and Walther, A. 2008. *Evaluating Derivatives*. Society for Industrial and Applied Mathematics. doi: 10.1137/1.9780898717761. 31

Grigoriu, M. 2012. *Stochastic Systems*. Springer London. doi: 10.1007/978-1-4471-2327-9. 5, 240

Gupta, R., Rossat, D., Dérobert, X., Baroth, J., Briffaut, M., Villain, G., and Dufour, F. 2022. Blind comparison of saturation ratio profiles on large RC structures by means of NDT and SFE—Application to the VeRCoRs mock-up. *Engineering Structures*, 258:114057. doi: 10.1016/j.engstruct.2022.114057. 213

Gérard, B., Breysse, D., Ammouche, A., Houdusse, O., and Didry, O. 1996. Cracking and permeability of concrete under tension. *Materials and Structures*, 29(3):141–151. doi: 10.1007/BF02486159. 105

Haario, H., Laine, M., Mira, A., and Saksman, E. 2006. DRAM: Efficient adaptive MCMC. *Statistics and Computing*, 16(4):339–354. doi: 10.1007/s11222-006-9438-0. 53

Haario, H., Saksman, E., and Tamminen, J. 2001. An adaptive Metropolis algorithm. *Bernoulli*, 7(2):223–242. doi: 10.2307/3318737. 53

Hadamard, J. 1923. *Lectures on the Cauchy Problem in Linear Partial Differential Equations*. Yale University Press, New Haven. 40

Hansen, P. C. 1987. The truncated SVD as a method for regularization. *BIT*, 27(4):534–553. doi: 10.1007/bf01937276. 40

Hart, J. and Gremaud, P. A. 2019. Robustness of the Sobol' Indices to Distributional Uncertainty. *International Journal for Uncertainty Quantification*, 9(5):453–469. doi: 10.1615/Int.J.UncertaintyQuantification.2019030553. 15, 193

Hasofer, A. M. and Lind, N. C. 1974. Exact and Invariant Second-Moment Code Format. *Journal of Engineering Mechanics*, 100(1):111–121. doi: 10.1061/JMCEA3.0001848. 36

Hastings, W. K. 1970. Monte Carlo sampling methods using Markov chains and their applications. *Biometrika*, 57(1):97–109. doi: 10.1093/biomet/57.1.97. 50, 51

Hauser, T., Keats, A., and Tarasov, L. 2011. Artificial neural network assisted Bayesian calibration of climate models. *Climate Dynamics*, 39(1-2):137–154. doi: 10.1007/s00382-011-1168-0. 56

Herman, G. T. 2009. *Fundamentals of Computerized Tomography*. Springer London. doi: 10.1007/978-1-84628-723-7. 40

Hesterberg, T. 1996. Estimates and confidence intervals for importance sampling sensitivity analysis. *Mathematical and Computer Modelling*, 23(8):79–85. doi: 10.1016/0895-7177(96)00041-6. 195

Hewitt, E. and Stromberg, K. R. 1965. *Real and Abstract Analysis*. Springer Berlin Heidelberg. doi: 10.1007/978-3-662-29794-0. 17

Higdon, D., Kennedy, M., Cavendish, J. C., Cafeo, J. A., and Ryne, R. D. 2004. Combining Field Data and Computer Simulations for Calibration and Prediction. *SIAM Journal on Scientific Computing*, 26(2):448–466. doi: 10.1137/s1064827503426693. 47

Hilaire, A. 2014. *Etude des déformations différées des bétons en compression et en traction, du jeune au long terme : application aux enceintes de confinement*. Theses, École normale supérieure de Cachan - ENS Cachan. 98, 99, 101, 102, 103, 105, 111

Hinton, G. E. and Salakhutdinov, R. R. 2006. Reducing the Dimensionality of Data with Neural Networks. *Science*, 313(5786):504–507. doi: 10.1126/science.1127647. 29

Hoeffding, W. 1948. A Class of Statistics with Asymptotically Normal Distribution. *The Annals of Mathematical Statistics*, 19(3):293 – 325. doi: 10.1214/aoms/1177730196. 32

Hohenbichler, M., Gollwitzer, S., Kruse, W., and Rackwitz, R. 1987. New light on first- and second-order reliability methods. *Structural Safety*, 4(4):267–284. doi: 10.1016/0167-4730(87)90002-6. 36

Hohenbichler, M. and Rackwitz, R. 1981. Non-Normal Dependent Vectors in Structural Safety. *Journal of the Engineering Mechanics Division*, 107(6):1227–1238. doi: 10.1061/JMCEA3.0002777. 21

Homma, T. and Saltelli, A. 1996. Importance measures in global sensitivity analysis of nonlinear models. *Reliability Engineering & System Safety*, 52(1):1–17. doi: 10.1016/0951-8320(96)00002-6. 33, 34

Hoseini, M., Bindiganavile, V., and Banthia, N. 2009. The effect of mechanical stress on permeability of concrete: A review. *Cement and Concrete Composites*, 31(4):213–220. doi: 10.1016/j.cemconcomp.2009.02.003. 105

Hénault, J.-M., Laviron, P., Desforges, S., Vautrin, D., Courtois, A., Martin, B., and Legrix, A. 2019. How to characterize the air tightness of containment structures - Overview of monitoring techniques tested on VeRCoRs mock up. In *Technological Innovation in Nuclear Civil Engineering (TINCE)*. 129

Idier, J. 2008. *Bayesian Approach to Inverse Problems*. ISTE. doi: 10.1002/9780470611197. 41

Iooss, B. 2009. *Contributions au traitement des incertitudes en modélisation numérique : propagation d'ondes en milieu aléatoire et analyse statistique d'expériences simulées*. Habilitation à diriger des recherches, Université Paul Sabatier - Toulouse III. 4, 31, 239

Iooss, B. and Le Gratiet, L. 2019. Uncertainty and sensitivity analysis of functional risk curves based on Gaussian processes. *Reliability Engineering & System Safety*, 187:58–66. doi: 10.1016/j.ress.2017.11.022, Sensitivity Analysis of Model Output. 15, 193

Iooss, B. and Lemaître, P. 2015. A review on global sensitivity analysis methods. In Meloni, C. and Dellino, G., Eds., *Uncertainty management in Simulation-Optimization of Complex Systems: Algorithms and Applications*. Springer. 5, 31, 32, 240

Iooss, B. and Prieur, C. 2019. Shapley effects for sensitivity analysis with correlated inputs: comparisons with Sobol' indices, numerical estimation and applications. *International Journal for Uncertainty Quantification*, 9(5):493–514. doi: 10.1615/int.j.uncertaintyquantification.2019028372. 32

Iooss, B., Vergès, V., and Larget, V. 2021. BEPU robustness analysis via perturbed law-based sensitivity indices. *Proceedings of the Institution of Mechanical Engineers, Part O: Journal of Risk and Reliability*. doi: 10.1177/1748006X211036569. 6, 15, 193, 194, 195, 205, 206, 210, 241

Isakov, V. 2006. *Inverse Problems for Partial Differential Equations*. Springer-Verlag. doi: 10.1007/0-387-32183-7. 41

Ishida, T., Maekawa, K., and Kishi, T. 2007. Enhanced modeling of moisture equilibrium and transport in cementitious materials under arbitrary temperature and relative humidity history. *Cement and Concrete Research*, 37(4):565–578. doi: 10.1016/j.cemconres.2006.11.015. 110

Jacquemain, D., Ed. 2015. *Nuclear Power Reactor Core Melt Accidents*, chapter Behaviour of Containment Buildings, pages 301–336. Institut de Radioprotection et de Sûreté Nucléaire. EDP Sciences. 3, 238

Jakeman, J. D., Franzelin, F., Narayan, A., Eldred, M., and Plfüger, D. 2019. Polynomial chaos expansions for dependent random variables. *Computer Methods in Applied Mechanics and Engineering*, 351:643 – 666. doi: 10.1016/j.cma.2019.03.049. 24

Janon, A., Klein, T., Lagnoux, A., Nodet, M., and Prieur, C. 2014. Asymptotic normality and efficiency of two Sobol index estimators. *ESAIM: Probability and Statistics*, 18:342–364. doi: 10.1051/ps/2013040. 34, 150

Jarner, S. F. and Hansen, E. 2000. Geometric ergodicity of Metropolis algorithms. *Stochastic Processes and their Applications*, 85(2):341–361. doi: 10.1016/S0304-4149(99)00082-4. 50

Jason, L., Pijaudier-Cabot, G., Ghavamian, S., and Huerta, A. 2007. Hydraulic Behaviour of a Representative Structural Volume for Confinement Buildings. *Nuclear Engineering and Design*, 237:1259–1274. doi: 10.1016/j.nucengdes.2006.09.035. 5, 114, 115, 135, 241

Jaynes, E. T. 1957. Information Theory and Statistical Mechanics. *Physical Review*, 106:620–630. doi: 10.1103/PhysRev.106.620. 43

Jefferys, W. H. and Berger, J. O. 1991. Sharpening Occam's Razor on a Bayesian strop. In *Bulletin of the American Astronomical Society*, volume 23, page 1259. 46

Jeffreys, H. 1946. An Invariant Form for the Prior Probability in Estimation Problems. *Proceedings of the Royal Society of London. Series A, Mathematical and Physical Sciences*, 186(1007):453–461. 42

Jeffreys, H. 1998. *Theory of Probability*. OUP Oxford. 46

Jensen, O. M. and Hansen, P. F. 2001. Autogenous deformation and RH-change in perspective. *Cement and Concrete Research*, 31(12):1859–1865. doi: 10.1016/S0008-8846(01)00501-4. 98

Jian, W., Zhili, S., Qiang, Y., and Rui, L. 2017. Two accuracy measures of the Kriging model for structural reliability analysis. *Reliability Engineering & System Safety*, 167:494–505. doi: 10.1016/j.ress.2017.06.028, Special Section: Applications of Probabilistic Graphical Models in Dependability, Diagnosis and Prognosis. 75

Johansen, S. and Juselius, K. 1990. Maximum Likelihood Estimation and Inference on Cointegration — with Applications to the Demand for Money. *Oxford Bulletin of Economics and Statistics*, 52(2):169–210. doi: 10.1111/j.1468-0084.1990.mp52002003.x. 20

Jolliffe, I. T. 2002. *Principal Component Analysis*. Springer-Verlag. doi: 10.1007/b98835. 29

Jones, D. R., Schonlau, M., and Welch, W. J. 1998. Efficient global optimization of expensive black-box functions. *Journal of Global Optimization*, 13(4):455–492. doi: 10.1023/a:1008306431147. 72

Jourdain, X. 2014. *Étude numérique méso-macro des propriétés de transfert des bétons fissurés*. PhD thesis, Ecole normale supérieure de Cachan. 116

Kaipio, J. and Somersalo, E. 2005. *Statistical and Computational Inverse Problems*. Springer. doi: 10.1007/b138659. 5, 6, 41, 42, 46, 87, 240

Kass, R. E. 1993. Bayes Factors in Practice. *Journal of the Royal Statistical Society: Series D (The Statistician)*, 42(5):551–560. doi: 10.2307/2348679. 45

Kass, R. E. and Wasserman, L. 1996. The Selection of Prior Distributions by Formal Rules. *Journal of the American Statistical Association*, 91(435):1343–1370. doi: 10.1080/01621459.1996.10477003. 42

Kaymaz, I. 2005. Application of kriging method to structural reliability problems. *Structural Safety*, 27(2):133–151. doi: 10.1016/j.strusafe.2004.09.001. 36

Kennedy, M. C. and O'Hagan, A. 2001. Bayesian calibration of computer models. *Journal of the Royal Statistical Society: Series B (Statistical Methodology)*, 63(3):425–464. doi: 10.1111/1467-9868.00294. 5, 47, 240

Kinda, J. 2021. *Impact of drying rate on delayed strain behavior of cement-based materials - experimental and numerical study*. PhD thesis, École Normale Supérieure Paris-Saclay. Thèse de doctorat dirigée par Benboudjema, Farid Génie civil université Paris-Saclay 2021. 101

Kinda, J., Bourdot, A., Charpin, L., Michel-Ponnelle, S., and Benboudjema, F. 2022. Investigation of Drying Shrinkage of Cement-Based Materials Assisted by Digital Image Correlation. *Journal of Materials in Civil Engineering*, 34(3). doi: 10.1061/(asce)mt.1943-5533.0004065. 99

Kirsch, A. 2011. *An Introduction to the Mathematical Theory of Inverse Problems*. Springer New York. doi: 10.1007/978-1-4419-8474-6. 41

Klinkenberg, L. J. 1941. The Permeability Of Porous Media To Liquids And Gases. *Drilling and Production Practice*, pages 200–213. 105, 115

Knothe, H. 1957. Contributions to the theory of convex bodies. *Michigan Mathematical Journal*, 4(1):39–52. doi: 10.1307/mmj/1028990175. 22

Konakli, K. and Sudret, B. 2016. Global sensitivity analysis using low-rank tensor approximations. *Reliability Engineering & System Safety*, 156:64–83. doi: 10.1016/j.ress.2016.07.012. 24

Koutsourelakis, P., Pradlwarter, H., and Schuëller, G. 2004. Reliability of structures in high dimensions, part I: algorithms and applications. *Probabilistic Engineering Mechanics*, 19(4):409–417. doi: 10.1016/j.probengmech.2004.05.001. 36

Krige, D. G. 1951. A statistical approach to some mine valuation and allied problems on the Witwatersrand. Master's thesis, University of the Witwatersrand. 24

Kucherenko, S. and Iooss, B. 2015. Derivative-Based Global Sensitivity Measures. In *Handbook of Uncertainty Quantification*, pages 1–24. Springer International Publishing. doi: 10.1007/978-3-319-11259-6_36-1. 32

Kucherenko, S., Tarantola, S., and Annoni, P. 2012. Estimation of global sensitivity indices for models with dependent variables. *Computer Physics Communications*, 183(4):937–946. doi: 10.1016/j.cpc.2011.12.020. 32

Kullback, S. and Leibler, R. A. 1951. On Information and Sufficiency. *The Annals of Mathematical Statistics*, 22(1):79–86. doi: 10.1214/aoms/1177729694. 44

Kupfer, H. B. and Gerstle, K. H. 1973. Behavior of Concrete under Biaxial Stresses. *Journal of Engineering Mechanics*, 99(4):853–866. doi: 10.1061/JMCEA3.0001789. 102

Lamboni, M., Monod, H., and Makowski, D. 2011. Multivariate sensitivity analysis to measure global contribution of input factors in dynamic models. *Reliability Engineering & System Safety*, 96(4):450–459. doi: 10.1016/j.ress.2010.12.002. 185

Landweber, L. 1951. An Iteration Formula for Fredholm Integral Equations of the First Kind. *American Journal of Mathematics*, 73(3):615. doi: 10.2307/2372313. 41

Lataniotis, C. 2019. *Data-driven uncertainty quantification for high-dimensional engineering problems*. PhD thesis, ETH Zurich. doi: 10.3929/ETHZ-B-000377865. 29

Lataniotis, C., Marelli, S., and Sudret, B. 2020. Extending classical surrogate modeling to high dimensions through supervised dimensionality reduction: a data-driven approach. *International Journal for Uncertainty Quantification*, 10(1):55–82. doi: 10.1615/int.j.uncertaintyquantification.2020031935. 29

Le Chatelier, H. 1904. *Recherches expérimentales sur la constitution des mortiers hydrauliques*. Dunod. 98

Le Gratiet, L., Marelli, S., and Sudret, B. 2017. *Metamodel-Based Sensitivity Analysis: Polynomial Chaos Expansions and Gaussian Processes*, pages 1289–1325. Springer International Publishing, Cham. doi: 10.1007/978-3-319-12385-1_38. 32, 34

Lebrun, R. and Dutfoy, A. 2009. Do Rosenblatt and Nataf isoprobabilistic transformations really differ? *Probabilistic Engineering Mechanics*, 24(4):577–584. doi: 10.1016/j.probengmech.2009.04.006. 22

Lelièvre, N., Beaurepaire, P., Mattrand, C., and Gayton, N. 2018. AK-MCSi: A Kriging-based method to deal with small failure probabilities and time-consuming models. *Structural Safety*, 73:1–11. doi: 10.1016/j.strusafe.2018.01.002. 75

Lemaire, M., Chateauneuf, A., and Mitteau, J.-C. 2009. *Structural Reliability*. ISTE. doi: 10.1002/9780470611708. 5, 35, 36, 240

Lemaître, P. 2014. *Analyse de sensibilité en fiabilité des structures*. PhD thesis, Université de Bordeaux. 177, 193, 194

Lemaître, P., Sergienko, E., Arnaud, A., Bousquet, N., Gamboa, F., and Iooss, B. 2015. Density modification-based reliability sensitivity analysis. *Journal of Statistical Computation and Simulation*, 85(6):1200–1223. doi: 10.1080/00949655.2013.873039. 6, 15, 177, 193, 194, 195, 205, 210, 212, 241

Li, G., Rosenthal, C., and Rabitz, H. 2001. High Dimensional Model Representations. *The Journal of Physical Chemistry A*, 105(33):7765–7777. doi: 10.1021/jp010450t. 32, 101

Li, J. and Marzouk, Y. M. 2014. Adaptive Construction of Surrogates for the Bayesian Solution of Inverse Problems. *SIAM Journal on Scientific Computing*, 36(3):A1163–A1186. doi: 10.1137/130938189. 56, 57

Lin, J. 1991. Divergence measures based on the Shannon entropy. *IEEE Transactions on Information Theory*, 37(1):145–151. doi: 10.1109/18.61115. 78

Lindley, D. V. 2000. The Philosophy of Statistics. *Journal of the Royal Statistical Society: Series D (The Statistician)*, 49(3):293–337. doi: 10.1111/1467-9884.00238. 14, 44

Llau, A. 2016. *Simulation methods for the nonlinear mechanical behavior of large reinforced and prestressed concrete structures : adaptive condensation in the probabilistic context and modelling of the heterogeneities*. Theses, Université Grenoble Alpes. 103

Loève, M. 1977. *Probability Theory I*. Springer New York. doi: 10.1007/978-1-4757-6288-4. 16, 29, 86

Lohtia, R. 1970. Mechanism of creep in concrete. *Roorkee University Research Journal*, 1-2(12):37–47. 100

Lu, F., Morzfeld, M., Tu, X., and Chorin, A. J. 2015. Limitations of polynomial chaos expansions in the Bayesian solution of inverse problems. *Journal of Computational Physics*, 282:138–147. doi: 10.1016/j.jcp.2014.11.010. 56

Lüthen, N., Marelli, S., and Sudret, B. 2021a. Sparse Polynomial Chaos Expansions: Literature Survey and Benchmark. *SIAM/ASA Journal on Uncertainty Quantification*, 9(2):593–649. doi: 10.1137/20m1315774. 24

Lüthen, N., Roustant, O., Gamboa, F., Iooss, B., Marelli, S., and Sudret, B. 2021b. Global sensitivity analysis using derivative-based sparse Poincaré chaos expansions. url: 10.48550/ARXIV.2107.00394. 26, 27, 182

MacKay, D. J. C. 2002. *Information Theory, Inference & Learning Algorithms*. Cambridge University Press, USA. 44

Mai, C. V. 2016. *Polynomial chaos expansions for uncertain dynamical systems - applications in earthquake engineering*. PhD thesis, ETH Zurich. doi: 10.3929/ethz-a-010735932. 172, 213

Manzoni, A., Pagani, S., and Lassila, T. 2016. Accurate Solution of Bayesian Inverse Uncertainty Quantification Problems Combining Reduced Basis Methods and Reduction Error Models. *SIAM/ASA Journal on Uncertainty Quantification*, 4(1):380–412. doi: 10.1137/140995817. 57

Marelli, S. and Sudret, B. 2014. UQLab: A framework for uncertainty quantification in Matlab. In *Proc. 2nd Int. Conf. on Vulnerability, Risk Analysis and Management (ICVRAM2014)*, pages 2554–2563, Liverpool, United Kingdom. 77, 146, 150, 184, 235

Marelli, S. and Sudret, B. 2018. An active-learning algorithm that combines sparse polynomial chaos expansions and bootstrap for structural reliability analysis. *Structural Safety*, 75:67–74. doi: 10.1016/j.strusafe.2018.06.003. 60, 72, 75, 92

Marelli, S., Wagner, P.-R., Lataniotis, C., and Sudret, B. 2021. Stochastic Spectral Embedding. *International Journal for Uncertainty Quantification*, 11(2):25–47. doi: 10.1615/Int.J.UncertaintyQuantification.2020034395. 55

Marrel, A., Iooss, B., Dorpe, F. V., and Volkova, E. 2008. An efficient methodology for modeling complex computer codes with Gaussian processes. *Computational Statistics & Data Analysis*, 52(10):4731–4744. doi: 10.1016/j.csda.2008.03.026. 69

Marzouk, Y. and Xiu, D. 2009. A Stochastic Collocation Approach to Bayesian Inference in Inverse Problems. *Communications in Computational Physics*, 6(4):826–847. doi: 10.4208/cicp.2009.v6.p826. 56, 71

Marzouk, Y. M. and Najm, H. N. 2009. Dimensionality reduction and polynomial chaos acceleration of Bayesian inference in inverse problems. *Journal of Computational Physics*, 228(6):1862–1902. doi: 10.1016/j.jcp.2008.11.024. 56, 86

Marzouk, Y. M., Najm, H. N., and Rahn, L. A. 2007. Stochastic spectral methods for efficient Bayesian solution of inverse problems. *Journal of Computational Physics*, 224(2):560–586. doi: 10.1016/j.jcp.2006.10.010. 56

Matallah, M., La Borderie, C., and Maurel, O. 2010. A practical method to estimate crack openings in concrete structures. *International Journal for Numerical and Analytical Methods in Geomechanics*, 34(15):1615–1633. doi: 10.1002/nag.876. 117

Mathelin, L. and Gallivan, K. A. 2012. A Compressed Sensing Approach for Partial Differential Equations with Random Input Data. *Communications in Computational Physics*, 12(4):919–954. doi: 10.4208/cicp.151110.090911a. 26

Matheron, G. 1963. Principles of Geostatistics. *Economic Geology*, 58(8):1246–1266. doi: 10.2113/gsecongeo.58.8.1246. 24

Mathieu, J.-P., Charpin, L., Sémété, P., Toulemonde, C., Rousseau Haelewyn, J., Hamon, F., Michel-Ponnelle, S., Jean-Marie, H., and Taillade, F. 2018. Temperature and humidity-driven ageing of the VeRCoRs mock-up. In *EURO-C 2018 - Computationnal Modelling of Concrete and Concrete Strucutres*. 129

Mazars, J. and Pijaudier-Cabot, G. 1989. Continuum Damage Theory - Application to Concrete. *Journal of Engineering Mechanics*, 115(2):345–365. doi: 10.1061/(ASCE)0733-9399(1989)115:2(345). 114, 117

McKay, M. D., Beckman, R. J., and Conover, W. J. 1979. A Comparison of Three Methods for Selecting Values of Input Variables in the Analysis of Output from a Computer Code. *Technometrics*, 21(2):239–245. doi: 10.2307/1268522. 26, 71, 146

Melchers, R. 1989. Importance sampling in structural systems. *Structural Safety*, 6(1):3–10. doi: 10.1016/0167-4730(89)90003-9. 36

Melchers, R. E., Ed. 1999. *Structural Reliability Analysis and Prediction*. John Wiley & Sons. 5, 36, 240

Mensi, R., Acker, P., and Attolou, A. 1988. Séchage du béton: analyse et modélisation. *Materials and Structures*, 21(1):3–12. doi: 10.1007/bf02472523. 109

Metropolis, N., Rosenbluth, A. W., Rosenbluth, M. N., Teller, A. H., and Teller, E. 1953. Equation of State Calculations by Fast Computing Machines. *The Journal of Chemical Physics*, 21(6):1087–1092. doi: 10.1063/1.1699114. 48, 50, 51

Metropolis, N. and Ulam, S. 1949. The Monte Carlo Method. *Journal of the American Statistical Association*, 44(247):335–341. doi: 10.1080/01621459.1949.10483310. 23, 36

Mivelaz, P. 1996. *Etanchéité des structures en béton armé - Fuites au travers d'un élément fissuré*. PhD thesis, Ecole Polytechnique Federale de Lausanne. 103, 106, 117

Monlouis-Bonnaire, J., Verdier, J., and Perrin, B. 2004. Prediction of the relative permeability to gas flow of cement-based materials. *Cement and Concrete Research*, 34(5):737–744. doi: 10.1016/S0008-8846(03)00071-1. 115

Montgomery, D. C. 2019. *Design and Analysis of Experiments, 10th Edition*. Wiley. 27

Morris, M. D. 1991. Factorial Sampling Plans for Preliminary Computational Experiments. *Technometrics*, 33(2):161–174. doi: 10.1080/00401706.1991.10484804. 32, 182

Moustapha, M., Marelli, S., and Sudret, B. 2022. Active learning for structural reliability: Survey, general framework and benchmark. *Structural Safety*, page 102174. doi: 10.1016/j.strusafe.2021.102174. 36, 60, 72, 75, 91, 92, 206, 213

Muskat, M. and Meres, M. W. 1936. The Flow of Heterogeneous Fluids Through Porous Media. *Physics*, 7(9):346–363. doi: 10.1063/1.1745403. 115

Möller, B. and Beer, M. 2004. *Fuzzy Randomness*. Springer Berlin Heidelberg. doi: 10.1007/978-3-662-07358-2. 15

Nagel, J. B. 2017. *Bayesian techniques for inverse uncertainty quantification*. PhD thesis, ETH Zurich. doi: 10.3929/ETHZ-A-010835772. 12, 42, 46, 48

Nagel, J. B., Rieckermann, J., and Sudret, B. 2020. Principal component analysis and sparse polynomial chaos expansions for global sensitivity analysis and model calibration: Application to urban drainage simulation. *Reliability Engineering & System Safety*, 195:106737. doi: 10.1016/j.ress.2019.106737. 148, 157, 216

Nagel, J. B. and Sudret, B. 2016a. Spectral likelihood expansions for Bayesian inference. *Journal of Computational Physics*, 309:267–294. doi: 10.1016/j.jcp.2015.12.047. 55

Nagel, J. B. and Sudret, B. 2016b. A unified framework for multilevel uncertainty quantification in Bayesian inverse problems. *Probabilistic Engineering Mechanics*, 43:68–84. doi: 10.1016/j.probengmech.2015.09.007. 43, 47, 211

Nataf, A. 1962. Détermination des distributions dont les marges sont données. *Comptes Rendus de l'Académie des Sciences*, 225:42–43. 22, 64

Neal, R. 2011. MCMC Using Hamiltonian Dynamics. In *Handbooks of Modern Statistical Methods*. Chapman and Hall/CRC. doi: 10.1201/b10905-6. 54

Nelsen, R. 2006. *An introduction to copulas*. Springer, New York. 20

Neville, A. 1996. *Properties of Concrete - Fourth Edition*. Pearson, Edinburgh. 95

Niederreiter, H. 1992. *Random Number Generation and Quasi-Monte Carlo Methods*. Society for Industrial and Applied Mathematics. doi: 10.1137/1.9781611970081. 27

Niyogi, A., Hsu, P., and Meyers, B. 1973. The influence of age at time of loading on basic and drying creep. *Cement and Concrete Research*, 3(5):633–644. doi: 10.1016/0008-8846(73)90100-2. 101

Novak, E. and Ritter, K. 1999. Simple Cubature Formulas with High Polynomial Exactness. *Constructive Approximation*, 15(4):499–522. doi: 10.1007/s003659900119. 26

O'Hagan, A. 2006. Bayesian analysis of computer code outputs: A tutorial. *Reliability Engineering & System Safety*, 91(10):1290–1300. doi: 10.1016/j.ress.2005.11.025, The Fourth International Conference on Sensitivity Analysis of Model Output (SAMO 2004). 56

Oukhemanou, E., Desforges, S., Buchoud, E., Michel-Ponnelle, S., and Courtois, A. 2016. VeRCoRs Mock-Up: Comprehensive Monitoring System for Reduced Scale Containment Model. In *Technological Innovation in Nuclear Civil Engineering (TINCE)*. 129

Oumouni, M., Schoefs, F., and Castanier, B. 2019. Modeling time and spatial variability of degradation through gamma processes for structural reliability assessment. *Structural Safety*, 76:162–173. doi: 10.1016/j.strusafe.2018.09.003. 234

Owen, A. B. 2014. Sobol' Indices and Shapley Value. *SIAM/ASA Journal on Uncertainty Quantification*, 2(1):245–251. doi: 10.1137/130936233. 32

Owhadi, H., Scovel, C., Sullivan, T. J., McKerns, M., and Ortiz, M. 2013. Optimal Uncertainty Quantification. *SIAM Review*, 55(2):271–345. doi: 10.1137/10080782X. 15

Papaioannou, I., Betz, W., Zwirglmaier, K., and Straub, D. 2015. MCMC algorithms for Subset Simulation. *Probabilistic Engineering Mechanics*, 41:89–103. doi: 10.1016/j.probengmech.2015.06.006. 38, 39, 54, 68, 192, 220, 221, 222

Parker, J. C., Lenhard, R. J., and Kuppusamy, T. 1987. A parametric model for constitutive properties governing multiphase flow in porous media. *Water Resources Research*, 23(4):618–624. doi: 10.1029/WR023i004p00618. 115

Parno, M. D. and Marzouk, Y. M. 2018. Transport Map Accelerated Markov Chain Monte Carlo. *SIAM/ASA Journal on Uncertainty Quantification*, 6(2):645–682. doi: 10.1137/17m1134640. 54

Parzen, E. 1962. On Estimation of a Probability Density Function and Mode. *Ann. Math. Statist.*, 33(3):1065–1076. doi: 10.1214/aoms/1177704472. 20

Paté-Cornell, M. 1996. Uncertainties in risk analysis: Six levels of treatment. *Reliability Engineering & System Safety*, 54(2):95–111. doi: 10.1016/S0951-8320(96)00067-1. 14, 15

Pearson, K. 1895. Note on regression and inheritance in the case of two parents. *Proceedings of the Royal Society of London*, 58(347-352):240–242. doi: 10.1098/rspl.1895.0041. 19

Pearson, K. 1901. LIII. On lines and planes of closest fit to systems of points in space. *The London, Edinburgh, and Dublin Philosophical Magazine and Journal of Science*, 2(11):559–572. doi: 10.1080/14786440109462720. 29

Perrin, F. 2008. *Prise en compte des données expérimentales dans les modèles probabilistes pour la prévision de la durée de vie des structures*. PhD thesis, Université Clermont-Ferrand 2. 155

Perrin, G. and Defaux, G. 2019. Efficient Evaluation of Reliability-Oriented Sensitivity Indices. *Journal of Scientific Computing*, 79(3):1433–1455. doi: 10.1007/s10915-018-00898-8. 15, 193, 194

Persson, B. 1998. Experimental studies on shrinkage of high-performance concrete. *Cement and Concrete Research*, 28(7):1023–1036. doi: 10.1016/S0008-8846(98)00068-4. 98

Peyré, G. and Cuturi, M. 2019. Computational Optimal Transport. *Foundations and Trends in Machine Learning*, 11(5-6):355–607. 44

Piasta, J. 1984. Heat deformations of cement paste phases and the microstructure of cement paste. *Materials and Structures*, 17(6):415–420. doi: 10.1007/BF02473981. 98

Picandet, V., Khelidj, A., and Bastian, G. 2001. Effect of axial compressive damage on gas permeability of ordinary and high-performance concrete. *Cement and Concrete Research*, 31(11):1525–1532. doi: 10.1016/S0008-8846(01)00546-4. 105, 115

Picandet, V., Khelidj, A., and Bellegou, H. 2009. Crack effects on gas and water permeability of concretes. *Cement and Concrete Research*, 39:537–547. doi: 10.1016/j.cemconres.2009.03.009. 105, 117

Pickett, G. 1942. The effect of change in moisture content on the creep of concrete under a sustained load. *Journal of the American Concrete Institute*, 38:333–355. 102

Pihlajavaara, S. 1974. A review of some of the main results of a research on the ageing phenomena of concrete: Effect of moisture conditions on strength, shrinkage and creep of mature concrete. *Cement and Concrete Research*, 4(5):761–771. doi: 10.1016/0008-8846(74)90048-9. 100, 101

Pijaudier-Cabot, G., Dufour, F., and Choinska, M. 2009. Permeability due to the Increase of Damage in Concrete: From Diffuse to Localized Damage Distributions. *Journal of Engineering Mechanics*, 135(9):1022–1028. doi: 10.1061/(ASCE)EM.1943-7889.0000016. 114

Poyet, S. 2009. Experimental investigation of the effect of temperature on the first desorption isotherm of concrete. *Cement and Concrete Research*, 39(11):1052–1059. doi: 10.1016/j.cemconres.2009.06.019. 97, 110

Prieur, C. and Tarantola, S. 2015. Variance-Based Sensitivity Analysis: Theory and Estimation Algorithms. In *Handbook of Uncertainty Quantification*, pages 1–23. Springer International Publishing. doi: 10.1007/978-3-319-11259-6_35-1. 32

Qiu, Z., Yang, D., and Elishakoff, I. 2008. Probabilistic interval reliability of structural systems. *International Journal of Solids and Structures*, 45(10):2850–2860. doi: 10.1016/j.ijsolstr.2008.01.005. 15

Rackwitz, R. and Flessler, B. 1978. Structural reliability under combined random load sequences. *Computers & Structures*, 9(5):489–494. doi: 10.1016/0045-7949(78)90046-9. 36

Rasmussen, C. E. and Williams, C. K. I. 2006. *Gaussian processes for machine learning*. MIT Press, Cambridge. 24, 77

Rastiello, G. 2013. *Influence de la fissuration sur le transfert de fluides dans les structures en béton. Stratégies de modélisation probabiliste et étude expérimentale*. PhD thesis, Université Paris-Est, IFSTTAR. 104, 106, 116

Rastiello, G., Tailhan, J. L., Rossi, P., and Dal Pont, S. 2015. Macroscopic probabilistic cracking approach for the numerical modeling of fluid leakage in concrete. *Annals of Solid and Structural Mechanics*, 7:1–16. doi: 10.1007/s12356-015-0038-6. 117

Reich, S. and Cotter, C. 2015. *Probabilistic Forecasting and Bayesian Data Assimilation*. Cambridge University Press. doi: 10.1017/CBO9781107706804. 5, 240

Reviron, N. 2009. *Etude du fluage des bétons en traction. Application aux enceintes de confinement des centrales nucléaires à eau sous pression*. Theses, École normale supérieure de Cachan. 111

Rizkalla, S. H., Lau, B. L., and Simmonds, S. H. 1984. Air Leakage Characteristics in Reinforced Concrete. *Journal of Structural Engineering*, 110(5):1149–1162. doi: 10.1061/(ASCE)0733-9445(1984)110:5(1149). 117

Robert, C. 2007. *The Bayesian choice : from decision-theoretic foundations to computational implementation*. Springer, New York. 41, 42, 43, 44, 48

Robert, C. P. and Casella, G. 2004. *Monte Carlo Statistical Methods*. Springer Series in Statistics. Springer, New York, 2nd edition. doi: 10.1007/978-1-4757-4145-2. 12, 23, 38, 49, 50, 62

Roberts, G. O. and Rosenthal, J. S. 1998. Optimal scaling of discrete approximations to Langevin diffusions. *Journal of the Royal Statistical Society: Series B (Statistical Methodology)*, 60(1):255–268. doi: 10.1111/1467-9868.00123. 221

Roberts, G. O. and Tweedie, R. L. 1996. Exponential Convergence of Langevin Distributions and Their Discrete Approximations. *Bernoulli*, 2(4):341. doi: 10.2307/3318418. 54

Rosenblatt, M. 1952. Remarks on a Multivariate Transformation. *The Annals of Mathematical Statistics*, 23(3):470 – 472. doi: 10.1214/aoms/1177729394. 22, 64

Rossat, D., Baroth, J., Briffaut, M., and Dufour, F. 2022a. Bayesian inversion using adaptive Polynomial Chaos Kriging within Subset Simulation. *Journal of Computational Physics*, 455:110986. doi: 10.1016/j.jcp.2022.110986. 60, 76

Rossat, D., Baroth, J., Briffaut, M., Dufour, F., Masson, B., Monteil, A., and Michel-Ponnelle, S. 2022b. Bayesian updating for nuclear containment buildings using both mechanical and hydraulic monitoring data. *Engineering Structures*, 262:114294. doi: 10.1016/j.engstruct.2022.114294. 118, 124

Rossat, D., Baroth, J., Briffaut, M., Dufour, F., Masson, B., Monteil, A., and Michel-Ponnelle, S. 2022c. Bayesian updating for predictions of delayed strains of large concrete structures: influence of prior distribution. *European Journal of Environmental and Civil Engineering*. doi: 10.1080/19648189.2022.2095441. 124, 172, 212

Rossat, D., Baroth, J., Briffaut, M., Dufour, F., Masson, B., Monteil, A., and Michel-Ponnelle, S. 2022d. Fast Bayesian inference with correction of model bias and global sensitivity analysis for Nuclear Containment Buildings. *Submitted*. 124

Rossat, D., Bouhjiti, D. E.-M., Baroth, J., Briffaut, M., Dufour, F., Monteil, A., Masson, B., and Michel-Ponnelle, S. 2021. A Bayesian strategy for forecasting the leakage rate of concrete containment buildings – Application to nuclear containment buildings. *Nuclear Engineering and Design*, 378:111184. doi: 10.1016/j.nucengdes.2021.111184. 117, 124

Rossi, P., Tailhan, J.-L., Le Maou, F., Gaillet, L., and Martin, E. 2012. Basic creep behavior of concretes investigation of the physical mechanisms by using acoustic emission. *Cement and Concrete Research*, 42(1):61–73. doi: 10.1016/j.cemconres.2011.07.011. 101

Rubio, P.-B. 2019. *Stratégies numériques innovantes pour l'assimilation de données par inférence Bayésienne*. PhD thesis, Université Paris-Saclay. 54

Ruggeri, F., Ríos Insua, D., and Martín, J. 2005. Robust Bayesian Analysis. In Dey, D. and Rao, C., Eds., *Bayesian Thinking*, volume 25 of *Handbook of Statistics*, pages 623–667. Elsevier. doi: 10.1016/S0169-7161(05)25021-6. 15, 43, 172, 212

Sabri, S. and Illston, J. M. 1982. *Isothermal Drying Shrinkage and Wetting Swelling of Hardened Cement Paste*, pages 63–72. Springer Netherlands, Dordrecht. doi: 10.1007/978-94-010-3716-7_6. 99

Sacks, J., Welch, W. J., Mitchell, T. J., and Wynn, H. P. 1989. Design and Analysis of Computer Experiments. *Statistical Science*, 4(4):409–423. doi: 10.1214/ss/1177012413. 24

Saltelli, A., Andres, T., and Homma, T. 1993. Sensitivity analysis of model output. *Computational Statistics & Data Analysis*, 15(2):211–238. doi: 10.1016/0167-9473(93)90193-w. 31

Saltelli, A. and Annoni, P. 2010. How to avoid a perfunctory sensitivity analysis. *Environmental Modelling & Software*, 25(12):1508–1517. doi: 10.1016/j.envsoft.2010.04.012. 32

Saltelli, A., Tarantola, S., Campolongo, F., and Ratto, M. 2004. *Sensitivity Analysis in Practice*. John Wiley & Sons, Ltd. doi: 10.1002/0470870958. 5, 31, 240

Samaniego, F. J. 2010. *A Comparison of the Bayesian and Frequentist Approaches to Estimation*. Springer New York. doi: 10.1007/978-1-4419-5941-6. 42

Santambrogio, F. 2015. *Optimal Transport for Applied Mathematicians*. Springer International Publishing. doi: 10.1007/978-3-319-20828-2. 21

Santner, T. J., Williams, B. J., and Notz, W. I. 2003. *The Design and Analysis of Computer Experiments*. Springer New York. doi: 10.1007/978-1-4757-3799-8. 24

Schilders, W. H. A., van der Vorst, H. A., and Rommes, J., Eds. 2008. *Model Order Reduction: Theory, Research Aspects and Applications*. Springer Berlin Heidelberg. doi: 10.1007/978-3-540-78841-6. 5, 240

Schuëller, G., Pradlwarter, H., and Koutsourelakis, P. 2004. A critical appraisal of reliability estimation procedures for high dimensions. *Probabilistic Engineering Mechanics*, 19(4):463–474. doi: 10.1016/j.probengmech.2004.05.004. 55

Schöbi, R. 2017. *Surrogate models for uncertainty quantification in the context of imprecise probability modelling*. PhD thesis, ETH Zurich. doi: 10.3929/ethz-a-010870825. 15, 69, 72, 73

Schöbi, R., Sudret, B., and Marelli, S. 2017. Rare Event Estimation Using Polynomial-Chaos Kriging. *ASCE-ASME Journal of Risk and Uncertainty in Engineering Systems, Part A: Civil Engineering*, 3(2). doi: 10.1061/ajrua6.0000870. 60, 70, 73

Schöbi, R., Sudret, B., and Wiart, J. 2015. Polynomial chaos based Kriging. *International Journal for Uncertainty Quantification*, 5(2):171–193. doi: 10.1615/int.j.uncertaintyquantification.2015012467. 24, 69, 77, 208

Schölkopf, B., Smola, A., and Müller, K.-R. 1998. Nonlinear Component Analysis as a Kernel Eigenvalue Problem. *Neural Computation*, 10(5):1299–1319. doi: 10.1162/089976698300017467. 29

Sciumè, G. and Benboudjema, F. 2017. A viscoelastic Unitary Crack-Opening strain tensor for crack width assessment in fractured concrete structures. *Mechanics of Time-Dependent Materials*, 21(2):223–243. doi: 10.1007/s11043-016-9327-7. 117

Scrivener, K. L., Juilland, P., and Monteiro, P. J. 2015. Advances in understanding hydration of Portland cement. *Cement and Concrete Research*, 78:38–56. doi: 10.1016/j.cemconres.2015.05.025, Keynote papers from 14th International Congress on the Chemistry of Cement (ICCC 2015). 96

Sellier, A. and Buffo-Lacarrière, L. 2009. Vers une modélisation simple et unifiée du fluage propre, du retrait et du fluage en dessiccation du béton. *European Journal of Environmental and Civil Engineering*, 13(10):1161–1182. doi: 10.1080/19648189.2009.9693184. 112

Sellier, A., Lacarrière, L., Multon, S., Vidal, T., and Bourbon, X. 2012. Nonlinear basic creep and drying creep modeling. In *SSCS 2012 :numerical modeling strategies for sustainable concrete structure*. 100

Sellier, A. and Millard, A. 2014. Weakest link and localisation WL2: a method to conciliate probabilistic and energetic scale effects in numerical models. *European Journal of Environmental and Civil Engineering*, 18(10):1177–1191. doi: 10.1080/19648189.2014.906368. 14

Sellier, A., Multon, S., Buffo-Lacarrière, L., Vidal, T., Bourbon, X., and Camps, G. 2016. Concrete creep modelling for structural applications: non-linearity, multi-axiality, hydration, temperature and drying effects. *Cement and Concrete Research*, 79:301–315. doi: 10.1016/j.cemconres.2015.10.001. 100

Shafer, G. 1976. *A Mathematical Theory of Evidence*. Princeton University Press. doi: 10.1515/9780691214696. 15

Silverman, B. W. 1986. *Density estimation for statistics and data analysis*. Chapman and Hall, London New York. 20

Sklar, A. 1959. Fonctions de répartition à n dimensions et leurs marges. *Publications de l'Institut de Statistique de L'Université de Paris*, 8:229–231. 20

Smith, A. F. M. and Gelfand, A. E. 1992. Bayesian Statistics without Tears: A Sampling–Resampling Perspective. *The American Statistician*, 46(2):84–88. doi: 10.1080/00031305.1992.10475856. 62

Smith, R. C. 2014. *Uncertainty Quantification: Theory, Implementation, and Applications*. Society for Industrial and Applied Mathematics. 4, 239

Snow, D. 1969. *A Parallel Plate Model of Permeable Fractured Media*. PhD thesis, University of California at Berkley. 116

Sobol', I. 1967. On the distribution of points in a cube and the approximate evaluation of integrals. *USSR Computational Mathematics and Mathematical Physics*, 7(4):86–112. doi: 10.1016/0041-5553(67)90144-9. 71

Sobol', I. 2001. Global sensitivity indices for nonlinear mathematical models and their Monte Carlo estimates. *Mathematics and Computers in Simulation*, 55(1):271–280. doi: 10.1016/S0378-4754(00)00270-6, The Second IMACS Seminar on Monte Carlo Methods. 32

Sobol', I. M. 1993. Sensitivity estimates for non linear mathematical models. *Mathematical Modelling and Computational Experiments*, 1:407–414. 32, 33

Sobol', I. M. and Gershman, A. 1995. On an alternative global sensitivity estimators. In *Proceedings of the Sensitivity Analysis on Model Output (SAMO) Conference*. 32

Soize, C. 2017. *Uncertainty Quantification*. Springer International Publishing. doi: 10.1007/978-3-319-54339-0. 4, 239

Soize, C. and Ghanem, R. 2004. Physical Systems with Random Uncertainties: Chaos Representations with Arbitrary Probability Measure. *SIAM Journal on Scientific Computing*, 26(2):395–410. doi: 10.1137/s1064827503424505. 25

Song, E., Nelson, B. L., and Staum, J. 2016. Shapley Effects for Global Sensitivity Analysis: Theory and Computation. *SIAM/ASA Journal on Uncertainty Quantification*, 4(1):1060–1083. doi: 10.1137/15M1048070. 32

Stavroulakis, G. E. 2001. *Inverse and Crack Identification Problems in Engineering Mechanics*. Springer US. doi: 10.1007/978-1-4615-0019-3. 40

Steinwart, I. and Christmann, A. 2008. *Support Vector Machines*. Springer-Verlag, New York. doi: 10.1007/978-0-387-77242-4. 24

Stenger, J. 2020. *Optimal uncertainty quantification of a risk measurement from a computer code*. PhD thesis, Université Toulouse 3. 15, 17, 212

Straub, D. and Papaioannou, I. 2015. Bayesian Updating with Structural Reliability Methods. *Journal of Engineering Mechanics*, 141(3):04014134. doi: 10.1061/(asce)em.1943-7889.0000839. 7, 55, 60, 61, 62, 79, 91, 208, 212, 242

Straub, D., Papaioannou, I., and Betz, W. 2016. Bayesian analysis of rare events. *Journal of Computational Physics*, 314:538–556. doi: 10.1016/j.jcp.2016.03.018. 78, 86, 199

Stroeven, P. 2000. A stereological approach to roughness of fracture surfaces and tortuosity of transport paths in concrete. *Cement and Concrete Composites*, 22(5):331–341. doi: 10.1016/S0958-9465(00)00018-4. 117

Stuart, A. M. 2010. Inverse problems : a Bayesian perspective. *Acta Numer.*, 19:451–559. doi: 10.1017/s0962492910000061. 41, 56

Stuart, A. M. and Teckentrup, A. L. 2017. Posterior consistency for Gaussian process approximations of Bayesian posterior distributions. *Mathematics of Computation*, 87(310):721–753. doi: 10.1090/mcom/3244. 56

Sudret, B. 2007. *Uncertainty propagation and sensitivity analysis in mechanical models - Contributions to structural reliability and stochastic spectral methods*. Université Blaise Pascal - Clermont II. Habilitation à Diriger des Recherches. 4, 25, 239

Sudret, B. 2008. Global sensitivity analysis using polynomial chaos expansions. *Reliability Engineering & System Safety*, 93(7):964 – 979. doi: 10.1016/j.ress.2007.04.002, Bayesian Networks in Dependability. 24, 32, 34

Sueur, R., Bousquet, N., Iooss, B., and Bect, J. 2016. Perturbed-Law based sensitivity indices for sensitivity analysis in structural reliability. In *Proceedings of the 8th International Conference on Sensitivity Analysis of Model Output (SAMO2016)*, Le Tampon, Réunion Island, France. 6, 15, 177, 193, 196, 205, 206, 210, 213, 241

Sueur, R., Iooss, B., and Delage, T. 2017. Sensitivity analysis using perturbed-law based indices for quantiles and application to an industrial case. In *10th International Conference on Mathematical Methods in Reliability (MMR 2017)*, Grenoble, France. 193

Sugiyama, T., Bremner, T. W., and Holm, T. A. 1996. Effect of Stress on Gas Permeability in Concrete. *ACI Materials Journal*, 93(5). doi: 10.14359/9848. 105

Sullivan, T. 2015. *Introduction to Uncertainty Quantification*. Springer International Publishing. doi: 10.1007/978-3-319-23395-6. 4, 239

Tarantola, A. 2005. *Inverse Problem Theory and Methods for Model Parameter Estimation*. Society for Industrial and Applied Mathematics. doi: 10.1137/1.9780898717921. 5, 6, 41, 240

Taylor, H. 1997. *Cement chemistry*. Thomas Telford Publishing, 2nd edition edition. doi: 10.1680/cc.25929. 95

Teckentrup, A. L. 2020. Convergence of Gaussian Process Regression with Estimated Hyper-Parameters and Applications in Bayesian Inverse Problems. *SIAM/ASA Journal on Uncertainty Quantification*, 8(4):1310–1337. doi: 10.1137/19M1284816. 56

Temam, R. 2001. *Navier-Stokes equations : theory and numerical analysis*. American Mathematical Society. 116

Thiery, M., Baroghel-Bouny, V., Bourneton, N., Villain, G., and Stéfani, C. 2007. Modélisation du séchage des bétons: analyse des différents modes de transfert hydrique. *Revue européenne de génie civil*, 11(5):541–577. 109

Tibshirani, R. 1996. Regression Shrinkage and Selection via the Lasso. *Journal of the Royal Statistical Society. Series B (Methodological)*, 58(1):267–288. doi: 10.1111/j.2517-6161.1996.tb02080.x. 157

Tierney, L. 1994. Markov Chains for Exploring Posterior Distributions. *The Annals of Statistics*, 22(4):1701 – 1728. doi: 10.1214/aos/1176325750. 50, 51

Tikhonov, A. N., Goncharsky, A. V., Stepanov, V. V., and Yagola, A. G. 1995. *Numerical Methods for the Solution of Ill-Posed Problems*. Springer Netherlands. doi: 10.1007/978-94-015-8480-7. 40

Torre, E., Marelli, S., Embrechts, P., and Sudret, B. 2019. Data-driven polynomial chaos expansion for machine learning regression. *Journal of Computational Physics*, 388:601–623. doi: 10.1016/j.jcp.2019.03.039. 25

Torrenti, J., Nguyen, V., Colina, H., Le Maou, F., Benboudjema, F., and Deleruyelle, F. 2008. Coupling between leaching and creep of concrete. *Cement and Concrete Research*, 38(6):816–821. doi: 10.1016/j.cemconres.2008.01.012. 100

Ulm, F. J. and Acker, P. 1998. Le point sur le fluage et la recouvrance des bétons. *Bulletin deliaison des Ponts et Chaussées spécial XX*, pages 73–82. 100, 101, 112

Uribe, F., Papaioannou, I., Betz, W., and Straub, D. 2020. Bayesian inference of random fields represented with the Karhunen–Loève expansion. *Computer Methods in Applied Mechanics and Engineering*, 358:112632. doi: 10.1016/j.cma.2019.112632. 55, 234

Uribe, F., Papaioannou, I., Marzouk, Y. M., and Straub, D. 2021. Cross-Entropy-Based Importance Sampling with Failure-Informed Dimension Reduction for Rare Event Simulation. *SIAM/ASA Journal on Uncertainty Quantification*, 9(2):818–847. doi: 10.1137/20M1344585. 36

Van Genuchten, M. T. 1980. A Closed-form Equation for Predicting the Hydraulic Conductivity of Unsaturated Soils. *Soil Science Society of America Journal*, 44(5):892–898. doi: 10.2136/sssaj1980.03615995004400050002x. 109, 115

Verdier, J. 2001. *Contribution à la caractérisation de l'évolution du taux de fuite des enceintes de confinement du parc nucléaire*. PhD thesis, Université Toulouse 3. 105, 115

Verdier, J., Rossat, D., Multon, S., Bouhjiti, D., Sogbossi, H., Baroth, J., Nehme, A., Dufour, F., Cagnon, H., and Briffaut, M. 2022. In-situ measurement and numerical modelling of air leakage in concrete: from the lab specimen up to structural scale. *Submitted*. 213

Villain, G., Baroghel-Bouny, V., Kounkou, C., and Hua, C. 2001. Mesure de la perméabilité aux gaz en fonction du taux de saturation des bétons. *Revue Française de Génie Civil*, 5(2-3):251–268. doi: 10.1080/12795119.2001.9692306. 115

Villani, C. 2003. *Topics in Optimal Transportation*, volume 58 of *Graduate Studies in Mathematics*. American Mathematical Society, Providence, Rhode Island. doi: 10.1090/gsm/058. 21, 54

Villani, C. 2009. *Optimal Transport*. Springer Berlin Heidelberg. doi: 10.1007/978-3-540-71050-9. 21, 22, 54

Wagner, P.-R. 2021. *Stochastic Spectral Embedding in Forward and Inverse Uncertainty Quantification*. PhD thesis, ETH Zurich. doi: 10.3929/ETHZ-B-000513631. 4, 12, 24, 30, 31, 44, 48, 239

Wagner, P.-R., Fahrni, R., Klippel, M., Frangi, A., and Sudret, B. 2020. Bayesian calibration and sensitivity analysis of heat transfer models for fire insulation panels. *Engineering Structures*, 205:110063. doi: 10.1016/j.engstruct.2019.110063. 148, 216

Wagner, P.-R., Marelli, S., and Sudret, B. 2021. Bayesian model inversion using stochastic spectral embedding. *Journal of Computational Physics*, 436:110141. doi: 10.1016/j.jcp.2021.110141. 55, 77, 87

Walley, P. 2000. Towards a unified theory of imprecise probability. *International Journal of Approximate Reasoning*, 24(2):125–148. doi: 10.1016/S0888-613X(00)00031-1. 15

Wang, Z. and Shafieezadeh, A. 2020. Highly efficient Bayesian updating using metamodels: An adaptive Kriging-based approach. *Structural Safety*, 84:101915. doi: 10.1016/j.strusafe.2019.101915. 57, 79, 92

Wasserman, L. 2000. Bayesian Model Selection and Model Averaging. *Journal of Mathematical Psychology*, 44(1):92–107. doi: 10.1006/jmps.1999.1278. 45, 211

Wiener, N. 1938. The homogeneous chaos. *Am. J. Math.*, 60:897–936. doi: 10.2307/2371268. 24

Wittmann, F. H. 1970. Einfluß des Feuchtigkeitsgehaltes auf das Kriechen des Zementsteines. *Rheologica Acta*, 9(2):282–287. doi: 10.1007/BF01973489. 101, 111

Wittmann, F. H. 1982. *Creep and Shrinkage in concrete structures*, chapter Creep and shrinkage mechanisms, pages 129–161. Wiley. 100

Xi, Y., Bažant, Z. P., Molina, L., and Jennings, H. M. 1994. Moisture diffusion in cementitious materials Moisture capacity and diffusivity. *Advanced Cement Based Materials*, 1(6):258–266. doi: 10.1016/1065-7355(94)90034-5. 96

Xiu, D. and Hesthaven, J. S. 2005. High-Order Collocation Methods for Differential Equations with Random Inputs. *SIAM Journal on Scientific Computing*, 27(3):1118–1139. doi: 10.1137/040615201. 26

Xiu, D. and Karniadakis, G. E. 2002. The Wiener–Askey Polynomial Chaos for Stochastic Differential Equations. *SIAM Journal on Scientific Computing*, 24(2):619–644. doi: 10.1137/S1064827501387826. 25

Yan, L. and Guo, L. 2015. Stochastic Collocation Algorithms Using l1-Minimization for Bayesian Solution of Inverse Problems. *SIAM Journal on Scientific Computing*, 37(3):A1410–A1435. doi: 10.1137/140965144. 56

Yan, L. and Zhang, Y.-X. 2017. Convergence analysis of surrogate-based methods for Bayesian inverse problems. *Inverse Problems*, 33(12):125001. doi: 10.1088/1361-6420/aa9417. 56

Yan, L. and Zhou, T. 2019. Adaptive multi-fidelity polynomial chaos approach to Bayesian inference in inverse problems. *Journal of Computational Physics*, 381:110–128. doi: 10.1016/j.jcp.2018.12.025. 56, 57

Yan, L. and Zhou, T. 2020. An Adaptive Surrogate Modeling Based on Deep Neural Networks for Large-Scale Bayesian Inverse Problems. *Communications in Computational Physics*, 28(5):2180–2205. doi: 10.4208/cicp.OA-2020-0186. 56, 57

Zahm, O., Constantine, P. G., Prieur, C., and Marzouk, Y. M. 2020. Gradient-Based Dimension Reduction of Multivariate Vector-Valued Functions. *SIAM Journal on Scientific Computing*, 42(1):A534–A558. doi: 10.1137/18M1221837. 92

Zahm, O., Cui, T., Law, K., Spantini, A., and Marzouk, Y. 2022. Certified dimension reduction in nonlinear Bayesian inverse problems. *Mathematics of Computation*. doi: 10.1090/mcom/3737. 92, 212

Zaki, M. and Meira, W. 2014. *Data Mining and Analysis*. Cambridge University Press. doi: 10.1017/cbo9780511810114. 73

Zhang, Z., Thiery, M., and Baroghel-Bouny, V. 2016. Investigation of moisture transport properties of cementitious materials. *Cement and Concrete Research*, 89:257–268. doi: 10.1016/j.cemconres.2016.08.013. 97

Zhdanov, M. S. 2015. *Inverse Theory and Applications in Geophysics*. Elsevier. doi: 10.1016/c2012-0-03334-0. 40

Zhu, X. and Sudret, B. 2020. Replication-based emulation of the response distribution of stochastic simulators using generalized lambda distributions. *International Journal for Uncertainty Quantification*, 10(3):249–275. doi: 10.1615/Int.J.UncertaintyQuantification.2020033029. 13

Zuev, K. M., Beck, J. L., Au, S.-K., and Katafygiotis, L. S. 2012. Bayesian post-processor and other enhancements of Subset Simulation for estimating failure probabilities in high dimensions. *Computers & Structures*, 92-93:283–296. doi: 10.1016/j.compstruc.2011.10.017. 37, 54, 67, 68, 220